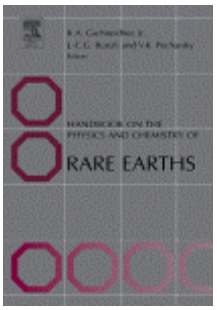

Handbook on the Physics and Chemistry of Rare Earths, **volume 12**

Elsevier, 1989

Edited by: Karl A. Gschneidner, Jr. and LeRoy Eyring
ISBN: 978-0-444-87105-3

Handbook on the Physics and Chemistry of Rare Earths, Vol. 12
edited by K.A. Gschneidner, Jr. and L. Eyring

PREFACE

Karl A. GSCHNEIDNER, Jr., and LeRoy EYRING

These elements perplex us in our rearches [sic], *baffle us in our speculations, and haunt us in our very dreams. They stretch like an unknown sea before us – mocking, mystifying, and murmuring strange revelations and possibilities.*

Sir William Crookes (February 16, 1887)

In our continuing quest to enlighten and inform the scientific and technical community on the rapidly expanding field of rare earth science, technology, and commercial utilization we have added eight more chapters to this vast body of knowledge, bringing the total number of chapters in the Handbook series to 87 in 12 volumes. In this volume two chapters are concerned with the preparation and growth of single crystals, three chapters deal with various aspects of the magnetic behaviors of lanthanide compounds, two chapters involve unusual states of rare earth matter – liquids and gaseous molecules – and one chapter is concerned with laser spectroscopy.

Ideally when one wishes to determine the intrinsic behavior of solid matter, be it electrical, magnetic, optical, mechanical, etc., one would like to make measurements on single crystals. Many times this ideal situation is not to be realized, and the few times it is attained a great deal of time and effort has been expended to obtain single crystals of the desired form, orientation and size to make meaningful measurements. Thus it is fitting that the Handbook added two chapters concerning this topic. J.S. Abell, and Z. Fisk and J.P. Remeika present their insights, acumen and perceptions, on growing metallic single crystal materials. Abell covers the more common methods used in the field – solid/solid growth (e.g. strain anneal), liquid/solid growth (e.g. float zoning, Bridgman) and vapor/solid growth. The chapter by Fisk and Remeika deals with growing intermetallic compounds from molten metal fluxes. The information in these two chapters should prove especially useful to neophytes and to those of us who only prepare crystals on an occasional basis.

The first of the three chapters on magnetism deals with one of the most important and fastest growing rare earth market – the Nd–Fe–B based permanent magnet materials. In this chapter E. Burzo and H.R. Kirchmayr cover the basic non-magnetic properties – phase relationships, crystal structures, etc. – in addition to the magnetic properties of the $R_2Fe_{14}B$ materials. Also included are the

two important ways of preparing the $Nd_2Fe_{14}B$-based permanent magnets, and their stabilities. The next chapter is by A. Szytula and J. Leciejewicz who discuss the crystallography, and the physical and magnetic properties of the rare earth ternary phases which form the $ThCr_2Si_2$-type structure, which W.B. Pearson has called the 'most populus of all known structures". This family of rare earth compounds are formed with a variety of d transition metals (Cr, Mn, Fe, Co, Ni, Cu, Ru, Rh, Pd, Ag, Os, Ir, Pt and Au occupying the Cr metal sites) and Si or Ge. The third chapter on magnetism, by H. Maletta and W. Zinn, deals with spin glass systems. Their review is primarily concerned with $Eu_xSr_{1-x}S$ based systems, but also covers the amorphous Gd_xAl_{1-x}, and Sc-rich and Y-rich intra rare earth alloys containing the heavy lanthanides. In addition a number of non-rare earth containing systems are discussed to give the reader a much better perspective of the physics and nature of spin glasses.

The vast body of knowledge of rare earth materials is concerned with the solid state, but in this volume we have included two reviews on other states of matter – the liquid rare earth metals and their alloys, and the gaseous rare earth elements and some of their gaseous compounds. In the former chapter, J. Van Zytveld discusses the physical, magnetic, electronic transport and thermodynamic properties and electronic structures of the liquid metals. When information is available about the liquid alloys, it is included in the various sections following the presentation of the molten element information. The other chapter on unusual states of matter is by M.S. Chandrasekharaiah and K.A. Gingerich, who discuss the thermodynamic properties of the gaseous rare earth metals and their gaseous compounds. The latter included compounds with other metallic elements, carbon, oxygen and the chalcogenides.

The last chapter in this volume is by W.M. Yen and deals with the impact of laser sources on the study of spectroscopic properties of the rare earths and the understanding that has resulted therefrom. The lanthanides, naturally, were initially used as laser sources and later as prototypical optical systems to demonstrate the laser spectroscopy technique, which has led to a much better understanding of the electronic nature and optical behavior of solids, and to a variety of devices and uses.

May 31, 1988

CONTENTS

CONTENTS OF VOLUMES 1–11

VOLUME 1: METALS

VOLUME 2: ALLOYS AND INTERMETALLICS

VOLUME 3: NON-METALLIC COMPOUNDS – I

VOLUME 4: NON-METALLIC COMPOUNDS – II

VOLUME 5

VOLUME 6

VOLUME 7

VOLUME 8

VOLUME 9

VOLUME 10: HIGH ENERGY SPECTROSCOPY

VOLUME 11: TWO-HUNDRED-YEAR IMPACT OF RARE EARTHS ON SCIENCE

Handbook on the Physics and Chemistry of Rare Earths, Vol. 12
edited by K.A. Gschneidner, Jr. and L. Eyring

Chapter 80

PREPARATION AND CRYSTAL GROWTH OF RARE EARTH ELEMENTS AND INTERMETALLIC COMPOUNDS

J.S. ABELL
Department of Metallurgy and Materials, University of Birmingham, UK

Contents

1. Introduction

Physical property measurements of rare earth elements and intermetallic compounds can be particularly sensitive to metallurgical factors such as impurity concentrations, phase distribution and crystallinity. For this reason, it is extremely important to perform measurements on well-characterised materials, and if possible on single crystals, produced under controlled conditions from the purest possible constituents. With this aim in view, this chapter is concerned with the preparation and crystal growth of the rare earth elements and their intermetallic compounds by solid state, melt and vapour condensation growth techniques.

Solid state recrystallisation methods are particularly applicable to the elements and intra-rare earth alloys while melt growth techniques have found application for certain of the elements, but most particularly for intermetallic compounds; use of the vapour–solid approach has been limited to the higher vapour pressure

elements. The discussion will centre on those methods most appropriate to rare earth-based materials which will include the elements, R–M binaries and R–M–M ternary intermetallics, including some of those ternaries where the third component is non-metallic but where the growth technique under discussion has been successfully applied to such a compound. The recent increase in research conducted on certain of these rare earth-based ternaries which exhibit interesting magnetic, superconducting, valence fluctuation and heavy fermion behaviour serves to justify their inclusion.

After a brief description of refining and purification of the elements which is often a necessary precursor to the production of good quality crystals, the discussion is organised into the three main sections of solid–solid, liquid–solid and vapour–solid crystal growth techniques. The melt growth section deals with those methods applicable to stoichiometric melts and specifically excludes flux growth and metal solution growth to be dealt with in Ch. 81 by Fisk and Remeika in this volume. The physical property measurements for which the majority of single crystals are grown benefit from well-characterised, specific geometry specimens and so the chapter ends with a brief description of the techniques most widely used for fabrication and assessment of specimens.

The preparation and basic properties of the rare earth elements have been described in detail by Beaudry and Gschneidner (1978) and other reviews have been written which have dealt with crystal growth both of the elements and of their compounds (Hukin and Jones 1976, Milstein 1976, Jones et al. 1978a, 1982, Vogt 1985). For more detailed discussion of crystal growth processes reference should be made to standard texts (e.g. Gilman 1963, Bunshah 1968, Laudise 1979, Jones 1974). The present work aims to give a comprehensive description of preparation and crystal growth techniques appropriate to both the elements and intermetallic compounds and to update references to the literature where the successful application of these techniques have resulted in single crystals suitable for a wide variety of physical property measurements. In many cases, full details of crystal growth are not given in the literature and so the lists of crystals presented here include references where only the technique is named with no further details; where no details at all are given, but single crystals have been used in the experiments, these references have been assembled in the Appendix.

2. Refinement of rare earth metals

Since a definite link exists between the purification or refinement of the rare earth metals and the successful growth of single crystals of both the elements and their compounds, it is appropriate to consider first these refinement techniques and to assess their role in enhancing the potential for good quality crystal growth by providing high purity starting materials. As some of the refinement techniques employ the same experimental hardware as used during subsequent crystal growth, it seems particularly relevant to introduce this aspect of materials preparation at this stage. These methods have been reviewed in some detail

elsewhere (Beaudry and Gschneidner 1978) and so the discussion will be brief, but it was nevertheless felt that, for completeness, reference to this important aspect of preliminary preparation should not be excluded.

Levels of contamination in commercially available rare earth metals vary widely. Various reasons exist for this including the different reactivities of individual elements, different production methods, unavoidable fluctuations in processing conditions and of course the manufacturer's grading (e.g. standard or high purity). The major contaminants are usually O, H, N and C, probably resulting from processing in industrial vacua, and are in some cases present at levels above the solid solubility limit (e.g. as discrete oxide particles). Other rare earths are often present together with contaminants from the ion exchange processing, crucibles and various reactants (e.g. Ca, Fe, Al, Si, Ta, W).

Appropriate refining routes, and also crystal growth methods, are determined predominantly by three physical properties of the rare earth elements: vapour pressure, melting point and reactivity. The most significant of these is the vapour pressure which determines whether the metal can be sublimed or distilled, and the extent to which impurities can be removed by volatilisation. In table 1 are listed various properties of the rare earth metals with the elements themselves being tabulated not in order of increasing atomic number, but increasing vapour pressure at the melting point. It can be seen that there is a wide range of vapour pressures – Ce and Tm differ by fourteen orders of magnitude. Also important in

TABLE 1
Vapour pressures, melting points and refinement techniques for rare earth elements.

Element	Vapour pressure (melting point) (torr)	Melting point (°C)	Refining technique[a]
Ce	8×10^{-13}	798	VR, ZR, SSE vac, SSE inert gas, DIS
La	3×10^{-10}	918	VR, ZR, SSE vac, SSE inert gas, DIS
Pr	2×10^{-9}	931	ZR, SSE vac, SSE inert gas, DIS
Nd	3×10^{-5}	1021	ZR, SSE vac, SSE inert gas, DIS
Gd	2×10^{-4}	1313	ZR, SSE vac, SSE inert gas, DIS
Tb	8×10^{-4}	1356	ZR, SSE vac, SSE inert gas, DIS
Y	2×10^{-3}	1522	ZR, SSE vac, SSE inert gas, DIS
Lu	8×10^{-3}	1663	ZR, SSE vac, SSE inert gas, DIS
Sc	8×10^{-2}	1541	ZR, SSE vac, SSE inert gas, DIS
Er	2×10^{-1}	1529	SSE inert gas, SUB
Ho	6×10^{-1}	1474	SSE inert gas, SUB
Dy	7×10^{-1}	1412	SSE inert gas, SUB
Eu	9×10^{-1}	822	SUB
Sm	7	1074	SUB
Yb	18	819	SUB
Tm	185	1545	SUB

[a] Abbreviations:
VR – Vacuum Remelting
ZR – Zone Refining
SSE – Solid State Electrotransport
SUB – Sublimation
DIS – Distillation

determining the appropriate processing route is the melting point of each element, which affects how easily the metal can be heated to, and contained at, the processing temperature. The reactivity of the rare earths also differs from element to element. For example, while La and Ce will completely decompose in air in a matter of days, the heavy metals are apparently inert in bulk form at room temperature; however, all the rare earths will degrade if heated for any length of time in anything but UHV or an inert gas of equivalent purity.

The physical properties of individual rare earths are so different that there is no single method of refining or crystal growth applicable to all the elements. Four of the commonly used routes for refining commercially available metals will be briefly discussed. To achieve a useful degree of refinement, two or sometimes three stages are normally necessary; it is unusual for a single technique to prove sufficient to refine a metal with respect to all contaminants. The term refinement is preferred to purification as a general classification since some of the techniques only re-distribute impurites and do not remove them completely.

2.1. *Vacuum re-melting*

Most rare earth elements benefit from re-melting in UHV which removes high vapour pressure contaminants. Many can be induction-heated to the melting point and above in a water-cooled 'cold boat' container as described by Hukin (1971), McMasters et al. (1987) and Fort et al. (1981), although the time held molten will be short for the higher vapour pressure metals. La and Ce can, however, be heated to several hundred degrees above their melting points for long periods. Beaudry and Gschneidner (1978) report that above ~1800°C significant purification with respect to most impurities including O, C and N is achieved. Ta or W containers are usually used for this super-heating and a secondary processing by zone-refining may be necessary to remove dissolved Ta or W.

Vacuum re-melting is the usual initial preparation stage for the low vapour pressure rare earth metals prior to either secondary refinement, crystal growth or alloy and compound formation.

2.2. *Sublimation/distillation*

Several rare earths have vapour pressures which allow purification by sublimation or distillation in UHV. The basic requirements are that the vapour pressure is high enough to give practicable transport rates, and that the process can be carried out well below the temperature at which the oxide co-sublimes or co-distills (generally ~1600°C). Also the condensate must be collected and handled in such a manner as to avoid recontamination. Beaudry and Gschneidner (1978) and Jones et al. (1982), describe the successful purification of Sc, Sm, Eu, Gd, Dy, Ho, Er, Tm and Yb by these techniques. The latter report a resistance ratio of ~60 for Dy starting with commercial quality material and similar results have now been obtained for Er. Double-stage processing can usually improve purity even further.

2.3. *Zone refining*

This technique involves the repeated passage in one direction of a molten zone along a rod of metal. Dissolved impurities which lower the melting point of the metal move with the zone to the end of the rod while those impurities which raise the melting point are transported in the opposite direction. The classic treatment of this subject is given by Pfann (1966). Unlike the previous two techniques, this process does not remove impurities, merely re-distributes them. Work at Ames and Birmingham (e.g. Fort et al. 1980, 1981, Jones et al. 1978b) has shown that zone refining in the rare earths is generally effective at moving metallic impurities (mostly with the zone) but less effective at moving non-metallic impurities (mostly against the zone); 20–30 passes at rates between 20 and 120 mm h^{-1} constitutes a typical processing. Reductions of metallic impurity levels by factors of several hundred have been achieved, although interstitial levels are rarely reduced by a factor of more than two or three. Zone refining can also redistribute some impurity precipitates (e.g. oxides). It is thought that lowering the interstitial level in the matrix adjacent to the precipitate to below the solubility limit can render the particle unstable. Dissociation takes place and the dissolved impurity is transported in the normal manner.

For the rare earths, zone refining can be regarded as a means of purification with respect to certain specific impurities (e.g. to reduce Ta and W levels in crucible-contaminated metal). The method is limited to those elements with a tractable vapour pressure. La, Ce, Pr, Nd, Gd, Tb and Y can be zoned in UHV or Argon, but for Dy, Ho and Er even the use of an atmosphere of inert gas does not sufficiently suppress volatilisation to allow more than a few controlled zone passes.

As well as creating a non-uniform impurity profile along the length of a rod, the technique has a tendency to promote crystal growth as will be discussed in section 4.3. It is not a technique that lends itself to alloys because of the problems of segregation of constituents.

2.4. *Solid state electrotransport (SSE)*

Preparation of the highest purity rare earth metals usually includes SSE as part of the refining treatment. A DC electric field is applied along a rod of metal and the resulting electron flow sweeps many impurities, but in particular O, H, N and C, to the anode end of the rod. The heating effect of the current serves to enhance impurity transport rates. The processing is carried out in a UHV chamber to prevent environmental recontamination. The re-distribution of impurities yields a section of the rod with substantially reduced impurity levels. Jordan (1974), Beaudry and Gschneidner (1978) and more recently Fort (1987) have reviewed the technique and its application to the rare earths.

The long processing times involved (e.g. 500–1000 h at 0.8–0.9 T_m) means that vapour pressure constraints limit the use of SSE in vacuum to Y, Ce, La, Pr, Nd, Gd and Tb, but Fort (1987) describes recent experiments using an inert gas

environment. This reduces volatilisation, but also has two other advantages: the gas reduces temperature gradients along the rod (and helps to prevent failure at hot spots) and allows higher currents to be used because of the cooling effect of the gas surround. However, disadvantages can arise from operating under inert gas conditions: the gas can provide an extra source of contamination and the system cannot be continuously pumped. It is extremely important to vacuum out-gas the chamber walls, electrodes and sample itself prior to introducing the inert gas.

SSE requires reasonably pure start material since only impurities in solution are transported directly. Precipitates can be effectively transported by dissolution as described for zone-refining but the process is very slow. The accumulation of impurities at the anode end of the rod can lead to failure by melting at 'hot spots' where high impurity levels have increased the electrical resistance or lowered the melting point. Some initial refinement of the melt is often to be recommended before subjecting it to SSE. This usually involves zone refining to remove metallic impurities although some work by Volkov et al. (1981) has shown that metallic impurities in Y can be redistributed by SSE. Grain growth often occurs during processing and a discussion of this crystal growth route will be presented in section 4.2. The yield of significantly improved material is generally low (20–25%) and together with the length of processing time renders this method an unsuitable source of start material for alloy or compound formation, except for small samples.

3. Synthesis of intermetallic compounds

Much of current research, both academic and technological, on rare earth-based materials is centered on intermetallic compounds. Areas of interest are much too numerous to mention here but several excellent reviews have been written (for example Wallace 1971, Buschow 1977, 1979, Gschneidner and Eyring 1979).

The interest in a wide range of rare earth-based intermetallic compounds, each with individual physical and metallurgical properties, presents the crystal grower with problems over and above those already encountered in discussion of the elements themselves. The use of UHV-rated environments and crucible-less techniques to minimise contamination is of paramount importance in the preparation of high purity rare earth elements. Adoption of the same stringent criteria is not always possible in the production of rare earth intermetallic compounds. The preparation technique employed has to take into account not only the physical properties of the rare earth metal, but also those of the other constituent(s) which can present equally difficult problems, e.g. the vapour pressure of molten zinc or the reactivity of molten Fe with W, a commonly used crucible material. These other constituent(s) also provide an additional potential source of contamination which can influence the quality of the compound prepared. Frequently, the main

difficulty encountered in the preparation and crystal growth of rare earth intermetallics is that arising from the complexities of the phase diagrams.

In a previous paper (Jones et al. 1982) the present author identified several constitutional criteria which can be adopted to simplify the choice of crystal growth process. While the choice of compound to be prepared is largely determined by a particular interest in its magnetic or related physical properties, these metallurgical guidelines bear repetition. Most melt growth processes are best applied to congruent line compounds in order to simplify the solidification process, to produce homogeneous stoichiometric material and to yield good quality single crystals. The compound should be a stable phase, i.e. possess a high melting point with respect to adjacent phases, and exhibiting no solid state reactions. The compound should be well-separated from adjacent phases in the phase diagram to minimise complications from the presence of additional phases. Simple structures having isotropic thermal expansion aid the cooling stage of brittle intermetallic compounds (and incidentally, often facilitates the interpretation of subsequent physical property measurements).

The refining routes described in section 2 do not all produce sufficient quantities of metal for subsequent compound formation; this applies particularly to SSE yields as has already been indicated. Vacuum remelting is readily achieved and should be applied to starting material where feasible. The relatively large yields of the sublimation and zone refining techniques mean that significantly improved rare earth metals are becoming available in quantities suitable for compound preparation on an academic research scale. If access to such material is not possible then the highest grade commercially available material should be used. In practice in many cases, initial crystal growth experiments are conducted using commercial purity material, and only if problems with either crystal growth or interpretation of subsequent physical property measurements can be identified as impurity related, is further refinement of start material contemplated.

Two main techniques form the basis of the majority of preparation methods employed for the synthesis of rare earth intermetallics – arc or induction melting. Induction melting in high vacuum in various designs of water-cooled cold cucible is the preferred route for the synthesis of non-volatile compounds from elements with low vapour pressure ($<10^{-3}$ torr at the melting temperature). A horizontal segmented cold boat for elongated samples and a Hukin-type crucible for regular-shaped ingots are the most common geometries employed (see fig. 1). The addition of high purity argon or helium can extend the range of tractable vapour pressure materials to ~100 torr, and for short periods even Tm (185 torr) can be held molten without too much loss by volatilisation. Prior to reaction the constituents should be high vacuum outgassed to as high a temperature as possible without loss. The alternative method of argon arc melting is particularly useful for high vapour pressure constituents and also for high melting point compounds beyond the capability of induction heating.

Synthesis in hot crucibles is also widely practiced. Induction melting in sealed crucibles, typically Ta or W, offers the only means of dealing with extremely high

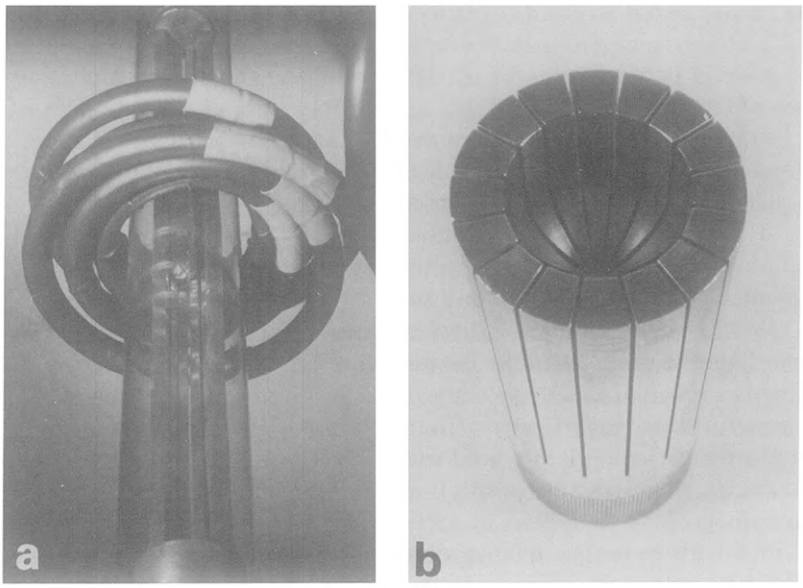

Fig. 1. Segmented cold crucibles for synthesis and crystal growth: (a) cold boat, (b) Hukin crucible.

vapour pressure constituents, e.g. Zn. Sealing of such crucibles is usually achieved by argon arc or electron beam welding. The risk of contamination from the crucible then exists but cannot really be avoided if the compound is to be formed at all. Reaction of constituents in other crucible materials have also been reported, including Al_2O_3, MgO and BN, of which the latter seems the most useful. Under these circumstances, compound formation and subsequent crystal growth are usually carried out in one operation to minimise the risk of contamination.

4. Crystal growth

4.1. *Introduction*

If the maximum information concerning a physical property of a rare earth element or intermetallic compound is to be obtained from experimental measurements, then the specimen on which the measurement is to be undertaken should be monocrystalline. Useful information can of course be extracted from powdered or polycrystalline samples, but definitive understanding of a property inevitably requires measurements on single crystals. This is particularly true for properties which show anisotropic behaviour and this applies to all measurements involving application of a magnetic field – the magnetic anisotropy of rare earth elements

and compounds is well documented (e.g. Wallace 1971, Buschow 1977, 1979, Kirchmayr and Poldy 1979).

As recently pointed out by Spirlet and Vogt (1984) in their review of actinide materials preparation, good experiments require good samples, and the best samples in this sense are usually single crystals. The processes involved in producing a single crystal, whether of the solid–solid, liquid–solid or vapour–solid type, invariably result in a purer, more homogeneous single phase specimen. The solid state re-distribution of impurities, impurity segregation at a solid–liquid interface, and separation associated with vapour transport all contrive to yield a better quality crystal as a result of the process. As we have seen in section 2, some purification methods can produce single crystals or large-grained material directly. In the case of compounds, single crystals will often only grow at the stoichiometric composition, thereby intrinsically controlling stoichiometry. Additional phases which may be present in polycrystalline material are thus precluded.

The crystal size and quality required will depend on the particular physical property to be measured, anything from a cubic millimetre to several cc. The smallest crystals can sometimes be cut from a polycrystalline matrix such as an as-cast ingot, but larger crystals require specific crystal growth methods. Requirements can differ widely. The largest crystals are in general needed for neutron inelastic scattering requirements, the highest crystallinity for magnetic domain studies and topography, and the best overall quality, both structural and chemical for Fermi surface studies such as dHvA experiments. The choice of crystal growth method therefore depends on the physical and chemical properties of the element or compound but also on the specific measurement to be performed and its sensitivity to specimen quality. Ideally, all experiments should be conducted on the best quality material, but the time and effort spent on producing a top quality specimen by, for instance, SSE processing (which could take several months) may not be warranted when a crystal of slightly inferior pedigree but produced more quickly and readily will suffice adequately.

4.2. *Solid–solid growth*

4.2.1. *Introduction*

Crystal growth in the solid state involves the re-arrangement of grains in a polycrystalline matrix to produce grains of considerable size if not a complete single crystal. Thus, while not strictly a single crystal growth method, solid state techniques do yield large grain material from which sizeable single crystals can be fabricated suitable for many physical property measurements.

Solid state growth is sometimes the final stage of a more complicated preparation route involving material in the liquid state to be discussed later; in these cases the final growth process involves a solid–solid interface. For instance, the existence of a structural modification below the melting point, which is the case for many rare earth elements means that the final stage of melt crystal growth is a solid–solid reaction even though this has been preceded by the passage of a liquid–solid interface through the material.

The general metallurgical term for these growth processes is recrystallisation, but various descriptions have been used in the literature including strain-anneal, grain growth, deformation growth, grain coarsening, transformation growth, secondary recrystallisation, etc. Often these terms are used interchangeably and it is not always possible to identify the specific mechanism involved. It is proposed here to deal with them separately in an attempt to distinguish between the processes associated with these various solid state techniques.

The generally accepted metallurgical view of the physical changes which a material undergoes as a result of heat treatment involve the terms recovery, recrystallisation and grain growth which describe the sequential effects occurring during the annealing process. Recovery involves the relief of strain by movement of defects prior to primary recrystallisation and the formation of new strain-free grains at the expense of the old deformed grains. It is this process which involves the concept of a critical amount of strain necessary to achieve primary recrystallisation. Primary grain growth then occurs by the migration of grain boundaries and leads to an increase in the average grain size in the material. Secondary recrystallisation (or exaggerated grain growth) can subsequently occur when certain grains grow and consume all other grains.

The precise mechanisms involved in individual cases of successful application of solid–solid techniques to crystal growth in rare earth-based materials are extremely difficult if not impossible to distinguish. The recipe for each element and compound is likely to be different and its determination is often a matter of trial and error, but the common factor in all solid–solid growth methods (Aust 1968) is that the annealing process is concerned with decreasing the strain energy which exists in the material either by design or as a result of previous treatment. The free energy of a polycrystalline system can be further reduced by a decrease in grain boundary area, and it is therefore energetically favourable for grains to grow and consume others resulting in a large-grained ingot. Recrystallisation techniques have been found to be applicable to certain elements and compounds to produce crystals which would be difficult to realise by other methods.

The distinct advantage of solid–solid growth techniques is that they avoid handling and containment in the molten state. This is particularly pertinent for the rare earths, which react in the molten phase with all other elements except the inert gases; it is thus extremely difficult to retain sample purity when molten for long periods of time. The methods are also applicable to constituents possessing high vapour pressure at their melting points where significant volatilisation would occur; in such cases a technique of crystal growth at temperatures well below the melting point can be most useful.

There exist other advantages of solid–solid growth techniques which are worth mentioning. Recrystallisation processes involve the movement of grain boundaries and not the redistribution of solute atoms; thus it is particularly applicable to alloys. A predetermined shape can be largely retained during growth which avoids subsequent fabrication with associated introduction of strain. Where the existence of a phase change close to the melting point causes problems, these methods can be employed to produce crystals below the phase transition. The solid state

approach avoids gross imperfections, such as lineage, which may result from solidification techniques. Although not as conveniently realised as for melt growth, the final orientation of a crystal can, in principle, be controlled by choice of a particular grain to promote throughout the ingot.

The limitations of solid state growth should also be pointed out. In a polycrystalline matrix, the density of nucleation sites can be high and it is therefore difficult to control the nucleation process to produce large single crystals. In the application of the strain-anneal route, particularly to high purity materials, difficulty is sometimes found in obtaining a fine grain matrix structure prior to critical strain and growth anneal, since grain growth occurs more readily in purer material. An accompanying problem in pure materials, particularly those with easily faulted structures, is the tendency to relieve strain by polygonisation or substructure formation rather than to recrystallise completely. A further problem can be encountered with hcp metals due to twin formation on introducing the critical strain. These can provide numerous nucleation sites during the subsequent heat treatment making large crystals difficult to achieve.

Solid state growth is characterised by the concept of a critical strain or maximum deformation which is a necessary pre-requisite for primary recrystallisation. The source of this critical strain allows solid–solid methods to be categorised as intrinsic or extrinsic. The critical strain can be introduced deliberately (extrinsic) either before the annealing process by room temperature deformation or during it by strain at elevated temperatures or by incorporating a phase transformation into the process or by quenching; alternatively, the strain can result from the method of preparation prior to the annealing process (intrinsic) and is likely to be thermal in origin. Discussion of the solid–solid crystal growth methods will be sub-divided according to the nature and application of this critical strain necessary for recrystallisation. Thus, the crystal growth methods will be considered under four sections: grain growth, where the strain is inherent and results from previous thermal history, strain-anneal involving a deliberate applied strain, and the phase transformation method, where the strain energy is associated with a structural modification at elevated temperature. The fourth section is a discussion of the application of solid state electrotransport, which involves the same mechanism as other solid–solid growth methods, but with the additional process of electromigration of defects under the influence of the applied electric field.

4.2.2. *Grain growth*

This section concerns the relief of strain and reduction of interfacial energy existing in a polycrystalline matrix by a simple anneal. The overall description grain growth includes terms such as grain coarsening, secondary recrystallisation and exaggerated grain growth frequently used in the literature. These mechanisms are also involved in other solid–solid techniques, but the present distinction relates to the lack of additional applied strain. The approach involves annealing a polycrystalline as-cast ingot at a temperature near the melting point but below any high temperature allotropic transformation. The casting can be produced in a

number of ways; in a hot crucible such as W or Ta (particularly when sealed for volatile compounds) or more commonly a cold crucible in the form of an arc furnace hearth or induction heated cold boat. For the hot crucible and induction cold crucible approach, the subsequent anneal is usually performed in situ, but arc-cast ingots are normally transferred to another system for heat treatment.

A genuine single crystal sample is unlikely to be produced but large enough grains from which experimental specimens can be fabricated, are often the result. The success of the technique is presumably based on the existence of large enough thermal strains in the as-cast material to provide the driving force for recrystallisation and grain growth at elevated temperatures. A typical example of large recrystallised grains in a Gd ingot is shown in fig. 2.

The original work of Nigh (1963) demonstrated the potential of the technique for Y and the heavy lanthanides Gd, Tb, Dy, Ho, Er and Tm, with the result on Gd being achieved with the use of a temperature gradient, a variation more commonly used in the strain-anneal method. Arc-melted as-cast ingots were used, with Gd and Tb being treated in vacuum, the others in an argon atmosphere to suppress volatilisation. A similar route was used by Savitskii et al. (1965). An alternative approach dates back to Whittaker (1968). Rods or ingots of rare earth material were prepared by cold crucible casting by induction heating and then annealed in situ. Relatively short anneals (8h) were found to produce significant grain growth. Inherent in this approach is the maintenance of a temperature gradient in the sample due to the presence of the water-cooled crucible which probably contributes to its success.

The dependence on purity of the success of this method in producing large grains was first reported by Savitskii et al. (1965) and Whittaker (1968) and confirmed by McEwen and Touborg (1973). Impurities can act as nucleation sites for new grains, and inhibit subsequent grain growth. Material refined by one of the methods in section 2 gives consistently better results in terms of grain size and crystal quality than commercially available material, but in the absence of additional refinement, use of the best quality commercial metal is always to be recommended.

McEwen and Touborg (1973) grew crystals of Y, Sm, Gd, Tb, Ho, Er and Tm

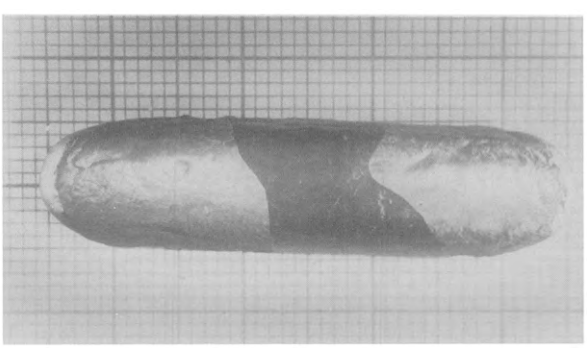

Fig. 2. Grain growth in a Gd ingot (1 div. = 1 mm). Courtesy of R.G. Jordan.

as well as many intra-rare earth alloys, sometimes in sealed Ta crucibles to prevent volatilisation losses. Beaudry and Gschneidner (1978) listed the largest single crystals of the rare earth elements produced at that time, many by the grain growth and strain anneal techniques. Their grain growth experiment on Gd involving the anneal at 1225°C for 24 h of an arc-melted button yielded a 7.5 cc crystal. Their most successful crystal growth experiments were conducted on high purity metals, that is metals refined on a laboratory scale at Ames, and they reported the recrystallisation temperatures of rare earth metals of laboratory purity and compared them with those measured on commercially available material. Differences of up to 200°C were observed.

Reed (1971) has grown large crystals of the low neutron capture cross-section isotopes of Sm, Dy and Er, by grain growth. The Sm^{154} crystal was grown by annealing an arc melted button at 917°C for 96 h. The metal would presumably be in the hexagonal phase at this temperature, being above the rhombohedral–hexagonal transition (731°C) and below the hexagonal–bcc transformation (922°C). Reed did not specify what structure the crystal possessed. Beaudry and Gschneidner (1978) speculated that the crystal was either in a metastable hexagonal form or had transformed to the normal rhombohedral structure. Recent work by Shi and Fort (1985) has shown that either modification can occur at room temperature depending on the precise thermal history, but that the hexagonal form is in fact the dhcp variant, only previously observed in thin films or under pressure. In fact grains exhibiting the two different structures can coexist in the same ingot (Shi and Fort 1986). The rhombohedral phase was always heavily twinned, and the grain size was always larger in ingots prepared from re-sublimed metal. The ingots were induction melted in a cold crucible under argon and subsequently annealed in Ta capsules. Sc and Y crystals produced by grain growth at Ames have recently been the subject of neutron scattering experiments to study the location of D in the hcp lattice (Khotamian et al. 1981, Saw et al. 1983).

The grain growth method is now widely used and has been particularly successful in preparing alloy single crystal specimens. The desired composition is produced by arc or induction melting and can then be heat treated as described. A list of references to crystals prepared in this way is contained in table 2. McMasters et al. (1978) have reported the preparation of single crystals of various elements and alloys by this method, including Sc, Y, Gd, Tb, Dy, Ho, Er, Lu and Y–Ce and Pr–Nd alloys. Reports on measurements on many intra-rare earth alloys prepared at Ames by recrystallisation appear in the literature and this approach has recently been extended to ternary systems of the type Gd–Y–Lu (Ito 1984). Achiwa and Kawano (1973) report crystals of Tb–Pr, Tb–La and Tb–Nd grown by this technique. A number of intra-rare earth alloy single crystals have been prepared at Birmingham and reported by various workers in the course of physical property measurements. Thus a series of Gd–Y single crystals were grown by grain growth ~100° below the transformation temperature in induction-cast ingots (Palmer et al. 1986). A similar series of Gd–Tb crystals were employed in work by Corner et al. (1985) but using SSE-refined start material.

TABLE 2
Selection of crystals prepared by grain growth.

Crystal	References
Single elements	Nigh (1963), Whittaker (1968), McEwen and Touborg (1973), McMasters et al. (1978), Beaudry and Gschneidner (1978)
Y–Ce	McMasters et al. (1978)
Y–Tb	Rainford et al. (1985), Yeshurun et al. (1985)
Y–Pr, Y–Nd	Daud et al. (1985)
Y–Er	Keller and Dixon (1976), Present work
Y–Ho	Present work
Pr–Nd	McMasters et al. (1978)
Pr–Ce, Pr–Tb, Pr–Er	Fort (1986)
Gd–Y	Palmer et al. (1986)
Gd–Tb	Corner et al. (1985)
Gd–Ho	Present work
Gd–Y–Lu	Ito (1984)
Tb–Sc	Corner and Welford (1978)
Tb–La, Tb–Pr, Tb–Nd	Achiwa and Kawano (1973)
Tb–Ho	Palmer and Greenough (1976)
Tb–Tm	Hansen and Lebech (1976)
Ho–La, Ho–Ce, Ho–Pr	Kawano and Achiwa (1983)
Er–Y, Er–Mg	Kjems et al. (1979)
RGa	Shohata (1977)
$LaSn_3$	Boulet et al. (1982)
R_2Co_7	Blaettner et al. (1978)
RCo_5	Klein et al. (1975)
$ErCo_{4.5}Cu$	Drzazga (1983)
Y_2Co_{17}	Perkins and Nagel (1975)
$GdMn_{0.8}Ni_{1.2}$	Slebarski and Byszewski (1982)

The same method has been successful with Gd–Ho and Y–Ho alloys. Y–Tb crystals from annealed arc-cast ingots (1400°C for 6 h) were reported by Rainford et al. (1985). Similar low-doped Y–Er crystals have been prepared in the same way. Crystals of Y–Tb (Yeshurun et al. 1985) and Y–Nd, Y–Pr (Daud et al. 1985) have also recently been prepared by this approach. Very few references to simple grain growth experiments being successful in rare earth intermetallics have been found. Blaettner et al. (1978) report crystals of R_2Co_7 (R = Ce, Pr, Nd) grown in this way, and Shohata (1977) has prepared $2 \times 2 \times 2\,mm^3$ cubes of several RGa (R = Pr, Nd, Sm, Tb, Dy, Ho, Er) compounds by annealing below the peritectic isotherm (1100–1350°C).

4.2.3. *Strain anneal*

Discussion in this section will be limited to those experiments where additional strain is deliberately introduced into the sample. Many of the references to crystal growth by this technique probably belong more properly to the previous section, since the intrinsic thermally produced strain quenched into the sample provides the only driving force for recrystallisation and grain growth.

Some workers make the distinction between the terms strain-anneal and deformation growth, with the former involving a strain being applied at elevated temperature during the anneal, and the latter with the strain applied prior to the anneal. As far as rare earth materials are concerned, the mechanical strain is invariably applied at room temperature, and the term strain-anneal is widely accepted to refer to this practice and therefore will be adopted in the present work. More important is the concept of a critical strain to be applied to induce recrystallisation. One of the potential advantages of this approach is that crystal orientation can be controlled in principle by using a temperature gradient to promote growth of a particular orientation grain. However, no specific demonstration of this to rare earth element and alloys has been reported. Strain anneal techniques have found limited applicability to intermetallic compounds because of their intrinsic restricted room temperature ductility. The possibility of applying the strain at elevated temperature to overcome this low ductility does not appear to have received much attention.

This method, involving the critical strain criterion, has been widely studied on non-rare earth metals as a result of which it was established that if the applied strain was less than this critical amount then no recrystallisation occurs on subsequent annealing; too much strain can cause too many grains to nucleate. That this criterion applies equally well to the rare earth metals was clearly illustrated by the work of Pederson et al. (1965) on Gd. A critical strain of 1–2% was established on a tapered tensile specimen, and when such a strain was applied to a cylindrical specimen followed by an anneal at 1200°C for 3 days large (2.5×1 cm diameter) crystals grew. A similar specimen strained 0.66% did not recrystallise.

The temperature at which secondary recrystallisation occurs is generally well above that necessary for primary recrystallisation but the precise temperature is clearly impossible to determine for each element or alloy. The procedure usually adopted is to heat slowly to within ~100°C of the melting point to allow grain growth to proceed. An alternative approach is to heat the sample in a temperature gradient or to physically move the sample through the gradient. This is designed to promote recrystallisation in a controlled manner from one end of the specimen to the other, rather than nucleation of new grains occurring simultaneously throughout the sample.

Beaudry and Gschneidner (1978) describe the repeated application of the strain-anneal technique to a large (20 cc) Ho arc melted ingot. After an initial anneal at 1340°C for 24 h, the selective application of a 'peening' strain to the smaller grains followed by a further anneal in order to encourage continued growth of one large grain eventually produced a single crystal ingot. A single

strain anneal (1220°C for 25 h) was sufficient to yield a similarly-sized Tb crystal. These examples typify the empirical approach which is usually adopted in this type of crystal growth. It is not possible to quantify the applied strain, the amount introduced being based largely on experience.

This method has recently been used to grow a crystal of Tm in the author's laboratory. Sublimed Tm from Ames was consolidated under argon in a water-cooled cold boat. An unquantified amount of mechanical strain was then introduced into the ingot prior to sealing off in a Ta crucible under $\frac{1}{2}$ atm argon. The crucible was held at 1300°C for 70 h in an argon pressure chamber, and then slowly cooled ($\sim 3° \text{ min}^{-1}$). A 0.3 cc crystal was extracted from the resulting ingot.

4.2.4. *Transformation growth*

Eleven of the sixteen rare earth elements (excluding Pm) exhibit at least one solid state phase transition, usually from hexagonal to cubic symmetry on heating. Generally, the occurrence of such structural modifications is a hindrance rather than a help to the crystal grower, because the transition involves a volume change and the associated strain can lead to the nucleation of new grains in the low temperature phase on cooling. However, if the progress of the transformation can be carefully controlled by the passage of a temperature gradient through the sample, it is in principle possible to transform a single crystal from a high to a low temperature form.

The mechanism involved in grain growth as a result of solid-state transformation have been discussed by Westlake (1968) and, in general, fall into two categories, appropriate to diffusion and shear-type transformations. In the former, a transformation can proceed through a sample under the influence of a traversing temperature gradient provided that the speed of traverse does not exceed that of the transformation front, in a manner analogous to passage of a solid–liquid interface in melt growth. But for a shear transformation, grain growth of new grains of the low temperature phase necessitates prolonged anneals just below the transition temperature, the critical strain being provided by the shear and associated volume change.

Which mechanism is appropriate to the rare earth metals has not been determined but the most common demonstration of the success of this technique in the rare earths is in relation to the growth of single crystals of the low temperature form of many of the metals by a float zone melting technique to be discussed in section 4. The single crystal of the high temperature phase crystallises from the molten zone and, as the zone passes through the bar, the transformation front follows. Thus, the method represents a combination of melt and solid state growth, and the successful transition of the single crystal to the low temperature structure depends critically on the stability of the molten zone (and its consequent control of the transformation front) and its uniform passage through the rod. Thus, this mechanism is an inherent part of the production of single crystals by the float zone melting technique as applied to those rare earths exhibiting a high temperature phase change, e.g. Sc, Y, Gd, Tb, Dy. This will be further discussed in the context of melt growth in section 4.3.

Another way in which the existence of a high temperature structural modification can be used to advantage in promoting crystal growth is by thermal cycling through the transition. The strain energy associated with the transformation is then harnessed and induces the nucleation of grains of the low temperature phase which are then persuaded to grow during an anneal below the transition temperature. This technique therefore qualifies as a genuine strain anneal method since the strain is effectively applied at elevated temperature by means of the structure change. The usual approach is to hold the sample both above and below the transformation for several hours, and repeat this temperature cycle a number of times, before a prolonged final anneal just below the transition temperature.

Tonnies and Gschneidner (1971) have grown crystals of Pr and Nd by this method. An arc melted rod of Pr (transition temperature 795°C) cycled several times between 850°C (~10 h) and 750°C (~20 h) followed by a final anneal of 1–2 weeks has yielded a grain ~5 cc. A similar treatment produced a 0.2 cc crystal in Nd. Nd seems consistently less amenable to this form of crystal growth, and this has also been the experience in work conducted in the author's laboratories, even when this technique has been applied to particularly pure material by a combination of SSE and thermal cycling as will be discussed in the next section.

More recently, crystals of a number of $Nd_{1-x}Pr_x$ intra-rare earth alloys have been prepared by a similar method at Birmingham (McEwen et al. 1986). Induction melted ingots were cycled several times in a copper cold boat before holding 4–8 days just below the transition temperature. A similar approach has also yielded usable crystals of $Pr_{95}Ce_5$ and $Sc_{90}Gd_{10}$ (Fort 1986).

For the other metals exhibiting a transformation at elevated temperature, all except La, Ce, Sm and Yb occur too close to the melting point to render the cycling technique feasible, and alternative methods are more attractive. La and Ce are complicated by other phase transitions at lower temperatures, but in each case this low temperature structural change is sluggish and rarely goes to completion. The α (dhcp) $\rightarrow \beta$ (fcc) transition in La occurs at ~310°C and $\beta - \gamma$ (bcc) at 865°C. The successful in situ growth at Ames of β-La by cycling high purity polycrystalline La contained in thin walled Ta crucibles mounted on a neutron diffractometer through the $\beta - \gamma$ transition has allowed diffraction studies to be performed on crystals of the stable β-phase at 825°C; cycling through the $\beta - \alpha$ transition has also produced crystals of β-La which have been examined at 385°C (Stassis et al. 1982). A sample which had been cycled through the $\beta - \gamma$ transition, annealed for several days at 335°C and then furnace cooled, was found to be in the metastable β-phase, thus allowing room temperature data to be collected as well (Stassis et al. 1985).

The structural transformations and other physical properties of Ce have been discussed in great detail by Koskenmaki and Gschneidner (1978). The γ (fcc) $\rightarrow \beta$ (dhcp) transition is also sluggish and rarely goes to completion. Single crystals of the γ-phase (~1 cc) have been grown by McMasters et al. (1978) by one thermal cycle through the $\gamma \rightarrow \delta$ transition (726°C), holding for one day above the transition and two days below. This treatment was performed on material which had been previously zone melted (see section 4.3.4) and strained

at room temperature. Thus, the success is based on a combination of three of the techniques discussed here, but it was found that strain anneal alone on as-cast metal did not yield appreciable crystal growth. The same approach has proved successful for Pr and Nd. Both Sm and Yb seem potential candidates for transformation growth, provided the samples are encapsulated. However, as we have seen in the previous section, the situation with Sm can be further confused by the possible co-existence of two room temperature modifications (Shi and Fort 1985).

The main limitations this method shares with other solid state growth mechanisms is the lack of control, in practice, over the number, size and orientation of the grains, together with the processing times involved. Moreover, the lack of detailed information on the precise nature of the transformations makes the appropriate number of cycles and isothermal anneal times impossible to predict. The subject will be returned to in the next section in the context of SSE crystal growth.

4.2.5. *SSE crystal growth*

The technique of solid state electrotransport has already been introduced in the context of metallic refinement and, together with zone refining, is a prime example of the inescapable link between purification and crystal growth. These two refinement methods have become the major means of purifying rare earth metals to the standards necessary for much academic research. For some research measurements, however, a single crystal of high crystalline quality can be as important a criterion as an element with high chemical purity. For instance, for dHvA measurements the long electron mean free paths required can only be achieved in high purity crystals with good crystallinity; similarly, neutron and X-ray topography require optimum crystal quality in relatively large specimens. Where requirements both of crystallinity and purity are to be satisfied, SSE processing must be used either on crystals previously grown by another method or on untreated polycrystalline material.

Early work using SSE was clearly directed primarily towards purification, but the observation of grain growth in processed samples led to the realisation of its potential as a crystal growth method in its own right (Whittaker 1968, Jordan et al. 1974a) or to achieve dramatic improvement in crystallinity (and of course purity) of previously grown single crystals (Jordan et al. 1974b). SSE processing of rare earth metals has been centered largely in two laboratories, Ames and Birmingham, and progress has been reported and reviewed periodically by Jordan (1974), Beaudry and Gschneidner (1978) and Jones et al. (1978a, 1982). More recently, Fort (1987) has discussed this subject in great detail and described the successful application of SSE to crystal growth in several rare earth elements. Although SSE processing has been applied to some compounds not involving the rare earths (Pratt and Sellors 1973) very little evidence has been found in the literature for the successful application of this technique to crystal growth in rare earth intermetallic compounds, and so the discussion centers almost entirely on the elements themselves.

The potential for crystal growth by SSE lies in the fact that, not only impurity atoms but also crystalline defects tend to migrate under the influence of an electric field (Pieri et al. 1973). This effect is reinforced by the Joule heating of the metal by the current flow which increases the electromigration rate and enhances the process of recovery, recrystallisation and grain growth essential to the production of large crystals.

The SSE crystal growth route could be thought to consist merely of an alternative method of annealing a sample to those already discussed. This certainly represents a major factor of this process, but the observation that electromigration of crystalline defects can promote grain growth and improve crystal quality within grains distinguishes SSE from straightforward thermotransport methods. Thus, in principle, the re-distribution of impurities and defects (including grain boundaries) is enhanced both by high electric fields and temperature. However, for the majority of rare earth metals processing at the highest possible temperature is not possible in practice due to excessive volatilisation, and so a compromise is usually sought between processing times and temperatures and volatilisation rates.

Theoretical considerations show that a long thin rod has the greatest potential for purification by SSE, the high surface to volume ratio increasing the effective current density. However, such a geometry is incompatible with the need for large volume crystals and so on larger diameter rods, processing times can be even longer when the end requirement is a usable crystal. In common with other crystal growth methods as applied to the majority of rare earth metals, the vapour pressure usually proves to be the most important intrinsic property affecting the choice of processing conditions. For La, Pr and Nd with relatively low vapour pressures even near the melting point, this represents no particular problem. For the remainder, Gd, Tb and Y can be processed in UHV, but only at reduced temperatures; for the rest, an inert gas environment is essential. A typical chamber used for SSE processing is shown in fig. 3.

The individual contributions from annealing and defect electromigration to the overall improvement cannot be readily distinguished, but Fort (1987) proposes three sub-categories to SSE processing based on the precise technique employed rather than on the mechanism involved. These follow the divisions commonly applied to other types of solid state growth and are those employed in this article, namely, (a) simple SSE annealing, (b) SSE strain annealing and (c) SSE transformation cycling. In the context of what has already been said, these subdivisions are self explanatory. SSE transformation cycling has been successfully applied to the dhcp–bcc transition in Pr and Nd, with the other methods applied to the remaining rare earths (where a transition does not exist or is at too high a temperature).

While SSE processing on polycrystalline start material has resulted in significant grain growth as well as purification in the rare earth metals, a totally monocrystalline sample is rarely achieved. An alternative approach involving float zoning followed by SSE has also been successfully applied (Jordan et al. 1974b). Float zoning will be discussed in section 4.3 but is a convenient means of first

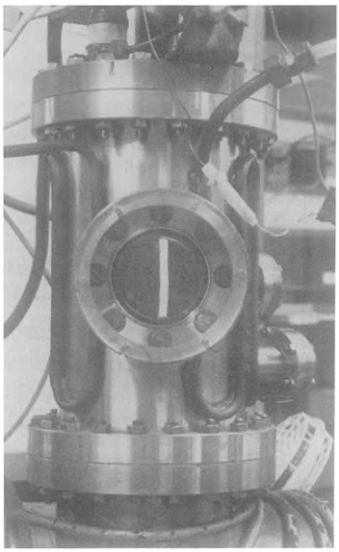

Fig. 3. SSE UHV chamber with rod being processed.

producing a single crystal rod which can then be subjected to SSE. In this way high quality and high purity single crystals can be prepared (Goddard et al. 1982).

Table 3 shows the results of crystal growth studies in the rare earth elements where SSE has formed part or all of the processing route. This represents work performed in Birmingham and Ames often in collaboration. It can be seen that for ten of the elements SSE can be wholly or partially responsible for the production of high quality crystals. Low temperature phase changes make Ce and La unlikely candidates, while the high vapour pressure elements Tm and Yb are also precluded because of extreme volatilisation problems. Sm has been tried but yields no better results than the other solid state methods already discussed. Of the successful SSE crystal growth experiments so far conducted, two have involved the transformation cycling method – Pr and Nd. Crystals of Nd are frequently of poorer quality, with 1–2° substructure quite common. A typical cycle would comprise purification for ~500 h in the bcc phase followed by cycling 3–5 times about the transformation, each cycle consisting of 16 h below and 8 h above, with a final anneal below for ~200 h prior to a slow cool over a similar period. Gd, Tb and Y have been treated in the hcp phase, the $\alpha-\beta$ transition being too close to the melting point for cycling. Good crystals have been produced both on poly- and mono-crystalline rods by simple SSE anneal or strain anneal (Jordan et al. 1974a, b, 1975). The problem of grain boundary sliding which can lead to catastrophic failure has been minimised by processing the rod vertically instead of horizontally. Dy and Ho have been processed in inert gas by simple annealing, Dy on polycrystalline and Ho on single crystal rods.

TABLE 3
Refinement and crystal growth by solid state electrotransport.

Element	Highest RR	Technique**	Ref.	Largest high quality crystal (cc)	Technique**	Ref.
Sc	520	SSE	a	0.4	SA + SSE	j
Y	>1000	RFFZ + SSE	b	2.0	RFFZ + SSE	b
La	260	SSE	c	—	—	
Pr	400	ZR + SSE	b	2.0	SSE/TC	b
Nd	120*	SSE	b	1.5	SSE/TC	b
Gd	800	ZR + SSE	b	1.7	EBFZ + SSE	e
Tb	>1000	EBFZ + SSE	d	>5.0	EBFZ + SSE	d
Dy	125	SUB + SSE	b	1.0	SSE	b
Ho	90	RFFZ + SSE	b	2.0	RFFZ + SSE	b
				0.8	SSE/SA	b
Er	60	SUB	f	—	—	
Lu	150	SSE	g	1.0	AZ + SSE	h

* $R_{293}/R_{1.2}$
** Abbreviations:

ZR	Zone Refining
RFFZ	RF Float Zoning
EBFZ	Electron Beam Float Zoning
SUB	Sublimation
SSE	Solid State Electrotransport
SSE/TC	SSE Transformation Cycling
SSE/SA	SSE Strain Anneal
AZ	Arc Zoning

a Schmidt and Carlson (1976).
b Fort (1987).
c Pan et al. (1980).
d Jones et al. (1982).
e Jordan et al. (1974b).
f Present work.
g Peterson and Schmidt (1969).
h Carlson et al. (1975).
j Stierman et al. (1983).

Fort (1987) points out that there seems no reason why this technique should not be successful for Sc, Lu, Er and Eu, but no such specific crystal growth attempts employing SSE have so far been reported. Carlson et al. (1975) report the SSE purification of a Lu single crystal previously produced by arc zone melting, and Schmidt and Carlson (1976) presented results on SSE in Sc but make no comment on grain growth. Similarly, Stierman et al. (1983) report magnetic susceptibility and electrical resistivity measurements on single crystals of Sc which were SSE refined subsequent to growth and Schirber et al. (1983) describe dHvA measurements on a crystal of Sc produced by SSE at Ames, implying a crystal of good quality. SSE has also been used to purify La (Pan et al. 1980) and to produce a single phase dhcp specimen by cycling through the $\alpha-\beta$ transition, but not specifically to promote crystal growth.

It is clear that the rigorous requirements of some physical property measurements can only be met by introducing SSE into the crystal growth route, whether on its own or in combination with another technique. In the latter case, it is usual for SSE to be the final stage of crystal growth or improvement in crystallinity, but in some instances it has been used as a precursor to another

method. Single crystals based on SSE-purified material have been grown when the desired quality would not have been possible with material not so processed (e.g. the Gd–Tb alloys referred to in section 4.2.2).

The main advantages of SSE crystal growth at a technical level are clear; working in UHV or inert gas equivalent, no contamination due to containment and purification being achieved simultaneously. However, it has to be appreciated that the technique has its limitations just like any other, primarily associated with the purification aspect of the process. To be really effective, reasonably good start material is necessary. Since the process only re-distributes impurities, difficulties arise with high initial impurity levels due to changes in resistivity at regions of high impurity densities (usually close to the anode for rare earth metals) leading to localised hot-spots and ultimately melting. In common with other solid–solid techniques, SSE does not readily allow crystal orientation control (except by processing a previously oriented rod), and, in general, the crystals produced are only small compared with those from melt growth techniques. However, perhaps the main limitation in practice is the long processing time involved (~1000 h), but when the restrictions on specimen quality associated with the particular experiment to be conducted are such that SSE offers the only realistic possibility, even this limitation is easily overlooked.

The possibility of differential migration rates of individual constituents has presumably prevented wider application of the method to alloys and compounds, although recent work at Birmingham on a Pr–Nd alloy has demonstrated the feasibility of applying SSE to crystal growth in alloy systems (Fort 1986). Only one reference to the application of SSE to a rare earth intermetallic compound has been found. Recently, Onuki et al. (1987) reported a significant reduction in resistivity in a rod of $CeCu_6$, which had been pulled from a W crucible, by means of SSE at 800°C for 700 h. No comment was made on any improvement in crystallinity.

4.3. *Liquid–solid growth*

4.3.1. *Introduction*

Solidification from the melt is the most widely used preparation and crystal growth method for rare earth metals and intermetallic compounds, certainly where large volume crystals are required. The main advantage in melt growth is that the solidification process can be subjected to considerable control with the associated benefit of being able to determine the orientation of the crystal. In addition, effective purification may occur simultaneously with crystal growth from the liquid phase due to segregation of impurities at the solid/liquid interface. Some of the disadvantages of this route include those associated with containment of the melt over lengthy periods. In general, the method only applies to elements and congruently melting compounds with tractable vapour pressures. Peritectic phases cannot normally be grown starting from the melt, but there are exceptions to this as will be seen later in this section.

Several methods are employed, some involving the use of crucibles, some not. One of the situations where use of a crucible is unavoidable is in the crystal growth from the melt of highly volatile compounds involving one or more high vapour pressure constituents. In these circumstances a sealed refractory material crucible is necessary; unlike the instance of volatile semi-conductor melts, encapsulated single crystal growth is not feasible due to the absence of a suitable encapsulant.

All melt growth processes are essentially ones of controlled solidification, involving the mechanisms of nucleation (most likely of the heterogeneous kind at some impurity or container site) and growth. Ideally, a stable solid–liquid interface is traversed in a uniform manner through the bulk of the material. To provide a stable interface and minimise constitutional supercooling effects, this is conventionally done in the presence of a significant temperature gradient normal to the growth interface.

Melt growth techniques can be classified into three sub-groups according to the method of melt containment: hot crucible, cold crucible and crucible-less, and in the following discussion of individual methods an attempt will be made to identify the type of melt containment used in specific crystal growth experiments in the literature.

4.3.2. *Melt containment*

Apart from float zone melting and skull melting all the melt growth techniques involve holding all the material molten for considerable periods of time. When dealing with such reactive metals as the rare earths, consideration must clearly be given to the method of containment and choice of suitable crucible material. Ideally the crucible material should not react with the molten metal and not be wetted by the melt. In practice, it is extremely difficult to meet both these criteria when melting rare earth based metals and so it is usually a matter of trying to minimise the effect of crucible containment. The refractory metals Mo, Ta and W are often used since their solubility in the molten rare earths is less than many other potential candidates, with W being distinctly less soluble in most of the rare earths (Dennison et al. 1966). However, for intermetallic compounds containing some of the transition metals, such as Fe and Co, reaction with this second constituent rather than the rare earth itself becomes the problem and other means of containment has to be found. Reports of the successful use of Al_2O_3 crucibles have appeared in the literature (e.g. Gignoux et al. 1975) but are best avoided in general because of the likelihood of melt reaction. Pyrolytic BN crucibles and BN coatings in Al_2O_3 crucibles have been more successful (Miller and Austin 1973, Katayama and Shibata 1974). A variation on this type of containment is reported by Purwins (1970). The inner wall of an Al_2O_3 crucible was coated with 30 μm W foil to prevent reaction.

With all these refractory material crucibles, considerable problems with wetting are encountered, leading to difficulty in extracting the boule subsequent to solidification. An additional problem resulting from wetting is the strain induced

in the boule on cooling due to the inevitable differential contraction rates between crucible and solidified melt. The degree of wetting and the dissolution rate of the crucible material can sometimes be reduced by polishing the internal surface of the crucible thus reducing the surface area of contact with the melt. The slight taper usually introduced into Bridgman crucible design is intended to ease extraction of the crystal boule subsequent to growth, but with these materials is not often very effective. More often than not a crucible can only be used for one experiment, which can introduce a significant financial factor into the crystal growth experiments: shaped W and BN crucibles cost typically £150 each.

The cold-crucible approach is being used increasingly in the preparation and crystal growth of rare earth elements and intermetallic compounds. This method avoids the reaction and wetting problems associated with the hot crucible methods. The crucible is water-cooled and usually constructed from a high electrical and thermal conductivity metal such as Cu or Ag. The nature of the contact between melt and crucible is not clear and probably depends on the type of heating employed. Thus, for arc-melting it is likely that a skull or skin of solid material exists between the melt and crucible, but with induction melting, the currents induced in the melt surface may cause some levitation away from the crucible giving rise to more complete melting.

Arc-melting employing a non-consumable electrode has found some application in crystal growth of rare earth based materials, apart from being a preparation route for the synthesis of intermetallic compounds as discussed in section 3. Some of the early crystal growth experiments on the rare earth elements themselves included attempts using arc zone melting (Carlson et al. 1964, 1975). An interesting development of this heating method and melt containment is the tri-arc system originally described by Reed and Pollard (1968). Three symmetrically arranged arcs and a water cooled hearth provide a melt source for Czochralski pulling. This modification will be discussed in section 4.3.6. In another development of the arc melting approach, known as arc transfer crystal growth (Drabble and Palmer 1966), the electrode is composed of the same material as the melt and acts as feedstock as growth proceeds; this has found no reported application to rare earth-based metals.

Developments of the cold crucible principle allied with induction heating have found application in crystal growth employing zone melting and crystal pulling techniques. In particular, segmented cold crucibles based on designs by Hukin (1971) and Smith (1979) have been used in many laboratories for the growth of intermetallic compounds by the Czochralski method. Here the cold crucible acts as a secondary and concentrator for an external primary RF coil, a combination which can hold the metal completely molten and slightly levitated. This represents a development of the earlier levitation-type geometries of induction cold crucible where the RF power is applied directly to the shaped coil itself rather than through a primary–secondary system (see Bunshah 1968). Water cooled cold boats, either segmented or not, coupled with induction heating form the basis of the horizontal zone melting approach to crystal growth and have also been used in

a modification by Oliver et al. (1972) as the container for the Czochralski method by pulling through the RF coil by means of a side arm in the chamber.

Crucible-less techniques require no physical containment and rely on the surface tension of a free floating molten zone in contact with the corresponding solid. This method of crystal growth is concerned primarily with vertical float zone melting with RF, electron beam or infra-red heating and will be discussed in section 4.3.4.

4.3.3. *Normal/controlled solidification*

Normal solidification of a rare earth element or compound will result in general in a polycrystalline ingot. However, directional freezing or even simply controlled solidification can often result in enlarged grain sizes. The crystal grower can then try and enhance this tendency by devising a geometry or temperature profile to suit the particular melt. Small single crystals can then be cut from the ingot or revealed by mechanical fragmentation (or the ingot can subsequently be subjected to solid state growth techniques already described). This approach can be equally well adopted in hot or cold crucible methods and several reports exist in the literature of the successful application of this route.

One way of achieving controlled solidification with the cold crucible containment is to reduce the RF power to a levitated or semi-levitated melt. The melt then comes into contact with the crucible and directional freezing occurs from the point of contact. Hukin (1971) used this method to advantage in producing crystals of Gd and Y (~2 cc) despite the phase transformation close to the melting point. Crystals of several rare earth intermetallic compounds have been produced by this means, but are usually small. Drewes et al. (1985, 1986) have produced crystals of $PrPd_3$ and $NdPd_3$ by slowly cooling the melt in an inductively-heated cold copper crucible, followed by an anneal. Magnetisation spheres 1.2 m diam. were prepared by spark erosion. 100 mg crystals of $GdCo_5$ have been cut from ingots slowly cooled in a cold crucible (Ballou et al. 1986a). Johnson et al. (1978) cut a crystal 200×35 μm from an ingot of YCo_5 induction melted in a cold boat and slowly cooled. A similar approach allowed Inoue et al. (1978) to extract a 100×40 μm crystal of Er_2Fe_{17}. Small crystals of $LaCu_4$ were also selected from an ingot crystallised in a temperature gradient for X-ray diffraction (Meyer-Liautard et al. 1985).

An alternative approach with a horizontal cold boat system with RF induction heating is to traverse the melt out of the work coil, thus driving a solid–liquid interface through the material. This method is sometimes referred to as the Chalmer's method or horizontal Bridgman technique. A cold finger can be introduced at one end to provide a specific nucleation site. This method has not found wide application for rare earth compounds.

Kletowski et al. (1985a) describe the successful crystal growth of a series of RSn_3 and RIn_3 compounds by a complicated slow cooling programme. These crystals were grown, however, from melts containing slight excesses of Sn or In, which lowered the melting point sufficiently to allow the use of Al_2O_3 crucibles.

This strictly constitutes growth from metal solution and more properly belongs in the discussion elsewhere in this volume (see Ch. 81 by Fisk and Remeika).

Interest in R-based ternary systems has expanded rapidly in recent years with the discovery of the coexistence of magnetic and superconducting states, and heavy fermion and mixed valence behaviour in some of these materials. While crystals of many of these ternary compounds are being grown by metal solution techniques, some attempts at growth from stoichiometric melts have been referred to in the literature. Small crystals of compounds in the Y–Rh–Si system (Paccard et al. 1985) and Ce–Pt–Se system (Dommann et al. 1985) have recently been taken from arc melted ingots. Ce–Cu–Al, Ce–Cu–Sn and Ce–Zn–Al ternaries slowly cooled in Al_2O_3 crucibles provided small crystals for structural analysis (Cordier et al. 1985). Chevalier et al. (1985) report crystals of $TbRh_2Si_2$ (1×1.5 mm) extracted from polycrystalline ingots. A variation of this approach involving argon plasma jet melting has yielded mg-size crystals of $PrMn_2Ge_2$ (Iwata et al. 1986). Crystals of the ternary $ErCo_2Ni_2$ were cut from an arc melted ingot (Drzazga 1985) and Barandiaran et al. (1986) report 25 mg crystals of $PrNi_2Si_2$ being cut from an ingot slowly cooled in an induction-heated cold crucible. A list of references to crystals produced in this way is given in table 4.

TABLE 4
Crystals grown by normal/controlled solidification.

Crystal	References
Gd, Y	Hukin (1971)
Tb_3Ni	Gignoux et al. (1982)
$Gd_{1-x}Ce_xAl_2$	Iwata et al. (1985)
$ErNi_2$	Gignoux and Givord (1983)
RSn_3, RIn_3	Kletowski et al. (1985a)
$PrPd_3$, $NdPd_3$	Drewes et al. (1985, 1986)
$LaCu_4$	Meyer-Liautard et al. (1985)
YCo_5	Johnson et al. (1978)
$Pr(Co_{1-x}Ce_x)_5$	Maeda (1978)
$GdCo_5$, $Gd_{0.5}Y_{0.5}Co_5$	Ballou et al. (1986a), Uehara (1980)
$CeCu_6$	Thompson (1985)
Er_2Fe_{17}	Inoue et al. (1978)
Y–Rh–Si	Paccard et al. (1985)
Ce–Pt–Si	Dommann et al. (1985)
Ce–Cu–Al, Ce–Cu–Sn, Ce–Zn–Al	Cordier et al. (1985)
$CeRu_2Si_2$	Thompson et al. (1985)
$CeRh_3B_2$	Kasaya et al. (1986)
$PrMn_2Ge_2$	Iwata et al. (1986)
$PrNi_2Si_2$	Barandiaran et al. (1986)
$SmMn_2Ge_2$	Fujii et al. (1985)
$TbRh_2Si_2$	Chevalier et al. (1985)
Tb–Y–Ni	Gignoux and Lemaire (1974)
$ErCo_2Ni_2$	Drzazga (1985)

4.3.4. *Float zone melting*

Crystal growth by the float zone melting technique is distinguished from the other melt growth routes by the fact that it involves the passage of two solid–liquid interfaces through the material rather than the more usual single interface; the two interfaces define the floating molten zone. Two modes are identifiable, horizontal (HFZ) and vertical (VFZ), and three sources of heating, DC arc, RF induction (RFFZ) and electron beam (EBFZ) are conventionally employed. The different variations are illustrated schematically in fig. 4.

The method derives directly from zone refining, discussed in section 2, and the frequent observation of grain growth as a by-product of the purification obtained by the repeated passage of the molten zone along a rod or bar of metal. The horizontal version is realised by arc or induction melting of the sample held in a water-cooled horizontal boat which can be traversed with respect to the electrode or RF coil. Both methods can be undertaken in argon atmosphere but the induction method can also be performed in high vacuum making it a more attractive and versatile approach. Semi-levitation is often achieved by this means but the success of the method is often hindered by the proximity of the cold boat and the inherent instability associated with the precarious nature of the levitation.

A more stable situation can be achieved in the vertical mode. The molten zone, which is in contact only with the solid parts of the rod, is stabilized by surface tension (and to some extent by RF levitation if this form of heating is used). High vacuum environments are possible with both forms of heating, RF coupling and electron beam, but the former again has the advantage of operation in inert gas for volatile materials. Passage of the molten zone often results in spontaneous crystal growth but seeding to produce a particular orientation single crystal is particularly straightforward with this technique. In the EB version, flexible power

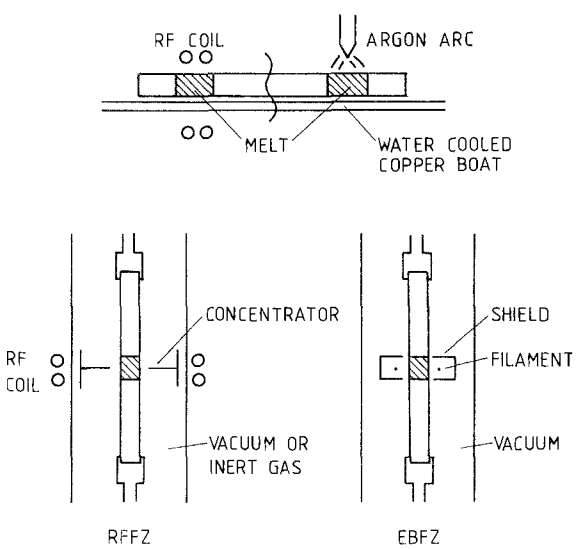

Fig. 4. Schematic representation of float zone melting.

leads to the electron source are relatively simple to arrange and so the source moves along a stationary rod. However, flexible RF leads are not as easy to arrange and, in this case, the specimen is invariably moved through a stationary work coil. Since it is desirable to arrange the source of heat as close to the rod as possible, provisions of a concentrator close to the rod coupled to an external primary coil is the more usual arrangement.

Designs can vary, but the essentials are the same. A rod typically 5–10 mm diam. and 100–150 mm in length is held vertically clamped at both ends. The top and bottom clamps can be moved independently to accommodate rods of different lengths and to allow fine adjustment if a seed and feed rod are being used. This also allows the grown crystal to be separated from the feed rod at the end of traverse to avoid the possibility of straining the crystal if it remained clamped during cooling. Rotation of one or both clamps is sometimes employed to provide stirring in the molten zone in a similar manner to the Czochralski technique (see section 4.3.6).

If a seed rod is to be used to grow a particular orientation along the axis of the rod, the seed should be fabricated to provide the required orientation; alternatively the seed can be mounted on a small goniometer attachment which replaces the bottom clamp, and the required orientation achieved by rotation of the goniometer arcs. The feed rod and seed are arranged to touch and then melted together, and the zone traversed up the feed rod, thus propagating the required orientation. Typical growth rates are 5–20 mm h^{-1}. The method is readily applied to elements and compounds and can, in principle, be extended to alloy systems provided any segregation resulting from a zone pass in one direction is compensated for by passing the zone in the reverse direction (zone-levelling). It may, in practice, be easier to reverse the rod rather than the direction of zoning. One of the advantages of the technique is the effective after-heating of the solidified crystal by conduction through the rod. This serves to improve the crystallinity of the grown crystal and, as discussed in section 4.2.1, allows the stable passage of the α–β transformation front along the rod in the case of those rare earth elements exhibiting this high temperature transition.

Some of the early crystal growth experiments on the rare earth elements employed arc zone melting. Carlson et al. (1975) grew a Lu crystal (7.8 cc) and subsequently Schmidt and Carlson (1976) an Er crystal (13 cc) by this method. Verhoeven et al. (1976) describe the application of arc zone melting to LaB_6, producing rods $\sim 20 \times 6$ mm at rates 50 μm s^{-1}, and this approach has been adopted by other workers for rare earth hexaborides (Gruhl and Winzer 1986).

Horizontal float zone melting using induction heating has also yielded single crystals. Hukin and Jones (1976) report the successful application of this approach to many of the rare earth elements and compounds including Sc, Y, Pr, Nd, Gd, Tb, Dy, Ho, Er, Lu together with many of their alloys, and $DyAl_2$, $DyFe_2$, $ErFe_2$ and $GdNi_5$. Their horizontal boat was machined and segmented from a solid Cu bar in a similar manner to that used for the original segmented cold crucible (Hukin 1971). Single crystals of Ce (1 cc) and Pr and Nd (2 cc) were grown by McMasters et al. (1978) by a combination of HFZ and strain-anneal

where straightforward recrystallisation had failed to promote appreciable crystal growth. A specially designed segmented copper boat (assembled from individual copper tubes) was used in this work and was also used successfully to grow crystals of RFe_2 ($R \equiv$ Tb, Dy) intermetallic compounds. Since $TbFe_2$ and $DyFe_2$ are peritectic phases, growth from stoichiometric melts was not possible; this potential difficulty was overcome by traversing a rare earth-rich molten zone along a stoichiometric bar at a speed ($0.8\,mm\,h^{-1}$) slow enough to allow diffusion across the molten zone thereby enabling the correct composition to solidify. A 1 cc single crystal of $TbFe_2$ and a 1 cc bi-crystal of $DyFe_2$ was thus obtained. This modification could, in principle, be applied to other peritectic phases but no such reports have been found.

Single crystals of the heavy rare earth metals Gd, Tb, Dy, Ho and Er, together with Sc and Y were grown by Whittaker (1968) by induction zone melting in argon in the vertical mode with a concentrator coupled with an external primary RF coil (RFFZ). Equipment based on that design is available commercially and is widely used for rare earth elements and intermetallic compounds. Crystals grown at the Ames Laboratory using VFZ include RAl_2 and $CePd_3$ (McMasters 1984) and this approach has been adapted to produce 'pseudo-crystals' of mixed ternary RFe_2 compounds such as $Dy_{0.73}Tb_{0.27}Fe_2$, a highly magnetostrictive compound produced in grain-oriented form at relatively high zoning speeds ($\sim 250\,mm\,h^{-1}$) (McMasters et al. 1986). More recently, crystals cut from the grain oriented rods were used as seeds to grow 'single crystals' by float zoning, but were found to be heavily twinned (Verhoeven et al. 1987). The method is used extensively in the author's laboratory and a recent modification (Fort 1986) has allowed crystals of Y, Dy and Ho to be grown in a system operated to UHV specifications. Single crystal rods several centimeters in length can be grown by this means.

This approach has been used to prepare single crystals of rare earth hexaborides at temperatures in excess of 2000°C (Tanaka et al. 1975, 1980). Many of these compounds are congruent melting, but the peritectic phase GdB_6 has also been grown in this way by using a B-rich molten zone together with slow zoning rates ($\sim 3\,mm\,h^{-1}$) and chuck rotation (10 rpm) to enhance mixing within the zone. As already mentioned a similar approach has been successful with RFe_2 peritectic phases in the horizontal mode. Laser-heating provides another way of achieving the high temperatures necessary for these compounds and such an approach has been adopted by Takagi and Ishii (1977). Crystals 50 mm long by 1 mm diameter have been grown at rates between $5–10\,cm\,h^{-1}$.

An alternative form of heating in the vertical mode involves the use of an infra-red image furnace and this version has recently been used to grow single crystals of ternary $R_2Fe_{14}B$ ($R \equiv$ Er, Tm, Sm) in an argon atmosphere (Hirosawa and Sagawa 1985, Hiroyoshi et al. 1985). Electron beam float zone melting in high vacuum has been successfully applied in Birmingham to crystal growth of some of the low vapour pressure elements such as Gd, Tb and Y. A seeded Tb rod grown in this way is shown in fig. 5. McEwen and Touborg (1973) report some limited success with Pr and Nd using this approach. Crystal rods grown by this means have been used as samples for subsequent SSE processing to improve

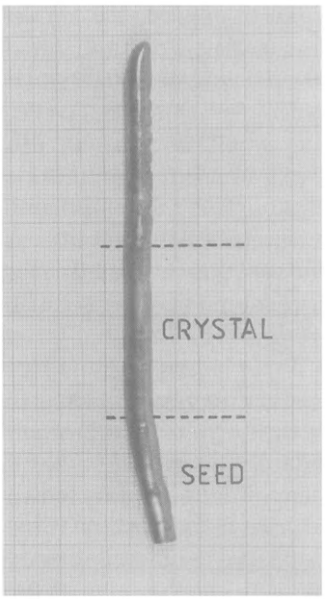

Fig. 5. Seeded rod of Tb grown by EBFZ (1 div. = 1 mm).

purity and crystallinity by Jordan et al. (1974b). Levin et al. (1980) report the growth of $PrNi_5$ crystals using the EBFZ method.

Some examples of float zone melting in a hot crucible to produce single crystals have also been reported. Float zoning in an Al_2O_3 crucible has been employed by Schweizer and Tasset (1980) to grow YCo_5 boules. The crucible used had a cone-shaped end resembling those used in the Bridgman technique. More recently, Onuki et al. (1987) zone melted $CeCu_6$ in a BN crucible but made no comment on crystal size. They concluded that the 'best quality' crystals were, however, produced by the Czochralski technique (see section 4.3.6). A list of some crystals grown by zone melting is shown in table 5.

4.3.5. *Bridgman technique*

Experimentally, the Bridgman (1925) method is perhaps the easiest melt growth method to realise. The technique is illustrated diagrammatically in fig. 6. The melt is contained vertically in a crucible, usually with a pointed end, and solidification from the lower end is achieved by passing the crucible through a steep temperature gradient containing the melting point. This can be realised by moving the heat source, lowering the crucible or progressively reducing the heat input while maintaining the temperature gradient.

The crucibles are normally cylindrical (sometimes with a slight taper to ease extraction) with a conical end. The cone is designed to minimise the number of nucleation sites, and ideally to provide a preferential site and thereby to promote single crystal growth. In other designs, one grain is encouraged to grow at the

TABLE 5
Crystals grown by float zone melting.

Crystal	References
Single elements	Whittaker (1968), McEwen and Touborg (1973), Jordan et al. (1974b), Carlson et al. (1975), Schmidt and Carlson (1976), Hukin and Jones (1976), McMasters et al. (1978), Fort (1986)
Y–Dy	Apostolov et al. (1986)
Ho–Tb, Ho–Gd	Bagguley and Howe (1986)
Tb–Y	Bagguley et al. (1981)
RAl_2	Hukin and Jones (1976), McMasters (1984)
RFe_2	Hukin and Jones (1976), McMasters et al. (1978, 1986), Verhoeven et al. (1987)
$ErCo_3$	Georges et al. (1975)
$CePd_3$	McMasters (1984)
YCo_5	Schweizer and Tasset (1980)
$LaNi_5$, $PrNi_5$	Levin et al. (1979, 1980)
$PrNi_5$	Kaplan and Williams (1980)
$GdNi_5$	Hukin and Jones (1976)
$CeCu_6$	Onuki et al. (1987)
RB_6	Tanaka et al. (1975, 1980), Verhoeven et al. (1976), Takagi and Ishii (1977), Kawakami et al. (1980), Flachbart et al. (1982), Gruhl and Winzer (1986)
$R_2Fe_{14}B$	Hiroyoshi et al. (1985), Hirosawa and Sagawa (1985)

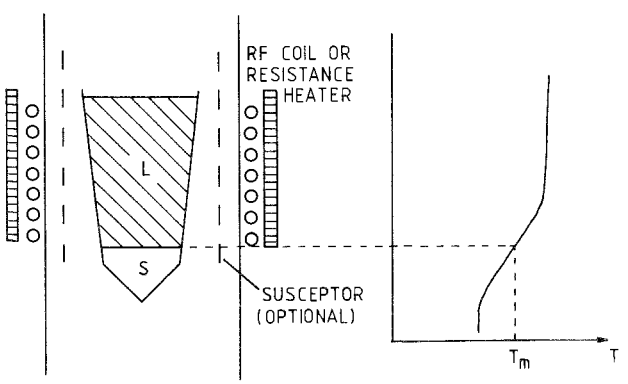

Fig. 6. Schematic representation of the Bridgman technique.

expense of others nucleated in the melt by a physical restriction in the crucible immediately above the conical end. Other geometries (e.g. square cross section) are, in principle, possible and this ability to determine the shape and size of the crystal by choice of crucible remains one of the main advantages of the technique. In Stockbarger's (1936) version of the method, a secondary furnace was used to promote the necessary temperature gradient. However, this effectively reduces the magnitude of the temperature gradient and increases the risk, due to super-cooling, of the whole melt being below the melting point before nucleation occurs, which can lead to rapid solidification and a polycrystalline boule. However, if a single crystal boule can be produced by this two-zone furnace arrangement, it has the merit of providing after-heating to the crystal which can improve crystallinity and homogeneity. In practice, with rare earth-based materials, the steep temperature gradient provided by the Bridgman method is usually preferred. A typical boule is shown in fig. 7.

Hurle (1962) has shown that the nature of the solid–liquid interface can influence the crystalline quality of the solidified boule. A melting point isotherm which is concave to the liquid will allow nucleation and growth of crystallites from the crucible wall into the bulk of the boule. Conversely, an interface convex with respect to the melt will inhibit the growth of such stray crystallities. Induction heating coupled directly with the crucible wall or low thermal conductivity crucible material can both increase the tendency towards a convex melting point isotherm and better quality crystals.

Seeding with a single crystal is, in principle, feasible by placing the seed at the base of the crucible and raising the temperature until melting of the charge and seed-tip only is achieved. This entails very close control of temperature and position and with no visual monitoring, as in float zone melting or Czochralski pulling, this proves difficult to realise in practice.

Being a hot crucible technique, a suitable choice of refractory material has to be made. Mo, Ta and W are frequently used and with induction heating, direct

Fig 7. Boule of PrAg grown by the Bridgman technique (1 div. = 1 mm).

coupling with the crucible is possible. With non-conducting crucible materials such as BN or Al_2O_3, a susceptor has to be incorporated into the experimental arrangement. Crystal growth can proceed under vacuum or inert gas and the small surface area exposed reduces the risk of contamination from the environment. However, the crucible itself remains the main source of contamination, but where other methods are not convenient and particularly for highly volatile constituents this method continues to be a relatively simple and invaluable route to single crystal growth. For growth of high vapour pressure systems, the constituents are usually sealed into Mo, Ta or W crucibles by argon arc or electron beam welding. Reaction melting of the components and crystal growth should then be performed in one operation, because once the melt has wetted the crucible, cooling and re-heating becomes difficult without straining, and sometimes cracking, the crucible walls due to differential expansion. This is particularly relevant to W and the insulating refractories which are more brittle than Ta. The introduction of stress on cooling the crystal boule due to wetting of the melt provides one of the major disadvantages of this technique, along with the associated problem of subsequent extraction from the crucible at room temperature.

The early work on crystal growth of the rare earth elements by the Bridgman method was reviewed by Beaudry and Gschneidner (1978) who point out that growth in Ta or W is more applicable to the light rare earths, in which Ta and W have lower solubility than the heavy elements (Dennison et al. 1966). Nevertheless crystals of Dy (Behrendt et al. 1958, Hall et al. 1960) and Er (Green et al. 1961) have been grown in Ta crucibles but with up to 1% atomic Ta levels. Beaudry and Gschneidner (1978) extended this technique to Yb by reducing the space above the melt by welding inside the Ta Bridgman crucible an inverted Ta crucible of smaller diameter to limit vapour transport. A 1 cc crystal was grown at 25 mm h^{-1}.

Several of the equiatomic RM compounds have been grown in sealed crucibles, where M is a volatile constituent such as Zn, Mg or Cd. Both W and Ta crucibles have been used as shown in table 6. Not many experimental details are available, but Sousa et al. (1983) grew a GdCd crystal in a thermal gradient of 2°mm^{-1}, and the present author has grown RZn boules in W and Ta crucibles sealed under half an atmosphere of argon at rates 6–10 mm h^{-1} (Abell et al. 1979a).

Single crystals of some RAl_2 (R ≡ Y, Gd, La) have also been grown by the Bridgman method in sealed Ta crucibles at Ames for elastic constant measurements (Schiltz and Smith 1974). A lowering rate of 15 mm h^{-1} produced boules from which cylindrical samples (~0.75 cc) were fabricated. Purwins (1970) also reported the successful Bridgman growth of several RAl_2 (R ≡ Er, Ho, Nd, Sm) compounds. The melt was contained in a Al_2O_3 crucible lined with 30 μm W foil in a pressure vessel at 20 atm He. Crystals (~1.5 cc) with misorientations <1.5° were grown at 25 mm h^{-1}. A similar approach has been adopted by Boucherle and Schweizer (1981) who used a 25 μm W foil inside a W crucible to reduce mechanical strains on cooling. Crystals of $NdAl_2$ were grown at 20 mm h^{-1} using a separate graphite susceptor. Barbara et al. (1980) point out that $CeAl_2$ and $NdAl_2$ boules grown in W crucibles contained only ~120 ppm atomic W,

TABLE 6
Crystals grown by the Bridgman technique.

Crystal	Crucible	References
Dy	Ta	Behrendt et al. (1958), Hall et al. (1960)
Er	Ta	Green et al. (1961)
Yb	Ta	Beaudry and Gschneidner (1978)
RAg		Giraud et al. (1983), Morin and Schmitt (1982), Giraud and Morin (1986), Present work
RCd	Ta	Sousa et al. (1983), Kitai et al. (1984), Morin (1984), Aleonard and Morin (1984, 1985)
TmCu	Ta	Morin (1984), Morin et al. (1984)
RMg	Ta	Aleonard et al. (1976), Morin et al. (1978), Giraud et al. (1986), Pierre et al. (1984)
RNi	Ta	Gignoux et al. (1985a), Fillion et al. (1984), Isikawa et al. (1983, 1985), Sato et al. (1986)
RZn	Ta, W	Morin et al. (1977, 1981), Morin (1984), Pierre et al. (1977), Givord et al. (1980b), Hamaguchi et al. (1980), Abell et al. (1979a), Rouchy et al. (1981), Kropp et al. (1984)
RAl_2	Ta, W Al_2O_3/W W/W	Schiltz and Smith (1974), Barbara et al. (1980) Purwins (1970) Boucherle and Schweizer (1981)
RCo_2	Al_2O_3	Gignoux et al. (1975, 1976a, 1979)
RFe_2	W	McMasters et al. (1978), Williams and Koon (1975)
$ErGa_2$		Doukoure and Gignoux (1982)
$HoNi_2$		Gignoux et al. (1975)
RIn_3	Mo, Al_2O_3	Kitazawa et al. (1985), Lawrence and Shapiro (1980), Kletowski et al. (1985a),
RSn_3	W, Mo	Johanson et al. (1981), Kletowski et al. (1985a), McMasters (1984), Kasaya et al. (1985), Shaheen et al. (1983), Stassis et al. (1981), Boucherle et al. (1986)
$GdCo_3$	Al_2O_3/BN	Katayama and Shibata (1981)
RCo_5	BN, Al_2O_3/BN	Miller and Austin (1973), Katayama and Shibata (1974, 1981), Shibata and Katayama (1983), Fidler and Kronmuller (1979), Ohkoshi et al. (1977), Givord et al. (1979), Patterson et al. (1986)
RNi_5		Gignoux et al. (1976b)
RCu_6	BN	Onuki et al. (1987)
Sm_2Co_7, Gd_2Co_7	BN Al_2O_3/BN	Fidler and Kronmuller (1979) Katayama and Shibata (1981)

TABLE 6 (continued)

Crystal	Crucible	References
R_2Co_{17}	Al_2O_3/BN	Katayama and Shibata (1974, 1981), Shibata and Katayama (1983), Slepowronski et al. (1983)
R_2Fe_{17}	BN	Christensen and Hazell (1980), Deportes et al. (1986)
$CeNi_2Ge_2$	BN	Kletowski (1983)
$CeCu_2Si_2$	BN, Al_2O_3	Kletowski (1983), Bredl et al. (1983), Assmus et al. (1984)
$CeInSn_2$	Ta	Benoit et al. (1985)
$CeRh_3B$		Kasaya et al. (1986)

compared with levels of 1–3% atomic Ta when grown in Ta crucibles. W crucibles have been used to yield small crystals of RFe_2 (R ≡ Tb, Dy, Er) compounds, but better results were obtained using zone melting (McMasters et al. 1978).

Large crystals of $LaSn_3$ (Stassis et al. 1981) and $CeSn_3$ (Johanson et al. 1981) have been grown in W crucibles by induction heating, but with a separate Ta susceptor to avoid direct RF coupling with the crucible (McMasters 1984). The ease with which the boules slipped out of the crucible indicated very little of the wetting normally encountered with direct coupling. Sealed Mo crucibles have recently been used by Kitazawa et al. (1985) for crystal growth of $PrIn_3$ and $LaIn_3$ and by Kasaya et al. (1985) for $SmSn_3$. Other isostructural members of the RM_3 group (with M ≡ Sn, In and Pb) have been grown by a solution crystallisation technique, not from a separate solvent but from a small excess of M (Kletowski et al. 1985a). This small excess lowered the melting point sufficiently to allow Al_2O_3 to be used, and this whole approach to crystal growth is discussed in detail elsewhere in this volume (see Ch. 81 by Fisk and Remeika).

The development of pyrolytic BN crucibles has renewed interest in this refractory material. Miller and Austin (1973) have grown $SmCo_5$ crystals in BN crucibles sealed in Ta containers under He. Because $SmCo_5$ is a peritectic phase, the crystals were grown from a melt containing excess Sm at extremely low rates (1 mm h^{-1}). Large (~100 g) crystals were obtained with sub-grain misorientations of 0.5 to 1.5 degrees. Crystals of this and other RCo_5 phases, together with $R_2(Fe_xCo_{1-x})_{17}$ compounds have also been grown by Katayama and Shibata (1974) using BN-coated Al_2O_3 crucibles, again from rare earth-rich melts. They claimed that the coated crucible was not only less expensive than a pyrolytic BN crucible, but was actually superior in terms of being less reactive towards the melt. Fidler and Kronmuller (1979) also report the use of BN crucibles to grow $SmCo_5$ crystals from a 1 wt% excess Sm melt at varying rates (6–80 mm h^{-1}) to study the decomposition behaviour of this compound by examining the precipitation of the 2:7 and 2:17 phases. More recently Onuki et al. (1987) report the Bridgman growth of the heavy fermion compound $CeCu_6$ in a BN crucible, together with the observation of dHvA oscillations in single crystals of other members of the RCu_6 group (R ≡ La, Pr, Nd and Sm). The ternary compounds

$CeNi_2Ge_2$ and $CeCu_2Si_2$ have also been crystallised from stoichiometric melts in BN crucibles in a Bridgman furnace slowly cooled at $8°h^{-1}$ with a temperature gradient of 50°C maintained down the crucible (Kletowski 1983).

4.3.6. *Czochralski technique*

By far the most widely used and most rewarding method of liquid–solid single crystal growth of rare earth elements and, in particular, intermetallic compounds is pulling from the melt by the Czochralski technique. The essential features are shown in fig. 8. The melt is contained in some form of crucible, hot or cold, which is ideally hemi-spherical in shape to encourage thorough mixing. A monocrystalline seed rod of the same composition as the melt is dipped into the melt to establish a solid–liquid interface. If a seed rod is not available a W or Mo rod can be used. The seed rod is then slowly extracted, usually with simultaneous rotation, and a crystal is pulled through the melting point isotherm. The shape and size of the crystal is determined by the power input to the melt and the extraction rate. Rotation of the crucible as well as the seed rod is sometimes incorporated into the technique to ensure thorough mixing and to minimise thermal gradients existing in the melt which could affect the solid–liquid interface. The ability to closely control the solid–liquid interface, the fact that the interface is not in contact with the crucible, the opportunity for visual observation of the interface, and lack of physical constraint of the growing crystal are among the major advantages of this technique.

If no single crystal is available for a seed rod, then a polycrystalline rod or a pull rod of W or Mo may be used in the same way. In either case, a single

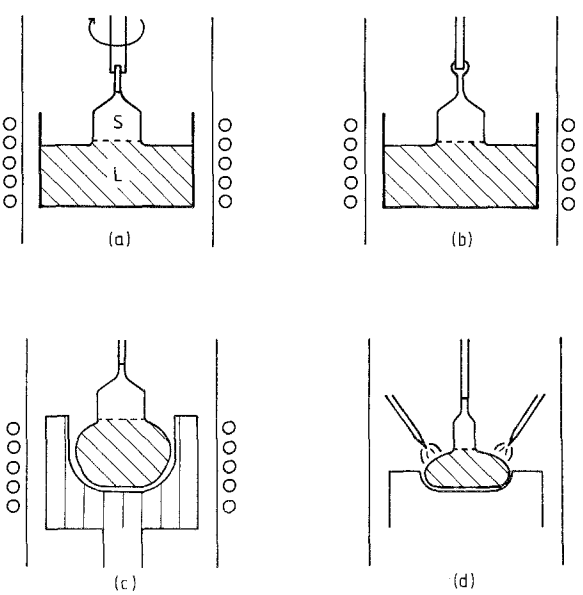

Fig. 8. Schematic representation of the Czochralski technique: (a) seeded growth from a hot crucible; (b) random orientation growth by 'necking'; (c) induction heated cold crucible, and (d) triarc cold crucible.

orientation grain is persuaded to grow from a polycrystalline matrix by reducing the diameter of the solidified material down to a thin 'neck'. On subsequently increasing the diameter, by fine adjustment of heat input and/or pulling speed, this single grain is propagated throughout the growing boule. The size of crystal can be varied by controlling the diameter, with the only restriction being the size of crucible which controls the volume of melt available and the maximum diameter of the boule. A typical boule grown in this way is shown in fig. 9.

Both hot and cold crucible versions of this technique have been used with effect, particularly for the growth of rare earth intermetallic compounds. As with other melt growth methods, both high vacuum and inert gas environments may be used. The method is capable of producing crystals having a high degree of crystal perfection but requires precise control of temperature and growth rate. Slight fluctuations in temperature can produce surface ridges on the grown crystal. The precise thermal conditions pertaining to Czochralski growth have been considered in detail by Rutter (1968) and Laudise (1970). The required temperature distribution in the melt is such that the melt is everywhere at a slightly higher temperature than at the solid–liquid isotherm, otherwise spurious nucleation will occur. The shape and position of the solid–liquid interface are all important in determining the success of the method. The interface can be concave, level, or convex to the melt surface depending on the particular growth conditions. A flat interface slightly above the melt level is usually considered desirable for good quality crystal growth. This requires isotherms in the solid and liquid to be nearly normal to the growth direction and implies good control over axial and radial heat flow. Factors such as depth of melt, speed of rotation, pull rate, after heating and latent heat of fusion are all significant in determining these isotherms. With no after heating the heat loss from the growing crystal is severe and the interface can

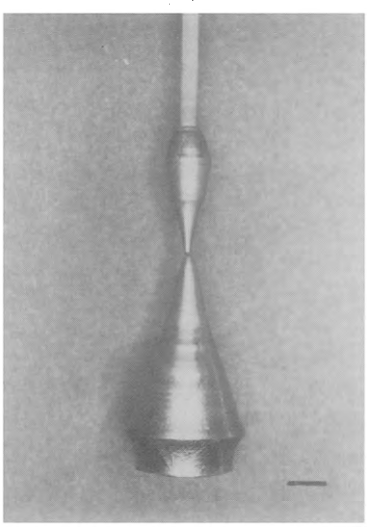

Fig. 9. RAl_2 boule grown from a W crucible with a W pull rod (marker = 5 mm).

become concave to the melt. However, if there is net heat flow to the crystal either by deliberate after heating or from the crucible wall as the melt level drops, then the interface is convex. Careful control therefore of both longitudinal and radial heat flow and a pull rate which is equal to the natural growth rate is required to maintain a flat interface. Radial thermal asymmetries can be minimised by rotation of the crystal and crucible. When reactivity with the crucible is a problem, as in the hot crucible version, the crucible and seed can be rotated at the same rate to achieve thermal symmetry without excessive stirring which would tend to accelerate crucible attack.

Some stirring is however desirable to prevent build up of impurities at the solid–liquid interface. Localised variations in growth rate due to temperature fluctuations arising from convection in the melt can produce bands of impurities in the growing crystal. Impurity content can also vary across the diameter of a boule. Solute rejected near the outer circumference is rapidly mixed into a larger volume of melt than at the centre thereby producing a higher impurity concentration at the core of the boule.

In practice, crystal growing experience based on experimentation counts for much in choosing suitable growth parameters for the wide variety of physical properties to be encountered in rare earth metals and compounds. There are three main versions of the Czochralski technique currently used throughout the rare earth crystal growing community. One employs a hot crucible, the other two use cold crucible containment.

Pulling from a hot crucible is still a widely used crystal growth method, particularly for rare earth intermetallic compounds. Early work on crystal pulling of Gd from a Ta crucible was described by Graham (1962), and a recent report by Winiarski (1985) of the growth of Ce single crystals using Ta crucibles shows that this refractory metal is still attracting attention as a crucible material. Crystal grains up to 2 mm of the γ-phase were obtained at room temperature, the grains being composed of mosaic blocks with spread $<1.5°$. However, W has become the main refractory metal crucible used for reasons of lower solubility already outlined. Godet et al. (1973) described the growth of $CeAl_2$ single crystals pulled from induction-heated W crucibles at 15 mm h^{-1}. A seed was cut from the first crystal which was then used to pull oriented boules. Various RAl_2 ($R \equiv$ La, Ce, Y and Tm) single crystals with random orientations have been grown in a similar manner by Beyss et al. (1980). These workers noted that the W content in the boules could be reduced by half (to ~280 ppm atomic) by polishing the internal walls of the crucible with SiC. Characterisation of their crystals was undertaken by means of X-rays, γ-rays and neutrons. Crystals of the ternary re-entrant superconducting series $La_{1-x}Ce_xAl_2$ grown by these workers have been used for dHvA measurements by Epstein et al. (1985). More recently, the present author has described the crystal growth and characterisation of other RAl_2 ($R \equiv$ Pr, Nd, Gd, Tb) phases also pulled from W crucibles (Abell et al. 1986). W levels of the order of 100 ppm atomic were noted and, in agreement with Beyss et al. (1980) it was observed that in general the crystal quality deteriorated down the length of the boule. Crystal growth of the RAl_2 series has now been extended to $R \equiv$ Dy,

Ho, Er and Tm using a high pressure chamber to suppress volatilisation (Abell 1988). A variation of this hot crucible approach was reported by Purwins (1970) who used Al_2O_3 crucibles lined with 30 μm W foil in a similar manner to his Bridgman experiments.

Various other reports exist of successful crystal growth from W crucibles. Sato et al. (1985) grew mixed (Ce, La)Al_2 crystals, and Leson et al. (1986) report the preparation of $TbAl_2$ and $ErAl_2$ crystals. Baberschke et al. (1978) grew $LaAl_2$ crystals from W crucibles of sufficient quality for dHvA oscillations to be observed, and similar observations have been made on a YAl_2 crystal (Seitz 1978) grown by Beyss et al. (1980). Recent interest in heavy fermion and mixed valence properties has led to attempts to grow single crystals of various intermetallic compounds exhibiting this behaviour. Onuki et al. (1986) have used W and BN crucibles from which to pull $CeCu_6$ crystals. From electrical resistivity measurements, they found that the 'best crystals' were those pulled from BN when compared with boules grown by other means such as Bridgman and float zone methods (Onuki et al. 1987). The same authors have grown the ternary compound $CeCu_2Si_2$ also from W and BN for magnetic and superconductivity measurements (Onuki et al. 1985).

Induction heated cold crucibles are now employed in a number of laboratories for Czochralski pulling. The early work by Hukin (1971) using his segmented design of cold crucible produced crystals of Y, Gd, Tb and their alloys up to 4 cc in volume. The growth of Pr, Nd and their alloys, and Eu crystals, from a similar crucible was reported by McEwen and Touborg (1973), who observed smaller mosaic spread in crystals grown in this manner than those produced by recrystallisation. Other methods such as float zone melting and SSE have largely taken over for crystal growth of the rare earth elements, but the technique has found wide application for the growth of rare earth intermetallic single crystals.

An early version of cold crucible melting and Czochralski pulling was described by Oliver et al. (1972). A side arm was introduced into a horizontal cold boat system passing through the turns of the RF coil. A boule was pulled directly from the melt in the cold boat with additional heating to the melt surface being achieved with the aid of two rod susceptors placed either side of the pulling rod. It was found particularly suitable for highly brittle materials such as YB_{66} which spontaneously shatter on cooling in the cold boat, but has not found much wider application.

Takke and Assmus (1980) describe the growth of $CePd_3$ from a levitated melt in a Hukin-type crucible where other methods such as float zone melting and tri-arc melting (see later in this section) had failed. Boules up to 7 cc have been grown at 3 mm h^{-1} but were found to be composed of several smaller crystallites. The boules were found to possess a Ce-rich layer (approx. 2 μm thick) on their outer as-grown surface, with the bulk of the crystal having the correct stoichiometry. The same workers have grown crystals of LaAg and CeAg under the same conditions (Takke et al. 1981). Several other reports exist of the application of this approach but with very few details. Thus, Gignoux et al. (1985b) report crystals of CeNi, and Chelkowski et al. (1985) list a series of RCu and

$R_{0.5}Gd_{0.5}Cu$ crystals pulled from a cold crucible. Givord et al. (1984) report the crystal growth from a cold crucible of the tetragonal ternary compound $Nd_2Fe_{14}B$, the matrix phase of a complex new permanent magnet material which is currently exciting a lot of interest. Full details of the successful crystal growth of this phase have recently been given by Swets (1986). Since this phase is peritectic the crystals were pulled from a non-stoichiometric melt. The first crystals pulled were random-oriented; these were then cut to provide seeds for subsequent growth of oriented boules. Pulling rates of $>5\,mm\,h^{-1}$ were found to result in the precipitation of a Nd-rich second phase, whereas boules pulled at $\sim 3\,mm\,h^{-1}$ showed no such defects.

This ternary phase and other members of the $R_2Fe_{14}B$ series have also been prepared by Czochralski pulling from a melt contained on a water cooled copper hearth in a tri-arc furnace (Koon et al. 1985). First described by Reed and Pollard (1968) the method now finds wide application in materials preparation and single crystal growth. Milstein et al. (1974) describe the growth of $Ho_{1-x}Tb_xFe_2$ crystals from 1% rare earth-rich melts using this method. Initial experiments with a stationary hearth were improved upon by rotating the hearth as well as the pull rod, and by using seed rods cut from the initial boules. Crystals up to 2 cc in size were pulled at $5\,mm\,h^{-1}$. Milstein (1978) subsequently compared these crystals with those pulled from an induction heated cold crucible and found the crystallinity to be superior in the tri-arc crystals. He examined various possible reasons for this discrepancy including the presence of surface dross in the induction melt which is dispersed in the tri-arc by the action of the arc, and the greater susceptibility to convection effects in the induction melt due to the exposure of the melt surface. However, the reference to after heating in the induction mode rendering the crystal more ductile and therefore liable to deform seems less likely to contribute to inferior crystallinity than fluctuations in the solid–liquid interface due to instabilities in the RF field.

Many binary and ternary intermetallics have been grown by the tri-arc method. Menovsky and Franse (1983) describe the successful application of this method to several intermetallics including $CeSi_2$, Ho_2Co_{17}, Ho_2Fe_{17}, $Ho_2Co_{14}Fe_3$, $Y_2(Co_{0.98}Ni_{0.02})_{17}$ and CePt. Pulling rates of 6–20 $mm\,h^{-1}$ with both pull rod and hearth rotation were used. This approach has also been successful for the ternary systems CeT_2Si_2 ($T \equiv Ni$, Pd, Pt) and $LaPd_2Si_2$, $LuPd_2Si_2$ and $LaRh_2Si_2$ (Menovsky et al. 1986). Their system can also be used for horizontal arc zone melting employing the rotating hearth and a specially designed mould. Sinnema et al. (1986) report crystals of Dy_2Co_{17} grown on the same equipment.

A list of references to single crystal growth of intermetallic compounds by the Czochralski method is given in table 7.

4.4. *Vapour–solid growth*

While condensation from the vapour is never going to yield large crystals it is nevertheless a feasible crystal growth technique for most of the rare earth metals. The method has the considerable advantage that it incorporates a purification

TABLE 7
Crystals grown by the Czochralski technique.

Crystal	Crucibles	References
Hot crucible		
Gd	Ta	Graham (1962)
γ-Ce	Ta	Winiarski (1985)
RAl_2	W	Godet et al. (1973), Baberschke et al. (1978), Beyss et al. (1980), Dobler et al. (1983), Sato et al. (1985), Abell et al. (1986), Leson et al. (1986)
	Al_2O_3/W	Purwins (1970)
$PrSn_3$		Knorr et al. (1985)
$CeCu_6$	W, BN	Onuki et al. (1986)
$CeCu_2Si_2$	W, BN	Onuki et al. (1985)
Induction cold crucible		
Single elements		Hukin (1971), McEwen and Touborg (1973)
LaAg, CeAg		Niksch et al. (1982), Takke et al. (1981)
CeNi		Gignoux et al. (1985b)
RCu		Chelkowski et al. (1985)
$HoCo_2$		Castets and Gignoux (1982)
RFe_2		Milstein (1978), Fuess et al. (1979), Givord et al. (1980a)
$CePd_3$		Takke and Assmus (1980)
YNi_3		Gignoux et al. (1980)
$GdCo_5$		Ballou et al. (1986a)
RNi_5		Butler et al. (1980), Aubert et al. (1981), Gignoux et al. (1981), Colinet and Pasturel (1983)
Dy_2Co_{17}, Ho_2Co_{17}		Christensen and Hazell (1980), Clausen and Lebech (1980)
R_2Fe_{17}		Christensen and Hazell (1980)
$Nd_2Fe_{14}B$, $Y_2Fe_{14}B$		Givord et al. (1984), Swets (1986)
Tri-arc cold crucible		
CePt		Menovsky and Franse (1983)
RCo_2		Rhyne et al. (1979), Koon and Rhyne (1981)
RFe_2		Milstein (1978), Rhyne et al. (1977), Savage et al. (1979), Williams (1977), Williams et al. (1980)
$CeSi_2$		Menovsky and Franse (1983)
$NdSn_3$		Hastings et al. (1980)
RB_4		Bressel et al. (1979)

TABLE 7 (continued)

Crystal	Crucible	References
Tri-arc cold crucible (cont'd)		
$GdCo_5$, $SmCo_5$		Milstein (1976)
$PrCu_5$		Andres et al. (1975)
R_2Co_{17}, Ho_2Fe_{17}		Menovsky and Franse (1983), Sinnema et al. (1986)
$R_2Fe_{14}B$		Koon et al. (1985)
RT_2Si_2		Menovsky et al. (1986)
$TbRh_2Si_2$		Quezel et al. (1984)

process into the technique. Sublimation and distillation are recognised refining routes but the methods have not been developed in terms of crystal growth, largely through the availability of more amenable procedures. Differential volatilisation rates make this an unlikely route for alloy or compound crystal growth. Attempts at a different approach for compounds using chemical as opposed to physical vapour deposition have been reported for $SmCo_5$ by Miller and Austin (1973). While appearing to have some potential for thin film preparation, this route did not prove promising for the growth of macro-crystals.

Schieber (1967) grew crystals of Sm, Eu, Tm and Yb from the vapour phase. The crystals of Eu, Tm and Yb were only a few mm long, but a Sm crystal up to 25 mm was grown; none were of particularly good quality. It was subsequently pointed out by Beaudry and Gschneidner (1978) that, for Sm at least, the deposition temperature was above the rhombohedral–hcp transition, which could account for poor crystallinity at room temperature. Indeed Shi and Fort (1986) have recently observed a high density of twinning in the rhombohedral phase. Cadieu and Douglass (1969) reported the growth of a 1 cc Gd crystal by a two-stage distillation-growth process. Gd distilled in a sealed Ta container onto a W rod was subsequently traversed in situ through a temperature gradient.

Winiarksi (1982) reports the growth of Yb crystals by vapour condensation from a Mo or Ta plate in a sealed silica ampoule under 0.1–0.3 atm argon. Both bcc and fcc crystals were obtained depending on the experimental conditions. With the Yb at 780°C and a temperature differential of 30°C, crystals grew on $\{110\}_{bcc}$ faces as rhombic dodecahedrons. On slow cooling, these transformed to the fcc phase with increased mosaic spread. However, with the temperature differential much greater, platelet crystals grew directly in the fcc phase on {111} faces up to 1.5 mm in size. Some evidence of a very slow transformation to the hcp phase at room temperature was observed. More recently Winiarski (1985) describes similar experiments on Ce, using a Ta crucible sealed under vacuum. The crystals were grown in the δ (bcc) temperature regime and formed on {100} faces with dimensions up to 0.1 mm. They were found to be in the γ (fcc) phase at room temperature, the platelets usually comprising two or three mosaic blocks.

An interesting recent development in the area of vapour–solid crystal growth

has arisen out of the current interest in the magnetic properties of rare earth superlattice structures. Coherent single crystal layers are being grown by UHV metal molecular beam epitaxy on sapphire substrates with a Nb buffer layer. Bulk magnetisation measurements have been reported on samples consisting of 40Å layers of Dy and Y (Sinha et al. 1986) and similar Gd–Y alloy layers (Kwo et al. 1986) which have been prepared by this technique. Recent neutron diffraction experiments on the Dy/Y layers have also been described (Rhyne et al. 1986). While not producing crystals on a macroscopic scale, this technique has allowed the new and interesting properties of these multi-layer structures to be investigated.

A crystal growth process which is receiving more attention for certain compounds is mineralisation which, although involving a complex series of mechanisms, certainly includes a vapour–solid stage. It is not intended to discuss this route here; but small crystals of many rare earth pnictides and chalcogenides have been grown in this manner.

5. Specimen fabrication

Many physical property measurements require oriented single crystal specimens with specific geometries. These requirements necessitate careful cutting and preparation stages using standard X-ray and slitting and/or spark erosion techniques. Beaudry and Gschneidner (1978) have discussed handling and preparative routes for the rare earth elements and many of these apply equally well to intermetallic compounds. The major difference, of course, is the relatively brittle nature of many of the compounds which means that spark-erosion methods are, in general, to be preferred to mechanical ones. Complicated geometries such as discs, spheres, cylinders, and parallel oriented faces are more easily achieved by spark erosion and usually impart less damage to the crystal.

However, spark erosion does yield an irregular surface on a microscopic scale, and if flat shiny surfaces are required there is no alternative but to resort to mechanical lapping and polishing. Care must be taken in polishing rare earth-based metals due to the affinity of rare earths for water-based solutions; oxidation can occur and in some cases hydride formation has been observed (Verhoeven et al. 1985). Non-aqueous solutions are to be preferred wherever possible. This process inevitably leaves residual strain in the surface which may not be a problem for many experimental measurements. However, where such surface strain could be significant, a recent development in the preparation of specimens (Abell et al. 1983a) has involved adapting an ion-beam thinning technique to the production of flat strain-free surfaces. Electron channelling patterns generated in the SEM from such surfaces have been used to monitor the improvement in surface crystallinity produced by this technique (Pelegrini et al. 1982). The significance to physical property interpretation has been demonstrated by the resolution of a surface anisotropy mode in the ferromagnetic resonance behaviour in some RAl_2 intermetallic compounds (Pelegrini et al. 1984). This ion-beam

planing approach may have potentially wider application for compounds, where the more conventional chemical polish or electro-polish route to strain-free surfaces is hindered by lack of detailed information on appropriate reactants and polishing parameters.

The shapes, sizes and qualities of crystals for particular measurements vary widely. Spirlet and Vogt (1984) have recently listed the specimen requirements for many experiments with regard to actinide elements and compounds, and similar criteria apply to rare earth-based specimens. The most demanding requirements, not only in terms of geometry but also chemical and structural purity are often for Fermi-surface studies, where high purity crystal spheres, fabricated from SSE crystals, are usually employed. Minimising demagnetising fields by use of large aspect ratio discs (approximating to ellipsoids) is a major consideration in many magnetic measurements. The largest crystals are usually required by neutron inelastic scattering experiments, and if one such crystal is not available, a composite made up of several aligned individual crystals can often suffice.

X-ray and neutron topographical measurements and TEM domain observations are extremely sensitive to crystal quality and residual strains, and very careful preparation and handling of specimens is required. For the elements, the best results have been obtained on SSE crystals (Chapman et al. 1981, Clark et al. 1982) and for what little work has been done on compounds, a combination of anneals and careful fabrication has resulted in some success (Goddard et al. 1982, Lord et al. 1982).

6. Characterisation

Early physical property measurements on the elements, particularly at low temperatures, using crystals available at that time were often found to differ markedly from those subsequently obtained on better quality material. Mass spectrometric analysis showed that many physical properties were sensitive to impurities, and crystallinity is clearly of paramount importance for topographic and domain studies. The crystal grower is always striving to improve the quality both chemical and structural, of the crystals that are grown, and physical property measurements on well-characterised crystals remain in the optimum interest of both the materials scientist and physicist.

Initial assessment of the outcome of a crystal growth experiment is usually carried out by Laue X-ray diffraction. Chemical etching (when possible) can reveal grain boundaries but the extent of a single grain is usually confirmed by XRD. The Laue technique can also provide an indication of crystal quality from the shape and nature of the individual spots. Often this is as far as characterisation proceeds, particularly where the intermetallic compounds are concerned.

Various other techniques are available to assess the quality of crystals. Residual resistance ratio provides a useful criterion by which overall chemical purity can be quantified and is particularly employed for the highest quality rare earth element crystals; values up to 1000 were reported by Jones et al. (1982). Similar

measurements on compounds have been reported; by comparison, values of 15 and 27 have been measured on $LaAl_2$ and YAl_2 (Seitz 1978) and 70 for $GdIn_3$ (Kletowski et al. 1985b). Crystallinity is best monitored by mosaic spread measurements using neutron, X-ray or γ-ray rocking curve experiments. Neutrons offer the distinct advantage of assessing the whole crystal. All three methods were used by Beyss et al. (1980) to assess some RAl_2 compounds, and similar measurements on these phases were reported by Abell et al. (1986). Typical mosaic spreads were found to be 0.1–0.5°. The availability of small good quality SSE crystals of the elements (mosaic spread ~0.1°) have allowed detailed neutron diffraction experiments to be performed (e.g. Baruchel et al. 1983). Milstein (1978) used neutron rocking curves to compare the crystallinity of Czochralski crystals grown by induction or tri-arc melting. He found that induction-grown crystals can have mosaic spreads up to ten times that of tri-arc grown crystals, and considered the thermal and thermodynamic factors which might explain this difference.

Conventional metallographic examination together with electron microprobe, TEM, XRF, SEM with energy and wavelength dispersive analysis can provide information on inclusions, defects, stoichiometry and phase distribution in the intermetallic compounds. An SEM operating in the back scattered electron mode can be a particularly powerful imaging technique for phase analysis. Auger and energy loss spectroscopy are also being employed to provide detailed analytical data (Verhoeven et al. 1985). Even if a crystal is not perfect a knowledge of the nature of the defects can facilitate the interpretation of a particular physical property. A striking example has been provided by the identification of a fine crystallographic array of oxide precipitates in an otherwise good quality ErZn crystal which allowed the anomalous magnetostriction behaviour to be interpreted in terms of an anisotropic domain distribution (Abell et al. 1979a). A similar domain distribution has been deduced from the magnetostrictive behaviour of some RAl_2 crystals (Abell et al. 1979b; 1983b) and the good crystallinity of these crystals (Goddard et al. 1982) has allowed domain observations to be made by Synchrotron X-ray topography in an attempt to understand this anisotropy (Clark et al. 1985).

Acknowledgements

The author wishes to thank Dr. D. Fort for reading the manuscript and for allowing access to his review of solid state electrotransport prior to publication, and to Mr. S.D. Sutton for his help with compiling the references.

Appendix

Crystals reported with no growth details.

Crystal	References
Ce	Rosina et al. (1985)
LaAg	Creuzet et al. (1982)
CeMg	Boulliot et al. (1985)
CeNi	Creuzet et al. (1985)
DyCu	Aleonard et al. (1984)
HoNi	Sato et al. (1983)
La_2Co_3	Gignoux et al. (1985c)
$CeCu_2$, $CeCu_6$	Soda et al. (1985)
$PrCu_2$	Ott et al. (1978)
$CeGa_2$	Burlet et al. (1987)
$TbGa_2$	Asmat et al. (1977)
$HoCo_2$	Castets et al. (1980), Rhyne et al. (1979)
$CeSn_3$	Blashko et al. (1984)
$CeSn_3$, Ce_2Sn_5, Ce_3Sn_7	Boucherle et al. (1987)
$NdIn_3$, $TmGa_3$	Czopnik et al. (1985)
$GdIn_3$	Kletowski et al. (1985b)
$ErAl_3$	Weber (1977)
Tb_2Co_7	Andreev et al. (1982)
$TbNi_5$	Gignoux and Rhyne (1986)
$ErNi_5$	Escudier et al. (1977)
$DyCo_5$	Tsushima and Ohokoshi (1983)
$HoCo_{5.6}$	DeCrop et al. (1983)
R_2Co_{17}	Deryagin and Kudrevatykh (1975), Ballou et al. (1986b)
$CeNi_{0.8}Pt_{0.2}$	Fillion et al. (1987)
$CePt_2Si_2$	Hiebl and Rogl (1985)
$SmCo_{3.5}Cu_{1.5}$	Uehara (1983)
$TbMn_2Si_2$	Shigeoka et al. (1986)

References

Abell, J.S., 1988, to be published.
Abell, J.S., A. del Moral and E.W. Lee, 1979a, Philos. Mag. B **39**, 197.
Abell, J.S., P. Hendy, E.W. Lee and K. Al-Rawi, 1979b, J. Phys. C **12**, 3551.
Abell, J.S., P.M. Marquis and D.W. Jones, 1983a, J. Mater. Sci. **18**, 299.
Abell, J.S., A. del Moral, R.M. Ibarra and E.W. Lee, 1983b, J. Phys. C **16**, 769.
Abell, J.S., D.W. Jones and E.W. Lee, 1986, J. Less-Common Met. **115**, 331.
Achiwa, N., and S. Kawano, 1973, J. Phys. Soc. Jpn. **35**, 303.
Aleonard, R., and P. Morin, 1984, J. Magn. & Magn. Mater. **42**, 151.
Aleonard, R., and P. Morin, 1985, J. Magn. & Magn. Mater. **50**, 128.
Aleonard, R., P. Morin, J. Pierre and D. Schmitt, 1976, J. Phys. F **6**, 1361.
Aleonard, R., P. Morin and J. Rouchy, 1984, J. Magn. & Magn. Mater. **46**, 233.
Andreev, A.V., E.N. Tarasov, A.V. Deryagin and S.M. Zadvorkin, 1982, Phys. Status Solidi a **71**, K245.
Andres, K., E. Bucher, P.H. Schmidt, J.P. Maita and S. Darack, 1975, Phys. Rev. B **11**, 4364.
Apostolov, A.V., M.T. Mikhov, T.L. Mydlarts, S.A. Nikitkin, N.A. Scheludko, O.P. Tchistyakov and O.P. Terekhova, 1986, Phys. Status Solidi a **96**, 265.
Asmat, H., D. Gignoux and R. Lemaire, 1977, Physica B **86–88**, 185.
Assmus, W., M. Herrmann, U. Rauchschwalbe,

S. Riegel, W. Lieke, H. Spille, S. Horn, G. Weber, F. Steglich and G. Cordier, 1984, Phys. Rev. Lett. **52**, 469.
Aubert, G., D. Gignoux, B. Hennion, B. Michelutti and A. Nait Saada, 1981, Solid State Commun. **37**, 741.
Aust, K.T., 1968, in: Techniques of Metals Research, ed. R.F. Bunshah (Wiley, New York) p. 991.
Baberschke, K., H.J. Jenrich and J. Nagel, 1978, Inst. Phys. Conf. Ser. **37**, 161.
Bagguley, D.M.S., and F.A. Howe, 1986, J. Magn. & Magn. Mater. **58**, 179.
Bagguley, D.M.S., J.P. Partington, J.A. Robertson and R.C. Woods, 1981, J. Magn. & Magn. Mater. **22**, 281.
Ballou, R., J. Deportes, B. Gorges, R. Lemaire and J.C. Ousset, 1986a, J. Magn. & Magn. Mater. **54–57**, 465.
Ballou, R., D. Gignoux, R. Lemaire, R. Mendia-Monterroso and J. Schweizer, 1986b, J. Magn. & Magn. Mater. **54–57**, 499.
Barandiaran, J.M., D. Gignoux and D. Schmitt, 1986, Solid State Commun. **57**, 941.
Barbara, B., M.F. Rossignol, J.X. Boucherle and C. Vettier, 1980, Phys. Rev. Lett. **45**, 938.
Baruchel, J., A. Drillat, D. Fort, D.W. Jones, S.B. Palmer and M. Schlenker, 1983, J. Magn. & Magn. Mater. **31–34**, 183.
Beaudry, B.J., and K.A. Gschneidner Jr, 1978, in: Handbook on the Physics and Chemistry of Rare Earths, Vol. 1, eds K.A. Gschneidner Jr and L. Eyring (North-Holland, Amsterdam) p. 173.
Behrendt, D.R., S. Legvold and F.H. Spedding, 1958, Phys. Rev. **109**, 1544.
Benoit, A., J.X. Boucherle, J. Flouquet, J. Sakurai and J. Schweizer, 1985, J. Magn. & Magn. Mater. **47&48**, 251.
Beyss, M., J.M. Welter and T. Kaiser, 1980, J. Cryst. Growth **50**, 419.
Blaettner, H.E., K.J. Strnat and A.E. Ray, 1978, in: Rare Earths in Modern Science and Technology, eds G.J. McCarthy and J.J. Rhyne (Plenum Press, New York) p. 421.
Blashko, O., G. Krexner, L. Pintschovius and W. Assmus, 1984, Solid State Commun. **51**, 971.
Boucherle, J.X., and J. Schweizer, 1981, J. Magn. & Magn. Mater. **24**, 308.
Boucherle, J.X., G. Fillion, J. Flouquet, F. Givord, P. Lejay and J. Schweizer, 1986, J. Magn. & Magn. Mater. **54–57**, 421.
Boucherle, J.X., F. Givord, P. Lejay, J. Schweizer and A. Stunault, 1987, J. Magn. & Magn. Mater. **63–64**, 575.
Bouillot, J., R.M. Galera and J. Pierre, 1985, Physica B **130**, 391.
Boulet, R.M., J.-P. Jan and H.L. Skriver, 1982, J. Phys. F **12**, 293.
Bredl, C.D., H. Spille, U. Rauchschwalbe, W. Luke, F. Steglich, G. Cordier, W. Assmus, H. Herrmann and J. Aarts, 1983, J. Magn. & Magn. Mater. **31–34**, 373.
Bressel, B., B. Chevalier, J.E. Etourneau and P. Hagenmuller, 1979, J. Cryst. Growth **47**, 429.
Bridgman, P.W., 1925, Proc. Am. Acad. Arts & Sci. **60**, 305.
Bunshah, R.F., 1968, Techniques of Metals Research (Wiley, New York).
Burlet, P., M.A. Fremy, D. Gignoux, G. Lapertot, S. Quezel, L.P. Regnault, J. Rossat-Mignod and E. Roudaut, 1987, J. Magn. & Magn. Mater. **63–64**, 34.
Buschow, K.H.J., 1977, Rep. Prog. Phys. **40**, 1123.
Buschow, K.H.J., 1979, Rep. Prog. Phys. **42**, 1285.
Butler, B., D. Givord, F. Givord and S.B. Palmer, 1980, J. Phys. C **13**, L743.
Cadieu, F.J., and D.H. Douglass, 1969, J. Appl. Phys. **40**, 2376.
Carlson, O.N., F.A. Schmidt and W.M. Paulson, 1964, ASM Trans. Q. **57**, 356.
Carlson, O.N., F.A. Schmidt and D.T. Peterson, 1975, J. Less-Common Met. **39**, 277.
Castets, A., and D. Gignoux, 1982, Phys. Rev. B **25**, 337.
Castets, A., D. Gignoux and B. Hennion, 1980, J. Magn. & Magn. Mater. **15–18**, 375.
Chapman, J.N., G.R. Morrison, D. Fort and D.W. Jones, 1981, J. Magn. & Magn. Mater. **22**, 212.
Chelkowski, A., E. Talik, J. Heimann and J. Szade, 1985, Physica B **130**, 231.
Chevalier, B., J. Etourneau, J.E. Greedan, J.M.D. Coey and A. Maaroufi, 1985, J. Less-Common Met. **111**, 171.
Christensen, A., and R.G. Hazell, 1980, Acta Chem. Scand. A **34**, 455.
Clark, G.F., B.K. Tanner, S.P. Farrant and D.W. Jones, 1982, J. Magn. & Magn. Mater. **29**, 71.
Clark, G.F., B.K. Tanner and J.S. Abell, 1985, J. Magn. & Magn. Mater. **49**, 317.
Clausen, K.N., and B. Lebech, 1980, J. Magn. & Magn. Mater. **15–18**, 347.
Colinet, C., and A. Pasturel, 1983, Phys. Status Solidi a **80**, K75.
Cordier, G., E. Czech, H. Schafer and P. Woll, 1985, J. Less-Common Met. **110**, 327.
Corner, W.D., and J. Welford, 1978, J. Phys. F **8**, 2203.
Corner, W.D., D.M. Paige, R.D. Hawkins, D. Fort and D.W. Jones, 1985, J. Magn. & Magn. Mater. **51**, 89.
Creuzet, G., I.A. Campbell and H.E. Hoenig, 1982, Solid State Commun. **44**, 733.
Creuzet, G., A. Fert, C. Gaonach and D. Gignoux, 1985, Physica B **130**, 138.
Czopnik, A., N. Iliew, B. Stalinski, C. Bazan, H. Madge and R. Pott, 1985, Physica B **130**, 259.
Daud, A., K.A. McEwen and J.C. Picoche, 1985, Physica B **130**, 233.
DeCrop, B., J. Deportes and R. Lemaire, 1983, J. Less-Common Met. **94**, 199.
Dennison, D.H., M.J. Tschetter and K.A. Gschneidner Jr, 1966, J. Less-Common Met. **11**, 423.
Deportes, J., B. Kebe and R. Lemaire, 1986, J. Magn. & Magn. Mater. **54–57**, 1089.
Deryagin, A.V., and N.V. Kudrevatykh, 1975, Phys. Status Solidi a **30**, K129.
Dobler, U., K. Baberschke and S.E. Barnes, 1983, Phys. Rev. B **27**, 6593.

Dommann, A., F. Hulliger, H.R. Ott and V. Gramlich, 1985, J. Less-Common Met. **110**, 331.
Doukoure, M., and D. Gignoux, 1982, J. Magn. & Magn. Mater. **30**, 111.
Drabble, J.R., and A.W. Palmer, 1966, J. Appl. Phys. **37**, 1778.
Drewes, W., A. Leson, W. Schelp, K. Bomken and H.-G. Purwins, 1985, Physica B **130**, 213.
Drewes, W., W. Schelp, A. Leson and H.-G. Purwins, 1986, J. Magn. & Magn. Mater. **54–57**, 476.
Drzazga, Z., 1983, Phys. Status Solidi a **76**, 647.
Drzazga, Z., 1985, Physica B **130**, 305.
Epstein, S.I., R.J. Higgins, D.H. Lowndes, F. Steglich and J.F. Smith, 1985, Phys. Rev. B **32**, 5683.
Escudier, P., D. Gignoux, D. Givord, R. Lemaire and A.P. Murani, 1977, Physica B **86–88**, 197.
Fidler, J., and H. Kronmuller, 1979, Phys. Status Solidi a **56**, 545.
Fillion, G., D. Gignoux, F. Givord and R. Lemaire, 1984, J. Magn. & Magn. Mater. **44**, 173.
Fillion, G., M.A. Fremy, D. Gignoux, J.C. Gomez-Sal and B. Gorges, 1987, J. Magn. & Magn. Mater. **63–64**, 117.
Flachbart, K., M. Reiffers, S. Janos, Y.B. Paderno and V.I. Lazorenko, 1982, J. Less-Common Met. **88**, L3, L11.
Fort, D., 1986, private communication.
Fort, D., 1987, J. Less-Common Met. **134**, 45.
Fort, D., B.J. Beaudry, D.W. Jones and K.A. Gschneidner Jr, 1980, in: Rare Earths in Modern Science and Technology, Vol. 2, eds G.J. McCarthy, J.J. Rhyne and H.B. Silber (Plenum Press, New York) p. 33.
Fort, D., D.W. Jones, B.J. Beaudry and K.A. Gschneidner Jr, 1981, J. Less-Common Met. **81**, 273.
Fuess, H., D. Givord, A.R. Gregory and J. Schweizer, 1979, J. Appl. Phys. **50**, 2000.
Fujii, H., T. Okamoto, T. Shigeoka and N. Iwata, 1985, Solid State Commun. **53**, 715.
Georges, R., J. Schweizer and J. Yakinthos, 1975, J. Phys. & Chem. Solids **36**, 415.
Gignoux, D., and D. Givord, 1983, J. Magn. & Magn. Mater. **31–34**, 217.
Gignoux, D., and R. Lemaire, 1974, Solid State Commun. **14**, 877.
Gignoux, D., and J.J. Rhyne, 1986, J. Magn. & Magn. Mater. **54–57**, 1179.
Gignoux, D., F. Givord and R. Lemaire, 1975, Phys. Rev. B **12**, 3878.
Gignoux, D., D. Givord, F. Givord, W.C. Koehler and R.M. Moon, 1976a, Phys. Rev. B **14**, 162.
Gignoux, D., D. Givord and A. del Moral, 1976b, Solid State Commun. **19**, 891.
Gignoux, D., F. Givord, R. Perrier de la Bathie and F. Sayetat, 1979, J. Phys. F **9**, 763.
Gignoux, D., R. Lemaire, P. Molho and F. Tasset, 1980, J. Magn. & Magn. Mater. **21**, 307.
Gignoux, D., D. Givord, R. Lemaire, A. Nait Saada and A. del Moral, 1981, J. Magn. & Magn. Mater. **23**, 274.
Gignoux, D., J.C. Gomez-Sal and D. Paccard, 1982, Solid State Commun. **44**, 695.
Gignoux, D., F. Givord, R. Lemaire and F. Tasset, 1985a, J. Magn. & Magn. Mater. **50**, 369.
Gignoux, D., F. Givord, B. Hennion, Y. Ishikawa and R. Lemaire, 1985b, J. Magn. & Magn. Mater. **52**, 421.
Gignoux, D., R. Lemaire, R. Mendia-Monterroso, J.M. Moreau and J. Schweizer, 1985c, Physica B **130**, 376.
Gilman, J.J., ed., 1963, in: The Art and Science of Growing Crystals (Wiley, New York).
Giraud, M., and P. Morin, 1986, J. Magn. & Magn. Mater. **58**, 135.
Giraud, M., P. Morin, J. Rouchy, D. Schmitt and E. du Tremolet de Lacheisserie, 1983, J. Magn. & Magn. Mater. **37**, 83.
Giraud, M., P. Morin, J. Rouchy and D. Schmitt, 1986, J. Magn. & Magn. Mater. **59**, 255.
Givord, D., J. Laforest and J. Schweizer, 1979, J. Appl. Phys. **50**, 2008.
Givord, D., A.R. Gregory and J. Schweizer, 1980a, J. Magn. & Magn. Mater. **15–18**, 293.
Givord, D., P. Morin and D. Schmitt, 1980b, J. Magn. & Magn. Mater. **15–18**, 525.
Givord, D., H.S. Li and R. Perrier de la Bathie, 1984, Solid State Commun. **51**, 857.
Goddard, P.A., G.F. Clark, W.D. Corner, B.K. Tanner, J.S. Abell, D. Fort and D.W. Jones, 1982, J. Magn. & Magn. Mater. **29**, 39.
Godet, M., E. Walker and H.-G. Purwins, 1973, J. Less-Common Met. **30**, 301.
Graham Jr, C.D., 1962, J. Phys. Soc. Jpn. **17**, 1310.
Green, R.W., S. Legvold and F.H. Spedding, 1961, Phys. Rev. **122**, 827.
Gruhl, H., and K. Winzer, 1986, Solid State Commun. **57**, 67.
Gschneidner Jr, K.A., and L. Eyring, eds, 1989, Handbook on the Physics and Chemistry of Rare Earths, Vol. 12 (North-Holland, Amsterdam).
Hall, P.M., S. Legvold and F.H. Spedding, 1960, Phys. Rev. **177**, 971.
Hamaguchi, Y., H. Betsuyaku and S. Funahashi, 1980, J. Magn. & Magn. Mater. **15–18**, 377.
Hansen, P., and B. Lebech, 1976, J. Phys. F **6**, 2179.
Hastings, J.M., L.M. Corliss, W. Kunnmann, R. Thomas, R.J. Begum and P. Bak, 1980, Phys. Rev. B **22**, 1327.
Hiebl, K., and P. Rogl, 1985, J. Magn. & Magn. Mater. **50**, 39.
Hirosawa, S., and M. Sagawa, 1985, Solid State Commun. **54**, 335.
Hiroyoshi, H., H. Yamauchi, Y. Yamaguchi, H. Yamamoto, Y. Nakagawa and M. Sagawa, 1985, Solid State Commun. **54**, 41.
Hukin, D.A., 1971, Report No. 24/71 (Clarendon Laboratory, Oxford, England).
Hukin, D.A., and D.W. Jones, 1976, Proc. 12th Rare Earth Research Conf., p. 891.
Hurle, D.T.J., 1962, Prog. Mater. Sci. **10**, 79.
Inoue, T., D.M. Sparlin and W.J. James, 1978, in: Rare Earths in Modern Science and Tech-

nology, eds G.J. McCarthy and J.J. Rhyne (Plenum Press, New York) p. 415.
Isikawa, Y., K. Higashi, T. Miyazaki and K. Sato, 1983, J. Magn. & Magn. Mater. **31–34**, 1057.
Isikawa, Y., K. Mori, K. Ueno, K. Sato and K. Maezawa, 1985, J. Magn. & Magn. Mater. **52**, 434.
Ito, T., 1984, Phys. Rev. B **29**, 6276.
Iwata, N., H. Fujii and T. Okamoto, 1985, J. Magn. & Magn. Mater. **46**, 312.
Iwata, N., T. Ikeda, T. Shigeoka, H. Fujii and T. Okamoto, 1986, J. Magn. & Magn. Mater. **54–57**, 481.
Johanson, W.R., G.W. Crabtree, A.S. Edelstein and O.D. McMasters, 1981, Phys. Rev. Lett. **46**, 504.
Johnson, P.E., W.J. James and R. Lemaire, 1978, in: Rare Earths in Modern Science and Technology, eds G.J. McCarthy and J.J. Rhyne (Plenum Press, New York) p. 395.
Jones, D.W., 1974, in: Crystal Growth, Vol. 1, ed. C.H.L. Goodman (Plenum Press, New York) p. 233.
Jones, D.W., S.P. Farrant, D. Fort and R.G. Jordan, 1978a, Inst. Phys. Conf. Ser. **37**, 11.
Jones, D.W., D. Fort and D.A. Hukin, 1978b, in: Rare Earths in Modern Science and Technology, eds G.J. McCarthy and J.J. Rhyne (Plenum Press, New York) p. 309.
Jones, D.W., J.S. Abell, D. Fort and J.K. Hulbert, 1982, J. Magn. & Magn. Mater. **29**, 20.
Jordan, R.G., 1974, Contemp. Phys. **15**, 375.
Jordan, R.G., D.W. Jones and P.G. Mattocks, 1974a, J. Less-Common Met. **34**, 25.
Jordan, R.G., D.W. Jones and M.G. Hall, 1974b, J. Cryst. Growth **24&25**, 568.
Jordan, R.G., D.W. Jones and V.J. Hems, 1975, J. Less-Common Met. **42**, 101.
Kaplan, N., and D.L. Williams, 1980, Phys. Rev. B **21**, 899.
Kasaya, M., B. Liu, M. Sera, T. Kasuya, D. Endoh, T. Goto and T. Fujimura, 1985, J. Magn. & Magn. Mater. **52**, 289.
Kasaya, M., S. Nakamura, T. Mitsuzuka and T. Kasuya, 1986, Presented at the Int. Conf. on Anomalous Rare Earths and Actinides, Grenoble.
Katayama, T., and T. Shibata, 1974, J. Cryst. Growth **24&25**, 396.
Katayama, T., and T. Shibata, 1981, J. Magn. & Magn. Mater. **23**, 173.
Kawakami, M., S. Kunii, T. Komatsubara and T. Kasuya, 1980, Solid State Commun. **36**, 435.
Kawano, S., and N. Achiwa, 1983, J. Magn. & Magn. Mater. **31–34**, 185.
Keller, G., and J.M. Dixon, 1976, J. Phys. F **6**, 819.
Khotamian, D., C. Stassis and B.J. Beaudry, 1981, Phys. Rev. B **23**, 624.
Kirchmayr, H.R., and C.A. Poldy, 1979, in: Handbook on the Physics and Chemistry of Rare Earths, Vol. 2, eds K.A. Gschneidner Jr and L. Eyring (North-Holland, Amsterdam) p. 55.
Kitai, T., H. Fujii, T. Okamoto and Y. Hashimoto, 1984, Solid State Commun. **52**, 407.
Kitazawa, H., I. Oguro, M. Hirai, Y. Kondo, T. Suzuki and T. Kasuya, 1985, J. Magn. & Magn. Mater. **47&48**, 251.
Kjems, J.K., P. Touborg and H. de Jong, 1979, J. Magn. & Magn. Mater. **14**, 277.
Klein, H.P., A. Menth and R.S. Perkins, 1975, Physica B **80**, 153.
Kletowski, Z., 1983, J. Less-Common Met. **95**, 127.
Kletowski, Z., N. Iliew, Z. Henkie and B. Stalinski, 1985a, J. Less-Common Met. **110**, 235.
Kletowski, Z., N. Iliew, B. Stalinski and M. Glinski, 1985b, Physica B **130**, 84.
Knorr, K., F. Feile, J.K. Kjems and W. Assmus, 1985, J. Magn. & Magn. Mater. **52**, 323.
Koon, N.C., and J.J. Rhyne, 1981, Phys. Rev. B **23**, 207.
Koon, N.C., B.N. Das, M. Rubinstein and J. Tyson, 1985, J. Appl. Phys. **57**, 4091.
Koskenmaki, D.C., and K.A. Gschneidner Jr, 1978, in: Handbook on the Physics and Chemistry of Rare Earths, Vol. 1, eds K.A. Gschneidner Jr and L. Eyring (North-Holland, Amsterdam) p. 337.
Kropp, H., E. Dormann, U. Köbler and W. Assmus, 1984, J. Phys. F **14**, 2177.
Kwo, J., E.M. Gyorgy, F.J. DiSalvo, M. Hong, Y. Yafet and D.B. McWhan, 1986, J. Magn. & Magn. Mater. **54–57**, 771.
Laudise, R.A., 1970, Growth of Single Crystals (Prentice-Hall, Englewood Cliffs, NJ).
Laudise, R.A., 1979, The Growth of Single Crystals (Prentice-Hall, Englewood Cliffs, NJ).
Lawrence, J.M., and S.M. Shapiro, 1980, Phys. Rev. B **22**, 4379.
Leson, A., W. Schelp, W. Drewes and H.-G. Purwins, 1986, J. Magn. & Magn. Mater. **54–57**, 473.
Levin, R., A. Grayevsky, D. Shaltiel, V. Zevin and D. Davidov, 1979, Phys. Rev. B **20**, 2624.
Levin, R., D. Davidov, A. Grayevsky, D. Shaltiel and V. Zevin, 1980, J. Phys. F **10**, 967.
Lord, D.G., H.T. Savage and R.G. Rosemeier, 1982, J. Magn. & Magn. Mater. **29**, 137.
Maeda, H., 1978, Phys. Status Solidi a **45**, 445.
McEwen, K.A., and P. Touborg, 1973, J. Phys. F **3**, 1903.
McEwen, K.A., B. Lebech and D. Fort, 1986, J. Magn. & Magn. Mater. **54–57**, 457.
McMasters, O.D., 1984, private communication.
McMasters, O.D., G.E. Holland and K.A. Gschneidner Jr, 1978, J. Cryst. Growth **43**, 577.
McMasters, O.D., J.D. Verhoeven and E.D. Gibson, 1986, J. Magn. & Magn. Mater. **54–57**, 849.
Menovsky, A.A., and J.J.M. Franse, 1983, J. Cryst. Growth **65**, 286.
Menovsky, A.A., C.E. Snel, T.J. Gortenmulder, H.J. Tan and T.T.M. Palstra, 1986, J. Cryst. Growth **74**, 231.

Meyer-Liautard, F., C.H. Allibert and J.M. Moreau, 1985, J. Less-Common Met. **110**, 81.
Miller, J.F., and A.E. Austin, 1973, J. Cryst. Growth **18**, 7.
Milstein, J.B., 1976, Proc. 12th Rare Earth Res. Conf., p. 904.
Milstein, J.B., 1978, in: Rare Earths in Modern Science and Technology, eds G.J. McCarthy and J.J. Rhyne (Plenum Press, New York) p. 315.
Milstein, J.B., N.C. Koon, L.R. Johnson and C.M. Williams, 1974, Mater. Res. Bull. **9**, 1617.
Morin, P., 1984, Phys. Rev. B **29**, 1425.
Morin, P., and D. Schmitt, 1982, J. Magn. & Magn. Mater. **28**, 188.
Morin, P., J. Rouchy and E. du Tremolet de Lacheisserie, 1977, Phys. Rev. B **16**, 3182.
Morin, P., J. Pierre, D. Schmitt and D. Givord, 1978, Phys. Lett. A **65**, 156.
Morin, P., D. Schmitt and C. Vettier, 1981, J. Phys. F **11**, 1487.
Morin, P., D. Schmitt and C. Vettier, 1984, J. Magn. & Magn. Mater. **40**, 287.
Nigh, H.E., 1963, J. Appl. Phys. **34**, 3323.
Niksch, M., B. Luthi, W. Assmus and J. Kubler, 1982, J. Magn. & Magn. Mater. **28**, 243.
Ohkoshi, N., H. Kobayashi, T. Katayama, M. Hirano and T. Tsushima, 1977, Physica B **86–88**, 195.
Oliver, D.W., G.D. Brower and F.H. Horn, 1972, J. Cryst. Growth **12**, 125.
Onuki, Y., T. Hirai, T. Komatsubara, S. Takayanagi, A. Sumiyama, A. Furukawa, Y. Oda and H. Nagano, 1985, J. Magn. & Magn. Mater. **52**, 338.
Onuki, Y., Y. Shimizu, T. Hirai, K. Shibutani, M. Nishihara, T. Komatsubara, A. Sumiyama, Y. Oda, H. Nagano, G. Oomi, A. Shibata and S. Minomura, 1986, J. Magn. & Magn. Mater. **54–57**, 389.
Onuki, Y., K. Shibutani, T. Yamazaki, T. Komatsubara, K. Maezawa and S. Wakabayoshi, 1987, J. Magn. & Magn. Mater. **63–64**, 306.
Ott, H.R., J.K. Kjems and K. Andres, 1978, Inst. Phys. Conf. Ser. **37**, 149.
Paccard, L., D. Paccard, J.M. Moreau, J.C. Gomez-Sal and M.A. Fremy, 1985, J. Less-Common Met. **110**, 315.
Palmer, S.B., and R.D. Grecnough, 1976, J. Magn. & Magn. Mater. **1**, 310.
Palmer, S.B., S. Bates, G.J. McIntyre, J.B. Sousa, D. Fort and B.J. Beaudry, 1986, J. Magn. & Magn. Mater. **54–57**, 519.
Pan, P.H., D.K. Finnemore, A.J. Bevolo, H.R. Shanks, B.J. Beaudry, F.A. Schmidt and G.C. Danielson, 1980, Phys. Rev. B **21**, 2809.
Patterson, C., D. Givord, J. Voiron and S.B. Palmer, 1986, J. Magn. & Magn. Mater. **54–57**, 891.
Pelegrini, F., R.W. Teale and J.S. Abell, 1982, J. Magn. & Magn. Mater. **29**, 105.
Pelegrini, F., R.W. Teale and J.S. Abell, 1984, J. Phys. F **14**, L247.
Perkins, R.S., and H. Nagel, 1975, Physica B **80**, 143.
Peterson, D.T., and F.A. Schmidt, 1969, J. Less-Common Met. **18**, 111.
Peterson, I.M., M. Smutz and E.H. Olson, 1965, J. Less-Common Met. **8**, 352.
Pfann, W.G., 1966, Zone Melting (Wiley, New York).
Pieri, J.C., A. Niazi and R. Jouty, 1973, J. Mater. Sci. **8**, 1426.
Pierre, J., D. Schmitt, P. Morin and B. Hennion, 1977, J. Phys. F **7**, 1965.
Pierre, J., R.M. Galeva and J. Bouillot, 1984, J. Magn. & Magn. Mater. **42**, 139.
Pratt, J.N., and R.G.R. Sellors, 1973, Electrotransport in Metals and Alloys (Trans. Tech., Switzerland).
Purwins, H.-G., 1970, Z. Phys. **233**, 27.
Quezel, S., J. Rossat-Mignod, B. Chevalier, P. Lejay and J.E. Etourneau, 1984, Solid State Commun. **49**, 685.
Rainford, B.D., H.B. Stanley and B.V.B. Sarkissian, 1985, Physica B **130**, 388.
Reed, R.E., 1971, Proc. 9th Rare Earth Res. Conf., Virginia, p. 657.
Reed, T.B., and E.R. Pollard, 1968, J. Cryst. Growth **2**, 243.
Rhyne, J.J., N.C. Koon, J.B. Milstein and H.A. Alperin, 1977, Physica B **86–88**, 149.
Rhyne, J.J., N.C. Koon and B.N. Das, 1979, J. Magn. & Magn. Mater. **14**, 273.
Rhyne, J.J., R.W. Erwin, M.B. Salomon, S. Sinha, J.E. Cunningham, J. Borchers and C.P. Flynn, 1986, J. Less-Common Met. **126**, 53.
Rosina, G., E. Bertel and F.P. Netzer, 1985, J. Less-Common Met. **111**, 285.
Rouchy, J., P. Morin and E. du Tremolet de Lacheisserie, 1981, J. Magn. & Magn. Mater. **23**, 59.
Rutter, J.W., 1968, in: Techniques of Metals Research, Vol. 1, ed. R.F. Bunshah (Wiley, New York) p. 923.
Sato, K., S. Iwasaki, K. Mori and Y. Isikawa, 1983, J. Magn. & Magn. Mater. **31–34**, 207.
Sato, K., Y. Yosida, Y. Isikawa and K. Mori, 1986, J. Magn. & Magn. Mater. **54–57**, 467.
Sato, S., T. Miyahara, T. Koide, T. Shidara, H. Kato, T. Komatsubara, Y. Onuki, K. Naito, H. Fukutani, M. Niwano, A. Fujimori, M. Yanagihara, S. Suzuki and T. Ishii, 1985, J. Magn. & Magn. Mater. **52**, 190.
Savage, H.T., R. Abbundi and A.E. Clark, 1979, J. Appl. Phys. **50**, 1671.
Savitskii, E.M., V.F. Terekhova, O.P. Naumkin and I.V. Burov, 1965, J. Cryst. Growth **6**, 111.
Saw, C.K., B.J. Beaudry and C. Stassis, 1983, Phys. Rev. B **27**, 7013.
Schieber, M., 1967, in: Crystal Growth, ed. H.S. Peiser (Pergamon Press, Oxford) p. 271.
Schiltz, R.J., and J.F. Smith, 1974, J. Appl. Phys. **45**, 4681.
Schirber, J.E., A.C. Switendick and F.A. Schmidt, 1983, Phys. Rev. B **27**, 6475.
Schmidt, F.A., and O.N. Carlson, 1976, J. Less-Common Met. **50**, 237.
Schweizer, J., and F. Tasset, 1980, J. Phys. F **10**, 2799.

Seitz, E., 1978, J. Phys. F **8**, L189.
Shaheen, S.A., J.S. Schilling, S.H. Lin and O.D. McMasters, 1983, Phys. Rev. B **27**, 4325.
Shi, N.L., and D. Fort, 1985, J. Less-Common Met. **113**, L21.
Shi, N.L., and D. Fort, 1986, Chin. J. Metal Sci. & Technol., in press.
Shibata, T., and T. Katayama, 1983, J. Magn. & Magn. Mater. **31–34**, 1029.
Shigeoka, T., N. Iwata, H. Fujii and T. Okamoto, 1986, J. Magn. & Magn. Mater. **54–57**, 1343.
Shohata, N., 1977, J. Phys. Soc. Japan **42**, 1873.
Sinha, S., J.E. Cunningham, R. Du, M.B. Salomon and C.P. Flynn, 1986, J. Magn. & Magn. Mater. **54–57**, 773.
Sinnema, S., J.J.M. Franse, A.A. Menovsky and R.J. Radwanski, 1986, J. Magn. & Magn. Mater. **54–57**, 1639.
Slebarski, A., and P. Byszewski, 1982, J. Magn. & Magn. Mater. **27**, 182.
Slepowronski, M., S. Warchol and A. Modrzejewski, 1983, J. Cryst. Growth **65**, 293.
Smith, B.A., 1979, Mater. Res. Bull. **14**, 431.
Soda, K., S. Asaoka, T. Mori, M. Taniguchi, K. Naito, Y. Onuki, T. Komatsubara, T. Miyahara, S. Sato and T. Ishii, 1985, J. Magn. & Magn. Mater. **52**, 347.
Sousa, J.B., R.P. Pinto, M.E. Braga, R. Aleonard, P. Morin and D. Schmitt, 1983, J. Phys. F **13**, 827.
Spirlet, J.C., and O. Vogt, 1984, in: Handbook on the Physics and Chemistry of the Actinides, eds A.J. Freeman and G.H. Lander (North-Holland, Amsterdam) p. 79.
Stassis, C., C.-K. Loong, J. Zarestky, O.D. McMasters and R.H. Nicklow, 1981, Phys. Rev. B **23**, 5128.
Stassis, C., C.-K. Loong and J. Zarestky, 1982, Phys. Rev. B **26**, 5426.
Stassis, C., G.S. Smith, B.N. Harmon, K.-M. Ho and Y. Chen, 1985, Phys. Rev. B **31**, 6298.
Stierman, R.J., K.A. Gschneidner Jr, T.-W.E. Tsang, F.A. Schmidt, P. Klavins, R.N. Shelton, J. Queen and S. Legvold, 1983, J. Magn. & Magn. Mater. **36**, 249.
Stockbarger, D.C., 1936, Rev. Sci. Instrum. **7**, 133.
Swets, D.E., 1986, J. Cryst. Growth **75**, 277.
Takagi, K., and M. Ishii, 1977, J. Cryst. Growth **40**, 1.
Takke, R., and W. Assmus, 1980, J. Cryst. Growth **49**, 97.
Takke, R., N. Dolezal, W. Assmus and B. Luthi, 1981, J. Magn. & Magn. Mater. **23**, 247.
Tanaka, T., E. Bannai, S. Kawai and T. Yamane, 1975, J. Cryst. Growth **30**, 193.
Tanaka, T., R. Nishitani, C. Oshima, E. Banai and S. Kawai, 1980, J. Appl. Phys. **51**, 3877.
Thompson, J.D., 1985, Phys. Rev. B **31**, 389.
Thompson, J.D., J.O. Willis, C. Godart, D.E. Maclaughlin and L.C. Gupta, 1985, J. Magn. & Magn. Mater. **47&48**, 281.
Tonnies, J.J., and K.A. Gschneidner Jr, 1971, J. Cryst. Growth **10**, 1.
Tsushima, T., and M. Ohokoshi, 1983, J. Magn. & Magn. Mater. **31–34**, 197.
Uehara, M., 1980, J. Appl. Phys. **51**, 5495.
Uehara, M., 1983, J. Magn. & Magn. Mater. **31–34**, 1017.
Verhoeven, J.D., E.D. Gibson, M.A. Noack and R.J. Conzemius, 1976, J. Cryst. Growth **36**, 115.
Verhoeven, J.D., A.J. Bevelo, D.T. Peterson, H.H. Baker, O.D. McMasters and E.D. Gibson, 1985, Metallography **18**, 277.
Verhoeven, J.D., E.D. Gibson, O.D. McMasters and H.H. Baker, 1987, Metall. Trans. A **18**, 223.
Vogt, O., 1985, Physica B **130**, 491.
Volkov, V.T., T.V. Nikiforova, A.M. Ionov, A.N. Pustovit and C.G. Nkharulidse, 1981, J. Less-Common Met. **79**, 199.
Wallace, W.E., 1971, Prog. Solid State Chem. **6**, 155.
Weber, K., 1977, Physica B **86–88**, 91.
Westlake, D.G., 1968, in: Techniques of Metals Research (Wiley, New York) p. 1145.
Whittaker, M., 1968, J. Cryst. Growth **3&4**, 317.
Williams, C.M., 1977, Physica B **86–88**, 147.
Williams, C.M., and N.C. Koon, 1975, Phys. Rev. B **11**, 4360.
Williams, C.M., N.C. Koon and B.N. Das, 1980, J. Magn. & Magn. Mater. **15–18**, 53.
Winiarski, A., 1982, J. Cryst. Growth **57**, 443.
Winiarski, A., 1985, Physica B **130**, 508.
Yeshurun, Y., L.J.P. Ketelsen and M.B. Salomon, 1985, Phys. Rev. B **32**, 7425.

Handbook on the Physics and Chemistry of Rare Earths, Vol. 12
edited by K.A. Gschneidner, Jr. and L. Eyring

Chapter 81

GROWTH OF SINGLE CRYSTALS FROM MOLTEN METAL FLUXES

Z. FISK
Los Alamos National Laboratory, Los Alamos, NM 87545 USA

J.P. REMEIKA†
AT&T Bell Laboratories, Murray Hill, NJ 07974 USA

Contents

1. Introduction

In research on the physical and chemical properties of intermetallic (and other) compounds, material in the form of single crystals is preferred. Ceramic or pressed powders of a given compound, wherein the particles are randomly oriented, not only present a much higher surface to bulk ratio than do single crystals; they also present problems of intergranular composition and porosity, and prevent any meaningful measurements of anisotropy. A generally higher level of purity is obtained in single crystals, and, more importantly, many macroscopic and (particularly) microscopic probes can only be effectively utilized with single crystal material. Fermi surface experiments, for example, using the de Haas–van Alphen effect, are in this category, as are many neutron and X-ray scattering

† Deceased

experiments. This makes the preparation of single crystals a matter of considerable importance for the condensed matter scientist.

The most important and simplest technique for crystal growth is growth from a pure melt of the substance desired. Even here there are numerous experimental techniques available, for example zone melting, crystal pulling and Bridgman cooling (see Ch. 80 by Abell in this volume). But such techniques are generally limited to cases when the material is congruently melting. And even in these cases there can be complications: the material may melt at an inconveniently high temperature or the vapor pressure of one or more of the components may be prohibitively large at the melting temperature. In such situations and in the more usual case where the compound melts incongruently, it is useful and often necessary to have other techniques available for the preparation of single crystals.

One such technique which is not widely used is the growth of single crystals from molten metal fluxes. We have no explanation for the relatively small attention given to this technique, which requires what amounts to the determination of part of the appropriate phase diagram, as do many crystal growth investigations. It is our purpose here to describe some of our experience in using this technique and give some general guidelines as to how we have gone about determining appropriate solvents (or fluxes) in particular cases. This choise of solvent is clearly the place where experience and imagination are put to the test, and it is similar to, but simpler than, the case with oxide systems.

It is not our intention to provide an introduction to the theory and practice of crystal growth. Such information can be obtained from a large number of good references (for example, see Elwell and Scheel 1975). It is rather our aim to indicate the general usefulness of the technique of growth from molten metals fluxes from the practical, how to do it, side, and to tabulate a number of instances where it has been successful. In this last, we are by no means familiar with all the work in this area. Computer searches of the literature actually turn up only literature references that we are already familiar with. The most effective way to research whether a metal flux method has been successful for single crystal growth of a particular compound is to search Chemical Abstracts under that compound. We have not done this compound by compound search, and what we present is in large part drawn directly from our own research work. This emphasis on our personal experience is in no way meant to draw attention from the importance of other work; rather it represents how we came to the subject, and it serves our particular purpose in this chapter.

What are the advantages of this particular technique? There are two general ones: (1) materials can be grown often well below their melting points, and this often produces material with fewer defects and much less thermal strain, and (2) molten metals offer a clean environment for growth, since the molten metal flux often getters impurities which do not subsequently appear in the crystal. In this respect, a molten metal flux can act, purity-wise, like a good vacuum. In addition to these advantages, there is the point to be made in favor of metal flux growth that it is a "poor man's" technique: it can be done with the simplest equipment, often even without a temperature controller, although a controller is necessary for the growth of large crystals. This enables a modestly equipped laboratory to get

into the business of single crystal growth without large capital equipment expenditure, an important advantage since the most reliable source for a single crystal is from your own operation.

To the above points can be added that occasionally other techniques will not yield crystals, that vapor pressure problems (as in a number of Yb and Eu compounds, for example) are often greatly reduced in solution and that in a number of cases completely new compounds have been discovered growing from metal flux systems.

There are, to be sure, a number of disadvantages to the technique. The first and foremost is that it is not always an applicable method: an appropriate metal flux from which the desired compound will crystallize may not be found. In addition, difficulties are encountered with some flux choices, when the flux, or some component of it, enters the crystal as an impurity. A further problem having to do with the actual growth situation is that flux inclusions often occur – the crystal grows around a pocket of flux. In this case special care must be taken with the growth rate conditions. The problem is really one of excessive nucleation which takes place either due to too fast a cooling rate, or supercooling of the melt by slow cooling with subsequent multiple nucleation and fast growth of large but imperfect crystals usually containing inclusions. It is under these conditions that the large crystals are imperfect, but after equilibrium is reached crystals nucleate at a much slower rate, and are of much higher quality. The flux growth method also suffers from a problem common to other growth methods, namely the container problem, which will be discussed at some length below. Finding a container to hold the melt at the temperature desired can be difficult, as secondary reactions often occur which one does not immediately expect. And finally, the ability to separate crystals from the flux at the conclusion of growth needs special consideration, and is also discussed at length below.

2. Description of technique

2.1. *Examples*

When crystals grow from a melt, we learn something about the relevant phase diagram. Conversely, knowledge of the relevant phase diagram will allow one to set carefully some of the conditions for crystal growth. We seldom have, needless to say, the phase diagram information necessary, and it is often much faster to optimize growth conditions without learning much in detail about the phase diagram. This is in part because factors other than those contained in the phase diagram also contribute to the process. Nevertheless, access to the tabulations of binary phase diagrams (i.e, Hansen 1958, Elliott 1965, Shunk 1969, and Moffatt 1981) is extremely useful when experimenting with possible fluxes for growth of a particular material.

The simplest way to introduce the concepts appropriate to growth of crystals from metal fluxes is with a simple binary eutectic system. Suppose we wish to produce crystals of Si. We know perfectly well that there is an entire industry built

on extremely high quality Si single crystals. Nevertheless, we might wish to perform some experiments on small crystals which we could easily produce ourselves. Si is chemically rather inert with respect to acids such as HNO_3, HCl and basic solutions such as NaOH. This would allow us to extract Si crystals from a metallic flux which is attacked by the above reagents. The simplest metals to consider as solvents are those with relatively low melting points: Al, Bi, Ga, In, Sn, and Zn. Zn has a high vapor pressure and is a poor solvent for Si, as we find out in Hansen. Bi is also a poor solvent. It dissolves about 5 a/o Si at 1000°C, Ga about 20 a/o and Sn something in the vicinity of 5 a/o. Al appears to be best in this respect, dissolving about 45 a/o at 1000°C, and the eutectic composition contains 11.3% Si (fig. 1). This makes the Al flux especially attractive for growing Si single crystals: large solubility at a reasonable temperature, ease of removal and reasonable composition range between eutectic composition and solubility at starting temperature. It is clear that if this last range is small, little material will be available for crystallization before the entire melt solidifies.

The small scale laboratory procedure for this Al flux growth of Si crystals then involves weighing out the appropriate amounts of the elements corresponding to the temperature where you wish growth to initiate and placing them in a suitable crucible. Al will attack SiO_2 when molten and SiO_2 cannot, therefore, be used. Al_2O_3 crucibles are readily available and will not be attacked by Al until, in our experience, temperatures near 1600°C when some solubility of Al_2O_3 in Al begins and where the vapor pressure of Al becomes an additional problem, partly because the thin oxide skin, which often covers molten Al, breaks up and loses its integrity, resulting in a much increased evaporation of Al. A protective atmos-

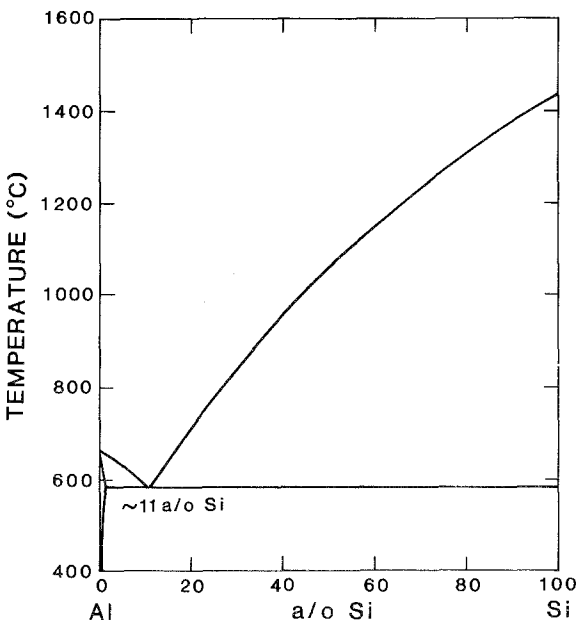

Fig. 1. Temperature–composition phase diagram for the Al–Si system. (After Hansen 1958.)

phere must be provided for the melt, and inert gas (He or Ar) is preferred over vacuum because more Al evaporation will occur in vacuum. The inert atmosphere can either be provided by sealing the crucible in a quartz tube, simply done at a glass bench, or using a gas atmosphere in a tube furnace arranged vertically to accommodate the crucibles. Horizontal tube furnaces can also be used if their bore is sufficient to accept the chosen crucible size as it stands up. In this case, the crucible(s) can be loaded in on a ceramic boat. There is an important point to remember when sealing a crucible into a quartz tube: the tube as it stands vertically will contact the Al_2O_3 crucible bottom at its end taper. Al_2O_3 has a much larger thermal expansion than quartz and will crack the quartz as the load is heated. This cracking can be prevented either by flattening the quartz tube bottom so that the crucible can rest there without contacting the sides, or a short stub of quartz can be used in the tube bottom to spring the crucible away from the nesting location. We also find some Al vapor attack on quartz tubes from the Al in the crucible load. This attack is slower, obviously, when the evaporation kinetics are hindered by an inert gas atmosphere in the quartz tube. It is reasonable to adjust the gas pressure in the tube so that it is of order 1 atm at the highest working temperature, although properly sealed quartz tubes of ~1 cm internal diameter can easily take 5 atm at temperatures up to 1200°C. While it is possible to use quartz above 1200°C, this is the range above which quartz starts to soften. Then it is important both to keep the quartz tubes scrupulously free of fingerprints and surface dirt (locations where devitrification starts) and to carefully adjust the gas pressure to be 1 atm at the operating temperature to prevent either the collapse or the expansion of the tube.

It is generally, but not always, the case that the larger the container, the larger the crystals. It becomes difficult, if you are not a professional glass blower, to seal off crucibles larger than about 2 cm in diameter in a quartz tube, and for crucibles above this size it is much easier to work in a tube furnace equipped with a tube through which inert gas is flowing. Mullite tubes (an Al_2O_3–SiO_2 ceramic) are relatively inexpensive and can be used to at least 1500°C, a common upper temperature limit of operation for furnaces heated with silicon carbide heating elements. Mullite tubes become somewhat porous at elevated temperatures, so that a slight over pressure of inert gas is recommended at all times. It is also important to realize that there is usually present trace amounts of unwanted gases such as H_2O and O_2 in high purity He and Ar delivered from gas bottles. The gas can be first run through a commercial gas purifier, or one can be constructed by packing a quartz tube with granular Zr metal, which is heated in a small tube furnace to 800°C and through which the gas is first passed. Even at the ppm level, O_2 can be gettered from the gas stream by the metal flux. It makes sense, therefore, to not flow more gas past the crucible then necessary. This can be accomplished by causing the gas flow to by-pass the tube, while maintaining a positive pressure within it, as shown in fig. 2. It is useful to know that the McDaniel Company which sells mullite tubes also sells gas tight end-cap sealing fixtures for their tubes which require no additional preparation of the mullite tubes.

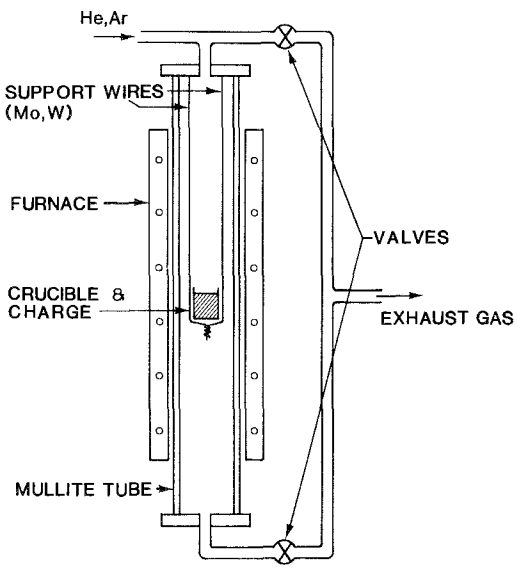

Fig. 2. Gas flow arrangement to maintain positive gas cover while not passing gas over hot crucible and charge. Lower valve open and upper valve closed allows for initial flushing of space, the reverse arrangement being used to maintain integrity of gas cover during heating and cooling cycle. The exit gas can conveniently be exhaused through a bubbler, allowing monitoring of flow rate.

Once the crucible has been loaded into the furnace, and the protective gas cover established, the furnace is then ramped to sufficient temperature to get the Si into solution. The kinetics of solution of various materials prove to be quite slow in many cases, and some experimentation is often required to establish the appropriate soak period required for complete solution. Then the furnace is ramped down: the slower the rate, generally the better the crystal growth, the fewer the inclusions and the higher the quality of the crystals. For the example given here, rates in the few degrees per hour should yield mm size crystals, although some crystals will be obtained if the furnace is just shut off at the soak temperature and then allowed to cool at its own rate. Indeed, for exploratory work aimed at determining the feasibility of using a particular solvent, it is often useful to use coolings rates of 100–200°C h^{-1}. This normal rate of cooling for a furnace can be slowed somewhat by increasing the thermal mass present, such as packing the crucible in SiO_2 sand.

Once the crucible is cold, it is then necessary to remove the Al. This is readily done in this case with NaOH solution. If the leaching reaction is slow, heating on a hot plate will speed things up. The Si crystals will remain after the reaction of the hydroxide with Al is complete. Crystals will in fact be visible on the surface of the melt before the leaching is begun.

This is a particularly simple example we have given of the technique, but there is really nothing additional involved in the general approach to crystal growth by

the flux method, only the phase diagrams becoming more complicated and often not known, and the separation of crystals requiring more care.

An example involving only slightly different considerations is the growth of UAl_3 crystals from Al (fig. 3). In this case there are a number of intermetallic phases present, UAl_2, UAl_3, and UAl_4, the last two melting incongruently. It turns out to be difficult to obtain clean, single phase samples of UAl_3 by arc melting, presumably because the UAl_3 peritectic horizontal intercepts the liquids at a composition (~17% U) rather far from the composition of the compound. Because of this, even if one has no interest in single crystals of UAl_3, if you want to know about the properties of the material it is best to attempt the single crystal growth, solely to get single phase material. Similar considerations apply for a number of Yb compounds where the high volatility of Yb makes arc melting an unattractive method for preparation of single phase, peritectic compounds.

In the growth of UAl_3 crystals, we see that we need to prepare a melt with U concentration between ~3% and ~10%. Additionally, especially if a quartz tube is used to contain the Al_2O_3 crucible, it will be advisible to keep the growth temperature below 1200°C. This restricts the U concentration between ~3% and ~7%. This is a narrow range from which to grow crystals, but it is easily done. When the melt has cooled to 730°C, the peritectic temperature of UAl_4, the furnace is shut off to discourage growth of sizable UAl_4 crystals. UAl_4 crystals, to be sure, can be grown from melts with U concentration between 1.7% and 2.6%. Again, extraction of the crystals can be accomplished by leaching out with NaOH solution.

A point to make here is that it is necessary to pay attention to the chemical

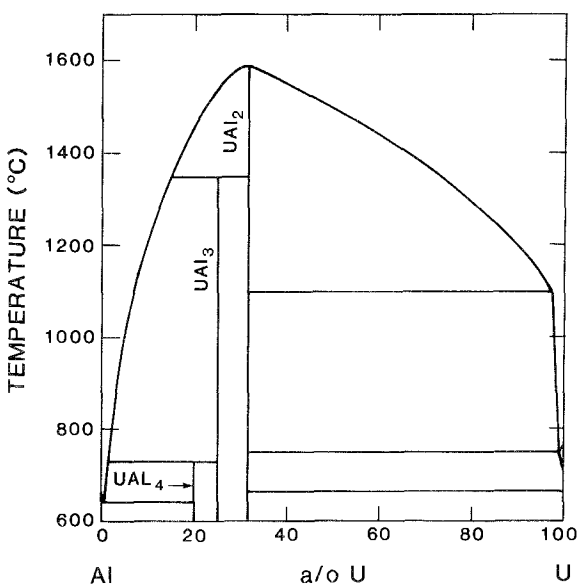

Fig. 3. The U–Al binary phase diagram. (After Hansen 1958.)

activity of species dissolved in the flux, in this case U. U is often quite reactive towards crucible materials, including Al_2O_3. In this case, however, the activity of U is sufficiently reduced by solution in molten Al so as not to be a problem. This sort of problem is generally worsened at elevated temperatures, and one can often detect attack on the crucible material from a discoloration of it. In some cases no product is obtained from a growth attempt because one solute in the melt has reacted out completely with the crucible.

The actual composition and temperature range conveniently available for growth of UAl_3 from excess Al is quite restricted. We have therefore investigated other possible fluxes from which to grow this material. A generally useful flux from which to grow a number of U compounds has proven to be Bi. In fig. 4 we show the U–Bi phase diagram. There are two peritectic intermetallics, UBi_2 and U_3Bi_4. UBi_2 melts at a rather low temperature, and the ability to grow intermetallic compounds of U from molten Bi is presumably due to the relative low stability of UBi_2, the U–Bi compound most likely to be in competition with the compounds one wishes to grow from Bi. In fig. 5 we show the Al–Bi phase diagram from Shunk (1969), two differing boundaries being given for the miscibility gap above the melting point of Al. What is important here for us in that something like 13 a/o Al can be dissolved in Bi at the melting point of Al.

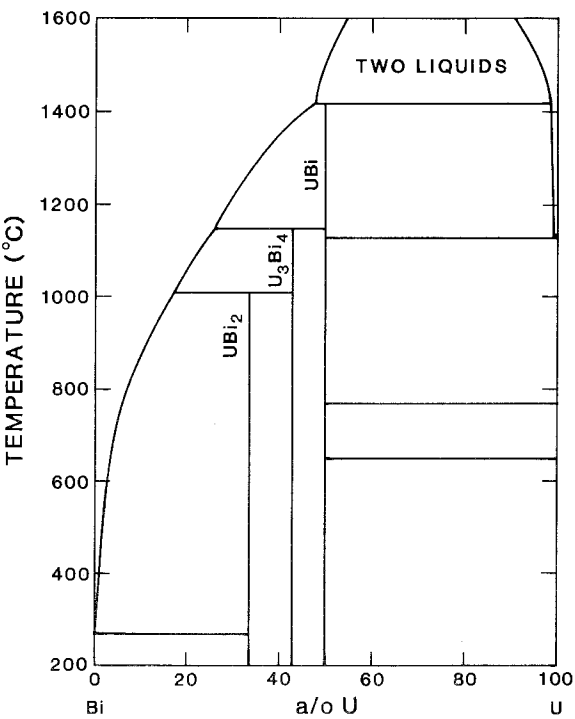

Fig. 4. The U–Bi binary phase diagram. (After Hansen 1958 and Elliott 1965.)

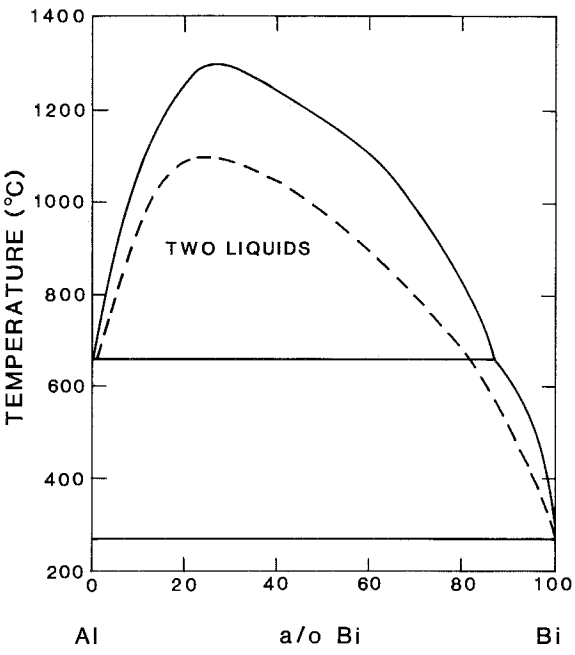

Fig. 5. The Al–Bi binary phase diagram. The two lines shown are from two different investigations of the system. (After Shunk 1969.)

Our original attempts at growing U–Al intermetallics from Bi were aimed at producing UAl_2 crystals. For reasons we do not fully understand, only UAl_3 crystals were obtained, even when compositions with U–Al ratio as large as U_2Al were tried. This is an interesting fact since, as we discuss further below, it is most often found that the congruently melting species in a binary phase diagram (here UAl_2) is the most likely to precipitate from the ternary melt with the solvent. The crystals of UAl_3 obtained from Bi flux were rectangular bars, with lateral dimensions of one or more millimeters and length in excess of 1 cm. The extraction of UAl_3 from the Bi flux is done by solution of Bi in moderately dilute HNO_3. It is a fact that many U intermetallics are quite stable chemically with respect to HNO_3. It is curious that many of these compounds will dissolve readily in HCl.

There is an alternative way to remove the Bi flux which proves to be extremely useful in situations where the crystals desired are attacked by HNO_3. This is by spinning off the flux in a centrifuge, and is useful for any low melting flux. What one does is to place the crucible in a furnace which is set to a temperature just sufficient to melt the flux, then place the inverted crucible in a centrifuge containing a base of glass or quartz wool, or glass beads, in the bottom, and spin out the molten flux. This is best done in an appropriately sealed glass tube with the coarse filter material in the bottom, but can be done in air when the rate of oxidation of the crystals will be small. We have been informed of situations where

heat was directly applied to the centrifuge buckets, which would allow solvents with melting points as high as that of Al (660°C) to be spun off. This could be a dangerous procedure, and should be used only as a last resort. In such a case, it would be necessary to replace the SiO_2 wool with Al_2O_3 granular material, which is not attacked by molten Al.

A concise description of growth of RIn_3 and RSn_3 from excess In and Sn, respectively, can be found in Kletowski et al. (1985).

2.2. *Choice of flux*

The general problem faced by materials physicists and chemists needing single crystals is, of course, the best way to grow the particular crystal they need. There are several general observations which can help in the examination of the possibility of successfully growing crystals from molten metal fluxes. The first is that it is generally easier to grow a congruently melting material from such a flux than an incongruently melting one, and that the higher this melting point is, the more readily the crystals will come out of the melt. We saw an exception to this above with the example of the growth of UAl_3 from Bi, when UAl_2 was the material expected to grow from Bi. It seems likely that at some presumably large concentration of UAl_2 in Bi, it will be possible to precipitate UAl_2. The temperatures involved will probably be quite high, and it would then be better to use another growth technique.

The second, fairly obvious, observation is that competing phases formed by the flux with the elements in the compound wanted can prevent growth of the desired compound. This translates into looking for potential solvent–solute binary phase diagrams with fairly low-melting, incongruent compounds.

An example illustrating these two observations is the growth of rare earth borides from molten Al. For the light rare earths, La through Eu, the hexaborides grow. Although there exist several Al borides, AlB_2 is the one most likely to cause trouble, and this melts incongruently at 975°C. These rare earth hexaborides melt congruently at temperatures over 2000°C, and in fact their solubilities in Al are quite modest. For example, LaB_6 has, very roughly, a solubility of 14 mg per gram Al near 1400°C. The interesting point is that for Gd and beyond, it is the tetraboride that comes down from the Al flux, and it is with these heavy rare earth borides that the tetraboride becomes congruently melting rather than the hexaboride, which is congruently melting in the light rare earth series. The cross over occurs near Sm, and it is possible to grow either the tetraboride or hexaboride of Sm by varying the composition of the charge. We also note that it is possible to separate, below the ppm level, Sm from Gd by growth of these borides: Gd will not dope into SmB_6 in Al melts, as has been shown by spin resonance experiments. The Gd comes down completely as tetraboride. An aside remark here is that Eu, which only forms an hexaboride, is a very volatile element, resembling the alkaline earths, and growth from Al is a very convenient preparation procedure for EuB_6, because the large disparity in melting points between Eu and B makes arc melting without large weight loss difficult.

There are further aspects of the growth of rare earth borides from Al which are worth mentioning. One point is that in many neutron experiments, it is important to use the ^{11}B isotope since the absorption of neutrons by ^{10}B is so high. It is often found that the ^{11}B isotope one can obtain has much lower purity than desired, and that a convenient preliminary step of purification can involve a boride growth which leaves these impurities behind. This has been done in the preparation of rare earth-Rh_4B_4 compounds.

A second point is that initial attempts to produce YbB_4 crystals from Al produced instead a ternary phase, $YbAlB_4$. This proved to be an interesting phase in its own right, and it was possible to also produce this phase with several other rare earths. In order to grow YbB_4 from Al, the starting growth temperature can be increased by going to higher YbB_4 concentration in the Al melt, so that crystallization starts above the melting point of $YbAlB_4$. Alternatively, YbB_4 can be grown from molten Yb in a sealed Ta tube.

A third general observation regarding metal flux growths is that certain metal fluxes work well for compounds containing certain elements, Bi for U compounds, for example. For this reason we have organized our listing of flux growths in appendix 1 by the solvent flux.

3. Further aspects of crystal growth from metallic fluxes

3.1. *Diagnostics*

In order to determine the suitability of various fluxes for the growth of single crystals of a particular compound, a number of small scale and fairly rapid trials are generally required. Crystals produced in this way will most often be small, and it is useful in such cases to examine the melt microscopically. This is especially the case when there are problems associated with chemically separating the crystals from the flux. We have found it worthwhile in these situations to saw with a diamond wheel through the crucible and melt, and then examine the cross-section after polishing it metallurgically. A cut vertically through the crucible gives the best representation of what is actually happening in the melt during cooling. It is perhaps not surprising that crystals often grow much larger in melts placed in special locations in a given furnace due to the local temperature gradients, and aspects of this will be visible in such metallurgical examinations. Elemental analysis of these cross-sections in an appropriately equipped SEM is also useful.

3.2. *Containers*

Containers are a central problem in crystal growth using metal fluxes. Aspects of this have been mentioned above. A short list of useful crucible materials is given in appendix 2. It is important to realize that solute reactivities in different melts vary enormously. For example, it was found possible to grow large rare

earth rhodium stannide crystals from excess molten tin in sealed quartz tubes. Some rare earth attack on the quartz was observed, being greatest for the light rare earth compounds, but this attack was sufficiently slow to allow large crystals to grow anyway. In view of the exceptional stability of rare earth oxides, this indicates that the rare earth–tin interaction is quite strong, reducing the rare earth activity in the melt substantially. By contrast, rare earths and U dissolved in molten Cu are found to be quite reactive towards container materials, and this might be guessed at by the low melting temperatures of compounds of rare earths and U formed with Cu. Crystals of rare earth-iridium C-15 Laves phase compounds have been grown from molten Cu. Ir dissolved in Cu will attack Ta, but the rate of this attack depends on which rare earth is in the melt. This attack problem was found to be severe for the case of $CeIr_2$, but not for $TmIr_2$. We were not able to find a completely suitable container for the $CeIr_2$ growth.

Ta, it should be said, is a convenient material to work with because tubing is readily available, and it is easily sealed shut in an arc furnace. When welding a melt load shut in Ta in the arc furnace, it is useful to hold the broad, flattened part of the tube shut in a clamp made from two Cu bars. This large thermal mass keeps the tube cool and prevents expansion of gases inside the Ta tube from spreading it apart in the region to be welded. Mo and W are also useful crucible materials, but are not ductile enough to crimp flat for welding. These crucibles can also be welded shut in an arc furnace if a fitted lid is fabricated. Some kind of copper clamp for holding the crucible while welding it shut is important. This holder should be bolted to the arc furnace hearth for effective heat exchange, since keeping the crucible charge cooled is important for these high temperature melting materials. Electron beam welding is, of course, a better alternative, but this is not as readily available.

3.3. *Flux incorporation*

One of the problems attendant to flux growth of single crystals is that macroscopic voids filled with the flux can often be found within crystals, and the presence of these voids is not necessarily evident from a simple visual inspection of the crystals. In the growth the U- and rare earth-Be_{13} crystals from Al, lamellae of Al are often found. We have often had to separate our crystals from these lammellae by spark machining, followed by leaching in NaOH solution. Any residual Al can be detected by looking for the diamagnetic signal of Al near 1.1 K. The presence of incorporated flux is generally due to unstable crystal growth conditions which usually occur in the initial growth stages, as discussed earlier. It is frequently possible to recognize where this initial growth occurred and mechanically remove this part of the material. Problems of this kind can be ameliorated by providing deliberate nucleation sites, although this complicates the experiment considerably. In the growth of rare earth rhodium stannides from excess Sn, we were never able to completely eliminate Sn inclusions, except in smaller crystals from a melt that had reached equilibrium.

3.4. *Stoichiometry*

Many materials exist over a range of compositions. This variable stoichiometry is a source of problems in flux growth because the melt composition as well as phase boundaries vary during the cooling cycle. This sometimes results in a composition gradient in the grown material. In a number of cases, one composition boundary is a vertical line in the phase diagram. This allows an excess to be added to the melt corresponding to forcing the growth always to occur at this limit of stoichiometry. It appears, for example, that the compound $CePt_2$ can form with deficient but not with excess Ce. We have grown crystals of this material from Pb melts, and found that we could approach quite closely the theoretical stoichiometry of 1:2 using large excess of Ce in the Pb melts. It is important to realize that these excesses may be much larger than one might expect, as we have found that certain melts "hold back" certain elements – namely, the material that grows is very different in composition from the charge.

The other important consideration concerns substitutional incorporation of flux in the growing crystals. For example, it has been found possible to grow $CeCu_2Si_2$ single crystals from In or Sn flux. Analysis shows that small amounts of In and Sn enter substitutionally into the $CeCu_2Si_2$. The properties of $CeCu_2Si_2$ are particularly sensitive to such substitutions, and for many experiments these crystals, therefore, proved to be unacceptable. There are many cases of this kind of problem, and this makes it important to examine each possible flux from this standpoint. Chemical or atomic size similarity of the elements in the flux to one of the components of a compound should alert one to this possibility.

3.5. *Separation of crystals and flux*

We have discussed in various places above the problem of flux removal. There are two general approaches, chemical and mechanical. Let us discuss chemical techniques first.

The stability of a compound in various acids and bases can be determined using polycrystalline material, and it is a good idea to investigate this before embarking on a lengthy attempt to grow crystals from a given flux. Specialized reagents do exist for certain elements, and it is often worthwhile to consult a practicing inorganic chemist for ideas connected with chemical etching. There are interesting effects, furthermore, which appear to result from electrochemical differences between fluxes and crystals. In the growth of rare earth rhodium stannides from excess Sn, the crystals can be leached out with dilute HCl. As long as the crystals are in contact with the Sn flux, they remain shiny and metallic. Crystals which have separated from the Sn, however, quickly form a black tarnish from which, microprobe analysis reveals, the rare earth has been extracted; and the black material appears to be an amorphous mixture of Rh and Sn. Thus, removal of the crystals from the leaching solution as soon as they are free of Sn flux is desirable.

As another case, we mention the growth of $CeCu_2Si_2$ from molten Cu. It was

reported that the Cu stoichiometry of $CeCu_2Si_2$ crystals was very relevant to its superconducting properties. We therefore felt that growing $CeCu_2Si_2$ from pure Cu would provide the limiting Cu stoichiometry for this material. The problem came with the Cu removal, since, although an examination of the crystallization runs showed the presence of well formed crystals, Cu and the crystals are chemically attacked at nearly the same rate. Ultimately, we were able to slowly extract crystals using acetic acid-hydrogen peroxide mixtures, the process taking approximately one month.

A less often used, but useful, technique is to electrochemically remove the flux, using it as an anode in an electrochemical cell. By suspending the melt anode in the bath, the crystals can fall free as the etching proceeds, and if this electrolyte does not attack the crystals, they can be easily recovered. The advantage of this technique is that the voltage used in the erosion is easily controlled. There can also be "protective" voltages developed between crystals and flux of the kind pointed out earlier in the chemical etching of stannide melts.

Another technique of some use is the solution of one metal by another after the growth is complete. As a case in point, we look at the growth of $CeIn_3$ crystals from excess In. The left over In after the growth can be dissolved in Hg. The crystals can then be removed from the liquid (at room temperature) In–Hg solution, and the Hg film remaining on the $CeIn_3$ crystals can be pumped into a trap in a vacuum system with gentle heating.

The usefulness of centrifuging off low melting fluxes has been discussed above. Such a process can easily be used in the $CeIn_3$–In case just mentioned. There is the additional possibility of flux removal of high vapor pressure metals by simple evaporation after the growth process in a pressure containing vessel. There is also the less elegant method of cutting crystals from melts, exactly as is done from zone refined rods.

3.6. *Solution kinetics*

Some flux growth attempts appear to fail because of problems having to do with slow solution kinetics. There are cases where such slow kinetics can be used to advantage, but more often it constitutes a nuisance. As an example we can look at Cu–B solutions. There are no compounds in the phase diagram, and there is a broad eutectic melting near 1000°C. If we can believe this reported phase diagram, this suggests that Cu should be a very promising solvent for growth of borides. A number of ternary superconducting borides have in fact been grown from Cu. A problem, however, is that B seems to dissolve into molten Cu very slowly. This means that a long soak time at the maximum running temperature is required. In addition, if the growth charge consists of the elements of the compound and Cu, it can happen that the elements other than B will dissolve in Cu first, and then react out on the B, possibly making further solution of B difficult. This can be avoided by pre-reacting the compound and using it in the charge, rather than the elements. It is also sometimes useful to make actual

solubility tests of a compound in a given flux. This can be done in an approximate manner by soaking arc-melted pellets of the compound in given amounts of flux at fixed temperatures, quenching to room temperature, and subsequently measuring the weight loss of the leached-out pill of compound.

4. Extensions of the technique

4.1. *Use of temperature gradient*

A variant of the growth technique utilizes a temperature gradient. This is most easily discussed with an example. In our discussion of the growth of single crystals of rare earth hexaborides from molten Al, we noted that hexaborides of the rare earths Gd and heavier did not occur, rather their tetraborides grew. We did finally succeed in preparing single crystals of GdB_6 by the following method. B has very low solubility in Ga, even at 1500°C. We therefore made a flux of 95 a/o Ga–5 a/o Al in which B will have very low solubility. An arc melted pill of GdB_6 was prepared, and its density is such that it floats on this Ga–Al mixture. Our Al_2O_3 crucible containing the flux and GdB_6 pill was placed in a furnace so that the crucible bottom was coldest, the temperature gradient along the 5 cm^3 crucible being about 50°C. The top of the crucible was maintained at 1500°C for several days; mm-size crystals of GdB_6 were found growing on the bottom of the crucible after shutdown. Our idea in this method was that we could force everything out of solution at lower temperatures that we put in at the higher temperature through the dynamic equilibrium. In a case where the compound is more dense than the flux, the temperature gradient can be reversed.

4.2. *Evaporation growth*

An alternative to precipitation of crystals by slow cooling is to supersaturate the flux solution via evaporation of the flux. This clearly requires the flux to be the most volatile species present. We have grown crystals of UPt_3 from Bi by such a method. The disadvantage associated with this method is that the supersaturation occurs at the evaporation surface, and it is difficult to prevent the formation of a large quantity of nuclei. In the case of Bi flux, it can be quite useful for high melting point materials which might be difficult to separate from Bi chemically although the centrifuge separation method is usually effective.

4.3. *Traveling solvent methods*

The use of molten metal solvents in the traveling solvent technique is clearly possible. The general aspects of the technique are discussed by Wolff and Mlavsky (1974) and can easily adapt to the various fluxes discussed here. This method is especially important when large crystals are desired.

4.4. *Miscellaneous*

We have made little mention of the uses of seeding melts, or of providing deliberate nucleation sites. These would clearly be useful in many situations. For the most part we have discussed only the simplest procedures, but it is clear that almost all of the technology adapted to produce large single crystals of oxides and similar materials can be suitably adapted to the growth of crystals from molten metal fluxes. This includes, in addition, the pulling of crystals from such metal fluxes. There is no need to repeat in our context the detail discussions of such methods as discussed, for example, in Elwell and Scheel (1975). The generalizations to this case are easily made.

Appendix 1

We present below a short list of representative intermetallic compounds grown from various solvents. Binary compounds grown from one of their constituent elements have not been included. For example, these include USn_3 from Sn, UGa_3 from Ga, $CeIn_3$ from In and $TiBe_2$ from the middle of the Ti–Be phase diagram. In our list, R means rare earth, although the rare earth compounds referred to cannot always be grown for all the rare earths.

Flux	Crystal*
Al	TiB_2, ZrB_2 $RAlB_4$ RB_4, UB_4, NpB_4, AmB_4 RB_6 RBe_{13}, UBe_{13}, $ThBe_{13}$, $PuBe_{13}$ Si(a), Ge(a)
Bi	UPt_3, $NpPt_3$ PtMnSb, NiMnSb UAl_3 UIr_3 GaP(a) $ZnSiP_2$, $CdSiP_2$(a)
Cu	RRh_4B_4 RCu_2Si_2 V_3Si RIr_2 UIr_3
Fe	BP(a) ZnS(a)
Ga	Si(a), Ge(a) GaSb(a)

Flux	Crystal*
Hg	InSb(a)
In	RCu_2Si_2 Si(a), Ge(a) RIn_3(c)
Pb	RPt_2, $YbPt_x$ GaSb(a)
Sb	$ZnSiP_2$(a), $CdSiP_2$(a) RSi_2
Sn	RCu_2Si_2 $R_3Rh_4Sn_{13}$ RFe_4P_{12}(b) $ZnSnP_2$(a) GaSb(a), GaP(a) $ZnSiP_2$(a), $CdSiP_2$(a) RSn_3(c)
Zn	InSb(a), GaSb(a), InAs(a) Si(a), Ge(a)

*References:
(a) Luzhnaya (1968); (b) Meisner (1982); (c) Kletowski et al. (1985).

Appendix 2

Containers for various molten metals. A more complete list can be found in Brown and Westbrook (1967).

The free energy of formation, ΔG, in kcal/mole O_2 for various oxide crucible materials is shown in fig. 6 [after Reed 1971]. The values are for reaction with one mole of O_2.

Metal	Container
alkali metals	Ta, steel
alkaline earth metals	Ta, graphite for Ba, steel
Al, Ga	Al_2O_3, MgO, BeO
Mg	MgO, Ta, graphite or steel
Mu	Al_2O_3
Cu, Ag, Au	graphite, MgO, Al_2O_3, Ta
Fe, Co, Ni	Al_2O_3, ZrO_2, ThO_2
Zn, Cd, Hg	Al_2O_3
In	Al_2O_3, Ta
rare earths	Ta, Mo, W, BeO
Bi, Sn	Al_2O_3, SiO_2, graphite
Sb	SiO_2, graphite

Melting points of oxide materials[a].

Oxide	Melting point (°C)
Al_2O_3	2015
BeO	2500
MgO	2800
SiO_2	1720 (softens ~1200)
ThO_2	3300

[a]SiO_2, Al_2O_3, and BeO have good thermal shock resistance, ThO_2 and MgO intermediate thermal shock resistance, and Y_2O_3 and ZrO_2 poor thermal shock resistance.

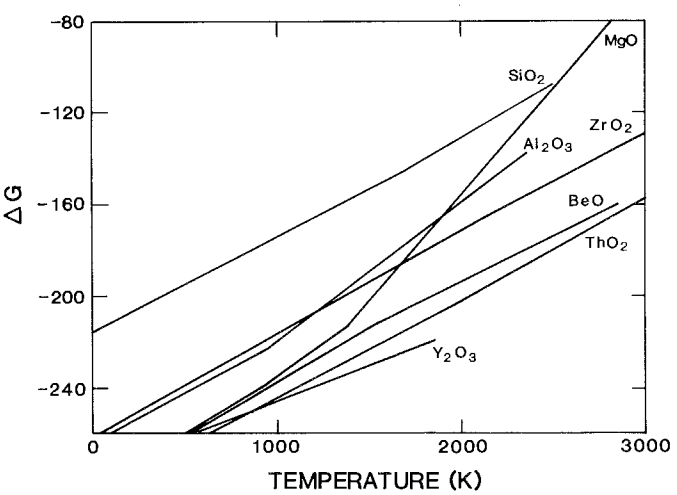

Fig. 6. Free energy of formation of oxides, for reaction with one mole of O_2.

References

Brown, A., and J.H. Westbrook, 1967, in: Intermetallic Compounds, ed. J.H. Westbrook (Wiley, New York) p. 303.

Elliott, R.P., 1965, Constitution of Binary Alloys, First Supplement (McGraw-Hill, New York).

Elwell, D., and H.J. Scheel, 1975, Crystal Growth from High-Temperature Solutions (Academic Press, New York).

Hansen, M., 1958, Constitution of Binary Alloys (McGraw-Hill, New York).

Kletowski, Z., N. Iliew, Z. Henkie and B. Stalinski, 1985, J. Less-Common Met. **110**, 235.

Luzhnaya, N.P., 1968, J. Cryst. Growth **3&4**, 97.

Meisner, G.P., 1982, Ph.D. Thesis, University of California, San Diego (unpublished).

Moffatt, W.G., 1981, Handbook of Binary Phase Diagrams (General Electric).

Reed, T.B., 1971, Free Energy of Formation of Binary Compounds (MIT Press, Cambridge, MA).

Shunk, F.A., 1969, Constitution of Binary Alloys, Second Supplement (McGraw-Hill, New York).

Wolff, G.A., and A.I. Mlavsky, 1974, in: Crystal Growth, Vol. 1, ed. C.H.L. Goodman (Plenum Press, New York) p. 193.

Handbook on the Physics and Chemistry of Rare Earths, Vol. 12
edited by K.A. Gschneidner, Jr. and L. Eyring

Chapter 82

PHYSICAL PROPERTIES OF $R_2Fe_{14}B$-BASED ALLOYS

E. BURZO
Central Institute of Physics, PO Box MG-06, Bucharest, Romania

H.R. KIRCHMAYR
Institute for Experimental Physics, Technical University Vienna
Wiedner Hauptstr. 8, A-1040 Vienna, Austria

Contents

Symbols

B_r	remanent induction	$\mathcal{H}$	one ion hamiltonian
B_s	saturation induction	$\mathcal{H}_{CEF}$	crystalline electric field hamiltonian
B_2^0, B_2^2	crystal field parameters		
C	Curie constant	H	external field
C_{Fe}	Curie constant of Fe ion	H_A	anisotropy field
C_R	Curie constant of R ion	H_{exch}	exchange field
c_{11}, c_{44}	stiffness constants	${}_BH_c$	coercive field
d_c	critical diameter	${}_MH_c$	intrinsic coercive field
d_{Fe-Fe}	distance between iron ions	H_{hf}	hyperfine field
d_k	grain diameter	H_N	nucleation field
E	Young's modulus	H_M	molecular field
E_A	anisotropy energy	$J_{ij}(i, j = R, Fe)$	molecular field coefficients
g_J	spectroscopic splitting factor	K_p, K, K_1, K_2, K_3	anisotropy constants
		M_s	saturation magnetization
g_{Fe}	spectroscopic splitting factor of iron	M_{eff}	effective moment
		M_{Fe}	iron moment

M_{4s}	4s polarization	$\alpha_{(BH)_{max}}$	reversible coefficient of energy product
n	demagnetizing coefficient	α_{H_c}	reversible coefficient of coercive field
r_0	halfwidth of soft magnetic region	α_J	Stevens factor
S_0	spin value of iron obtained from saturation data	γ	critical exponent
S_p	spin value of iron obtained from paramagnetic data	γ_W	domain wall energy
S_v	after effect constant	δ_W	wall width
t	time	θ_D	Debye temperature
T	temperature	θ_p	paramagnetic Curie temperature
T_c	Curie temperature	λ	spin–orbit coupling constant
T_m	melting temperature		
T_t	eutectic temperature	λ_a	magnetostriction coefficient along a-axis
x	concentration		
α_a	thermal dilation coefficient along a-axis	λ_c	magnetostriction coefficient along c-axis
α_c	thermal dilation coefficient along c-axis	λ_v	volume magnetostriction
		μ_B	Bohr magneton
α_v	volume dilatation coefficient	μ_0	vacuum permeability
		ν	Poisson ratio
α_{B_r}	reversible coefficient of remanent induction	φ	canting angle
		χ	magnetic susceptibility

1. Introduction

Based on the earlier work by Croat (1981, 1982) on binary amorphous Nd–Fe alloys, and by Koon and Das (1981) on B additions to R–Fe alloys, researchers from Sumitomo Metals Co. showed that a phase in the Nd–Fe–B system, with an approximate composition $Nd_{12}Fe_{82}B_6$ has remarkable magnetic properties, namely saturation induction $B_s = 1.35$ T, Curie temperature $T_c = 585$ K, an intrinsic coercive force at room temperature of 960 kA/m and an energy product of 290 kJ/m^3 (Sagawa et al. 1984a). Later on, starting from these materials, permanent magnets with an energy product up to 360 kJ/m^3 have been obtained (Sagawa et al. 1984b, 1985a, b, Narasimhan 1985a). The price of these magnets is lower than that of rare-earth-cobalt magnets.

Initially, the composition of a tetragonal phase which possesses remarkable magnetic properties has been a controversial matter. Sagawa et al. (1984a) give the composition $Nd_2Fe_xB_y$ with $10.3 \leqslant x \leqslant 10.7$ and $1.0 \leqslant y \leqslant 1.1$. These alloys contain small quantities of a neodymium rich phase. Chaban et al. (1979) reported the presence of a $Pr_2Fe_{10.7}B_{0.67}$ compound. Stadelmaier et al. (1983) showed that the composition of the phase is $R_2Fe_{14}B_{0.67}$, where R is a rare earth. The studies performed both by neutron diffraction (Herbst et al. 1984) and X-ray measurements (Givord et al. 1984a, Shoemaker et al. 1984) lead to the determination of the crystal structure, the compositions being $R_2Fe_{14}B$. The presence of other compounds having composition close to the above has not been evidenced (Stadelmaier et al. 1984).

The rare-earth–cobalt permanent magnets are based on RCo_5 and R_2Co_{17}-type structures. The high Curie temperatures of the above compounds are mainly determined by the magnetic interactions between the cobalt atoms. The magnetic coupling between magnetizations of transition metals and those of the rare earths allows that the high anisotropy characteristic of the 4f ions, at 4.2 K, is being preserved to room temperature. Since in the above systems the cobalt atoms have uniaxial anisotropy, while the iron atoms have the anisotropy in the basal plane, the "classical" rare-earth magnets are based essentially on cobalt. The α_J Stevens factor is positive for Sm and negative for Pr and Nd (Givord et al. 1984a). The positive α_J value favours the uniaxial anisotropy, while the negative α_J values determine a basal plane anisotropy. Consequently, samarium is used as main component in the cobalt-based magnets.

Sagawa et al. (1984a) showed that in the tetragonal phase of the Nd–Fe–B system, both Nd and Fe show uniaxial anisotropy. This is opposite to what is evidenced in the rare-earth–cobalt compounds. In order to obtain magnets from this generation, neodymium may be partially or wholly substituted by other rare earths (Sagawa et al. 1984b). Similarly, a fraction of iron may be replaced by cobalt or some metals which have beneficial effect on the properties of the above systems (Herget 1984, 1985a).

Considerable work has been done on the above systems both in order to elucidate their basic properties as well as technological aspects connected with the manufacture of permanent magnets. In this context, the studies were directed towards: (1) obtaining hard magnetic materials based on $R_2Fe_{14}B$ compounds with high Curie temperatures, saturation magnetization and anisotropy fields, (2) to improve technological processes in order to obtain better magnetic characteristics of the permanent magnets.

Two types of processes have been used to manufacture these permanent magnets. One is obtained by sintering the crystalline hard magnetic phase. An excess of rare earth is used to obtain a phase with low melting point, of great importance, in the liquid phase sintering. The second one is obtained by melt-spinning the alloys, to obtain amorphous ribbons; after processing they show good magnetic properties.

In this review we survey the phase diagrams of the ternary R–Fe–B systems; the crystal structure of the hard magnetic phase, $R_2Fe_{14}B$; and the lattice parameters as well as the preparation methods. Then, we present the magnetic properties of $R_2Fe_{14}B$-based alloys: Curie temperatures, magnetizations, anisotropy fields and paramagnetic behaviour. Some data obtained by analysing the systems with compositions slightly different from the above are also given. The physical properties of the sintered and rapidly-solidified magnets are described in connection with compositions and manufacturing procedures. The review covers mainly the literature up to June 1986.

The results of studies performed on $R_2Fe_{14}B$ compounds in various stages of researches were reviewed by Livingston (1985b), Burzo (1984), Coey et al. (1984), Kirchmayr (1984, 1985), Burzo et al. (1985d), Buschow (1986) and Givord et al. (1986b).

2. Phase diagrams and crystal structures

2.1. *Phase diagrams*

The phase diagrams of some R–Fe–B systems have been reported by various authors (Bilonizhko and Kuzma 1972, Kuzma et al. 1977, Chaban et al. 1979, Stepanchikova and Kuzma 1980, Stadelmaier and Park 1981, Stadelmaier et al. 1983 and 1984, Matsuura et al. 1985b, Oesterreicher 1985). In fig. 1 is plotted the phase diagram of the Nd–Fe–B system and in fig. 2 a section at $T \simeq 600°C$ in the above phase diagram (Oesterreicher 1985). For $Nd_2Fe_{14}B$ a melting temperature $T_M \simeq 1450°C$ is evidenced (Stadelmaier et al. 1984, Stadelmaier and El Masry 1985). The ternary borides crystallize from the melt. At the composition $Nd_2Fe_{14}B$, the primary crystallization product is δ-Fe. Annealing at 1200°C causes $Nd_2Fe_{14}B$ to recrystallize into much larger grains. It also causes the amount of iron, which is now γ-Fe, to decrease by coalescence into fewer particles. One may observe the presence of a three phase region $R_2Fe_{14}B$–$R_{1+\varepsilon}Fe_4B_4$–R, with a low melting eutectic suitable for liquid-phase sintering.

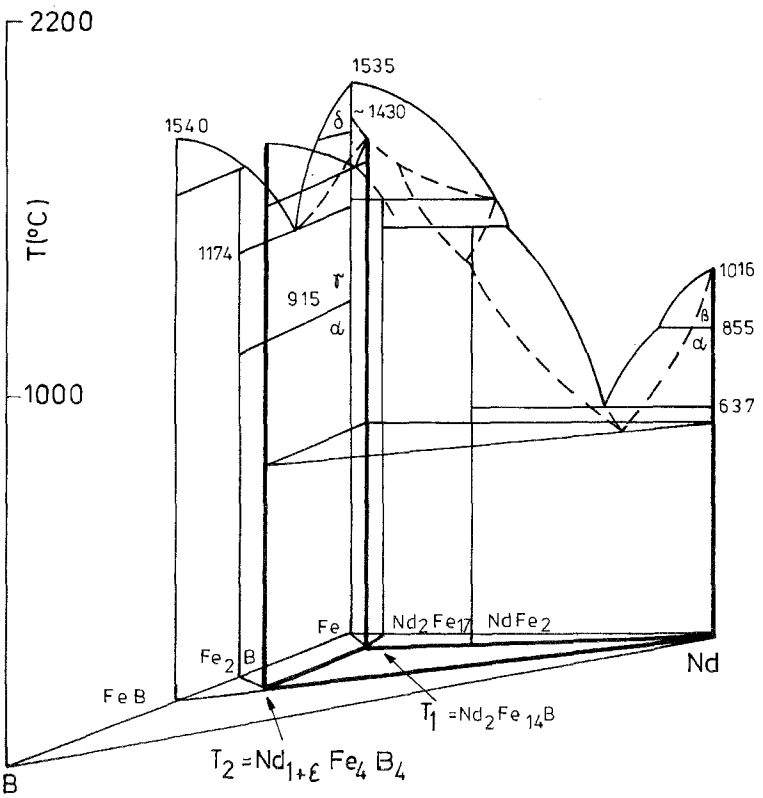

Fig. 1. Phase diagram of Nd–Fe–B system.

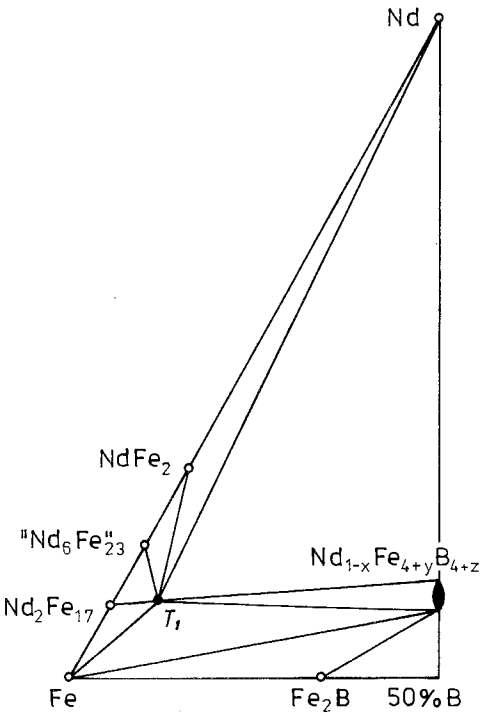

Fig. 2. Phase equilibria in Nd–Fe–B system at 600°C.

According to Oesterreicher (1985) the RFe_4B_4 compounds appear to allow for a slightly higher R concentration as compared to the stoichiometric one. Matsuura et al. (1985b) reported the existence of the $R_{1+\varepsilon}Fe_7B_6$ composition. Crystallographic studies show the presence of the $R_{1+\varepsilon}Fe_4B_4$ composition (R = Ce, Pr, Nd, Sm, Gd and Tb) with 0.11 (Pr) $\leq \varepsilon \leq$ 0.15 (Tb) (Bezinge et al. 1985, Braun et al. 1982, Givord et al. 1985a, b, Givord et al. 1986a, b). For R = Pr, Nd and Gd the structure is of the Pccn space group, while for R = Ce and Sm, the structure can be described by the space group $P4_2/m$. In addition, weak superstructure reflections were observed (Bezinge et al. 1985, Givord et al. 1985b, 1986a). These correspond to a periodic modulation of the Fe tetrahedra induced by interactions with the R sublattice in order to increase the shortest Fe–R interatomic distances. Chang and Qiang (1986) reported that the tetragonal boron rich phase is one-dimensional.

An eutectic composition with low melting temperature is also shown. After Stadelmaier et al. (1984), the eutectic constituent found in the magnet alloys have 70 at% Nd with little boron.

The experimental study of the liquidus projection in the phase diagram of Nd–Fe–B ternary system has been also carried out (Matsuura et al. 1985b). In the Nd-poor region it is found that two phases, Fe_2B and T_2 ($Nd_{1+\varepsilon}Fe_4B_4$ or $Nd_2Fe_7B_6$) coexist with the liquid. Two monovariant curves $L \rightleftharpoons Fe + Fe_2B$ and $L \rightleftharpoons Fe_2B + T_2$, join and form the transition reaction, $L + Fe_2B \rightleftarrows T_2 + Fe$. The end point of the liquid in the Nd-poor region is the ternary eutectic point

$L \rightleftarrows Fe + Nd_2Fe_{14}B(T_1) + T_2$. In the Nd-rich region T_1 phase, T_2 phase and rich-Nd solid solutions solidify from the liquid at the end point of the liquid.

The phase diagram of as-cast buttons and melt-spun ribbons with the composition $La_{15}Fe_{77}B_8$ and $La_{16}Fe_{76}B_8$ was investigated by Hadjipanayis et al. (1985c). The crystallization and stability of the tetragonal $La_2Fe_{14}B$ phase was analyzed by Stadelmaier et al. (1985b). It has been suggested that in the $P4_2/mnm$-type structure boron can be replaced to some extent by carbon (Stadelmaier and El Masry 1985, Stadelmaier and Park 1981). An iron-rich phase having the composition $Gd_3Fe_{20}C$ was initially reported in the Gd–Fe–C system (Stadelmaier and Park 1981). The study of the Gd–Fe–C phase diagram allows one to identify this phase as $Gd_2Fe_{14}B$ (Stadelmaier and El Masry 1985). No such carbide was found in the Ce–Fe–C system (Park et al. 1982). This phase has been observed in the R–Fe–C system with R = Dy or Er (Pedziwiatr et al. 1986c).

2.2. *Crystal structure of $R_2Fe_{14}B$ compounds*

The crystal structure of $Nd_2Fe_{14}B$ compound has been determined by neutron diffraction study (Herbst et al. 1984) and by X-ray measurements (Givord et al. 1984a, Shoemaker et al. 1984). This phase is tetragonal belonging to the space group $P4_2/mnm$ (fig. 3).

The crystalline cell is constructed from four $Nd_2Fe_{14}B$ units, 68 atoms, respectively. This structure is formed also with other lanthanides, yttrium and thorium. The R ions occupy two distinct crystallographic sites, the iron ions share six non-equivalent sites, while B is located on one site. The positions of the atoms in lattice are given in table 1 (Herbst et al. 1984).

The above structure is related to the sigma phase (Bergman and Shoemaker 1954) and may be described in terms of nets perpendicular to z-axis. There are triangular nets formed by $Nd_1(4f)$, $Nd_2(4g)$, $Fe_1(4e)$ and B atoms in the mirror planes at $z = 0$ and $1/2$. Between each pair of adjacent planes, there are sandwiched two puckered sigma-phase main layer-type nets ($z \simeq 1/8$ and $3/8$) formed by $Fe_2(4c)$, $Fe_3(8j_1)$, $Fe_5(16k_1)$ and $Fe_6(16k_2)$ atoms and one sigma-

TABLE 1
Atomic sites and coordinates x, y, z (in units of the lattice constants) for $Nd_2Fe_{14}B$ obtained from analysis of room temperature neutron diffraction data.

Atom	Site	x	y	z
Nd_1	4f	0.2679(5)	0.2679(5)	0
Nd_2	4g	0.1403(4)	−0.1403(4)	0
Fe	4c	0	0.5000	0
Fe	4e	0.5000	0.5000	0.1139(5)
Fe	$8j_1$	0.0979(3)	0.0979(3)	0.2045(2)
Fe	$8j_2$	0.3167(3)	0.3167(3)	0.2464(3)
Fe	$16k_1$	0.2234(3)	0.5673(3)	0.1274(2)
Fe	$16k_2$	0.0375(3)	0.3698(3)	0.1758(2)
B	4g	0.3711(9)	0.3711(9)	0

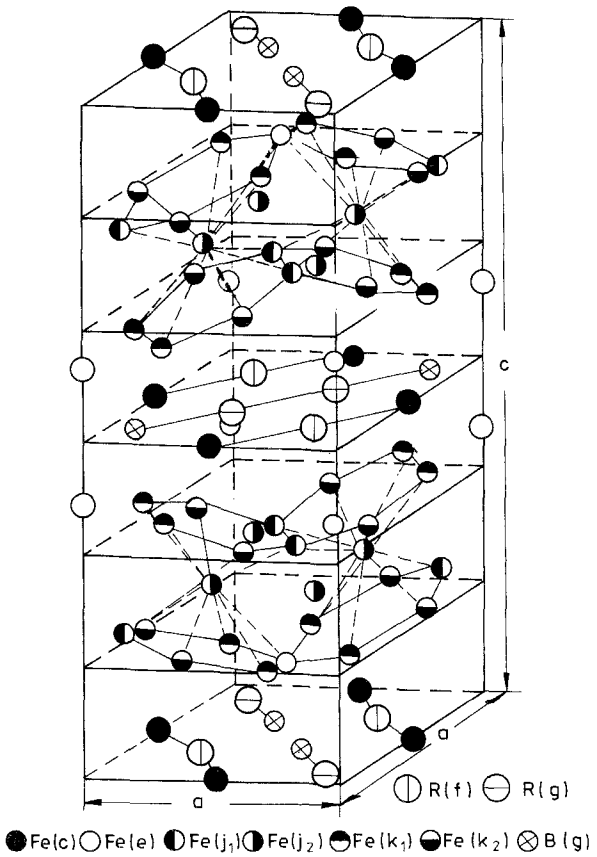

Fig. 3. The crystal structure of $R_2Fe_{14}B$ compounds.

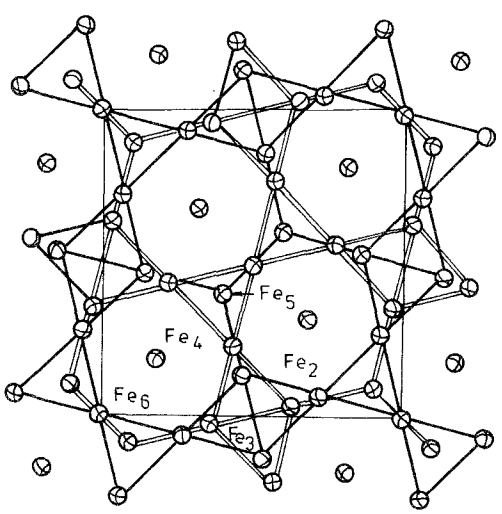

Fig. 4. The schematic representation of iron layers and σ-phase showing the antiprisms occupied by $Fe_4(8j_2)$ atoms.

TABLE 2
The interatomic distances in $Nd_2Fe_{14}B$

Site	Interatomic distances (Å)			
$Fe_1(4e)$	2 $Nd_2(4g)$	3.192	2 $Fe_3(8j_1)$	2.491
	2 B	2.095	2 $Fe(8j_2)$	2.754
	1 $Fe_1(4e)$	2.826	4 $Fe_5(16k_1)$	2.496
$Fe_2(4c)$	2 $Nd_1(4f)$	3.382	4 $Fe_5(16k_1)$	2.573
	2 $Nd_2(4g)$	3.118	4 $Fe_6(16k_2)$	2.492
$Fe_3(8j_1)$	2 $Nd_1(4f)$	3.306	1 $Fe_4(8j_2)$	2.784
	1 $Nd_2(4g)$	3.296	2 $Fe_5(16k_1)$	2.587
	1 $Fe_1(4e)$	2.491	2 $Fe_6(16k_2)$	2.396
	1 $Fe_3(4f_1)$	2.433		
	2 $Fe_4(8j_2)$	2.633		
$Fe_4(8j_2)$	1 $Nd_1(4f)$	3.143	2 $Fe_5(16k_1)$	2.748
	1 $Nd_2(4g)$	3.049	2 $Fe_5(16k_1)$	2.734
	1 $Fe_1(4e)$	2.754	2 $Fe_6(16k_2)$	2.640
	2 $Fe_3(8j_1)$	2.633	2 $Fe_6(16k_2)$	2.662
	1 $Fe_3(8j_1)$	2.784		
$Fe_5(16k_1)$	1 $Nd_1(4f)$	3.066	1 $Fe_4(8j_2)$	2.734
	1 $Nd_2(4g)$	3.060	1 $Fe_4(8j_2)$	2.748
	1 B	2.096	1 $Fe_5(16k_1)$	2.592
	1 $Fe_1(4e)$	2.496	1 $Fe_6(16k_2)$	2.527
	1 $Fe_2(4c)$	2.573	1 $Fe_6(16k_2)$	2.536
	1 $Fe_3(8j_1)$	2.587	1 $Fe_6(16k_2)$	2.462
$Fe_6(16k_2)$	1 $Nd_1(4f)$	3.279	1 $Fe_5(16k_1)$	2.527
	1 $Nd_2(4g)$	3.069	1 $Fe_5(16k_1)$	2.462
	1 $Fe_2(4c)$	2.492	1 $Fe_5(16k_1)$	2.536
	1 $Fe_3(8j_1)$	2.396	1 $Fe_6(16k_2)$	2.542
	1 $Fe_3(8j_2)$	2.662	2 $Fe_6(16k_2)$	2.549
	1 $Fe_4(8j_2)$	2.640		

phase subsidiary layer-type net ($z = 1/4$) formed by $Fe_4(8j_2)$ atoms (fig. 4). Similarly, as in $CaCu_5$-type structure, the R atoms occupy the center of a hexagonal prism. The B atoms are at the center of a trigonal prism of iron atoms, occupying the lattice sites similar to the 2c-type in $CaCu_5$ structure.

The coordination of the atoms and also the distances between them, in $Nd_2Fe_{14}B$, are given in table 2 (Givord et al. 1984a). In these systems short distances ($d < 2.50$ Å) between some iron sites appear similar to those found in R_2Fe_{17}-type compounds (Givord and Lemaire 1974).

2.3. *Lattice parameters of $R_2Fe_{14}B$ compounds*

A survey of the composition dependence of the lattice constants of $R_2Fe_{14}B$ compounds was given already by Livingston (1985b). In fig. 5 we plotted the up-to-date reported values (Sagawa et al. 1984a, Givord et al. 1984a, Shoemaker et al. 1984, Abache and Oesterreicher 1985, Sinnema et al. 1984, Yamamoto et al. 1984, Stadelmaier et al. 1985a, Andreev et al. 1985, Burzo 1984, Hirosawa et

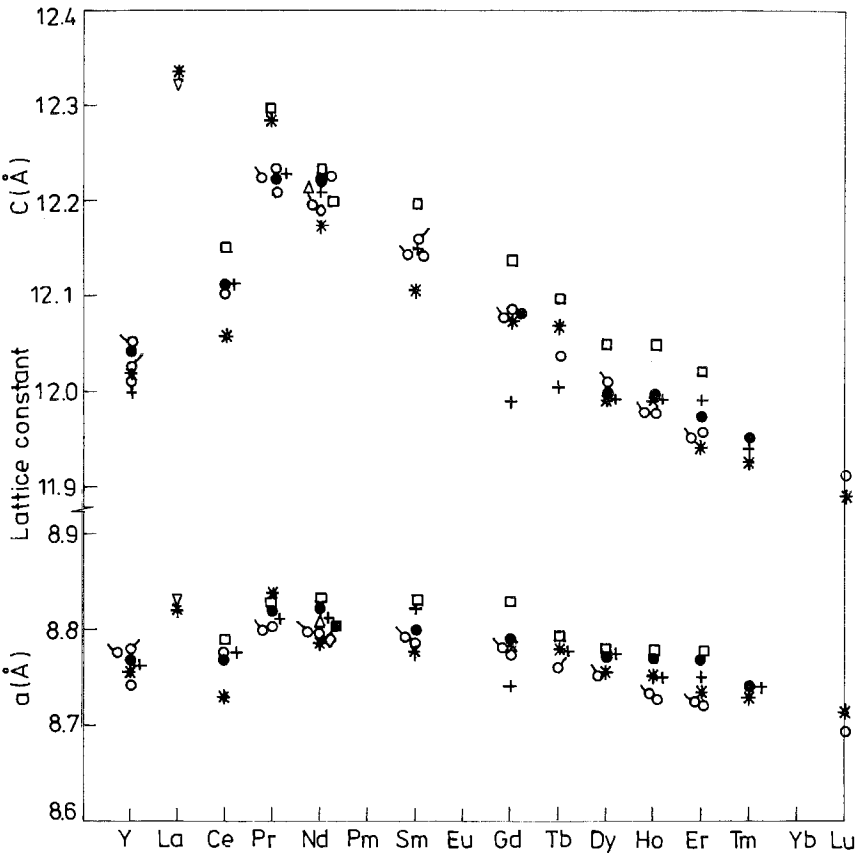

Fig. 5. The composition dependence of the lattice parameters: ○ Abache and Oesterreicher (1985), * Sinnema et al. (1984), □ Sagawa et al. (1984a, b), ● Yamamoto et al. (1984), △ Shoemaker et al. (1984), ▽ Stadelmaier et al. (1985b), ○ Andreev et al. (1985), ○ Burzo (1984), ◇ Givord et al. (1984a), + Hirosawa et al. (1985a), ■ Deryagin et al. (1984).

al. 1985a, Deryagin et al. 1984). These decrease as the lanthanide atomic number increases, following the lanthanide contraction. Such a behaviour is more evident in the *c* direction. According to Herbst et al. (1985) these features are connected with the structural stability of the trigonal prisms formed by each boron atom and its six nearest iron neighbours. The anomalously small lattice parameters of $Ce_2Fe_{14}B$ compound are associated with the tetravalent state of cerium.

The crystal structure and lattice parameters of $R_2Fe_{14-x}T_xB$ alloys with T = Co, Si, Al, Cu, Mn, Cr, etc., were also studied. The $R_2Fe_{14-x}Si_xB$ compounds (R = Pr, Nd, Er and Y) crystallize in a tetragonal structure of $P4_2/mnm$-type up to a silicon content $x = 2$. The lattice parameters decrease as the Si content increases (Pedziwiatr et al. 1987a, b). The $R_2Fe_{14-x}Co_xB$ compounds with R = Pr, Nd, Gd, and Y have a tetragonal structure for the entire composition range (Sagawa et al. 1984b, Arai and Shibata 1985, Burzo et al. 1985a, b, Matsuura et al. 1985a, Pedziwiatr et al. 1986b, L'Heritier and Fruchart 1985, Fuerst et al.

1986). The lattice parameters decrease with increasing the cobalt content. The $R_2Fe_{14}B$-type structure was preserved when replacing iron by aluminium (Burzo et al. 1986a, Yang et al. 1986a). Single phase compounds were obtained when substituting iron by ruthenium up to $x = 2.0$ (Pedziwiatr et al. 1986a, Ku et al. 1986). In $Y_2Fe_{14-x}Cu_xB$ alloys a single phase is observed up to a copper content $x = 1.5$ (Pedziwiatr et al. 1987a). Diffraction studies on $Er_2Fe_{14-x}T_xB$ with T = Mn or Co show the presence of a tetragonal structure for T = Mn up to $x = 9$ and up to $x = 5$ for Co (Meisner and Fuerst 1986). The lattice parameters of $Er_2Fe_{14-x}Mn_xB$ exhibit a minimum between $x = 2$ and $x = 3$. The lattice parameters of $Nd_{15}(Fe_{1-x}T'_x)_{78}B$ with $x < 0.5$ and T' = Mn or Cr increase with raising the Mn or Cr content (Yang et al. 1985a, b, Ho et al. 1985). The structure of $Gd_2Fe_{14-x}Mn_xB$ (L'Heritier and Fruchart 1985) and $Nd_2Co_2Fe_{12-x}Mn_xB$ (Jurczyk and Wallace 1986) was also analysed. Maocai et al. (1985b) replaced Fe in $Nd_{15}(Fe_{1-x}T''_x)_{77}B_8$ by Cr, Zr, Ti, Ni, Mn and Cu. No data on the structure of the above alloys were reported.

2.4. *Preparation of the alloys*

In the following we present some preparation methods of R–Fe–B alloys. The steps involved in manufacturing permanent magnets will be surveyed in section 4.1. Both the $R_2Fe_{14}B$ magnetic phase as well as alloys having a composition slightly different from the above are obtained. For manufacturing permanent magnets, alloys with an approximate composition $R_{15}Fe_{77}B_8$ are used. The alloys are multiphases and always contain in addition to the $R_2Fe_{14}B$ hard magnetic phase a low-melting eutectic phase with ~70 at% Nd as well as $R_{1+\varepsilon}Fe_4B_4$ phase.

The most common method to produce R–Fe–B alloys consists in melting the respective metals in an inert atmosphere, in induction furnace (Sagawa et al. 1984a) or in arc furnace (Tokunaga and Harada 1985). Sometimes, the melting is performed in vacuum. The melting in vacuum has no advantage as compared to that in inert gas, since there is a loss of weight of some components by volatilization. The Nd may be prepared in the conventional way by electrolysis of the chloride, or thermal reduction of the fluoride by using calcium as the reductant. Variations include preparing a low melting Nd-rich Nd–Fe master alloy by the above two processes. The use of this master alloy is interesting technically as well as commercially.

Stadelmaier et al. (1985a) prepared R–Fe–B alloys by the reaction of elemental Fe and Nd powder in combination with a master alloy of Fe_2B-type along a ternary diffusion path.

$R_2Fe_{14}B$ single crystals were also produced. Givord et al. (1984a) obtained crystals by the Czochralski method from a levitation melt in a so-called cold crucible. Koon et al. (1986a) prepared R–Fe–B single crystals using the Czochralski method and arcs to keep the charge molten. Typical growth rates were 5 mm/h. Hiroyoshi et al. (1985) have grown $R_2Fe_{14}B$ single crystals in an infrared imaging furnace filled with argon by floating-zone melting technique.

After cooling the samples are annealed at temperatures between 900 and 1100°C in an inert gas atmosphere or in vacuum.

The R–Fe–B alloys may be prepared by reducing with calcium, at high temperature, the respective rare-earth oxides, in the presence of a mixture of transition metals in powder form plus some transition metal oxides (Herget 1985a). Two versions of calciothermic processes for making rare-earth alloys were proposed: the reduction–diffusion (R–D) process (Cech 1974, McFarland 1973) and the co-reduction process (Herget and Domazer 1975, Domazer and Strnat 1976). The last one consists of a simultaneous reduction of rare-earth and transition metal oxides in the presence of transition metal powder, followed by diffusional alloys formation. The process may be divided into two steps:

$$\tfrac{15}{2}Nd_2O_3 + 72Fe^* + \tfrac{4}{30}Fe_{40}B^\circ_{60} + \tfrac{45}{2}Ca \xrightarrow[\text{vacuum}]{1200^\circ C} Nd_{15}Fe_{77}B_8 + \tfrac{45}{2}CaO$$

*iron metal powder; ◦ commercial powdered ferroboron,

$$Ca^\circ + 2CaO + 2H_2O \xrightarrow{RT} 2Ca(OH)_2$$

◦ excess calcium metal from reduction.

Since the eutectic phase is a region of heavy corrosion, a leaching procedure has been developed (Herget 1985a) that enables us to remove the excess calcium and the CaO by-product in spite of the corrosive nature of Nd–Fe–B alloys.

Another procedure used to obtain R–Fe–B alloys is the so called melt-spinning method. Thus, the amorphous precursor or the fine-grained metastable structure are produced directly. Such a method involves melting of the alloy or constituent elements in quartz tube. The melt under argon pressure is sprayed through an orifice in a quartz tube into a rotating water-cooled copper wheel or disc. The quench rate varies by changing the substrate velocity. Cooling rates in excess of 10^6 K s^{-1} are produced (Ormerod 1984, 1985). A fine grained metastable structure could be obtained by annealing treatment.

The method of liquid dynamic compaction (LDC) (Chin et al. 1986, Tanigawa et al. 1986) is based on the process of gas atomization (Anand et al. 1980). In gas atomization a stream of molten alloy is broken into a spray of fine particles by a jet of high-velocity gas and the rapidly solidified particles are collected. In LDC, a cooled substrate is placed beneath the atomization core at a distance such that most of the sprayed droplets are partially solidified. The rapidly solidified alloy builds up on the substrate at controllable rates, which can easily exceed 1 cm/min. Rapid solidification is made possible by the supercooling of the high-velocity atomized particles and the good thermal contact with a water-cooled copper substrate.

3. Magnetic properties of $R_2Fe_{14}B$ compounds

The essential components of the permanent magnets based on R–Fe–B alloys are the tetragonal $R_2Fe_{14}B$ compounds. Consequently, it is of interest to analyse the magnetic behaviour of these phases, which determine mainly the magnetic characteristics of the magnets. The Curie temperatures, magnetizations, anisotropy fields as well as the magnetic behaviour of $R_2Fe_{14}B$ compounds above the Curie temperatures are presented below.

3.1. *The Curie temperature*

The Curie temperatures, T_c of $R_2Fe_{14}B$ compounds, where R is a rare earth, reported by various authors are plotted in fig. 6. The T_c values are mainly

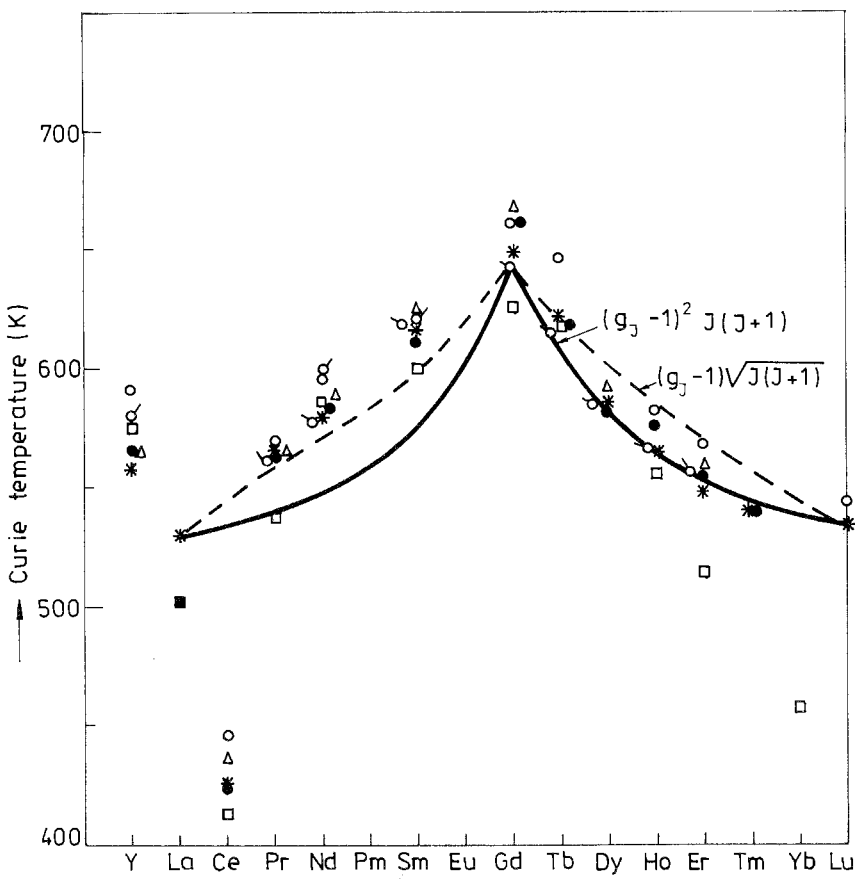

Fig. 6. The composition dependence of the Curie temperatures: ○ Abache and Oesterreicher (1985), * Sinnema et al. (1984), □ Sagawa et al. (1984a, b), ● Yamamoto et al. (1984), ■ Stadelmaier et al. (1985b), ○ Andreev et al. (1985), ○ Burzo (1984), △ Boltich et al. (1985), Huang et al. (1985b).

determined by the magnetic interactions involving iron atoms. A dependence on the rare earth partner is also observed.

The Curie temperatures are due to the cumulative effect of the magnetic interactions between iron atoms, J_{Fe-Fe} between iron and rare earth, J_{R-Fe}, as well as between rare earths, J_{R-R}. Supposing that the magnetic interactions between the iron atoms are not dependent on the rare earth element, two simplified analyses may be performed:

(a) If the exchange interactions between two lanthanides are smaller than those of J_{R-Fe} type, the J_{R-R} values may be neglected. In this case the T_c values may be described by a relation of the form $T_c = T_0 + a_1(g_J - 1)\sqrt{J(J+1)}$ (Sinnema et al. 1984). The predictions of the above relation are plotted in fig. 6 by the broken line.

(b) The lanthanide contribution to T_c values is proportional to the De Gennes factor, $T_c = T_0 + a_2(g_J - 1)^2 J(J+1)$ (Burzo 1984, Burzo et al. 1985d, Pszczola and Krop 1986). This relation is plotted in fig. 6 by the solid line.

Both relations reasonably describe the Curie temperatures of the heavy lanthanide compounds. For light lanthanide compounds, a deviation from these predictions is shown, particularly in the case (b). This fact may be attributed to the variations of exchange interactions between iron atoms, as the distances between them vary, as result of the modification of the lattice parameters. This matter will be analysed below.

The Curie temperatures of $R_2Fe_{14}B$ compounds are about 55% of the Curie point of metallic iron. Low Curie points were also reported in R_2Fe_{17}-type compounds (Givord and Lemaire 1974). The arrangement of the iron atoms in $P4_2/mnm$-type lattice is rather complex and consequently the distances between them cover a large range of values. The interactions between the iron atoms situated at distances $d_{Fe-Fe} < 2.50$ Å are negative (Givord and Lemaire 1974). The interactions between iron atoms situated at distances greater than 2.50 Å are positive. For example in case of $Nd_2Fe_{14}B$ compound, the interactions between $Fe_3(8j_1)$ and $Fe_6(16k_2)$ atoms situated at $d_{Fe-Fe} = 2.396$ Å are strongly negative, while those between $Fe_3(8j_1)$ and $Fe_3(8j_1)$ located at $d_{Fe-Fe} = 2.433$ Å are also negative but of a lesser strength. The magnetic couplings between $Fe_3(8j_1)$ and those situated in $Fe_4(8j_2)$ and $Fe_5(16k_1)$ sites, at distances $d_{Fe-Fe} = 2.633$ Å and 2.587 Å, respectively are supposed to be positive and impose a parallel alignment of iron moments as experimentally observed (Givord et al. 1985a). The negative interactions between iron atoms are not satisfied since they are smaller than the positive ones and consequently a considerable magnetic energy is stored. Similar as in R_2Fe_{17} compounds, the magnetic energy varies greatly with distance. As the d_{Fe-Fe} values are greater, the positive interactions increase while the negative ones decrease. Thus, the competition between elastic and magnetic energies leads to anomalies in the thermal dilatation, as observed in $Y_2Fe_{14}B$ compounds (fig. 7) (Givord and Li 1984, Givord et al. 1984b, c). Such anomalies in the thermal variation of the lattice parameters determine a decrease of the magnetic energy at the expense of the elastic one.

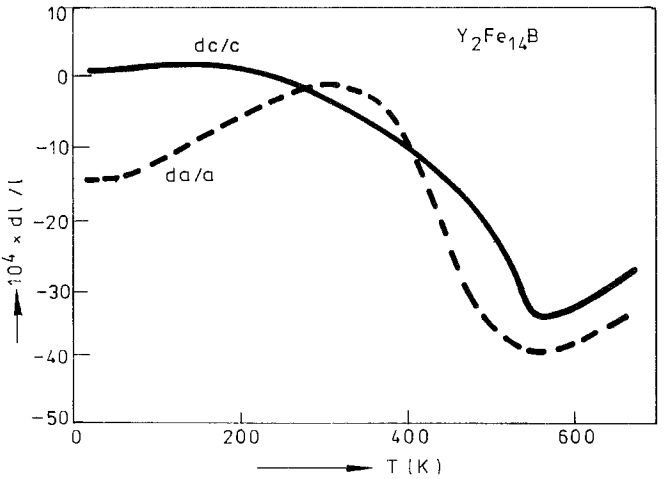

Fig. 7. Thermal variations of the reduced values of lattice parameters, da/a and dc/c in $Y_2Fe_{14}B$ compounds.

The temperature dependence of the lattice parameters of $R_2Fe_{14}B$ compounds (R = Y, Nd and Sm) in the temperature range 4.2–800 K was studied also by Andreev et al. (1985). The thermal dilatation coefficients for $R_2Fe_{14}B$ (R = Y, Nd and Sm) are given in table 3. In this table the magnetostriction constants λ_a and λ_c along the a and c axes as well as the volume magnetisriction λ_v at 4.2 K are presented. The spontaneous volume magnetostriction is high (~2%) and does not depend on the rare earth or the type of anisotropy and is determined by the iron sublattice. Szymczak (1985) calculated the magnetostriction constants of $Nd_2Fe_{14}B$ and compared them with the experimental data. Graham and Flanders (1986) reported the room temperature linear magnetostriction as function of the applied field and magnetization of $Nd_2Fe_{14}B$-type permanent magnet materials. The magnetostriction was relatively small and showed substantial hysteresis at the applied field levels. The elastic constants of $R_2Fe_{14}B$ compounds with R = Y, Pr and Nd were studied by Turilli et al. (1985). These are given in table 4. Since the magnetostriction constants are small, one may conclude that magnetostrictive strains do not significantly contribute to the elastic constants.

TABLE 3
The magnetostriction and thermal dilatation coefficients of $R_2Fe_{14}B$ (R = Y, Nd, Sm) compounds

Compounds	Magnetostriction coefficients at 4.2 K × 10^{-3}			Thermal dilatation coefficients × $10^{-3}K^{-1}$		
	λ_a	λ_c	λ_v	α_a	α_c	α_v
$Y_2Fe_{14}B$	8.5	2.5	19.5	1.21	1.20	3.61
$Nd_2Fe_{14}B$	8.7	1.7	19.0	1.24	0.93	3.41
$Sm_2Fe_{14}B$	8.2	2.7	19.2	1.23	1.09	3.55

TABLE 4
The elastic constants, Debye temperature, θ_D, Young modulus E and Poisson ratio ν for some $R_2Fe_{14}B$ compounds.

Compound	Elastic constants $\times 10^{12}$ N m^{-2}		θ_D	ν	E
	C_{11}^{eff}	C_{44}^{eff}	(K)		(10^{12} N m^{-2})
$Y_2Fe_{14}B$	146	66.9	429	0.077	144
$Pr_2Fe_{14}B$	147	59.5	390	0.085	138
$Nd_2Fe_{14}B$	161	70.1	414	0.114	156

As a result of the low Curie points great variations in the temperature dependence of the magnetic properties are evidenced. An improvement of the magnetic properties around room temperature may be obtained by increasing the Curie points. In this framework, the effect of iron substitution by various metals was studied. In fig. 8 we plotted the composition dependence of the Curie

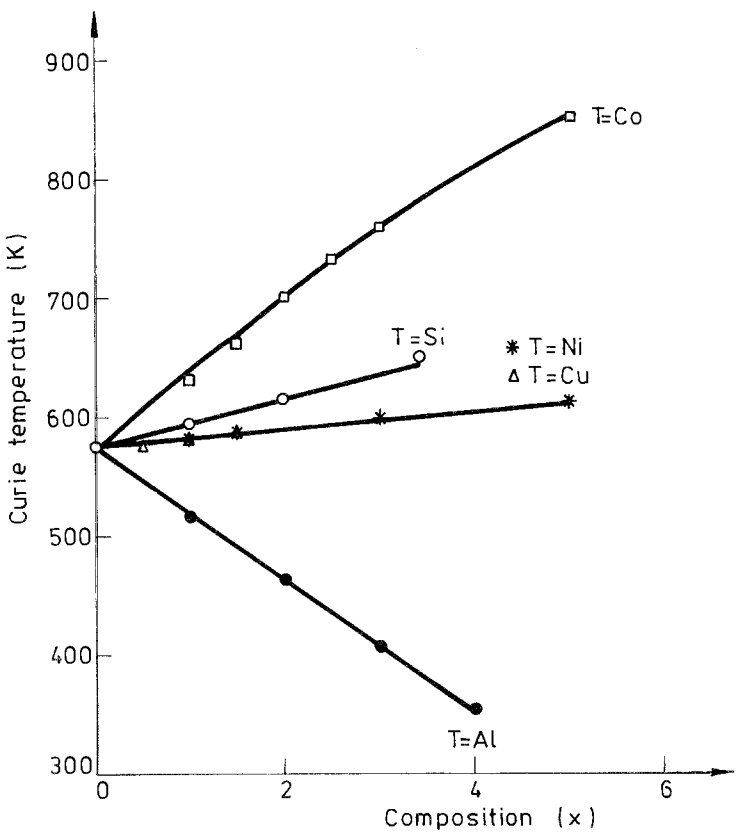

Fig. 8. The effect of iron substitution on the Curie temperatures of $Y_2Fe_{14-x}T_xB$ compounds (T = Co, Ni, Al, Si and Cu).

temperatures in $Y_2Fe_{14-x}T_xB$ alloys with T = Co, Ni, Al, Si and Cu (Pedziwiatr et al. 1987a, Burzo et al. 1985b, 1986b, Yang et al. 1986a, b). The Curie temperatures increase strongly when iron is substituted by cobalt. In this case the composition dependence of T_c values is not linear. A mean increase of ~60 K per substituted iron atom is observed (Burzo et al. 1986b). The replacement of iron by nickel, silicon, or copper slightly increases the Curie point, while in case of aluminium the Curie temperature is lowered.

When substituting Fe by Co, the positive exchange interactions between the transition metals increase and the negative ones decrease, cobalt replacing a fraction of $Fe_6(16k_2)$ sites (Burzo et al. 1985b, d). Because of the similarity in the composition dependence of the Curie temperatures in crystalline and amorphous alloys, a random distribution of cobalt in iron sites was also supposed, especially for high cobalt concentration. Later on (Van Noort and Buschow 1985) it has been reported that for low cobalt content the cobalt shows a strong preference for $Fe_6(16k_2)$ sites and avoids $Fe_4(8j_2)$ sites in $Nd_2(FeCo)_{14}B$ system. The composition dependence of the Curie temperatures in $Pr_2Fe_{14-x}Co_xB$ alloys was analysed also in the above models (Pedziwiatr et al. 1986b).

When replacing iron by silicon or nickel, generally, there is a decrease of the exchange interactions and at first sight it is expected that the T_c values decrease. For Fe–Si alloys with low silicon content, variations in T_c values of −3.5 K/at% Si (Stoner 1946) or −2 K/at% Si (Stoelinga et al. 1971) were reported. Arajs (1965) shows that the composition dependence of the Curie temperatures in iron–silicon alloys is not linear. In the composition range up to 7 at% Si, the T_c values decrease by ~31 K. Supposing a similar diminution of the exchange interactions occurs in the $Y_2Fe_{14-x}Si_xB$ compounds, a decrease of ~31 K for an iron atom replaced by silicon atom is expected (each replacement of an iron corresponds to an addition of 7 at% Si). Consequently, the increase of the Curie points may be attributed to a higher positive contribution than the previous one, which may be ascribed only to the diminution of the negative exchange interactions. This takes place if Si atoms occupy Fe sites involved in antiferromagnetic exchange interactions, namely $Fe_6(16k_2)$. The experimentally determined composition dependence of T_c values in this case is due to two competitive effects since $Fe_3(8j_1)$ atoms interact in two ways: antiferromagnetically with the $Fe_6(16k_2)$ and $Fe_3(8j_1)$ atoms and ferromagnetically with the $Fe_4(8j_2)$ and $Fe_5(16k_1)$ atoms. If there is a diminution of the positive exchange interactions, which leads to a variation of T_c values by −31 K for a substituted iron by silicon, it may be concluded that there must be a decrease of negative exchange interactions which increases the Curie point by ~52 K, when replacing iron in sites involved in antiferromagnetic interactions. The last value is ~70% of the variations of the T_c values when iron is replaced by cobalt. The presence of both mechanism leads to an increase of the Curie temperature by ~21 K per substituted iron by silicon.

An increase of the Curie temperatures may be also evidenced when replacing Fe by Cu or Ni. This is a variation of ~9 K per substituted iron. In these cases it is expected that the Cu or Ni atoms occupy iron sites involved both in ferromagnetic and antiferromagnetic exchange interactions with a slight preference for the

former. In the copper system the lattice parameters increase and consequently this leads to a diminution of negative exchange interactions and to an increase of the positive ones. For aluminium substitutions the Curie temperature decreases rapidly, namely by ~70 K per substituted iron. This seems to be connected with the site distributions of these atoms.

The composition dependences of the Curie temperatures in some $Nd_2Fe_{14}B$-based compounds are given in fig. 9 (Sagawa et al. 1984b, Pedziwiatr et al. 1986a, 1987b, Jurczyk and Wallace 1986, Ku et al. 1986). The substitution of Fe by Ru rapidly decreases the Curie points (Pedziwiatr et al. 1986a, Ku et al. 1986). The comparative analysis of the lattice constants of $Nd_2Fe_{14-x}Ru_xB$ and $R_2Fe_{14}B$ compounds show that the observed variations in the dimensions of lattice constants do not have much influence on the T_c values. Thus, the sharp decrease

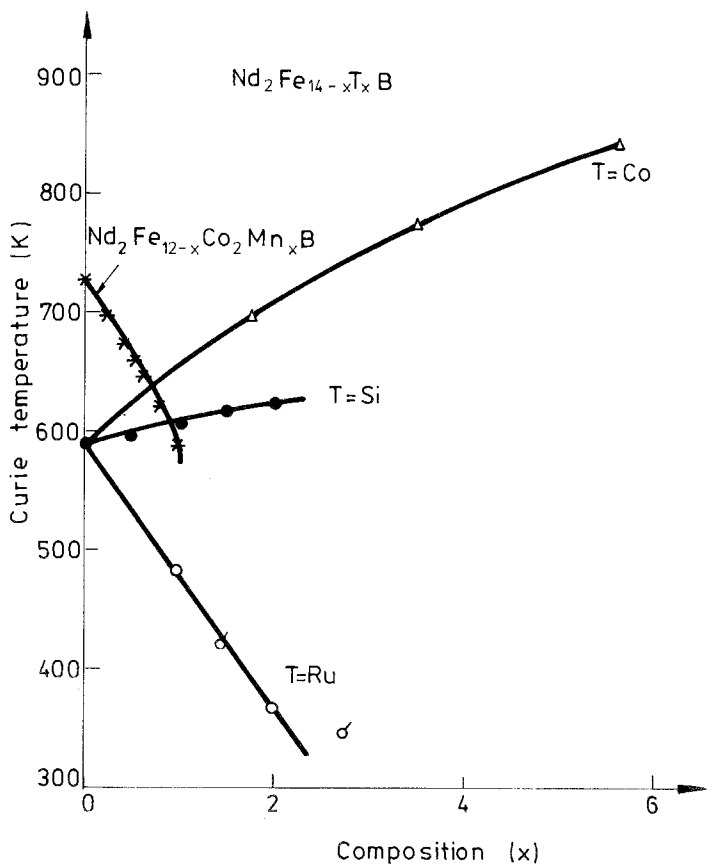

Fig. 9. The composition dependence of the Curie temperatures in $Nd_2Fe_{14-x}T_xB$ (T = Co, Si and Ru) and in $Nd_2Fe_{12-x}Co_2Mn_xB$ alloys: △ Sagawa et al. (1984b), ● Pedziwiatr et al. (1987b), * Jurczyk and Wallace (1986), ○ Pedziwiatr et al. (1986a), Ó Ku et al. (1986).

of the Curie points, as in case of Fe–Ru solid solutions (Ono 1971) may be due to the presence of an antiferromagnetic or mictomagnetic-type ordering. The presence of manganese (Jurczyk and Wallace 1986, L'Heritier and Fruchart 1985) strongly decreases the Curie points. In $Nd_2Fe_{12-x}Co_2Mn_xB$ alloys, for example, this decrease is ~130 K per substituted iron and in $Gd_2Fe_{12-x}Co_2Mn_xB$ ~128 K. As in ruthenium alloys the presence of a mictomagnetic behaviour may explain the experimental data. The replacement of Fe by Al in $Nd_2Fe_{14}B$-based compounds decrease the Curie points by ~70 K per substituted Fe atom, close to the value found in the yttrium compounds (Burzo et al. 1987, Yang et al. 1986b).

The effect of Fe substitution by both Co and Al in $Nd_2Fe_{14-x-y}Co_xAl_yB$ alloys was also investigated (Burzo et al. 1987, Yang et al. 1986b). In the composition range $0 \leqslant x \ll 3$ and $0 \leqslant y \leqslant 1$, the Curie temperatures increase by ~60 K when substituting an iron atom by cobalt and decrease by ~70 K when this is replaced by aluminium.

Higher Curie temperatures than in $R_2Fe_{14}B$ system have been observed in $R_2Co_{14}B$ compounds (R = Y, La, Pr, Nd, Sm, Gd and Tb). The T_c values range from 955 K (R = La) to 1050 K (R = Gd) (Buschow et al. 1985b). In $Nd_2Fe_{14-x}Co_xB$, $Pr_2Fe_{14-x}Co_xB$ and $Gd_2Fe_{14-x}Co_xB$ compounds, the T_c values increase when replacing Fe by Co, over the whole composition range (Sagawa et al. 1984b, Fuerst et al. 1986, Pedziwiatr et al. 1986b, L'Heritier and Fruchart 1985, Huang et al. 1986).

The Curie temperatures of $(R'_xR''_{1-x})_2Fe_{14}B$ vary smoothly between T_c values of $R'_2Fe_{14}B$ and $R''_2Fe_{14}B$ compounds (Huang et al. 1985a, Bolzoni et al. 1986).

Finally we mention that the Curie temperatures of $R_2Fe_{14}C$ compounds are ~40 K lower than those of corresponding boron-based systems (Pedziwiatr et al. 1986c).

3.2. *Magnetic moments*

The composition dependences of the saturation magnetizations at 4.2 K as well as the data obtained at room temperature on $R_2Fe_{14}B$ compounds by several authors are plotted in fig. 10. Other measurements on single-crystals (Sagawa et al. 1985a, Hirosawa et al. 1986, Yamauchi et al. 1986, Hiroyoshi et al. 1985, 1986, Tokuhara et al. 1985) or on polycrystalline samples (Yamauchi et al. 1985, Buschow et al. 1985c, Ho et al. 1985, Sinnema et al. 1985) are not shown in fig. 10. There may are significant differences between the values reported by various authors. These may be attributed to different intensities of external field in which the measurements have been performed and also to the procedure used to obtain the spontaneous magnetizations. Greater values of the saturation magnetizations are evidenced in light lanthanide compounds. As in binary rare-earth transition metal compounds (Taylor 1971, Wallace 1973, Buschow 1977, Kirchmayr and Poldy 1979) the magnetic moments of the light lanthanides are coupled parallel to those of transition metal atoms. For the heavy compounds the R and Fe moments are oriented antiparallel to each other.

Because of local environment effects, the iron magnetic moments are depen-

dent on the lattice sites they occupy. By magnetic measurements only the mean value may be obtained. In case of $Y_2Fe_{14}B$, where yttrium is not magnetic, the mean iron moment determined by saturation measurements is 2.11 μ_B. In $Gd_2Fe_{14}B$, where gadolinium is in S-state, a value of 2.27 μ_B was determined (Burzo et al. 1985d, Burzo 1985a). Substituting yttrium by a magnetic lanthanide, the mean magnetic contribution of iron increased up to 8%.

Data concerning the site dependence of the iron moments may be obtained by neutron diffraction measurements (Herbst et al. 1984, 1985, Herbst and Yelon 1986, Givord et al. 1985a) or may be estimated from ^{57}Fe hyperfine fields. In table 5 we give a summary of the neutron diffraction measurements performed on $R_2Fe_{14}B$ compounds (R = Y, Ce, Pr, Nd and Dy). Differences between magnetic moments of Nd and Fe reported by various authors in $Nd_2Fe_{14}B$ compounds are shown.

Mössbauer effect measurements on ^{57}Fe in $R_2Fe_{14}B$ compounds have been carried out by several investigators. The studied $R_2Fe_{14}B$ compounds are with

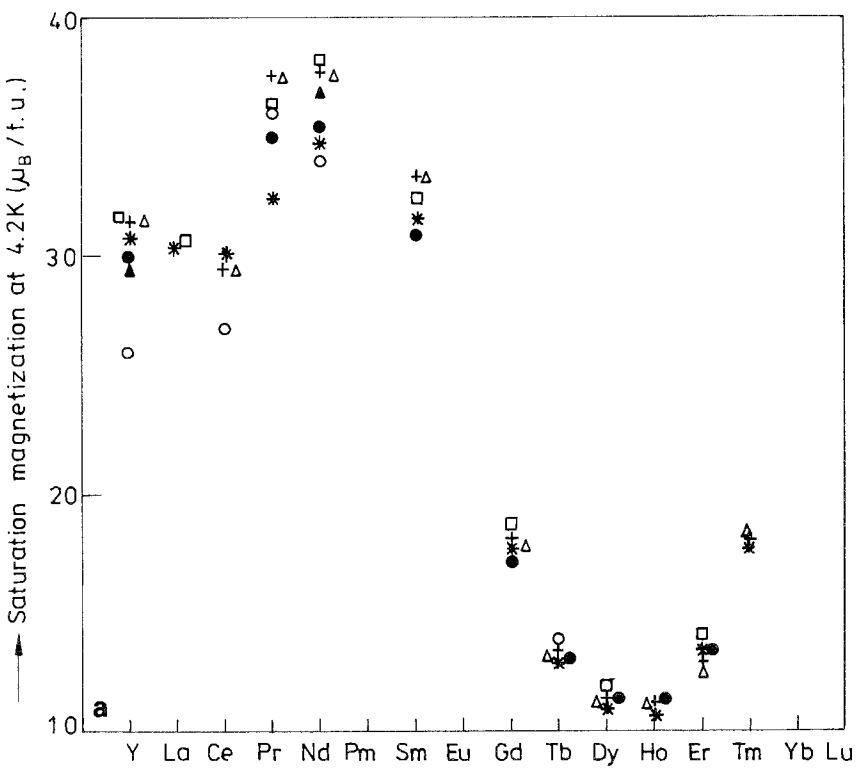

Fig. 10. The saturation magnetizations at 4.2 K (a) and 293 K (b) in $R_2Fe_{14}B$ compounds. At 4.2 K: ○ Abache and Oesterreicher (1985), * Sinnema et al. (1984), □ Boltich et al. (1985), ● Burzo (1984), ▲ Givord et al. (1984b), △ Yamauchi et al. (1986). At 293 K: ○ Abache and Oesterreicher (1985), □ Boltich et al. (1985a, b), + Hirosawa et al. (1985a, b), ● Yamamoto et al. (1984), ▲ Givord et al. (1984b), * Sagawa et al. (1984b). △ Koon et al. (1985).

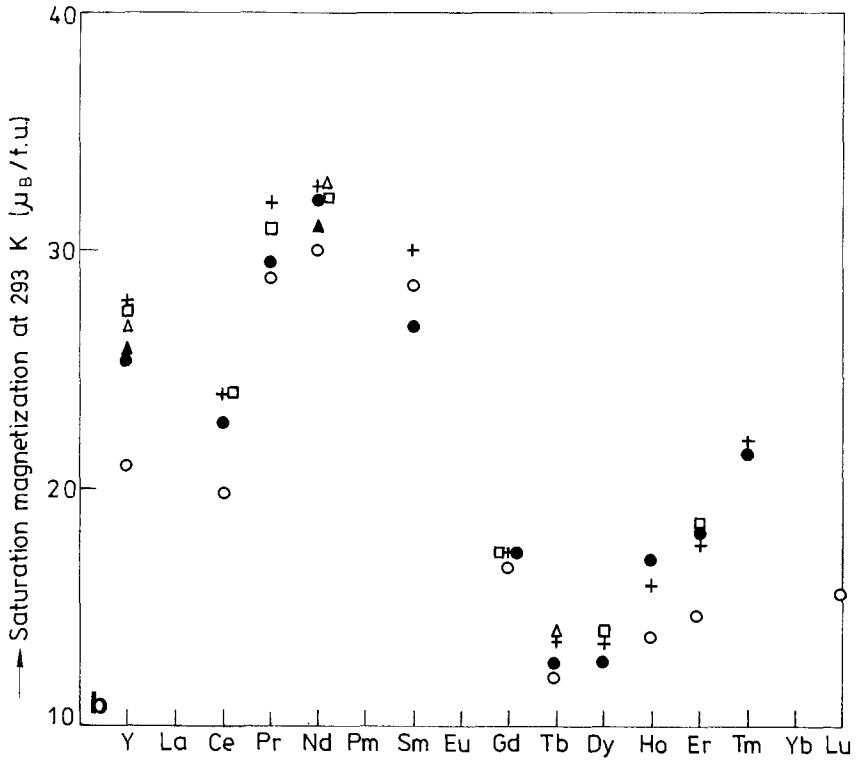

Fig. 10(b)

R = Pr, Nd, Dy and Er (Wallace et al. 1985), R = Nd (Kamal and Anderson 1985, Ling et al. 1986, Rani and Kamal 1986, Rani et al. 1986), R = Y, La, Ce, Pr, Nd, Gd, Dy and Ho (Rosenberg et al. 1985, 1986a, b), R = Y, Ce, Pr, Nd, Gd, Dy and Ho (Pinkerton and Dunham 1985), R = Nd (Onodera et al. 1984, Buschow et al. 1985b, Rong et al. 1985, Koon et al. 1986b), R = Dy (Friedt et al. 1984), R = Ce, Dy, Er, Y (Friedt et al. 1986a, b), R = Ce, Nd, Gd and Y (Van Noort et al. 1985, 1986), R = Pr (Rotenberg et al. 1985), R = Y, Pr, Gd, Tb, Dy and Er (De Réotier et al. 1985), R = Y, Nd, Gd, Dy and Lu (Berthier et al. 1986), R = Tm (Price et al. 1986), $(Er_{1-x}Gd_x)_2Fe_{14}B$ (Vasquez and Sanchez 1986), $Y_{2-x}Nd_xFe_{14}B$ compounds (Bolzoni et al. 1986) as well as on $Nd_{15}Fe_{85-x}B_x$ alloys with $x = 0$–8 (Jueyun et al. 1985). The Mössbauer spectra consist of six sextets, corresponding to the nonequivalent iron sites in $P4_2/mnm$ lattice. The above studies suggest that the electronic configuration of iron atoms are nearly the same for all these compounds and that iron 3d shell dominates the conduction electron polarization contribution to the ^{57}Fe hyperfine fields. The mean ^{57}Fe hyperfine fields scale linearly with the Curie temperature (Pinkerton and Dunham 1985). In case of a single-crystal $Nd_2Fe_{14}B$ sample cut with its c-axis normal to the sample face, the canting angle of the iron spins was measured. The iron spins rotate away from c-axis by about 27° at 4.2 K (Koon et al. 1986b).

The iron magnetic moments may be also obtained from the ^{57}Fe hyperfine

TABLE 5
The rare-earth and iron moments in the $R_2Fe_{14}B$ compounds

		$R_1(4f)$	$R_2(4g)$	$Fe_1(4e)$	$Fe_2(4c)$	$Fe_3(8j_1)$	$Fe_4(8j_2)$	$Fe_5(16k_1)$	$Fe_2(16k_2)$	Ref
a) Neutron diffraction										
$Y_2Fe_{14}B$	T = 4.2 K	–	–	2.15	1.95	2.40	2.80	2.25	2.25	[1]
$Nd_2Fe_{14}B$	T = 4.2 K	2.30	2.25	2.10	2.75	2.30	2.85	2.60	2.60	[1]
$Nd_2Fe_{14}B$	T = 77 K	2.3(1)	3.2(1)	1.1(2)	2.2(3)	2.7(1)	3.5(1)	2.4(1)	2.4(1)	[2, 3]
$Er_2Fe_{14}B$	T = 77 K	2.6(1)	2.8(1)	1.7(2)	1.7(2)	2.4(1)	3.3(1)	2.6(1)	2.5(1)	[3]
$Dy_2Fe_{14}B$	T = 77 K	−8.9(1)	−9.2(1)	2.4(1)	2.5(1)	2.5(1)	3.0(1)	2.6(1)	2.5(1)	[3]
$Ce_2Fe_{14}B$	T = 77 K	–	–	2.1(2)	2.4(1)	2.7(2)	3.4(1)	2.7(1)	2.2(1)	[4]
$Lu_2Fe_{14}B$	T = 77 K	–	–	1.7(3)	2.2(2)	2.9(2)	3.6(2)	2.8(2)	2.4(2)	[4]
b) Mössbauer effect data										
$Nd_2Fe_{14}B$	T = 77 K	–	–	2.33	2.16	1.87	2.60	2.24	2.55	[5]
$Er_2Fe_{14}B$	T = 77 K	–	–	2.41	2.19	1.99	2.65	2.25	2.35	[5]
c) Band calculation										
$Nd_2Fe_{14}B$		–	–	2.42	2.49	2.33	2.61	2.40	2.40	[6]
		–	–	2.28	2.32	2.16	2.84	2.41	2.11	[7]

[1] Givord et al. (1985b), [2] Herbst et al. (1984), [3] Herbst et al. (1985), [4] Herbst and Yelon (1986), [5] Wallace et al. (1985), [6] Szpunar and Szpunar (1985), [7] Inoue and Shimizu (1986a).

fields. In binary iron rare-earth compounds the ratio between the ^{57}Fe hyperfine field, H_{hf}, and the iron moment M_{Fe} is $H_{hf}/M_{Fe} \simeq 147\ kG/\mu_B$ (Gubbens et al. 1978, Burzo and Ursu 1979). Some M_{Fe} values thus obtained are listed in table 5. According to the peculiar environment, the iron moments may differ up to 23%.

The mean iron moment determined by polarized neutron study in $Y_2Fe_{14}B$ is 2.32 μ_B, while in $Nd_2Fe_{14}B$ a value of 2.56 μ_B was obtained (Givord et al. 1985a). These values are somewhat larger than 2.11 μ_B as obtained by magnetic measurements in $Y_2Fe_{14}B$ or 2.28 μ_B estimated from ^{57}Fe hyperfine field values in $Nd_2Fe_{14}B$ (Wallace et al. 1985). This fact suggests the presence of negative 4s polarization (Givord and Li 1984). The negative polarization, M_{4s}, estimated from the above data is $-0.28\mu_B$ in case of $Nd_2Fe_{14}B$ and $-0.21\mu_B$ in $Y_2Fe_{14}B$ compound. These values are close to $-0.25\mu_B$ found in pure iron (Shull and Yamada 1962). By using a value $M_{4s} = -0.25\mu_B$ for all the $R_2Fe_{14}B$ compounds, the mean iron moments deduced from magnetic and Mössbauer effect measurements were corrected. The mean M_{Fe} values thus obtained are listed in table 6. Assuming for iron a value $g_{Fe} = 2.10$ as determined in rare-earth-iron compounds (Burzo 1983), S_0, the mean spin values of iron were obtained. These are in the range $1.105 \leq S_0 \leq 1.24$, see table 6.

The effect of substitution of Y or a non-magnetic rare earth by a magnetic one, on the iron magnetic contributions was analysed by Givord et al. (1985c). In $Y_2Fe_{14}B$, small iron moments are evidenced in $Fe_2(4c)$ sites, $M_{Fe_2}(4c) = 1.95\mu_B$. This site has four Y atoms as nearest neighbours as well as four $Fe_5(16k_1)$ and

TABLE 6
Some magnetic data obtained by measurements on $R_2Fe_{14}B$ compounds

	Y	Pr	Nd	Gd	Dy	Ho	Er
Effective iron moments, M_{eff}(fe), (μ_B)	3.98	4.02	4.04	4.12	4.09	4.07	4.10
The iron spins obtained from paramagnetic data, S_p	1.460	1.485	1.490	1.525	1.510	1.505	1.515
Mean iron moment (μ_B)							
Neutron diffraction at 4.2 and 77 K (*) [2, 3]	2.32	2.61*	2.56	–	2.61*	–	–
Mössbauer effect	–	2.28	2.28	–	2.31	2.32	2.30
Saturation magnetization[1)]	2.11	–	–	2.27	2.26	2.27	2.25
Corrected values considering 4s negative polarization M_c(Fe)	2.32	2.61	2.58	2.52	2.61	2.52	2.55
The iron spins determined from M_c(Fe)	1.105	1.243	1.228	1.20	1.243	1.20	1.214
$r = S_p/S_0$	1.321	1.195	1.213	1.270	1.214	1.254	1.24

[1)] Using the M_R moment given by gJ value.
[2] Givord et al. (1985a)
[3] Herbst et al. (1985), Herbst and Yelon (1986)

four $Fe_6(16k_2)$ atoms. As result of a greater number of Y atoms as nearest neighbours, the exchange interactions involving $Fe_2(4c)$ atoms are small. Consequently, a smaller exchange splitting of $Fe_2(4c)$ band is supposed. When substituting Y by a magnetic lanthanide, due to 4f–3d exchange interactions, there is an increase in the exchange splitting of iron 3d band, and $M_{Fe_2}(4c)$ increase to a value of $2.75\mu_B$. By exchange interactions between $Fe_2(4c)$ atoms and $Fe_5(16k_1)$ and $Fe_6(16k_2)$ nearest neighbours, their magnetic moments increase from $2.25\mu_B$ up to $2.60\mu_B$ when Y is substituted by Nd (table 5).

The study of spin polarized band energy in $Nd_2Fe_{14}B$ (Szpunar and Szpunar 1985) leads to the theoretical determination of the iron magnetic moments in various crystallographic sites (table 5). A reasonable agreement with the experimental data, especially in predicting a greater magnetic moment on the $Fe_4(8j_2)$ sites may be observed. The electronic structure and magnetic moments in $Y_2Fe_{14}B$ were calculated using a first principle method. The calculated values show a substantial degree of local environment effects (Gu and Ching 1986a, b).

Inoue and Shimizu (1986a) calculated the electronic density of states (DOS) in $Y_2Fe_{14}B$ by the recursion method. The total DOS is similar to that in Y_2Fe_{17}. The values of the low temperature specific heat coefficient, the local magnetic moment on non-equivalent iron sites and the high-field spin susceptibility at 0 K and the temperature variation of the paramagnetic spin susceptibility are calculated and compared with the experimental results. The iron moments are given in table 5. A reasonable agreement with the experimental data is shown.

In $Nd_2Fe_{14}B$, according to Givord et al. (1985c), the low values obtained at 4.2 K for Nd moments suggest that the magnetic structure determined by a competition between 3d–4f exchange interactions and crystal field interactions, is not collinear. Thus, only the projection of the Nd moment along the direction of the spontaneous magnetization is measured. Herbst et al. (1984) show in $Nd_2Fe_{14}B$ at 77 K, that the magnetic arrangement is ferromagnetic with all moments parallel to the *c*-axis. No evidence for spin reorientation or canting was reported. The Nd(g) moments are no longer equal within statistics, with the Nd(f) moment smaller. A Mössbauer study on ^{155}Gd in $Gd_2Fe_{14}B$ (Bogé et al. 1985, 1986) has shown the main axis of the electric field gradient to have different directions at the two rare earth sites. A non-collinear spin structure, at low temperatures was found in $Tm_2Fe_{14}B$ compound (Yamada et al. 1985).

The lanthanide contributions to the magnetization, determined by magnetic measurements coincides generally with the gJ values (Burzo 1984, 1985b, Boltich et al. 1985, Yamauchi et al. 1986). Friedt et al. (1984) and Gubbens et al. (1985, 1986) confirmed this by Mössbauer effect measurements on ^{161}Dy in $Dy_2Fe_{14}B$ compounds.

The magnetic properties of $R_2Co_{14}B$ compounds were also investigated. Sinnema et al. (1985) reported the magnetization measurements up to 35 T on field oriented samples with R = Y, La, Pr, Nd and Sm. $Nd_2Co_{14}B$ exhibits a spin rotation in the (110) plane at low temperature. The *c*-axis is of easy magnetization at 300 K (Le Roux et al. 1985). Another reorientation occurs at 543 K toward the (001) plane. This plane is favoured by cobalt anisotropy. The magnetic and zero field spin echo NMR investigations for $Nd_2Co_{14}B$ and $Y_2Co_{14}B$ compounds were

reported by Kapusta et al. (1986). The anisotropy field and anisotropy constant K_1 derived from the experimental data for $Nd_2Co_{14}B$ are strongly temperature dependent. In $Nd_2Co_{14}B$ the easy direction of magnetization deflects up to ~26° from the *c*-axis in the temperature range from about 130 K down to 4.2 K.

Density of states of $Y_2Co_{14}B$ and also the local density of states of Y and Co atoms are calculated by making use of the tight-binding d-band model and by recursion method. Local magnetic moments on Co atoms are calculated from the computed local density of states (Inoue and Shimizu 1986b).

The effect of iron substitution by other metals in $R_2Fe_{14}B$ based compounds was also analysed. The composition dependence of the saturation magnetizations in $Y_2Fe_{14}B$-based compounds at 4.2 K are plotted in fig. 11 (Pedziwiatr et al. 1987, Burzo et al. 1985b, 1986b). The magnetization of $Y_2Fe_{14-x}Co_xB$ compounds have a small composition dependence, with a maximum at $x = 4$ to 5, i.e. 28–35 at% Co. The above behaviour is similar with that observed in Co_yFe_{1-y} alloys or in pseudobinary R–Fe–Co system (Collins and Forsyth 1963, Abel and Craig 1968, Burzo 1978b). In these cases a peak in the composition dependence of

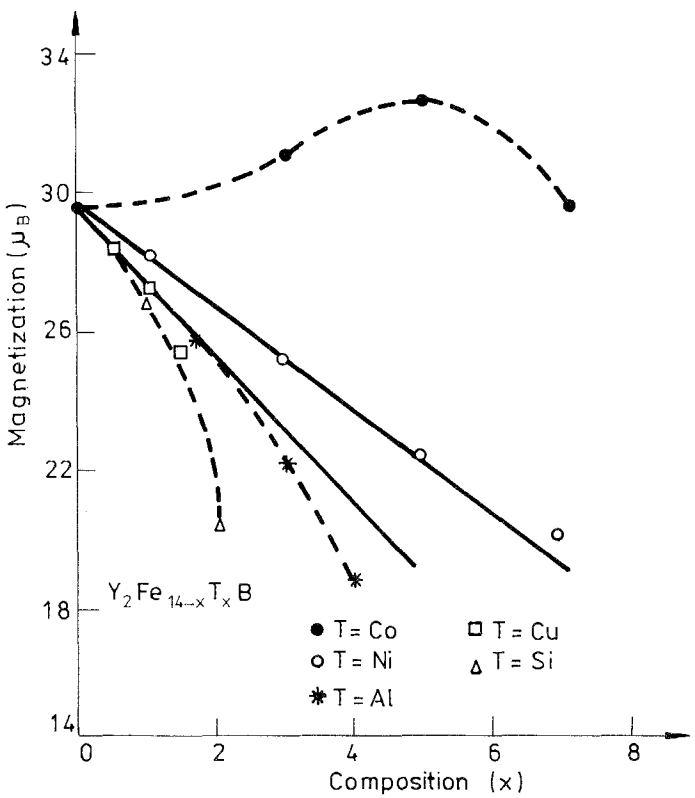

Fig. 11. The composition dependence of the magnetizations at 4.2 K in some $Y_2Fe_{14}B$-based compounds. The solid lines for T = Al and Ni are calculated from a simple dilution model.

the magnetization is observed at $y \simeq 30$ at% Co. The magnetizations decrease when substituting Fe by T = Ni, Al, Cu or Si. In simple dilution model the magnetizations, M_S, may be described by the relation $M_S = 14M_{Fe} - x(M_{Fe} - M_T)$. Assuming that the nickel moment is $M_{Ni} = 0.61\mu_B$ as in pure metal and Al, Cu or Si are not magnetic, the M_S values were computed according to the above relation. These data are plotted in fig. 11 by solid lines. The simple dilution model describes reasonably well the magnetizations of $Y_2Fe_{14-x}Ni_xB$ compounds as well as of $Y_2Fe_{14-x}Cu_xB$ in the high iron concentration range. If the iron is substituted by silicon or aluminium the magnetizations decrease more rapidly than those described by the simple dilution model. The above data suggest a decrease of mean iron moment as compared to 2.11 μ_B evidenced in the $Y_2Fe_{14}B$ compound. This behaviour is attributed to the diminution of the exchange interactions leading to smaller exchange splitting of iron 3d states (Azoulay and Ley 1979).

The composition dependences of the magnetizations in some $Nd_2Fe_{14}B$-based compounds are plotted in fig. 12 (Pedziwiatr et al. 1986a, 1987b, Jurczyk and Wallace 1986). Similar trends as in yttrium systems are shown. The mean iron moments decrease when Fe is replaced by Si, Cu, Mn or Ru as shown for example in $Y_2Fe_{14-x}Cu_xB$, $Y_2Fe_{14-x}Si_xB$ and $Nd_2Fe_{14-x}Si_xB$ compounds (fig. 13). A peak value of magnetization is observed at $x = 1.5$ when iron is substituted by cobalt. The saturation magnetizations of $Pr_2Fe_{14-x}Co_xB$ compounds behave in a similar way. At 77 K these increase slightly up to a maximum at a composition $x \simeq 1$ and then decrease monotonically for larger x values (Pedziwiatr et al. 1986b).

If a Fe atom is replaced by Mn in $R_2Fe_{14}B$-based compounds (R = Nd or Pr) the magnetic moment per formula unit decreases by $6.9\mu_B$ (Jurczyk and Wallace

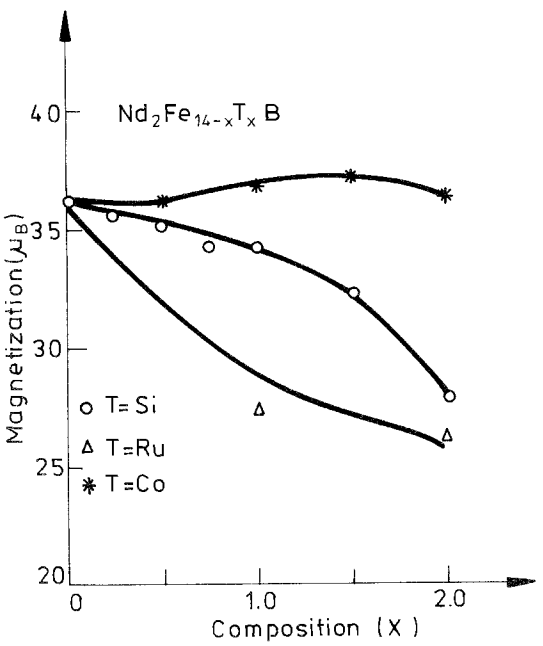

Fig. 12. The composition dependence of the magnetizations at 4.2 K in some $Nd_2Fe_{14}B$-based compounds.

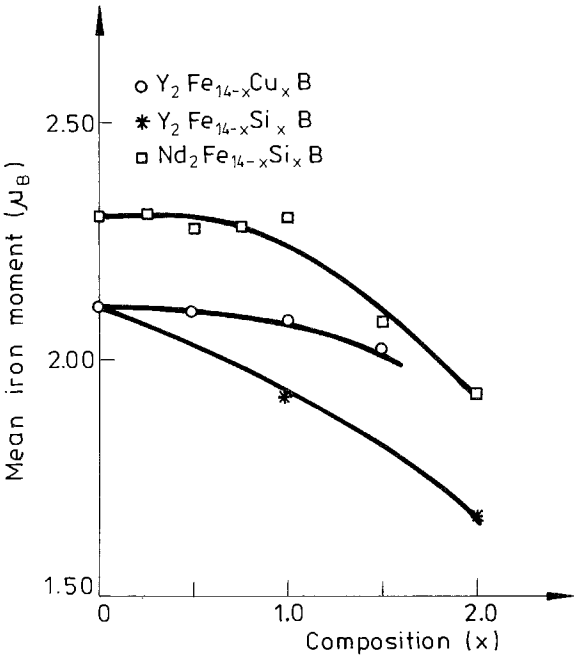

Fig. 13. The composition dependence of the mean iron moment in some $R_2Fe_{14}B$-based compounds.

1986). Such a high decrease of the magnetization may be attributed only to a deviation from a collinear magnetic structure or to a mictomagnetic-type behaviour. In S-state compounds as gadolinium, the decrease of the magnetic moment is $3.1\mu_B$ per substituted iron by manganese, more than twice smaller than in Pr- and Nd-based compounds (Jurczyk and Wallace 1986, L'Heritier and Fruchart 1985). This resembles the magnetic behaviour of amorphous RFe_2 compounds (Rhyne 1979).

In case of $Gd_2Fe_{14-x}Al_xB$ alloys, ferrimagnetic-type ordering is evident (Burzo et al. 1986a). The magnetizations decrease when iron is substituted by aluminium. Similar effects are evidenced in $Nd_2Fe_{14}B$-based compounds (Yang et al. 1986a, b, Burzo et al. 1987).

The effect of iron substitution by Co, Al, Mo, Cr, Zr and Ti in $Nd_{15}Fe_{77}B_8$-based compounds was studied by Maocai et al. (1985a, b). Ho et al. (1985) replaced iron by Co and Mn in the same system, while Szytula and Drajewicz (1986) replaced Fe by T = Mn, Co and Ni in $Y_{15}Fe_{77-x}T_xB_8$ alloys.

Information on the magnetic properties of $R'_{1-x}R''_xFe_{14}B$ compounds were also obtained. In $Gd_{2-x}Y_xFe_{14}B$ the mean iron moment is dependent on the composition (Burzo 1985a). Similar behaviour was evidenced in $R_{2-x}Th_xFe_{14}B$ alloys with R = Y, Dy or Er (Pedziwiatr et al. 1986d). In agreement with our previous discussion, the variation of the mean iron moment seems to be due to some peculiar sites. Substituting Y or Th by a magnetic rare earth, due to 4f–3d exchange interactions, a polarization of $Fe_2(4c)$ moment takes place. This is proportional to the rare-earth content which influence the magnitude of exchange

interactions. By exchange interactions between $Fe_2(4c)$ and $Fe_5(16k_1)$ and $Fe_6(16k_2)$ atoms, there is also an increase in the magnetic contributions of the last two sites. The effect of neodymium substitution by R′ = Er and Dy was investigated in $Nd_{2-x}R'_xFe_{14}B$ alloys (Huang et al. 1985a). Koon et al. (1986a) analysed the magnetic properties of $(Y_{0.9}R_{0.1})_2Fe_{14}B$ with R = Er and Tb. Grössinger et al. (1985b) studied the magnetic behaviour of $(Nd_{1-x}R''_x)_{15}Fe_{77}B_8$ with R″ = Y, La and Ce. Sagawa et al. (1984b) and Rodewald (1985a, b) analysed the magnetic properties of $Nd_{15-x}Dy_xFe_{77}B_8$. The saturation magnetization was calculated from the magnetizations of $Nd_2Fe_{14}B$ and $Dy_2Fe_{14}B$ compounds. The experimental results coincide with the calculated values. Maocai et al. (1985a) substituted Nd by Pr and mischmetal in $(Nd_{1-x}R_x)_{16}Fe_{76}B_8$. When R = Pr, no significant changes in the magnetic properties were observed.

3.3. *Anisotropy fields*

The composition dependence of the anisotropy fields, H_A, of $R_2Fe_{14}B$ compounds, at room temperature is given in fig. 14. Discrepancies between the data given by various authors are also observed. These are mainly due to the different procedures in the determination of the anisotropy fields, to the alignment degree as well as to the strength of the external fields used to determine H_A values.

In compounds with yttrium or non-magnetic lanthanide as La and Ce the magnetization is oriented along *c*-axis. Similar behaviour was observed in $Gd_2Fe_{14}B$ compound. Since Y, La and Ce are not magnetic and gadolinium is in S-state, the anisotropy fields are determined by the iron sublattice. The temperature dependences of the anisotropy fields in $R'_2Fe_{14}B$ compounds (R′ = Th, Y, La, Ce and Lu) was studied by Grössinger et al. (1985b, c, 1986b). The anisotropy fields increase by increasing the temperature, showing a flat maximum at a characteristic temperature. These suggest that the iron atoms on different sites have opposite contributions to the bulk anisotropy.

In compounds with R = Pr, Nd, Tb, Dy or Ho, where the α_j Stevens coefficients are negative, the magnetizations at room temperature are also oriented along *c*-axis. The anisotropy field at 295 K of $Pr_2Fe_{14}B$ is ~79 kOe and of $Nd_2Fe_{14}B$ is ~71 kOe (Boltich et al. 1985). The anisotropy constants of $R_2Fe_{14}B$ compounds, at 4.2 K, are listed in table 7 (Yamauchi et al. 1986). Anisotropy constants were also reported by Hirosawa et al. (1985a).

By decreasing the temperature, the anisotropy fields in $Nd_2Fe_{14}B$ increase up to 140 K, from which the easy axis of magnetization rotates, by lowering the temperature, up to 30°, from the *c*-axis, in the (110) plane (Givord et al. 1984b, Sagawa et al. 1984a). In $Pr_2Fe_{14}B$ as in $Nd_2Fe_{14}B$ compound a spin reorientation was found to occur below room temperature (Grössinger et al. 1985c). The anisotropy constant, K_1, of $Nd_2Fe_{14}B$ changes its sign at a temperature close to 140 K (Yamada et al. 1986, Durst and Kronmüller 1986, Yingchang et al. 1985). Asti et al. (1985) studied $R_2Fe_{14}B$ compounds with R = Nd 90.92, Pr 6.68, La 1.47, Ce 0.47, Sm 0.46 wt%. Both the anisotropy field and the critical field of the first order magnetization process observed below 210 K are not different from

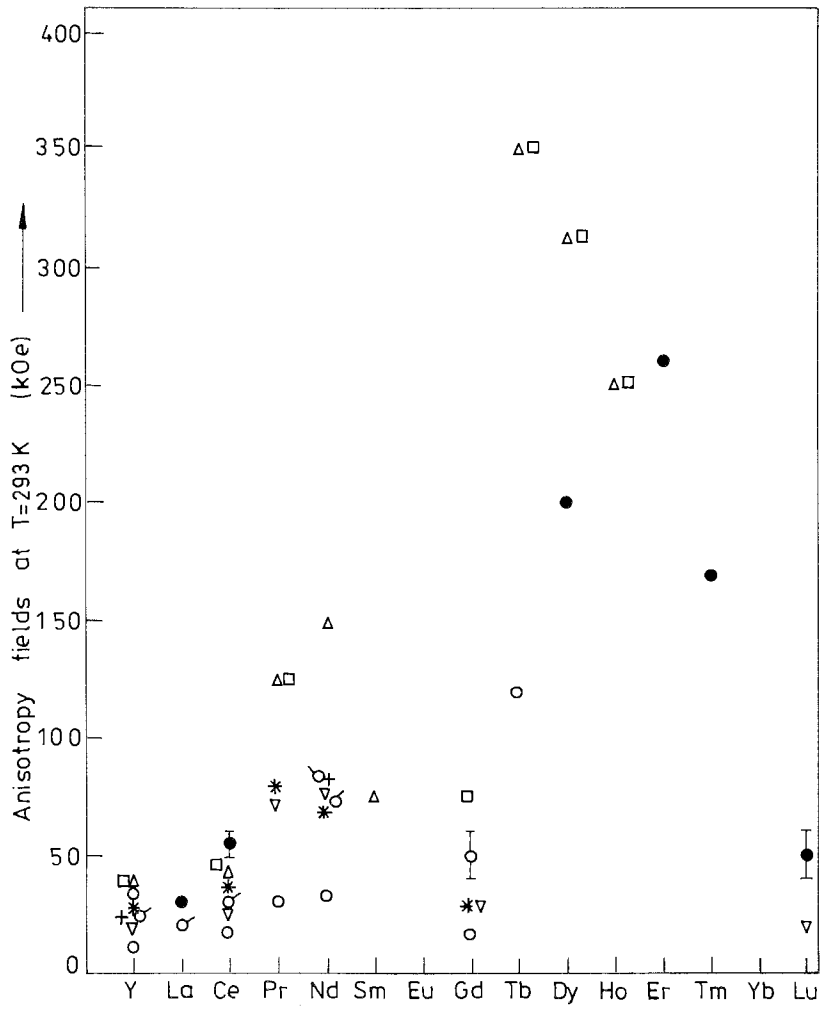

Fig. 14. The room temperature anisotropy field in $R_2Fe_{14}B$ compounds: ○ Abache and Oesterreicher (1985), □ Sagawa et al. (1984b), * Boltich et al. (1985), △ Yamamoto et al. (1984), ● Sinnema et al. (1984), + Yang et al. (1985a, b), ▽ Oesterreicher et al. (1984), Ò Asti et al. (1984), Ó Grössinger et al. (1985b).

TABLE 7
Anisotropy constants at 4.2 K of $R_2Fe_{14}B$ single-crystals

R	Y	Ce	Pr	Nd	Sm	Gd	Tb	Dy	Ho	Er	Tm
K_1 (10^6 J/m^3)	0.90	1.80	24	−16	−26	0.75	6.9	3.8	−1.1	−1.4	−3.6
K_2 (10^6 J/m^3)				28					4.4		
K^3 (10^6 J/m^3)				0.45	−1.4				0.12	−0.29	−0.70

those measured in $Nd_2Fe_{14}B$ compound. In order to justify this behaviour Givord et al. (1984b) computed the crystal field parameters in the second order, considering a point charge model for Nd^{3+} ions. The electrical charge of other ions was considered nil. The spin reorientation, at 140 K, is interpreted by a non-collinear arrangement of Nd magnetic moments on f and g sites. Buschow (1984) shows that the two rare-earth sites in $R_2Fe_{14}B$ compounds contribute with a different sign to the magnetocrystalline anisotropy at low temperatures. Abache and Oesterreicher (1985) and Oesterreicher et al. (1984) considered the contribution of B^{3-} and Nd^{3+} ions and attributed the spin reorientation to the competition to the anisotropy of the f and g sites, respectively. Cadogan and Coey (1984) computed the crystalline field parameters up to the sixth order, summing the contributions of Nd^{3+}, $Fe^{9/14-}$ and B^{3-} ions in a sphere having a radius $r = 60$ Å. It is shown that both neodymium sites have an easy axis of magnetization along c direction. In analysing the contribution of crystalline field, Boltich and Wallace (1985) included a term involving the exchange interactions. It is to be mentioned that $Nd_2Fe_{14}B$ may have a conical easy axis of magnetization, at low temperature, when the crystalline field parameters have adequate values. A similar type of analysis was made by Sankar and Narasimhan (1985) who added to the previous Hamiltonian a $B_2^2O_2^2$ term. Honma et al. (1986) analysed also the contribution of rare earth to the magneto-crystalline anisotropy of $Nd_2Fe_{14}B$, by using a single ion model and a Hamiltonian of the form

$$H = \lambda \boldsymbol{L}\boldsymbol{S} + H_{\mathrm{CEF}} + 2\mu_{\mathrm{B}}\boldsymbol{H}_{\mathrm{exch}}\boldsymbol{S} .$$

The Nd^{3+} ions in all the lattice sites, under the action of both crystalline and exchange fields have uniaxial anisotropy. The contribution of Nd^{3+} ions to the magneto-crystalline anisotropy of $Nd_2Fe_{14}B$ intermetallic compound was calculated also by single ion theory (Xiaojia et al. 1985). By adjusting the shielding factor, the calculated $K_1(T)$ and $K_2(T)$ anisotropy constants agree with the experimental curves. This shows that the shielding factor is material independent.

The point charge model was used to compute the magnetocrystalline anisotropy and magnetoelastic constants for $Nd_2Fe_{14}B$ (Szymczak 1985). It was shown that the experimentally observed spin reorientation phenomena result from the ground state level crossing.

Miyajima et al. (1986) investigated the magnetization process of $Nd_{13}Fe_{81}B_8$ from 4.2 to 300 K, as function of the angle between the c-axis and the magnetic field. The magnetic properties are interpreted in terms of orbital quenching of Nd moment, in the distorted hexagonal crystalline field. Magnetization reversals of several Nd–Fe–B magnets were measured at temperatures between 4.2 K and 300 K, the external field being applied parallel or perpendicular to c-axis (Kuntze et al. 1985). It appears that the constriction in the magnetization curve visible near $H = 0$, may have several causes. At temperatures above 150 K it was found to be associated with sample oxidation. Below 150 K, additional effects seem to play a role: a boron rich phase with Curie point around 50 K, and the spin reorientation phenomena. Ming et al. (1985) analysed the magnetization rotation

from c-axis in $Nd_{16.7}Fe_{75.5}B_{7.8}$ alloy at smaller temperatures than 140 K and attributed the observed effect to the competition between the exchange interactions and the crystalline electric field. Magnetization processes in $R_2Fe_{14}B$ (R = Pr, Nd) were analysed by Pareti et al. (1985a, b).

Adam et al. (1986) within a model independent approach proved that four distinct rare-earth sites exist with respect to the crystalline electric fields and a relationship is established between the corresponding crystal-field coefficients. Generalized Stevens parametrizations of the crystal-field coefficients are derived at three levels of approximation for the interatomic forces inside the crystal. The computation of the crystal-field coefficients in $Nd_2Fe_{14}B$ leads to results which raise a question about the validity of the simple Coulomb point-charge model. In case of a $Nd_2Fe_{14}B$ single crystal Tokuhara et al. (1985) show that below the spin reorientation temperature, the magnetization value, in the direction of easy magnetization, increases anomalously with decreasing temperature. The direction of easy magnetization tilts from [001] axis to [110] one. Hiroyoshi et al. (1985) show that there is no evidence for spin canting of Nd moments in $Nd_2Fe_{14}B$ compound even at 4.2 K.

The $Gd_2Fe_{14}B$ compound was investigated by means of ^{155}Gd Mössbauer spectroscopy (Buschow et al. 1985a, Bogé et al. 1986). The experimental values for the corresponding second order crystal field parameters, B_2^0, were determined. The two rare earth sites in $R_2Fe_{14}B$ compounds experience different types of crystal field. The B_2^0 mainly governs the magnetocrystalline anisotropy in related permanent magnets such $Nd_2Fe_{14}B$.

In addition to light rare-earth compounds some $R_2Fe_{14}B$ systems with heavy rare earth have high values of the anisotropy fields (fig. 14). For technical applications this fact is counterbalanced by the relative low saturation magnetization as result of the antiparallel coupling of lanthanide and iron sublattice magnetizations. In order to increase the anisotropy field and to preserve as much as possible the magnetization value of $Nd_2Fe_{14}B$ compound, the $Nd_{2-x}R_xFe_{14}B$ systems (R = Tb or Dy) were analysed (Sagawa et al. 1984b).

For $R''_2Fe_{14}B$ compounds with R'' = Sm, Er and Tm, the α_J values, for lanthanide ions, are positive. The easy direction of magnetization is determined by the anisotropies of the R and Fe sublattice. As mentioned above, the iron sublattice has an easy c-axis. In case of R'' = Sm, Er and Tm, the R'' sublattice magnetization has an easy direction perpendicular to the c-axis and there is a competition between the R'' and Fe sublattice anisotropies. In these cases the magnetization is in the basal plane at room temperature. Since the lanthanide anisotropy decreases more rapidly than that of iron sublattice, the last one may dominate at higher temperature and spin reorientation phenomena appear. The anisotropy changes from the basal plane to uniaxial one (Sinnema et al. 1984, Hirosawa and Sagawa 1985, Davis et al. 1985). The spin reorientation seems to influence also the magnetic structure. Neutron diffraction measurements (Davis et al. 1985) suggest that $Tm_2Fe_{14}B$ is a basal plane ferrimagnet at 294 K and a c-axis ferrimagnet at 340 K. This study was unable, however, to exclude the possibility of tilting of individual Fe or Tm moments at either temperatures. Later on (Yamada et al.

1985), a neutron diffraction study revealed in this compound a non-collinear spin structure at low temperatures where the magnetization vector lies in the *c*-plane. Favourable parameters are found to reproduce the observed spin structure. The canting angles of Tm moment at f and g sites are $\varphi_f = (34.1 \pm 6.4)°$ and $\varphi_g = (14.9 \pm 1.8)°$.

The relative intensities of Mössbauer spectra in an $Er_2Fe_{14}B$ single crystal (Vasquez et al. 1985), as mentioned, show a spin reorientation from basal plane to *c*-axis. However, a small deviation from expected intensities for the so called 2 and 5 Mössbauer lines in the spectra recorded above 328 K are observed. Although these were attributed to possible non-homogeneous grain size, it may be also suggested to be the non-collinearity of Fe spins. Hirosawa and Sagawa (1985) show large anisotropy in the saturation magnetization at 296 K in $Er_2Fe_{14}B$. It is about 4% greater in the [001] direction than in the basal plane. It was not possible to ascribe this phenomena to the appearance of non-collinear spin structure or to intrinsic single-ion properties of erbium ions. In case of $Er_{2-x}Th_xFe_{14}B$ compounds two stages for spin reorientations are evident (Pedziwiatr et al. 1986d). The spin reorientation temperatures decrease linearly as the thorium content is greater.

In case of $Sm_2Fe_{14}B$ single crystal (Hiroyoshi et al. 1985) the easy direction of the magnetization lies along [100] in the tetragonal structure. Magnetic anisotropy energies at 290 K along [110] and [001] have been estimated to be 5.8×10^5 and 1.1×10^2 J/m^3, respectively, both becoming much larger at lower temperatures.

In $Pr_2Fe_{14-x}Co_xB$ compounds both at 77 K and 295 K there is an initial decrease of H_A values. As more cobalt is introduced to the system, H_A reaches a flat minium and finally increases rapidly to relatively high values (Pedziwiatr et al. 1986b). For cobalt rich samples, both in $Nd_2Fe_{14-x}Co_xB$ and $Pr_2Fe_{14-x}Co_xB$ alloys it was found that at temperatures higher than ambiant, a second spin reorientation takes place. This is ascribed to the competing effect of the Nd sublattice anisotropy and the 3d sublattice anisotropy (Pedziwiatr et al. 1986b, Grössinger et al. 1986c).

Spin reorientation phenomena were also studied in $(R'_xR''_{1-x})_2Fe_{14}B$ mixed systems. The substitution of Nd by Sm in $(Nd_{1-x}Sm_x)_2Fe_{14}B$ results in increasing spin reorientation temperature. A change in easy magnetization direction from the *c*-axis toward the basal plane is observed at room temperature by increasing Sm content (Yang et al. 1986a). The effect of substitution of Nd with Pr is reverse to that with Sm substitutions. The studies performed on $(Y_{0.9}R_{0.1})_2Fe_{14}B$ with R = Er and Tb (Koon et al. 1986a) show that the addition of Er decreases the anisotropy at room temperature slightly, but at low temperature induces a spin reorientation in the (100) plane toward the [010], stopping at an angle of 78° from [001]. The addition of Tb increases the anisotropy favouring the [001] direction at all temperatures. In case of $Y_{2-x}Nd_xFe_{14}B$ system, the Nd ions give the main contribution to the anisotropy and are responsible for first order magnetization processes and spin reorientations observed at low temperatures (Bolzoni et al. 1986). In case of $(Er_{1-x}Gd_x)_2Fe_{14}B$ compounds a single-ion model for the free energy explains the magnetocrystalline anisotropy and describes qualitatively the

composition dependence of the spin reorientation temperature (Vasquez and Sanchez 1986). The anisotropy fields $R_2Fe_{14-x}T_xB$ systems were also analysed. In fig. 15 we give the anisotropy field at room temperature for the $Y_2Fe_{14-x}T_xB$ compounds with T = Co, Al, Ni, Si and Cu (Pedziwiatr et al. 1987a, Burzo et al. 1985c, 1986b). The H_A values at room temperature, generally decrease when Fe is substituted by T = Co, Si, Al or Ni. For T = Al the decrease of the anisotropy field at room temperature is mainly due to the thermal effects. The H_A values for T = Cu increase as compared to the anisotropy field of $Y_2Fe_{14}B$ compound, for a copper content $x = 1.5$.

The anisotropy fields in $Nd_2Fe_{14}B$-based compounds were also analysed. A small amount of Mn (Jurczyk and Wallace 1986), Si (Pedziwiatr et al. 1987b) or Al (Burzo et al. 1987) increases the room temperature H_A values. Due to thermal effects, for higher substitutions, the anisotropy fields decrease.

Grössinger et al. (1985b) studied the anisotropy fields of the mixed crystal series $(Nd_xY_{1-x})_{15}Fe_{77}B_8$, $(Nd_xLa_{1-x})_{15}Fe_{77}B_8$ and $(Nd_xCe_{1-x})_{15}Fe_{77}B_8$ between 77 K and Curie temperature. The temperature dependence of the anisotropy field was analysed using the one ion model. Substituting Nd by a non-magnetic element like Y, La or Ce, always the anisotropy field is reduced because the main part of the anisotropy is caused by the Nd sublattice.

The anisotropy fields of $(NdR')_2Fe_{14}B$ compounds with R' = Er and Dy were investigated by Huang et al. (1985a). The H_A values, at room temperature, decrease with Nd substitution by Er and increase when replacing Nd by Dy.

The anisotropy of $Nd_2Fe_{14}B$ films sample was also analysed (Cadieu et al. 1986a, b). For relatively low substrate deposition temperatures, the *c*-axis texture was predominantly in the plane of the substrate.

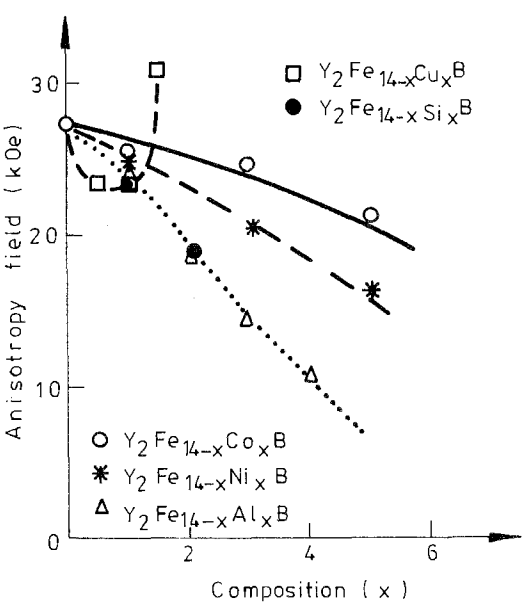

Fig. 15. The composition dependence of the anisotropy field in $Y_2Fe_{14-x}T_xB$ alloys (T = Al, Co, Si, Cu or Ni).

Estimated values of anisotropy fields in $R_2Co_{14}B$ compound are 0.6 T for R = La and 7.5 T for R = Pr (Buschow et al. 1985c). The cobalt sublattice anisotropy favours an easy magnetization direction perpendicular to *c*-axis, whereas the crystal field induced anisotropy of the 4f sublattice corresponds to the second order Stevens factor α_J of R component.

3.4. *Paramagnetic behaviour*

Information on the magnetic properties of $R_2Fe_{14}B$ compounds may be obtained analysing their properties above the Curie points. Some studies were devoted to this subject.

The thermal variations of reciprocal susceptibility, χ^{-1} in $R_2Fe_{14}B$ ferromagnetic compounds (R = Y, Pr and Nd) follow a Curie–Weiss law (fig. 16) (Burzo 1984, Burzo et al. 1985d, e).

$$\chi = C(T - \theta_p)^{-1}, \tag{1}$$

where C is the Curie constant and θ_p is the paramagnetic Curie temperature.

At higher temperatures but close to the Curie points a deviation from the Curie–Weiss behaviour is observed. In this temperature range the susceptibilities are described by a relation of the form $\chi \propto t^{-\gamma}$ where $t = |T - T_c| T_c^{-1}$ and $\gamma = (1.30\text{–}1.40)$, see table 6. The critical exponents, γ, are close to those predicted theoretically for a Heisenberg ferromagnet (De Jongh and Miedema 1974).

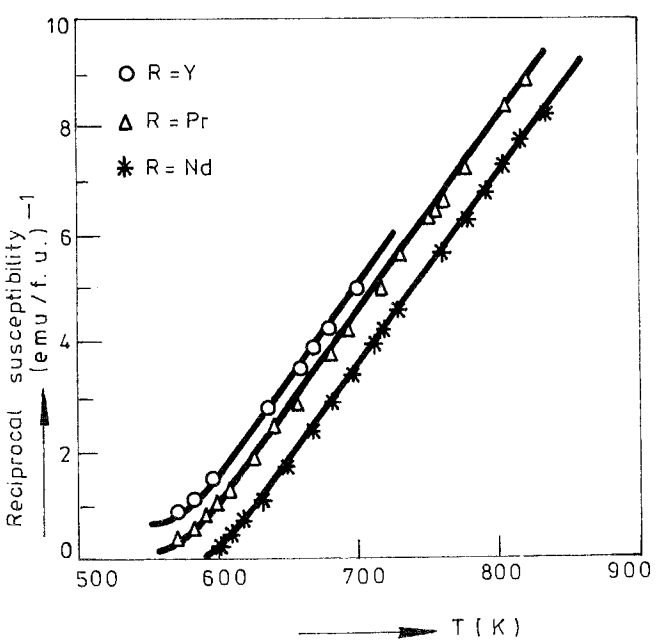

Fig. 16. Thermal variation of the reciprocal susceptibility for some ferromagnetic $R_2Fe_{14}B$ compounds (R = Y, Pr and Nd).

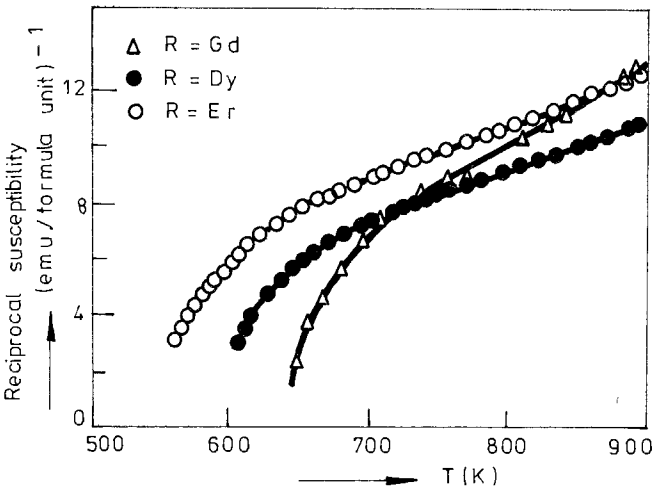

Fig. 17. Thermal variation of reciprocal susceptibility for ferrimagnetic $R_2Fe_{14}B$ compounds (R = Gd, Dy and Er).

The reciprocal susceptibilities for ferrimagnetic $R_2Fe_{14}B$ compounds obey a non-linear temperature dependence described by the relation (fig. 17):

$$\chi^{-1} = \chi_0^{-1} + TC^{-1} - \sigma(T-\theta)^{-1} . \tag{2}$$

By χ_0, σ and θ are denoted parameters connected to the molecular field coefficients and C is the Curie constant. Some data obtained by paramagnetic measurements on these compounds are listed in table 8.

Previously (Farrell and Wallace 1966, Burzo and Laforest 1972) it was noted that the effective lanthanide moments in transition metal compounds are identical with those of the free R^{3+} ions. Taking this into account, according to the additional law of susceptibilities, the iron contributions to the Curie constants and effective iron moments, M_{eff}(Fe) were determined. The effective iron moments are listed in table 4. The errors which appear in determining the M_{eff}(Fe) values, suggest that there are no significant differences between them.

TABLE 8
Data obtained from paramagnetic measurements

Compound	C (emu/fu)	C_R (emu/fu)	C_{Fe} (emu/fu)	θ_p (K)	γ
$Y_2Fe_{14}B$	27.70	–	27.70	563	1.30
$Pr_2Fe_{14}B$	31.60	3.28	28.32	573	1.37
$Nd_2Fe_{14}B$	32.10	3.30	28.40	602	1.41
$Gd_2Fe_{14}B$	45.45	15.95	29.50		
$Dy_2Fe_{14}B$	57.65	28.32	29.33		
$Ho_2Fe_{14}B$	57.40	28.32	29.08		
$Er_2Fe_{14}B$	53.30	24.45	29.35		

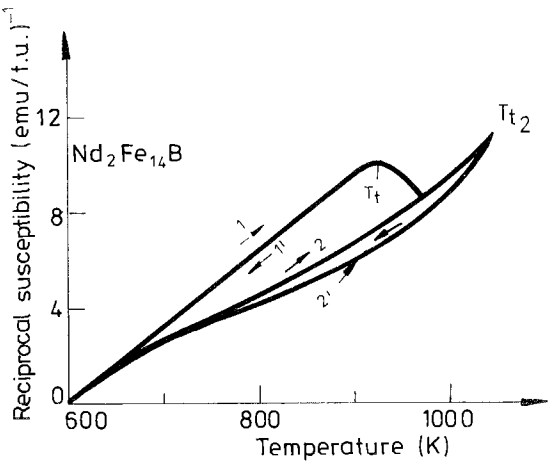

Fig. 18. The temperature dependence of χ^{-1} for $Nd_2Fe_{14}B$ compound by heating several times at temperatures higher than T_t.

An interesting feature of $R_2Fe_{14}B$ compounds is constituted by the deviation of $\chi = f(T)$ curve from the expected behaviour, beginning with a characteristic temperature, T_t, see fig. 18. If the measurements are performed up to a temperature T_t, the magnetic susceptibilities are the same, both by heating and cooling the sample. By cooling the sample from a temperature $T > T_t$, the χ values are greater (curve 2') as compared to the values determined by heating (curve 2). The form of $\chi = f(T)$ curves is dependent on the maximum heating temperature. This behaviour may be correlated with the presence of low melting temperature of the eutectic phase, of great interest in the sintering and postsintering thermal treatment. The temperatures T_t determined in some $R_2Fe_{14}B$ compounds are plotted in fig. 19.

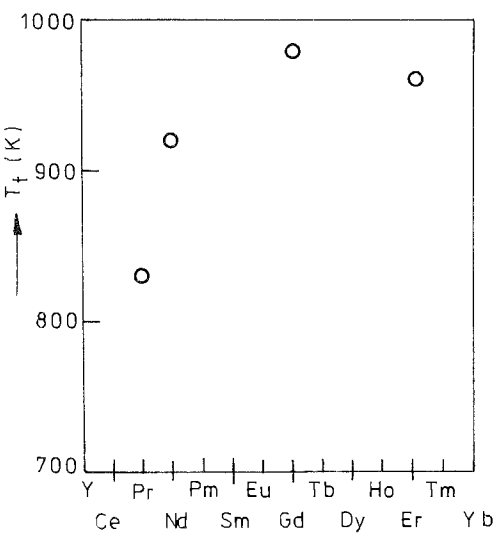

Fig. 19. Some characteristic T_t temperatures for $R_2Fe_{14}B$ compounds.

The paramagnetic behaviour of other systems has been also studied. In case of ferrimagnetic $Gd_2Fe_{14-x}Al_xB$ (Burzo et al. 1986a) and $Gd_{2-x}Y_xFe_{14}B$ (Burzo 1985a) compounds, the reciprocal susceptibilities follow a non-linear temperature dependence described by the relation (2). In $Y_2Fe_{14-x}T_xB$ (T = Co, Si, Cu) compounds Curie–Weiss dependence for χ values are found (Burzo et al. 1985c, Pedziwiatr et al. 1987a).

Considering a two sublattice ferrimagnet and using the molecular field approximation, the mean values of the exchange interactions inside and between magnetic sublattices were determined (Burzo et al. 1985a). The exchange interactions between lanthanides as well as those between iron and the lanthanide are smaller than those inside the iron sublattice. The exchange fields, H_{exch}, acting on the lathanides and iron were estimated. For example the exchange field acting on erbium in $Er_2Fe_{14}B$ is $2\mu_B H_{exch} = 250$ K (Pedziwiatr et al. 1987b) and on Gd in $Gd_2Fe_{14}B$ of 370 K (Bogé et al. 1985). In $Nd_2Fe_{14}B$ we have $2\mu_B H_{exch} = 385$ K (Givord et al. 1986b). These values are close to that obtained in $GdFe_2$, $2\mu_B H_{exch} = 300$ K (Burzo 1975), suggesting that the mechanism involving magnetic interactions in ternary R–Fe–B compounds is not significantly modified from that in the binary lanthanide–transition metal systems. The exchange fields acting on the lanthanides are of the same order of magnitude as the overall splitting of the multiplets (Givord et al. 1986b). This suggests that the lanthanide moments are not significantly influenced by the crystal field effects. The exchange field acting on the iron sublattice is substantially greater, $2\mu_B H_{exch} \simeq 1.5 \times 10^3$ K. Consequently, the iron magnetization as function of temperature diminishes more slowly than that of the lanthanide.

From the effective iron moments, the mean spin values, S_p, were computed according to the relation $M^2_{eff}(Fe) = g^2_{Fe} S_p(S_p + 1)$ (Burzo et al. 1985d). The S_p values thus determined are listed in table 6. These are somewhat greater than the spin values, S_0, obtained from the mean saturation iron moments.

A measure of the localization of iron moments is given by the ratio $r = S_p/S_o$, between the number of spins deduced from the Curie constants and those obtained from saturation data (Burzo 1978a). In case of Fe, Co and Ni metals, the r values are 1.05, 1.34 and 1.46, respectively. The r values for iron moments in $R_2Fe_{14}B$ compounds are around 1.22 (table 6). These data do not suggest a great degree of itineracy.

3.5. *Magnetic properties of $R_2Fe_{14}B$ hydrides*

The $R_2Fe_{14}B$ compounds absorb up to 6 hydrogen atoms per formula unit (Fruchart et al. 1984, Pourarian et al. 1986). The Curie temperature increases with the hydrogen content. This increase is particularly strong for the case of R = Ce, indicating a change of the electronic state of the ion. Neutron diffraction studies allow us to determine the interstitial sites filled by deuterium. The magnetic structure of $Y_2Fe_{14}BD_x$ ($x = 0$ and $x = 3.55$) has been determined. The different iron sites carry a magnetic moment comparable to that of iron metal, within ±20%. In case of $Nd_{15}Fe_{77}B_8$ alloy an increase in the magnetization and ^{57}Fe hyperfine field is observed (Wiesinger et al. 1987). The hydrogen absorption

substantially reduces the anisotropy contribution of the Nd sublattice. The spin reorientation temperature is shifted at lower values. The occupation numbers of certain Fe sites deviate from those found in the parent compound. This together with the selective oxidation of Nd may cause the formation of free metallic iron.

L'Heritier and Fruchart (1985) and L'Heritier et al. (1985) studied also the magnetic properties of $R_2Fe_{14}BH_x$ compounds with R = Y, Lu and Dy. The presence of hydrogen increases the lattice parameters, Curie temperatures and the magnetizations. Ferreira et al. (1985) and Fruchart et al. (1984) studied by magnetization measurements and Mössbauer effect on ^{57}Fe and ^{161}Dy, the $Dy_2Fe_{14}BH_x$ system with $0 \leqslant x \leqslant 4.7$. The ^{57}Fe spectra in $DyFe_{14}BH_{3.3}$ and $ErFe_{14}BH_{2.6}$ reveal both a significant line broadening and an increase in the average field compared with the original materials (Friedt et al. 1986a). The saturation hyperfine field H_{hf} is increased by ~2% in the hydrides as compared with the original materials. The significantly enhanced H_{hf} observed in the hydrides at room temperature by reference to the original alloys arises primarily from the higher ordering temperatures. The local Fe moments depend sensitively on the Fe coordination number, on the nature of R element and on the presence of hydrogen. This is connected with the changes of the magnetic exchanges coupling, which depend on the Fe–Fe interatomic distances. The enhanced ordering temperature of the hydride probably arises from the lattice expansion, i.e. decreased negative exchange interactions. The structure and magnetic properties of $Nd_2Fe_{14}BH_{2.7}$ were investigated by Oesterreicher and Oesterreicher (1984a). The hydrogen decrepitation of an $Nd_{15}Fe_{77}B_8$ magnetic alloy was reported by Harris et al. (1985).

4. Rare earth–iron–boron magnets

4.1. *Sintered R–Fe–B magnets*

The Nd–Fe–B type magnets have been obtained since 1983, by a procedure similar to that used in manufacturing rare-earth-cobalt ones (Sagawa et al. 1984a). The production of the magnets involves certain steps (Ormerod 1985). After casting, the samples are crushed under a nitrogen atmosphere prior to the final milling, that is when Nd–Fe–B alloys involve dimensions smaller than 500 μm. The alloys prepared by calciothermic method are generally of particle size suitable for direct milling. The fine powder may be obtained by ball milling in on organic liquid (cyclohexane, toluene, freon), under an inert atmosphere, the powder being then dried under vacuum, or by heating under argon. Another frequently used method is jet milling. The milling conditions are selected in such a way to give the required particle size distribution and at the same time to pick-up the smallest possible quantity of oxygen.

The effect of milling time in the vibration ball in the presence of freon, on the oxygen pick-up, is given in fig. 20a and in fig. 20b, the correlation between the milling time and particle dimensions is shown (Ormerod 1984, 1985). The oxygen

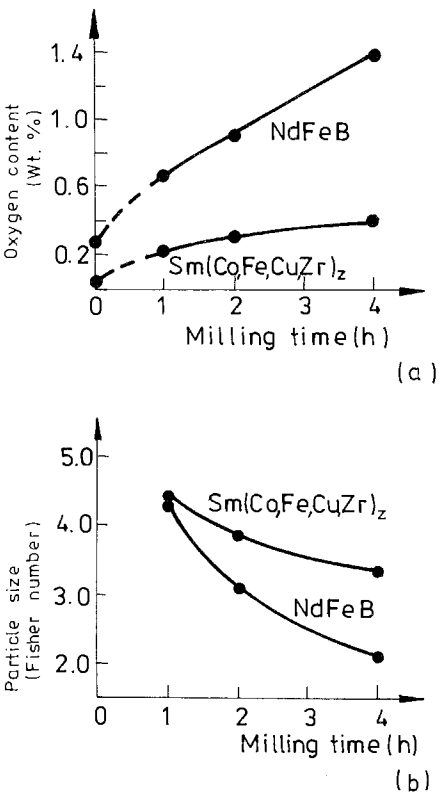

Fig. 20. Effect of milling time during vibration ball-milling in freon on the oxygen pick-up (a) and on the particle size of Nd–Fe–B and Sm(Co, Fe, Cu, Zr)$_z$ alloys (b).

pick-up in Nd–Fe–B alloys is higher than in Sm–Co magnets, while the size reduction is more pronounced than in Sm–Co alloys.

The powder compaction is made by die-pressing or by isostatic pressing. In the first case the external field necessary for alignment is set up in the cavity of a non-magnetic die with its axis lying either in the direction of pressing or perpendicular to it. The pressure used for compacting is thus selected to ensure to a powder compact with sufficient mechanical strength to be handled, but not so high to lead to misorientation of the particles. Isostatic pressing is normally carried out on powders prealigned in a pulsed magnetic field, 3–4 time greater than used in uniaxial pressing. This improves the degree of particle alignment which is maintained during the isostatic pressing.

The sintering of Nd–Fe–B magnets is performed in vacuum or in inert atmosphere. Commonly, the density is greater than 95% from theoretical value. The dependence of magnetic properties on the sintering temperature has been analysed by Sagawa et al. (1984a). The optimum magnetic properties may be obtained for a large range of sintering temperatures (fig. 21). The coercivity of Nd–Fe–B magnets further increases after a post sintering thermal treatment, which may include several different steps at temperatures between 900°C and 600°C and different cooling rates in between. The magnets are e.g. kept at 630°C for 1 h. Following Sagawa et al. (1984a), the enhancement of the coercivity is due

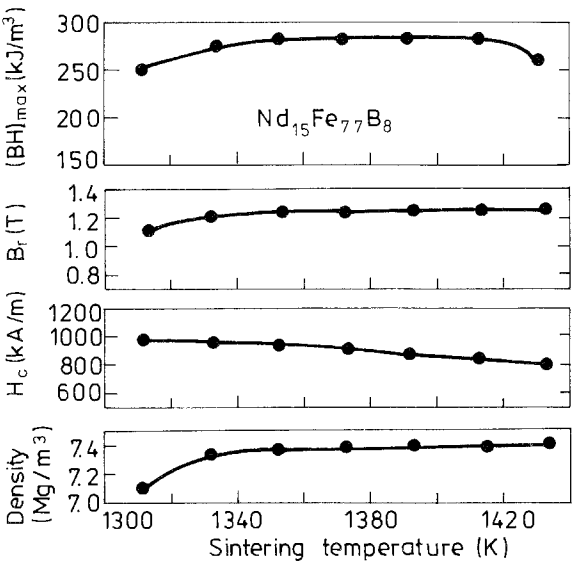

Fig. 21. The influence of the sintering temperatures on the magnetic properties of $Nd_{15}Fe_{77}B_8$ magnets.

to the removal of damaged particle surfaces by the action of a grain boundary liquid phase. Stadelmaier et al. (1983) suggest that the liquid phase, during sintering, inhibits grain growth and maintains or even reduces the milled particle size.

Strnat (1985) reviewed the spectrum of modern permanent magnet materials with emphasis on those based on Nd–Fe–B. Falconnet (1984) analysed some industrial and economical problems of Nd–Fe–B magnets in the short and long term. Ervens (1984) compared the properties of Nd–Fe–B magnets with those of Sm–Co–type, while Grand (1984) made some technico-economic considerations on Nd–Fe–B magnets. The current patent situation in the field of Nd–Fe–B permanent magnets was given by Herget (1984, 1985b).

The most recent results in the science and technology of Nd–Fe–B based magnets have been listed by Capellen et al. (1986) and are contained in the proceedings of the INTERMAG 87 conference, April 1987 Tokyo, Japan (to appear in September 1987 in the "Transactions on Magnetics") and in the proceedings of the "Ninth International Workshop on Rare-Earth Magnets and the Fifth International Symposium on Magnetic Anisotropy and Coercivity in Rare-Earth–Transition Metal Alloys". August/September 1987, Bad Soden (near Frankfurt) Federal Republic of Germany.

The structure inside the $Nd_2Fe_{14}B$ matrix grain is clean and faultless. The average grain size is 5–20 μm, much larger than the single domain particle (~0.26 μm). Thus, the multidomain structure is most stable (Sagawa et al. 1984a, b, Durst and Kronmüller 1985).

Generally, the microstructure studies on Nd–Fe–B magnets reveal at least three phases (Livingston 1985b, Ormerod 1985, Fidler and Yang 1985, Oesterreicher and Oesterreicher 1984b, Kostikas et al. 1985):

- $Nd_2Fe_{14}B$ which occupies a volume fraction of 80–85%.

- A boron-rich phase, $Nd_{1+\varepsilon}Fe_4B_4$ (or $Nd_2Fe_7B_6$) irregularly distributed, which occupies a volume fraction of 5–8%.
- A neodymium rich phase which, together with pores and neodymium oxide, has a volume fraction of 10–15%.

Fidler and Yang (1985) reported the presence of α-Fe in an as-cast sample as well as of the $Nd(FeCo)_2$ Laves phase in cobalt-containing magnets. The structure of neodymium rich phase is still a controversial matter. It has been reported that this is of fcc-type (Sagawa et al. 1984b, Chang and Qiang 1986), bcc (Stadelmaier et al. 1983, Sagawa et al. 1985a) or hcp (Fidler 1985, Fidler and Yang 1985). This phase appears heavily faulted. As mentioned the melting temperature of this phase is ~920 K (~650°C) (Sagawa et al. 1984a, Oesterreicher 1985). The eutectic reaction between Nd-rich phase and $Nd_2Fe_{14}B$ is believed to enhance the liquid phase sintering (Sagawa et al. 1984a). The distribution of the neodynium rich phase within the grains may effectively reduce the grain size (Oesterreicher and Oesterreicher 1984b, Handstein et al. 1985).

We now present some data on the magnetic properties of sintered magnets.

Sagawa et al. (1984a) prepared $Nd_{15}Fe_{77}B_8$ magnets by sintering the aligned powders at 1100°C, the samples being then rapidly cooled. After a post-sintering thermal treatment at 600°C, magnets with $B_r = 1.23$ T, ${}_MH_c = 0.96$ MA/m and $(BH)_{max} = 290$ kJ/m^3 have been obtained. The partial replacement of iron by cobalt (Sagawa et al. 1984b) raise the Curie temperature of $Nd_2Fe_{14}B$ compound, and thus improves the temperature coefficient of remanence. The intrinsic coercive force, however, is decreased by the cobalt addition. For example this is the case for $Nd_{15}(Fe_{0.8}Co_{0.2})_{77}B_8$ samples, where the magnetic characteristics are $B_r = 1.21$ T, ${}_MH_c = 0.82$ MA/m and $(BH)_{max} = 260$ kJ/m^3; the reversible coefficient of magnetization decreasing in absolute magnitude for the above sample from -0.123%/K for $Nd_{15}Fe_{77}B_8$ to -0.074%/K (Sagawa et al. 1984b). Tianduo and Xijian (1985) also investigated the magnetic properties of $Nd_{16.7}(Fe_{1-x}Co_x)_{75.5}B_{7.8}$ alloys. The coercivity and energy product show a rapid decrease at $x = 0.4$. The reversible coefficient of magnetization around room temperature decreases in absolute magnitude from -0.13%/K for $x = 0$ to -0.058%/K for $x = 0.4$. Nd–Fe–B based magnets having similar properties are now already the industrial standard.

Arai and Shibata (1985) obtained magnets having the nominal composition $Nd_{23-y}Fe_{77-2x}Co_{2x}B_y$ with $x = 0$ to 10 and $y = 5$ to 10. After crushing, the powders were aligned in a magnetic field of 0.96 kA/m, pressed at $p = 500$ MPa, sintered and thermally treated. In fig. 22, the composition dependence of the magnetic properties of $Nd_{15}Fe_{77-2x}Co_{2x}B_8$ alloys is plotted. The maximum energy product of 336 kJ/m^3 has been obtained in case of $Nd_{16}Fe_{66}Co_{11}B_7$ alloy. The reversible coefficient of remanent induction, in this case, is -0.02%/K. It has been suggested that highly heat resistant magnets may be produced when cobalt distributes only in the tetragonal matrix phase.

Lidong et al. (1985) studied the system $Pr_{16}Fe_{84-y}B_y$ in order to produce permanent magnets. Energy products in excess of 300 kJ/m^3 were obtained.

The effect to Dy_2O_3 sintering additive on the coercivity of $Nd_{15}Fe_{77}B_8$ magnets was studied (Ghandehari 1986). The ${}_MH_c$ values increase from 0.936 to 1.08 and

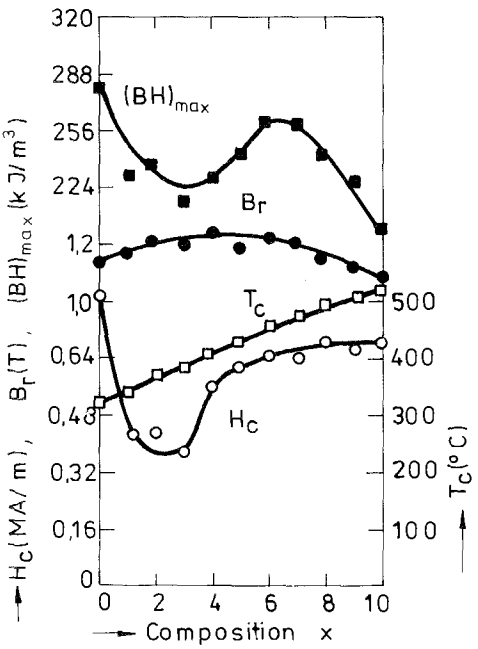

Fig. 22. The influence of cobalt on the magnetic properties of $Nd_{15}Fe_{77-2x}Co_{2x}B$ alloys.

1.28 MA/m as Dy_2O_3 concentration is increased from 0 to 2 and 4 wt%, respectively. There is also a decrease in remanence and a corresponding diminution of the energy product, characteristic of the Dy-containing magnets.

Wang et al. (1985) prepared sintered magnets having the composition $Nd_{15.5-16.5}Fe_{77.5-75.5}B_{7-8}$. The optimum magnetic properties are $B_r = 1.32$ T, ${}_BH_c = 0.692$ MA/m. The demagnetization curve has a perfect squareness. Tokunaga and Harada (1985) investigated the properties of $Pr(Fe, B)_z$ and $Pr(Fe, Si)_z$. The magnetic properties of sintered $Pr(Fe_{0.9}B_{0.1})_5$ magnets are comparable with those of Nd–Fe–B alloys. Cumulative aging enhanced ${}_MH_c$ to 1.16 MA/m. High ${}_MH_c$ values were not obtained in $Pr(Fe_{1-x}Si_x)_5$ alloys.

Narasimhan (1985a, b, c) prepared sintered Nd–Fe–B magnets having the composition $RFe_{5.3}B_{0.3}$ by a similar method as used in manufacturing the $SmCo_5$ ones. The maximum energy product was 360 kJ/m^3. By a slight increase of the intrinsic coercive field the energy product would be of 380 kJ/m^3, corresponding to $(BH)_{max} = B_r^2/4\mu_0$. Stadelmaier et al. (1985a) prepared Nd–Fe–B magnets by sintering the $Nd_2Fe_{14}B$ compound or starting from neodymium and iron particles having $d \simeq 100$ μm and $d \simeq 38$ μm, respectively mixed with Fe_2B powders ($d <$ 38 μm). By compacting the above powders at $p = 700$ MPa and sintering in quartz tubes under vacuum, the powders react and form the $Nd_2Fe_{14}B$ phase. The high coercive field is attributed to small dimensions of particles resulting from the above reaction. The dimensions depend essentially on temperature and duration of the process.

The demagnetizing curves for $Nd_{15}Fe_{77}B_8$ as well as for $Nd_{13.5}Dy_{1.5}Fe_{77}B_8$ magnets are plotted in fig. 23 (Sagawa et al. 1984b). The coercive field increases

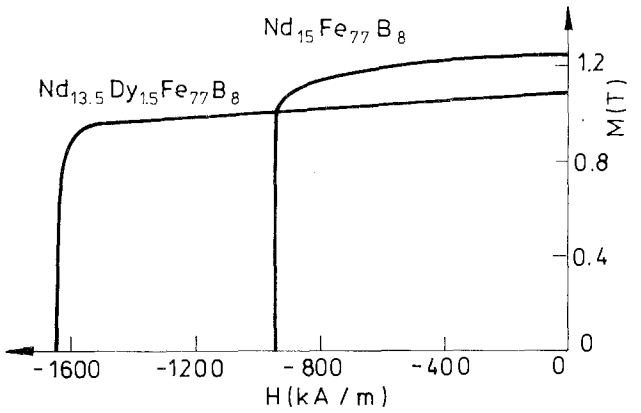

Fig. 23. Some demagnetizing curves for Nd–Fe–B magnets.

substantially by partial replacing of Nd by Dy. This substitution has negative effect on the remanent induction. The saturation inductions of the sintered $Nd_{15-x}Dy_xFe_{77}B_8$ magnets were calculated from those of intermetallic $Nd_2Fe_{14}B$ and $Dy_2Fe_{14}B$ compounds (Rodewald 1985a, b). The experimental data coincide with the calculated values and indicate that other phases in the alloy do not carry appreciable magnetic moments.

Lidong et al. (1985) in case of the magnets with nominal composition $Pr_{16}Fe_{76}B_8$ obtained $B_r = 1.29$ T, ${}_MH_c = 0.936$ MA/m and $(BH)_{max} = 296$ kJ/m^3. The magnetocrystalline anisotropy constant, $K_1 = 4.2 \times 10^6$ J/m^3, is somewhat higher than in Nd–Fe–B magnets. Okada and Homma (1985), Okada et al. (1985) and Homma et al. (1985) studied the possibility to replace neodymium by didymium (Nd–10 wt% Pr) and cerium in Nd–Fe–B magnets. In fig. 24 the magnetic properties of some magnets with the composition (32.5–34.5) didymium–5 Ce–(1–1.6) B are plotted as function of sintering temperature. Better magnetic characteristics are evidenced in case of Fe–33.5 wt% (Di–5 Ce) and 1 wt%B namely $B_r = 1.32$ T, ${}_MH_c = 0.816$ MA/m and $(BH)_{max} = 320$ kJ/m^3. The cerium enhances the wettability of Nd-rich liquid phase to $R_2Fe_{14}B$ compound. In addition, it helps to form the reactive surface of hard magnetic phase by deoxidation effects. At 70°C, the coercive force of (Ce, Di)–Fe–B magnets is by about 15% greater than in alloys without cerium and at 150°C by about 20%. Thus, the presence of cerium in Nd–Fe–B permanent magnets is desirable. The microstructure of didymium–iron–boron was also studied (Ramesh et al. 1986). The main phase is $R_2Fe_{14}B$. In all samples, a triple junction fcc phase which frequently extended into two-grain junctions, was observed with a lattice parameter of 5.24 Å enriched in Ce, Pr and Nd. The magnets with poorer properties have considerable amounts of rare-earth oxides.

For $Nd_{15}Fe_{75}B_8$ + 4 wt% Nd, magnets with $(BH)_{max} = 248$ kJ/m^3, ${}_BH_c = 0.656$ MA/m and $B_r = 1.18$ T were obtained (Deryagin et al. 1984).

The effect of various substitutions on the properties of $Nd_{15}(Fe_{1-x}T_x)_{77}B_8$ sintered magnets has been studied (Maocai et al. 1985b). The substitution of iron by cobalt lowers the reversible coefficient of induction but increases the irrevers-

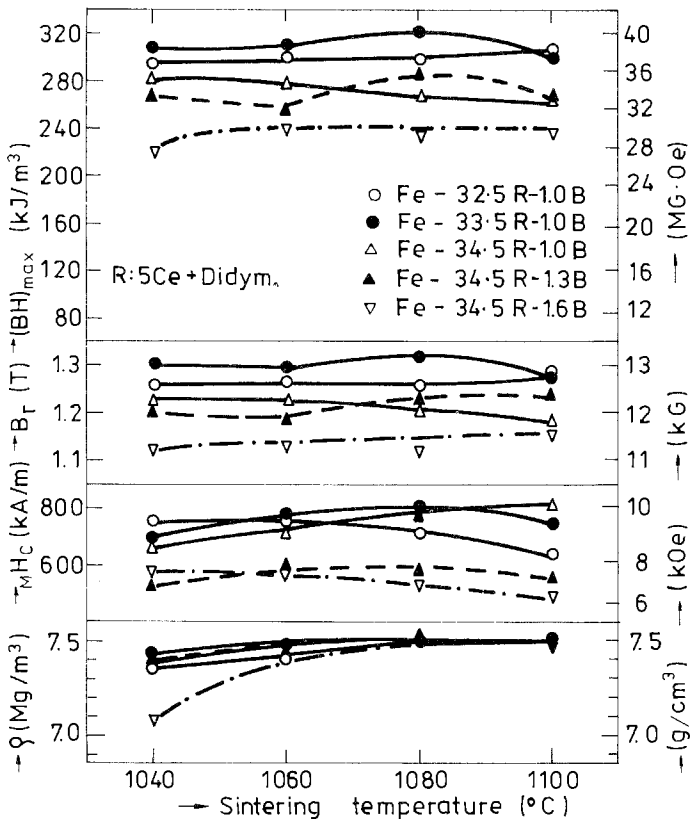

Fig. 24. Magnetic properties and density as function of sintering temperatures for Fe–(32.5 to 34.5) 5Ce–didymium–(1 to 1.6)B alloys.

ible loss of the open-circuit remanent induction. Aluminium and molybdenum enhance the intrinsic coercive field. The addition of Y, Er, Cr, Zr, Ti and especially Ni, Mn and Cu deteriorate the magnetic properties of Nd–Fe–B magnets. When 50% Nd is replaced by mischmetal, the magnets still exhibit rather good magnetic properties with $(BH)_{max}$ ranging from 160 to 200 kJ/m^3.

The magnetic behaviour of $Nd_{16}(Fe_{1-x}Al_x)_{76}B_8$ alloys are plotted in fig. 25 (Maocai et al. 1985b). The coercive fields, $_MH_c$, increase nearly linearly by increasing the aluminium content. The energy product decreases as result of the diminution of the remanent induction.

Tokunaga et al. (1985) analysed the effect of heat treatment on the coercive force of R–Fe–B magnets. The following heat treatments were used: (1) heating at 900°C for 2 h, followed by the continuous cooling at the rate of 1.3°C/min at room temperature, (2) heating at a temperature smaller than 700°C for 1 h and quenching. When using this heat treatment, the following magnetic properties were obtained for $Nd(Fe_{0.92}B_{0.08})_6$, $B_r = 1.38$ T, $_BH_c = 734$ kA/m and $(BH)_{max} = 352$ kJ/m^3.

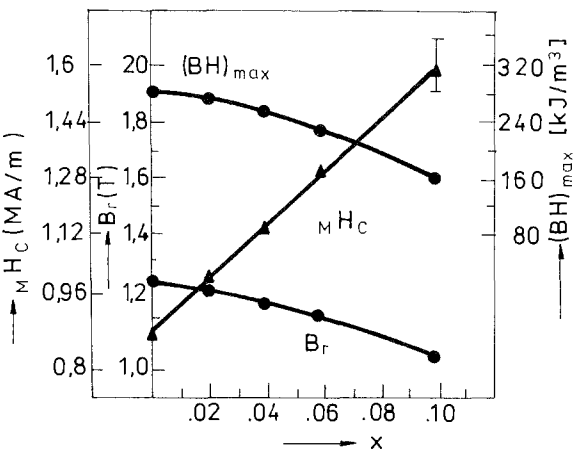

Fig. 25. The composition dependence of B_r, $_MH_c$ and $(BH)_{max}$ values in $Nd_{16}(Fe_{1-x}Al_x)_{76}B_8$ sintered magnets.

Bolzoni et al. (1985) analysed the carbon influence on the magnetic properties of $Nd_2Fe_{14}B_{1-x}C_x$ system. The room temperature anisotropy field increases with the carbon content from 6.84 MA/m ($x = 0$) to 7.72 MA/m ($x = 0.75$). Liu and Stadelmaier (1986) show also that isostructural R–Fe–C systems have high magnetocrystalline anisotropy. In a preliminary study an intrinsic coercivity of 25 T has been obtained in Dy–Fe–C alloy. The advantages of these materials are: (1) it is possible to develop high coercivities without recourse to special processing such as powder metallurgy or melt spinning, and (2) unlike sintered boride magnets, the carbides are not sensitive to coercivity loss by comminution.

The microstructures of R–Fe–B magnets were also analysed. Rong et al. (1985) studied the phase composition of the $Nd_xFe_{100-x-y}B_y$ alloys with $x = 15, 16$ and $y = 4$ to 10, by means of the Mössbauer spectroscopy. The alloy without B consists of α-Fe and Nd_2Fe_{17} phases. By adding 4 at% B, the Nd_2Fe_{17} phase disappears and the tetragonal $Nd_2Fe_{14}B$ phase forms. Increasing the amount of B up to 7 at%, the α-Fe disappears and in addition to the $Nd_2Fe_{24}B$ phase a Nd-rich phase and a B-rich phase emerge. By further increasing the B content, the quantity of B-rich phase tends to increase. Fidler (1985) and Fidler and Yang (1985) showed that the rare-earth–iron magnets produced by powder metallurgical process exhibit "single phase" microstructure of $R_2Fe_{14}B$-type, with additional grains and precipitates of soft magnetic phases. These soft magnetic phases lower the remanence and, therefore, the energy product of the final magnet, but they also act as nucleation sites for reversed domains and therefore, as center for the magnetization reversal. The intrinsic coercive force is determined by the nucleation and expansion of reversed domains. The coercive force is dependent on the external field (Hadjipanayis et al. 1985d, f). Both in sintered and melt-spin samples the pinning of domain walls at the grain boundaries has been observed (Hadjipanayis et al. 1985d, f, Mishra et al. 1986). The formation of thin intergranular Nd-rich layer extending to pockets of polycrystalline fcc Nd crystals has

been evidenced in sintered magnets annealed at 650°C (Mishra et al. 1986). The $Nd_{1+\varepsilon}Fe_4B_4$ phase is an unavoidable product of the sintering process but for good coercivity it is not necessary to be present.

Hiraga et al. (1985) examined the grain boundaries of sintered $Nd_{15}Fe_{77}B_8$ magnets. A bcc phase with lattice constant $a = 2.9$ Å was found at most of boundaries of $Nd_2Fe_{14}B$ grains. The bcc phase and $Nd_2Fe_{14}B$ grains are joined with smooth interfaces in the samples annealed at 870 K, which have a coercivity as high as 1 MA/m. In samples quenched from 1350 K with a coercivity of about 0.5 MA/m, however, thin plates of bcc phase extend from the interfaces to the inside of the $Nd_2Fe_{14}B$ grains and deform the lattice spacing of (001) planes of the $Nd_2Fe_{14}B$ matrix. These thin plates are considered to act as nucleation centers of reverse magnetic domains which reduce the coercivity of the samples.

Harris and Bailey (1984) show a two stage precipitation process in the $Nd_{15}Fe_{77}B_8$ alloy on aging at 600°C, this process involves fine precipitates. Ogilvy et al. (1984) analysed the influence of cooling rate during solidification and boron concentration on the constitution and microstructure of Nd–Fe–B alloys. The approximate minimum cooling rate required to avoid the presence of the ferrite iron was also determined for some Nd–Fe–B magnets.

Studies were performed to analyse the domain–wall surface energy, γ_W. For $Nd_2Fe_{14}B$ compound values of 3.5×10^{-2} J/m^2 (Livingston 1985a) or 4.2×10^{-2} J/m^2 (Szymczak et al. 1985) were determined. In the $Pr_2Fe_{14}B$ the domain–wall surface energy is 3.3×10^{-2} J/m^2 (Szymczak et al. 1985) or 3.16×10^{-2} J/m^2 (Shouzeng et al. 1986). These values are about half of the value determined in $SmCo_5$ magnet.

Domain patterns of a sintered Nd–Fe–B permanent magnet with different magnetic states at $H = 0$ were observed on the pole and side surfaces using the Kerr effect and the Bitter technique, respectively (Tiesong et al. 1986). During the magnetization process, most of the single domain grains persist as single domains apparently only reversing the direction of magnetization (Li and Strnat 1985), while reverse domains in multidomain grains grow. As the value of the demagnetization field approaches and exceeds that of the coercivity, some reverse domains in multi-domain grains extend across grain boundaries. It seems that the growth and shrinkage of reverse domains with the variation of the field characterizes the recoil lines. Suzuki and Hiraga (1986) analysed static and dynamical walls in $Nd_{15}Fe_{77}B_8$ sintered magnets. A 180° wall near a triple junction of the grains constituting of a bcc phase boundary region can be a strong pinning site. Other walls by increasing the field easily moved and disappeared. The observation of 180° walls moving under the influence of the applied field is also discussed. The magnetic domains and the changes in magnetic properties of sintered Pr–Fe–B magnets during the course of annealing at 580°C have been investigated (Shouzeng et al. 1986). The mean width of surface domains in the tetragonal phase is about 0.9 μm. The magnetic properties are related to the concentration gradient in the phase boundaries.

Otani et al. (1986) show that the hysteresis loop of $Nd_{15}Fe_{77}B_8$ can be decomposed in hysteresis loops of two magnetic phases; one with a comparatively

low coercivity and the other with a high coercivity. The volume ratio of these phases depends on the temperature and the angle between the external field and the pseudo c-axis.

Grössinger et al. (1986b) analysed the temperature dependence of the anisotropy field, the anisotropy energy, the ratio between wall energy and magnetization and the nucleation field for reversed magnetic domains in Nd–Fe–B magnets. It was found that coercive force is neither purely pinning-controlled nor purely nucleation-controlled.

The sintered Nd–Fe–B magnets have the grain size $d = 5$–15 μm while those obtained by spin melting have $d = 200$–800 Å. Since the critical diameter for single domain particles is ~ 0.3 μm, in the first case the particles are greater while in the second one are smaller than the critical size (Livingston 1985b)

The Nd–Fe–B magnets behave somewhat similar as the $SmCo_5$ fine particle magnets (Handstein et al. 1985, Heinecke et al. 1985). The division into individual particles of the $Nd_2Fe_{14}B$ phase is caused mainly by Nd-rich phase. The major contribution to the coercivity of sintered Nd–Fe–B magnets may be attributed to an appropriate particle size. Much higher ${}_MH_c$ values are found when the magnetization reversal occurs independently in each particle. This is evidenced if there is no exchange contact across the boundaries of the particles and or the growth/movement of the domain walls is hindered by surface inhomogeneities of the particles (Livingston 1981). The initial magnetizing curve, the demagnetizing curves for sintered Nd–Fe–B magnets after thermal demagnetizing as well as after demagnetizing by suitable selection of external field are plotted in fig. 26 (Handstein et al. 1985). The observed behaviour is typical for magnets constituted from fine particles, where the magnetization reversal is due to the nucleation processes. This fact was also evidenced by Hilscher et al. (1986). The model calculation for an assembly of non-interacting magnetically uniaxial particles may be used for a description of the magnetization processes in sintered Nd–Fe–B magnets (Heinecke et al. 1985).

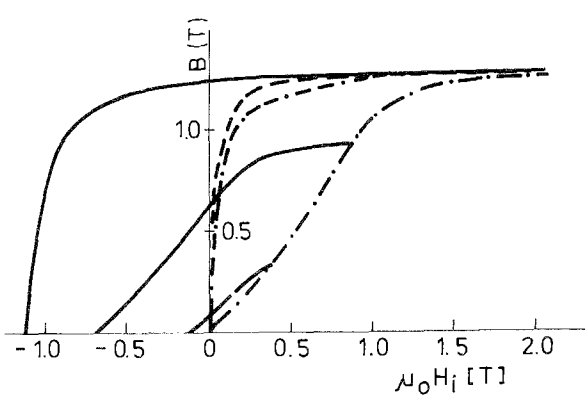

Fig. 26. Demagnetizing curves for Nd–Fe–B magnets after thermal demagnetizing (– – –) and the demagnetizing by an external field (– · – · – · –). The demagnetizing curves after saturation in a field of 5.2 MA/m and in field of lower intensities are also plotted (——). The curve (· – – –) connects the tops of the minor loops obtained by increasing the field.

The domain walls are strongly pinned near grain boundaries. The thickness of the domain wall (~40 Å) is thinner than the width of Nd-rich phase surrounding the grains. The local pinning of domain walls by grain boundaries involves the presence of other phases along the boundaries or compositional (structural) changes which lead to variation in the anisotropy or exchange energies along the boundaries (Livingston 1985b, Li and Strnat 1985). Thus, the coercive field is not only determined by the material parameters of $R_2Fe_{14}B$-phase, but also by the properties of the surface imperfect regions. The surface energy term provides the energy barrier that resists the formation of reverse domains. Both the height of the energy barrier and the breakaway radius of the reverse domain, decrease by increasing external field and makes the nucleation more difficult (Durst and Kronmüller 1985).

It is important that the Nd-rich phase surrounds the $Nd_2Fe_{14}B$ particle grains. In samples with low coercivities the grain boundary phase extended into the grains. This fact has not been observed in samples with high coercivities, where a thin layer of 200–500 Å is observed around the particles (Hiraga et al. 1985). Probably the platelets form nuclei for reversed domains and thus the coercivity decreases. The soft magnetic phase acts as nucleation sites, determining the magnetization reversal and therefore limits the coercivity of the magnets. Thus, it seems that the magnetically inhomogeneous transition region primarily controls the nucleation field of the reversed domains.

Some models have been developed in order to analyse the coercive fields of Nd–Fe–B permanent magnets (Durst and Kronmüller 1985, Chikazumi 1986, Givord et al. 1985c, Herzer et al. 1986, Grössinger et al. 1986a).

Durst and Kronmüller (1985) considered the nucleation field, H_N, for the reversal of the magnetization within a planar, magnetically soft region of width $2r_0$, embedded within a magnetically hard region. The H_N value is given by (Kronmüller 1982)

$$\mu_0 H_N = 2K_p/M_s - (2K_1/M_s)\delta W/\pi r_0 , \tag{3}$$

where K_p and K_1 denote the anisotropy constants within the magnetically soft and hard regions and δW is the wall width of magnetically hard component. In $Nd_2Fe_{14}B$-type magnets, $\delta W \simeq 40$ Å and thus the ideal nucleation field $H_N \simeq K_1/M_s\mu_0$ (about 4.8 MA/m) is reduced two times for a magnetically soft region, having the width $2r_0 \simeq 50$ Å (Durst and Kronmüller 1985). The above data suggest that high-quality magnets can be produced if the extension of the magnetically soft region is smaller than 50 Å. This discussion may explain the increase of coercivity by annealing at 870 K (600°C). The platelets evidenced in quenched samples after annealing disappear completely and smooth and flat interfaces are formed. This fact is reflected in an increase of the coercive field.

In Nd–Fe–B sintered magnets the coercive field, ${}_MH_c$, falls to zero at remarkably lower temperatures than the anisotropy field does (Grössinger et al. 1985a, e, Ma and Narasimhan 1986, Schneider et al. 1985), see fig. 27. An explanation may be given if it is considered that nucleation occurs in the strong opposite field

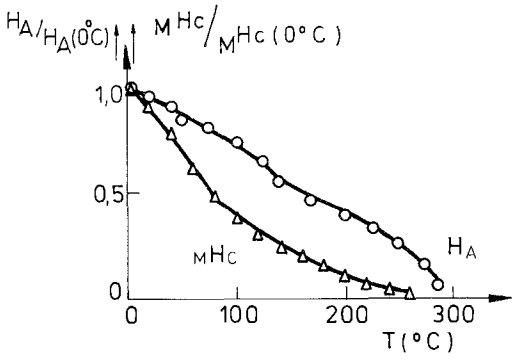

Fig. 27. The temperature dependence of the anisotropy field and coercive force in Nd–Fe–B magnets.

which is created by grains with reverse polarization. Such grains always exist in real magnets. The temperature dependence of the coercive field may be given by the relation (Adler and Hamann 1985):

$$_{M}H_{c} = c_1 H_A - 2M_s - H_n \tag{4}$$

where $c_1 H_A$ is the field required to create a stable nucleus and $H_A = 2K/M_s\mu_0$ is the anisotropy field. The c_1 value decreases by increasing the exchange coupling at the boundaries ($c_1 = 1$ if there is a complete decoupling with respect to the exchange interactions of crystallites). If the exchange coupling is very strong c_1 drops to zero (soft magnetic case) and the nucleus can grow without restraint. The coercivity is then determined by the grain diameter, d_k:

$$\mu_{0\,M}H_c \simeq 3\,\frac{\gamma_w}{d_k M_s} \tag{5}$$

where γ_w is the domain wall energy.

The third therm represents the field characterising the thermal aftereffect. This is given by

$$H_n = S_v(Q + \ln t) \tag{6}$$

where Q is approximately constant and of the order of 40 and S_v for $Nd_2Fe_{14}B$ at room temperature, is 80 A/cm. The time is denoted by t.

The decrease of the coercivity by increasing the temperature shows a thermal activation from the nucleus in addition to the decrease of the anisotropy constants and wall energy.

Herzer et al. (1986) based on the so-called homogeneous rotation mode of nucleation show that in uniaxial ferromagnets, the nucleation fields are influenced by the second anisotropy constant K_2 and may be expressed by the relation

$$\mu_0 H_N = \frac{2K_1}{M_s} + \frac{4K_2 f(K_1/K_2)}{M_s}\,. \tag{7}$$

This relation holds for a wide range of K_1 and K_2 values ($-2K_2 < K_1 < 4K_2$) irrespective whether the magnetic easy direction is parallel or oblique to the c-axis. The analysis also reveals that K_2 controls the form of the hystersis loop. There is an evidence that the low temperature increase in coercivity of $Nd_2Fe_{14}B$ sintered magnets is due to the temperature dependence of K_2. The model may be a partial aspect of the actual magnetization reversal of a grain in a sintered magnet. It is suggested that the magnetostatic stray fields expressed by a phenomenological relation similar to (4) play another important part

$$ {}_M H_c = c_1 H_N - n M_s , \tag{8} $$

where H_N is given by the relation (7), n is the "demagnetizing factor" which gives the local stray field at the grain boundary and the parameter c_1 has the same significance as in relation (4).

Grössinger et al. (1986b) analysed the temperature dependence of the anisotropy field and coercivity in some commercial Nd–Fe–B magnets. A theoretical analysis predicts a correlation between ${}_M H_c$ and certain power of the nucleation field, H_n ($H_n = K_1/\mu_0 M_s$)

$$ {}_M H_c \propto H_n^b , \tag{9} $$

with values of $1/2 \leqslant b \leqslant 5/2$. Assuming that H_n can be replaced by H_A, they have tried to correlate the experimentally ${}_M H_c(T)$ with $H_A(T)$. From the slope $\ln({}_M H_c(T))$ vs $\ln H_A(T)$ a value $b = 5/2$ was estimated. From a theoretical analysis a 5/2 power relation is expected if the coercivity is determined by volume pinning.

Givord et al. (1985c) analysed the larger decrease of the coercivity than the anisotropy field as the temperature increases. This behaviour is found in systems where the coercivity is governed by pinning of domain walls. The occurrence of thermal aftereffects in these systems reveals that thermal activation induces an additional decrease of the coercivity. In magnets where the pinning of walls occurs, due to the high anisotropy, the displacement of walls occurs step by step through processes which involve simultaneously pinning and nucleation (Barbara and Uehara 1978). The temperature dependence of the coercive field is given by

$$ \frac{1}{H_c(T)} = \frac{1}{c H_A(T)} + \frac{37}{c' v E_A H_M} T . \tag{10} $$

The first term describes the dependence of the coercivity on the anisotropy field. In an ideal system, the phenomenological coefficient c would be one and is reduced to about 0.1 in a real system. The second term describes the thermal activation effects. E_A denotes the anisotropy energy, H_M is the molecular field and c' is a phenomenological coefficient, which gives an account for the decrease of anisotropy and/or exchange interactions at defect position. The experimental data show that $(1/H_c - 1/cH_A)H_c^0$ has a quadratic-like behaviour which means

that the activation processes become more and more effective at high temperature. Such a behaviour is expected from the relation (10) as a result of the decrease of exchange interactions and anisotropy as temperature increases. The decrease of coercivity with temperature results both from the decrease of the anisotropy and thermal activation.

Chikazumi (1986) considers the case in which the size of the grains in Nd–Fe–B magnets is well above the critical size, so that the coercivity is governed by nucleation of reverse domains at the grain boundaries. One of the features of this mechanism is that the coercivity is increased by increasing the previously applied magnetic field. In order to explain this feature, a mechanism of magnetically locked pinning of domain walls is proposed. It is assumed a number of regions which are magnetized permanently either in a positive or negative sense. These regions called "magnetic seeds" may be highly distorted or highly anisotropic regions at the grain boundaries or on the surface of inclusions. The model seems to explain almost all the experimental facts, including the high field experiments.

The wide range of coercivities obtainable with Nd–Fe–B materials indicates the dependence of ${}_{M}H_{c}$ on the surface properties. A usual high ratio (for a metallic system) of ${}_{M}H_{c}/H_{A} \simeq 0.5$ for the highest value of ${}_{M}H_{c}$ that has been achieved so far for $Nd_2Fe_{14}B$. This high ratio appears, above all, to be due to the ideal surface structures obtainable in a system with a low melting eutectic and with the fact that the matrix of the other two components in the three phase field is not magnetic at room temperature.

Summarizing it must be stated, however, that at present the problem of a Nd–Fe–B based permanent magnet with sufficient high coercivity to reach the maximum energy product corresponding to

$$\frac{B_r^2}{4\mu_0}$$

at 150°C to 200°C has not been solved yet. Such a temperature region is of great interest for many applications. Furthermore a magnet must be stable at this temperature for a long time. Therefore more investigations of the above mentioned substituted alloys and magnets and especially a deeper understanding of the pinning and nucleation mechanisms in multicomponent Nd–Fe–B based magnets is needed.

4.2. *Magnets obtained by splat-cooling*

The researchers from General Motors obtained in 1983 isotropic Nd–Fe–B magnets by splat cooling (Croat et al. 1984a, b). These are manufactured by pushing the melt alloy under pressure, in argon atmosphere, by a quartz aperture, onto a rotating disk. Optimum magnetic properties are obtained for a disk speed which results in grain dimensions of the $Nd_2Fe_{14}B$ phase in the range 200–500 Å. If the disk speed is higher, optimum magnetic properties are obtained by annealing the samples. The thermal treatment determines an increase of the particle size.

The composition dependence of the magnetic properties of $Nd_{1-x}(Fe_{0.95}B_{0.05})_x$ amorphous alloys is plotted in fig. 28 (Croat et al. 1984b). The maximum energy product for this isotropic magnet is obtained for $x = 0.87$, namely $(BH)_{max} = 112.8\,kJ/m^3$. This composition is rich in neodymium and poor in boron in comparison with the $Nd_2Fe_{14}B$ compound.

Hadjipanayis et al. (1983, 1985d, e, 1986, Dickenson et al. 1985) analysed the magnetic properties of melt-spun magnets. By adding Si and B to R–Fe–B alloys, amorphous ribbons with energy products up to $104\,kJ/m^3$ were obtained (Hadjipanayis et al. 1983). The as-quenched R–Fe–B alloys are usually magnetically soft, but some of them show large magnetic hysteresis when annealed around 700°C. In case of $Pr(Nd)_{16}Fe_{76}B_8$ samples, coercivities in excess of 0.8 MA/m were obtained (Hadjipanayis et al. 1985e). Relatively large anisotropies were observed in Y and Gd containing samples. The partial substitution of Fe by Ni and Mn leads to a significant decrease of the Curie points. The magnetic

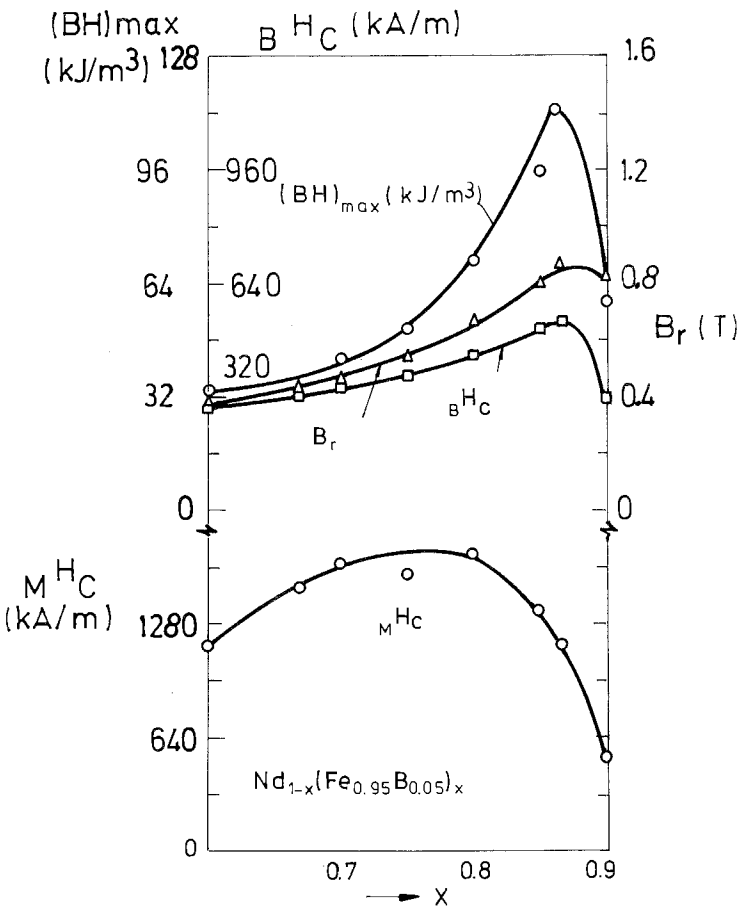

Fig. 28. The magnetic properties of $Nd_{1-x}(Fe_{0.95}B_{0.05})_x$ amorphous alloys.

behaviour of $R_{15}Fe_{77}B_8$ melt-spun ribbons with R = Y, La, Pr, Nd, Sm, Gd, Tb, Dy and Er was also studied (Aly et al. 1986). The ordering temperatures of these alloys were found to be in the range 90–300°C, well below the crystallization temperatures. Fairly large magnetic hysteresis (120–640 kA/m) is observed at 4.2 K for alloys containing Er, Sm, Dy and Tb. The coercivities of melt-spun Nd–Fe–B magnets decrease drastically by increasing the temperature and are small at temperatures considerably lower than the Curie points (Hadjipanayis and Tao 1985). The magnetic properties of the melt-spun R–Fe–B magnets have been correlated with the microstructure and domain structure (Hadjipanayis et al. 1985d, Aly et al. 1986). As in crystalline systems, four different phases with composition $Nd_2Fe_{14}B$, $Nd_{1+\varepsilon}Fe_4B_4$, α-Fe and a high Nd-content phase have been found. The major phase observed in all the studied alloys is $Nd_2Fe_{14}B$, with much finer grains in melt-spun ribbons than in sintered magnets. Herbst et al. (1985) showed that the mean dimension of the particles obtained by neutron diffraction in $Nd_{0.13}Fe_{0.83}B_{0.08}$ ribbons is ~300 Å, while by electron microscopy studies the dimension of the particles, in the range 200 Å and 800 Å, are observed.

Grössinger et al. (1985d) and Eibler et al. (1984) show a maximum in ${}_MH_c$ values of $Nd_{15}Fe_{77}B_8$ and $Nd_{14}Fe_{81}B_5$ amorphous alloys for a disk speed $v \simeq$ 15 m/s close to the value of 19 m/s reported by Croat et al. (1984a, b). In $Pr_{16}(Fe_{100-x}Co_x)_{76}B_8$ alloys for a disk speed $v = 20$–30 m/s a value ${}_MH_c \simeq$ 1.6 MA/m is obtained (Overfeld and Becker 1984).

Narasimhan (1985a) manufactured Pr–Fe–B magnets in the form of amorphous ribbon having composition close to that reported by Hadjipanayis et al. (1983). By increasing the praseodymium content, the intrinsic coercive fields are greater. An alloy having the composition $Pr_{12}Fe_{76}B_{12}$ has ${}_MH_c = 0.512$ MA/m. By crystallization of the $Pr_{0.15}Fe_{0.60}B_{0.17}$ alloy a coercive field ${}_MH_c = 23$ MA/m was obtained.

Tao and Hadjipanayis (1985) studied recrystallization of the rare-earth–iron metalloid alloys. It was pointed out that the $R_2Fe_{14}B$ phase is stable for R = Ce to Tm. The recrystallized samples have coercive field up to 0.48 MA/m.

Koon and Das (1984) reported the properties of rapidly quenched R–Fe–B alloys (R = La, Pr, Nd, Tb) and Becker (1984) studied melt spun $R_{16}Fe_{76}B_5Si_3$ (R = Pr, Nd, Sm) alloys. Coercivities ${}_MH_c > 1.6$ MA/m were obtained.

Yamasaki et al. (1986) analysed the composition dependence of the anisotropy field of rapidly quenched $MM_yFe_{100-y-x}B_x$ ribbons with $5 < x < 9$ and $15 < y < 17$ at substrate speed $v = 25$ and 30 m/s. The ${}_MH_c$ exhibits a tendency to increase with increasing x and y. The largest coercive field was 0.752 MA/m for $MM_{10}Fe_{75}B_9$ ribbons. Intrinsic coercive forces up to 0.512 MA/m were reported in melt-spun $Tb_{0.135}Fe_{0.813}B_{0.052}$ and $Dy_{0.135}Fe_{0.813}B_{0.052}$ alloys after magnetic hardening by rapid solidification (Pinkerton 1986). The peak coercivities are obtained only within a narrow range of substrate velocities and are associated with a microstructure consisting of small particles of $R_2Fe_{14}B$ with size distribution from 30 to 600 nm.

Jiangao et al. (1985) studied the magnetizations and coercivities of $(Nd_xFe_{1-x})_{94}B_6$ metallic glasses. Sellmyer et al. (1984) obtained good permanent

magnets in case of $Nd_{16}Fe_{76}B_6$ amorphous alloy after heat treatment at ~700°C for 30 min.

The magnetic hardening of melt-spun Nd–Fe–B and Pr–Fe–B alloys is achieved by either quenching directly from the melt or by annealing an over-quenched precursor (Croat 1985). Samples with optimum properties have a uniform finely crystalline microstructure with an average particle size less than 50 nm. The quenched ribbons may be also consolidated into bulk magnets by conventional powder metallurgy processing and hot press/hot form techniques (Lee et al. 1985). Energy products up to 320 kJ/m^3 have been achieved by hot deformation.

Hadjipanayis et al. (1985a) analysed the hysteresis and crystallization behaviour of an amorphous $Nd_{54}Co_{36}B_{10}$ alloy. Magnetic measurements on melt-spun ribbons reveal a coercivity of 0.48 MA/m at 4.2 K. The coercivity at 4.2 K of a sample heat treated at 210°C is increased to 0.64 MA/m but is reduced gradually upon annealing at higher temperatures. The origin of magnetic hardening in Nd–Fe–B alloys was also investigated (Hadjipanayis et al. 1985b). Initial magnetization studies, magnetic viscosity data, the temperature dependence of coercivity and magnetic domain studies all indicate domain wall pinning at grain boundaries.

The good magnetic properties of amorphous ribbons were obtained only in Nd–Fe–B and Pr–Fe–B systems. The partial substitution of Nd by Dy and Tb leads to the increase of the coercive field, decreasing the remanent induction. Replacement of Nd by La, Ce or Sm decreases the coercive field. The alloys, having high magnetocrystalline anisotropy, were obtained only by using boron. The substitution by C, P, Si, Ge or Al had a negative influence on magnetic properties.

Transmission electron microscopy was used to characterize the microstructure of melt-spun ribbons having the composition $Nd_{13}Fe_{82.6}B_{4.4}$ (Chen 1985). The microstructure consists of fine grains which are practically single-phase materials. There are also very thin grain boundary films surrounding the grains. The grain size varies from 100 to 800 Å, with an average of about 150 Å. The good magnetic properties are probably due to the fine grained $Nd_2Fe_{14}B$ compound (i.e. single domain fine particles).

Mishra (1986) shows that the best magnetic properties of melt-spun magnets are obtained in materials with a two phase microstructure where 20–30 nm size $Nd_2Fe_{14}B$ grains are completely surrounded by a 1–2 nm thick amorphous film of Nd-rich and B-deficient phase. This phase acts as a pinning site for the magnetic domain walls. The presence of this amorphous phase is explained by the fact that nuclei of $Nd_2Fe_{14}B$ grains form homogeneously during cooling from the melt (or during annealing). As these grains grow, all the B diffuses into the grains and is consumed while the material outside the $Nd_2Fe_{14}B$ grains gets enriched in Nd. The coercive force is highest when the grain boundary area to grain volume is highest, providing maximum pinning sites. The small grain size makes reverse domain nucleation relatively easy in the melt spun magnets, but the pinning is much more effective due to the two-phase microstructure.

Low field dc thermomagnetic measurements on Nd–Fe–B magnets were performed in order to obtain information on the microscopic magnetic behavior (Rao et al. 1985). Heat treating of these materials in the temperature range 400 to 600°C is found to change the constitution of the alloy and significantly modify the magnetic properties.

The effect of changing the melt-spinning roll material on the value of roll velocity corresponding to the peak value of $(BH)_{max}$ for $Fe_{81.75}Nd_{13.5}B_{4.75}$ alloy, was studied in correlation with differential scanning calorimetry and microscopic observations (Ogilvy et al. 1984).

Lee (1985) and Lee et al. (1985) analysed the possibilities to manufacture magnets from over quenched melt-spin ribbons of the nominal composition $Nd_{0.14}(Fe_{0.91}B_{0.09})_{0.86}$ by hot-pressing at 700–750°C and 100 kPa. The resulting material is only slightly magnetically aligned with $B_r = 0.8$ T, ${}_MH_c = 1.52$ MA/m. Die upsetting, however, to thickness reduction of 50%, produces $B_r \simeq 1.1$ T, ${}_MH_c = 0.96$ MA/m and is accompanied by a lateral plastic flow of the ribbons and a corresponding ribbon thickness reduction resulting in an anisotropic magnet. The alignment arises from anisotropic grain growth and grain rotation which produces platelet shaped grains oriented perpendicular to the press direction.

A new rapid solidification processing technique, liquid dynamic compaction (LDC), has been used to make bulk permanent magnets of composition $Nd_{15}Fe_{57}Co_{20}B_8$ (Chin et al. 1986). In this process, molten metal is spray atomized onto a cooled substrate in a protective atmosphere. Subsequent heat treatment at 450°C of the LDC material resulted in isotropic permanent magnets with intrinsic coercivity and remanence approaching to ${}_MH_c = 0.64$ MA/m, and $B_r = 0.6$ T. Tanigawa et al. (1986) used LDC method in making bulk, oxide free Nd–Fe–Co–B magnets of high quality directly from the molten state. Intrinsic coercivities ${}_MH_c \simeq 0.64$ MA/m and $B_r = 0.6$ T were achieved after one hour heat treatment at 450°C. Magnets with wider range of compositions were then produced. Processing by LDC method allows for sufficient quench rate control to produce microstructures with grain sizes on the submicron scale or up to several tens of microns. The inter-granular material is enriched in Nd – relative to grains themselves. Later on (Chin et al. 1986), the magnetic hardening of dynamically compacted liquid Nd–Fe–Co–B magnets was studied. A great improvement in the coercivity occurs after heat treatment around 450°C.

The amorphous R–Fe–B alloys obtained by melt-spinning have been also studied by Mössbauer effect (Grössinger et al. 1985d, Niarchos et al. 1985, Rotenberg et al. 1985). The spectra show slight differences with respect to those obtained from annealed ingots.

In case of rapidly solidified magnets, $d < d_c$ and thus a part of the grains are single-domains (Livingston 1985b). The magnets are isotropic and consequently a fraction of the permeability is determined by magnetization rotation. In order to obtain a peak value of the coercivity it is necessary to have a rotating speed of the disk, which ensures single domain particles. For a higher speed, superparamagnetic behaviour may be observed, while for a lower one, multi-domain particles are evidenced. In both cases, the coercivity decreases. As in crystalline systems,

domain wall pinning has been observed at the grain boundaries. The domain walls move easily inside the grains. The slower increase of the initial magnetization with applied field observed in ribbons is due to the randomness of $R_2Fe_{14}B$ grains orientation. This fact needs much higher fields to align them as compared to those of sintered Nd–Fe–B magnets. The randomness also leads to smaller values of the magnetic induction and lower energy product. Auger electron spectroscopic studies in these magnets indicate considerable compositional inhomogeneities at the surface. After Hilscher et al. (1986) the coercivity for melt-spun ribbons with optimum cooling rate appears to be dominated by domain wall pinning.

4.3. *The stability of R–Fe–B permanent magnets*

The absolute values of the temperature coefficients of B_r, ${}_BH_c$ and $(BH)_{max}$ up to 100°C, are two times greater in Nd–Fe–B magnets than in $SmCo_5$ ones and three times as large for ${}_MH_c$ (Li et al. 1985). The losses which appear may be covered, as result of thermal demagnetization, by heating at $T > T_c$ and remagnetizing the sample. For a Nd–Fe–B magnet having $(BH)_{max} = 256\,kJ/m^3$ and ${}_BH_c = 0.904\,MA/m$, the reversible coefficient of coercive field $\alpha_{H_c} = -1.09\%/°C$ and of the energy product $\alpha_{(BH)_{max}} = -0.398\%/°C$ (Potenziani et al. 1985).

In case of Nd–Fe–B magnets heated at 300°C for 3 h in argon atmosphere, irreversible losses are small (~0.5%) (Narasimhan 1985a). The changes in demagnetizing curves by heating the samples are shown in fig. 29. By heating at 150°C, the coercive force diminished considerably.

The irreversible losses in remanent induction of a Nd–Fe–B magnet with ${}_BH_c = 0.9\,MA/m$ and $B_r = 1.15\,T$ after exposure for 3 h at various temperatures are plotted in fig. 30. The relative small irreversible losses suggest that Nd–Fe–B magnets may be used up to 100°C. For magnets having $B_r = 1.285\,T$, ${}_BH_c = 0.916\,MA/m$ and $(BH)_{max} = 310\,kJ/m^3$, the thermal variations of B_r values in

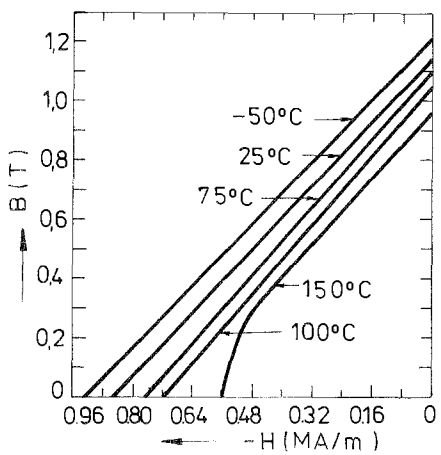

Fig. 29. Some demagnetizing curves for Nd–Fe–B magnets.

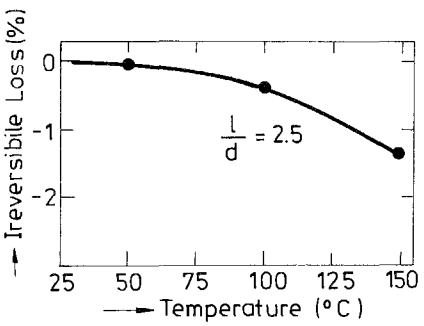

Fig. 30. The temperature dependence of the irreversible losses of the remanent induction.

$\alpha_{B_r} = -0.10\%/°C$ and $\alpha_{{}_MH_c} = -0.6\%/°C$. For magnets with higher coercivities $\alpha_{B_r} = -0.089\%/°C$ and $\alpha_{{}_MH_c} = -0.54\%/°C$ were reported (Narasimhan 1985a).

Strnat et al. (1985) analysed the magnetic properties of Nd–Fe–B magnets in the temperature range −200°C to +200°C. As result of the great decrease of ${}_MH_c$ values in the temperature range 100–150°C, the irreversible losses for remanent induction in this temperature region are large, especially for high values of the permeance.

Narasimhan (1985a) analysed the integrity of magnets after exposure at temperatures 100 to 150°C in moisture conditions. After 16 h, the magnets are stable. It is suggested that the Nd–Fe–B magnets may be used up to 150°C for a limited time.

The temperature coefficient of remanent induction for hot pressed and die-upset ribbons is −0.25%/°C (Lee et al. 1985). The temperature coefficient of ${}_MH_c$ for hot pressed is −0.25%/°C and for die-upset ribbons −0.45%/°C. By aging in air at high temperatures the losses are smaller than for sintered magnets.

The temperature coefficient of irreversible polarization losses are smaller, the stronger the coercive field. Partial substitution of Nd by Dy increases coercivity and the irreversible polarization losses decreases. The polarization losses due to thermal aftereffect decrease with temperature (Rodewald 1985a, b).

In our opinion the most urgent problems to be solved in the near future are the magnetic stability at elevated temperatures up to 200°C and the corrosion in humid atmosphere, for a real breakthrough for these magnets in a multitude of applications to happen.

References

Abache, C., and H. Oesterreicher, 1985, J. Appl. Phys. **57**, 4112.
Abel, A.W., and R.S. Craig, 1968, J. Less-Common Met. **16**, 77.
Adam, S., Gh. Adam and E. Burzo, 1986, J. Magn. & Magn. Mater. **61**, 260.
Adler, E., and P. Hamann, 1985, Proc. 8th Int. Workshop on Rare Earth Permanent Magnets and Their Applications, Dayton, OH, ed. K.J. Strnat, p. 747.
Aly, S.H., G.N. Nicolaides, Y.F. Tao and G.C. Hadjipanayis, 1986, J. Phys. F **16**, L21.
Anand, V., A.J. Kaufman and N.J. Gant, 1980, in: Rapid Solidification Processing II, eds R. Mehrabian, B. Kear and M. Cohen (Claitor's, Baton Rouge, FL) p. 273.

Andreev, A.V., A.V. Deryagin, S.M. Zadvorkin and S.V. Terentiev, 1985, Fiz. Tverd. Tela **27**, 1641.
Arai, S., and T. Shibata, 1985, IEEE Trans. Magn. **MAG-21**, 1952.
Arajs, S., 1965, Phys. Status Solidi **11**, 121.
Asti, G., F. Bolzoni, F. Leccabue, L. Pareti and R. Panizzieri, 1984, in: Nd–Fe Permanent Magnets – Their Present and Future Applications, ed. I.V. Mitchell (Commission of the European Communities, Brussels) p. 161.
Asti, G., F. Bolzoni, L. Pareti, W. Lianchong and Z. Hongru, 1985, in: New Frontiers in Rare Earth Science and Applications, Vol. II, eds X. Guangxian and X. Jimei (Science Press, Beijing, China) p. 937.
Azoulay, J., and L. Ley, 1979, Solid State Commun. **31**, 131.
Barbara, B., and M. Uehara, 1978, Int. Phys. Conf. **37**, 203.
Becker, J.J., 1984, J. Appl. Phys. **55**, 2067.
Bergman, G., and D.P. Shoemaker, 1954, Acta Crystallogr. **7**, 875.
Berthier, Y., M. Bogé, G. Czjzek, D. Givord, C. Jeandey, H.S. Li and J.L. Oddou, 1986, J. Magn. & Magn. Mater. **54–57**, 589.
Bezinge, A., H.F. Braun, J. Muller and K. Yvon, 1985, Solid State Commun. **55**, 131.
Bilonizhko, N.S., and Y.B. Kuzma, 1972, Izv. Akad. Nauk SSSR, Neorg. Mater. **8**, 183.
Bogé, M., J.M.D. Coey, G. Czjzek, D. Givord, C. Jeandey, H.S. Li and J.L. Oddou, 1985, Solid State Commun. **55**, 295.
Bogé, M., G. Czjzek, D. Givord, C. Jeandey, H.S. Li and J.L. Oddou, 1986, J. Phys. F **16**, L67.
Boltich, E.B., and W.E. Wallace, 1985, Solid State Commun. **55**, 529.
Boltich, E.B., E. Oswald, M.Q. Huang, S. Hirosawa, W.E. Wallace and E. Burzo, 1985, J. Appl. Phys. **57**, 4106.
Bolzoni, F., F. Leccabue, L. Pareti and J.L. Sanchez, 1985, J. Phys. (France) **46**, C6-305.
Bolzoni, F., A. Deriu, F. Leccabue, L. Pareti and J.L. Sanchez, 1986, J. Magn. & Magn. Mater. **54–57**, 595.
Braun, H.F., M. Pelizzone and K. Yvon, 1982, Proc. VIIth Int. Conf. on Solid Compounds of Transition Elements, Grenoble.
Burzo, E., 1975, Invited Lecture, Symposion on Metal Physics, Zloty Potok, Poland, Reprint SR-12 (IFA, Bucharest) p. 87.
Burzo, E., 1978a, Phys. Rev. B **17**, 1914.
Burzo, E., 1978b, Solid State Commun. **25**, 525.
Burzo, E., 1983, J. Magn. & Magn. Mater. **31–34**, 213.
Burzo, E., 1984, Proc. 2nd Int. Conf. on Physics of Magnetic Materials, Jadwisin, Poland, p. 304.
Burzo, E., 1985a, J. Appl. Phys. **57**, 3232.
Burzo, E., 1985b, Stud. Cercet. Fiz. **37**, 717.
Burzo, E., and J. Laforest, 1972, Int. J. Magnet. **3**, 161.
Burzo, E., and I. Ursu, 1979, J. Appl. Phys. **50**, 1971.
Burzo, E., D.P. Lazăr and W.E. Wallace, 1985a, in: New Frontiers in Rare Earth Science and Applications, Vol. II, eds X. Guangxian and X. Jimei (Science Press, Beijing, China) p. 924.
Burzo, E., L. Stanciu and W.E. Wallace, 1985b, J. Less-Common Met. **111**, 83.
Burzo, E., L. Stanciu and W.E. Wallace, 1985c, in: New Frontiers in Rare Earth Science and Applications, Vol. II, eds X. Guangxian and X. Jimei (Science Press, Beijing, China) p. 914.
Burzo, E., E.B. Boltich, M.Q. Huang and W.E. Wallace, 1985d, Proc. 8th Int. Workshop on Rare Earth Magnets and Their Applications, Dayton, OH, ed. K.J. Strnat, p. 771.
Burzo, E., E. Oswald, M.Q. Huang, E.B. Boltich and W.E. Wallace, 1985e, J. Appl. Phys. **57**, 4109.
Burzo, E., I. Lupsa and A.T. Pedziwiatr, 1986a, J. Phys. F **16**, L83.
Burzo, E., N. Plugaru, V. Pop, L. Stanciu and W.E. Wallace, 1986b, Solid State Commun. **58**, 803.
Burzo, E., A.T. Pedziwiatr and W.E. Wallace, 1987, Solid State Commun. **61**, 57.
Buschow, K.H.J., 1977, Rep. Prog. Phys. **40**, 1179.
Buschow, K.H.J., 1984, Nd–Fe Permanent Magnets – Their Present and Future Applications, ed. I.V. Mitchell (Commission of the European Communities, Brussels) p. 155.
Buschow, K.H.J., 1986, Mater. Sci. Rep. **1**, 1.
Buschow, K.H.J., J.W.C. De Vries and R.C. Thiel, 1985a, J. Phys. F **15**, L93.
Buschow, K.H.J., H.M. Van Noort and D.B. De Mooij, 1985b, J. Less-Common Met. **109**, 79.
Buschow, K.H.J., D.B. De Mooij, S. Sinnema, R.J. Radwanski and J.J.M. Franse, 1985c, J. Magn. & Magn. Mater. **51**, 211.
Cadieu, F.J., T.D. Cheung and L. Wickramasekara, 1986a, J. Magn. & Magn. Mater. **54–57**, 535.
Cadieu, F.J., T.D. Cheung, L. Wickramasekara and N. Kamprath, 1986b, IEEE Trans. Magn. **MAG-22**, 752.
Cadogan, J.M., and J.M.D. Coey, 1984, Phys. Rev. B **30**, 7326.
Capellen, J., K.A. Menzel and K.A. Gschneidner Jr, 1986, Source Book on Neodymium–Iron–Boron Permanent Magnets (Rare Earth Information Center, Iowa State University, Ames, IA, USA).
Cech, R.E., 1974, J. Met. **26**, 32.
Chaban, N.F., Y.B. Kuzma, N.S. Bilonizhko, O.O. Kachmar and N.V. Petrov, 1979, DAN SSSR Ser. A, Fiz. Mat. Tekh. Nauk. **10**, 873.
Chang, Y.S., and Y.R. Qiang, 1986, Phys. Status Solidi a **93**, 573.
Chen, Y.L., 1985, IEEE Trans. Magn. **MAG-21**, 1967.
Chikazumi, S., 1986, J. Magn. & Magn. Mater. **54–57**, 1551.
Chin, T.S., Y. Hara, E.J. Lavernia, R.C. O'Handley and N.J. Grant, 1986, J. Appl. Phys. **59**, 1297.

Coey, J.M.D., J.M. Cadogan and D.H. Ryan, 1984, Nd–Fe Permanent Magnets – Their Present and Future Applications, ed. I.V. Mitchell (Commission of the European Communities, Brussels) p. 143.
Collins, M.F., and J.B. Forsyth, 1963, Philos. Mag. **8**, 401.
Croat, J.J., 1981, J. Appl. Phys. Lett. **39**, 357.
Croat, J.J., 1982, J. Appl. Phys. **53**, 3161.
Croat, J.J., 1985, in: New Frontiers in Rare Earth Science and Applications, Vol. II, eds X. Guangxian and X. Jimei (Science Press, Beijing, China) p. 887.
Croat, J.J., J.F. Herbst, R.W. Lee and F.E. Pinkerton, 1984a, Appl. Phys. Lett. **44**, 148.
Croat, J.J., J.F. Herbst, R.W. Lee and F.E. Pinkerton, 1984b, Appl. Phys. Lett. **44**, 2078.
Davis, R.L., R.K. Day and J.B. Dunlop, 1985, Solid State Commun. **56**, 181.
de Jongh, D.J., and A.R. Miedema, 1974, Adv. Phys. **23**, 1.
De Reotier, P.D., D. Fruchart, P. Wolferms, R. Guillen, P. Vuillet, A. Yaouanc, R. Fruchart and P. L'Heritier, 1985, J. Phys. (France) **46**, C6-323.
Deryagin, A.V., E.N. Tarasov, A.V. Andreev, V.N. Moskalev and A.I. Kozlov, 1984, Pis'ma v Zh. Eksp. & Teor. Fiz. **39**, 516.
Dickenson, R.C., G.C. Hadjipanayis and K.R. Lawless, 1985, J. Appl. Phys. **57**, 4097.
Domazer, H.G., and K.J. Strnat, 1976, Proc. 2nd Int. Workshop on Rare Earth–Cobalt Permanent Magnets, University of Dayton, OH, ed. K.J. Strnat, p. 348.
Durst, K.D., and H. Kronmüller, 1985, Proc. 8th Int. Workshop on Rare Earth Magnets and Their Applications, Dayton, OH, p. 725.
Durst, K.D., and H. Kronmüller, 1986, J. Magn. & Magn. Mater. **59**, 86.
Eibler, R., R. Grössinger, G. Hilscher, H.R. Kirchmayr, O. Mayerhofer, H. Sassik, Y.K. Sun and G. Wiesinger, 1984, Nd–Fe Permanent Magnets – Their Present and Future Applications, ed. I.V. Mitchell (Commission of the European Communities, Brussels) p. 167.
Ervens, W., 1984, Nd–Fe Permanent Magnets – Their Present and Future Applications, ed. I.V. Mitchell (Commission of the European Communities, Brussels) p. 111.
Falconnet, P., 1984, Nd–Fe Permanent Magnets – Their Present and Future Applications, ed. I.V. Mitchell (Commission of the European Communities, Brussels) p. 15.
Farrell, J., and W.E. Wallace, 1966, J. Inorg. & Nucl. Chem. **5**, 105.
Ferreira, L.P., F. Cullen, P. Vuillet, A. Yaouanc, D. Fruchart, P. Wolfers and P. L'Heritier, 1985, J. Magn. & Magn. Mater. **53**, 145.
Fidler, J., 1985, IEEE Trans. Magn. **MAG-21**, 1955.
Fidler, J., and L. Yang, 1985, Proc. 8th Int. Workshop on Rare Earth Magnets and Their Applications, Dayton, OH, ed. K.J. Strnat, p. 647.
Friedt, J.M., J.P. Sanchez, P. L'Heritier and R. Fruchart, 1984, Nd–Fe Permanent Magnets – Their Present and Future Applications, ed. I.V. Mitchell (Commission of the European Communities, Brussels) p. 179.
Friedt, J.M., A. Vasquez, J.P. Sanchez, P. L'Heritier and R. Fruchart, 1986a, J. Phys. F **16**, 651.
Friedt, J.M., A. Vasquez, J.P. Sanchez, P. L'Heritier and R. Fruchart, 1986b, Hyperfine Interactions **28**, 611.
Fruchart, D., P. Wolfers, P. Vuillet, A. Yaouanc, R. Fruchart and P. L'Heritier, 1984, Nd–Fe Permanent Magnets – Their Present and Future Applications, ed. I.V. Mitchell (Commission of the European Communities, Brussels) p. 173.
Fuerst, C.D., J.F. Herbst and E.A. Alson, 1986, J. Magn. & Magn. Mater. **54–57**, 567.
Ghandehari, M.H., 1986, Appl. Phys. Lett. **78**, 578.
Givord, D., and R. Lemaire, 1974, IEEE Trans. Magn. **MAG-10**, 109.
Givord, D., and H.S. Li, 1984, Nd–Fe Permanent Magnets – Their Present and Future Applications, ed. I.V. Mitchell (Commission of the European Communities, Brussels) p. 131.
Givord, D., H.S. Li and L.M. Moreau, 1984a, Solid State Commun. **50**, 497.
Givord, D., H.S. Li and R. Perrier de la Bathie, 1984b, Solid State Commun. **5**, 857.
Givord, D., H.S. Li, J.M. Moreau, R. Perrier de la Bathie and E. du Tremolet de Lacheisserie, 1984c, Physica B **130**, 323.
Givord, D., H.S. Li and F. Tasset, 1985a, J. Appl. Phys. **57**, 4091.
Givord, D., J.M. Moreau and P. Tenaud, 1985b, Solid State Commun. **55**, 303.
Givord, D., J. Laforest, H.S. Li, A. Lienard, R. Perrier de la Bathie and P. Tenaud, 1985c, J. Phys. (France) **46**, C6-213.
Givord, D., J.M. Moreau and P. Tenaud, 1986a, J. Less-Common Met. **115**, L7.
Givord, D., H.S. Li, J.M. Moreau and P. Tenaud, 1986b, J. Magn. & Magn. Mater. **54–57**, 445.
Graham Jr, C.D., and P.J. Flanders, 1986, IEEE Trans. Magn. **MAG-22**, 749.
Grand, G., 1984, Nd–Fe Permanent Magnets – Their Present and Future Applications, ed. I.V. Mitchell (Commission of the European Communities, Brussels) p. 123.
Grössinger, R., R. Krewenka, K.S.V.L. Narasimhan and M. Sagawa, 1985a, J. Magn. & Magn. Mater. **51**, 160.
Grössinger, R., X.K. Sun, R. Eibler and H.R. Kirchmayr, 1985b, Proc. 8th Int. Workshop on Rare Earth Magnets and Their Applications, Dayton, OH, ed. K.J. Strnat, p. 553.
Grössinger, R., X.K. Sun, R. Eibler, K.H.J. Buschow and H.R. Kirchmayr, 1985c, J. Phys. (France) **46**, C6-221.
Grössinger, R., G. Hilscher, H.R. Kirchmayr, H. Sassik, R. Strnat and G. Wiesinger, 1985d, Physica B **130**, 307.

Grössinger, R., H.R. Kirchmayr, R. Krewenka, K.S.V.L. Narasimhan and M. Sagawa, 1985e, Proc. 8th Int. Workshop on Rare Earth Magnets and Their Applications, Dayton, OH, ed. K.J. Strnat, p. 565.
Grössinger, R., R. Krewenka, K.S.V.L. Narasimhan and H.R. Kirchmayr, 1986a, IEEE Trans. Magn. **MAG-22**, 760.
Grössinger, R., X.K. Sun, R. Eibler, K.H.J. Buschow and H.R. Kirchmayr, 1986b, J. Magn. & Magn. Mater. **58**, 55.
Grössinger, R., R. Krewenka, X.K. Sun, K.H.J. Buschow, R. Eibler and H.R. Kirchmayr, 1986c, J. Less-Common Met. **124**, 165.
Gu, Z.Q., and W.Y. Ching, 1986a, J. Magn. & Magn. Mater. **54–57**, 525.
Gu, Z.Q., and W.Y. Ching, 1986b, Phys. Rev. B **33**, 2868.
Gubbens, P.C.M., A.M. van der Kraan and K.H.J. Buschow, 1978, Solid State Commun. **26**, 107.
Gubbens, P.C.M., A.M. Van der Kraan and K.H.J. Buschow, 1985, Phys. Status Solidi b **130**, 575.
Gubbens, P.C.M., A.M. van der Kraan and K.H.J. Buschow, 1986, J. Magn. & Magn. Mater. **54–57**, 591.
Hadjipanayis, G.C., and Y.F. Tao, 1985, J. Phys. (France) **46**, C6-237.
Hadjipanayis, G.C., R.C. Hazelton and K.R. Lawless, 1983, Appl. Phys. Lett. **43**, 797.
Hadjipanayis, G.C., S.H. Aly and D.J. Sellmyer, 1985a, J. Appl. Phys. **57**, 4133.
Hadjipanayis, G.C., K.R. Lawless and R.C. Dickenson, 1985b, J. Appl. Phys. **57**, 4097.
Hadjipanayis, G.C., Y.F. Tao and K. Gudimetta, 1985c, Appl. Phys. Lett. **47**, 757.
Hadjipanayis, G.C., Y.F. Tao and K.R. Lawless, 1985d, Proc. 8th Int. Workshop on Rare Earth Magnets and Their Applications, Dayton, OH, ed. K.J. Strnat, p. 657.
Hadjipanayis, G.C., C.P. Wong and Y.F. Tao, 1985e, in: Rapidly Quenched Metals, eds S. Steeb and H. Warlimont (North-Holland, Amsterdam) p. 1307.
Hadjipanayis, G.C., Y.F. Tao, K.R. Lawless and D.J. Sellmyer, 1985f, Mater. Lett. **3**, 270.
Hadjipanayis, G.C., R.C. Dickenson and K.R. Lawless, 1986, J. Magn. & Magn. Mater. **54–57**, 557.
Handstein, A., J. Schneider, D. Stephan, W. Fischer, U. Heinecke, R. Grössinger, H. Sassik and H.R. Kirchmayr, 1985, Mater. Lett. **3**, 200.
Harris, I.R., and T. Bailey, 1984, Nd–Fe Permanent Magnets – Their Present and Future Applications, ed. I.V. Mitchell (Commission of the European Communities, Brussels) p. 99.
Harris, I.R., C. Noble and T. Bailey, 1985, J. Less-Common Met. **106**, L1.
Heinecke, U., A. Handstein and J. Schneider, 1985, J. Magn. & Magn. Mater. **53**, 236.
Herbst, J.F., and W.B. Yelon, 1986, J. Magn. & Magn. Mater. **54–57**, 570.
Herbst, J.F., J.J. Croat, F.E. Pinkerton and W.B. Yelon, 1984, Phys. Rev. B **29**, 4176.
Herbst, J.F., J.J. Croat and W.B. Yelon, 1985, J. Appl. Phys. **57**, 4086.
Herget, C.S., 1984, Nd–Fe Permanent Magnets – Their Present and Future Applications, ed. I.V. Mitchell (Commission of the European Communities, Brussels) p. 245.
Herget, C.S., 1985a, Proc. 8th Int. Workshop on Rare Earth Magnets and Their Applications, Dayton, OH, ed. K.J. Strnat, p. 407.
Herget, C.S., 1985b, Proc. 8th Int. Workshop on Rare Earth Magnets and Their Applications, Dayton, OH, ed. K.J. Strnat, p. 441.
Herget, C.S., and H.G. Domazer, 1975, Goldschmidt Informiert **4/75**(35), 3.
Herzer, G., W. Fernengel and E. Adler, 1986, J. Magn. & Magn. Mater. **58**, 48.
Hilscher, G., R. Grössinger, S. Heisz, H. Sassik and G. Wiesinger, 1986, J. Magn. & Magn. Mater. **54–57**, 577.
Hiraga, K., M. Hirabayashi, M. Sagawa and Y. Matsuura, 1985, Japan J. Appl. Phys. **24**, L30.
Hirosawa, S., and M. Sagawa, 1985, Solid State Commun. **54**, 355.
Hirosawa, S., Y. Matsuura, H. Yamamoto, S. Fujimura and M. Sagawa, 1985a, in: New Frontiers in Rare Earth Science and Applications, Vol. II, eds X. Guangxian and X. Jimei (Science Press, Beijing, China) p. 928.
Hirosawa, S., Y. Matsuura, H. Yamamoto, S. Fujimura, M. Sagawa and H. Yamauchi, 1985b, Japan J. Appl. Phys. **24**, L803.
Hirosawa, S., Y. Matsuura, H. Yamamoto, S. Fujimura, M. Sagawa and H. Yamauchi, 1986, J. Appl. Phys. **59**, 873.
Hiroyoshi, H., H. Yamauchi, Y. Yamaguchi, H. Yamamoto, Y. Nakagawa and M. Sagawa, 1985, Solid State Commun. **54**, 41.
Hiroyoshi, H., N. Saito, G. Kido, Y. Nakagawa, S. Hirosawa and M. Sagawa, 1986, J. Magn. & Magn. Mater. **54–57**, 583.
Ho, W.W., H.Y. Chen, Y.C. Yang, J. Wang, B. Liao, C. Lin, F. Xing, Z.X. Liu and J. Lan, 1985, Proc. 8th Int. Workshop on Rare Earth Magnets and Their Applications, Dayton, OH, ed. K.J. Strnat, p. 635.
Homma, M., M. Okada and S. Sugimoto, 1985, in: New Frontiers in Rare Earth Science and Applications, Vol. II, eds X. Guangxian and X. Jimei (Science Press, Beijing, China) p. 888.
Honma, H., N. Shimotomai and M. Doyama, 1985, J. Magn. & Magn. Mater. **52**, 309.
Huang, M.Q., E.B. Boltich, E. Oswald and W.E. Wallace, 1985a, in: New Frontiers in Rare Earth Science and Applications, Vol. II, eds X. Guangxian and X. Jimei (Science Press, Beijing, China) p. 974.
Huang, M.Q., E. Oswald, E.B. Boltich, S. Hirosawa, W.E. Wallace and E. Schwab, 1985b, Physica B **130**, 319.
Huang, M.Q., E.B. Boltich, W.E. Wallace and E. Oswald, 1986, J. Magn. & Magn. Mater. **60**, 270.
Inoue, J., and M. Shimizu, 1986a, J. Phys. F **16**, 1051.

Inoue, J., and M. Shimuzu, 1986b, J. Phys. F **16**, L157.
Jiangao, Z., S. Baogen and Z. Wenshan, 1985, in: New Frontiers in Rare Earth Science and Applications, Vol. II, eds X. Guangxian and X. Jimei (Science Press, Beijing, China) p. 895.
Jueyun, P., L. Zhengwen and M. Ruzhang, 1985, in: New Frontiers in Rare Earth Science and Applications, Vol. II, eds X. Guangxian and X. Jimei (Science Press, Beijing, China) p. 982.
Jurczyk, N., and W.E. Wallace, 1986, IEEE Trans. Magn. **MAG-22**, 755.
Kamal, R., and Y. Anderson, 1985, Phys. Rev. B **32**, 1785.
Kapusta, Cz., Z. Kakol, H. Figiel and R.J. Radwanski, 1986, J. Magn. & Magn. Mater. **59**, 169.
Kirchmayr, H.R., 1984, Proc. 2nd Int. Conf on Phys. Magnetic Materials, Jadwisin, Poland, p. 338.
Kirchmayr, H.R., 1985, in: New Frontiers in Rare Earth Science and Applications, Vol. II, eds X. Guangxian and X. Jimei (Science Press, Beijing, China) p. 879.
Kirchmayr, H.R., and C.A. Poldy, 1979, in: Handbook on the Physics and Chemistry of Rare Earths, Vol. 2, eds K.A. Gschneidner Jr and L. Eyring (North-Holland, Amsterdam) p. 55.
Koon, N.C., and B.N. Das, 1981, J. Appl. Phys. Lett. **39**, 870.
Koon, N.C., and B.N. Das, 1984, J. Appl. Phys. **55**, 2063.
Koon, N.C., B.N. Das, M. Rubinstein and J. Tyson, 1985, J. Appl. Phys. **57**, 4091.
Koon, N.C., B.N. Das and C.M. Williams, 1986a, J. Magn. & Magn. Mater. **54–57**, 523.
Koon, N.C., M. Abe, E. Callen, B.N. Das, J. Foster, S.H. Liou, A. Martinez and R. Segnan, 1986b, J. Magn. & Magn. Mater. **54–57**, 593.
Kostikas, A., V. Papaefthyniou, A. Simopoulos and G.C. Hadjipanayis, 1985, J. Phys. F **15**, L129.
Kronmüller, H., 1982, Proc. 6th Int. Workshop on Rare Earth Permanent Magnets, ed. J. Fidler, Vienna, p. 555.
Ku, H.C., J.C. Chen and L.S. Yen, 1986, J. Magn. & Magn. Mater. **54–57**, 533.
Kuntze, K., D. Kohake, R. Beranek, S. Stieler and C. Heiden, 1985, J. Phys. (France) **46**, C6-253.
Kuzma, Y.B., N.S. Bilonizhko and S.I. Svaricheskaya, 1977, Interaction of Rare Earth Metals with Transition Metals and Boron [Tugoplavkie Boridy i Silitsidy] (Naukova Dumka, Kiev) p. 67.
Le Roux, D., H. Vincent, P. L'Heritier and R. Fruchart, 1985, J. Phys. (France) **46**, C6-243.
Lee, R.W., 1985, J. Appl. Phys. Lett. **46**, 790.
Lee, R.W., E.G. Brewer and N.A. Schaffel, 1985, IEEE Trans. Magn. **MAG-21**, 1958.
L'Heritier, P., and R. Fruchart, 1985, J. Phys. (France) **46**, C6-319.
L'Heritier, P., P. Chaudonet, R. Madar, A. Rouanet, J.P. Senateur and R. Fruchart, 1985, C. Rend. Acad. Sci. Paris **299**, 849.
Li, D., and K.J. Strnat, 1985, J. Appl. Phys. **57**, 4143.
Li, D., H.F. Mildrum and K.J. Strnat, 1985, J. Appl. Phys. **57**, 4140.
Lidong, Z., L. Lin, H. Qin and Z. Shouzeng, 1985, in: New Frontiers in Rare Earth Science and Applications, Vol. II, eds X. Guangxian and X. Jimei (Science Press, Beijing, China) p. 918.
Ling, Q., J.M. Cadogan and J.M.D. Coey, 1986, Hyperfine Interactions **28**, 655.
Liu, N.C., and H.H. Stadelmaier, 1986, Mater. Lett. **4**, 377.
Livingston, J.D., 1981, J. Appl. Phys. **52**, 2544.
Livingston, J.D., 1985a, J. Appl. Phys. **57**, 4137.
Livingston, J.D., 1985b, Proc. 8th Int. Workshop on Rare Earth Magnets and Their Applications, Dayton, OH, ed. K.J. Strnat, p. 423.
Ma, B.M., and K.S.V.L. Narasimhan, 1986, J. Magn. & Magn. Mater. **54–57**, 559.
Maocai, Z., M. Deqing, H. Qin and L. Shiqiang, 1985a, in: New Frontiers in Rare Earth Science and Applications, Vol. II, eds X. Guangxian and X. Jimei (Science Press, Beijing, China) p. 967.
Maocai, Z., M. Deqing, J. Xiuling and L. Shiqiang, 1985b, Proc. 8th Int. Workshop on Rare Earth Magnets and Their Applications, Dayton, OH, ed. K.J. Strnat, p. 541.
Matsuura, Y., S. Hirosawa, H. Yamamoto, S. Fujimura and M. Sagawa, 1985a, Appl. Phys. Lett. **46**, 308.
Matsuura, Y., S. Hirosawa, H. Yamamoto, S. Fujimura, M. Sagawa and H. Osamura, 1985b, Japan J. Appl. Phys. **24**, L365.
McFarland, C.M., 1973, Proc. Xth Rare Earth Research Conf., Oak Ridge, TN, eds C.J. Kavane and T.H. Moeller, p. 692.
Meisner, G.P., and C.D. Fuerst, 1986, IEEE Trans. Magn. **MAG-22**, 744.
Ming, Y.F., Z.X. Chao, Z.R. Wen, Z.X. Jian and S.T. Duo, 1985, Proc. 8th Int. Workshop on Rare Earth Magnets and Their Applications, Dayton, OH, ed. K.J. Strnat, p. 529.
Mishra, R.K., 1986, J. Magn. & Magn. Mater. **54–57**, 450.
Mishra, R.K., J.K. Chen and G. Thomas, 1986, J. Appl. Phys. **59**, 2244.
Miyajima, H., Y. Otani, S. Chikazumi, S. Hirosawa and M. Sagawa, 1986, J. Magn. & Magn. Mater. **54–57**, 587.
Narasimhan, K.S.V.L., 1985a, J. Appl. Phys. **57**, 4081.
Narasimhan, K.S.V.L., 1985b, Proc. 8th Int. Workshop on Rare Earth Magnets and Their Applications, Dayton, OH, ed. K.J. Strnat, p. 459.
Narasimhan, K.S.V.L., 1985c, in: New Frontiers in Rare Earth Science and Applications, Vol. II, eds X. Guangxian and X. Jimei (Science Press, Beijing, China) p. 947.
Niarchos, D.G., B.D. Dunlap, G.C. Hadjipanayis and D.R. Jones, 1985, J. Appl. Phys. **57**, 4133.

Oesterreicher, H., 1985, Proc. 8th Int. Workshop on Rare Earth Magnets and Their Applications, Dayton, OH, ed. K.J. Strnat, p. 705.
Oesterreicher, H., F. Spada and C. Abache, 1984, Mater. Res. Bull. **19**, 1069.
Oesterreicher, K., and H. Oesterreicher, 1984a, Phys. Status Solidi a **85**, K61.
Oesterreicher, K., and H. Oesterreicher, 1984b, J. Less-Common Met. **104**, L19.
Ogilvy, A.J.W., G.P. Gregan and H.A. Davies, 1984, in: Nd–Fe Permanent Magnets – Their Present and Future Applications, ed. I.V. Mitchell (Commission of the European Communities, Brussels) p. 93.
Okada, M., and M. Homma, 1985, in: Proc. 8th Int. Workshop on Rare Earth Magnets and Their Applications, Dayton, OH, ed. K.J. Strnat, p. 507.
Okada, M., S. Sugimoto, C. Ishizaka, T. Tanaka and M. Homma, 1985, J. Appl. Phys. **57**, 4146.
Ono, H., 1971, J. Phys. Soc. Jpn. **31**, 92.
Onodera, H., Y. Yamaguchi, H. Yamamoto, M. Sagawa, Y. Matsuura and H. Yamamoto, 1984, J. Magn. & Magn. Mater. **46**, 151.
Ormerod, J., 1984, in: Nd–Fe Permanent Magnets – Their Present and Future Applications, ed. I.V. Mitchell (Commission of the European Communities, Brussels) p. 69.
Ormerod, J., 1985, J. Less-Common Met. **111**, 49.
Otani, Y., H. Miyajima, S. Chikazumi, S. Hirosawa and M. Sagawa, 1986, J. Magn. & Magn. Mater. **60**, 168.
Overfeld, R.A., and J.J. Becker, 1984, J. Appl. Phys. Lett. **44**, 925.
Pareti, L., F. Bolzoni and O. Moze, 1985a, Phys. Rev. B **32**, 7604.
Pareti, L., H. Szymczak and H.K. Lachowicz, 1985b, Phys. Status Solidi a **92**, K65.
Park, H.K., H.H. Stadelmaier and L.T. Jordan, 1982, Z. Metallkd. **73**, 399.
Pedziwiatr, A.T., W.E. Wallace and E. Burzo, 1986a, J. Magn. & Magn. Mater. **61**, 173.
Pedziwiatr, A.T., S.Y. Jiang and W.E. Wallace, 1986b, J. Magn. & Magn. Mater. **62**, 29.
Pedziwiatr, A.T., W.E. Wallace and E. Burzo, 1986c, J. Magn. & Magn. Mater. **59**, L179.
Pedziwiatr, A.T., W.E. Wallace and E. Burzo, 1986d, J. Magn. & Magn. Mater. **61**, 177.
Pedziwiatr, A.T., W.E. Wallace, E. Burzo and V. Pop, 1987a, Solid State Commun. **61**, 61.
Pedziwiatr, A.T., W.E. Wallace and E. Burzo, 1987b, IEEE Trans. Magn. **MAG-23**, 1795.
Pinkerton, F.E., 1986, J. Magn. & Magn. Mater. **54–57**, 579.
Pinkerton, F.E., and W.R. Dunham, 1985, J. Appl. Phys. **57**, 4121.
Potenziani, E., H.A. Leupold, J.P. Clarke and A. Tauber, 1985, J. Appl. Phys. **57**, 4152.
Pourarian, F., M.Q. Huang and W.E. Wallace, 1986, J. Less-Common Met. **120**, 63.
Price, D.C., R.K. Day and J.B. Dunlop, 1986, J. Appl. Phys. **59**, 3587.
Pszczola, J., and K. Krop, 1986, J. Magn. & Magn. Mater. **59**, 95.
Ramesh, R., K.M. Krishnan, E. Goo, G. Thomas, M. Okada and M. Homma, 1986, J. Magn. & Magn. Mater. **54–57**, 563.
Rani, M., and R. Kamal, 1986, J. Less-Common Met. **125**, 97.
Rani, M., M.S. Saini and R. Kamal, 1986, Phys. Lett. A **118**, 103.
Rao, K.V., R. Malmhall and G.C. Hadjipanayis, 1985, J. Phys. (France) **46**, C6-229.
Rhyne, J.J., 1979, in: Handbook on the Physics and Chemistry of Rare Earths, Vol. 2, eds K.A. Gschneidner Jr and L. Eyring (Amsterdam, North-Holland) p. 259.
Rodewald, W., 1985a, Proc. 8th Int. Workshop on Rare Earth Magnets and Their Applications, Dayton, OH, ed. K.J. Strnat, p. 737.
Rodewald, W., 1985b, J. Less-Common Met. **111**, 77.
Rong, Q.X., J.H. Juan, X.G. Qing, W.L. Hong and Z. Yi, 1985, in: Proc. 8th Int. Workshop on Rare Earth Magnets and Their Applications, Dayton, OH, ed. K.J. Strnat, p. 693.
Rosenberg, M., P. Deppe, M. Wojcik and H.H. Stadelmaier, 1985, J. Appl. Phys. **57**, 4124.
Rosenberg, M., P. Deppe, K. Erdmann, M. Sostarich and H.H. Stadelmaier, 1986a, J. Magn. & Magn. Mater. **54–57**, 599.
Rosenberg, M., P. Deppe and H.H. Stadelmaier, 1986b, Hyperfine Interactions **28**, 503.
Rotenberg, L.R.K., R.F. Oliveira, H.R. Rechenberg and F.P. Missell, 1985, J. Appl. Phys. **57**, 4127.
Sagawa, M., S. Fujimura, N. Togawa, H. Yamamoto and Y. Matsuura, 1984a, J. Appl. Phys. **55**, 2083.
Sagawa, M., S. Fujimura, H. Yamamoto, Y. Matsuura and K. Hiraga, 1984b, IEEE Trans. Magn. **MAG-20**, 1584.
Sagawa, M., S. Fujimura, H. Yamamoto, Y. Matsuura, S. Hirosawa and K. Hiraga, 1985a, in: Proc. 8th Int. Workshop on Rare Earth Magnets and Their Applications, Dayton, OH, ed. K.J. Strnat, p. 587.
Sagawa, M., S. Fujimura, H. Yamamoto, Y. Matsuura and S. Hirosawa, 1985b, J. Appl. Phys. **57**, 4094.
Sankar, S.G., and K.S.V.L. Narasimhan, 1986, J. Magn. & Magn. Mater. **54–57**, 530.
Schneider, J., R. Grössinger, R. Krewenka, A. Handstein, U. Heinecke and H. Sassik, 1985, Mater. Lett. **3**, 401.
Sellmyer, D.J., A. Ahmed, G. Muench and G.C. Hadjipanayis, 1984, J. Appl. Phys. **55**, 2088.
Shoemaker, C.B., D.P. Shoemaker and R. Fruchart, 1984, Acta Crystallogr. Sect. C **40**, 1665.
Shouzeng, Z., L.I. Lin, Z. Lidong and H.U. Qin, 1986, J. Magn. & Magn. Mater. **54–57**, 521.
Shull, C.G., and Y. Yamada, 1962, J. Phys. Soc. Jpn. **17**, B III-1.
Sinnema, S., R.J. Radwanski, J.J.M. Franse, D.B. De Mooij and K.H.J. Buschow, 1984, J. Magn. & Magn. Mater. **44**, 333.
Sinnema, S., J.J.M. Franse, R.J. Radwanski and K.H.J. Buschow, 1985, J. Phys. (France) **46**, C6-260.

Stadelmaier, H.H., and N.A. El Masry, 1985, in: Proc. 8th Int. Workshop on Rare Earth Magnets and Their Applications, Dayton, OH, ed. K.J. Strnat, p. 613.
Stadelmaier, H.H., and H.K. Park, 1981, Z. Metallkd. **92**, 417.
Stadelmaier, H.H., N.A. El Masry and S.F. Cheng, 1983, Mater. Lett. **2**, 169.
Stadelmaier, H.H., N.A. El Masry, N.C. Liu and S.F. Cheng, 1984, Mater. Lett. **2**, 411.
Stadelmaier, H.H., N.A. El Masry and S.R. Stallard, 1985a, J. Appl. Phys. **57**, 4149.
Stadelmaier, H.H., N.C. Liu and N.A. El Masry, 1985b, Mater. Lett. **3**, 130.
Stepanchikova, G.F., and Y.B. Kuzma, 1980, Poroshk. Metall. **10**, 44.
Stoelinga, J.M., A.J.T. Grimberg, R. Gesdorf and G. De Vrie, 1971, J. Phys. (France) **32**, C1-831.
Stoner, E.G., 1946, Rep. Prog. Phys. **47**, 11.
Strnat, K.J., 1985, in: New Frontiers in Rare Earth Science and Applications, Vol. II, eds X. Guangxian and X. Jimei (Science Press, Beijing, China) p. 872.
Strnat, K.J., D. Li and H.F. Mildrum, 1985, in: Proc. 8th Int. Workshop on Rare Earth Magnets and Their Applications, Dayton, OH, ed. K.J. Strnat, p. 575.
Suzuki, T., and K. Hiraga, 1986, J. Magn. & Magn. Mater. **54–57**, 527.
Szpunar, B., and J.A. Szpunar, 1985, J. Appl. Phys. **57**, 4130.
Szymczak, H., 1985, J. Phys. (France) **46**, C6-225.
Szymczak, H., E. Burzo and W.E. Wallace, 1985, J. Phys. (France) **46**, C6-309.
Szytula, A., and J. Drajewicz, 1986, Solid State Commun. **57**, 509.
Tanigawa, S., I. Hara, E.J. Lavernia, R.C. O'Handley and N.J. Grant, 1986, IEEE Trans. Magn. **MAG-22**, 746.
Tao, Y.F., and G.C. Hadjipanayis, 1985, J. Appl. Phys. **57**, 4103.
Taylor, K.N.R., 1971, Adv. Phys. **20**, 551.
Tianduo, S., and Z. Xijian, 1985, in: Proc. 8th Int. Workshop on Rare Earth Magnets and Their Applications, Dayton, OH, ed. K.J. Strnat, p. 527.
Tiesong, Z., J. Hanmin, D. Jingouan, W. Fengwen, S. Jihua and S. Yan, 1986, J. Magn. & Magn. Mater. **54–57**, 573.
Tokuhara, K., Y. Ohtsu, F. Ono, O. Yamada, M. Sagawa and Y. Matsuura, 1985, Solid State Commun. **56**, 333.
Tokunaga, M., and H. Harada, 1985, in: Proc. 8th Int. Workshop on Rare Earth Magnets and Their Applications, Dayton, OH, ed. K.J. Strnat, p. 475.
Tokunaga, M., M. Meguro, M. Endoh, S. Tanigawa and H. Harada, 1985, IEEE Trans. Magn. **MAG-21**, 1964.
Turilli, H., H. Szymczak and H.K. Lachowicz, 1985, Phys. Status solidi a **90**, K143.
Van Noort, H.M., and K.H.J. Buschow, 1985, J. Less-Common Met. **113**, L9.
Van Noort, H.M., D.B. De Mooij and K.H.J. Buschow, 1985, J. Appl. Phys. **57**, 5414.
Van Noort, H.M., D.B. De Mooij and K.H.J. Buschow, 1986, J. Less-Common Met. **115**, 155.
Vasquez, A., and J.P. Sanchez, 1986, 17th Rare Earth Conf., Hamilton, Canada.
Vasquez, A., J.M. Friedt, P. L'Heritier and R. Fruchart, 1985, Solid State Commun. **55**, 783.
Wallace, W.E., 1973, Rare Earth Intermetallics (Academic Press, New York).
Wallace, W.E., E. Burzo, D. Barb, M. Morariu and M. Rogalski, 1985, unpublished data.
Wang, D.W., W.T. Xiao, F.S. Zhao, D.N. Lan, G.P. Hua and J.H. Zhu, 1985, in: Proc. 8th Int. Workshop on Rare Earth Magnets and Their Applications, Dayton, OH, ed. K.J. Strnat, p. 525.
Wiesinger, G., G. Hilscher and R. Grössinger, 1987, J. Less-Common Met. **131**, 409.
Xiaojia, L., X. You, Y. Guilin and Z. Hongru, 1985, in: Proc. 8th Int. Workshop on Rare Earth Magnets and Their Applications, Dayton, OH, ed. K.J. Strnat, p. 683.
Yamada, M., Y. Yamaguchi, H. Kato, H. Yamamoto, Y. Nakagawa, S. Hirosawa and M. Sagawa, 1985, Solid State Commun. **56**, 663.
Yamada, O., H. Tokuhara, F. Ono, M. Sagawa and Y. Matsuura, 1986, J. Magn. & Magn. Mater. **54–57**, 585.
Yamamoto, H., Y. Matsuura, S. Fujimura and M. Sagawa, 1984, J. Appl. Phys. Lett. **45**, 1141.
Yamasaki, J., H. Soeda, M. Yanagida, K. Mohri, T. Teshima, O. Kohmoto and T. Yoneyama, 1986, IEEE Trans. Magn. **MAG-22**, 763.
Yamauchi, H., H. Hiroyoshi, Y. Yamaguchi, H. Yamamoto, M. Sagawa, Y. Matsuura and H. Yamamoto, 1985, J. Magn. & Magn. Mater. **49**, 210.
Yamauchi, H., M. Yamada, Y. Yamaguchi, H. Yamamoto, S. Hirosawa and M. Sagawa, 1986, J. Magn. & Magn. Mater. **54–57**, 575.
Yang, Y.C., W.W. Ho, N.Y. Chen, J. Wang and J. Lan, 1985a, J. Appl. Phys. **57**, 4118.
Yang, Y.C., H.Y. Chen, Z.X. Liu, B. Liao, F. Xing and W.W. Ho, 1985b, J. Appl. Phys. **57**, 4115.
Yang, Y.C., W.J. James, H.Y. Chen and H. Sun, 1986a, J. Magn. & Magn. Mater. **54–57**, 895.
Yang, Y.C., W.J. James, X.D. Li and L.G. Xu, 1986b, IEEE Trans. Magn. **MAG-22**, 757.
Yingchang, Y., C. Haiying, L. Chin, X. Feng, L. Zunxiao and H. Wenwang, 1985, in: New Frontiers in Rare Earth Science and Applications, Vol. II, eds X. Guangxian and X. Jimei (Science Press, Beijing, China) p. 941.

Handbook on the Physics and Chemistry of Rare Earths, Vol. 12
edited by K.A. Gschneidner, Jr. and L. Eyring

Chapter 83

MAGNETIC PROPERTIES OF TERNARY INTERMETALLIC COMPOUNDS OF THE RT_2X_2 TYPE

Andrzej SZYTUŁA
Institute of Physics, Jagellonian University, 30-059 Kraków, Reymonta 4, Poland

Janusz LECIEJEWICZ
Institute of Nuclear Chemistry and Technology, 03-195 Warszawa, Dorodna 16, Poland

Contents

Symbols and abbreviations

a, b, c	unit cell parameters
$\boldsymbol{a}^*$, $\boldsymbol{b}^*$, $\boldsymbol{c}^*$	basic vectors in reciprocal lattice
a_m, b_m, c_m	lattice parameters of monoclinic unit cell
a_t, c_t	lattice parameters of tetragonal unit cell
$\|a_+\rangle$, $\|a_-\rangle$, $\|b_+\rangle$, $\|b_-\rangle$	wave functions
A_1^m, B_1^m	crystal field parameters
CEF	crystalline electric field
DOS	density of states
E	energy of a spin system
E_a	anisotropy energy
E_F	the Fermi energy
$F(\boldsymbol{k})$	function described by Yosida and Watabe
g	the Landé factor
H	magnetic field
H_c	critical field
H_{tot}	total Hamiltonian
H_{exch}	Hamiltonian describing the exchange interactions
H_{cf}	Hamiltonian describing the crystal electric field
H_{ms}	Hamiltonian describing the magnetostriction effect
H_{ext}	Hamiltonian describing the influence of the external magnetic field
H_{eff}	the effective magnetic field
$\mathcal{J}$	a constant
J	total angular momentum
J_x, J_z	x and z component of total angular momentum
$J(\boldsymbol{k})$	the Fourier transform of the exchange integral
J_K	the Kondo coupling constant
$J(\boldsymbol{R}_i - \boldsymbol{R}_j)$	the exchange integral between i and j magnetic ions
J_{sf}	coupling constant between a 4f and a conduction electron
k	the Boltzman constant
$\boldsymbol{k}$	wave vector of a magnetic structure
k_x, k_y, k_z	x, y and z component of wave vector of a magnetic structure
k_F	the Fermi vector
K_1, K_2	anisotropy constant
L	transition heat
$\Delta l/l$	thermal expansion
m	electron rest mass
m^*	effective electron mass
M	magnetization
M_s	saturation magnetization
$m_0(\chi)$	the Brillouin function
N	total number of magnetic ions
$N(E_F)$	electron density of states at the Fermi level
n_c	magnetic carrier number derived from the Curie constant
n_s	magnetic carrier number derived from spontaneous moment at 0 K
O_n^m	crystal field operator equivalent (Stevens operator)
p	pressure
Q_s	saturated quadrupole moment
Q_{zz}	quadrupolar operator
R	chemical symbol for rare earth
R_a	interatomic distance between Mn atoms in a-constant direction
R_c	interatomic distance between Mn atoms in c-constant direction
R_i, R_j	interatomic distance between magnetic atoms
R_0	universal gas constant
S	entropy
T	chemical symbol for 3d, 4d and 5d metal
T	temperature
T_C	the Curie temperature (ferromagnetic or ferrimagnetic ordering)
T_K	the Kondo temperature
T_m	temperature of the phase transition from ferri- to antiferromagnetic state

T_{max}	spin-fluctuation temperature	θ_p	paramagnetic Curie temperature
T_N	the Néel temperature (antiferromagnetic ordering)	μ	magnetic moment
		$\langle \mu \rangle$	average value of the magnetic moment
T_s	superconductor transition temperature	μ_x, μ_z	magnetic moment in x and z direction
V	volume	μ_B	the Bohr magneton
V_2^0	second order crystal field parameter	μ_{eff}	effective paramagnetic moment
x	concentration	μ_{Mn}	magnetic moment of Mn atom (in μ_B)
X	silicon or germanium		
XAS	X-ray absorption spectroscopy method	μ_s	ordered moment (in μ_B)
z	position parameter of silicon or germanium atoms in $ThCr_2Si_2$-type structure	μ_R	magnetic moment of R atoms (in μ_B)
		ρ	resistivity
		$\chi(T)$	magnetic susceptibility
z_i	position parameters of atoms in $CaBe_2Ge_2$-type structure	$\chi(0)$	low temperature susceptibility
		χ_z, χ_c	magnetic susceptibility measured for $H \parallel a$ and $H \parallel c$
Z	number of free electrons per magnetic ion		
γ, $\gamma(0)$	electronic specific heat coefficient (extrapolated at $T = 0$ K)	ϕ	angle between magnetization vector and a-axis
		φ	angle between magnetic moment and tetragonal axis
θ	angle between magnetization vector and c-axis		

1. Introduction

During the past few years, the intermetallic compounds containing rare earth elements have been a subject of intensive studies because of their intriguing physical properties, which have both fundamental and practical significance.

One of the many "families" of intermetallic systems, which turned out to be particularly interesting, consists of compounds exhibiting the tetragonal $BaAl_4$ type of crystal structure and its modifications. A few hundred of these compounds have been synthesized up to now and their properties investigated. Their general chemical formula is RT_2X_2, where R is a rare earth, T is a transition 3d, 4d, or 5d metal and X is silicon or germanium.

The question arises, why these compounds are so interesting. There are several reasons for it:

- they are stable over a large temperature range and they appear in a strict stoichiometric ratio of 1:2:2,
- their crystal structure is fairly simple, generally of a tetragonal symmetry with a large c/a ratio equal to about 2.5 in all cases, so one may expect a large anisotropy of physical properties,
- some of them were found to be superconductors at low temperatures,

– $CeCu_2Si_2$ and $CeRu_2Si_2$ were discovered to be heavy fermion systems,
– they exhibit various, often surprising magnetic properties.

The ternary RT_2X_2 compounds crystallize in two allotropic modifications of the tetragonal $BaAl_4$ type structure (Andress and Alberti 1935).

Most compounds have the body-centered tetragonal $ThCr_2Si_2$ type structure (Ban and Sikirica 1964). Some exhibit the primitive tetragonal $CaBe_2Ge_2$-type structure (Eisenmann et al. 1972).

The space group of $ThCr_2Si_2$-type structure is I4/mmm, the atoms are distributed as follows:

R(Th) in 2(a) site: 0, 0, 0,
T(Cr) in 4(d) site: $0, \frac{1}{2}, \frac{1}{4}; \frac{1}{2}, 0, \frac{1}{4}$;
X(Si) in 4(e) site: $0, 0, z; 0, 0, \bar{z}$;
+ body centering translation.

The unit cell of $ThCr_2Si_2$-type is displayed in fig. 1. This type of crystal structure consists of tetrahedra composed of X atoms with a transition metal inside. The X–X distances are usually close to the sum of covalent radii of X atoms, similarly as are the T–X contacts. Thus strong chemical interactions are expected within the layers composed of tetrahedra which in turns, consist of 4X atoms. The bond lengths are critically dependent on the magnitude of the z parameter and the c/a ratio (a, c are the lattice constants).

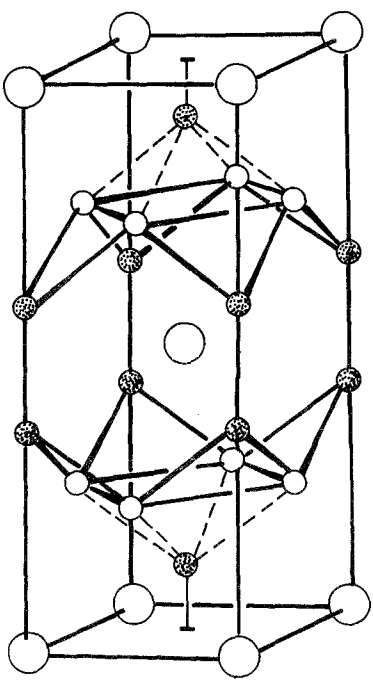

Fig. 1. Crystal structure of RT_2X_2 compounds of $ThCr_2Si_2$ type.

In the case of a regular tetrahedron:

$$z = \frac{1}{4} + \frac{1}{2\sqrt{2}} \frac{a}{c} = \frac{3}{8} \qquad \text{if} \qquad c/a = 2(2)^{1/2}.$$

The crystal structure of $ThCr_2Si_2$ type is characterized by two parameters: the free parameter z and the a/c ratio. The values of these parameters for rare-earth compounds change with the kind of transition metal (Szytuła and Leciejewicz 1987a). The z values oscillate around 0.375 value. For compounds containing Pd and Cu $z > 0.375$, in contrast to compounds containing Ru and Os for which $z < 0.375$. The a/c values observed are in the range from 0.366 to 0.424. The values of these parameters indicate that the tetrahedra deviate from the regular shape.

The shortest distance between two X atoms belonging to two adjacent layers of 4X tetrahedra is $(1\text{-}2z)c$ implying strong X–X interactions.

The layers form a sandwich framework with R atoms in between. Each R atom coordinates 8X atoms and 8T atoms at the corners of a cube at a distance which is smaller than the corresponding sum of ionic radii but larger than the sum of covalent radii. The distortion of the R-8X cube is also dependent on the magnitude of the z parameter.

The crystal structure of $CaBe_2Ge_2$ type is described in the space group P4/nmm with atoms distributed among the following sites:

R in 2(c) site: $\frac{1}{4}, \frac{1}{4}, z_1$; $\frac{3}{4}, \frac{3}{4}, \bar{z}_1$;

T1 in 2(c) site: $\frac{1}{4}, \frac{1}{4}, z_2$; $\frac{3}{4}, \frac{3}{4}, \bar{z}_2$;

T2 in 2(a) site: $\frac{3}{4}, \frac{1}{4}, 0$; $\frac{1}{4}, \frac{3}{4}, 0$;

X1 in 2(b) site: $\frac{3}{4}, \frac{1}{4}, \frac{1}{2}$; $\frac{1}{4}, \frac{3}{4}, \frac{1}{2}$;

X2 in 2(c) site: $\frac{1}{4}, \frac{1}{4}, z_3$; $\frac{3}{4}, \frac{3}{4}, \bar{z}_3$.

The unit cell of $CaBe_2Ge_2$ type structure is displayed in fig. 2. Two kinds of coordination polyhedra can be distinguished: 4X tetrahedra with T atoms in their centers and a sequence of pyramids composed of 5X atoms and the T atom inside.

The R atoms lie approximately in the center of the holes between the layer of tetrahedra and the layer of pyramids.

The $CaBe_2Ge_2$ structure is described in terms of successive nets of atoms as:

$$-R-T-X-T-R-X-T-X-T-.$$

For comparison, the $ThCr_2Si_2$ type structure is

$$-R-X-T-X-R-X-T-X-R-.$$

Both structures may be considered as consisting of a three dimensional

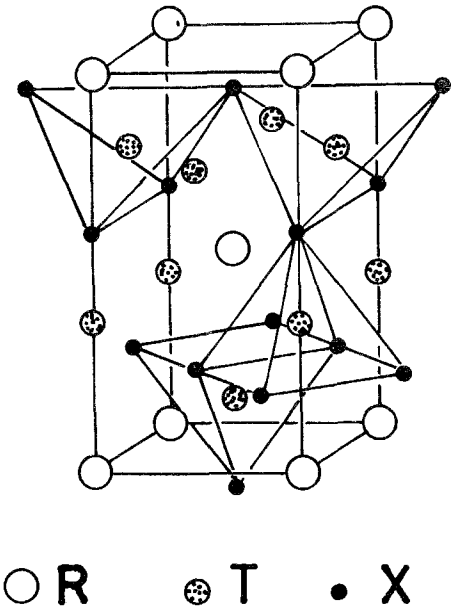

Fig. 2. Crystal structure of RT_2X_2 compounds of $CaBe_2Ge_2$ type. The origin of the unit cell of $CaBe_2Ge_2$ type is shifted by $(\frac{3}{4}, \frac{3}{4}, \frac{1}{4})$ so that it corresponds to a unit cell of $ThCr_2Si_2$ type.

framework with short bond distances, where R atoms occupy the largest open spaces.

The RIr_2Si_2 compounds have both structures: the low-temperature modification has a body centered unit cell, the high-temperature phase shows the primitive unit cell (Braun et al. 1983). The c/a ratio is smaller for the primitive cell which implies a smaller deformation of unit cell.

For the detailed description of the crystallographic structure the reader is referred to the contribution by Parthé and Chabot (1984) in vol. 6, ch. 48 of this Handbook. The crystallographic data for ternary silicides are presented in Rogl's paper (1984) in vol. 7, ch. 51 of this Handbook.

The results concerning the magnetic properties of the ternary metal silicides and germanides with R elements (R = Y, and lanthanides) basing on magnetometric, neutron diffraction and the Mössbauer data are discussed in the second section. Section 3 gives information concerning the magnetic interactions.

The magnetic properties of RT_2X_2 compounds were already reviewed by Leciejewicz (1982), Rogl (1984) and Suski (1985).

2. Magnetic properties

2.1. *RCr_2X_2 compounds*

Data concerning the magnetic properties of the $ThCr_2Si_2$ type compounds with the chromium are scarce.

The magnetic susceptibility of $GdCr_2Si_2$ in the temperature range 4.2–800 K (Buschow and de Mooij 1986) satisfies the Curie–Weiss law with the paramagnetic Curie temperature $\theta_p = +10$ K and the effective magnetic moment $\mu_{eff} = 7.95\ \mu_B$/f.u. The Mössbauer effect measurements performed at 4.2 K by Nowik et al. (1980) gave the hyperfine field $H_{eff} = -244(2)$ kOe.

The temperature dependence of the susceptibility (Nowik et al. 1983) suggests that $DyCr_2Ge_2$ is an antiferromagnet with the Néel temperature $T_N = 16$ K and the hyperfine field 5658(10) kOe at 4.2 K. Strongly time dependent magnetization phenomena are observed in this case.

2.2. *RMn_2Si_2 and RMn_2Ge_2 compounds*

In the past years magnetic properties of RMn_2Si_2 and RMn_2Ge_2 compounds were studied extensively by magnetometric and neutron diffraction methods.

The magnetometric measurements (see fig. 3) indicate that the RMn_2X_2 compounds have two critical magnetic ordering temperatures (Szytuła and Szott 1981):

- at low temperatures the magnetic moments localized on Mn and R atoms are ordered,

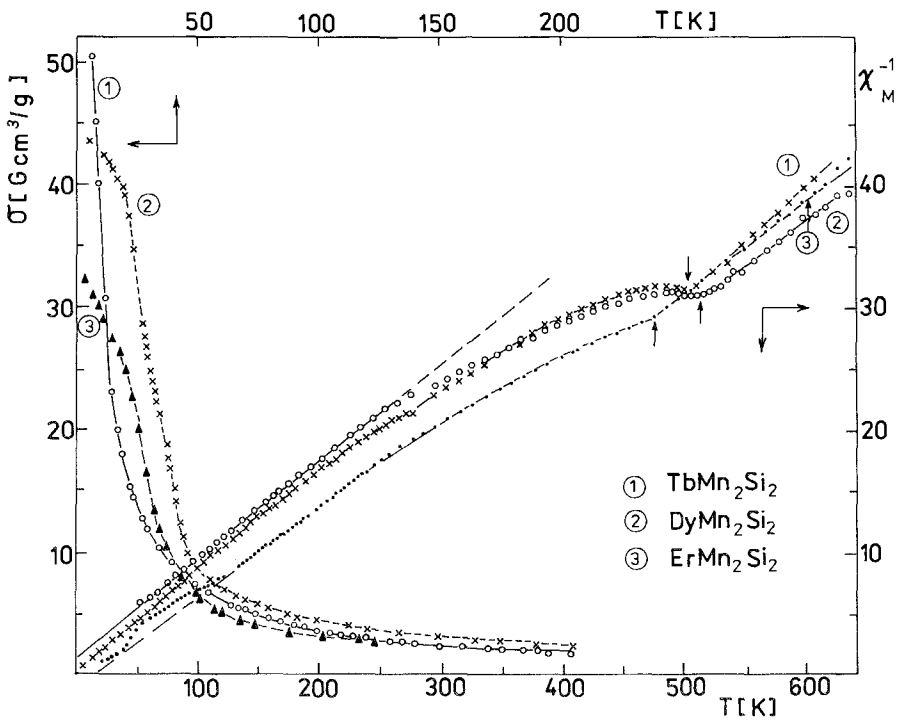

Fig. 3. Temperature dependence of magnetization and reciprocal susceptibility for $TbMn_2Si_2$, $DyMn_2Si_2$ and $ErMn_2Si_2$ (Szytuła and Szott 1981).

– at high temperatures the magnetic moments on Mn atoms show either ferromagnetic or antiferromagnetic ordering.

A ferromagnetic ordering is observed in the case of $LaMn_2Si_2$ (Narasimhan et al. 1975) and in the RMn_2Ge_2 compounds (where R is La, Ce, Pr, Nd, Eu) (Narasimhan et al. 1976).

For $LaMn_2Ge_2$ and $PrMn_2Ge_2$ measurements of magnetization were made on single crystal samples. In both cases the easy axis of magnetization of Mn sublattices is the [001] axis.

For $LaMn_2Ge_2$ the values of the magnetic moment and the anisotropy constant K_1 were estimated to be 1.55 μ_B per Mn atom and 2.25×10^6 erg/cm^3 at 0 K. The magnetic moment descreases with an increasing temperature following the $T^{3/2}$ law while K_1 decreases as $\{M(T)/M(0)\}^{1.6}$ (Shigeoka et al. 1985).

For $PrMn_2Ge_2$ the magnetization and magnetocrystalline anisotropy constant at 0 K were estimated to be 5.9 μ_B/f.u. and 5.3×10^7 erg/cm^3. If we assume that the magnetic moment of Mn atom is 1.55 μ_B, as estimated from the data obtained for $LaMn_2Ge_2$, and that the moment is coupled parallel to Pr moments, we can deduce the Pr moment to be 2.8 μ_B (Iwata et al. 1986a).

Other RMn_2X_2 compounds are antiferromagnets; as determined from neutron diffraction investigations carried out for a number of RMn_2X_2 systems. In $CeMn_2Si_2$, the Mn moments from an antiferromagnetic sublattice are stable between 80 and 379 K (the Néel point) with a magnetic moment of 2.3 μ_B at 80 K (Siek et al. 1978). The magnetic moments lie along the four-fold axis with the sequence + − + − (see fig. 4). No information about the ordering of Ce moments below 80 K is available. The absence of magnetic ordering of Pr and Nd moments at 1.8 K is shown by neutron diffraction studies of $PrMn_2Si_2$ and $NdMn_2Si_2$ (Siek et al. 1981) contrary to the results of magnetometric measurements which gave a ferromagnetic coupling of Nd and Mn sublattices (Narasimhan et al. 1975). In $PrMn_2Si_2$ and $NdMn_2Si_2$ as well as in YMn_2Si_2 and YMn_2Ge_2, the manganese moments order antiferromagnetically in the same way as in $CeMn_2Si_2$.

Interesting results were obtained from magnetometric measurements performed on a single crystal sample of $SmMn_2Ge_2$. In the temperature range between 196 K and the Curie point at 348 K ferromagnetic properties were found. At a temperature lower than 196 K a collinear antiferromagnetic ordering stabilizes. It disappears at 64 K and a reentrant ferromagnetism is observed below this temperature (Fujii et al. 1985). The easy axis of magnetic moments is parallel to the [110] direction below 196 K, while at higher temperature it is parallel to the [100] direction (see fig. 5).

It should be noted that different values of the phase transition temperatures were published for $SmMn_2Ge_2$ (see table 1) (Duraj et al. 1987, Gyorgy et al. 1987).

A susceptibility measurement has been used to determine the various transition temperatures as a function of pressure. The pressure–temperature diagram for $SmMn_2Ge_2$ displayed in fig. 6 shows the paramagnetic, ferromagnetic and antiferromagnetic regions. The temperature T_c separating the paramagnetic and the ferromagnetic regions decreases slightly when the pressure increases. The critical

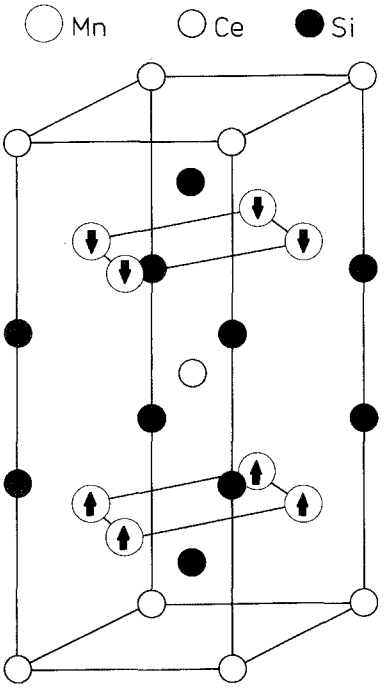

Fig. 4. The chemical and magnetic unit cells of $CeMn_2Si_2$.

temperature between the ferromagnetic and the antiferromagnetic regions increases almost linearly with p until about 330 K and 1.0 GPa when the ferromagnetic phase disappears. The second critical temperature of the ferro–antiferro phase transition decreases rapidly with p.

The X-ray data obtained for $SmMn_2Ge_2$ at the atm pressure show that in the antiferromagnetic region the lattice parameter "a" decreases and shows a discontinuity at the phase transition temperature. The lattice parameter "c" does not change throughout the phase transition region (Gyorgy et al. 1987).

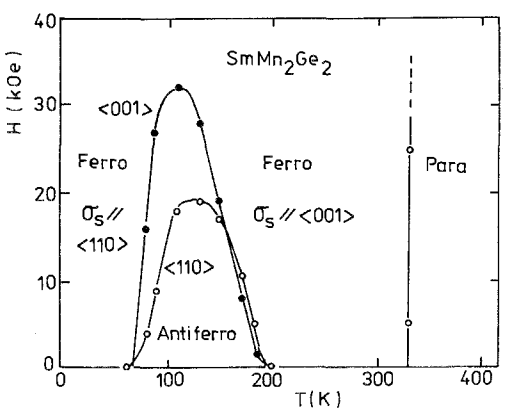

Fig. 5. Magnetic phase diagram of $SmMn_2Ge_2$. The critical fields along the [110] and [100] directions are indicated by open and filled circles, respectively (Fujii et al. 1985).

TABLE 1
Magnetic data of the ternary silicides RMn_2Si_2 and germanides RMn_2Ge_2.

R	RMn_2Si_2								RMn_2Ge_2							
	type of magnetic ordering	$T_{C,N}$ (K)	θ_p (K)	μ_{eff} (μ_B)	μ_s (μ_B)	μ_R (μ_B)	μ_{Mn} (μ_B)	Ref.	type of magnetic ordering	$T_{C,N}$ (K)	θ_p (K)	μ_{eff} (μ_B)	μ_s (μ_B)	μ_R (μ_B)	μ_{Mn} (μ_B)	Ref.
Y	AF	460	385	3.5			2.4	a, b	AF	395	385	3.8			2.95	a, b
	AF	516						c								
La	F	303		4.8	3.08			a	F	306		4.7	3.0			a
	F	310	310	4.5				c	F	306			3.0			d
	F	303			3.08			e	F	310	270	3.5	3.1			f
Ce	AF	379	330	5.1			2.3	a, g	F	316			3.1			d, e
Pr	AF	348	290	5.1			2.48	a, b	F	334			3.9			d, e
									F	329			5.9	2.77	1.55	h
Nd	AF	365	290	5.1			2.57	a, b	F	334			6.0			d, e
	F, AF	32,380			5.14			e								
Sm	AF	398	301	3.3				a	F	350		3.4	3.0			a
									F, AF, F	64,196,348			4.18			i
									F, AF, F	100,150,350						j
									F, AF, F	105,142,346						k

Eu								AF, F	9,330	52						l
Gd	F, AF	65,453	8.4	4.37			a	F, AF	97,365			3.6				a
	F, AF	60,485	8.2				m	F, AF	96,365							d, e
								F, AF	96,365							l
								F, AF	96,365	100	8.8	3.6				n
Tb	AF	501	9.8	5.6			a	F, AF	33,413		9.6	6.0				a
	F, AF	65,550		7.0	9.0	1.7	o	F, AF	95,414	100	10.4	5.3	8.0	1.7		n
								F, AF	110,413				7.8	2.3		p
Dy	F, AF	55,473	11.0	6.5			a	F, AF	47,383		9.9		3.5			a, d, e
								F, AF	40,438	100	10.8	6.2				n
Ho	AF	453	10.5	6.65			a	F, AF	37,403		8.5	5.5				a, d, e
								F, AF	4.2,459	100	10.0					n
Er	F, AF	10,508	10.2	4.22	8.9	2.3	a, r	F, AF	8.5,390		9.0	6.0	7.7	2.3		a, r
								F, AF	4.2,475	224	9.4	8.3				n
Tm	AF	498	3.7				a	AF	458		6.2					a
Yb	AF	513	4.6				a	AF	338		5.8					a
Lu	AF	464	4.2				a	AF	453		3.8					a

References:

(a) Szytuła and Szott (1981), (b) Siek et al. (1981), (c) Sampathkumaran et al. (1983), (d) Narasimhan et al. (1976), (e) Narasimhan et al. (1975), (f) Shigeoka et al. (1985), (g) Siek et al. (1978), (h) Iwata et al. (1986), (i) Fujii et al. (1985), (j) Gyorgy et al. (1987), (k) Duraj et al. (1987), (l) Felner and Nowik (1978), (m) Buschow and de Mooij (1986), (n) Shigeoka (1984), (o) Shigeoka et al. (1986), (p) Leciejewicz and Szytuła (1984), (r) Leciejewicz et al. (1984).

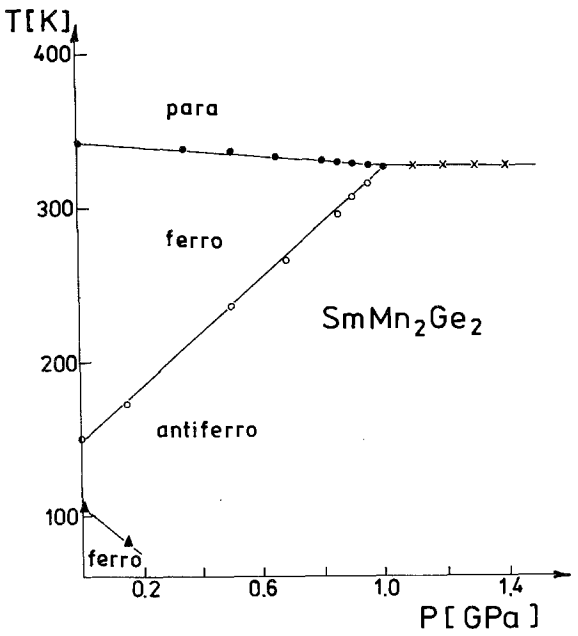

Fig. 6. The pressure–temperature diagram of $SmMn_2Ge_2$ showing the paramagnetic, ferromagnetic, and antiferromagnetic regions (Duraj et al. 1987).

Measurements with a differential scanning calorimeter show that the phase transition near 150 K is endothermic with the transition heat $L = 0.04(1)$ cal/g (Gyorgy et al. 1987).

No data concerning the magnetic properties of $EuMn_2Si_2$ are known.

The magnetometric data indicate that in $EuMn_2Ge_2$ the Mn moments order ferromagnetically at 330 K and change to an antiferromagnetic order when Eu moments order ferromagnetically (9 K) (Felner and Nowik 1978).

Szytuła and Szott (1981), Narasimhan et al. (1976) and Łątka (1987a) investigated the magnetic behaviour of $GdMn_2Si_2$.

Antiferromagnetic ordering occurs at $T_N = 453$ K and an additional magnetic transition is observed at $T_m = 65$ K. The value obtained for the spontaneous magnetic moment $\mu_s = 4.0\ \mu_B$ at low temperatures suggests ferrimagnetic ordering below T_m (Łątka 1987a). Assuming that each Gd atom has its full 7 μ_B magnetic moment coupled antiparallel to the Mn moment and taking into account the resultant 4.0 μ_B per f.u. moment, one obtains the value of 1.5 μ_B per Mn atom. The temperature dependence of the hyperfine magnetic field shows that magnetic ordering in Gd sublattice disappears at 65 K (Łątka 1987a). Above this temperature an antiferromagnetic ordering in Mn sublattice is observed.

The magnetic data (Felner and Nowik 1978, Shigeoka 1984, Iwata et al. 1986) indicate that $GdMn_2Ge_2$ is ferrimagnetic at low temperatures. It changes to an antiferromagnet undergoing a first-order transition at 95 K. Below this temperature the magnetic moment is localized on Gd and Mn sublattices, and above it only on Mn sublattice. The Mn sublattice orders antiferromagnetically at 365 K.

The analysis of the temperature dependence of the magnetization at low

temperatures carried out in terms of the molecular-field approximation shows that Gd–Mn interaction is antiferromagnetic (Iwata et al. 1986).

The Mössbauer studies of $GdMn_2Si_2$ (Łątka 1987a) and $GdMn_2Ge_2$ (Felner and Nowik 1978) with ^{155}Gd indicate that the magnetic moment of Gd^{3+} ions lies in the basal plane of the unit cell.

A different conclusion was drawn from the results of a magnetometric measurement on the single crystal of $GdMn_2Ge_2$. The magnetization curve at 4.2 K (see fig. 7) shows that the easy magnetization axis is along the c-axis direction (Shigeoka 1984).

The field dependence of magnetization of $ErMn_2Si_2$ and $DyMn_2Si_2$ suggested that these compounds are ferrimagnets. The magnetization disappears at 34 K for $ErMn_2Si_2$ and 55 K for $DyMn_2Si_2$, respectively (Szytuła and Szott 1981).

Detailed magnetic studies were performed on some RMn_2Ge_2 single crystal samples (Shigeoka 1984, Shigeoka et al. 1983). The [001] direction (the tetragonal axis) was found to be the easy magnetization axis in (Gd, Tb, Dy, Ho) Mn_2Ge_2 while in $ErMn_2Ge_2$ it was the direction [110] (see fig. 7). The saturation magnetic moments per molecule at 4.2 K are much smaller than the theoretical value expected for a free R^{3+} ion, indicating ferrimagnetic or noncollinear ordering.

The magnetization curves in the easy and hard directions of magnetization shown in fig. 7 suggest that the magnetic anisotropy is large.

A temperature dependence of the magnetization for (Gd, Tb, Dy)Mn_2Ge_2 indicates that the magnetic transition at T_m (see fig. 8) is the ferrimagnetic–antiferromagnetic transition of the first order (Shigeoka 1984).

The temperature dependence of the electrical resistivity and the thermal expansion of RMn_2Ge_2 compounds have been measured to explain the character of magnetic transitions. As an example, fig. 9 shows the resistivity ρ vs T curve for $GdMn_2Ge_2$. As marked by arrows, a sharp jump and a bend appear at the temperatures corresponding to T_m and T_N, respectively. A similar behaviour was found for $TbMn_2Ge_2$ and $DyMn_2Ge_2$ (Shigeoka 1984).

The temperature dependence of the thermal expansion $\Delta l/l$ of the RMn_2Ge_2 polycrystalline samples is shown in fig. 10. Sharp jumps correspond to the first order transition at the T_m's. Bends indicating the second order transitions are seen at the T_N's.

The magnetic structure in $TbMn_2Si_2$ was determined in the course of magnetization and neutron diffraction studies. It was found that the $TbMn_2Si_2$ compound exhibits:

- a collinear ferromagnetic structure at Tb sublattice and a canted structure at Mn sublattice at $T \leqslant 53$ K,
- two magnetic sublattices: ferromagnetic Tb and antiferromagnetic Mn at $53\ \text{K} \leqslant T < 65$ K,
- a collinear Mn antiferromagnetic sublattice at $65\ \text{K} < T \leqslant 550$ K (Shigeoka et al. 1986).

The magnetic moment of both sublattices in ferro- and antiferromagnetic phase is parallel to c-axis.

$TbMn_2Ge_2$ exhibits also an interesting magnetic behaviour (Leciejewicz and

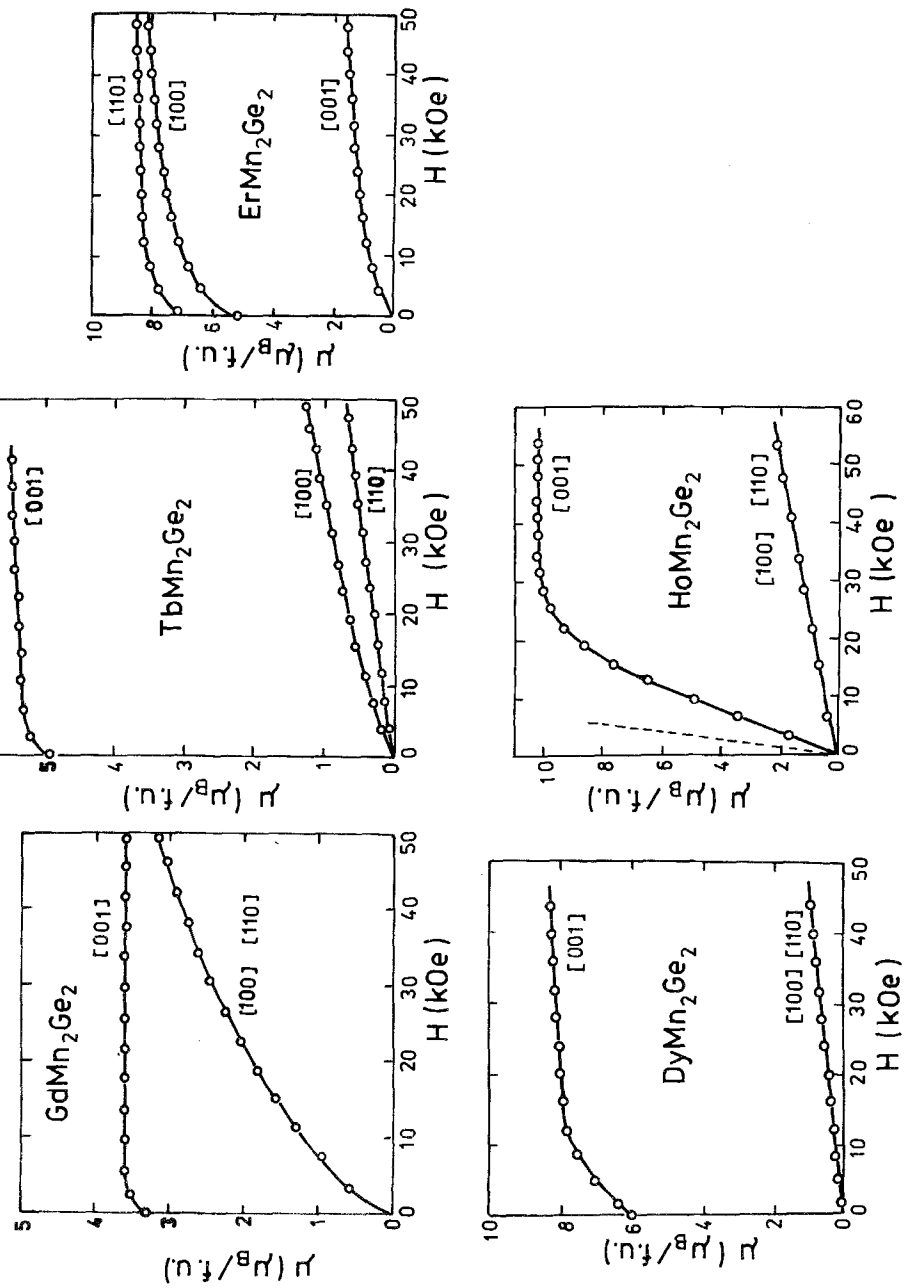

Fig. 7. Magnetization curves along each principal axis of RMn_2Ge_2 (R = Gd, Tb, Dy, Ho, Er) single crystals at 4.2 K (Shigeoka 1984).

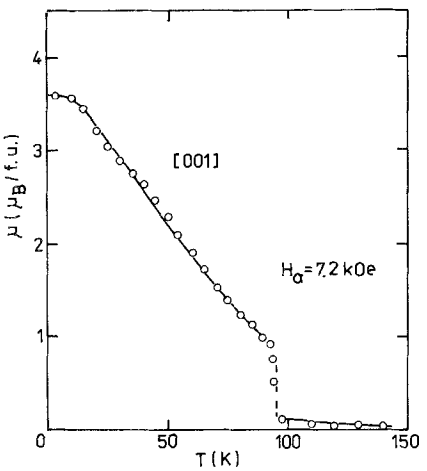

Fig. 8. Temperature dependence of the magnetization along the [001] direction at 7.2 kOe for single crystal $GdMn_2Ge_2$ (Iwata et al. 1986).

Szytuła 1984). The neutron diffraction study of $TbMn_2Ge_2$ gave following results:
- in the temperature range between 4.2 K and $T_N = 413$ K the magnetic moments localized on Mn atoms order antiferromagnetically as in $CeMn_2Si_2$,
- below $T_m = 110$ K a collinear ferromagnetic order of Tb moments along the fourfold axis is observed,
- at $T_t = 26$ K the terbium collinear ferromagnetic sublattice transforms into an antiferromagnetic one. The magnetic moments have two components:
  a) ferromagnetic, which is parallel to the c-axis of the tetragonal unit cell,
  b) antiferromagnetic, parallel to the [120] direction in a monoclinic unit cell. The monoclinic unit cell transforms into tetragonal one by the following transformation:

$$\boldsymbol{a}_m = 2\boldsymbol{a}_t, \qquad \boldsymbol{b}_m = \boldsymbol{a}_t + \boldsymbol{c}_t, \qquad \boldsymbol{c}_m = \boldsymbol{a}_t.$$

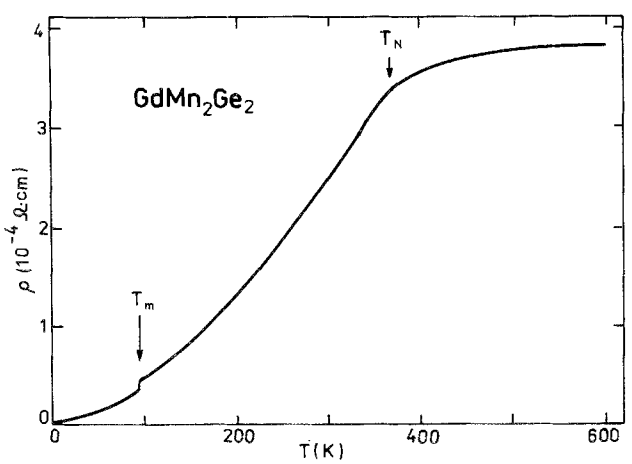

Fig. 9. Temperature dependence of electrical resistivity for $GdMn_2Ge_2$ compound (Shigeoka 1984).

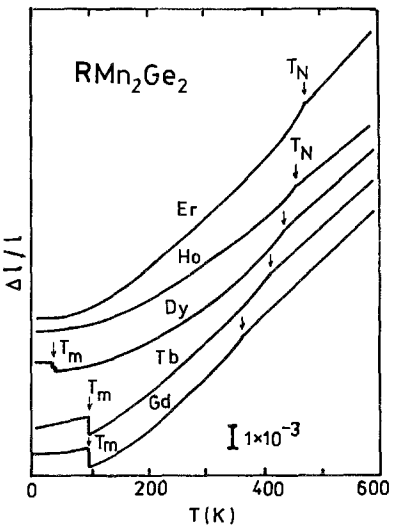

Fig. 10. Temperature dependence of thermal expansion for RMn_2Ge_2 (R = Gd, Tb, Dy, Ho and Er) compounds (Shigeoka 1984).

The magnetic unit cell of $TbMn_2Ge_2$ at 4.2 K is shown in fig. 11.

The neutron diffraction study of $ErMn_2Si_2$ and $ErMn_2Ge_2$ (Leciejewicz et al. 1984) provides the following results:

- the manganese sublattice orders antiferromagnetically like in $CeMn_2Si_2$,
- the Er sublattice is ferromagnetic with moments perpendicular to fourfold axis.

The Curie points are small: 10 ± 5 K for $ErMn_2Si_2$ and 8.5 ± 3 K for $ErMn_2Ge_2$.

Siek and Szytuła (1979) investigated the magnetic properties of the $CeMn_2(Si_xGe_{1-x})_2$. The magnetic phase diagram obtained on the basis of the magnetization and the susceptibility measurements in weak external magnetic fields is presented in fig. 12. Three concentration ranges can be distinguished:

- for $x < 0.45$ the samples are ferromagnetic,
- for $0.45 < x < 0.7$ the samples undergo a transition from ferromagnetic to antiferromagnetic states via a transient state. Two critical temperatures are observed as temperature rises: T_1 from antiferromagnetic to transient state and T_2 from the transient to ferromagnetic state. The third critical temperature is connected with the transition to paramagnetic state,
- the samples with $x > 0.75$ exhibit antiferromagnetic properties.

The following three systems: $La_{1-x}Y_xMn_2Si_2$ (Sampathkumaran et al. 1983), $YMn_2(Si_{1-x}Ge_x)_2$ (Kido et al. 1985) and $Y_{1-x}La_xMn_2Ge_2$ (Fujii et al. 1986) show different magnetic structures depending on the concentration parameter x.

Magnetization studies of $La_{1-x}Y_xMn_2Si_2$ show that a ferromagnetic ordering occurs for $x < 0.2$ and an antiferromagnetic ordering set in for $x > 0.2$. A complex magnetic behaviour is observed for $x = 0.2$.

The temperature dependence of magnetic susceptibilities for the $YMn_2(Si_{1-x}Ge_x)_2$ system indicates that all compounds are antiferromagnetic with $T_N = 475$ K, 456 K, 436 K, and 326 K for $x = 0.2$, 0.4, 0.6, and 0.8, respectively.

The measurements of temperature dependence of magnetization, susceptibility

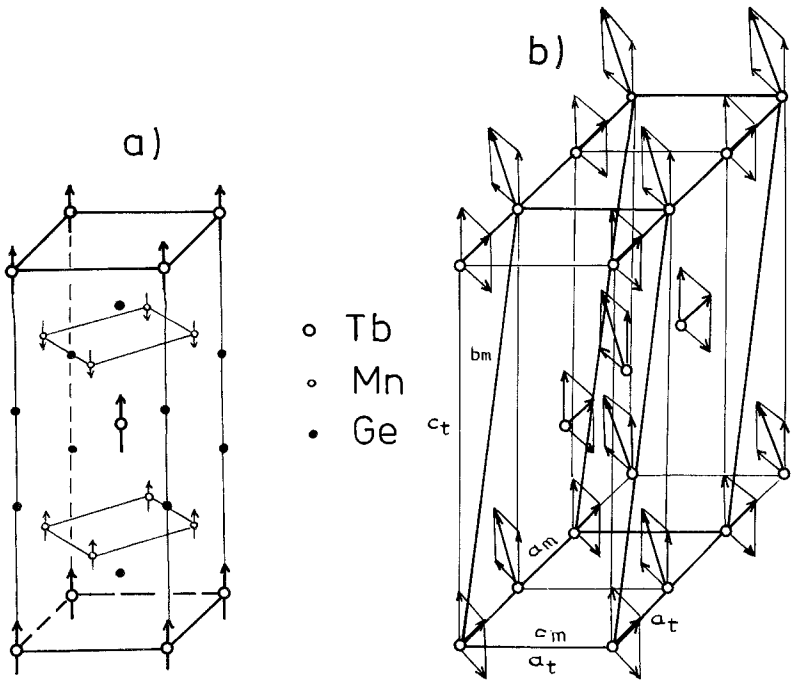

Fig. 11. Magnetic structure of $TbMn_2Ge_2$: (a) tetragonal unit cell with the Tb and Mn sublattices at 85 K, (b) monoclinic unit cell with Tb sublattice at 4.2 K.

and lattice constants for $Y_{1-x}La_xMn_2Ge_2$ system show that in the Y rich region ($x \leqslant 0.2$) the same antiferromagnetic structure exists for YMn_2Ge_2 (Siek et al. 1981). In the La-rich range ($x \geq 0.4$) the ferromagnetic coupling between the ferromagnetic Mn sublayers becomes dominant.

Magnetic properties of the $Ce_{1-x}La_xMn_2Si_2$ system were investigated by the neutron diffraction and the magnetometry (Szytuła and Siek 1982). The samples with low La concentration ($x \leqslant 0.5$) show antiferromagnetic properties. For

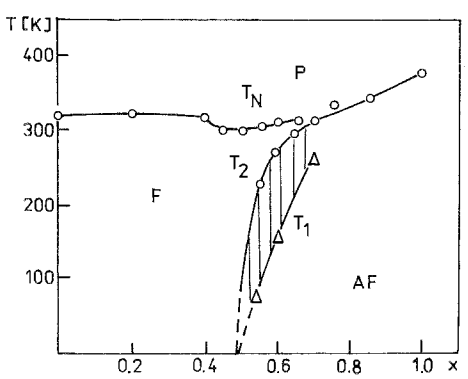

Fig. 12. Magnetic phase diagram of the $CeMn_2(Si_xGe_{1-x})_2$. The transition temperatures T_1, T_2, T_N correspond to the transition from AF to the transient state, from the transient state to F and from F to the paramagnetic state, respectively (Siek and Szytuła 1979).

$x = 0.6$ the magnetic ordering changes from antiferro- to ferromagnetic when increasing temperature is observed. The increase in La content leads to ferromagnetism. A collinear magnetic structure was deduced from neutron diffraction data.

In all pseudoternary systems the nature of the magnetic ordering depends on the Mn–Mn distance.

The magnetic data for RMn_2Si_2 and RMn_2Ge_2 systems are summarized in table 1.

2.3. *RFe_2Si_2 and RFe_2Ge_2 compounds*

Over the last fifteen years almost all compounds of the RFe_2Si_2 and RFe_2Ge_2 groups have been studied by the magnetometric, the Mössbauer effect and the neutron diffraction methods.

First results of magnetometric and the Mössbauer effect experiments suggested, that RFe_2Si_2 and RFe_2Ge_2 compounds were weak ferromagnets below a temperature of about 700 K (Bauminger et al. 1974, Felner et al. 1975). Antiferromagnetic ordering at low temperatures was reported for RFe_2Si_2 compounds (R = Nd, Gd, Tb, Dy, Ho and Er). No long range ordering at 1.2 K was found in Tm and Yb compounds (Umarji et al. 1983, Noakes et al. 1983). $LaFe_2Si_2$ and $CeFe_2Si_2$ show a weak paramagnetic behaviour which was explained by the presence of tetravalent Ce^{4+} and trivalent La^{3+} ions in these structures.

The information about the magnetic properties of RFe_2Ge_2 systems is rather scarce. Felner et al. (1975) reported that $NdFe_2Ge_2$ and $GdFe_2Ge_2$ were antiferromagnetically ordered below the Néel point of 13 K and 11 K, respectively, while other RFe_2Ge_2 compounds (R = La, Ce, Pr, Sm and Dy) were not ordered down to 4.2 K. Malik et al. (1976) investigated the magnetic properties of RFe_2Ge_2 (R = Pr, Gd, Tb and Er). The compounds with Pr, Gd and Tb were reported to be antiferromagnetic with the Néel temperatures of 14 K, 11 K and 7.5 K, respectively. The $ErFe_2Ge_2$ is paramagnetic down to 4.2 K.

$PrFe_2Ge_2$ shows a particularly complicated magnetization curve at 4.2 K (see fig. 13). It contains two ranges of a rapid growth. The first one below 1 kOe provides the evidence for a weak anisotropy field, the second one at about 10 kOe is probably connected with a metamagnetic phase transition. The ferromagnetic order is induced by an applied external magnetic field, but even the field of 50 kOe does not produce the saturation.

Neutron diffraction data give the information about the magnetic structure of the compounds. The magnetic moments in $NdFe_2Si_2$ localized on Nd atoms order antiferromagnetically at 4.2 K. The magnetic structure of $NdFe_2Si_2$ is antiferromagnetic of a collinear $+ - - +$ type, with a magnetic unit cell twice as big as the chemical one in the direction of he c-axis (so called type AFII – see fig. 23) (Pinto and Shaked 1973). $PrFe_2Ge_2$ and $NdFe_2Ge_2$ are collinear antiferromagnets of the same kind as $NdFe_2Si_2$ with the Néel points at 13 ± 1 K and 9 ± 1 K, respectively (Szytuła et al. 1983).

$TbFe_2Si_2$ exhibits a rather complex magnetic structure below the Néel point

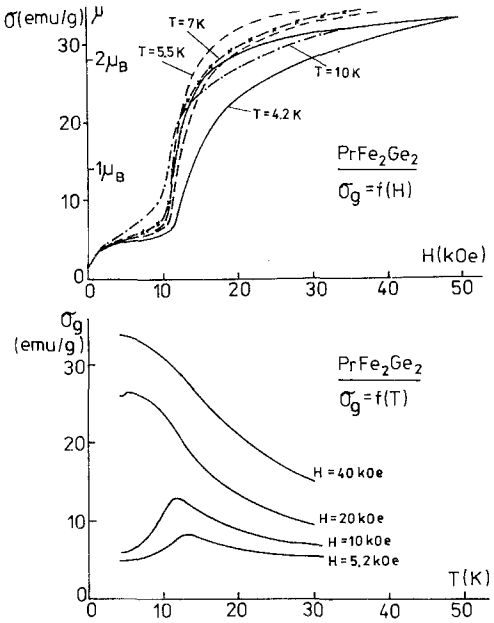

Fig. 13. Magnetization vs applied field for $PrFe_2Ge_2$ compound at different temperatures. Magnetization vs temperature at different applied fields (Leciejewicz et al. 1983a).

$T_N = 10.5$ K (Pinto et al. 1985). It is described as a helicoidal alignment of magnetic moments with a propagation vector $\boldsymbol{k} = (0, 0.3226, 0.1708)$. The magnetic ordering is represented by a static linear transverse spin wave displayed in fig. 23 (LSW IV). The magnetic moment localized on Tb atoms is parallel to c-axis (Bażela et al. 1988).

Neutron diffraction measurements performed on $TbFe_2Ge_2$ gave different results:

- Pinto et al. (1985) confirmed, that $TbFe_2Ge_2$ is antiferromagnetic below $T_N = 7.5$ K with the incommensurate magnetic structure, while Bażela et al. (1988) did not observe the long-range magnetic ordering down to 1.8 K.

$HoFe_2Si_2$ has a magnetic structure similar to $TbFe_2Si_2$ type with a propagation vector $\boldsymbol{k} = (0, 0.328, 0.152)$. The angle between the magnetic moment direction and the c-axis is $15 \pm 5°$ (Leciejewicz and Szytuła 1985a).

For $ErFe_2Si_2$ a collinear antiferromagnetic structure of $+ - - +$ type was found. The magnetic moment of Er atoms is perpendicular to the c-axis (Leciejewicz et al. 1984).

The Mössbauer effect data indicate that in $EuFe_2Si_2$, the Eu-ion is trivalent. There are no data concerning the magnetic properties of this compound (Bauminger et al. 1973).

According to ^{155}Gd Mössbauer data obtained at 4.2 K, the Gd magnetic moment in $GdFe_2Si_2$ and $GdFe_2Ge_2$ is aligned perpendicularly to the c-axis (Bauminger et al. 1974, Łątka et al. 1979, Nowik et al. 1980, Felner and Nowik 1978).

In all the RFe_2X_2 systems studied either by ^{57}Fe Mössbauer spectroscopy or

neutron diffraction, no magnetic moment on iron atom was detected within the accuracy of the particular method. The ^{57}Fe Mössbauer spectra of $GdFe_2Si_2$ at 300 K, 80 K and 4.2 K are shown in fig. 14 (Łątka 1988). The spectra in the paramagnetic state (300 K and 80 K) give the value of the isomer shift (0.19 ± 0.02 mm/s). The absence of a quadrupole splitting is in favour of the low-spin divalent iron with the $3d^6$ configuration in contradiction to that of $3d^{10}$ in similar compounds as suggested by Felner (1975). The ^{57}Fe Mössbauer spectra taken at 4.2 K display the Zeeman hyperfine interaction. The hyperfine magnetic field $H_{eff} = 10$ kOe is transferred from Gd spins. Similar effects are observed in the case of (Nd, Tb, Dy, Ho, Er) Fe_2Si_2 compounds (Umarji et al. 1983, Noakes et al. 1983, Görlich et al. 1982). The available Mössbauer data for RFe_2Si_2 systems allow to draw important conclusions concerning the influence of crystal electric field (CEF) on their magnetic characteristics. They are discussed in detail in Chapter 3.

The magnetic data for the RFe_2Si_2 and RFe_2Ge_2 systems are listed in table 2.

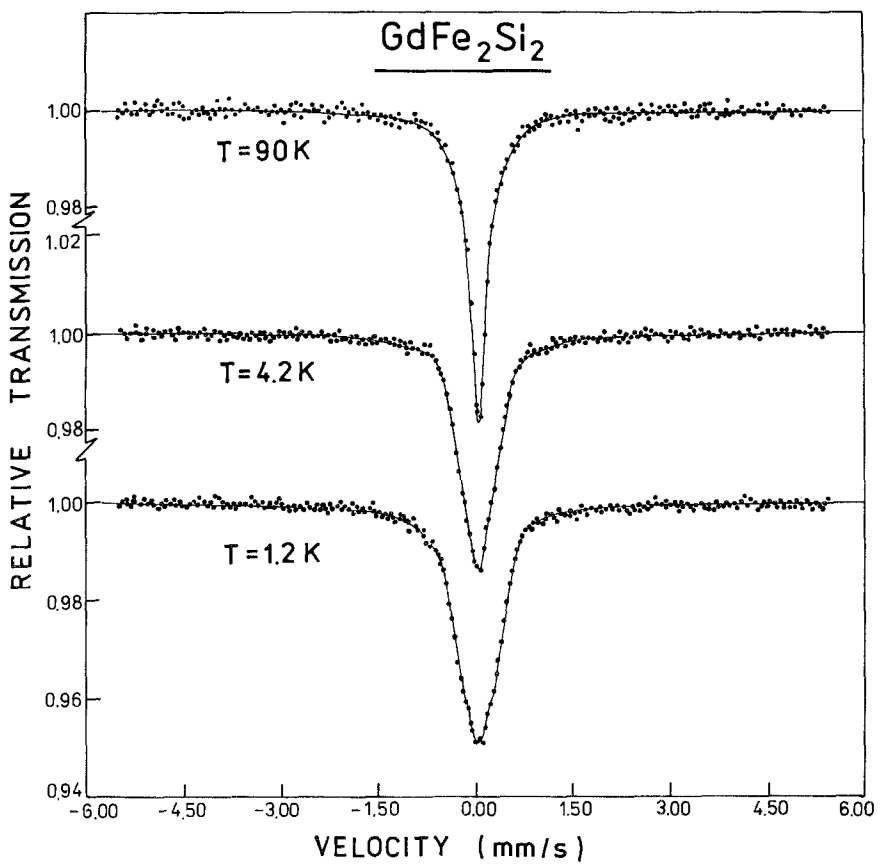

Fig. 14. ^{57}Fe (14.4 keV) Mössbauer absorption spectra of $GdFe_2Si_2$ at 90 K, 4.2 K and 1.2 K (Łątka 1988).

TABLE 2
Magnetic data for RFe_2Si_2 and RFe_2Ge_2 compounds.

R	RFe_2Si_2							RFe_2Ge_2					
	type of magnetic ordering	$T_{C,N}$(K)	θ_p(K)	$\mu_{eff}(\mu_B)$	$\mu_s(\mu_B)$	$(\mu_R(\mu_B)$	Ref.	type of magnetic ordering	$T_{C,N}$(K)	θ_p(K)	$\mu_s(\mu_B)$	$\mu_R(\mu_B)$	Ref.
La	WF	668			0.29		a						
Ce								WF	605		0.77		a
Pr	WF	693			0.23		a	AF	9(1)			3.44(8)	b
								AF	14				c
Nd	AF	15.6				3.1(3)	d	AF	13(1)			3.38(7)	b
	AF	14					e	WF, AF	665,13				a
Gd	WF, AF	738,7			0.32		a	AF	11				f
	AF	8.4					e	AF	11				c
	AF	8.4	+3	8.18			g						
	AF	9.0					h						
Tb	AF	5.8					e	AF	7.5				c
	AF	10.5					i	AF	7.5				i
Dy	WF	753			0.39		a	AF	6				j
	AF	3.8					e						
	AF	3.7					j						
Ho	AF	2.2					e						
	AF	2.3				7.4(5)	k						
Er	AF	2.6					e						
	AF	2.9				7.4(3)	l						

References:
(a) Felner et al. (1975), (b) Szytuła et al. (1983), (c) Malik et al. (1976), (d) Pinto and Shaked (1973), (e) Noakes et al. (1983), (f) Felner and Nowik (1978), (g) Łątka et al. (1979), (h) Nowik et al. (1980), (i) Pinto et al. (1985), (j) Nowik et al. (1983), (k) Leciejewicz and Szytuła (1985a), (l) Leciejewicz et al. (1984).

2.4. *RCo_2Si_2 and RCo_2Ge_2 compounds*

The results of magnetometric measurements for the RCo_2Si_2 and RCo_2Ge_2 systems are collected in table 3. The following features are evident:

1. The RCo_2X_2 compounds with R = La, Ce, Lu and Y are the Pauli paramagnets. Their susceptibilities are independent of the temperature.
2. The reciprocal magnetic susceptibility of the RCo_2X_2 compounds (R = Sm, Er, Tm) obeys the Curie–Weiss law down to 4.2 K. This shows the lack of ordering of magnetic moments above 4.2 K.
3. The temperature dependence of the magnetic susceptibility for the compounds RCo_2Si_2 (R = Pr, Nd, Gd, Tb, Dy and Ho) and RCo_2Ge_2 (R = Pr, Nd, Tb, Dy and Ho) shows characteristic maxima connected with the Néel temperatures. Above the Néel temperatures, the reciprocal magnetic susceptibility obeys the Curie–Weiss law.
4. For the samples $PrCo_2X_2$ and $NdCo_2Ge_2$ below the Néel temperature there is a jump in the magnetic susceptibility at 12 and 10 K, respectively. It suggests the existence of an additional magnetic phase.

For the antiferromagnetic compounds additional measurements of the magnetic field dependence on the magnetization were made up to $H = 50$ kOe at 4.2 K. The results show that:

1. The field dependence of the magnetization of $GdCo_2X_2$ is linear up to 50 kOe.
2. For the remaining compounds the variation of magnetization as a function of the external field has a complex character. In low external fields the magnetization vs magnetic field is linear. In high external fields, deviations from linearity are observed.
3. For all compounds the values of the magnetic moments at $T = 4.2$ K and $H = 50$ kOe are smaller than those expected for the R^{3+} free-ion (gJ) (Kolenda et al. 1982).

Neutron diffraction investigations were performed for the majority of RCo_2Si_2 and RCo_2Ge_2 compounds (Szytuła et al. 1980, Leciejewicz et al. 1982, 1983, 1983a, Leciejewicz and Szytuła 1983, Yakinthos et al. 1983, Nguyen et al. 1983, Schobinger-Papamantellos et al. 1983, Yakinthos et al. 1984, Pinto et al. 1979, 1983, 1985). At low temperatures reflections indexable assuming a magnetic unit cell of the same dimensions as the crystallographic one were observed (see fig. 15). A simple antiferromagnetic structure was deduced. Magnetic moments localized on the lanthanide atoms form ferromagnetic basal planes. The magnetic coupling between adjacent planes is antiferromagnetic. The magnetic structure could be displayed as a piling up the ferromagnetic sheets along the *c*-axis with the sequence + − + − etc. This type of a magnetic structure is usually denoted as AFI type (see fig. 23).

In the case of RCo_2X_2 compounds, where R is Pr, Nd, Tb, Dy and Ho the absence of (001) reflections indicates that the magnetic moments are parallel to the *c*-axis. In the case of R = Er and Tm compounds the presence of magnetic reflections (001) indicates that the magnetic moment on Er or Tm atoms lies in

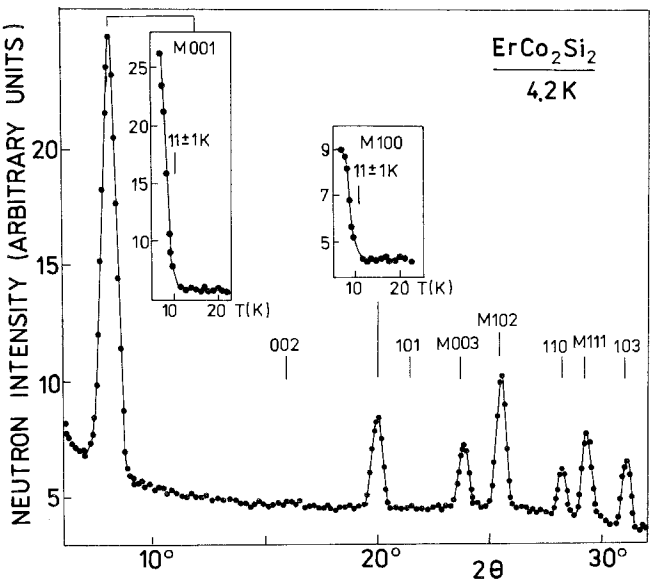

Fig. 15. Neutron diffraction pattern of $ErCo_2Si_2$ at 4.2 K. Peak height vs temperature curves are shown for M001 and M100 magnetic reflections (Leciejewicz et al. 1983).

the basal plane, i.e. it is perpendicular to the tetragonal axis (Leciejewicz et al. 1983, Leciejewicz and Szytuła 1983). Slightly different parameters were obtained from an independent neutron diffraction study by Yakinthos et al. (1983). The resulting magnetic moment of Er is 6.75 μ_B at an angle of 56.2° with the c-axis. The corresponding magnetic space group was derived to be $P_{2_s}\bar{1}(Sh_2^7)$.

A different distribution of magnetic peaks has been observed for $PrCo_2Ge_2$ (Pinto et al. 1979, Szytuła et al. 1980). The coherent magnetic reflections could be successfully interpreted as the satellite pairs associated with each reciprocal lattice point, representing the body-centered nuclear reflections with $h + k + l = 2n$. The propagation vector is $\boldsymbol{k} = (0, 0, k_z)$ with $k_z = 0.73$. From the analysis of magnetic peak intensities, the following model of a spiral magnetic structure was obtained:

- the magnetic moment is localized only on Pr atoms,
- the magnetic structure is sinusoidal modulated along the c-axis (see LSWI in fig. 23).

The ^{155}Gd Mössbauer spectra of $GdCo_2Si_2$ and $GdCo_2Ge_2$ show that the magnetic moments are aligned perpendicularly to c-axis (Łątka et al. 1979, Nowik et al. 1980, Felner and Nowik 1978).

The magnetometric and the Mössbauer effect measurements indicate that $EuCo_2Ge_2$ is an antiferromagnet with the Néel point 23 K and the magnetic moment makes an angle 29° with the c-axis (Felner and Nowik 1978).

TABLE 3
Magnetic data for RCo_2Si_2 and RCo_2Ge_2.

R	RCo_2Si_2							RCo_2Ge_2						
	type of magnetic ordering	T_N(K)	θ_p(K)	$\mu_{eff}(\mu_B)$	$\mu_R(\mu_B)$	H_c(T)	Ref.	type of magnetic ordering	T_N(K)	θ_p(K)	$\mu_{eff}(\mu_B)$	$\mu_R(\mu_B)$	H_c(T)	Ref.
Y	Pauli paramagnetic						a	Pauli paramagnetic						a, b
La								Pauli paramagnetic						b
Ce	Pauli paramagnetic						c			−151.9	2.74			b
Pr	AF	30	−40	3.7		2.4	d	AF	13,28	−8.7	2.87			b
	AF	49			3.19		e	AF	28	−9	2.9	3.98	1.5	f
	AF	31			3.19		g							
Nd	AF	26			3.39		e	AF	26,5, 30	−5.5	4.1	3.24		h
								AF	28	−32.5	3.34			b
Sm										−43.8	1.12			b
Eu								AF	23	−19				i
Gd	AF	43	−40	8.3			d	AF	40	−40				i
	AF	44	−55	9.9			a	AF	40	−39.5	6.96			b
	AF	45	−29	8.19			k							
Tb	AF	45	−73	10.2	8.9	0.78	l	AF	32	−22	10.3	8.3	2.0	l
	AF	8	−16	9.4			a	AF	30	−43.9	9.27			b
	AF	46			9.12		g							
	AF	30			8.8		m							

	AF	46			9.2		n						
Dy	AF	19.5	−27	10.5		2.1	c	AF	14.5	−4.7	10.17		b
	AF	21			9.4		p	AF	16			9.5	n
	AF	21	−35	10.2			a	AF	17				o
	AF	25					o						
	AF	21			9.5		r						
Ho	AF	11.2	−10	10.5		1.0	d	AF	8	6	10.38		b
	AF	15	−8	10.7			a	AF	8	−10	10.0		d
	AF	10			10.4		e	AF	8	−10	10.0	8.64	f
	AF	12			9.85		u	AF	8.5			8.12–8.28	j
	AF	13			8.1		m						
Er	AF	6	−9	10.4			a			8.7	7.6		b
	AF	11			8.7		e	AF	4.2	−8	8.7	7.32	h
	AF	6			6.75		s	AF	4.2			7.3	n
Tm	AF	−8	−8	6.9			d			−0.8	5.89		b
	AF	3			6.2		p						
Lu								Pauli paramagnetic					b
Yb	Pauli paramagnetic						t	Pauli paramagnetic					b, t

References:

(a) Yakinthos et al. (1980), (b) McCall et al. (1973), (c) Palstra et al. (1986), (d) Kolenda et al. (1982), (e) Leciejewicz et al. (1983), (f) Szytuła et al. (1980), (g) Yakinthos et al. (1984), (h) Leciejewicz et al. (1983a), (i) Felner and Nowik (1978), (j) Pinto et al. (1982), (k) Łątka et al. (1979), (l) Leciejewicz et al. (1982), (m) Nguyen et al. (1983), (n) Pinto et al. (1985), (p) Leciejewicz and Szytuła (1983), (o) Nowik et al. (1983), (r) Pinto et al. (1983), (s) Yakinthos et al. (1983), (t) Kolenda and Szytuła (1987), (u) Schobinger-Papamantellos et al. (1983).

2.5. *RNi_2Si_2 and RNi_2Ge_2 compounds*

$CeNi_2Si_2$ was prepared as a single crystal (Menovsky et al. 1988). It was found to be a temperature-independent Pauli paramagnet down to 1.4 K with a linear magnetization up to 50 kOe (Palstra 1986a).

Magnetic properties of $PrNi_2Si_2$ were reported by Barandiaran et al. (1986). Below $T_N = 18$ K a collinear modulated antiferromagnetic structure with $\boldsymbol{k} = (0, 0, 0.87)$ is observed. Ni is nonmagnetic, Pr moments lie along the c-axis with a maximum value of 2.6(1) μ_B at 5.5 K. Magnetic measurements performed on a single crystal reveal a large uniaxial magnetocrystalline anisotropy. From the anisotropy of the paramagnetic susceptibility, the second-order crystal field parameter $V_2^0 = +190$ K was deduced. The stability of the modulated structure at low temperature could be associated with a crystal field splitting of the Pr^{3+} multiplet which gives rise to a nonmagnetic singlet ground state.

Magnetic measurements of RNi_2Si_2 (R = Gd, Tb, Dy, Ho, Er, Tm) compounds were performed in the temperature range 4.2–200 K and in magnetic fields up to 20 kOe (Yakinthos and Ikonomou 1980). It was found that $GdNi_2Si_2$, $TbNi_2Si_2$ and $DyNi_2Si_2$ order antiferromagnetically below $T_N = 15.5$ K, 14 K and 7 K, respectively. The compounds with R = Ho, Er and Tm were found to be paramagnetic at 4.2 K. A dependence of the reciprocal susceptibility versus temperature in the case of $ErNi_2Si_2$ attains curvilinear shape for the temperatures above 200 K, while for $HoNi_2Si_2$ and $TmNi_2Si_2$ it follows the Curie–Weiss law.

Neutron diffraction data available for $TbNi_2Si_2$ indicate that it is an antiferromagnet below the ordering temperature $T_N = 10 \pm 1$ K with a magnetic unit cell doubled in the direction of the a-axis {see AFIII in fig. 23 (Nguyen et al. 1983)}. Magnetic moments are localized on Tb atoms only and they are aligned along the tetragonal axis. Ni atoms have no magnetic moment. In contrast to the RCo_2Si_2 series, antiferromagnetic interactions are dominant in the [001] plane. On the neutron diffraction pattern of $DyNi_2Si_2$ only a broad magnetic maximum is observed at 1.4 K indicating the presence of a short-range magnetic order at this temperature, while $HoNi_2Si_2$ exhibits a long-range magnetic ordering at 1.4 K, associated with two wave vectors $\boldsymbol{k} = (0, 0, 1)$ and $\boldsymbol{k} = (0.517, 0, 0)$ resulting in a magnetic structure of rather complex character (Nguyen et al. 1983).

Pinto et al. (1985) investigated $HoNi_2Si_2$, $TbNi_2Ge_2$ and $HoNi_2Ge_2$ compounds by neutron diffraction. The low temperature patterns (at 4.2 K and 2.1 K) show the existence of incommensurate structures. The magnetic reflections yield two transition temperatures in each compound: 4.2 and 3.1 K in $HoNi_2Si_2$ and 16 and 9 K in $TbNi_2Ge_2$. In $HoNi_2Ge_2$ the incommensurate magnetic structure at 2.1 K is consistent with a spiral with a propagation vector $\boldsymbol{k} = (0, 0, 0.76)$ and a turning axis along this propagation vector. The magnetic moment is 8 μ_B and it is perpendicular to the c-axis.

$EuNi_2Ge_2$ is an antiferromagnet below $T_N = 30$ K with the magnetic moment at an angle 44° to the c-axis (Felner and Nowik 1978).

The ^{61}Ni Mössbauer spectra in $GdNi_2Si_2$ show no hyperfine splitting down to 1.2 K, which confirms that the 3d moment is zero (Łątka et al. 1979). The ^{155}Gd

TABLE 4
Magnetic data for RNi_2Si_2 and RNi_2Ge_2.

R	RNi_2Si_2						RNi_2Ge_2					
	type of magnetic ordering	T_N(K)	θ_p(K)	$\mu_{eff}(\mu_B)$	$\mu_R(\mu_B)$	Ref.	type of magnetic ordering	T_N(K)	θ_p(K)	$\mu_{eff}(\mu_B)$	$\mu_R(\mu_B)$	Ref.
La												
Ce	Pauli paramagnetic					a						
Pr	AF	18		3.67	2.6	b						
Nd			−85	2.75		c	AF	16	−10	3.69		c
Gd	AF	15.5	−6	8.0		d	AF	22	−19	8.6		e
		15	−1	7.97		f						
		11.6				g						
		14	0	7.9		h						
Eu							AF	30	−8	7.7		e
Tb	AF	14	9	10.2		d	AF	16, 9				i
	AF	10			8.1	j						
Dy	AF	7	−4	10.7		d	AF	11				k
	AF	7				k						
Ho			1.4	9.4		d	AF	6			8.0	i
	AF	4.2, 3.1				i						
Er			8	7.6		d						

References:
(a) Palstra (1986a), (b) Barandiaran et al. (1986), (c) Zygmunt and Szytuła (1988), (d) Yakinthos and Ikonomou (1980), (e) Felner and Nowik (1978), (f) Łątka et al. (1979), (g) Nowik et al. (1980), (h) Buschow and De Mooij (1986), (i) Pinto et al. (1985), (j) Nguyen et al. (1983), (k) Nowik et al. (1983).

Mössbauer spectra of $GdNi_2Si_2$ and $GdNi_2Ge_2$ show that the angle between the Gd moments and c-axis is approximately 70° for $GdNi_2Si_2$ (Nowik et al. 1980) and 75° for $GdNi_2Ge_2$ (Felner and Nowik 1978), respectively.

The magnetic data for the RNi_2Si_2 and RNi_2Ge_2 systems are listed in table 4.

2.6. *RCu_2Si_2 and RCu_2Ge_2 compounds*

In the last few years the RCu_2Si_2 and RCu_2Ge_2 systems were studied thoroughly.

Routsi and Yakinthos (1981) investigated the magnetic behaviour of $LaCu_2Si_2$ in the temperature range from 4.2 K to 150 K and at the magnetic fields up to 18 kOe. No details about the susceptibility values were given except that they were small.

The susceptibility of $CeCu_2Si_2$ follows the Curie–Weiss law above 50 K with the Curie–Weiss temperature $\theta_p = -164$ K and the effective moment of $\mu_{eff} = 2.62\ \mu_B$ (Sales and Viswanathan 1976). Assmus et al. (1984) and Batlogg et al. (1984) measured an anisotropy in the susceptibility of $CeCu_2Si_2$ and found it to be quite large at $T \cong 0$ K varying by a factor 2 in the different crystal directions.

The temperature dependence of the specific heat indicates that $CeCu_2Si_2$ is a superconductor below 0.5 K. The electronic specific heat constant $\gamma = 1100\ \text{mJ/mol K}^2$ suggests that $CeCu_2Si_2$ is a heavy-fermion system with an effective mass $\sim 100 m_0$ (Stewart 1984).

The band structure of $CeCu_2Si_2$ and of the isostructural $LaCu_2Si_2$ was calculated using the self-consistent semirelativistic, linear Muffin-tin orbital method (LMTO) (Andersen 1975, Jarlborg and Arbman 1977). The Ce-4f levels are situated mainly above the Fermi energy E_F. The density-of-states at E_F is large and heavily concentrated around the Ce-4f band (Jarlborg et al. 1983).

Aliev et al. (1984) drew a magnetic phase diagram on the basis of the magnetic susceptibility measurements of $Ce_xLa_{1-x}Cu_2Si_2$ system (fig. 16). The theoretical analysis of the diagram is reported in the paper of Brandt and Moshchalkow (1984). The interplay between the two competing processes, the indirect exchange interaction of Ce^{3+} ions via the RKKY oscillations and the effective suppression of the Ce^{3+} magnetic moments due to the Kondo spin fluctuations

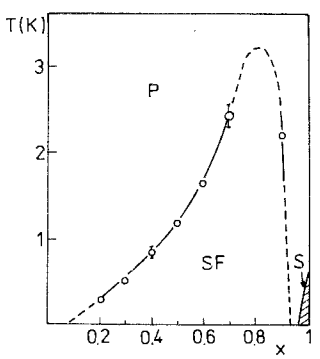

Fig. 16. The T versus x phase diagram of magnetic properties of $Ce_xLa_{1-x}Cu_2Si_2$ alloys: P is the paramagnetic phase, S the superconducting phase and SF the spin frozen state (Aliev et al. 1984).

explains the variation of the magnetic properties with the Kondo coupling constant J_K.

Magnetic, calorimetric and transport measurements characterize $CeCu_2Ge_2$ as a Kondo-lattice system which orders antiferromagnetically below $T_N = 4.15(5)$ K. (de Boer et al. 1987).

The crystal structure and the magnetic properties of $CeCu_2Si_{2-x}Ge_x$ ($0 \leq x \leq 2$) system were reported in the paper of Rambabu and Malik (1987). The evolution of a heavy-fermion system into a normal one was investigated in these compounds. The inverse susceptibility for $CeCu_2Si_{2-x}Ge_x$ compounds shows a linear dependence on T at high temperatures, while at low temperatures there are some deviations from linearity. The effective magnetic moment, deduced from the fit of the susceptibility data between 150 K and 300 K, shows a small decrease (~4%) from a value of $\mu_{eff} = 2.58\ \mu_B$ in $CeCu_2Si_2$. The large negative θ_p value for $CeCu_2Si_2$ ($\theta_p = -78$ K) gradually rises to -3.4 K for $CeCu_2Ge_2$.

The temperature dependence of the magnetic susceptibility, the resistivity and the magnetostriction for the RCu_2Si_2 compounds (R = Pr, Nd, Sm, Gd, Tb, Dy, Ho, Er and Tm) indicate that all compounds (except $NdCu_2Si_2$) order antiferromagnetically at low temperatures (Schlabitz et al. 1982). The (Ce, Eu, Yb)Cu_2Si_2 have unstable 4f shells (intermediate valence) (Sales and Viswanathan 1976). The temperature dependence of the magnetic susceptibility gives no evidence of the magnetic order in $EuCu_2Si_2$. The observed value of the susceptibility in $EuCu_2Si_2$ is intermediate between the values of Eu^{2+} and Eu^{3+}. At high temperature the susceptibility of $YbCu_2Si_2$ follows the Curie–Weiss law with the Curie–Weiss temperature $\theta_p = -90$ K and an effective moment $\mu_{eff} = 4.19\ \mu_B$, which is smaller than the theoretical value of $\mu_{eff} = 4.5\ \mu_B$ resulting from the Hund rule. There is no evidence of a magnetic order at low temperatures. The low temperature magnetization curves are linear. The susceptibility of single crystal was found to be highly anisotropic. At room temperature the susceptibility for $H \| a$ was $\chi_a = 4.6 \times 10^{-3}$ emu/mol while for $H \| c$ it was $\chi_c = 6.48 \times 10^{-3}$ emu/mol. For both orientations the susceptibility follows the Curie–Weiss law at high temperatures with $\mu_{eff} = 4.19\ \mu_B$. The Curie–Weiss temperatures are -160 K for $H \| a$ and -42 K for $H \| c$. Below 75 K the susceptibility curve flattens in both directions.

The saturated magnetostriction (Rüßmann et al. 1982) and $\Delta(c/a)$ anomalies (Schlabitz et al. 1982) imply that the axis of the magnetic moment is perpendicular to the c-axis in Pr, Nd, Tb, Dy and Ho, while for Sm, Er and Tm it is parallel to it.

The electrical resistivity measurements between 1.3 K and 300 K for RCu_2Si_2 (R = Gd–Lu) (Cattaneo and Wohlleben 1981) indicate that the disorder resistivities and the Néel temperatures deviate strongly from the de Gennes factor.

The temperature dependence of the specific heat of $TmCu_2Si_2$ gives the magnetic ordering temperature of about 2.8 K and shows that the Schottky anomaly corresponds to two lowest singlet levels. The separation of these two levels is about 7 K, while the distance to the higher excited levels is approximately 10 times larger (Kozłowski 1986).

The magnetic susceptibility and specific heat measurements performed in the temperature range 1–100 K for $Tm_{1-x}Lu_xCu_2Si_2$ ($x = 0$, 0.025, 0.05, 0.1, 0.25, 0.5 and 1.0) systems indicate that the Néel temperature decreases from $T_N = 2.80(5)$ K for $x = 0$ to $T_N = 2.30(5)$ K for $x = 0.1$. Other samples are paramagnets down to 1 K. The crystal level scheme was also determined (Kozłowski et al. 1987).

No indication of any long range magnetic order was found in $CeCu_2Si_2$ by neutron diffraction even at the mK range, only transitions between the Kramers ground state and two excited crystal field doublets of Ce^{4+} ion were determined by an inelastic scattering of high energy neutrons. Consequently the crystal field level scheme was determined (Horn et al. 1981).

$NdCu_2Si_2$ was found to remain paramagnetic below 4.2 K, while $PrCu_2Si_2$ order antiferromagnetically below 19 K (Schlabitz et al. 1982). Its magnetic structure was determined to be of AFI type with magnetic moments localized on Pr^{3+} ion lying along the tetragonal axis. $PrCu_2Ge_2$ shows the same magnetic ordering (Szytuła et al. 1983).

$DyCu_2Si_2$ (Pinto et al. 1983), $TbCu_2Si_2$ and $HoCu_2Si_2$ (Pinto et al. 1985, Leciejewicz et al. 1986) were also studied by neutron diffraction and their magnetic structures were determined at low temperatures. The magnetic ordering may be described as ferromagnetic [101] planes of R^{3+} ions coupled antiferromagnetically with the sequence $+ - + -$. Such structure requires the doubling of unit cell dimensions along the a and c axes which results in an orthorhombic unit cell. The magnetic moments are perpendicular to c-axis, but make different angles with the a-axis: 23.4(1.3)° in $TbCu_2Si_2$, 11.1(1.1)° in $DyCu_2Si_2$ and 7.5(3.1)° in $HoCu_2Si_2$. This type of magnetic ordering is denoted as AFIII type. It is displayed in fig. 23.

The ^{155}Gd Mössbauer and magnetometric data indicate that magnetic moments of Gd^{3+} ions in $GdCu_2Si_2$ and $GdCu_2Ge_2$ order antiferromagnetically at low temperatures. The easy axis of magnetization is in the basal plane (Felner and Nowik 1978, Łątka et al. 1979, Nowik et al. 1980).

$TmCu_2Si_2$ was studied by the Mössbauer spectroscopy (Stewart and Żukrowski 1982). The CEF level scheme of the Tm^{3+} ion was determined. The Mössbauer data suggest that in the ordered state below 2.8 K it is a magnetically ordered 2-singlet system.

Oesterreicher (1977) and Kotsanidis and Yakinthos (1981) reported a large amount of data concerning the magnetic properties of RCu_2Ge_2 compounds. The temperature dependence of the reciprocal magnetic susceptibility of RCu_2Ge_2 follows the Curie–Weiss law with negtive paramagnetic Curie temperatures. The compounds with R = Pr, Nd, Gd, Tb, Dy, Ho, Er and Tm are anitferromagnetic. Newly published neutron diffraction data (Kotsanidis et al. 1984, Schobinger-Papamantellos et al. 1984, Yakinthos 1985) gave the information about the magnetic ordering in $TbCu_2Ge_2$, $DyCu_2Ge_2$, $HoCu_2Ge_2$ and $ErCu_2Ge_2$. They are antiferromagnetics at 4.2 K except $ErCu_2Ge_2$ which shows antiferromagnetic ordering at 1.9 K. The magnetic unit cell is four times larger than the chemical one with the wave vector $\boldsymbol{k} = (\frac{1}{2}, 0, \frac{1}{2})$. The magnetic moments of R^{3+} ions

belonging to the same (101) plane of the magnetic unit cell are coupled ferromagnetically while those belonging to the adjacent (101) planes are coupled antiferromagnetically. The moment directions and its values at low temperatures are as follows:

in $TbCu_2Ge_2$: $\mu = 8.46(6)\ \mu_B$. It is aligned along the [111] direction of the tetragonal crystallographic unit cell and it is perpendicular to the tetragonal axis,

in $DyCu_2Ge_2$: $\mu = 8\ \mu_B$. It makes an angle of 30° with the *a*-axis and 70° with the *c*-axis of the tetragonal unit cell,

in $HoCu_2Ge_2$: $\mu = 6.5(1)\ \mu_B$. It makes an angle of 80° with the *a*-axis and 81.4° with the *c*-axis,

in $ErCu_2Ge_2$: $\mu = 8.0(4)\ \mu_B$. It is aligned along the tetragonal axis.

$EuCu_2Ge_2$ was studied by the Mössbauer spectroscopy and the magnetic susceptibility. It is antiferromagnetic with the Néel temperature of 13 K and the magnetic moment which makes an angle 52° with the *c*-axis (Felner and Nowik 1978).

The magnetic data determined for the RCu_2Si_2 and RCu_2Ge_2 systems are gathered in table 5.

2.7. *RRu_2Si_2 and RRu_2Ge_2 compounds*

Ternary RRu_2Si_2 silicides and RRu_2Ge_2 germanides of $ThCr_2Si_2$ type with all rare-earth elements except Pm were intensively investigated during the 1983–1987 period.

Magnetometric measurements were carried out in the temperature range from 1.5 K to 1100 K by several groups (Hiebl et al. 1983, Felner and Nowik 1984, Ślaski and Szytuła 1982, Felner and Nowik 1985). It was found that (Y, La, Lu)Ru_2Si_2 compounds are Pauli paramagnets. In the case of $CeRu_2Si_2$ the temperature dependence of the magnetic susceptibility above 20 K can be described by the Van Vleck paramagnetism of widely spaced multiplets. The derived effective paramagnetic moment $\mu_{eff} = 2.12\ \mu_B$ shows that about 85% of cerium ions are in the Ce^{3+} state. At low temperatures $CeRu_2Si_2$ is a non-magnetic heavy fermion ($\gamma = 355\ J/mol\ K^2$) (Thompson et al. 1985). This system does not exhibit superconductivity down to 40 mK (Gupta et al. 1983). The magnetization measured at low temperature and at high magnetic fields shows a saturation effect (Besnus et al. 1985). $CeRu_2Ge_2$ is a ferromagnet with the Curie temperature 11 K (Umarji et al. 1986).

Recent magnetic susceptibility studies of the pseudoternary $CeRu_2Si_{2-x}Ge_x$ series show that as x increases the system progresses from a heavy electron paramagnet ($x = 0$) to an antiferromagnet, and eventually, at $x = 2$, it becomes ferromagnetic. The unit cell volume of these compounds also increases with the increase in x. In $CeRu_2Si_{2-x}Ge_x$ compounds magnetic ordering is observed for samples with $x = 0.5$, 1.0 and 1.5. Their Néel or Curie temperatures are $T_N = 8$ K, 9.2 K and $T_c = 10$ K, respectively (Umarji et al. 1986, Godart et al. 1987).

The magnetic properties of $Ce_{1-x}R_xRu_2Si_2$ compounds (where R is La or Y)

TABLE 5
Magnetic data of the ternary silicides RCu_2Si_2 and germanides RCu_2Ge_2.

R	RCu_2Si_2						RCu_2Ge_2					
	type of magnetic ordering	T_N(K)	θ_p(K)	$\mu_{eff}(\mu_B)$	$\mu_R(\mu_B)$	Ref.	type of magnetic ordering	T_N(K)	θ_p(K)	$\mu_{eff}(\mu_B)$	$\mu_R(\mu_B)$	Ref.
Y	Pauli paramagnetic					a						
La	Pauli paramagnetic					a						
Ce			−164	2.62		b	AF	4.2				c
			−140	2.68		d						
Pr	AF	20.8		2.61		e	AF	16				f
	AF	15	−2	3.41		g	AF	16			2.53	h
	AF	19			2.51	h						
Nd				2.39		e						
			−7	3.7		a						
Sm	AF	9		1.12		e						
Eu	Van Vleck susceptibility					b	AF	13	−20	8.0		i
Gd	AF	14.2		7.93		e	AF	11				f
	AF	12.5	−21	8.03		j	AF	12	−30	7.8		k
	AF	10	−10	7.28		g	AF	14	−24	8.0		i
	AF	12	−20	7.75		b	AF	11				c
	AF	13.5				m	AF	14	−24	8.0		l
	AF	10	−14	7.95		n						
Tb	AF	12.5		9.28		e	AF	15	−21.5	9.7		k

	AF	12	−12	9.35		g	AF	13			8.48	o
	AF	11		8.5	8.5	p	AF	13			8.6	r
	AF	13		8.6	8.6	r						
Dy	AF	11.8		10.58		e	AF	8	−15	10.6		k
	AF	10	−4	10.5		a	AF	8	−15		8.0	q
	AF	11			8.3	s	AF	10				t
	AF	11				t						
	AF	11				u						
	AF	10.9				m						
Ho	AF	7.7		10.42		e	AF	6.4	−6	10.6		k
	AF	8	−3	10.3		a	AF	6			6.5	o
	AF	10			8.2	p	AF	6.5				r
	AF	8			6.5	r						
	AF	6.8				m						
Er	AF	1.6		9.49		e			−4.5	10.7		k
			−3	9.4		a	AF	1.9			8.0	v
	AF	4.8				m						
Tm	AF	7.0, 3.0		7.14		e		−2	−2	7.5		k
		6.9				m						
			−2	7.4		a						
Yb			−90	4.19		b						

References:

(a) Kotsanidis and Yakinthos (1981), (b) Sales and Viswanathan (1976), (c) Gottwick et al. (1987), (d) Lieke et al. (1982), (e) Schlabitz et al. (1982), (f) Oesterreicher (1977), (g) Oesterreicher (1976), (h) Szytuła et al. (1983), (i) Felner and Nowik (1978), (j) Łątka et al. (1987), (k) Kotsanidis and Yakinthos (1981a), (l) De Vries et al. (1985), (m) Cattaneo and Wohlleben (1981), (n) Buschow and de Mooij (1986), (p) Leciejewicz et al. (1986), (r) Schobinger-Papamantellos et al. (1984), (q) Kotsanidis et al. (1984), (s) Pinto et al. (1979), (t) Nowik et al. (1983), (u) Görlich et al. (1982), (v) Yakinthos (1985).

were investigated by Besnus et al. (1987). When Ce ions are replaced by Y or La ions an internal pressure changes because atomic radii are different: $R(\mathrm{Ce}) = 1.8247$ Å, $R(\mathrm{La}) = 1.8791$ Å, $R(\mathrm{Y}) = 1.8012$ Å, respectively. The substitution of Ce atoms by La atoms causes a negative lattice pressure, while Y's in the place of Ce atoms produce a positive lattice pressure. Figure 17 shows the results of the investigations of $Ce_{1-x}R_xRu_2Si_2$ systems.

The $Ce_xLa_{1-x}Ru_2Si_2$ compounds where $0.1 \leq x \leq 0.85$ are antiferromagnetics with the Néel temperatures changing from 0.9 K for $x = 0.1$ to 6.3 K for $x = 0.85$.

The $Ce_xY_{1-x}Ru_2Si_2$ system does not show any magnetic ordering.

$PrRu_2Si_2$ (Hiebl et al. 1983) and $PrRu_2Ge_2$ (Felner and Nowik 1985) are ferromagnets with the Curie temperature of 17.8 K and 18 K, respectively. The magnetic moment of Pr atoms is parallel to c-axis (Ślaski et al. 1984).

$NdRu_2Si_2$ and $NdRu_2Ge_2$ exhibit two magnetic transitions at 10 K and 26 K for $NdRu_2Si_2$ (Felner and Nowik 1984) and 7 K and 21 K for $NdRu_2Ge_2$ (Felner and Nowik 1985). Neutron diffraction data indicate that $NdRu_2Si_2$ exhibits a complicated magnetic structure: below $T_N = 26$ K it developes a sine-wave modulation $\boldsymbol{k} = (0.13, 0.13, 0)$ of the magnetic moments, with an amplitude 3.23 μ_B/Nd atom, then a squaring of the magnetic structure occurs at about 15 K. At $T < 10$ K a ferromagnetic order takes place with the moments always along the c-axis. The square-modulated phase decreases but persists until $T = 2.8$ K where both phases coexist (Chevalier et al. 1985).

Heat capacity, electrical resistivity and neutron diffraction studies performed on $NdRu_2Ge_2$ indicate that in the temperature range from 17 K to 10 K, the compound exhibits two types of sine-wave modulated magnetic structures, having the wave vectors $\boldsymbol{k} = (0.19, 0.05, 0.125)$ and $\boldsymbol{k} = (0.12, 0.12, 0)$ with the amplitude of the moment along the c-axis. At 10 K, a first-order transition to a ferromag-

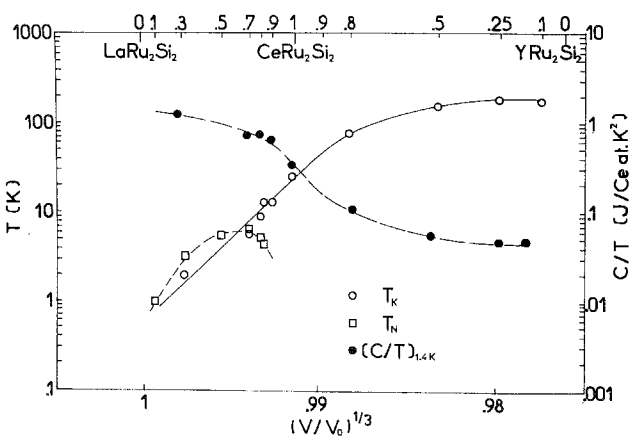

Fig. 17. Kondo temperatures (T_K), Néel temperatures (T_N) and electronic term of the specific heat at 1.4 K ($C/T_{1.4\,K}$) in the (Ce–La)Ru_2Si_2 and (Ce–Y)Ru_2Si_2 systems vs normalized atomic volumes ($V_0 = V_{LaRu_2Si_2}$ (lower scale). Upper scale: alloy compositions. The lines are guides to the eye (Besnus et al. 1987).

netic state occurs with a moment of 3.64(13) μ_B aligned along the tetragonal axis (Szytuła et al. 1987a).

In $SmRu_2Si_2$, the effective paramagnetic moment is only 0.54 μ_B. It corresponds to $J = 5/2$ ground level for free Sm^{3+} and a low lying excited level with $J = 7/2$. At the temperatures above 15 K the magnetic susceptibility as a function of temperature follows the Van Vleck function for the free Sm^{3+} ion (Hiebl et al. 1983). In $SmRu_2Ge_2$ a small part of samarium moments 0.23(10) μ_B orders magnetically below 10 K (Felner and Nowik 1985).

$EuRu_2Si_2$ and $EuRu_2Ge_2$ are antiferromagnets with the Néel temperatures of 78 K and 63 K, respectively (Felner and Nowik 1984, 1985). The values of the hyperfine interactions parameters for $EuRu_2Ge_2$ indicate, that at 4.1 K the Eu spins are in the basal plane. Due to low magnetic anisotropy, small fields are sufficient to saturate the magnetization (Felner and Nowik 1985).

$GdRu_2Si_2$ and $GdRu_2Ge_2$ are also antiferromagnets. The Néel type transition of $GdRu_2Si_2$ is strongly field dependent and moves to lower temperatures when the external field increases (Ślaski et al. 1984, Buschow and de Mooij 1986). This compound undergoes a spin–flop transition at relatively low magnetic fields.

(Tb, Dy, Ho, Er)Ru_2Si_2 (Hiebl et al. 1983, Ślaski and Szytuła 1982, Felner and Nowik 1984) and (Tb, Dy, Ho)Ru_2Ge_2 (Felner and Nowik 1985) systems were reported to be antiferromagnetic at low temperatures. These results were verified by neutron diffraction experiments.

Neutron diffraction data for (Tb, Dy, Ho, Er)Ru_2Si_2 collected at 4.2 K are interpreted in terms of a helicoidal magnetic ordering of a linear transverse wave mode. The static moment propagating along the b-axis with a wave vector $\boldsymbol{k} = (0, k_y, 0)$. It is polarized in the direction of the tetragonal c-axis in the case of (Tb, Dy, Ho)Ru_2Si_2 and it is perpendicular to it in the case of $ErRu_2Si_2$ (Ślaski et al. 1983, 1984). In the case of $TbRu_2Si_2$ at low temperatures a squaring of the modulation develops, giving rise to a square-wave modulation at $T = 3.1$ K (Chevalier et al. 1985a) and $T = 4.2$ K (Szytuła et al. 1987).

Neutron diffraction measurements performed on $TbRu_2Ge_2$ indicate that the magnetic structure of the compound is sine modulated below 32 K (the Néel point). It becomes square modulated at 4.2 K with the terbium magnetic moment amounting to 9.06 μ_B and the propagation vector $\boldsymbol{k} = (0.2331, 0, 0)$. The magnetic moment is directed along the c-axis (Yakinthos 1986, Szytuła et al. 1987).

The holmium ions order antiferromagnetically in the $HoRu_2Ge_2$ compound at the Néel temperature $T_N = 20$ K. This compound exhibits a square modulated structure with a propagation vector $\boldsymbol{k} = (0.2216, 0.0111, 0)$ and a holmium magnetic moment of 6.6 μ_B, parallel to the c-axis (Yakinthos and Roudaut 1987).

The ^{161}Dy Mössbauer spectra in $DyRu_2Ge_2$ were measured in the temperature range from 4.2 K to 63 K. $DyRu_2Ge_2$ is an antiferromagnet with the Néel temperature of 22 K. Above T_N, relaxation spectra are observed. H_{eff} value at 4.2 K gives the magnetic moment of about 10 μ_B. The ground state of the Dy^{3+} ion in this compound must be close to 15/2. The first excited state $\pm(13/2)$ occurs at a distance of 209.9 cm^{-1} from the ground state $\pm(15/2)$ (Yakinthos et al. 1987).

TABLE 6
Magnetic data of the ternary silicides RRu_2Si_2 and germanides RRu_2Ge_2.

R	RRu_2Si_2								RRu_2Ge_2						
	type of magnetic ordering	$T_{N,C}$(K)	θ_p(K)	$\mu_{eff}(\mu_B)$	$\mu_s(\mu_B)$	$\mu_R(\mu_B)$	H_c(T)	Ref.	type of magnetic ordering	T_N(K)	θ_p(K)	$\mu_{eff}(\mu_B)$	$\mu_s(\mu_B)$	$\mu_R(\mu_B)$	Ref.
Y	Pauli paramagnetic							a							
La	Pauli paramagnetic							a	Pauli paramagnetic						b
Ce			0.5	2.12				a	F	11	−70	2.3	0.67		b
		10	−18	2.46				c							
Pr	F	17.8	46.8	3.49				a	F	18	27	3.85	1.82		b
	F	18				3.18		d							
Nd	F	17.4	29.9	3.54				a	F	7.21	44	3.44	1.66		b
	F, AF	26, 10	−6	3.56				c	F, AF	10, 17			3.64		e
	F	18				3.63		d							
	F, AF	10, 23.5	29	3.64				f							
Sm	AF	7	14.4	0.54				a	F	10					b
Eu	AF	78	−63	3.95				a	F	62	62	7.53	5.0		b
Gd	AF	31	54.7	8.02				a	AF	32	39	8.2	5.4		b
	AF	45	40	8.2				c							
	AF	49	57	7.51	5.8		1.17	d							
	AF	44	39.6	7.96				g							
Tb	AF	55	100	9.65				a	AF	30	−3	12.1	2.0		b
	AF	58	10	11.02	5.06	8.77	1.6	d	AF	30	+1	10.9	4.9	9.1	h
Dy	AF	25	100	10.59				a	AF	22	−8	10.5	2.8		b
	AF	29	7	10.98				c							
	AF	29	12	11.4	6.1	9.33	0.8	d							
Ho	F	6.4	47	10.6				a	AF	3	−64	11.13	1.4		b
	AF	19	11.6	11.1	6.8	9.25	0.45	d	AF	20				6.6	i
Er	F	4.5	39.6	9.66				a			−1	9.65			b
	AF	8	−4	10.0				c							
	AF	5	2	9.48	6.0	6.6	0.25	d							
Tm	F	1	65.7	7.38				a			−6	7.1			b
Yb			−18	3.54				a							

References:
(a) Hiebl et al. (1983), (b) Felner and Nowik (1985), (c) Felner and Nowik (1984), (d) Ślaski et al. (1984), (e) Szytuła et al. (1987a), (f) Chevalier et al. (1985a), (g) Łątka (1988), (h) Szytuła et al. (1987), (i) Yakinthos and Roudaut (1987).

The magnetic data determined for RRu_2Si_2 and RRu_2Ge_2 systems are listed in table 6.

2.8. *RRh_2Si_2 and RRh_2Ge_2 compounds*

Susceptibility data obtained for $LaRh_2Si_2$ and YRh_2Si_2 compounds indicate the presence of a magnetic phase transition at 7 K and 5 K, respectively, connected with the onset of an itinerant electron magnetic ordering below these temperatures. Both compounds become superconducting at 3.8 K and 3.1 K, respectively (Felner and Nowik 1983, 1984). New data reveal that no superconductivity is observed for YRh_2Si_2 and $LuRh_2Si_2$ down to 0.33 K and that $LaRh_2Si_2$ is superconducting only below 0.074 K (Palstra 1986, Palstra et al. 1986a).

$LaRh_2Ge_2$ and YRh_2Ge_2 are neither itinerant magnets nor superconductors down to 1.4 K (Felner and Nowik 1985).

The magnetic properties of the other RRh_2Si_2 and RRh_2Ge_2 compounds were intensively studied by several authors. The results show that at 4.2 K the compounds containing the lanthanide elements from Ce to Er are antiferromagnetic, while $LuRh_2Si_2$ and $YbRh_2Si_2$ remain paramagnetic down to 1.4 K. For majority compounds two maxima are observed in the temperature against the magnetic susceptibility curves: first (at higher temperature) corresponding to the Néel temperature and second corresponding to a change in the magnetic structure.

In the case of $TbRh_2Si_2$ the magnetic susceptibilities were measured parallel and perpendicular to the unique axis of a single crystal. In the temperature range 200–300 K the Curie–Weiss law is satisfied for both orientations, with the parameters:

$$\chi_c(T)\text{: } \mu^c_{\text{eff}} = 10.3\ \mu_B/\text{Tb atom}, \quad \theta^c_p = 50(5)\ \text{K, and}$$
$$\chi_a(T)\text{: } \mu^a_{\text{eff}} = 10.5\ \mu_B/\text{Tb atom}, \quad \theta^a_p = -70(5)\ \text{K}$$

(Chevalier et al. 1985).

The changes in the Néel temperatures under the influence of an external pressure were measured for $GdRh_2Si_2$ and $TbRh_2Si_2$. Fig. 18 shows plots of the induced voltage versus temperature for several values of the applied pressure and the dependence of the Néel temperature as a function of the pressure. No changes are observed for $TbRh_2Si_2$, while a linear decrease is apparent for $GdRh_2Si_2$ (Szytuła et al. 1986a).

An anomaly of the temperature dependence of the lattice constants at the Néel temperature was observed in $CeRh_2Si_2$ ($T_N = 37$ K) (Godart et al. 1983) and $TbRh_2Si_2$ ($T_N = 92$ K) (Szytuła et al. 1986a). No anomalies were noticed near $T_N = 99$ K for the temperature dependence of a and c lattice constants in $GdRh_2Si_2$ (Szytuła et al. 1986a).

Specific heats have been measured for polycrystalline $LaRh_2Si_2$ and $HoRh_2Si_2$ (Sekizawa et al. 1987). $LaRh_2Si_2$ is not magnetically ordered above 1.3 K. $HoRh_2Si_2$ has two peaks in the specific heat vs. temperature curve, a broad peak

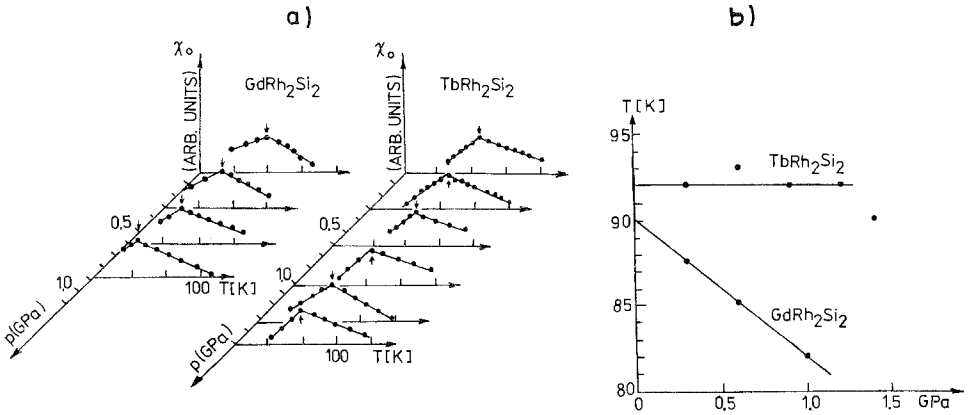

Fig. 18. The temperature dependence of small field (15 Oe) a.c. susceptibility of $GdRh_2Si_2$ and $TbRh_2Si_2$ and pressure dependence of the transition temperatures (Szytuła et al. 1986a).

at 11 K and a very sharp one at 27 K. The magnetic part of the specific heat, obtained by subtraction of the specific heat of $LaRh_2Si_2$ from that of $HoRh_2Si_2$, provides a total entropy $S = 24$ J/mol K, which is close to $R_0 \ln(2J + 1)$ for $J = 8$. This fact suggests that the excess entropy can be attributed to the ground state multiplet of Ho^{3+} ion ($^5I_8$). Takano et al. (1987) claim that the temperature dependence of the magnetic heat capacity of $HoRh_2Si_2$ can be reproduced remarkably well using three crystal field parameters and one isotropic exchange constant with appropriate values of the parameters. The lower transition temperature (11 K) is the temperature at which the perpendicular component of the magnetization disappears. The higher transition point is that one at which the parallel component of the magnetization disappears (Néel point). A good fit to the experimental data is obtained for the following set of the parameters: $B_2^0 = -0.14$ K, $B_4^0 = +0.0004$ K, $B_4^4 = -0.002$ K.

The ^{155}Gd Mössbauer spectra at liquid temperatures in $GdRh_2Si_2$ show that Gd magnetic moments are ordered in the basal plane, i.e. perpendicular to the fourfold symmetry axis (Nowik et al. 1980, Łątka 1988). An evaluation of Mössbauer spectra of ^{161}Dy in $DyRh_2Si_2$ shows that the magnetic moment localized on Dy^{3+} ion to be 10 μ_B, suggesting the presence of weak crystalline field effects in respect to strong Dy–Dy exchange interactions (Felner and Nowik 1984). The Mössbauer studies performed on ^{151}Eu nuclei embedded in $EuRh_2Si_2$ and $EuRh_2Ge_2$ show that in both compounds the Eu ions are in the divalent state and the conduction electrons are mainly responsible for the magnetic properties of both systems (Felner and Nowik 1984, 1985).

$CeRh_2Si_2$ exhibit the magnetic structure described by the wave vector $\boldsymbol{k} = (\frac{1}{2}, 0, \frac{1}{2})$ (see AFIII in fig. 23) (Quezel et al. 1984). A different type of magnetic structure is observed for $CeRh_2Si_2$ by Grier et al. (1984). Below the Néel point ($T_N = 39$ K) it exhibits another second order transition: at 27 K it changes to a complex commensurate structure with modulated moments.

Neutron diffraction studies (Ślaski et al. 1983, Szytuła et al. 1984, Quezel et al.

1984, Melamud et al. 1984, Chevalier et al. 1985a) carried out for Nd, Tb, Dy, Ho and Er compounds show, that at 4.2 K in all of them the ordering is antiferromagnetic of the AFI type {wave vector $\boldsymbol{k} = (0, 0, 1)$} similarly as in RCo_2Si_2 system (see section 2.4). In $NdRh_2Si_2$ and $TbRh_2Si_2$ the magnetic moment localized on the R atom is aligned along the fourfold symmetry axis, in $ErRh_2Si_2$ it is perpendicular to it, while in $HoRh_2Si_2$ it makes an angle of $28 \pm 3°$. Below $T_N = 52$ K the magnetic structure of $DyRh_2Si_2$ is of the AFI type with the magnetic moment on Dy^{3+} amounting to 9.9(1) μ_B. It is aligned along the fourfold symmetry axis, however neutron diffraction data indicate that below 18 K it makes an angle of approximately 19° with the tetragonal axis (Melamud et al. 1984).

$TbRh_2Ge_2$ orders antiferromagnetically in the AFI type structure with a magnetic moment of 9.4(3) μ_B at 4.2 K localized on Tb^{3+} ion (Szytuła et al. 1987).

The comparison of magnetic data available for the RRh_2Si_2 and RRh_2Ge_2 systems shows large similarities but the magnetic interactions in RRh_2Ge_2 compounds seem to be weaker, perhaps due to the larger size of the Ge atom (Felner and Nowik 1985).

The magnetic data determined for RRh_2Si_2 and RRh_2Ge_2 systems are listed in table 7.

2.9. *RPd_2Si_2 and RPd_2Ge_2 compounds*

$LaPd_2Si_2$ and $LaPd_2Ge_2$ are superconductors with the transition temperatures of $T_s = 0.39$ K for $LaPd_2Si_2$ (Palstra et al. 1986) and 1.12 K for $LaPd_2Ge_2$ (Hull et al. 1981). Also YPd_2Si_2 and YPd_2Ge_2 are superconductors below 0.47 K and 1.14 K, respectively (Palstra et al. 1986, Hull et al. 1981).

$CePd_2Si_2$ was reported by Murgai et al. (1982) to order antiferromagnetically below $T_N = 10$ K, but Hiebl et al. (1986) did not find a magnetic transition in $CePd_2Si_2$. On the other hand neutron diffraction data for $CePd_2Si_2$ indicate collinear antiferromagnetic ordering of AFIII type (see fig. 23). The magnetic moment configuration is described as ferromagnetic planes with the moment perpendicular to the (110) plane. The magnitude of the Ce moment was determined to be 0.62(3) μ_B at 4.2 K (Grier et al. 1984).

In the case of $Ce_{1-x}Y_xPd_2Si_2$ $(0 \leqslant x \leqslant 1)$ system the results of heat capacity, resistivity and susceptibility measurements (Besnus et al. 1987) show that a partial substitution of Ce by Y leads to a rapid decrease in the Néel temperature. Spontaneous magnetism and the Kondo effect coexist up to $x = 0.4$ ($T_N = 3$ K) where T_K is estimated as $3T_N$. For higher Ce dilution the magnetic moment of the ground state doublet has become completely quenched and a genuine heavy fermion behaviour is evident, for example, $\gamma = 0.875$ J/K^2 Ce atom and $T_K = 10$ K at $x = 0.5$ and $\gamma = 0.58$ J/K^2 Ce atom and $T_K = 15$ K at $x = 0.75$.

The temperature variation of the lattice parameters, the magnetic susceptibility and the ^{151}Eu Mössbauer measurements indicate the occurrence of a mixed valency in $EuPd_2Si_2$ with a continuous valence transition near 140 K. From these

TABLE 7
Magnetic data for RRh_2Si_2 and RRh_2Ge_2 compounds.

R	RRh_2Si_2						RRh_2Ge_2					
	type of magnetic ordering	T_N(K)	θ_p(K)	$\mu_{eff}(\mu_B)$	$\mu_R(\mu_B)$	Ref.	type of magnetic ordering	T_N(K)	θ_p(K)	$\mu_{eff}(\mu_B)$	$\mu_R(\mu_B)$	Ref.
Y	AF	5	−8	0.2		a, b	No ordered down to 1.4 K					c
	No ordered down to 1.4 K					c						
La	AF	7	−41	2.0		a, b	No ordered down to 1.4 K					c
	No ordered down to 1.4 K					c						
	No ordered down to 1.3 K					d						
Ce	AF	36, 5	−81	2.9		a, b	AF	15, 3	−3	2.7		c
	AF	36	−61	2.56	1.5	e						
	AF	39, 27			2.54	f						
	AF	37	−163	2.43		g						
	AF	37	−72	2.9		h						
	AF	36	−26	2.33		i						
Nd	AF	56, 8	−4	4.7		a, b	AF	46	0	3.8		c
	AF	55	7	3.59	3.25	j						
	AF	57	27	3.78	3.24	k						
Pr							AF	47, 4	−14	3.90		c
Sm	AF	46, 8				a, b	AF	7, 3.5				c
Eu	AF	25	22	7.2		a, b	AF	14	13	7.94		c
Gd	AF	132, 16	25	5.6		a, b	AF	90, 7	20	7.60		c
	AF	101	−7	7.51		l						

	AF	106, 18	−2.5	8.17		m						
	AF	99				n						
			+24	7.91		o						
			+31	6.9		p						
Tb	AF	92, 12	−26	8.4		a, b	AF	77, 8	−12	10.3		c
	AF	88	−10	10.1		l	AF	67	0	9.9	9.4	q
	AF	98			8.92	r						
	AF	94	43	10.0	8.5	e, k						
	AF	94		10.4		s						
	AF	55	−1	11.4		l	AF	44, 9	−3	10.68		c
Dy	AF	52, 18			9.9	t						
	AF	55, 15	7	10.6		a, b						
	AF	57				u						
Ho	AF	27, 14	3	9.3		a, b	AF	40, 5	−27	10.8		c
	AF	27	8	10.2		l						
	AF	27			8.8	r						
	AF	29, 10				d						
Er	AF	103, 13	8	7.6		a, b						
	AF	12.8	−2	9.45	7.74	j						
Tm	AF	4.2			4.2	v						
Lu			−28	0.7		a, b						

References:

(a) Felner and Nowik (1983), (b) Felner and Nowik (1984), (c) Felner and Nowik (1985), (d) Sekizawa et al. (1987), (e) Quezel et al. (1984), (f) Grier et al. (1984), (g) Palstra et al. (1986), (h) Godart et al. (1983), (i) Hiebl et al. (1986), (j) Szytuła et al. (1986), (k) Chevalier et al. (1985a), (l) Zygmunt and Szytuła (1984), (m) Łątka et al. (1988), (n) Szytuła et al. (1986), (o) Buschow and de Mooij (1986), (p) Slaski and Szytuła (1982), (r) Ślaski et al. (1983), (s) Chevalier et al. (1985a), (t) Melamud et al. (1984), (u) Nowik et al. (1983), (v) Yakinthos (1986a), (q) Szytuła et al. (1987).

investigations the average valence of Eu ion in $EuPd_2Si_2$ was derived to be ~2.3 at 300 K and ~2.7 at 120 K (Sampathkumaran et al. 1981).

The magnetic data show an antiferromagnetic ordering only in $GdPd_2Si_2$ and $TbPd_2Si_2$ below 13 and 20 K, respectively, while compounds with Dy, Ho and Er are paramagnetic at 4.2 K (Yakinthos and Gamari-Seale 1982).

Neutron diffraction investigations were performed up to now only on $HoPd_2Si_2$ (Leciejewicz and Szytuła 1985a), $TbPd_2Si_2$ (Szytuła et al. 1986) and $TdPd_2Ge_2$ (Szytuła et al. 1988a). Based on neutron diffraction measurements a magnetic structure of a helicoidal character was suggested to exist in these compounds. In the helicoidal magnetic order the configuration of magnetic moments is represented by a static linear transverse spin wave. The wave propagation vectors are:

$\boldsymbol{k} = (0.58, 0, 0.15)$ for $HoPd_2Si_2$ below $T_N = 21 \pm 1$ K,
$\boldsymbol{k} = (0.602, 0, 0.148)$ for $TbPd_2Si_2$ below $T_N = 15 \pm 1$ K,
$\boldsymbol{k} = (0.572, 0, 0.185)$ for $TbPd_2Ge_2$ below $T_N = 4.2$ K.

The magnetic moments localized on the rare-earth atoms make angles with the tetragonal axis: for $HoPd_2Si_2$ $\mu = 10.9(2)\ \mu_B$, the angle is 63(5)°, for $TbPd_2Si_2$ $\mu_B = 7.9(1)\ \mu_B$ at 4.2 K, the angle is 90°, and for $TbPd_2Ge_2$ $\mu = 8.4(2)\ \mu_B$ at 1.8 K, the angle is 62°.

The temperature dependence of the magnetic susceptibility of $YbPd_2Si_2$ attains a peak at $T_{max} = 30$ K and it tends to a constant value below 10 K. Above 120 K, χ^{-1} is a linear function of temperature. The determined effective magnetic moment $\mu_{eff} = 4.5(1)\ \mu_B$ is close to the moment expected for the free Yb^{3+} ion ($\mu_{eff} = 4.54\ \mu_B$). From an extrapolation of the high-temperature course of χ^{-1} a paramagnetic Curie temperature $\theta_p = -70$ K is determined. Such a large negative θ_p is characteristic of homogeneously mixed-valent compounds (Sampathkumaran et al. 1984). Below 16 K, a T^2 dependence of the susceptibility reflects the Fermi liquid nature of the ground state (Dhar et al. 1987a). This compound is a superconductor below 1.17 K (Hull et al. 1981).

The magnetic data for the RPd_2Si_2 and RPd_2Ge_2 systems are summarized in table 8.

2.10. *RAg_2Si_2 and RAg_2Ge_2 compounds*

From among RAg_2Si_2 and RAg_2Ge_2 systems, only $CeAg_2Si_2$, $GdAg_2Si_2$ and $CeAg_2Ge_2$ have been studied.

The resistivity and susceptibility measurements (Murgai et al. 1982) reveal a transition in $CeAg_2Si_2$ to an antiferromagnetic state near 10 K and a small ferromagnetic component of $gJ = 0.03\ \mu_B$ below this point. From the neutron diffraction data it may be concluded that the magnetic ordering in $CeAg_2Si_2$ at 4.2 K may be described as an incommensurate longitudinal wave of magnetization propagating along *a*-axis (Grier et al. 1984).

Magnetometric and the Mössbauer data obtained for $GdAg_2Si_2$ indicate, that it orders antiferromagnetically below 10 K (Nowik et al. 1980).

TABLE 8
Magnetic data for RPd_2Si_2 and RPd_2Ge_2 compounds.

R	RPd_2Si_2						RPd_2Ge_2					
	type of magnetic ordering	T_N(K)	θ_p(K)	$\mu_{eff}(\mu_B)$	$\mu_R(\mu_B)$	Ref.	type of magnetic ordering	T_N(K)	θ_p(K)	$\mu_{eff}(\mu_B)$	$\mu_R(\mu_B)$	Ref.
Ce	AF	10.5	−57	2.55		a						
	AF	10	−75		0.62	b						
			−19	2.31		c						
Gd	AF	13	2	8.8		d						
	AF	19	−45.5	8.05		e						
	AF	16	−48	8.02		f						
	AF	17.7				g						
			−39	8.7		h						
Tb	AF	20	−1	9.8		d	AF	4.2			8.4	i
	AF	15			9.3	j						
Eu	AF	10				k						
Dy			−4	10.8		d						
			−25	6.8		h						
Ho			−5	10.5		d						
	AF	21			7.7	l						
			0	10.0		h						
Er			−3	9.5		d						
			−20	7.3		h						
Yb			−70	4.5		m						

References:
(a) Palstra et al. (1986a), (b) Grier et al. (1984), (c) Hiebl et al. (1986), (d) Yakinthos and Gamari-Seale (1982), (e) Łątka et al. (1987), (f) Buschow and de Mooij (1986), (g) Nowik et al. (1980), (h) Ślaski and Szytuła (1982), (i) Szytuła et al. (1988a), (j) Szytuła et al. (1986), (k) Felner and Nowik (1985), (l) Leciejewicz and Szytuła (1985), (m) Sampathkumaran et al. (1984).

TABLE 9
Magnetic data of ternary silicides RAg_2Si_2.

R	type of magnetic ordering	T_N(K)	θ_p(K)	$\mu_{eff}(\mu_B)$	Ref.
Ce	AF	9.5	−36	2.54	a
	AF	10			b
Gd	AF	10	−29.4	7.98	c
	AF	8	−18	7.89	d

References:
(a) Palstra et al. (1986a), (b) Grier et al. (1984), (c) Łątka et al. (1987), (d) Buschow and de Mooij (1986).

The temperature dependence of the resistivity of $CeAg_2Ge_2$ has a peak near 8 K below which $\rho(T)$ decreases rather steeply, indicating that magnetic ordering occurs in this compound. The measurement of the d.c. susceptibility (Rauchschwalbe et al. 1985) suggests an antiferromagnetic phase transition in $CeAg_2Ge_2$.

The magnetic data for the RAg_2Si_2 systems are listed in table 9.

2.11. *ROs_2Si_2 compounds*

Magnetic properties of ROs_2Si_2 are very similar to the magnetic properties of RRu_2Si_2. ROs_2Si_2 compounds with R = Y, La, Lu are paramagnets. The determined paramagnetic moment of Ce in $CeOs_2Si_2$ $\mu = 0.98\ \mu_B$ (Hiebl et al. 1983a) or 1.53 μ_B (Hiebl et al. 1986) is compatible with a rather small concentration of Ce^{3+} ions. The effective moment in $SmOs_2Si_2$ $\mu_{eff} = 0.47\ \mu_B$ per Sm atom agrees with the magnetic moment of free Sm^{3+} ion with the $J = 5/2$ ground state. At the temperatures above 25 K the magnetic susceptibility dependence on temperature corresponds to the Van Vleck curve for a free Sm^{3+} ion with closely spaced multiplets $J = 5/2$ and $J = 7/2$.

ROs_2Si_2 compounds with R = Pr, Nd, Ho, Er and Tm are ferromagnets while the compounds with R = Sm, Gd, Tb and Dy show an antiferromagnetic behaviour at low temperatures (Hiebl et al. 1983). Magnetometric measurements performed at 4.2 K for $TbOs_2Si_2$ and $HoOs_2Si_2$ indicate that they become ferromagnetic at critical fields of 10 and 2 kOe, respectively (see fig. 19) (Kolenda et al. 1985).

Neutron diffraction experiments reveal that at low temperatures $TbOs_2Si_2$, $HoOs_2Si_2$ and $ErOs_2Si_2$ exhibit a magnetic structure which can be described as an incommensurate longitudal static magnetization wave. The magnetic moments in $TbOs_2Si_2$ and $HoOs_2Si_2$ are aligned along the c-axis but the magnetic wave propagates along the b-axis. In the case of $ErOs_2Si_2$ the magnetic moments are aligned along b-axis. The propagation wave vector is $\boldsymbol{k} = (0, \frac{1}{3}, 0)$ in all three cases (Kolenda et al. 1985).

The ^{155}Gd Mössbauer data indicate that in $GdOs_2Si_2$ the magnetic moment of

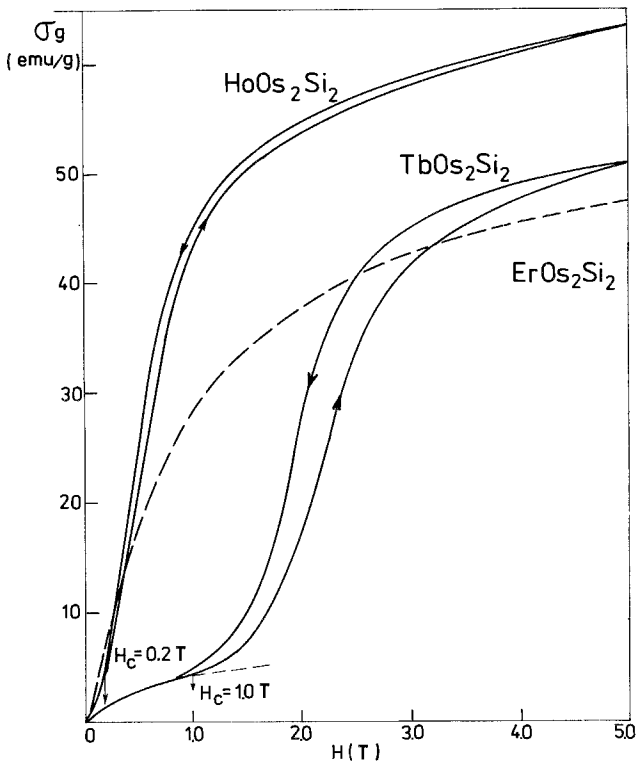

Fig. 19. Magnetization isotherms at 4.2 K measured at different values of the external magnetic field for $TbOs_2Si_2$, $HoOs_2Si_2$ and $ErOs_2Si_2$ (Kolenda et al. 1985).

Gd^{3+} ion has a complex structure similar to that observed in metallic erbium between 20 and 52 K (Cable et al. 1965, Łątka 1987a).

No ROs_2Ge_2 compounds have been synthetized to date.

The available magnetic data of ROs_2Si_2 system are listed in table 10.

2.12. *RIr_2Si_2 compounds*

Ternary RIr_2Si_2 silicides have two allotropic forms. At low temperatures they crystallize in the $ThCr_2Si_2$-type structure (space group I4/mmm) which is adopted by several other ternary silicides such as RT_2Si_2. The form stable at high temperatures is isostructural with $CaBe_2Ge_2$ (space group P4/nmm). Both structural types are ordered ternary derivatives of the binary $BaAl_4$-type structure (Parthé et al. 1983).

The polymorphism and the superconductivity of $LaIr_2Si_2$ was studied by Braun et al. (1983). The solid state transition between P-$LaIr_2Si_2$ and I-$LaIr_2Si_2$ was determined at 1720(10)°C, where P and I mean "primative" and "body-centered", respectively. P-$LaIr_2Si_2$ is superconducting at 1.58 K whereas I-$LaIr_2Si_2$ does not show any superconductivity down to 1 K.

For I-$CeIr_2Si_2$ the inverse susceptibility deviates considerably from the Curie–

TABLE 10
Magnetic data of the ternary silicides ROs_2Si_2.

R	Type of magnetic ordering	$T_{C,N}$(K)	θ_p(K)	$\mu_{eff}(\mu_B)$	$\mu_s(\mu_B)$	$\mu_R(\mu_B)$	H_c(T)	Ref.
Y	Pauli paramagnetic							a
La	Pauli paramagnetic							a
Ce			−5	0.23				a
Pr	F	12.6	53	3.53				a
Nd	F	2.9	19	3.56				a
Sm	AF	5	12	0.47				a
Gd	AF	26	27	8.12				a
	AF	29	24	8.04				a
Tb	AF	42	100	9.64				a
	AF	41	20	10.5	5.43	8.85	1.0	c
Dy	AF	23	101	10.35				a
Ho	F	8.5	30	10.61				a
	AF	19	6.5	10.9	6.83	9.9	0.2	c
Er	F	5.1	30	9.7				a
	AF		−16	9.58	5.13	8.24^{++}		c
Tm	F	1	64	7.34				a
Yb			−21	4.38				a
Lu	Pauli paramagnetic							

μ_s–magnetometric data $T = 4.2$ K, $H = 5$ T, μ_n–neutron diffraction data, $^{++}$ at 1.8 K.
References:
(a) Hiebl et al. (1983a), (b) Buschow and de Mooij (1986), (c) Kolenda et al. (1985).

Weiss law at temperatures below 200 K and it ceases to depend on the temperature at lower temperatures. The P-$CeIr_2Si_2$ exhibits a broad maximum in χ_g^{-1} curve below 700 K, a fact commonly observed in intermediate valence systems (Hiebl et al. 1986).

Measurements of the ^{151}Eu Mössbauer spectra and magnetic susceptibility show that the 4f configuration of the Eu ion in $EuIr_2Si_2$ changes continuously with the temperature from $4f^{6.2}$ at 4.2 K to $4f^{6.7}$ at 290 K (Chevalier et al. 1986).

$GdIr_2Si_2$ orders antiferromagnetically with reported Néel points of 92 K (Buschow and de Mooij 1986) and 77 K (Zygmunt and Szytuła 1984). The results of the ^{155}Gd Mössbauer measurements indicate that the magnetic moment is perpendicular to c-axis (Lątka 1988).

Both forms of $TbIr_2Si_2$ are antiferromagnetic: I-form with $T_N = 80$ K and $\theta_p = +42$ K, and P-form with $T_N = 13$ K and $\theta_p = +13$ K (Hirjak et al. 1984). Since the Tb^{3+}–Tb^{3+} intra- and interplane distances are similar in both phases, a change in the density of states at Fermi level (RKKY-type interaction) could explain small T_N and θ_p values observed in the P-form.

Only I-$TbIr_2Si_2$ phase was studied by neutron diffraction (Ślaski et al. 1983). A collinear, antiferromagnetic ordering of AFI type with the moments aligned along the tetragonal axis {wave vector $\boldsymbol{k} = (0, 0, 1)$} was discovered.

The magnetic susceptibility of $DyIr_2Si_2$, $HoIr_2Si_2$ and $ErIr_2Si_2$ follows the

TABLE 11
Magnetic data of ternary silicides RIr_2Si_2.

R	type of magnetic ordering	T_N(K)	θ_p(K)	$\mu_{eff}(\mu_B)$	$\mu_R(\mu_B)$	Ref.
La-P	No order down to 1.2 K					a
La-I	No order down to 1.2 K					a
Ce-P			−360	1.9		b
Ce-I			−116	2.05		b
Gd	AF	77	−8	8.42		c
	AF	81	−4	7.96		d
	AF	92	−16	7.83		e
Tb-P	AF	13	13	9.78		f
Tb-I	AF	80	42	9.97		f
	AF	75	−21	10.4		c
	AF	72			8.1	g
Dy			−2	10.0		c
Ho			+2	11.1		c
Er			+7	8.64		c
			−27	6.8		h

References:
(a) Braun et al. (1985), (b) Hiebl et al. (1986), (c) Zygmunt and Szytuła (1984), (d) Lątka (1988), (e) Buschow and de Mooij (1986), (f) Hirjak et al. (1984), (g) Ślaski et al. (1983), (h) Ślaski and Szytuła (1982).

Curie–Weiss law down to 4.2 K indicating the absence of a long range ordering above 4.2 K (Zygmunt and Szytuła 1984).

The field dependence of magnetization is linear up to 50 kOe for $GdIr_2Si_2$ and $TbIr_2Si_2$. In the cases of $DyIr_2Si_2$, $HoIr_2Si_2$ and $ErIr_2Si_2$ they all exhibit a typical behaviour for paramagnetic compounds (Zygmunt and Szytuła 1984).

The RIr_2Ge_2 compounds were not synthesized as yet.

The available magnetic data at RIr_2Si_2 systems are listed in table 11.

2.13. *RPt_2Si_2 compounds*

The crystal structure of all ternary RPt_2Si_2 silicides (R = La, Ce, Pr, Nd, Sm, Gd, Tb, Dy, Ho, Er, Tm, Yb and Lu) is of the $CaBe_2Ge_2$ type. The magnetic properties were determined in the temperature range from 1.5 K to 1100 K in the presence of external magnetic fields up to 13 kOe revealing a typical paramagnetism of free R^{3+} ions at the temperatures larger than 200 K (Hiebl and Rogl 1985). Susceptibilities of (Y, La, Lu)Pt_2Si_2 are almost temperature independent. Characteristic molar susceptibilities at the room temperature are collected in table 12.

YPt_2Si_2, $LaPt_2Si_2$ (Shelton et al. 1984) and $LaPt_2Ge_2$ (Hull et al. 1981) are superconductors below T_s = 1.42–1.31 K, 1.70–1.58 K and 0.55 K, respectively.

The temperature dependence of the magnetic susceptibility of $CePt_2Si_2$ similar

TABLE 12
Magnetic data of ternary silicides RPt_2Si_2.

R	type of magnetic ordering	T_N(K)	θ_p(K)	$\mu_{eff}(\mu_B)$	Ref.
Y	Pauli paramagnetic				a
La	Pauli paramagnetic				a
Ce				2.24	a
			−85	2.42	b
			−33	2.24	c
			−86	2.57	d
Pr			7	3.46	a
Nd			−4.5	3.55	a
Sm			0	0.7	a
Gd	AF	10	−7	8.13	a
	AF	9.7	−5	8.14	e
	AF	7.2			f
	AF	8	−8	8.10	g
Tb	AF	6.5	58.5	9.55	a
Dy	F?	>3	37	10.59	a
	AF	7			h
Ho	F?	>3	11	10.56	a
	No ordered down to 2K			10.0	i
Er	F?	>3	26	9.57	a
Tm	F?	>3	65	7.32	a
Yb			−180	3.5	a
La	Pauli paramagnetic				a

References:
(a) Hiebl and Rogl (1985), (b) Palstra et al. (1987), (c) Hiebl et al. (1986), (d) Gignoux et al. (1986), (e) Łątka (1988), (f) Nowik et al. (1980), (g) Buschow and de Mooij (1986), (h) Nowik et al. (1983), (i) Leciejewicz et al. (1984).

to the susceptibility of the Kondo lattice and the Fermi liquid system below 2 K (Gignoux et al. 1986).

The magnetic susceptibility versus temperature curves for $PrPt_2Si_2$, $NdPt_2Si_2$ and $YbPt_2Si_2$ follow closely the Curie–Weiss law down to 1.8 K. Magnetic data for $SmPt_2Si_2$ ($\mu_{eff} = 0.7\ \mu_B$) show that the Sm ion behaves as an ideal Van Vleck Sm^{3+} ion with the ground state $J = 5/2$ and the low-lying first excited state $J = 7/2$. Antiferromagnetic ordering is observed below 10 K and 6.5 K in the case of $GdPt_2Si_2$ and $TbPt_2Si_2$, respectively, whereas (Dy, Ho, Er, Tm)Pt_2Si_2 are ferromagnets below 3 K (Hiebl and Rogl 1985).

$DyPt_2Si_2$ is antiferromagnetic below 7 K (Nowik et al. 1983). Long range magnetic order at 1.8 K was found by neutron diffraction in $HoPt_2Si_2$ (Leciejewicz et al. 1984a).

The RPt_2Ge_2 compounds were not synthetized as yet.

The magnetic data for the RPt_2Si_2 system are summarized in table 12.

TABLE 13
Magnetic data of the ternary silicides RAu_2Si_2.

R	type of magnetic ordering	$T_{C,N}$(K)	θ_p(K)	$\mu_{eff}(\mu_B)$	$\mu_R(\mu_B)$	Ref.
Ce	AF	6.6	−2.8	2.54		a
	AF	10.1	−18	2.43		b
	AF	10.0			1.29	c
Pr			−9.2	3.58		a
Nd			−6.1	3.62		a
Sm	AF	15.9	2.5	0.63		a
Eu	F	15.5	−5.0	6.7		a
Gd	AF	5.7	−4.9	8.7		a
	AF	12.5	−35.0	7.96		d
	AF	18	−25.0	7.87		e
	AF	14.8	−14.8	8.9		a
Dy	AF	7.5	−3.6	10.6		a
		7.0				f
Ho	F	14.8	−2.1	10.6		a
Er	F	40.0	13.0	9.0		a

References:
(a) Felner (1975), (b) Palstra et al. (1986a), (c) Grier et al. (1984), (d) Łątka et al. (1988), (e) Buschow and de Mooij (1986), (f) Nowik et al. (1983).

2.14. *RAu_2Si_2 compounds*

Magnetic parameters were determined for all RAu_2Si_2 compounds with R = Ce–Er (Felner 1975). Antiferromagnetic ordering was found in compounds with R = Ce, Sm, Gd, Tb and Dy. The Néel points range from 5.7 to 15.9 K. $EuAu_2Si_2$, $HoAu_2Si_2$ and $ErAu_2Si_2$ order ferromagnetically at 4.2 K, while $PrAu_2Si_2$ and $NdAu_2Si_2$ remain paramagnetic.

The Mössbauer data obtained for $GdAu_2Si_2$ (Nowik et al. 1980) and $DyAu_2Si_2$ (Nowik et al. 1983) confirm the presence of a long range magnetic order below 19 K and 7 K, respectively. The Mössbauer spectra indicate that the magnetic structure consists of ferromagnetic Gd planes nearly perpendicular to *c*-axis, stacked in a sequence which does not yield antiferromagnetic order. The angle between the Gd moments and the *c*-axis was found to be approximately 60°.

A neutron diffraction study was carried out only for $CeAu_2Si_2$ (Grier et al. 1984). Its magnetic structure is of the AFI type. The magnetic moment of $\mu = 1.29(5)\ \mu_B$ is localized on the Ge^{3+} ion. It is parallel to the tetragonal axis.

RAu_2Ge_2 compounds have not yet been synthetized.

The available magnetic data of RAu_2Si_2 system are listed in table 13.

2.15. *Solid solution compounds*

Investigations of solid solutions between the ternary systems with $ThCr_2Si_2$ type of crystal structure provide valuable information on the magnetic interactions

between the magnetic moments of rare earth and transition metal ions and allow one to draw conclusions about their electronic structure.

Magnetometric measurements performed on the $Ce(Mn_{1-x}T_x)_2\ Si_2$ (T = Fe, Co, Cu) (Siek and Szytuła 1979, Szytuła and Siek 1982a) indicate that the compositions with $x \leq 0.5$ are ordered antiferromagnetically. The Néel temperatures decreases with T concentration (see fig. 20). The magnetization dependence on the applied external field obtained at 4.2 K for $CeMnFeSi_2$ and $CeMnCuSi_2$ compounds shows transitions of metamagnetic type at the critical fields of 12.5 and 60 kOe, respectively.

In the case of $Ce(Mn_{1-x}Cr_x)_2Si_2$ it is observed that there is a strong Mn 3d antiferromagnetism and a decrease of T_N with increasing Cr concentration (Johnston et al. 1988).

Also, in the case of $Nd(Mn_{1-x}Cr_x)_2Si_2$ system (Obermyer et al. 1979) the rise of Cr concentration leads to the decrease of the Néel temperatures of the Mn ordered sublattice from 380 K to 260 K and 200 K for the compositions with $x = 0$, 0.2 and 0.3, respectively.

An evolution of a heavy-fermion behaviour in $CeCu_2Si_2$ from strong mixed valence in $CeNi_2Si_2$ is demonstrated in the $CeCu_{2-x}Ni_xSi_2$ system. Heavy-fermion behaviour, as probed by the low-temperature susceptibility, $\chi(0)$, is destroyed at $x = 0.65$ (Sampathkumaran and Vijayaraghavan 1986).

This problem was also studied by the magnetic susceptibility (4.2–300 K) and the resistance (1.2–300 K) measurements for the series of $CeCu_{2-x}Co_xSi_2$ (Dhar et al. 1987). There is a significant drop in the low temperature susceptibility $\chi(0)$ for $x = 0.5$. For higher concentrations of Ce, χ is nearly temperature independent which is typical for strongly mixed valent systems.

The magnetic susceptibility of a number of compositions in the $CeOs_xRu_{2-x}Si_2$ system was recently studied (Hiebl et al. 1984). For all concentrations, the temperature dependence of cerium valence state could be satisfactorily represented using the ICF model (Sales and Wohlleben 1975).

Sampathkumaran et al. (1987) reported the influence of various chemical substituents at the Rh site on T_N by the measurements of magnetic susceptibility

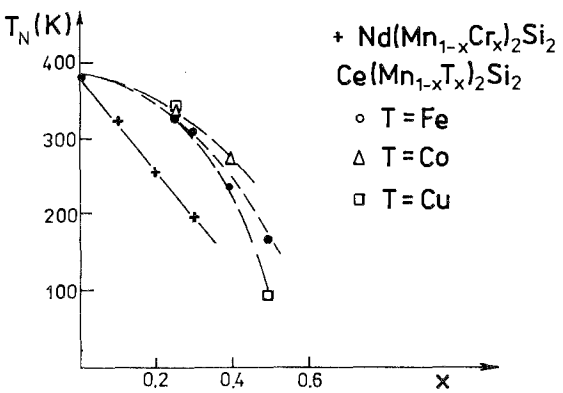

Fig. 20. Néel temperatures of $Nd(Mn_{1-x}Cr_x)_2Si_2$ and $Ce(Mn_{1-x}T_x)_2Si_2$ (T = Fe, Co, Cu) vs x.

in the series $CeRh_{1.8}T_{0.2}Si_2$ (T = Co, Ni, Cu, Ru, Pd, Os, Au). The results suggested that all these substituents have a general tendency to suppress T_N, but the degree of suppression varies from one substituent to the other.

The magnetic properties of $Ce(Rh_{1-x}Ru_x)_2Si_2$ solid solutions was investigated by the magnetometric, specific heat and neutron diffraction methods (Lloret et al. 1987). The magnetic ordering of AFII type is observed up to $x = 0.4$. Magnetic moments are always found to be parallel to c-axis and their values are strongly depressed when x increases ($\mu = 1.5\ \mu_B$/Ce atom for $x = 0$ and $\mu = 0.65\ \mu_B$/Ce atom for $x = 0.4$). The variation of T_N with the ruthenium concentration is quite anomalous (see fig. 21). For small concentrations ($0 \leq x \leq 0.15$) a sharp decrease in T_N is observed (from 36 K to 12 K) whereas for $0.15 < x \leq 0.4$ T_N keeps a nearly constant value of about 11 K.

Neutron diffraction studies of $Nd(Rh_{1-x}Ru_x)_2Si_2$ system at 4.2 K give the following magnetic structures:

- $x = 0.25$, the coexistence of collinear antiferromagnetic AFI and modulated structure with propagation vector $\boldsymbol{k} = (0, 0, 0.838)$ is observed,
- $x = 0.4$, 0.5 and 0.75, the modulated structure is observed,
- $x = 0.9$, the coexistence of ferromagnetic and modulated structure is observed.

For all samples the observed magnetic moment is the same as the free ion magnetic moment $\mu = 3.27\ \mu_B$ (Jaworska et al. 1987).

In $TbRh_{2-x}Ru_xSi_2$ systems magnetic susceptibilities satisfy the Curie–Weiss law at the temperature higher than 130 K. The magnetic moment of the rare earth atom is larger than the magnetic moment of the free Tb^{3+} ion (9.27 μ_B). A similar effect is observed in the case of $TbRh_{2-x}Ir_xSi_2$ system (Jaworska and Szytuła 1987).

A difference is observed in the concentration dependence of the Néel temperature (see fig. 22). In the case of the $ThRh_{2-x}Ir_xSi_2$ system the Néel temperature decreases from 92 K for $x = 0$ to 75 K for $x = 0.5$ and for higher concentrations it remains constant. For $TbRh_{2-x}Ru_xSi_2$ system the T_N decreases rapidly to 10 K for $x = 0.5$ and next it increases from 10 K for $x = 1.0$ to 55 K for $x = 2.0$ (Jaworska and Szytuła 1988). A modified RKKY theory which included the interaction

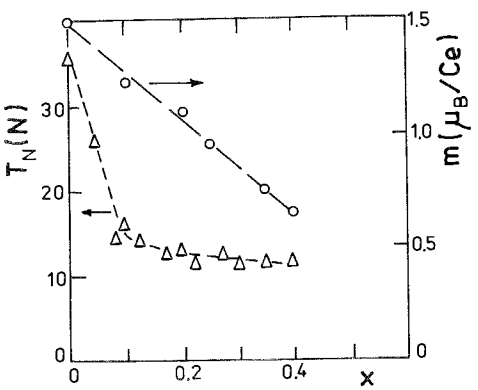

Fig. 21. The Néel temperature and the Ce^{3+} magnetic moment determined by neutron scattering of $Ce(Rh_{1-x}Ru_x)_2Si_2$ vs x (Lloret et al. 1987).

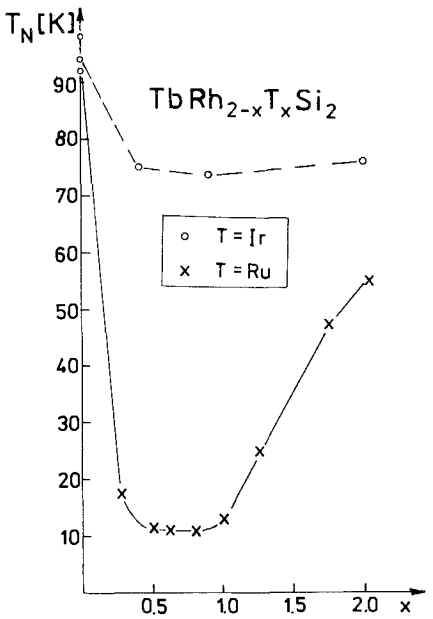

Fig. 22. The Néel temperature of $TbRh_{2-x}T_xSi_2$ (T = Ir, Ru) vs x (Jaworska and Szytuła 1988).

between the conduction electrions was applied to explain the variation of properties of the compounds.

The crystallographic and magnetic properties of $Ce(Ir_{1-x}Rh_x)_2Si_2$ are reported by Sujata Patil et al. (1987). Alloys with $x \leqslant 0.3$, in the as-cast state, crystallize in $CaBe_2Ge_2$-type primitive tetragonal structure and undergo a crystallographic transformation ($ThCr_2Si_2$-type body-centered structure) upon annealing at 875 K for two weeks. As-cast, as well as annealed alloys with $x \geqslant 0.4$ crystallize in the $ThCr_2Si_2$ type structure. The magnetic susceptibility $\chi(T)$ of the alloys of $CaBe_2Ge_2$ structure is essentially temperature independent with the Curie-like "impurity" tail at low temperatures. Cerium is in a strongly mixed valent state in these alloys. The $\chi(T)$ of the annealed alloys with a low Rh-concentration is characterised by a "$CeSn_3$ like" behaviour (Misawa 1974) whereas the $\chi(T)$ behaviour of the alloys with $x \geqslant 0.4$ suggests that the valence of Ce in these alloys is close to 3+. θ_p varying between -158 K and -47 K for $0.4 \leqslant x \leqslant 1.0$. The mixed valent behaviour of Ce atoms in $CaBe_2Ge_2$ type structure is observed.

$Eu(Pd_{1-x}Au_x)_2Si_2$ with $x \leqslant 0.25$ was investigated by means of the temperature dependent susceptibility, an electric resistivity and a high magnetization at 4.2 K and by the ^{151}Eu Mössbauer effect (Gupta et al. 1983, Segre et al. 1982). For $0 \leqslant x \leqslant 0.175$ the system undergoes a valence transition with the temperature (non-magnetic ground state). For $x \geqslant 0.2$ the system has antiferromagnetic transitions: $T_N = 32(1)$ K at $x = 0.2$ and $T_N = 28(1)$ K at $x = 0.25$.

3. Influence of physical properties on magnetism in RT_2X_2 compounds

Neutron diffraction data indicate that the rare earth sublattices exhibit a large variety of ordering schemes (see fig. 23):

1. collinear ferromagnetism (F) was found in $TbMn_2X_2$ and $ErMn_2X$ (X = Si, Ge),
2. four types of collinear antiferromagnetic structures:
   - type AFI with the wave vector $\boldsymbol{k} = (0, 0, 1)$ was observed in RCo_2X_2 (R = Pr–Tm), RRh_2Si_2 and RRh_2Ge_2 (R = Nd–Tm), $TbIr_2Si_2$, $PrCu_2X_2$ and $CeAu_2Si_2$,
   - type AFII with $\boldsymbol{k} = (0, 0, \frac{1}{2})$ was found in $NdFe_2Si_2$, $NdFe_2Ge_2$, $PrFe_2Ge_2$ and $ErFe_2Si_2$,

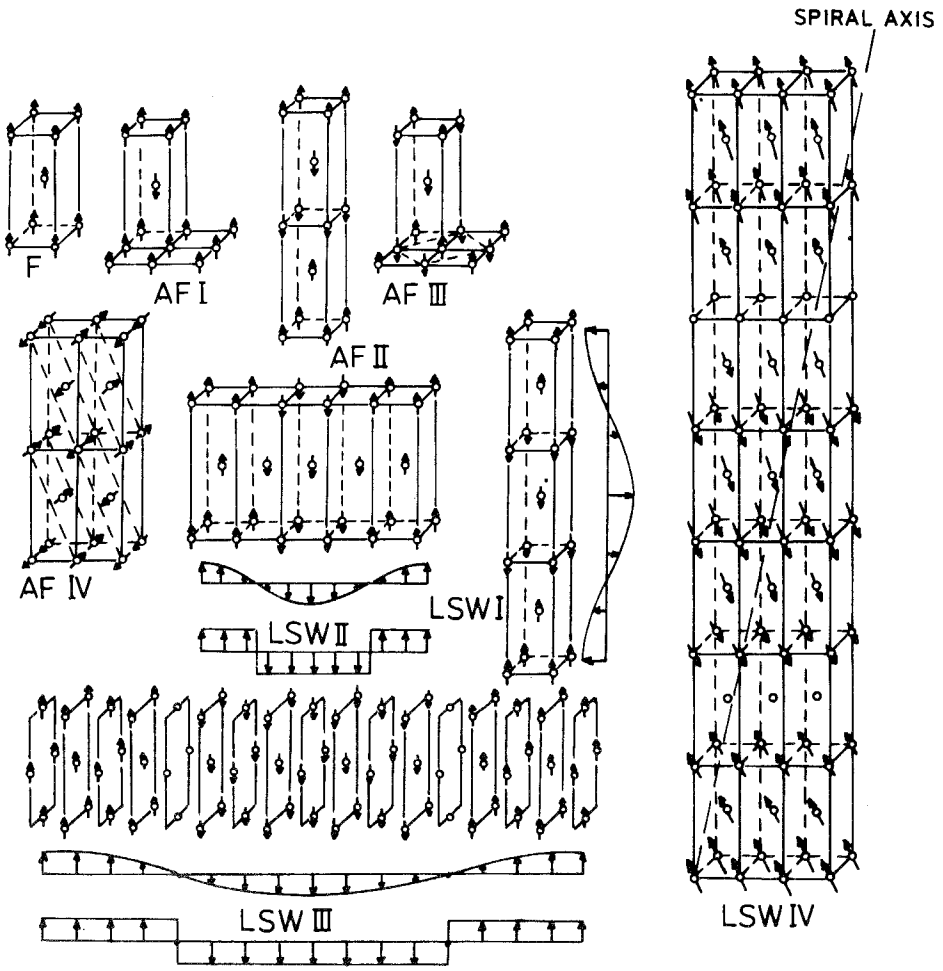

Fig. 23. The magnetic ordering of the R sublattice in RT_2X_2 compounds.

- type AFIII described by $\boldsymbol{k} = (\frac{1}{2}, \frac{1}{2}, 0)$ is adopted by $TbNi_2Si_2$, $CeRh_2Si_2$ and $CePd_2Si_2$,
- type AFIV with $\boldsymbol{k} = (\frac{1}{2}, 0, \frac{1}{2})$ is exhibited by RCu_2X_2 (R = Tb–Er).

3. a number of different non-collinear structures was also discovered:
   - cosinusoidally modulated longitudinal spin wave LSW I propagating along the c-axis was found in $PrCo_2Ge_2$, $HoNi_2Ge_2$ and $PrNi_2Si_2$,
   - cosinusoidally modulated longitudinal spin wave LSW II propagating along the a-axis operates in RRu_2Si_2 (R = Tb–Er), $TbRu_2Ge_2$, ROs_2Si_2 (R = Tb, Ho, Er) and $CeAg_2Si_2$. In the case of $TbRu_2Si_2$ and $TbRu_2Ge_2$ at low temperatures this type of magnetic structure transforms to the square modulated phase.
   - $NdRu_2Si_2$ and $NdRu_2Ge_2$ have complex magnetic structures. Below $T = 10$ K they are ferromagnetic with the moments parallel to c-axis. Above $T = 10$ K $NdRu_2Si_2$ has a cosinusoidally modulated longitudinal spin wave, LSW III, propagating along the [110] direction. A squaring of the magnetic structure is observed below $T = 15$ K. $NdRu_2Ge_2$ exhibits two types of sine wave modulated magnetic structures, having wave vectors $\boldsymbol{k} = (0.19, 0.05, 0.125)$ and $\boldsymbol{k} = (0.12, 0.12, 0)$ with the amplitude of the moment along the c-axis,
   - LSW IV is an incommensurate structure with two component wave vectors $\boldsymbol{k} = (k_x, 0, k_z)$ occurs in $TbFe_2Si_2$, $HoFe_2Si_2$, $TbPd_2Si_2$, $HoPd_2Si_2$ and $TbPd_2Ge_2$.

The Hamiltonian which describes the magnetic properties of an R ion is usually presented in the form:

$$H_{\text{tot}} = H_{\text{coul}} + H_{\text{exch}} + H_{\text{cf}} + H_{\text{ms}} + H_{\text{ext}},$$

where the term: H_{coul} represents the Coulomb interactions, H_{exch} describes the exchange interactions which in the case of rare-earth systems are usually described in terms of the RKKY theory, H_{cf} is the crystal electric field term, H_{ms} is bound to the magnetostriction effect, H_{ext} takes into account the interaction within an external magnetic field.

The available experimental data clearly indicate that the terms H_{exch} and H_{cf} are dominant in the description of the magnetic properties of the R ion in a crystal, so we shall discuss them in detail. But first we shall briefly summarize the information related to the magnetic ordering schemes which have been observed up to now in the ternary RT_2X_2 systems. They will be essential in further discussions.

3.1. *Exchange interactions*

Since the interatomic distances between two R atoms are always about 0.4 nm in the basal plane and about 0.6 nm along the c-axis, the assumption of the Heisenberg type interaction is not justified. The models involving indirect coupling are usually adopted to explain the stability of particular magnetic structures.

Since the 4f electrons are strongly localized and the RT_2X_2 systems show a metallic type of electric conductivity, the exchange interactions of 4f electrons can be described in terms of the well-known RKKY theory, which postulates the coupling between the moments via conduction electrons.

The other factors are the interaction of the f-electron shells with the crystal field CEF and the interactions with valence electrons of the anionic lattice via the hybridization orbitals.

The competition of these factors causes a large variety of magnetic structures in RT_2X_2 systems to occur. To estimate which of them plays the more important role in the particular compound, a plot of the observed Néel points against the de Gennes factor $(g-1)^2J(J+1)$ was constructed (see fig. 24). The following conclusions can be drawn from it:

- the de Gennes function is not obeyed in RT_2X_2 compounds containing light rare-earth ions. In many cases the compounds remain paramagnetic above 1.8 K,
- in the case of heavy rare-earth ions, the Néel points follows in principle the de Gennes function, however, large discrepancies are observed when T = Cu, Ru, Os.

These observations suggest that different mechanisms of interaction are decisive

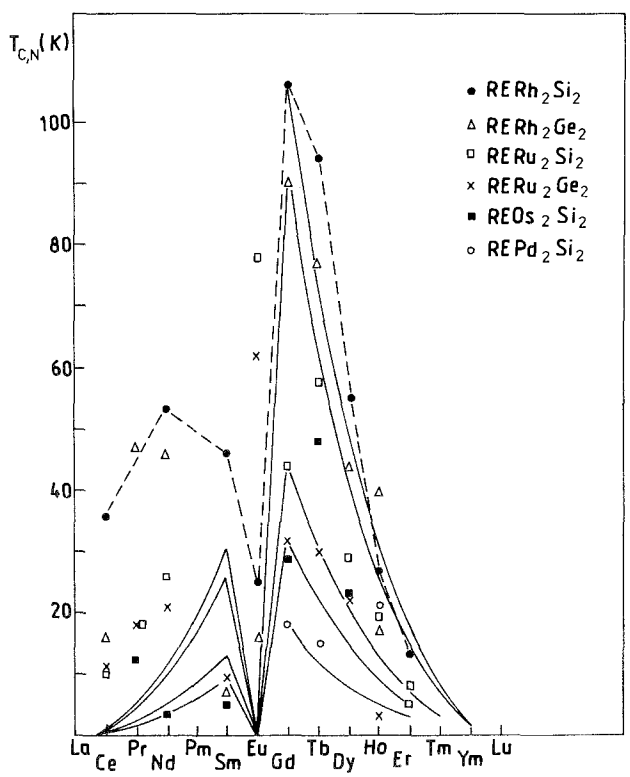

Fig. 24. The Néel or the Curie temperatures observed for RT_2X_2 compounds and their relation to the de Gennes function.

in the magnetic structure of the RT_2X_2 systems with light and heavy rare-earth ions.

Attempts to connect the Néel points with the interatomic distances along the *a*- and *c*-axes do not provide any satisfactory correlations (Szytuła and Leciejewicz 1987), however, in the TbT_2X_2 series the oscillatory character of the Néel or Curie temperature is caused by the increase in d-electron number (see fig. 25). Similar effect is observed in magnetically isostructural ErT_2Si_2 (Leciejewicz et al. 1983), EuT_2Ge_2 and GdT_2Ge_2 (Felner and Nowik 1978) compounds suggesting that while the magnetic interactions may be discussed in terms of the RKKY model, the number of free electrons donated to the conduction band depends on the number of d-electrons. In the RFe_2Si_2 systems where the absence of a local moment on the Fe atom has been found, the observed magnetic fields on the ^{57}Fe site are in reasonable agreement with conduction electron polarization by rare earth moments (Noakes et al. 1983).

In an isotropic RKKY model with a spherical Fermi surface, the Fermi vector is strongly dependent on the c/a ratio and on the number of free electrons Z per magnetic ion:

$$2k_F = \frac{2\pi}{a}\sqrt{\frac{6Z}{\pi}\frac{a}{c}}.$$

The analysis of a/c values determined for a large number of RT_2X_2 systems containing heavy rare-earth ions (R = Tb–Tm) shows, that when $a/c < 0.415$, a simple collinear antiferromagnetic ordering is observed, while the compounds

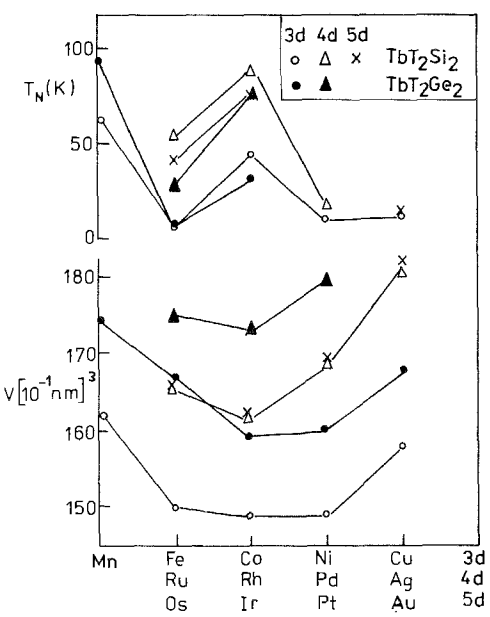

Fig. 25. The dependence the Néel temperatures and the atomic volumes for TbT_2X_2 compounds (T = 3d, 4d and 5d transition metal, X = Si or Ge) in the function of the atomic numbers of T elements.

with $a/c > 0.415$ exhibit oscillatory magnetic structures (Leciejewicz and Szytuła 1987).

Following the RKKY theory, the energy E of a spin system with an oscillatory character of ordering is given by:

$$E = -N\langle \mu^2 \rangle J(\boldsymbol{k}),$$

where N is the total number of magnetic ions in the system, $\langle \mu \rangle$ is the average value of the magnetic moment, $J(\boldsymbol{k})$ represents the Fourier transform of the exchange integral $J(\boldsymbol{R}_i - \boldsymbol{R}_j)$ between i and j magnetic ions, positions of which are given by the vectors $\boldsymbol{R}_i$ and $\boldsymbol{R}_j$, respectively. Assuming that the interaction integral $J(\boldsymbol{k})$ remains constant, the energy E is directly proportional to a function expressed as

$$-F(\boldsymbol{k}) \sim -[J(\boldsymbol{k}) - J(0)].$$

The stability of a particular magnetic structure means that the functions $F(\boldsymbol{k})$ exhibits a maximum for non-zero values of $\boldsymbol{k}$ (the wave vector of the magnetic structure) (Yosida and Watabe 1962).

The computation of $F(\boldsymbol{k})$ function against $\boldsymbol{k}$ for particular values of k_F (or Z) permits one to select those values of $\boldsymbol{k}$ for which $F(\boldsymbol{k})$ exhibits a maximum. Figure 26 shows the range of $\boldsymbol{k} = (k, 0, 0)\boldsymbol{a}^*$ for which $F(\boldsymbol{k})$ attains maxima, plotted against the number of free electrons per Tb^{3+} ion in $TbRu_2Si_2$ (Ślaski et al. 1984). For these compounds the observed value of the magnetic structure vector $\boldsymbol{k}$ is $0.233\boldsymbol{a}^*$. It corresponds to $Z = 3.13$ free electrons per Tb^{3+} ion. The Z and k values obtained for a number of RT_2X_2 compounds are listed in table 14. In RT_2X_2 compounds the observed magnetic ordering scheme requires 3 free electrons per R^{3+} ion. It could indicate that 6s and 5d electrons of R^{3+} ion are donated to the conduction band. Valence electrons of the other atoms contribute to the chemical bonding. On the other hand the chemical shift measurements performed by the X-ray absorption spectroscopy method (XAS) indicate that electrons of all constituents i.e. of R, T and X atoms contribute to the conduction

TABLE 14
The values of k and Z obtained for RT_2X_2 compounds.

Compound	k	Z	Ref.	Compound	k	Z	Ref.
$TbRu_2Si_2$	$0.233a^*$	3.13	a	RCo_2X_2	$1.0c^*$	2.75–3.75	d
$DyRu_2Si_2$	$0.22a^*$	3.136	a	RRh_2Si_2	$1.0c^*$	2.77–3.39	d
(Ho, Er)Ru_2Si_2	$0.2a^*$	3.16	a	$TbRh_2Ge_2$	$1.0c^*$	2.84–3.2	e
$TbRu_2Ge_2$	$0.235a^*$	3.0	b	$NdRu_2Si_2$	$0.0c^*$	2.67–3.4	d
$TbOs_2Si_2$	$0.312a^*$	3.0	c	$NdFe_2Si_2$	$0.5c^*$	1.4	d
(Ho, Er)Os_2Si_2	$0.295a^*$	3.02	c				

References:
(a) Ślaski et al. (1984), (b) Yakinthos (1986a), (c) Kolenda et al. (1985), (d) Leciejewicz and Szytuła (1987), (e) Szytuła et al. (1987).

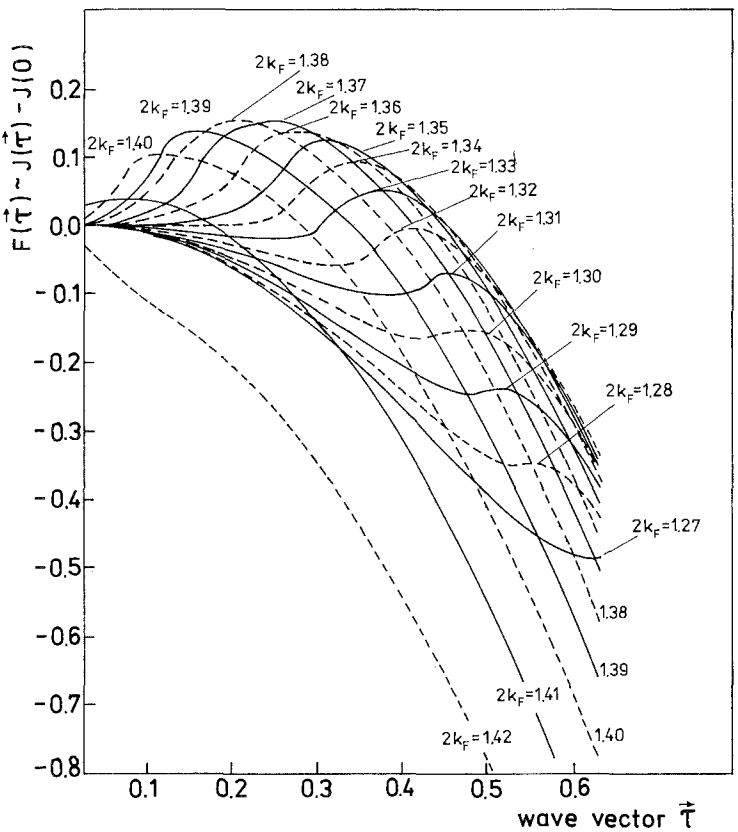

Fig. 26. A plot of the $F(k)$ function against the wave vector k for different values of $2k_F$ (Fermi vector) in $TbRu_2Si_2$ (Ślaski et al. 1984).

band (Darshan et al. 1984). The Fourier map of the electron density obtained recently for $DyCo_2Si_2$ (Szytuła et al. 1988) shows Si–Co–Si layers that form an independent sandwich with saturated electric charge.

The comparison of the effective hyperfine magnetic fields H_{eff} in DyT_2X_2 compounds and of the respective magnitudes of the ordered magnetic moment u derived from neutron diffraction experiments gives the relation $H_{eff}(\text{kOe}) \sim 600\mu$ (μ_B). This result may be considered as evidence for the localization of 4f electrons (Pinto et al. 1983).

3.2. *Crystalline electric fields*

The interaction of crystalline electric fields (CEF) with the multiple moments of R atom electrons in a site of a crystal lattice of 4/mmm point symmetry is given by the Hamiltonian

$$H_{cf} = B_2^0 O_2^0 + B_4^0 O_4^0 + B_4^4 O_4^4 + B_6^0 O_6^0 + B_6^4 O_6^4,$$

where O_n^m is the Stevens operator, B_n^m is a CEF parameter defined by Hutchings (1964). The c-axis of a tetragonal unit cell was chosen as a quantization axis.

The values of the B_n^m coefficient can be derived from experimental data obtained from the magnetic susceptibility, the Schottky specific heat, the hyperfine structure, the magnetic form factor and the neutron inelastic scattering measurements. The B_n^m values are shown in table 15. It can be seen that the B_2^0 coefficient is dominant since the others are smaller by an order of magnitude.

The orientation of the magnetic moment in respect to the tetragonal axis can be connected with the sign of the B_2^0 coefficient. It was shown (Greedan and Rao 1973) that when the magnetic moment is normal to the tetragonal axis or makes an angle φ with it, B_2^0 is positive. For a negative value of B_2^0 coefficient the magnetic moment is parallel to the c-axis. Table 16 contains the values of B_2^0 coefficients determined for a number of RT_2X_2 compounds. These data indicate that the correlation between the signs of the B_2^0 coefficient and the orientation of magnetic moments agrees with that deduced from neutron diffraction experiments. However, it has been shown, that the sign of B_2^0 depends also on the number of 4f and nd electrons, but the lack of data does not permit us to plot a detailed diagram.

The influence of a crystal field on the direction and magnitude of magnetic moments in RT_2X_2 systems where R = Pr, Tb, Er and Tm will be discussed further.

The determined values of B_n^m coefficients for $PrNi_2Si_2$ (Barandiaran et al. 1986) indicate that the ground state is a non-magnetic singlet. Another non-magnetic singlet is the first excited state separated by 2 K in the energy scale. A doublet at 73 K is the second excited state. Such level scheme is consistent with the modulated magnetic structure observed below 5.5 K.

The CEF splittings in TbT_2X_2 indicate that the ground state of Tb^{3+} is formed by two very close singlets $\frac{1}{2}\{|6\rangle + |-6\rangle\}$ and $\frac{1}{2}\{|6\rangle + |-6\rangle\}$. In this case the magnetic moments are quenched along the c-axis giving rise to the Ising-like behaviour. The first excited state is at 100 K in $TbFe_2Si_2$ (Noakes et al. 1983) and 50 K in $TbRu_2Ge_2$ (Yakinthos 1986). In all TbT_2X_2 compounds the magnitude of the magnetic moment localized on Tb^{3+} ion equals the magnetic moment value of the Tb^{3+} free ion $gJ = 9\ \mu_B$.

In all ErT_2X_2 systems the magnetic moment on Er^{3+} is smaller than the free ion value of 9 μ_B. The magnetic moment is perpendicular to the tetragonal axis in all ErT_2X_2 compounds except $ErCu_2Ge_2$. The case of $ErCu_2Ge_2$ may be explained by considering the influence of CEF. The level scheme for the Er^{3+} ion was deduced assuming that the charge is localized on the Er and is zero on Cu. The magnetic moment is given by:

$$\mu_x = \mu_B g \langle a_+ | J_x | a_- \rangle \qquad \mu_z = \mu_B g \langle a_+ | J_z | a_- \rangle$$

where $|a_+\rangle$ and $|a_-\rangle$ are two wave functions of the fundamental doublet, $|a_-\rangle$ is the time conjugate of $|a_+\rangle$, g is the Lande factor, J_x and J_z are x- and z-component of the rare-earth total angular momentum, μ_x and μ_z as the

TABLE 15
The values of B_n^m coefficients of crystal electric field.

Compound	$CeCu_2Si_2$ [a]	$TmCu_2Si_2$ [b]	$TmFe_2Si_2$ [c]	$DyCo_2Si_2$ [d]	$DyFe_2Si_2$ [d]	$HoRh_2Si_2$ [e]	$PrNi_2Si_2$ [f]
B_2^0(K)	-3.0 ± 1.0	$+0.12 \pm 0.02$	+2.53	−1.0	−1.8	−0.22	−3.99
B_6^0(K)	-0.4 ± 0.1	−0.0312(3)	−0.017	−0.0062	−0.0039	+0.0011	+0.0016
B_4^4(K)	-0.24 ± 0.1	−0.049(3)	+0.049			−0.002	+0.156
B_6^4(K)		−0.00014	0	+0.00003	+0.000025		+0.00013
B_6^6(K)		+0.00126	+0.002				−0.00032

References:
(a) Horn et al. (1981), (b) Stewart and Żukrowski (1982), (c) Umarji et al. (1984), (d) Görlich (1980), (e) Takano et al. (1987), (f) Barandiaran et al. (1986).

TABLE 16
The values of B_2^0 coefficients and direction of magnetic moment for RT_2Si_2 compounds.

R/T	Mn	Fe	Co	Ni	Cu	Rh
Ce					-3.0^{r}	$\perp c^{x}$
Pr	-0.7^{a}, $\|c^{a}$		$\|c^{k,j}$	-3.99^{q}, $\|c^{q}$	$\|c^{s}$	
Nd		-0.63^{d}, $\|c^{e}$	$\|c^{k}$			$\|c^{A}$
Tb	$\|c^{b}$	-3.0^{d}, $\|c^{f}$	$\|c^{j,k,l,m}$	$\|c^{l}$	$+0.8^{t}$, $\perp c^{u,m}$	-2.4^{w}, $\|c^{z,w}$
Dy	-1.35^{c}	-1.8^{cd},	-1.0^{c}, $\|c^{i,n}$	$+0.17^{c}$	$+0.57^{c}$, $\perp c^{n}$	φ^{B}
Ho		-0.61^{d}, φ^{g}	$\|c^{k,m,o,l}$		$+0.175^{t}$, $\perp c^{u,m}$	-0.22^{y}, φ^{z}
Er	c^{h}	$+0.67^{d}$, $\perp c^{h}$	$\perp c^{k}$, φ^{p}		-0.2^{t}	$\perp c^{A}$
Tm		$+2.54^{d}$	$\perp c^{i}$		-0.79^{t}, $+0.12^{v}$	$\perp c^{C}$
Yb		$+7.65^{d}$				

References:
(a) Iwata et al. (1986), (b) Shigeoka et al. (1986), (c) Görlich et al. (1982), (d) Noakes et al. (1983), (e) Pinto and Shaked, (1973), (f) Szytuła et al. (1987b), (g) Leciejewicz and Szytuła (1985), (h) Leciejewicz et al. (1984), (i) Leciejewicz and Szytuła (1983), (j) Yakinthos et al. (1984), (k) Leciejewicz et al. (1983), (l) Nguyen et al. (1983), (m) Pinto et al. (1985), (n) Pinto et al. (1983), (o) Schobinger-Papamantellos et al. (1983), (p) Yakinthos et al. (1983), (q) Barandiaran et al. (1986), (r) Horn et al. (1981), (s) Szytuła et al. (1983), (t) Budkowski et al. (1987), (u) Leciejewicz et al. (1986), (v) Stewart and Żukrowski (1982), (w) Chevalier et al. (1985), (z) Ślaski et al. (1983), (x) Quezel et al. (1984), (y) Takano et al. (1987), (A) Szytuła et al. (1984), (B) Melamud et al. (1984), (C) Yakinthos (1986a).

magnetic moment in x and z directions (x is normal to z). The wave functions were calculated to be:

$$|a_{\pm}\rangle = 0.156|\pm 7/2\rangle + 0.984|\pm 1/2\rangle + 0.081|\pm 9/2\rangle$$

hence $\mu_x = 4.8\ \mu_B$ and $\mu_z = 0.5\ \mu_B$. However, the model does not agree with experimental data. If one assumes that the charge on Cu ion is non-zero, the splitting of the $|\pm 15/2\rangle$ multiplet is reversed and the fundamental doublet has $|\pm 15/2\rangle$ as its strongest component. The calculated wave functions for $q_{Cu} = 0.6^{+}$ are:

$$|b_{\pm}\rangle = 0.920|\pm 15/2\rangle + 0.249|\pm 9.2\rangle + 0.297|\pm 1/2\rangle$$

and then the moments are $\mu_x = 0.4\ \mu_B$ and $\mu_z = 7.9\ \mu_B$. The direction of the magnetic moment is along the c-axis of the crystal. These results are in agreement with the neutron diffraction experiment (Yakinthos 1985).

In the case of $TmRh_2Si_2$, $TmFe_2Si_2$ and $TmCu_2Si_2$, the ground state of Tm is deduced to be $|0\rangle$ and the first excited state is $|\pm 1\rangle$ at 49 K for $TmRh_2Si_2$ (Yakinthos 1986a), 8 K for $TmCu_2Si_2$ (Stewart and Żukrowski 1982) and 8 K for $TmFe_2Si_2$ (Umarji et al. 1984). Such splitting leads to the reduction of the magnetic moment value on Tm^{3+} ion yielding 4.2 μ_B in $TmRh_2Si_2$ (Yakinthos 1986a) and 3.2 μ_B in $TmCu_2Si_2$ (Kozłowski 1986). Both μ values are smaller than the free Tm^{3+} ion value of 7 μ_B.

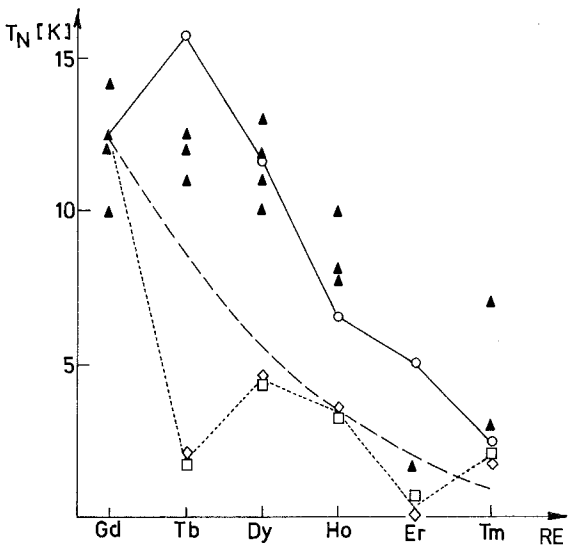

Fig. 27. Comparison of experimental (solid triangles) and calculated magnetic transition temperatures T_N for the RCu_2Si_2 family. Dashed smooth line represents the de Gennes rule. Broken lines are trends obtained on the basis of the molecular field model (Noakes and Shenoy 1982) including CEF effects. Broken solid line (open circles) indicates T_N's predicted by the B_2^0 model with A_2^0 as for $GdCu_2Si_2$ (Łątka et al. 1979). Broken dashed line (open squares) represents calculations with full CEF Hamiltonian ($5A_l^m$ parameters are, according to Stewart and Żukrowski (1982) –□ and according to Kozłowski (1986) –◇).

The observed values of magnetic transition temperatures of RCu_2Si_2 compounds do not follow the de Gennes rule (see fig. 27), but if a CEF Hamiltonian H_{cf} is added to the exchange Hamiltonian, the agreement with the de Gennes function improves rapidly (Noakes and Shenoy 1982):

$$H = -2\mathcal{J}(g-1)^2 J_z \langle J_z \rangle + B_2^0[3J_z^2 - J(J+1)].$$

The magnetic ordering temperature is given by

$$T_N = 2\mathcal{J}(g-1)^2 \sum_{J_z} J_z^2 \exp(-3B_2^0 J_z^2/T_N) \times \left\{ \sum_{J_z} \exp(-3B_2^0 J_z^2/T_N) \right\}^{-1}.$$

The deduced values of B_2^0 are as follows: 0.8 K for Tb, 0.5 K for Dy, 0.175 K for Ho, −0.199 K for Er and −0.789 K for Tm (Budkowski et al. 1987).

The results show that the crystal electric field has a significant effect on the magnetic properties of these compounds.

3.3. *Magnetocrystalline anisotropy*

The magnetization curves determined along the easy and hard directions of magnetization for RMn_2X_2 compounds (see fig. 7) suggest that the magnetic

anisotropy is large. The anisotropy energy E_a in the tetragonal lattice is expressed as

$$E_a = K_1 \sin^2 \theta + K_2 \sin^4 \theta + K_3 \sin^4 \theta \sin^2 \phi \cos^2 \phi,$$

where K_n are the nth order anisotropy constants, θ and ϕ are the angles between the magnetization vector and the c- and a-axes, respectively. The anisotropy constants K_1 and K_2 can be determined from the relation:

$$\frac{H_{\text{eff}}}{M} + \frac{2K_1}{M_s^2} + \frac{4K_2}{M_s^4} M^2$$

in the case when the easy axis is parallel to c-axis and

$$\frac{H_{\text{eff}}}{M} = -2\frac{K_1 + 2K_2}{M_s^2} + \frac{4K_2}{M_s^4} M^2,$$

when the easy axis is perpendicular to the c-axis. The H_{eff} term is the effective magnetic field, M is the magnetization and M_s is the saturation magnetization. The K_1 and K_2 coefficients for RMn_2X_2 compounds are listed in table 17. The large anisotropies observed in these compounds originate mainly from a single ion anisotropy due to the crystal field effect. Since Gd^{3+} ion is in the S state, the anisotropy energy in $GdMn_2Ge_2$ is smaller than in the other compounds.

3.4. *Linear magnetostriction*

A systematic study of rare-earth single ion magnetostriction was reported for the first time in the $R_xY_{1-x}Cu_2Si_2$ compounds with $x = 0.05$ for R = Pr, Nd, Sm, Gd with $x = 0.1$ for R = Tb–Tm and in $ErCu_2Si_2$ (Rüßmann et al. 1982). Figure 28 shows the isothermal longitudinal magnetostriction MS curves. The MS values are positive in the case of R = Sm, Tm, Er impurity and negative for Pr, Nd, Gd, Tb, Dy and Ho impurities.

For a quantitative analysis of the MS curves the knowledge of the crystal field effect is required. It is assumed that there is an anisotropic charge distribution bound axially to the 4f magnetic moment localized on the R^{3+} ion. It causes a distortion of the lattice when the magnetic moment becomes aligned either by an external or internal magnetic fields. The dominant factor of the charge distribution and hence the dominant distortion of the lattice around a R^{3+} ion is the quadrupolar moment (Nicholson et al. 1978). In fact, all MS curves look similar to that which is expected for a thermal average of the quadrupolar operator

$$Q_{zz} = 3J_z^3 - J(J+1)$$

as a function of $\chi = (g\mu_B/k)(H/T)$

$$\frac{\Delta l}{l} = xQ_s(2J-1)^{-1}[2(J+1) - 3m_J(\chi)\,\text{ctgh}(\chi/2)]$$

TABLE 17
The values of anisotropy constants K_1 and K_2 for RMn_2X_2 compounds.

	RMn_2Ge_2							
R	La	Pr	Gd	Tb	Dy	Ho	Er	$TbMn_2Si_2$
K_1 (erg/cm^3)	2.2×10^6	5.3×10^7	5.4×10^6	8.4×10^7	1.3×10^8	-4.2×10^8	2.2×10^8	
K_2 (erg/cm^3)	10^4		3.6×10^6					
direction of magnetic moment	[001]	[001]	[001]	[001]	[001]	[001]	[110]	[001]
Ref.	a	b	c	c	c	c	c	d

References:
(a) Shigeoka (1985), (b) Iwata et al. (1986), (c) Shigeoka (1984), (d) Shigeoka et al. (1986).

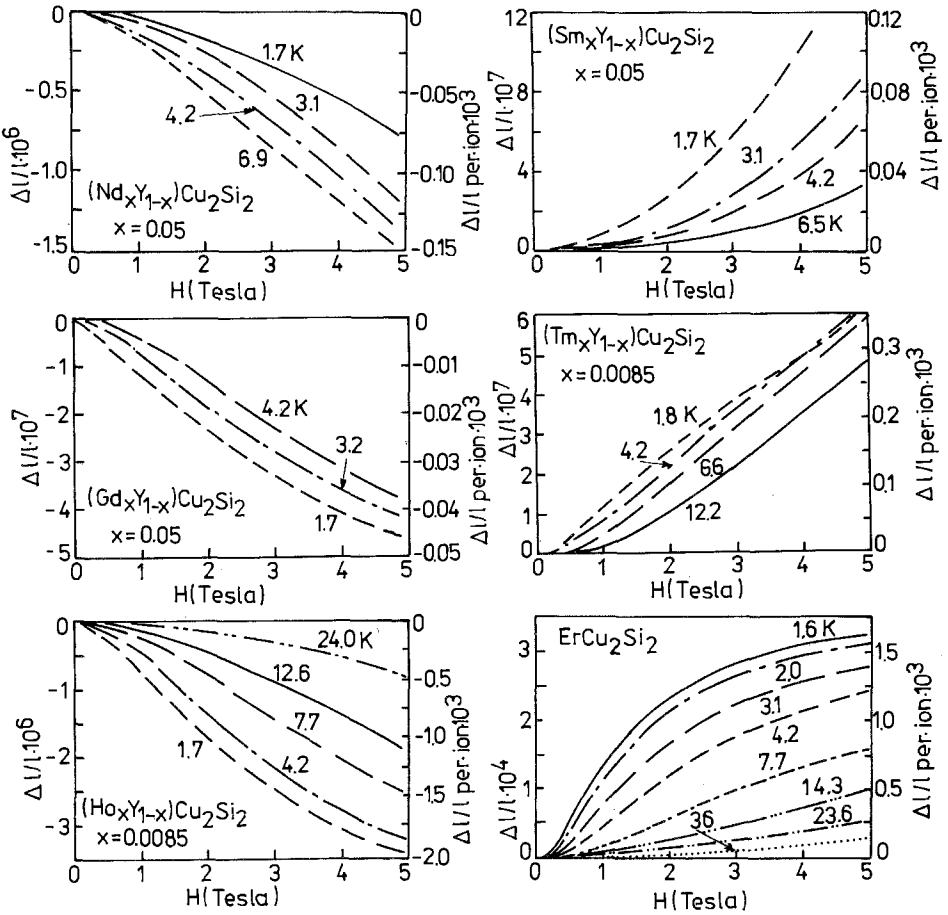

Fig. 28. Magnetostriction of R-impurities in $Y_{1-x}R_xCu_2Si_2$ (R = Nd, Sm, Gd, Ho and Tm) and $ErCu_2Si_2$ (Rüßmann et al. 1982).

where $m_J(\chi)$ is the Brillouin function, x is the concentration of R^{+3} impurity, Q_s is the saturated quadrupole moment. The values of Q_s are listed in table 18, and are supported by the lattice data $\Delta(c/a)$ and $\Delta c/c$ (Schlabitz et al. 1982). Both types of lattice distortions are caused by the asphericity of the rare earth charge distribution due to aspherical screening of the nuclear charge. This asphericity has an axis permanently bound to the axis of the magnetic moment. The results listed in table 18 imply that in R = Pr, Nd, Tb, Dy, Ho the axis of the magnetic moment is aligned along the axis of the charge distribution shaped like an oblate spheroid (the negative sign of the Stevens factor), while for R = Sm, Er and Tm, the magnetic moment is parallel to the axis of a prolate spheroid (the positive sign of the Stevens factor). The positive sign of the c-axis anomaly (Schlabitz et al. 1982) indicates, that for R = Sm, Er and Tm the axis of the magnetic moment at low temperatures is parallel to the tetragonal symmetry axis (the c-axis of the unit

TABLE 18
Saturation values Q_s, obtained by fit experimental data $\Delta l/l$ and structural data for $Y_{1-x}R_xCu_2Si_2$[(a)].

R	Pr	Nd	Sm	Gd	Tb	Dy	Ho	Er	Tm
Q_s (10^3 ion)	−4.9	−0.38	+1.5	−0.1[(x)]	−6.3	−9.3	−3.1	+2.5	+1.2

(x) estimated value.
References:
(a) Rüßmann et al. (1982).

cell), while for R = Pr, Nd, Tb, Dy and Ho it is perpendicular to it. Neutron diffraction data obtained for RCu_2X_2 compounds (R = Tb, Dy, Ho) (Pinto et al. 1983, Kotsanidis et al. 1984, Schobinger-Papamantellos et al. 1984, Pinto et al. 1985, Leciejewicz et al. 1986) indicate that the magnetic moment localized on the R^{3+} ions lie in the basal plane i.e. perpendicularly to the c-axis, while for R = Er and Pr (Yakinthos 1985, Szytuła et al. 1983) they are aligned along it. Only in the case of $PrCu_2X_2$ compounds the Stevens rule does not work.

3.5. *Magnetoelastic effects*

There is a number of elastic properties which influence the magnetism of investigated compounds.

The temperature dependence of the thermal expansion $\Delta l/l$ of the RMn_2Ge_2 polycrystalline samples are shown in fig. 10 (Shigeoka 1984). Sharp jumps are observed at T_m, corresponding to the first order transition. Bends are observed at T_N. For example, in $GdMn_2Ge_2$ a discontinuous lattice contraction of $\Delta l/l \sim 10^{-3}$ occurs at T_m. The magnetoelastic energy can be estimated to be of the order of 0.1 K per magnetic atom, which is smaller than the energy of the exchange interaction but only slightly smaller than the energy of the magnetocrystalline anisotropy ($E_a \sim 1$ K/Gd atom).

3.6. *Magnetic ordering in transition metal sublattice*

The characteristic feature of RT_2X_2 system is that, except for Mn compounds, no magnetic moment is localized on the transition metal atom. This comment is based on magnetometric and neutron diffraction measurements, and is supported, in the case of RFe_2X_2 and RNi_2X_2 compounds, by the Mössbauer studies (Łątka et al. 1979, Noakes et al. 1983). Line broadenings observed at liquid helium and subhelium temperatures are attributed to the conduction electron polarization at the iron site caused by the magnetic ordering of the R sublattice. Only in the RMn_2X_2 systems does the Mn sublattice exhibit a long range magnetic ordering apart from the ordering of R magnetic moments. The ordering temperatures of RMn_2X_2 are in the range of 300–500 K and they are larger than those of the f-electron metal sublattice.

The Mn sublattice is either ferromagnetic or antiferromagnetic (see fig. 29). It

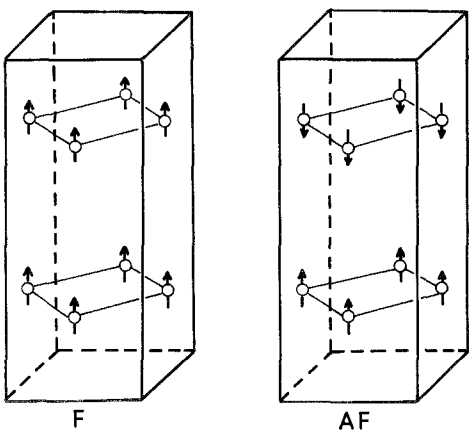

Fig. 29. The magnetic structure of Mn sublattices in RMn_2X_2 compounds.

consists of ferromagnetic layers stacked along the c-axis and coupled either ferromagnetically (sequence + + + +) or antiferromagnetically (sequence + − + −).

The magnetic moment equals 1.5–3.0 μ_B per Mn atom and it is observed to be aligned along the c-axis.

To decide whether the magnetism of RMn_2X_2 compounds may be discussed in terms of itinerant or localized moments, the ratio n_c/n_s should be estimated. The n_c and n_s are the magnetic carrier numbers derived from the Curie constant and the spontaneous moment at zero K. The n_c/n_s ratio in the range of 1.0–2.87 indicates that the magnetic properties of RMn_2X_2 compounds cannot be explained in terms of the itinerant model only.

The electronic structures of antiferromagnetic YMn_2Ge_2, a ferromagnetic $LaMn_2Ge_2$ and a paramagnetic $LaCo_2Ge_2$ were calculated by KKR method (Asano and Yamashita 1972) using LSD (Local Spin Density) approximation (Ishida et al. 1986). A crystal potential of the muffin-tin type was used. The density of state (DOS) curves of 3d electrons belonging to Mn or Co atoms and of 5d and 4f electrons of Y and La atoms are shown in fig. 30. The results obtained for YMn_2Ge_2 indicate that s-bands of Ge atoms and their p-states strongly hybridize with Mn d-states in the region from 0.2 to 0.7 Ryd. The values of DOS at the Fermi level $N(E_F)$ are 20 states/(atom spin Ryd.) and 29 states/(atom spin Ryd.) for antiferromagnetic YMn_2Ge_2 and ferromagnetic $LaMn_2Ge_2$, respectively, and they satisfy the Stoner condition for ferromagnetism. The threshold value of $N(E_F)$ is expected to be in the range from 15 to 20 states/(atom spin Ryd.) when the Stoner condition is fulfilled. In $LaCo_2Ge_2$ the Co band is below the Fermi level. The value of $N(E_F)$ is 8 states/(atom spin Ryd.). The Stoner condition is thus not fulfilled. Consequently $LaCo_2Ge_2$ is a paramagnet. The majority of $\uparrow$-spin states and the minority $\downarrow$-spin states for ferromagnetic $LaMn_2Ge_2$ are displayed in fig. 31. The calculated magnetic moment of Mn atom is 1.95 μ_B and it is much larger than the experimental value of 1.55 μ_B (Shigeoka et al. 1985).

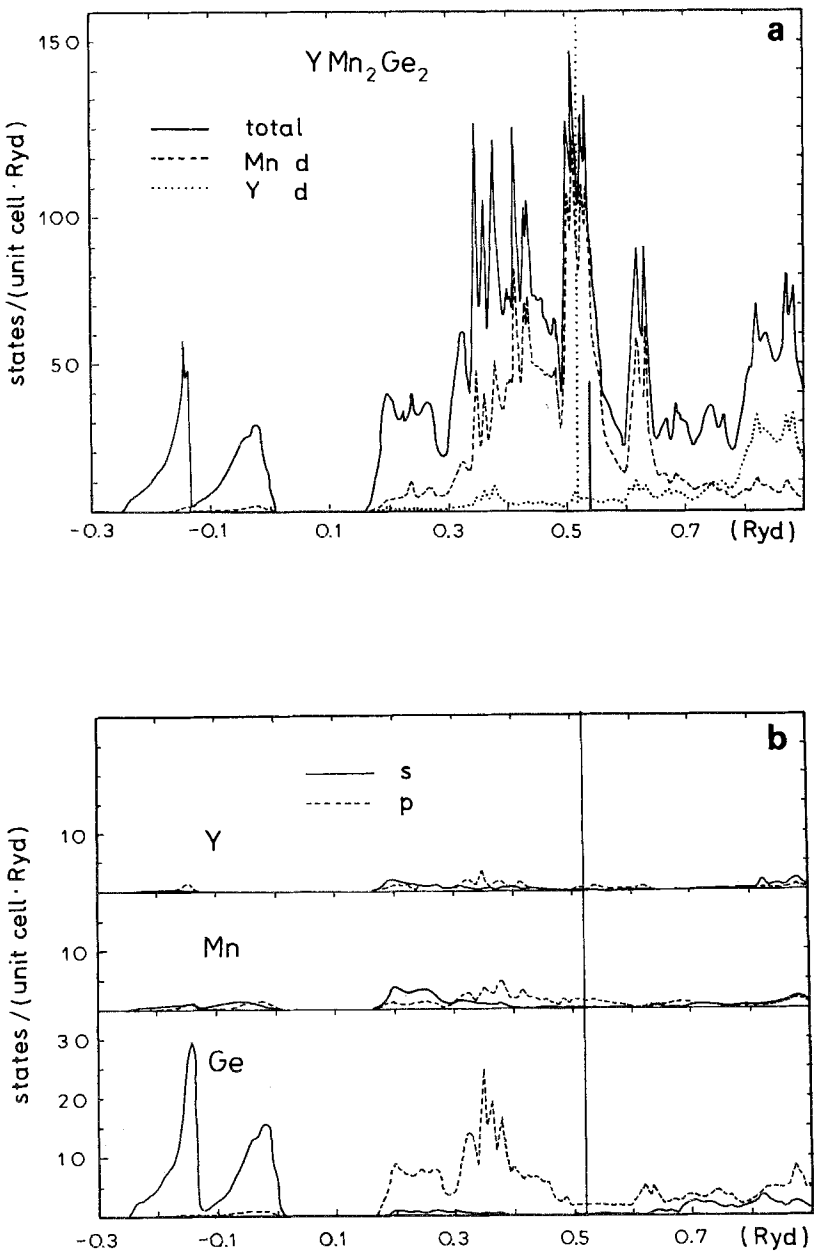

Fig. 30. The density-of-states (DOS) curves of YMn_2Ge_2. (a) The DOS curves of d states of Y and Mn are shown by the dotted and broken curves, respectively. The Fermi level is shown by the vertical dotted line. The Fermi level of YFe_2X_2 (X = Si, Ge) is also shown by the vertical solid line, assuming that the rigid-band-model is reasonable. (b) The DOS curves of s and p states are shown by the solid and broken curves for Y, Mn and Ge (Ishida et al. 1986).

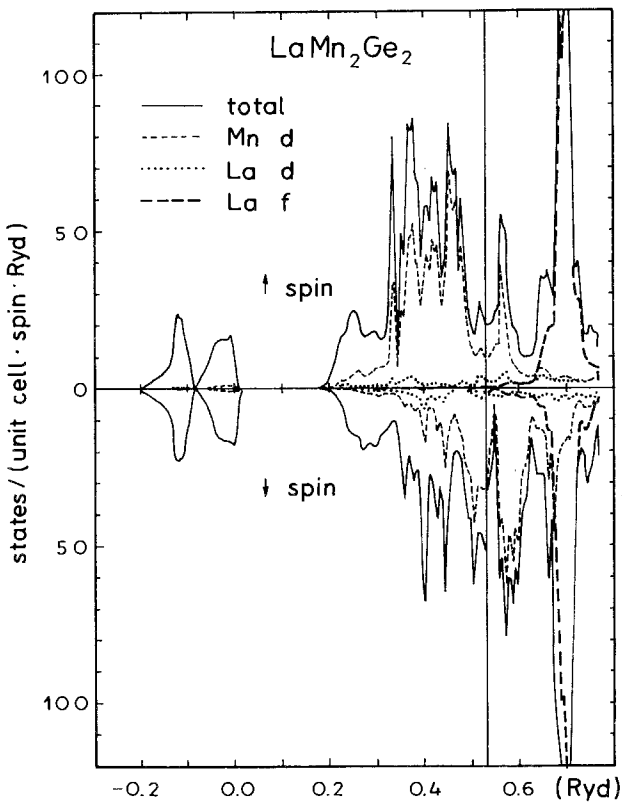

Fig. 31. The DOS curves of d and f states of La and d state of Mn are shown for both spin-states by the dotted, dashed and broken curves, respectively (Ishida et al. 1986).

The magnetic transition temperatures of RMn_2X_2 compounds are plotted in fig. 32 against the Mn–Mn distances within the layer R_a and between two Mn–Mn layers R_c. It appears that the respective temperatures follow a curve that is a function of R_a but it is not a function of R_c. It is seen that there is a critical distance of R_a of about 0.285 nm. Antiferromagnetic coupling exists when R_a is less than 0.285 nm and ferromagnetism appears for $R_a > 0.285$ nm. Similar critical distances were observed in many Mn alloys with transition metals (Tebble and Craik 1969).

Goodenough (1963) suggested that the localization–delocalization effect of 3d electrons occurred when the critical distance in Mn compounds was 0.285 nm.

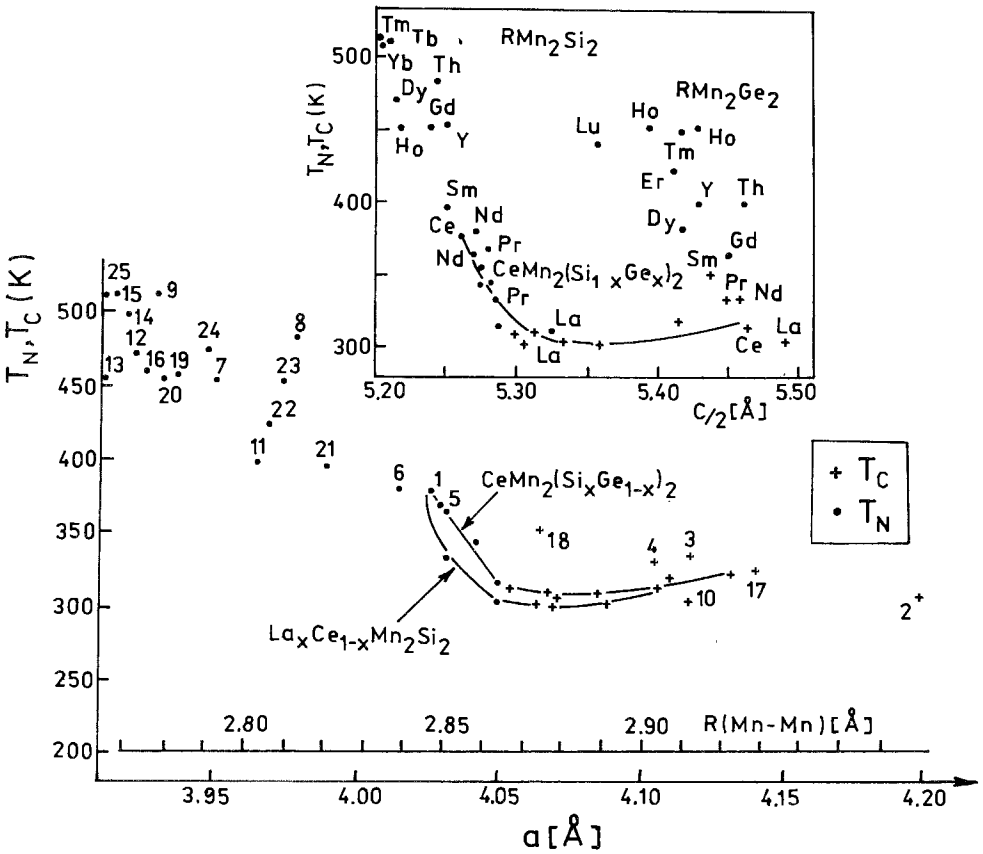

Fig. 32. The dependence of Néel or Curie temperature upon interlayer (*c*-constants) and intralayer (*a*-constants) distances (Szytuła and Siek, 1982). 1–$PrMn_2Si_2$, 2–$LaMn_2Ge_2$, 3–$PrMn_2Ge_2$, 4–$NdMn_2Ge_2$, 5–$GdMn_2Ge_2$, 6–$NdMn_2Si_2$, 7–$GdMn_2Si_2$, 8–$DyMn_2Ge_2$, $DyMn_2Ge_2$, 9–$TbMn_2Si_2$, 10–$LaMn_2Si_2$, 11–$SmMn_2Si_2$, 12–$DyMn_2Si_2$, 13–$HoMn_2Si_2$, 14–$ErMn_2Si_2$, 15–$YbMn_2Si_2$, 16–YMn_2Si_2, 17–$CeMn_2Ge_2$, 18–$SmMn_2Ge_2$, 19–$TmMn_2Ge_2$, 20–$LuMn_2Ge_2$, 21–YMn_2Ge_2, 22–$ErMn_2Ge_2$, 23–$HoMn_2Ge_2$, 24–$TbMn_2Ge_2$.

4. Recent developments

4.1. *RMn_2Ge_2 compounds*

The ^{55}Mn NMR (Nuclear Magnetic Resonance) in RMn_2Ge_2 (R = Nd and Gd) was observed as a function of temperature (Hiraoka et al. 1987). ^{55}Mn frequencies exhibit anomalous temperature dependences which is caused by the rare earth sublattice effect. The ordering temperatures of the Nd and Gd sublattices are found to be 30 and 95 K, respectively.

The specific heat and the resistivity measurements of $ErMn_2Ge_2$ show a phase

transition at 5.1 K corresponding to the disordering temperature of magnetic moments in rare earth sublattice (Szytuła et al. 1988b).

Based on the temperature dependence of the magnetisation the magnetic phase diagram of $Sm_{1-x}Gd_xMn_2Ge_2$ was determined (Duraj et al. 1988). In the case of $x \leqslant 0.6$ the samples are ferromagnetic at low temperatures, an increase in the temperature leads to antiferromagnetic ordering and finally to a new ferromagnetism. The samples with $x > 0.6$ are ferromagnetic at low temperatures and they become antiferromagnetic when the temperature increases. The (p, T) magnetic phase diagram for samples with $x = 0$, 0.15 and 0.6 show that the Curie temperature decreases linearly with pressure while the temperature of the ferro–antiferro transition increases almost linearly with pressure. With an increase in Gd concentration the region of antiferromagnetic order increases. The value of the critical point decreases from $T_c = 330$ K and $p_c = 1.0$ GPa for $x = 0$ to $T_c = 310$ K and $p_c = 0.39$ GPa for $x = 0.6$.

4.2. *RCo_2Si_2 and RCo_2Ge_2 compounds*

Magnetic phases of $PrCo_2Si_2$ were studied by measurements of magnetization, neutron diffraction and electrical resistivity (Shigeoka et al. 1987). For $T < 9$ K, the magnetic structure is stable and the propagation vector is $\boldsymbol{k} = (0, 0, 1)[2\pi/c]$. An incommensurate magnetic structure with the propagation vectors $\boldsymbol{k} = (0, 0, 0.926)$ and $(0, 0, 0.777)$ is observed in the temperature ranges $9\text{ K} < T < 17\text{ K}$ and $17\text{ K} < T < 30\text{ K}$, respectively. In the whole temperature range the magnetic moment is parallel to the c-axis. The magnetization curves measured for a single crystal of $PrCo_2Si_2$ at various temperatures as a function of an applied magnetic field up to 57 kOe gave the following information:

- the magnetization in the c-plane changes linearly with an applied field and is small, i.e., 0.09 μ_B/f.u. at 57 kOe for 4.2 K,
- the magnetization curve along the c-axis differs from the in-plane behaviour noted above. For $T = 4.2$ K sharp jumps are observed at critical fields $J_1 = 13$ kOe and $H_2 = 36$ kOe. For $T = 10$ K the transition at H_1 disappears while the transition at H_2 disappears above 17.7 K. The magnetization curve becomes linear above 17.7 K with the applied field.

The specific heat and the resistivity studies of $NdCo_2Ge_2$ and $ErCo_2Ge_2$ compounds give the Néel temperature at 28 K for $NdCo_2Ge_2$ and 4.9 K for $ErCo_2Ge_2$ (Ślaski et al. 1988, Szytuła et al. 1988b).

4.3. *RNi_2Si_2 and RNi_2Ge_2 compounds*

Barandiaran et al. (1987) reported studies of the magnetic properties of RNi_2Si_2 compounds where R = Pr, Nd, Gd, Tb, Dy, Ho, Er and Tm. The results of resistivity, neutron diffraction, susceptibility and magnetization experiments are summarized in table 19. For all compounds the antiferromagnetic ordering of the incommensurate structure is observed. The magnetic moment of the lan-

TABLE 19
Magnetic data of RNi_2Si_2 [a].

Rare earth	Pr	Nd	Gd	Tb	Dy	Ho	Er	Tm
T_N (K)	18	6.2	14.5	15	6	4.3	3	1.7
T_t (K)				9				
θ_p (K)	−6	−4	−7	16	2	0	4	6.5
μ_{eff} (μ_B)	3.67	3.73	8.05	9.93	10.74	10.58	9.58	7.64
μ_R (μ_B)	2.6	2.6		8.8		9.6	6.4	5.6
Magnetic structure type	a.m.	a.m.		a.m.(1) AF(2)		a.m.	a.m.	a.m.
Moment direction	[0, 0, 1]	⊥[0, 0, 1]		[0, 0, 1]		[0, 1, 0]	[0, 1, 0]	[1, 1, 0]
Propagation vector	(0, 0, 0.87)	(0, 0, 0.885)		(0.574, 0.426, 0) (1) (0.5, 0.5, 0) (2)		(0.206, 0, 0.863)	(0.204, 0, 0.842)	(0.068, 0.068, 0.835)

a.m.: amplitude modulated, AF: simple antiferromagnetic
(1) Between T_m and T_N
(2) Below T_m
[a]Barandiaran et al. (1987)

thanide ions are parallel to the c-axis in the compounds with R = Pr, Tb, while the magnetic moment of R = Nd, Ho, Er and Tm lie in the basal plane. In the case of $TbNi_2Si_2$ the commensurate structure with propagation vector $\boldsymbol{k} = (\frac{1}{2}, \frac{1}{2}, 0)$ is observed in the temperature range 3.4–9 K. Above 9 K it changes to the incommensurate structure with $\boldsymbol{k} = (0.586, 0.414, 0)$.

The neutron diffraction and magnetometric measurements of $NdNi_2Ge_2$ indicate the presence of the magnetic ordering at $T_N = 16$ K of the modulated antiferromagnetic structure with a propagation vector $\boldsymbol{k} = (0, 0, 0.805)$ in a reduced unit cell and a magnetic moment parallel to the c-axis (Szytuła et al. 1988c). It differs from the situation observed in $NdNi_2Si_2$, where the magnetic moment is perpendicular to the c-axis.

4.4. *RCu_2Si_2 compounds*

Neutron diffraction measurements performed on a polycrystalline sample of $TmCu_2Si_2$ indicate that the compound is antiferromagnetic below the Néel temperature of 3.6 K. The magnetic structure is cosinusoidally modulated along the [110] direction with the propagation vector $\boldsymbol{k} = (0.147, 0.147, 0)$. The thulium magnetic moment of 5.1 μ_B makes an angle of 33(3)° with the c-axis (Allain et al. 1988).

4.5. *RRu_2Si_2 and RRu_2Ge_2 compounds*

The heat capacity and the electrical resistivity studies of $NdRu_2Si_2$ and $NdRu_2Ge_2$ indicate two magnetic phase transitions observed at temperatures 10 K and 23 K for $NdRu_2Si_2$ and 10 K and 17 K for $NdRu_2Ge_2$, respectively. Two phase transition temperatures correspond to the transitions from ferro- to antiferro- and from antiferro- to paramagnetic states for both compounds. The magnitude of the Schottky anomaly due to the nuclear hyperfine splitting (in the low temperature region, below 1 K) suggests that the magnetic moment in the crystal ground state is about 80% of the free-ion value of Nd^{3+} for the $NdRu_2Ge_2$ compound and it equals the free-ion value in the case of $NdRu_2Si_2$ compound (Ślaski et al. 1988).

4.6. *RRh_2Si_2 compounds*

The magnetic anisotropy of RRh_2Si_2 (R = Nd, Tb, Ho, Er) which has an AFI type magnetic structure can be explained by using a R^{3+} ion Hamiltonian which includes the crystal field term and the isotropic exchange term under the two-dimensional molecular field approximation, when the appropriate crystal field parameters are adopted. The crystal field parameters calculated are listed in table 20 (Takano et al. 1987a).

TABLE 20
Experimental and calculated values of the Néel temperature and the tilting angle at 4.2 K and the values of the parameters which are used in the calculations[(a)].

Compound	Experimental		Crystal field parameters			Molecular field constant	Calculated tilting angle (°)
	T_N (K)	Tilting angle (°)	B_2^0(K)	B_4^0(K)	B_4^4(K)	T_N(K)	
$NdRh_2Si_2$	56	0	−0.915	0.0189	−0.0344	46	36
$TbRh_2Si_2$	92	0	−1.09	−0.0047	−0.00854	48	0
$HoRh_2Si_2$	27	28	−0.22	0.0011	−0.002	20	36
$ErRh_2Si_2$	103	90	0.241	−0.00135	−0.00246	97	90

[(a)]Takano et al. (1987a).

4.7. *Other compounds*

Mixed valence compounds CeT_2Si_2 with T = Co, Ni show an enhanced Pauli paramagnetism with the fluctuation temperature around 150 K for Co and Ni which was established in the magnetic measurements in the temperature range of 1.6 to 600 K. The electrical resistivity measurements show that the compounds with T = Fe, Co and Ni do not become superconducting down to 18 mK and that the Fermi liquid behavior exists in the temperature range of 40 to 70 K (Ammarguellat et al. 1987).

^{170}Yb Mössbauer measurements show that magnetic ordering occurs within the Yb sublattices of $YbCo_2Si_2$ and $YbFe_2Si_2$ at 1.7 and 0.75 K, respectively. The saturated magnetic moments are 1.4 and 2.0 μ_B and they lie in a plane making a small angle with the basal plane (Hodges 1987).

The electron spin resonance (ESR) spectra measured for GdT_2Si_2 (T = Co, Ni, Cu, Ru, Rh, Pd) in the temperature range of 100–300 K give the values of g-factors which are close to $g_{isol} = 1.993$ observed for Gd^{3+} ion. The $La_{0.873}Gd_{0.127}Cu_2Si_2$ sample was also investigated. The results obtained indicate that the exchange coupling constant between conduction electrons and magnetic moments is probably positive for $GdCu_2Si_2$. The change of the electronic structure of the GdT_2Si_2 compounds, when the different 3d and 4d transition metals are the T elements, visibly influences the ESR spectra (Kwapulińska et al. 1988).

Acknowledgments

The authors would like to thank Dr. H. Hrynkiewicz for useful discussions and editing of the text of this paper.

References

Aliev, F.G., N.B. Brandt, V.V. Moshchalkov and S.M. Chudinov, 1984, J. Low Temp. Phys. **57**, 61.

Allain, Y., F. Bourée-Vigneron, A. Oleś and A. Szytuła, 1988, J. Magn. & Magn. Mater., to be published.

Ammarguellat, C., M. Escorne, A. Mauger, E. Beaurepaire, M.F. Ravet, G. Krill, F. Lapierre, P. Haen and C. Godart, 1987, Phys. Stat. Sol. b **143**, 159.

Andersen, O.K., 1975, Phys. Rev. B **12**, 3060.

Andress, K.R., and E. Alberti, 1935, Z. Metallkd. **27**, 12.

Asano, S., and J. Yamashita, 1972, Prog. Theor. Phys. **49**, 373.

Assmus, W., M. Herrmann, U. Rauchschwalbe, S. Riegel, W. Licke, H. Spille, S. Horn, G. Weber, F. Steglich and G. Cordier, 1984, Phys. Rev. Lett. **52**, 469.

Ban, Z., and M. Sikirica, 1964, Acta Crystallogr. **18**, 594.

Barandiaran, J.M., D. Gignoux, D. Schmitt and J.C. Gomez-Sal, 1986, Solid State Commun. **57**, 941.

Barandiaran, J.M., D. Gignoux, D. Schmitt, J.C. Gomez-Sal and J. Rodriguez Fernandez, 1987, J. Magn. & Magn. Mater. **69**, 61.

Batlogg, B., J.P. Remeika, A.S. Cooper and Z. Fisk, 1984, J. Appl. Phys. **55**, 2001.

Bauminger, E.R., et al., 1973, referred to on pp. 18,19.

Bauminger, E.R., I. Felner, D. Froindlich, A. Grill, D. Lebenbaum, I. Meyer, I. Nowik, S. Ofer and M. Schieber, 1974, Proc. Int. Conf.

on Magnetism, Vol. 5, Moscow, 1973 (Nauka, Moscow) p. 56.
Bazela, W., J. Leciejewicz, H. Ptasiewicz-Bak and A. Szytuła, 1988, J. Magn. & Magn. Mater. **72**, 85.
Besnus, M.J., J.P. Kappler, P. Lehmann and A. Meyer, 1985, Solid State Commun. **55**, 779.
Besnus, M.J., P. Lehmann and A. Meyer, 1987, J. Magn. & Magn. Mater. **63–64**, 323.
Brandt, N.B., and V.V. Moshchalkov, 1984, Adv. Phys. **33**, 373.
Braun, H.F., N. Engel and E. Parthé, 1983, Phys. Rev. B **28**, 1389.
Braun, H.F., T. Jarlborg and A. Junod, 1985, Physica B **135**, 397.
Budkowski, A., J. Leciejewicz and A. Szytuła, 1987, J. Magn. & Magn. Mater. **67**, 316.
Buschow, K.H.J., and D.B. De Mooij, 1986, Philips J. Res. **41**, 55.
Cable, J.W., E.O. Wollan, W.C. Koehler and M.K. Wilkinson, 1965, Phys. Rev. **140**, 1896.
Cattaneo, E., and D. Wohlleben, 1981, J. Magn. & Magn. Mater. **24**, 197.
Chevalier, B., J. Etourneau, J.E. Greedan, J.M.D. Coey and A. Moaroufi, 1985, J. Less-Common Met. **111**, 171.
Chevalier, B., J. Etourneau, J. Hagenmuller, P.H. Quezels and J. Rossat-Mignod, 1985a, J. Less-Common Met. **111**, 161.
Chevalier, B., J.M.D. Coey, B. Lloret and J. Etourneau, 1986, J. Phys. C **19**, 4521.
Darshan, B., B.D. Padalia, R. Nagarajan and R. Vijayaraghavan, 1984, J. Phys. C **17**, L445.
De Boer, F.R., J.C.P. Klaasse, P.A. Veenhuizen, A. Böhm, C.D. Bredl, U. Gottwick, H.M. Mayer, L. Pawlak, U. Rauchschwalbe, H. Spille and F. Steglich, 1987, J. Magn. & Magn. Mater. **63–64**, 91.
De Vries, J.W.C., R.C. Thiel and K.H.J. Buschow, 1985, J. Less-Common Met. **111**, 313.
Dhar, S.K., E.V. Sampathkumaran, J. Ray and G. Chandra, 1987, Proc. Int. Conf. on Valence Fluctuations, Bangalore, India, p. A22.
Dhar, S.K., E.V. Sampathkumaran, R. Vijayaragharan and R. Kuentzler, 1987a, Solid State Commun. **61**, 479.
Duraj, M., R. Duraj, A. Budkowski and A. Szytuła, 1987, Acta Magn. Suppl. **87**, 201.
Duraj, M., R. Duraj and A. Szytuła, 1988, J. Phys. (France), Suppl., to be published.
Eisenmann, B., N. May, W. Müller and H. Schafer, 1972, Z. Naturforsch. b **27**, 1155.
Felner, I., 1975, J. Phys. Chem. Solids **36**, 1063.
Felner, I., and I. Nowik, 1978, J. Phys. Chem. Solids **39**, 763.
Felner, I., and I. Nowik, 1983, Solid State Commun. **47**, 831.
Felner, I., and I. Nowik, 1984, J. Phys. Chem. Solids **45**, 419.
Felner, I., and I. Nowik, 1985, J. Phys. Chem. Solids **46**, 681.
Felner, I., I. Meyer, A. Grill and M. Schieber, 1975, Solid State Commun. **16**, 1005.
Fujii, H., T. Okamoto, T. Shigeoka and N. Iwata, 1985, Solid State Commun. **53**, 715.
Fujii, H., M. Isoda, T. Okamoto, T. Shigeoka and N. Iwata, 1986, J. Magn. & Magn. Mater. **54–57**, 1345.
Gignoux, D., D. Schmitt, M. Zerguine, C. Ayache and E. Bonjour, 1986, Phys. Lett. A **117**, 145.
Godart, C., L.C. Gupta and M.F. Ravet-Krill, 1983, J. Less-Common Met. **94**, 187.
Godart, C., A.M. Umarji, L.C. Gupta and R. Vijayaraghavan, 1987, J. Magn. & Magn. Mater. **63–64**, 326.
Goodenough, J.B., 1963, Magnetism and Chemical Bond (Wiley–Interscience, New York) p. 240.
Görlich, E.A., 1980, Thesis (Institute of Physics, Jagellonian University, Kraków).
Görlich, E.A., A.Z. Hrynkiewicz, R. Kmieć and K. Tomala, 1982, J. Phys. C **15**, 6049.
Gottwick, U., R. Held, G. Sparun, F. Steglich, K. Vey, W. Assmus, H. Rietschel, G.R. Stewart and A.L. Giorgi, 1987, J. Magn. & Magn. Mater. **63–64**, 341.
Greedan, J.E., and V.U.S. Rao, 1973, J. Solid State Chem. **6**, 387; **8**, 368.
Grier, B.H., J.M. Lawrence, V. Murgai and R.D. Parks, 1984, Phys. Rev. B **29**, 266.
Gupta, L.C., D.E. MacLaughlin, Tien Cheng, M.A. Edwards and R.D. Parks, 1983, Phys. Rev. B **28**, 3673.
Gyorgy, E.M., B. Batlogg, J.P. Remeika, R.B. van Dover, R.M. Felming, H.E. Bair, G.P. Espinosa, A.S. Cooper and R.G. Maines, 1987, J. Appl. Phys. **61**, 4237.
Hiebl, K., and P. Rogl, 1985, J. Magn. & Magn. Mater. **50**, 39.
Hiebl, K., C. Horvath, P. Rogl and M.J. Sienko, 1983, J. Magn. & Magn. Mater. **37**, 287.
Hiebl, K., C. Horvath, P. Rogl and M.J. Sienko, 1983a, Solid State Commun. **48**, 211.
Hiebl, K., C. Horvath, P. Rogl and M.J. Sienko, 1984, Z. Phys. B **56**, 201.
Hiebl, K., C. Horvath and P. Rogl, 1986, J. Less-Common Met. **117**, 375.
Hiraoka, K., T. Hihara, T. Shigeoka, H. Fujii and T. Okamoto, 1987, J. Magn. & Magn. Mater. **70**, 255.
Hirjak, M., B. Chevalier, J. Etourneau and P. Hagenmuller, 1984, Mater. Res. Bull. **19**, 727.
Hodges, J.A., 1987, Europhys. Lett. **4**, 749.
Horn, S., E. Holland-Moritz, M. Loewenhaupt, F. Steglich, H. Schener, A. Benoit and J. Flouquet, 1981, Phys. Rev. B **23**, 3171.
Hull, G.W., J.H. Wernick, T.H. Geballe, J.V. Waszczak and J.E. Bernardini, 1981, Phys. Rev. B **24**, 6715.
Hutchings, N.T., 1964, Solid State Phys. **16**, 227.
Ishida, S., S. Asano and J. Ishifa, 1986, J. Phys. Soc. Jpn. **55**, 936.
Iwata, N., T. Ikeda, T. Shigeoka, H. Fujii and T. Okamoto, 1986, J. Magn. & Magn. Mater. **54–57**, 481.
Iwata, N., K. Hattori and T. Shigeoka, 1986, J. Magn. & Magn. Mater. **53**, 318.
Jarlborg, T., and G. Arbman, 1977, J. Phys. F **7**, 1635.

Jarlborg, T., H.F. Braun and M. Peter, 1983, Z. Phys. B **52**, 295.
Jaworska, T., and A. Szytuła, 1987, Solid State Commun. **57**, 813.
Jaworska, T., and A. Szytuła, 1988, Solid State Commun., to be published.
Jaworska, T., A. Szytuła, H. Ptasiewicz-Bak and J. Leciejewicz, 1987, Acta Magn. Suppl. **87**, 211; cf. Solid State Commun. 65 (1988) 261.
Johnston, D.C., G. Liang, M. Croft, N. Anbalagan and T. Mihalisian, 1988, to be published.
Kido, H., T. Hishikawa, M. Shimada and M. Kotzumi, 1985, Phys. Status Solidi a **87**, K61.
Kolenda, M., and A. Szytuła, 1987, Acta Magn. Suppl. **87**, 213.
Kolenda, M., A. Szytuła and A. Zygmunt, 1982, in: Crystalline Electric Field Effects in f-electron Magnetism, eds R.P. Guertin, W. Suski and Z. Zołnierek (Plenum, New York) p. 309.
Kolenda, M., A. Szytuła and J. Leciejewicz, 1985, J. Magn. & Magn. Mater. **49**, 250.
Kotsanidis, P.A., and J.K. Yakinthos, 1981, Phys. Status Solidi a **68**, K153.
Kotsanidis, P.A., and J.K. Yakinthos, 1981a, Solid State Commun. **40**, 1041.
Kotsanidis, P.A., J.K. Yakinthos and E. Roudaut, 1984, Solid State Commun. **50**, 413.
Kozłowski, A., 1986, Thesis (Institute of Physics, Polish Academy of Sciences, Warsaw).
Kozłowski, A., A. Maksymowicz, Z. Tarnawski, A. Lewicki, J. Zukrowski and L. Anioła-Jędrzejek, 1987, J. Magn. & Magn. Mater. **68**, 95.
Kwapulińska, E., K. Kaczmarska and A. Szytuła, 1988, J. Magn. & Magn. Mater. **73**, 65.
Łątka, K., 1987, Acta Magn. Suppl. **87**, 205.
Łątka, K., 1987a, Acta Phys. Pol. A **72**, 73.
Łątka, K., 1988, Report (Institute of Nuclear Physics, Kraków) to be published.
Łątka, K., H. Schmidt, V. Oestreich, P. Götz and G. Czjzek, 1979, Progress Report KfK 2881 (IAK, Kernforschungszentrum Karlsruhe) p. 79.
Leciejewicz, J., 1982, in: Crystalline Electric Field Effects in f-electron Magnetism, eds R.P. Guertin, W. Suski and Z. Zołnierek (Plenum, New York) p. 279.
Leciejewicz, J., and A. Szytuła, 1983, Solid State Commun. **48**, 55.
Leciejewicz, J., and A. Szytuła, 1984, Solid State Commun. **49**, 361.
Leciejewicz, J., and A. Szytuła, 1985, Solid State Commun. **56**, 1051.
Leciejewicz, J., and A. Szytuła, 1985a, J. Magn. & Magn. Mater. **49**, 177.
Leciejewicz, J., and A. Szytuła, 1987, J. Magn. & Magn. Mater. **63–64**, 190.
Leciejewicz, J., S. Siek, A. Szytuła and A. Zygmunt, 1982, Crystalline Electric Field Effects in f-electron Magnetism, eds R.P. Guertin, W. Suski and Z. Zołnierek (Plenum, New York) p. 327.
Leciejewicz, J., M. Kolenda and A. Szytuła, 1983, Solid State Commun. **45**, 145.
Leciejewicz, J., A. Szytuła and A. Zygmunt, 1983a, Solid State Commun. **45**, 149.
Leciejewicz, J., S. Siek and A. Szytuła, 1984, J. Magn. & Magn. Mater. **40**, 265.
Leciejewicz, J., A. Szytuła, M. Ślaski and A. Zygmunt, 1984a, Solid State Commun. **52**, 475.
Leciejewicz, J., M. Kolenda and A. Szytuła, 1986, J. Magn. & Magn. Mater. **53**, 309.
Lieke, W., U. Rauchschwalbe, C.D. Bredl, F. Steglich, J. Aorts and F.R. de Boer, 1982, J. Appl. Phys. **53**, 2111.
Lloret, B., B. Chevalier, B. Buffat, J. Etourneau, S. Quezel, A. Lamharrar, J. Rossat-Mignod, R. Calemczuk and E. Bonjour, 1987, J. Magn. & Magn. Mater. **63–64**, 85.
Malik, S.K., S.G. Sankar, V.U.S. Rao and R. Obermyer, 1976, AIP Conf. Proc. **34**, 87.
McCall, W.M., K.S.V.L. Narasimhan and R.A. Butera, 1973, J. Appl. Phys. **44**, 4724.
Melamud, H., H. Pinto, I. Felner and H. Shaked, 1984, J. Appl. Phys. **55**, 2034.
Menovsky, A.A., C.E. Snel, T.J. Gortenmulder, H.J. Tan and T.T.M. Palstra, 1988, J. Cryst. Growth, to be published.
Misawa, S., 1974, Solid State Commun. **15**, 507.
Murgai, V., S. Raen, L.C. Gupta and R.D. Parks, 1982, in: Valence Instabilities, eds P. Wachter and H. Boppart (North-Holland, Amsterdam) p. 537.
Narasimhan, K.S.V.L., V.U.S. Rao, W.E. Wallace and I. Pop, 1975, AIP Conf. Proc. **29**, 594.
Narasimhan, K.S.V.L., V.U.S. Rao, R.L. Bergner and W.E. Wallace, 1976, J. Appl. Phys. **46**, 4957.
Nguyen, V.N., F. Tcheou, J. Rossat-Mignod and R. Ballestracci, 1983, Solid State Commun. **45**, 209.
Nicholson, K., H.U. Häfner, E. Müller-Hartmann and D. Wohlleben, 1978, Phys. Rev. Lett. **41**, 1325.
Noakes, D.R., and G.K. Shenoy, 1982, Phys. Lett. A **91**, 35.
Noakes, D.R., A.M. Umarji and G.K. Shenoy, 1983, J. Magn. & Magn. Mater. **39**, 309.
Nowik, I., I. Felner and M. Seh, 1980, J. Magn. & Magn. Mater. **15–18**, 1215.
Nowik, I., I. Felner and M. Seh, 1983, Proc. Int. Conf. on Magnetism of Rare Earths and Actinides, eds E. Burzo and M. Rogalski (Central Institute of Physics, Bucharest) p. 112.
Obermyer, R., S.G. Sankar and V.U.S. Rao, 1979, J. Appl. Phys. **50**, 2312.
Oesterreicher, H., 1976, Phys. Status Solidi a **34**, 723.
Oesterreicher, H., 1977, Phys. Status Solidi a **39**, K75.
Palstra, T.T.M., 1986, Thesis (University of Leiden, Leiden).

Palstra, T.T.M., A.A. Menovsky, G.J. Nieuwenhuys and J.A. Mydosh, 1986, J. Magn. & Magn. Mater. **54–57**, 435.
Palstra, T.T.M., A.A. Menovsky, G.J. Nieuwenhuys and J.A. Mydosh, 1986a, Phys. Rev. B **34**, 4566.
Palstra, T.T.M., et al., 1987, referred to on p. 41.
Parthé, E., and B. Chabot, 1984, in: Handbook on the Physics and Chemistry of Rare Earths, Vol. 7, eds K.A. Gschneidner Jr and L. Eyring (North-Holland, Amsterdam) ch. 48.
Parthé, E., B. Chabot, H.F. Braun and N. Engel, 1983, Acta Crystallogr. B **39**, 588.
Pinto, H., and H. Shaked, 1973, Phys. Rev. B **7**, 3261.
Pinto, H., M. Melamud and E. Gurewitz, 1979, Acta Crystallogr. A **35**, 533.
Pinto, H., M. Melamud and H. Shaked, 1982, in: Neutron Scattering 1981, ed. J. Faber Jr (AIP, Argonne National Laboratory, New York) p. 315.
Pinto, H., M. Melamud, J. Gal, H. Shaked and G.M. Kalvius, 1983, Phys. Rev. B **27**, 1861.
Pinto, H., M. Melamud, M. Kuznietz and H. Shaked, 1985, Phys. Rev. B **31**, 508.
Quezel, S., J. Rossat-Mignod, B. Chevalier, P. Lejay and J.E. Etourneau, 1984, Solid State Commun. **49**, 685.
Rambabu, D., and S.K. Malik, 1987, Proc. Int. Conf. Valence Fluctuations, Bangalore, India, p. A24.
Rauchschwalbe, U., U. Gottwick, U. Ahlheim, H.M. Mayer and F. Steglich, 1985, J. Less-Common Met. **111**, 265.
Rogl, P., 1984, in: Handbook on the Physics and Chemistry of Rare Earths, Vol. 7, eds K.A. Gschneidner Jr and L. Eyring (North-Holland, Amsterdam) ch. 51.
Routsi, Ch., and J.K. Yakinthos, 1981, Phys. Status Solidi a **68**, K183.
Rüßmann, N., H.U. Häfner and D. Wohlleben, 1982, in: Crystalline Electric Field Effects in f-electron Magnetism, eds R.P. Guertin, W. Suski and Z. Żołnierek (Plenum, New York) p. 333.
Sales, B.C., and R. Viswanathan, 1976, J. Low Temp. **23**, 449.
Sales, B.C., and D.K. Wohlleben, 1975, Phys. Rev. Lett. **35**, 1240.
Sampathkumaran, E.V., and R. Vijayaraghavan, 1986, Phys. Rev. Lett. **56**, 2861.
Sampathkumaran, E.V., L.C. Gupta, R. Vijayaraghavan, K.V. Gopalakrishnan, R.G. Pillay and H.G. Devare, 1981, J. Phys. C **14**, L237.
Sampathkumaran, E.V., R.S. Changhule, K.V. Gopalakrishnan, S.K. Malik and R. Vijayaraghavan, 1983, J. Less-Common Met. **92**, 35.
Sampathkumaran, E.V., K.H. Frank, G. Kalkowski, G. Kaindl, M. Domke and G. Wortmann, 1984, Phys. Rev. B **29**, 5702.
Sampathkumaran, E.V., S.K. Dhar and S.K. Malik, 1987, Proc. Int. Conf. Valence Fluctuations, Bangalore, India, p. B13.
Schlabitz, W., J. Baumann, G. Neumann, D. Plümacher and K. Reggentin, 1982, in: Crystalline Electric Field Effects in f-electron Magnetism, eds R.P. Guertin, W. Suski and Z. Żołnierek (Plenum, New York) p. 289.
Schobinger-Papamantellos, P., Ch. Routsi and J.K. Yakinthos, 1983, J. Phys. & Chem. Solids **44**, 875.
Schobinger-Papamantellos, P., A. Niggli, P.A. Kotsanidis and J.K. Yakinthos, 1984, J. Phys. & Chem. Solids **45**, 695.
Segre, C.U., M. Croft, J.A. Hodges, V. Murgai, L.C. Gupta and R.D. Parks, 1982, Phys. Rev. Lett. **49**, 1947.
Sekizawa, K., Y. Takano, H. Takigami and Y. Takahashi, 1987, J. Less-Common Met. **127**, 99.
Shelton, R.N., H.F. Braun and E. Musick, 1984, Solid State Commun. **52**, 797.
Shigeoka, T., 1984, J. Sci. Hiroshima Univ. A **48**(2), 103.
Shigeoka, T., H. Fujii, H. Fujiwara, K. Yagasaki and T. Okamoto, 1983, J. Magn. & Magn. Mater. **31–34**, 209.
Shigeoka, T., N. Iwata, H. Fujii and T. Okamoto, 1985, J. Magn. & Magn. Mater. **53**, 58.
Shigeoka, T., N. Iwata, H. Fujii and T. Okamoto, 1986, J. Magn. & Magn. Mater. **63–64**, 1343.
Shigeoka, T., N. Iwata, H. Fujii, T. Okamoto and Y. Hashimoto, 1987, J. Magn. & Magn. Mater. **70**, 239.
Siek, S., and A. Szytuła, 1979, J. Phys. **40**, C5-162.
Siek, S., A. Szytuła and J. Leciejewicz, 1978, Phys. Status Solidi a **46**, K101.
Siek, S., A. Szytuła and J. Leciejewicz, 1981, Solid State Commun. **39**, 863.
Ślaski, M., and A. Szytuła, 1982, J. Less-Common Met. **87**, L1.
Ślaski, M., A. Szytuła and J. Leciejewicz, 1983, J. Magn. & Magn. Mater. **39**, 268.
Ślaski, M., A. Szytuła, J. Leciejewicz and A. Zygmunt, 1984, J. Magn. & Magn. Mater. **46**, 114.
Ślaski, M., J. Kurzyk, A. Szytuła, B.D. Dunlap, Z. Sungaila and A. Umezawa, 1988, J. Phys. (France), Suppl., to be published.
Stewart, G.A., and J. Żukrowski, 1982, in: Crystalline Electrid Field Effects in f-electron Magnetism, eds R.P. Guertin, W. Suski and Z. Żołnierek (Plenum, New York) p. 319.
Stewart, G.R., 1984, Rev. Mod. Phys. **56**, 755.
Sujata Patil, A.M. Umarji, B.D. Padalia, L.C. Gupta and R. Vijayaraghavan, 1987, Proc. Int. Conf. Valence Fluctuations, Bangalore, India, p. B14.
Suski, W., 1985, Physica B **130**, 195.
Szytuła, A., and J. Leciejewicz, 1987, Acta Magn. Suppl. p. 39.
Szytuła, A., and J. Leciejewicz, 1987a, Acta Sci. Litt., Schedae Physicae (Universitas Jagellonica, Fascilus 26).

Szytuła, A., and S. Siek, 1982, J. Magn. & Magn. Mater. **27**, 49.
Szytuła, A., and S. Siek, 1982a, Proc. VII Int. Conf. on Solid Compounds of Transition Elements, Grenoble, IIA11.
Szytuła, A., and I. Szott, 1981, Solid State Commun. **40**, 199.
Szytuła, A., J. Leciejewicz and H. Bińczycka, 1980, Phys. Status Solidi a **58**, 67.
Szytuła, A., W. Bażela and J. Leciejewicz, 1983, Solid State Commun. **48**, 1053.
Szytuła, A., M. Ślaski, H. Ptasiewicz-Bąk, J. Leciejewicz and A. Zygmunt, 1984, Solid State Commun. **52**, 395.
Szytuła, A., J. Leciejewicz and M. Ślaski, 1986, Solid State Commun. **58**, 683.
Szytuła, A., A. Budkowski, M. Ślaski and R. Zach, 1986a, Solid State Commun. **57**, 813.
Szytuła, A., J. Leciejewicz, W. Bażela, H. Ptasiewicz-Bąk and A. Zygmunt, 1987, J. Magn. & Magn. Mater. **69**, 299.
Szytuła, A., A. Oleś, M. Perrin, M. Ślaski, W. Kwok, Z. Sungaila and B.D. Dunlap, 1987a, J. Magn. & Magn. Mater. **69**, 305.
Szytuła, A., D. Matković-Calogović and Z. Ban, 1988, Croat. Chim. Acta, to be published.
Szytuła, A., H. Ptasiewicz-Bąk, J. Leciejewicz and W. Bażela, 1988a, Solid State Commun. **66**, 309.
Szytuła, A., M. Ślaski, J. Kurzyk, B.D. Dunlap, Z. Sungaila and A. Umezawa, 1988b, J. Phys. (France), Suppl., to be published.
Szytuła, A., A. Oleś, Y. Allain and G. André, 1988c, J. Magn. & Magn. Mater., to be published.
Takano, Y., K. Ohhata and K. Sekizawa, 1987, J. Magn. & Magn. Mater. **66**, 187.
Takano, Y., K. Ohhata and K. Sekizawa, 1987a, J. Magn. & Magn. Mater. **70**, 242.
Tebble, R.S., and D.J. Craik, 1969, Magnetic Materials (Wiley-Interscience, New York) p. 61.
Thompson, J.D., J.O. Willis, C. Godart, D.E. MacLaughlin and L.C. Gupta, 1985, Solid State Commun. **56**, 169.
Umarji, A.M., D.R. Noakes, P.J. Vaccaro, G.K. Shenoy, A.T. Aldred and D. Niarchos, 1983, J. Magn. & Magn. Mater. **36**, 61.
Umarji, A.M., G.K. Shenoy and D.R. Noakes, 1984, J. Appl. Phys. **55**, 2297.
Umarji, A.M., C. Godart, L.C. Gupta and R. Vijayaraghavan, 1986, Pramana-J. Phys. **27**, 321.
Yakinthos, J.K., 1985, J. Magn. & Magn. Mater. **46**, 300.
Yakinthos, J.K., 1986, J. Phys. **47**, 673.
Yakinthos, J.K., 1986a, J. Phys. **47**, 1239.
Yakinthos, J.K., and H. Gamari-Seale, 1982, Z. Phys. B **48**, 251.
Yakinthos, J.K., and P.F. Ikonomou, 1980, Solid State Commun. **34**, 777.
Yakinthos, J.K., and E. Roudaut, 1987, J. Magn. & Magn. Mater. **68**, 90.
Yakinthos, J.K., Ch. Routsi and P.F. Ikonomou, 1980, J. Less-Common Met. **72**, 205.
Yakinthos, J.K., Ch. Routsi and P. Schobinger-Papamantellos, 1983, J. Magn. & Magn. Mater. **30**, 355.
Yakinthos, J.K., Ch. Routsi and P. Schobinger-Papamantellos, 1984, J. Phys. & Chem. Solids **45**, 689.
Yakinthos, J.K., M. Bogé, C. Jeandey and L. Oddou, 1987, Solid State Commun. **61**, 427.
Yosida, K., and A. Watabe, 1962, Prog. Theor. Phys. **28**, 361.
Zygmunt, A., and A. Szytuła, 1984, Acta Magn. Suppl. **84**, 193.
Zygmunt, A., and A. Szytuła, 1988, Solid State Commun., to be published.

Handbook on the Physics and Chemistry of Rare Earths, Vol. 12
edited by K.A. Gschneidner, Jr. and L. Eyring

Chapter 84

SPIN GLASSES

H. MALETTA and W. ZINN
Institut für Festkörperforschung der Kernforschungsanlage Jülich, D-5170 Jülich, Postfach 1913, Fed. Rep. Germany

Contents

Symbols

a-	amorphous
a_0	lattice parameter
ac-χ	susceptibility in a small alternating field
AFM	antiferromagnet
AT	de Almeida–Thouless transition
C	specific heat
D	magnetic anisotropy
DM	Dzyaloshinskii–Moriya interaction
d_l	lower critical dimension
d_u	upper critical dimension
E	energy
E_A	anisotropy energy
E_{DM}	anisotropy energy due to DM-interaction
EA	Edwards–Anderson model for a spin glass

ESR	electron spin resonance
F	free energy
FC	cooling the sample in a magnetic field
FM	ferromagnet
GT	Gabay–Toulouse transition
$\hbar$	Planck's constant
H	magnetic field
H_A	anisotropy field
$\mathcal{H}$	Hamiltonian
IRM	isothermal remanent magnetization (after ZFC)
$J_{1,2}$	exchange constant for nearest and next-nearest ion interactions, respectively
K	anisotropy constant
k_B	Boltzmann's constant
M	magnetization
M_{nl}	nonlinear magnetization
M_r	remanent magnetization
MCS	Monte-Carlo steps per spin
NSE	neutron spin echo
NMR	nuclear magnetic resonance
q	wave vector
q	order parameter in a spin glass
RAM	random anisotropy-axis model
RSG	reentrant spin glass
SG	spin glass
SK	Sherrington–Kirkpatrick model for a spin glass
t	time
T	temperature
T_c	ferromagnetic ordering (Curie) temperature
T_f	spin-glass freezing temperature
T_N	antiferromagnetic ordering (Néel) temperature
TRM	thermo-remanent magnetization (after FC)
x	concentration of magnetic atoms
ZFC	cooling the sample in zero magnetic field
z	dynamic critical exponent
α	critical exponent of specific heat
β	critical exponent of magnetization
γ	critical exponent of magnetic susceptibility
Γ	torque
δ	critical exponent of critical isotherm
η	critical exponent of correlation decay
θ	angle
θ_p	paramagnetic Curie–Weiss temperature
κ	inverse magnetic correlation length
μ_B	Bohr magneton
μSR	muon spin relaxation
ν	critical exponent of correlation length
ξ	magnetic correlation length
σ	neutron cross-section
τ	relaxation time
χ	magnetic susceptibility
χ'	real part of ac-χ
χ''	imaginary part of ac-χ
ω	frequency

1. Introduction

In recent years there has been an upsurge of interest in the research on the spin-glass phenomenon. The term "spin glass" was introduced in 1968; now about one paper per day is published which uses this word in its title or abstract (for recent reviews see: Fischer 1983a and 1985, Binder and Young 1986, Huang 1985).

There is now general agreement on the "definition" of a spin glass: Spin glass refers to a magnetic state of a system in which interactions between the magnetic moments are "in conflict" with each other due to disorder so that the spins order in a non-periodic fashion – they "freeze" into *random* directions. Additionally, the state is characterized by very slow equilibration after perturbation and significant history-dependence. Taking these features together means that we are going to apply the term "spin glass" here in the restricted sense, as mostly done, and not to all random non-collinear ordered magnets, e.g. not to systems with random anisotropy axes (see section 9) or to systems with random fields. The new type of magnetic order is represented schematically in fig. 1 where its magnetiza-

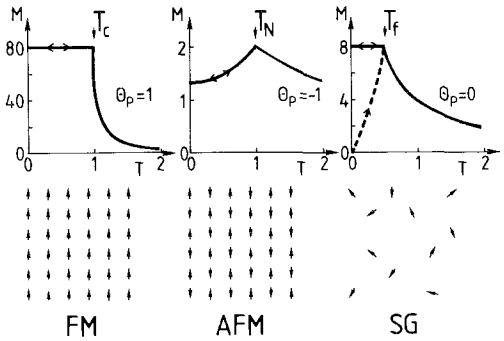

Fig. 1. Comparison of the magnetization measured in a small applied field for (a) a ferromagnet (FM), (b) an antiferromagnet (AFM), and (c) a spin glass (SG). The dashed line indicates the zero-field-cooled behavior of the spin glass. The curves are schematic and the units arbitrary, but the same average magnitude of the exchange interaction is chosen for all three. Values of the paramagnetic Curie–Weiss temperature θ_p are indicated. At the bottom the corresponding ordering of the magnetic moments is sketched schematically (from Moorjani and Coey 1984).

tion measured in a small applied field is compared (in its magnitude and temperature dependences) with that of two well known types of collinear magnetic order.

The increasing interest in spin glasses may have the following reasons:

(i) Spin-glass properties are fairly universal. They have been observed in a wide variety of different systems with competing interactions between the spins, e.g. in crystalline metals Fe_xAu_{1-x} (Cannella and Mydosh 1972), in crystalline insulators $Eu_xSr_{1-x}S$ (Maletta and Crecelius 1976) as well as in amorphous alloys Gd_xAl_{1-x} (Mizoguchi et al. 1977).

(ii) Spin-glass behavior is novel; it is an intrinsic effect of disorder and competition of the magnetic interactions. Attempts to understand the origin and behaviour of the spin-glass state have led to the appreciation of several new concepts and to the recognition that the fundamental ingredients for these concepts are much more widespread in occurrence than spin glasses. This study has had important impact in statistical mechanics, and recently also applications on complex optimation problems (Kirkpatrick et al. 1983) and biological problems {memory (Hopfield 1982), prebiological evolution (Anderson 1983)} have been discussed.

(iii) In spite of more than 2000 publications with many important results and in spite of a close interaction between experiment, computer simulation and analytical model calculation the essential questions for instance about the nature of the spin-glass transition and the spin-glass state are still controversially discussed. Spin glasses are still a challenge to solid state physics.

The present review attempts to give a survey of the field, including discussions of the most exciting questions which have come up. Obviously, it is nearly impossible to cite all the papers on spin glasses, hence the authors apologize at the outset to those whose work is not explicitely referenced. Additional references are found in other reviews (Fischer 1983a and 1985, Binder and Young 1986, Huang 1985).

The organization of this chapter is as follows: First, two questions are discussed in sec. 2: How to classify any material as a spin glass? What are the ingredients a system needs to be a potential spin glass? Section 3 is concerned with some basic requirements for any type of magnetic order such as interactions and anisotropies, and an introduction of some typical systems out of the large variety of rare-earth spin-glasses. We then summarize in sec. 4 the present understanding of the mean-field model of spin glasses, and present briefly numerical results on short-range models, because no analytical results are available for realistic models. Section 5 is devoted to the unusual properties of spin glasses at low temperatures, including irreversibilities, anisotropy and excitations. The upsurge of interest in spin glasses in recent years is related to the "spin-freezing" process near the spin-glass temperature T_f, which is discussed in sections 6 and 7. Experimental work on the dynamics of spin-glass freezing is reviewed in sec. 6, while attempts devoted to analyzing the data in terms of a phase transition at T_f are discussed in sec. 7. We then give in sec. 8 recent results of studies concerned with the magnetic behavior in the crossover regime from spin-glass to long-range ferro- or antiferromagnetic order. A brief discussion on systems with random anisotropy axis is included in sec. 9. Finally, sec. 10 contains some concluding remarks.

2. Characteristics of a spin glass

Before beginning a survey of experimental results on rare-earth spin glasses and their interpretation by model calculations, we would first suggest a brief discussion on two questions: How to classify any material as a spin glass? What are the ingredients a system needs to be a potential spin glass?

2.1. *Classification of a spin glass*

There is no unique experiment which is able to definitely identify a sample as a spin glass. Some of the characteristic properties of spin glasses which will be discussed below also occur for other sorts of magnets, so in practice it is necessary to observe *several* characteristics before classifying any material as a spin glass. As an example, we present experimental data in fig. 2 on the spin glass sample, $Eu_{0.40}Sr_{0.60}S$, which may be taken as a possible collection of defining properties:

(a) In the ac-susceptibility: A peak in $\chi(T)$ at low magnetic fields. It defines the spin-glass temperature T_f, not necessarily the phase transition temperature T_c (if it exists at all) because T_f is often dependent on the measuring frequency.

(b) In the neutron diffraction spectrum: No magnetic Bragg peaks. That means, the spin "freezing" (associated with feature a) is accompanied with no periodic long-range order at $T \leqslant T_f$.

(c) In the magnetic specific heat: no anomaly in $C(T)$ at T_f. A broad peak exists at higher temperature (at about $1.3T_f$).

(d, e) In the magnetization: Below T_f severe history dependence (the magnetization measured after zero-field cooling, ZFC, is different from that in field cooling,

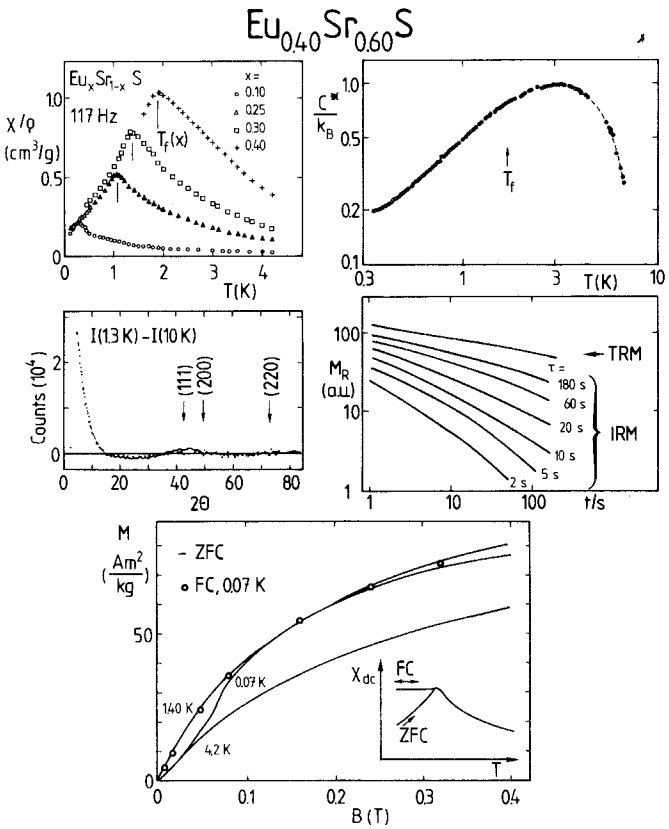

Fig. 2. Collection of defining properties of a spin-glass. Data of $Eu_{0.40}Sr_{0.60}S$ are taken from measurements of (a) ac-susceptibility $\chi(T)$ (Maletta and Felsch 1979b), (b) neutron diffraction $I(T = 1.3\,\mathrm{K}) - I(T = 10\,\mathrm{K})$ (Maletta and Felsch 1979b), (c) magnetic specific heat $C(T)$ (Meschede et al. 1980), (d) slowly decaying remanent magnetizations, TRM and IRM, for different values of the acquisition time τ, as indicated, at $T = 1.32\,\mathrm{K}$ and $H = 40\,\mathrm{Oe}$ (Ferré et al. 1981), and (e) magnetizations M after field-cooling (FC) or zero-field-cooling (ZFC) (Maletta and Felsch 1979b). The inset shows the corresponding dc-susceptibilities, $\lim_{H\to 0} \mathrm{d}M/\mathrm{d}H$.

FC), remanence (TRM measured after FC, IRM measured after ZFC) and slow (non-exponential) relaxation exist after magnetic perturbation (TRM denotes the thermoremanent magnetization, and IRM the isothermal remanent magnetization).

2.2. *Ingredients for a spin glass*

In order to answer the second question above, we compare the magnetic phase diagrams of two systems, $Eu_xSr_{1-x}O$ and $Eu_xSr_{1-x}S$ (see also Westerholt et al. 1977), displayed in fig. 3. Both insulating systems are based upon a ferromagnet, EuO ($T_c = 69\,\mathrm{K}$) and EuS ($T_c = 16.6\,\mathrm{K}$), and are magnetically diluted with Sr. These two Eu-monochalcogenides are rather similar chemically, and crystallize in

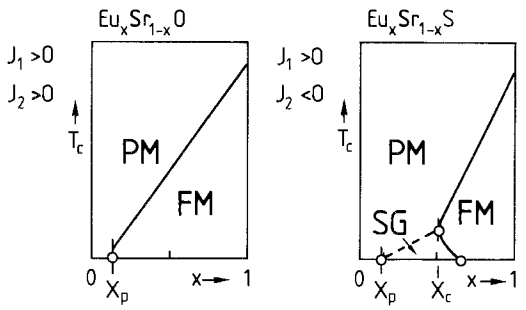

Fig. 3. Schematic magnetic phase diagrams for $Eu_xSr_{1-x}O$ and $Eu_xSr_{1-x}S$. PM = paramagnet; FM = ferromagnet; SG = spin glass; x_p = percolation threshold. The exchange interactions to the first (J_1) and second nearest neighbors (J_2) are of equal or of opposite sign in $Eu_xSr_{1-x}O$ or $Eu_xSr_{1-x}S$, respectively.

the NaCl structure. The magnetic moments at the divalent Eu ions are coupled via short-range exchange interactions to the first (J_1) and second (J_2) nearest Eu neighbors. Thus, in both dilution systems the percolation threshold (depending on the crystal structure and range of interaction only) is the same and equal to $x_p = 0.13$. It means that for Eu concentrations $x < x_p$ the system consists exclusively of independent *finite* magnetic clusters (superparamagnet), whereas from geometrical arguments within percolation theory *long*-range magnetic order may be possible for all $x > x_p$ (i.e. as long as there exist infinite continuous exchange paths joining magnetic Eu ions). Figure 3 demonstrates, however, that the systems do not exhibit the same type of magnetic phase diagram.

By dilution of a ferromagnet one expects the Curie temperature $T_c(x)$ first to decrease linearly with $(1 - x)$ due to the linear decrease in the effective exchange field, and, as x is further decreased, ferromagnetism to persist down to the critical concentration x_p where T_c has to go to zero. This happens in the dilution series $Eu_xSr_{1-x}O$.

The origin of the fundamental difference in magnetic ordering observed in $Eu_xSr_{1-x}S$ has been proposed (Maletta and Convert 1979a) to lie in the presence of *competing* exchange interactions. Both exchange couplings, J_1 and J_2, are positive in EuO, whereas in EuS they are of opposite sign, with ratio $J_2/J_1 = -0.5$ (Zinn 1976, Wachter 1979).

The important role played by the competing exchange is confirmed in Monte Carlo simulations by Binder et al. (1979, 1980). In a realistic model for $Eu_xSr_{1-x}S$, considering an fcc lattice with $J_2/J_1 = -0.5$, they even find quantitative agreement with experimental results without adjusting parameters by calculating the concentration dependences of the Curie temperature $T_c(x)$ and the magnetization (fig. 4). Obviously, the ferromagnetic state in EuS is unstable against dilution with SrS already at $x_c = 0.50$, far above the percolation threshold $x_p = 0.13$.

To understand this behavior, we consider in fig. 5 as a simple model the ground state of a diluted square lattice with $J_1 > 0$ and $J_2 < 0$. Due to the competition between positive J_1 (full lines) and negative J_2 (broken lines) there occur spins or

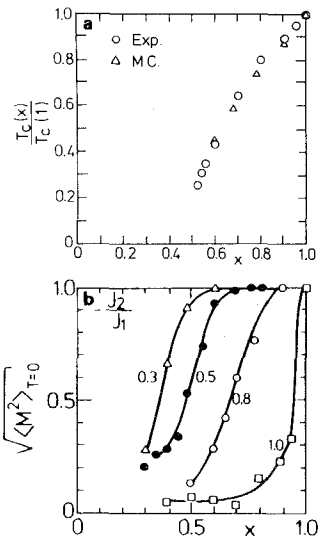

Fig. 4. (a) Simulated Curie temperatures T_c (triangles) of a fcc Heisenberg ferromagnet with $J_2/J_1 = -1/2$ plotted vs concentration x of magnetic ions (Binder et al. 1980). Circles denote experimental data for $Eu_xSr_{1-x}S$ (Maletta and Convert 1979a). (b) Ground-state magnetization of a classical fcc Heisenberg ferromagnet as a function of concentration x for various ratios J_2/J_1 of exchange interactions, as obtained from Monte Carlo simulations (from Binder et al. 1979).

spin clusters near the non-magnetic atoms (open circles) which are aligned antiparallel to the ferromagnetic environment (in the Ising model), or which are turned away from the spontaneous magnetization direction by an angle φ (in the XY and Heisenberg model) which is dependent on the ratio of the exchange interactions $R = J_2/J_1$. Even more interesting is the behavior shown between the double arrows in fig. 5. For instance in the lower left part it is favorable to have either one of two spins (in the middle) antiparallel to the ferromagnetic network but it is undecided which of them, and hence the states with these two spin configurations, are *degenerate*. As a result, bulk magnetization is reduced, this

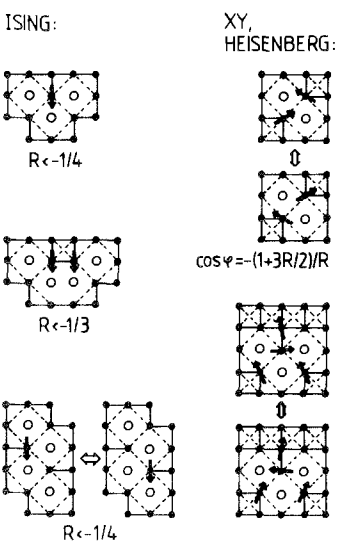

Fig. 5. Spin configurations near nonmagnetic atoms (circles) of a diluted ferromagnet with competing nearest (J_1) and next-nearest (J_2) neighbor interactions, $R = J_2/J_1 < 0$. Only the spins which are not aligned in the direction of the spontaneous magnetization (pointing upwards) are indicated by arrows. The most simple cases of both the Ising and XY or Heisenberg model are shown (from Maletta 1981b).

two-spin cluster is only weakly coupled to the ferromagnetic environment, in both states some interactions are unfavorable (*"frustrated"* bonds). Systems with frustration (Toulouse 1977) cannot minimize simultaneously the energy because of competition between different requirements. This high ground-state degeneracy due to frustration is a basic feature of spin glasses.

Similar frustration effects occur in XY- and Heisenberg-spin systems (Kinzel and Binder 1981, Dunlop and Sherrington 1985) as illustrated in fig. 5. Thus, as dilution proceeds, we expect that more and more spins are effectively decoupled from the ferromagnetic alignment within the long-range ferromagnetic order, until ferromagnetism breaks down completely already above x_p, as observed experimentally in $Eu_xSr_{1-x}S$ (Maletta and Convert 1979a). A new type of order, the spin glass, occurs instead characterized by these two ingredients: *disorder and frustration*. Disorder in the Eu ions alone as induced in the dilution series by substitution with Sr will not destroy ferromagnetic order for $x > x_p$ ($Eu_xSr_{1-x}O$), unless competition in the exchange couplings comes into play ($Eu_xSr_{1-x}S$). On the other hand, frustration alone is also not sufficient to create a spin glass; for example a system on a triangular lattice with antiferromagnetic bonds to nearest neighbors, or the Mattis model (Mattis 1976), both are frustrated systems but without disorder, i.e. no spin glasses.

3. Lanthanide spin glasses

The basic requirements for any type of magnetic order in a solid are the existence of magnetic moments associated with unpaired electrons on the atoms, and interactions to couple them.

3.1. *Interactions*

In systems with lanthanides the 4f shell builds up a well-localized moment $g\mu_B S_i$ which may be coupled to neighboring moments by the *isotropic Heisenberg exchange*

$$\mathcal{H}_{ij} = -2J_{ij}\boldsymbol{S}_i \cdot \boldsymbol{S}_j \tag{1}$$

where J_{ij} is the exchange parameter between spins at site i and site j. It is positive for ferromagnetic coupling and negative for antiferromagnetic coupling. The insulating Eu-monochalcogenides EuO and EuS are believed to be some of the most ideal realizations of the isotropic Heisenberg model of ferromagnetism (Zinn 1976, Wachter 1979).

In metallic systems with 4f atoms the most prominent source of long-range interaction between magnetic moments is the mechanism first described by Ruderman and Kittel (1954), Kasuya (1956) and Yosida (1957), which involves the conduction-electron sea as mediator of the interaction. Distinctive features of the *RKKY-interactions* are its long range and oscillatory nature:

$$J(R) = V_0 \frac{\cos(2k_F R + \phi)}{(k_F R)^3}, \quad k_F R \gg 1. \tag{2}$$

The effective exchange parameter J between spins of distance R falls off as R^{-3} and oscillates in sign and magnitude with R, so the coupling can give ferro- as well as antiferromagnetic alignments. Here, k_F is the Fermi wave number, ϕ a phase factor, and V_0 is proportional to J_{fs}^2 where J_{fs} is the exchange interaction between the localized f-electrons of the lanthanide and the conduction electrons of the host metal. The oscillations arise when the Fermi surface is sharply defined. For further discussions on the RKKY interactions in disordered systems we refer to the literature (de Gennes 1962, Kaneyoshi 1975, de Châtel 1981, Levy and Zhang 1986).

3.2. *Anisotropies*

The interactions discussed so far are isotropic in nature. Anisotropy, however, may influence the magnetic ordering substantially. Here, we are going to distinguish between three main sources of *anisotropy*:

(i) Magnetic *dipolar* interaction

$$\mathcal{H}_{ij}^{\text{dip}} = \frac{\boldsymbol{\mu}_i \cdot \boldsymbol{\mu}_j}{r_{ij}^3} - \frac{3(\boldsymbol{\mu}_i \cdot \boldsymbol{r}_{ij})(\boldsymbol{\mu}_j \cdot \boldsymbol{r}_{ij})}{r_{ij}^5} \tag{3}$$

tends to align the two moments $\boldsymbol{\mu}_i$ and $\boldsymbol{\mu}_j$ parallel, along the line joining their sites, $\boldsymbol{r}_{ij}$.

This anisotropy is of order 1 K only and probably not important for typical metallic spin glasses. It may be relevant for insulating spin glasses $Eu_xSr_{1-x}S$ (Binder and Kinzel 1983).

(ii) *Dzyaloshinskii–Moriya* (*DM*) interaction (Dzyaloshinskii 1958, Moriya 1960):

$$\mathcal{H}_{ij}^{\text{DM}} = -\boldsymbol{D}_{ij} \cdot (\boldsymbol{S}_i \times \boldsymbol{S}_j) \tag{4}$$

with the vector $\boldsymbol{D}_{ij} = -\boldsymbol{D}_{ji}$. Hence, a conduction electron of the host metal is first scattered by the spin $\boldsymbol{S}_i$, then via spin–orbit interaction by another (non-magnetic) impurity T (where D is proportional to the spin–orbit coupling constant), and finally by a second spin $\boldsymbol{S}_j$. The same mechanism, but without the process at T, leads to the RKKY interaction, thus the DM interaction is of third order in perturbation theory.

Fert and Levy (1980, 1981) propose this DM interaction to be responsible for observed anisotropy effects in metallic spin glasses. The anisotropy field D is randomly distributed (like the T atoms), i.e. there is *no global* anisotropy axis, but with eq. 4 one gets a macroscopic anisotropy energy of unidirectional character

$$E_{\mathrm{DM}} = -K \cdot \cos\theta \quad \text{with} \quad K \sim D^2 . \tag{5}$$

E_{DM} is only dependent on the angle θ of spin rotation from any axis, there is no preferred direction. In this sense the DM interaction in spin glasses leads to an "isotropic anisotropy".

(iii) *Single-ion anisotropy*

$$\mathcal{H}_i^{\mathrm{si}} = -D(S_i^z)^2 \tag{6}$$

in uniaxial crystals where z being the easy-axis direction. This anisotropy is also related to the spin–orbit coupling which is rather strong in 4f atoms. It occurs in systems containing non-S state ions, mostly from interaction between the non-spherical electronic charge distribution and the local crystalline field created by the surroundings. Due to the uniaxial character of this type of anisotropy one expects to observe a preferred direction (z) in magnetic properties of such crystals.

3.3. *Spin-glass systems*

Let us consider ingredients of typical systems out of the large variety of substances containing rare earths, for which some spin-glass properties have been reported (see also Durand and Poon 1979).

Insulating crystals: The system $Eu_xSr_{1-x}S$ has been studied in great detail in recent years (Maletta 1982a) and is nowadays regarded as the standard system for spin-glass properties in insulating compounds. Its model character is due to the stable, well-localized, spin-only magnetic moment of $\mu_i = 2\mu_B S_i = 7\mu_B$ carried by the $4f^7 - {}^8S_{7/2}$ groundstate of the Eu^{2+} ion at a site i of the NaCl lattice of EuX, which is coupled to each of the z_r Eu spins S_r in the r-th neighbor shell by the isotropic Heisenberg interaction yielding the sum

$$\mathcal{H} = -\sum_{r=1}^{R} 2z_r J_r \boldsymbol{S}_i \cdot \boldsymbol{S}_r . \tag{7}$$

Recent detailed study of the spin-wave dispersion by Bohn et al. (1980) in a single crystal of EuS (enriched with ^{153}Eu) by inelastic neutron scattering technique (fig. 6a) confirms previous assumptions that the range of the exchange interactions is essentially limited to the second nearest neighbors: $J_1/k_B = 0.220$ K and $J_2/k_B = -0.100$ K, while the exchange interactions to more distant neighbors decrease to a few percent of J_2 only. The dependence of J_1 and J_2 on the Eu–Eu pair distance $R_r = a/\sqrt{2}$ (a = lattice parameter) for each of the four members of the EuX series is summarized in fig. 6b. EuO with the shortest R_r values obviously is a special case where both J_1 and J_2 are positive, otherwise J_1 and J_2 are opposite in sign. Obviously, going from EuO to EuTe, i.e. in the direction of increasing lattice constants and covalent character of the chemical bond, J_r shifts to more negative (or smaller positive) values. In the theory of Kasuya (1973) the following exchange mechanisms for J_1 and J_2 are proposed:

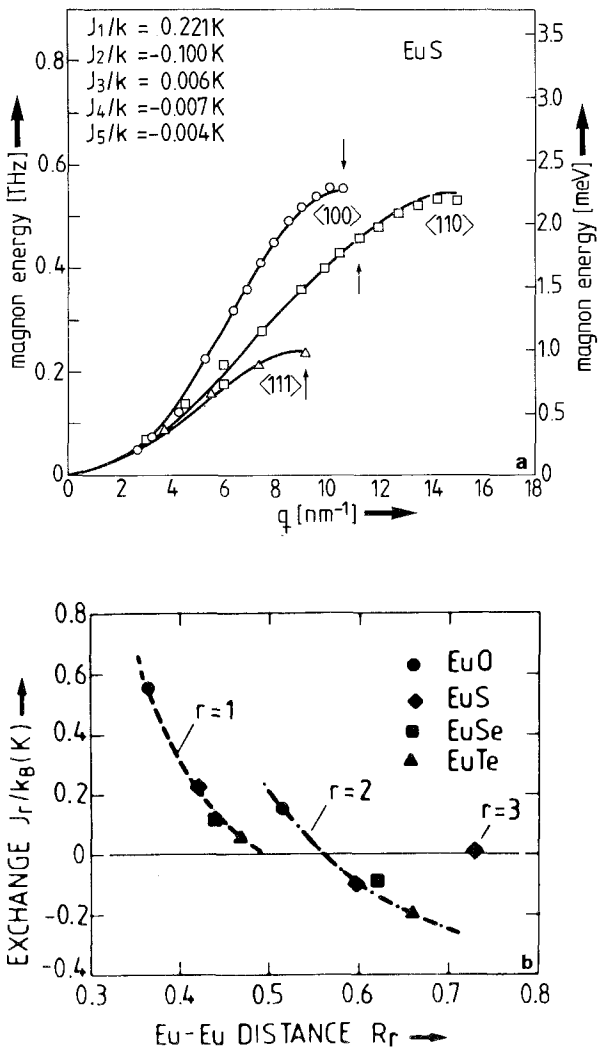

Fig. 6. (a) Spin-wave dispersion in EuS, measured by inelastic neutron scattering at $T = 1.3$ K ($T_c = 16.6$ K). The solid lines represent the best fit using up to fifth neighbors exchange interactions. The arrows indicate the boundary of the first Brillouin zone in the various symmetry directions (from Bohn et al. 1980). (b) Dependence of the exchange interactions, J_1 and J_2, on the Eu–Eu distance R_r in the Eu-chalcogenides.

– An Eu–Eu superexchange with virtual transfer of a 4f electron to the 5d-t_{2g} excited state of a Eu nearest neighbor (J_1; $z_1 = 12$).
– An indirect superexchange between Eu next-nearest neighbors involving the antibonding 5d-e_g orbitals of the Eu and the p orbitals of the anion (J_2; $z_2 = 6$).
For further discussions on EuX see Wachter (1979).

A careful analysis of the high-temperature susceptibility of $Eu_zSr_{1-x}S$ versus Eu concentration by Köbler and Binder (1980) has been used to search for possible deviations in the atomic arrangement from the ideal random mixing (see also Binder 1982). No indication for chemical short-range order in $Eu_xSr_{1-x}S$ is found. The experimental data can be quantitatively understood over the whole Eu-concentration range by taking only into account the weak dependence of the

exchange parameters on concentration and temperature via lattice expansion (EuS: $a_0 = 0.597$ nm, SrS: $a_0 = 0.602$ nm).

The presence of well-known competing exchange interactions of short range, J_1 and J_2, in $Eu_xSr_{1-x}S$ over the whole x-range has made this system a famous spin-glass material where the conditions for spin-glass behavior discussed above are clearly realised. For this reason a lot of different experiments has been performed on this material, and experimental results on this rare-earth system will be somewhat emphasized in this review.

In EuS the dominant interaction (J_1) leads to ferromagnetism, in EuTe the dominant interaction (J_2) to antiferromagnetism, both possessing competing exchange, J_1 and J_2. Thus, as expected from discussions above, spin-glass behavior is observed in both dilution systems, in the diluted ferromagnets $Eu_xSr_{1-x}S$ (Maletta and Felsch 1979b) and in the diluted antiferromagnets $Eu_xSr_{1-x}Te$ (Börgermann et al. 1986a, b). Their magnetic phase diagrams are displayed in fig. 7.

Westerholt and Bach (1981a, b) started by mixing the ferromagnet EuS with the metastable antiferromagnet EuSe together, EuS_ySe_{1-y}. From ac susceptibility and specific heat measurements they claim to obtain a narrow concentration regime around $y = 0.10$ with spin-glass or "mictomagnetic" properties (fig. 8a). Theoretical work often predicts in such a phase diagram an intermediate region with mixed ferro- and antiferromagnetic order, instead (Fishman and Aharony 1980). As long as neutron diffraction studies have not yet been performed, a definite decision on the type of magnetic order is still open in that case. The same authors proceed by diluting this system with Sr which stabilizes the spin-glass ordering, and broad spin-glass regimes versus Eu concentration are observed (fig. 8b) in

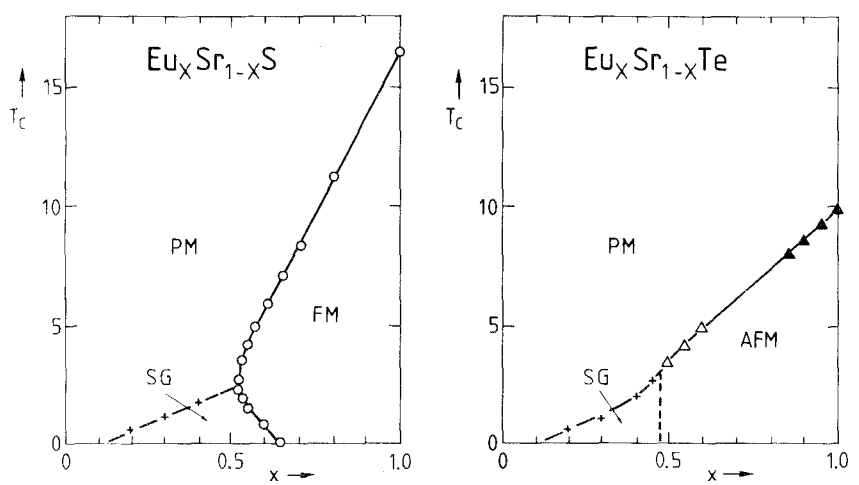

Fig. 7. Magnetic phase diagrams for the diluted ferromagnet $Eu_xSr_{1-x}S$ (Maletta and Felsch 1979b) and the diluted antiferromagnet $Eu_xSr_{1-x}Te$ (Börgermann et al. 1986b). PM = paramagnet; FM = ferromagnet; AFM = antiferromagnet; SG = spin glass. Note that the boundary between SG and AFM in $Eu_xSr_{1-x}Te$ has not been studied by neutron scattering technique.

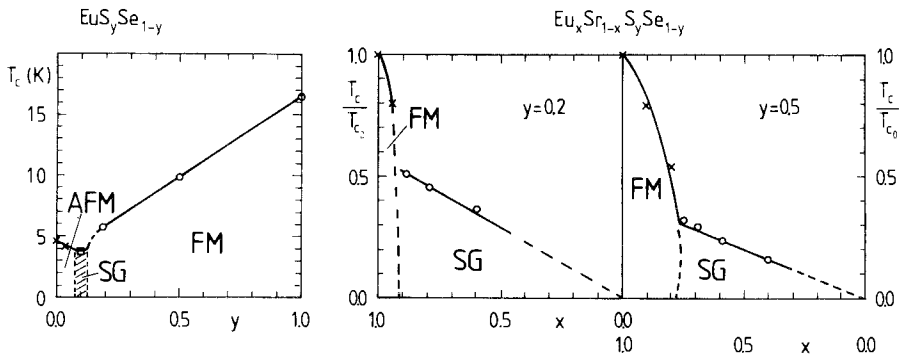

Fig. 8. Magnetic phase diagrams for EuS_ySe_{1-y} for $0 \leq y \leq 1$, and $Eu_xSr_{1-x}S_ySe_{1-y}$ with $y = 0.2$ and $y = 0.5$ for $0 \leq x \leq 1$. FM = ferromagnet; AFM = antiferromagnet; SG = spin glass (from Westerholt and Bach 1981b).

$Eu_xSr_{1-x}S_ySe_{1-y}$. This can be understood by systematically changing the ratio J_2/J_1 with concentration y, for instance they estimate $J_2/J_1 \approx -0.75$ for the system with $y = 0.2$, and $J_2/J_1 \approx -0.6$ for $y = 0.5$. This feature is in qualitative agreement with model calculations in 2 dimension by Binder et al. (1979) where just this behavior has been predicted.

Semimetallic crystals: The next system being introduced in this section is the dilution system $Eu_xSr_{1-x}As_3$ based upon the semimetal $EuAs_3$. $EuAs_3$ and $SrAs_3$ are again isostructural, namely monoclinic, with nearly equal lattice parameters (Bauhofer et al. 1981). The antiferromagnet $EuAs_3$ undergoes two successive magnetic transitions (Bauhofer et al. 1985 and 1986, Chattopadhyay et al. 1986) at 11.2 K and 10.3 K. First, a transition to an incommensurate magnetic structure occurs which is followed by a lock-in transition to a commensurate antiferromagnetic phase at 10.3 K where the magnetic moments are oriented in the crystallographic b direction. Together with a careful neutron diffraction study, a detailed theoretical investigation of the incommensurate state has been performed (Thalmeier 1986, Chattopadhyay et al. 1986), suggesting that there exist competing exchange interactions to the nearest and next-nearest Eu^{2+} neighbors.

Therefore, it is not astonishing that Lecomte et al. (1984, 1986a) observe a spin-glass regime in $Eu_xSr_{1-x}As_3$. Very recently, a study of the directional dependence of the ac susceptibility (Schröder et al. 1986) reveals *anisotropic* spin-glass behavior: by lowering the temperature longitudinal (i.e. for the ac driving field parallel to the b direction) and subsequently transverse freezing occurs at different temperatures. Figure 9 shows the magnetic phase diagram of $Eu_xSr_{1-x}As_3$.

Metallic crystals: Metallic systems, like Fe impurities in *Au*, are often cited as "classical" spin glasses, referring to the pioneering experiment by Cannella and Mydosh (1972) when a "cusp" in the ac susceptibility, $\chi(T)$, in low magnetic fields is observed in these dilute alloys. In such systems, however, the interactions are rather complicated and not precisely known:

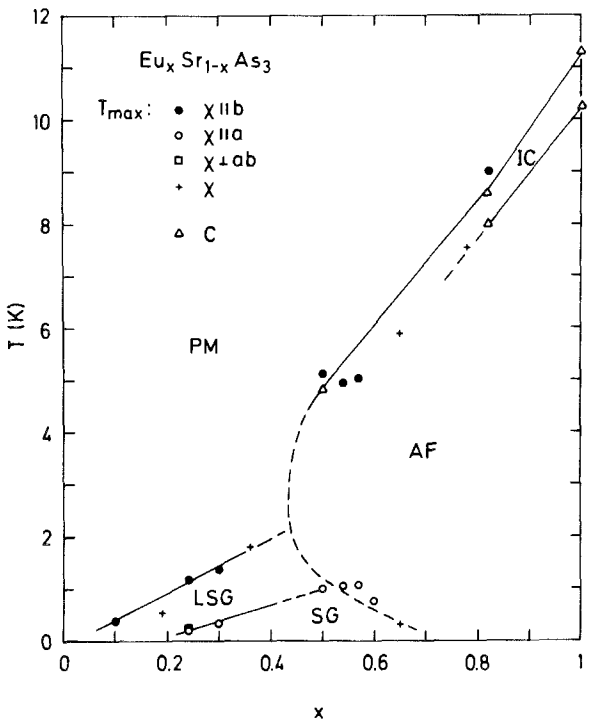

Fig. 9. Magnetic phase diagram for $Eu_xSr_{1-x}As_3$. PM = paramagnet; AF = antiferromagnet; IC = incommensurate antiferromagnet; LSG = longitudinal spin glass (freezing only for $\chi \| b$); SG = spin glass (additional freezing of transverse components). Triangles denote specific-heat results, other symbols denote the temperature of the maximum in the ac susceptibility χ. The crosses denote χ-measurements in unspecified directions. Note that the "reentrant" phase boundary (dashed line) is only tentative, neutron-scattering studies are in progress (from Schröder et al. 1986).

– Magnetism created by 3d electrons is not properly described by localized moments, at least for concentrations of about 10 atom% or even more, as often used in experiments. Modifications of the far too idealized RKKY interaction and additional direct overlap of the d electrons have to be included in realistic model calculations.
– The situation is even more complicated as sometimes an interplay with atomic short-range order occurs.

A careful analysis of the paramagnetic susceptibility by Morgownik and Mydosh (1983) confirms both complications being present in 3d systems, e.g. in Cu, Au and Pt host-metals with even low ($\lesssim$8 atom%) Mn and Fe impurity concentrations. Nevertheless, there exist competing interactions which are responsible for the appearance of the spin-glass state in such systems.

Here we will concentrate on lanthanide systems which built up well-localized moments. In the class of dilute lanthanide metals and intermetallic compounds for which spin-glass behavior has been reported, one topic involves 4f-impurities in superconducting hosts. Already a small amount of paramagnetic impurities, as

example 1 atom% Gd in *La*, destroys superconductivity. Above this critical concentration Hein et al. (1959) have observed the first striking low-field susceptibility maxima (fig. 10) already in 1959 which today we take as characteristic of spin-glass freezing (see also Finnemore et al. 1968, for an additional neutron diffraction study). In case of a very weak depression of the superconducting transition temperature T_c with magnetic impurity concentration x, as in $Nd_xTh_{1-x}Ru_2$, Hüser et al. (1983a) have given experimental evidence for even a coexistence of the spin-glass and superconducting state. Its phase diagram is shown in fig. 11. For recent reviews on the competition between superconductivity and magnetic order, with more complete references on experimental systems studied, we refer to the literature (Maple 1976, Roth 1978).

Another subject class is concerned with diluted 4f metals. Sarkissian and Coles (1976) have tried to distinguish between spin-glass freezing and helical ordering in solid solutions of Gd, Tb and Dy in Y and Sc by means of resistivity and susceptibility measurements (fig. 12). These materials have attracted recent interest again, because some are candidates for anisotropic spin glasses (Baberschke et al. 1984). It also turned out that spin-glass behavior in yttrium based alloys occurs at much lower concentrations than previously claimed.

Furthermore, diluted intermetallic compounds with 4f atoms also reveal spin-glass properties, for example (Gd, *La*)Al_2 (von Löhneysen et al. 1978b), (Gd, *Y*)Al_2 (Besnus and Kappler 1980), (Gd, *La*)B_6 (Felsch 1978), and (Er, *Y*)Al_2 (Bruss et al. 1979).

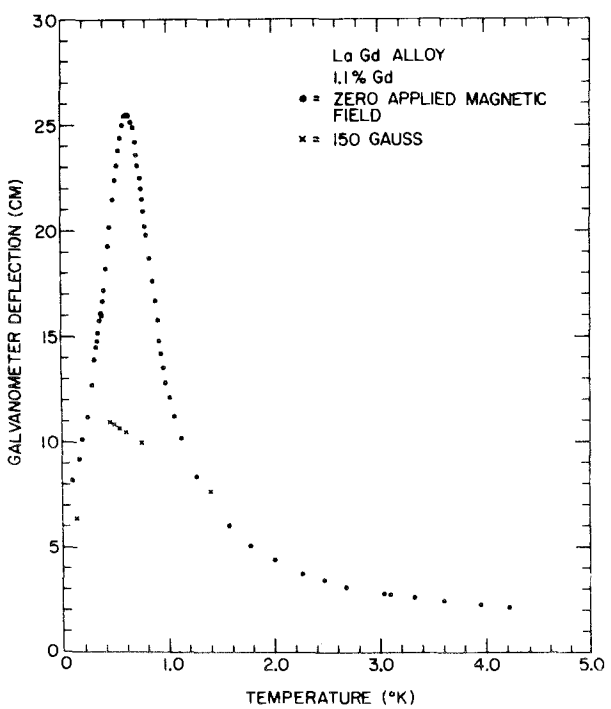

Fig. 10. Galvanometer deflection (proportional to the ac-susceptibility) in *La*Gd 1.1 atom% as a function of temperature at $H = 0$ and $H = 150$ G (from Hein et al. 1959).

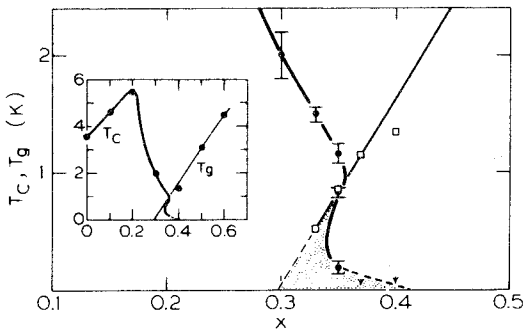

Fig. 11. Superconducting (T_c) and magnetic (T_g) phase diagram for $Th_{1-x}Nd_xRu_2$. The lines are a visual guide (from Hüser et al. 1983a).

Amorphous alloys: This class of structural disorder contains for instance a-Gd_xAl_{1-x} where detailed studies provide evidence for spin-glass behavior in the concentration range $0.30 \leqslant x \leqslant 0.40$ (see phase diagram in fig. 13, McGuire et al. 1978).

On the other hand, amorphous systems like a-DyCu whose magnetic orders are highly influenced by the random distribution of local anisotropy axes (due to single-ion anisotropy of non-S-state rare-earth atoms) will be called "*speromagnets*" (Moorjani and Coey 1984) and not discussed here, but in section 9. Remember that we decided to adopt the term "spin glass" to denote disordered magnets whose magnetic properties are due to a broad distribution of positive and negative interactions.

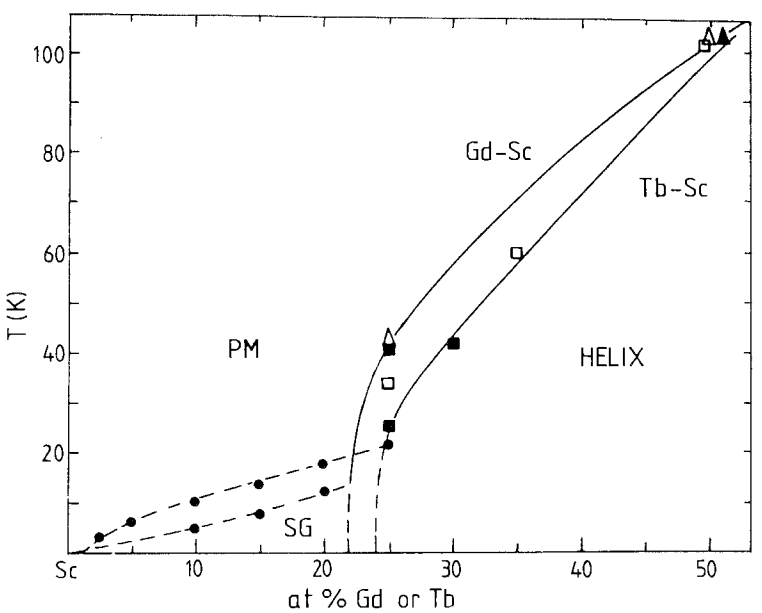

Fig. 12. Magnetic phase diagrams for Gd–*Sc* and Tb–*Sc* alloys. PM = paramagnet; HELIX = helical spin structure; SG = spin glass (from Sarkissian and Coles 1976).

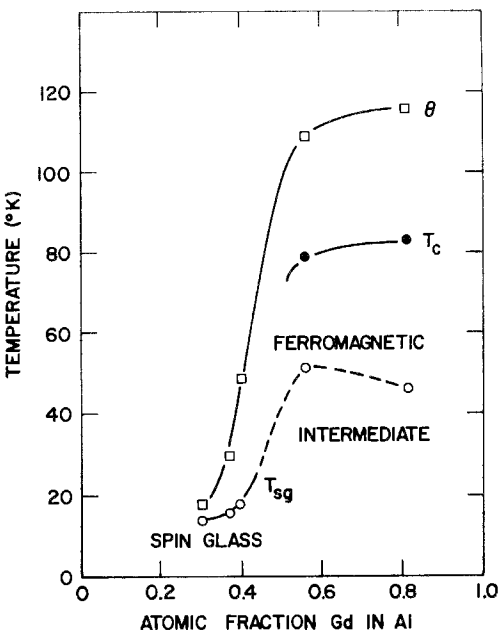

Fig. 13. Magnetic phase diagram for amorphous Gd–Al alloys showing temperatures for susceptibility peaks (T_{sg}), ferromagnetic Curie points (T_c), and paramagnetic θ values (from McGuire et al. 1978).

4. Model calculations

To discuss this new type of ordered phase in spin glasses, one would like to have a microscopic model where the actual interactions and anisotropies are considered and the average over a realistic description of the site dilution disorder is performed. Clearly this is a difficult task and up to now no realistic model of a spin glass has been solved analytically. In addition, there exists another difficulty because a proper treatment of systems with quenched disorder like spin glasses involves averaging the free energy F rather than the partition function Z

$$F = [F\{x\}]_{av} = -\frac{k_B T}{N} [\ln Z\{x\}]_{av} \tag{8}$$

where F depends on a large set of variables $\{x\}$ describing the randomness.

4.1. *Edwards–Anderson model*

In 1975 Edwards and Anderson (EA) published a paper (Edwards and Anderson 1975) which revolutionized the statistical mechanics of disordered spin systems. Stimulated by Cannella and Mydosh's observation of a cusp in the temperature dependence of the ac magnetic susceptibility of dilute alloys such as *Au*Fe and *Cu*Mn (Cannella and Mydosh 1972), EA propose a model to study this problem and a method of solving it. They consider the Hamiltonian

$$\mathcal{H} = -\sum_{ij} J_{ij} \boldsymbol{S}_i \boldsymbol{S}_j - g\mu_B \boldsymbol{H} \sum_i \boldsymbol{S}_i \tag{9}$$

where classical spins $\boldsymbol{S}_i$ are put onto the sites of a regular lattice, and disorder is introduced by a suitable distribution $P(J_{ij})$ of exchange interactions. $\boldsymbol{H}$ is an external magnetic field. For instance a Gaussian distribution of the J_{ij} can be taken

$$P(J_{ij}) \propto \exp - \frac{(J_{ij} - J_0)^2}{2\Delta J^2} \,. \tag{10}$$

For $|J_0| < \Delta J$ there are ferromagnetic ($J_{ij} > 0$) as well as antiferromagnetic ($J_{ij} < 0$) couplings.

EA present the following picture of a spin glass below the "freezing temperature": If one observes a given spin pointing in a certain direction, then there is a finite probability for a long period of time to find the spin pointing in the same direction. They propose a new type of order parameter which describes long-*time* correlations (instead of long-range *spatial* spin correlations)

$$q_{EA} = \lim_{t \to \infty} [\langle S_i(t) S_i(0) \rangle_T]_{av} \tag{11}$$

where $\langle \ldots \rangle_T$ denotes a statistical mechanics average for a given set of interactions and $[\ldots]_{av}$ is an average over the distribution of interactions (=configurational average). It should be emphasized that what differentiates the spin-glass phase from the paramagnetic state is precisely the non-vanishing value of the local autocorrelation function in time. Thus a "memory" effect prevails in the spin-glass state.

In order to avoid averaging ln Z, EA use the so-called replica trick, where one averages quantities such as Z^n when n is an integer. The relevance of averaging Z^n instead of ln Z lies in the relationship

$$\ln Z = \lim_{n \to 0} \frac{1}{n} (Z^n - 1) \,. \tag{12}$$

Another way of getting around this difficulty is studying time-dependent phenomena in spin glasses (De Dominicis 1978).

The EA model contains the two essential ingredients for a spin glass – disorder and competition as discussed above – but it is a crude approximation to real spin glasses. Therefore at the beginning we have to discuss how well this model reproduces spin-glass properties. Up to now there is no analytic solution available for the short-range EA model. Even modern methods like real space renormalization yield inconclusive results (Kinzel and Fischer 1978, Tatsumi 1978). Hence numerical methods like the Monte Carlo simulation have been applied to answer this question the results of which will be briefly summarized now. Then the mean-field analysis of the EA model will be discussed, and finally the question

about the existence of a phase transition in real spin glasses is taken up in the last part of this section. We restrict ourselves, however, to describing always some typical results only; further details of the model calculations are deferred to the following sections where they are presented in direct comparison with experimental data.

4.2. *Monte Carlo simulations*

Extensive studies of the 2-dimensional EA–Ising model with Gaussian distributed nearest neighbor bonds by Monte Carlo simulations (Binder and Schröder 1976, Kinzel 1979, Kinzel and Binder 1984) provide evidence that the EA model reproduces many experimental findings on real spin glasses remarkably well. For instance

- A peak in the time dependent susceptibility $\chi(T)$ at T_f (fig. 14b).
- A broad maximum in the magnetic specific heat $C(T)$ above T_f (fig. 14a).
- A plateau in the field-cooled magnetization $M(T)$ (fig. 14c) and an S-shaped curve of $M_{ZFC}(H)$ (fig. 14d).
- The existence of different remanences, TRM and IRM, and their dependence on temperature, field and time (fig. 27).

Some of these results are shown in fig. 14 and fig. 27 which can be compared with fig. 2.

4.3. *Mean-field theory (Sherrington–Kirkpatrick model)*

4.3.1. *Ising spins*

The *infinite*-range model of Sherrington and Kirkpatrick (SK) (1975) was originally introduced as a model for which the mean field analysis of EA would be exact. Here, each spin couples equally with every other spin in the system. One takes in eq. 10 the mean $[J_{ij}]_{av} = J_0/N$ and the variance $\Delta J = \tilde{J}/\sqrt{N}$ in order to get a non-trivial thermodynamic limit (N is the number of spins in the system).

But while the formulation of mean field theory, e.g. for an infinite-range ferromagnet, is rather trivial, the formulation for spin glasses has been a major challenge of theoretical physics. It has taken eight years to achieve an essentially complete understanding of the thermodynamics of this model. In fact, this model starts from an unphysical assumption, but equally as for conventional pure problems it has proven instructive, and many experimental results are in remarkable qualitative agreement with the SK model's predictions.

It has been shown that the SK model has a true phase transition in thermal equilibrium at a finite temperature T_f, with a cusp both in the magnetic susceptibility $\chi(T)$ and the magnetic specific heat $C(T)$. The latter prediction is in serious disagreement with experimental specific heat data. In magnetic fields the cusp in $\chi(T)$ does get rounded, however, the fields required for the rounding are approximately twenty times stronger than the ones observed experimentally.

In the original solution of this model by SK the low-temperature phase is characterized by a single order parameter, q_{SK}, defined by

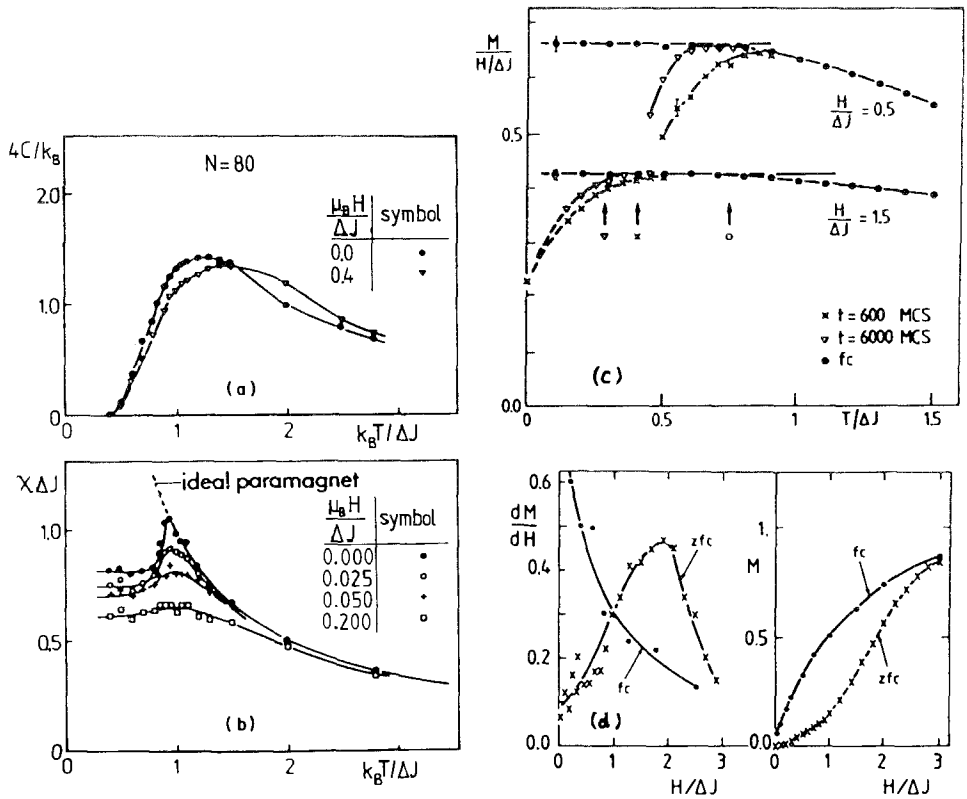

Fig. 14. Collection of some results from Monte Carlo simulations for a 2-dimensional EA-Ising model with Gaussian distributed nearest-neighbor bonds: (a) Specific heat C vs temperature for two values of the magnetic field H. (b) Susceptibility χ vs. temperature for four values of the magnetic field H (Binder and Schröder 1976). (c) Susceptibility M/H vs temperature for two values of the field H. The solid circles show the field-cooled magnetization. The other symbols show the magnetization obtained from zero-field cooling and then applying the field H for a given time as indicated (MCS = Monte-Carlo steps per spin). Arrows identify critical fields as shown in figs. 65 and 66. (d) Magnetization M and its derivative dM/dH at zero temperature for the field-cooled (circles) and zero-field cooled (crosses) case (Kinzel and Binder 1984).

$$q_{SK} = [\langle S_i \rangle_T^2]_{av} . \tag{13}$$

$q_{SK}(T)$ vanishes at T_f as $q_{SK} \propto 1 - T/T_f$ and is unity at $T = 0$. The cusp in $\chi(T)$ at T_f is given by

$$\chi(T) = \frac{C}{T}(1 - q_{SK}) . \tag{14}$$

This solution was subsequently shown by *de Almeida and Thouless* (*AT*) (1978) to be unstable below a line in the H–T plane terminating at $T = T_f$ for $H = 0$, and

varying for small fields as

$$\delta T_f(H)/\tilde{J} = (3/4)^{1/3}(H/\tilde{J})^{2/3} \tag{15}$$

with

$$\delta T_f = T_f(H=0) - T_f(H) .$$

It turned out that this instability is not an artifact of the method employed, but it represents an inherent difficulty of the spin-glass problem, and its study has pointed the way to the essential physics.

Below the AT line (at which the symmetry between replicas is broken) a single order parameter description is no longer correct, but a whole *order parameter function* $q(x)$ is necessary, monotonic in the range $0 \leq x \leq 1$, to describe the static properties (Parisi 1979). The meaning of this function $q(x)$ was initially obscure. It has been obtained by the replica method together with a selfsimilar replica symmetry breaking (fractal structure; see e.g. De Dominicis 1983), but $q(x)$ is also given by a dynamical formulation where the parameter x is related to a set of time scales (Sompolinsky and Zippelius 1981). There have been various discussions of the relation between the two approaches (Houghton et al. 1983, De Dominicis and Young 1983a). These considerations clarified the characteristics of the phase below the AT line in the SK model.

Sompolinsky (1981) shows that there are relaxation times which *diverge* exponentially in the thermodynamic limit ($N \to \infty$). This idea is connected with the fact that the mean-field equations of Thouless, Anderson and Palmer (TAP) (1977) which describe the magnetizations for a particular set of J_{ij}, have *many* solutions (Bray and Moore 1980, De Dominicis et al. 1980): for a system of N spins the number of states metastable against single spin flip scales as $N_s(N) \propto \exp(\alpha(T) \cdot N)$ where $\alpha(T)$ is non-zero for T below the AT line. These minima in phase space ("valleys") are stable at finite temperatures if they are separated from each other by an energy barrier whose height diverges when $N \to \infty$. Sompolinsky's divergent time scales presumably correspond to the rare fluctuations over these barriers which can occur for finite N.

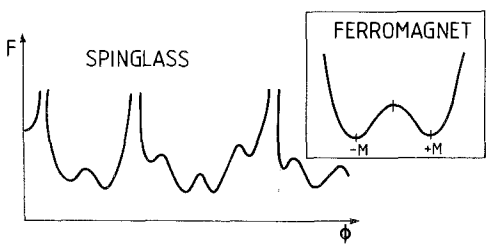

Fig. 15. Schematic plot of the free energy F of a spin glass as a function of a phase-space coordinate ϕ which measures the projection of the considered state on a particular ordered state. The inset shows the situation in an Ising ferromagnet for comparison.

Thus spin-glass ordering is *non-unique*: there exists a large number of equivalent states with the same macroscopic properties but with different microscopic spin configurations – contrary to usual periodic order where only one state occurs (up to rotation or $S_i = \pm 1$ Ising symmetry). In fig. 15 a schematic picture of the free energy is shown as function of one coordinate in phase space, with many "valleys" separated by high free energy barriers.

Now the meaning of the order parameter function $q(x)$ can be understood for instance in terms of dynamics: if one takes $N \to \infty$ before the time t tends to infinity, the system will stay in a single valley and one will measure q_{EA}. However, if we study the *infinite* time limit of a finite system then the system will move between different valleys in phase space and the time average will be equivalent to the average from equilibrium statistical mechanics, q:

$$q_{\mathrm{EA}} = \lim_{t\to\infty} \lim_{N\to\infty} q(t) \tag{16}$$

$$q = \lim_{\tilde{H}\to 0} \lim_{N\to\infty} \lim_{t\to\infty} q(t)\,. \tag{17}$$

Here in the time dependent autocorrelation function

$$q(t) = [\langle S_i(0) S_i(t)\rangle_{t'}]_{\mathrm{av}} \tag{18}$$

the time average $\langle \ldots \rangle_{t'}$ is performed over the observation time. The canonical Gibbs average must be evaluated with a small field $\tilde{H}$ which breaks the spin reversal symmetry ($S_i \to -S_i$ for all i) and which is taken to zero after taking $N \to \infty$.

The parameter x labels a spectrum of relaxation times $\tau(x)$ where $\tau(x)$ decreases with x: The shortest time marked by $x = 1$ defines

$$q(x = 1) = q_{\mathrm{EA}} \tag{19}$$

for which the system remains in a single valley, whereas the statistical mechanics order parameter q is associated with the longest time (marked by $x = 0$)

$$q(x = 0) = q \tag{20}$$

which leads to an average over all valleys.

From the monotonic increase of the lifetimes with N it follows that in the thermodynamic limit the SK model is *non-ergodic* (Palmer 1982) below $T_{\mathrm{f}}(H)$: the time average of the order parameter q_{EA} does *not* agree with the ensemble average q. Monte Carlo simulation yields for the time average

$$\begin{aligned} &1 - q_{\mathrm{EA}}(T) \propto T^2 \\ &\tilde{\chi}(T) = \frac{C}{T}(1 - q_{\mathrm{EA}}) \propto T \end{aligned} \qquad \text{for } T \ll T_{\mathrm{f}}\,. \tag{21}$$

For the ensemble average one obtains

$$1 - q(T) \propto T$$
$$\chi_{\mathrm{eq}}(T) = \frac{C}{T}(1 - q) = \text{const}. \tag{22}$$

These two limiting processes in $\chi(T)$ are sketched in fig. 16.

The Parisi order parameter function $q(x)$ with $0 \leq x \leq 1$ is shown to be related to "overlap functions" between different valleys. Defining an overlap

$$q_{12} = \frac{1}{N} \sum_i \langle S_i^1 \rangle \langle S_i^2 \rangle \tag{23}$$

between two states $\langle S_i^1 \rangle$ and $\langle S_i^2 \rangle$ (or two valleys), then the probability distribution $P(q)$ of phases having overlap equal to q is just the derivative of the inverse function $x(q)$:

$$P(q) = \mathrm{d}x/\mathrm{d}q \tag{24}$$

(Parisi 1983, Young 1983b, De Dominicis and Young 1983b).

Looking at overlaps between *three* valleys (Mézard et al. 1984) it turned out to one's surprise that there are restrictions on the values these overlaps can take: there is no probability associated with all three overlaps different. Such restrictions characterize an *ultrametric* space. Physically it arises from a hierarchical structure of "valleys within valleys within. . .".

Summarizing the theoretical picture of the SK model of a spin glass, there are many thermodynamic states below the phase transition at T_{f} which can be characterized by a whole order parameter function $q(x)$. In a single thermodynamic state ("valley") the order parameter is the largest value of the Parisi function, i.e. $q(x = 1) = q_{\mathrm{EA}}$. The many-valley structure of phase space leads to diverging relaxation times and to nonergodic behavior. The freezing temperature T_{f} signals the onset of irreversibility (= replica symmetry breaking).

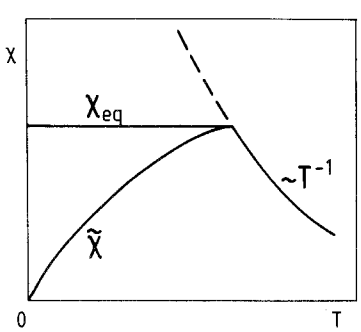

Fig. 16. Susceptibilities, eqs. 21 and 22, vs temperature as obtained for the SK model with infinite-range interactions.

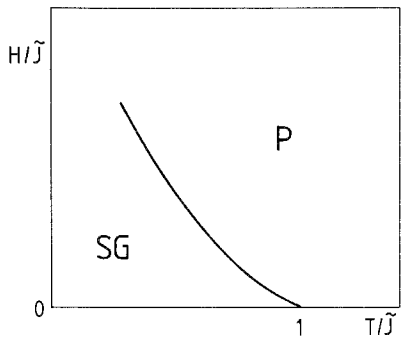

Fig. 17. Plot of the deAlmeida–Thouless (AT) line for the SK model (Ising spins) with $J_0 = 0$ (eq. 15). To the right of the AT line (P) the SK solution with a single order parameter is correct, while to the left of the AT line (SG) the Parisi's order-parameter function is believed exact. The AT line signals the onset of irreversibility.

These properties are also found in an *external magnetic field H* below the *AT line* (see eq. 15 and fig. 17). There is an analogous transition when $H = 0$ but the mean of the exchange distribution $J_0 > 0$: As shown in fig. 18, then the AT line is the boundary between the ferromagnetic phase FM and a modified ferromagnetic phase F′ with irreversibility (often called a "*mixed*" phase). The F′–SG phase boundary is vertical in the T–J_0 phase diagram in the Parisi theory.

4.3.2. *Heisenberg spin glasses in magnetic field*

Up to now we always considered Ising spins in the SK model. Let us now discuss briefly the generalization to m component vector spin glasses ($m = 3$: Heisenberg spins) (Sherrington 1983). It turned out that isotropic vector spin glasses within the SK model are rather similar to the Ising case. Interesting new features, however, occur in the presence of a magnetic field H, as first discussed by Gabay and Toulouse (1981) (see also Cragg et al. 1982a).

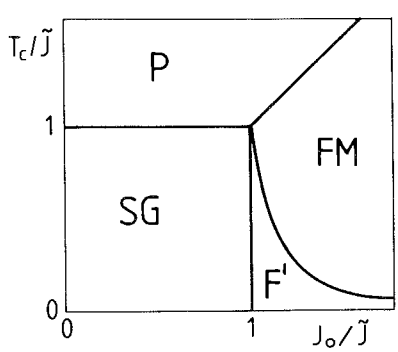

Fig. 18. Magnetic phase diagram for the SK model (EA model for Ising spins with infinite-range couplings). $\tilde{J}$ and J_0 denote the width and mean of the exchange distribution. P = paramagnet; FM = ferromagnet; SG = spin glass. F′ is a ferromagnetic phase with replica symmetry breaking, i.e. irreversibility ("mixed phase") and is separated from FM by an AT line.

The EA-Hamiltonian in eq. 9 is now written for classical vector spins S_i with m components S_i^μ, $\mu = 1, \ldots, m$. The $\mu = 1$ component is defined to be parallel to the field H. The SG order parameter is then a tensor in spin space with

$$q_\parallel = [\langle S_i^1 \rangle_T^2]_{\text{av}} \tag{25}$$

$$q_\perp = [\langle S_i^\mu \rangle_T^2]_{\text{av}} \quad \text{with } \mu = 2, \ldots, m\,. \tag{26}$$

In the presence of a field one always has $M = [\langle S_i^1 \rangle_T]_{\text{av}} \neq 0$ and $q_\parallel \neq 0$, but Gabay and Toulouse (GT) predicted a *transverse freezing*, with $q_\perp \neq 0$, below the *GT line* (for small H):

$$\frac{\delta T_f(H)}{\tilde{J}} = \frac{m+4}{2(m+2)} \left(\frac{H}{\tilde{J}}\right)^2 . \tag{27}$$

This feature is sketched in fig. 19. Thus, a vector spin system in a field H within the SK model exhibits a phase with spin-glass order transverse to the field, reminiscent of a spin-flop phase of a pure antiferromagnet. Just below the GT line, only weak irreversibilty occurs in the longitudinal component $q_\parallel$, but there is a crossover to strong irreversibility in $q_\parallel$ at a region which goes as $H^{2/3}$ like the AT line (indicated by the dashed line in fig. 19).

Again we also report on the corresponding behavior in the T–J_0 phase diagram, as sketched in fig. 20. There is an analogous GT-transition, when $H = 0$ but $J_0 > 0$, from a collinear ferromagnet FM to a "canted FM state" F′, where the spins are not all parallel because $q_\perp \neq 0$ as well as $M \neq 0$. Thus, in vector spin glasses with $J_0 > 0$ a "mixed" phase F′ is predicted in the SK model where ferromagnetism coexists with transverse spin-glass order. The F′–SG phase boundary is again vertical.

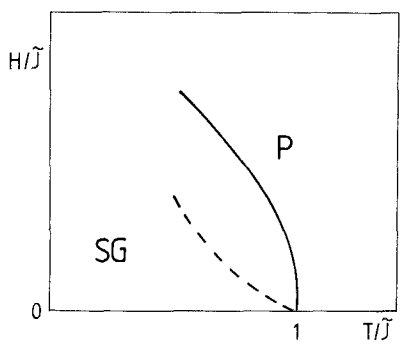

Fig. 19. Plot of the Gabay–Toulouse (GT) line (solid line) for an infinite-range vector-spin glass (eq. 27). The low-temperature phase (SG) has nonzero transverse spin-glass ordering. The deAlmeida–Thouless (AT) line (dashed line) strictly no longer occurs but there is a well-defined crossover region which follows a similar curve.

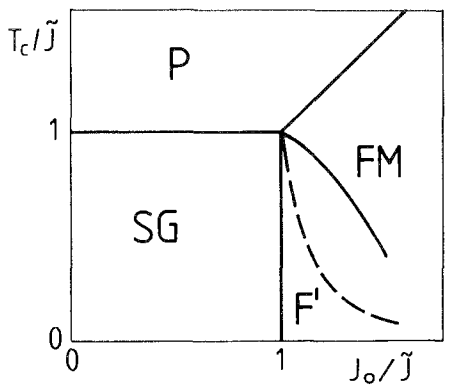

Fig. 20. Magnetic phase diagram for an infinite-range vector-spin glass with nonzero mean, J_0, in the exchange distribution. P = paramagnet; FM = ferromagnet; SG = spin glass. The "mixed phase" F' where ferromagnetism coexists with transverse spin-glass order is separated from FM by a GT line (solid line). The dashed line indicates a crossover region as in fig. 19.

4.3.3. *Anisotropic spin glasses*

Now we turn to the effect of single-ion *uniaxial anisotropy* which in general leads to a preferred "easy" axis of magnetization. Recent mean-field calculations (Cragg and Sherrington 1982b, Roberts and Bray 1982) have predicted a rather rich magnetic phase diagram (fig. 21) for such uniaxial anisotropic spin glasses. The Hamiltonian is given by

$$\mathcal{H} = -\sum_{ij} J_{ij} \boldsymbol{S}_i \boldsymbol{S}_j - D \cdot \sum_i (S_i^1)^2 \tag{28}$$

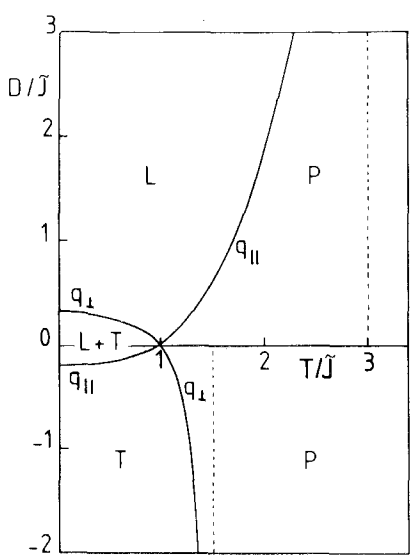

Fig. 21. Magnetic phase diagram for an infinite-range vector spin glass with uniaxial anisotropy D (Cragg and Sherrington 1982b, Roberts and Bray, 1982). Longitudinal (L) and transverse (T) spin-glass order occurs as well as both together (L + T).

where the anisotropy energy D is allowed any magnitude or sign. The limiting models are (i) $D \to +\infty$, Ising; (ii) $D \to -\infty$, planar XY; $D = 0$, Heisenberg. Let us consider the case $J_0 = H = 0$.

If the anisotropy $D > 0$ is weak compared to the exchange $\tilde{J}$, *two* successive transitions are expected (fig. 21): As the temperature is decreased, spin components along the easy axis ("1"-direction) freeze at T_f (longitudinal spin-glass phase L-SG, with $q_\parallel \neq 0$ and $q_\perp = 0$). Then, at a lower critical temperature T_2 the transverse components freeze as well (LT-SG, with $q_\parallel \neq 0$ and $q_\perp \neq 0$). The second transition does not exist for sufficiently strong anisotropy. Corresponding features are found if $D < 0$ which favors transverse freezing (T − SG, with $q_\perp \neq 0$).

4.3.4. *Dynamics*

The non-ergodicity of the spin glass as described by the SK model suggests that an understanding of spin-glass dynamics is essential. It has been studied for Ising spins in mean-field theory either in the Glauber model or in the "soft spin" version (in which the length of the spins is not fixed) (Kirkpatrick and Sherrington 1978, Sompolinsky and Zippelius 1981 and 1982). We have already discussed above the central feature of Sompolinsky's theory which introduces time-dependent order parameters and obtains a spectrum of timescales which *diverge* in the thermodynamic limit below the AT line.

For temperatures *above* T_f one has exponential decay of the spin correlations with a characteristic time τ and critical slowing down with a divergence of τ at T_f, as expected from dynamical scaling (Hohenberg and Halperin 1977):

$$\tau \propto \xi^z \propto \left(\frac{T - T_f}{T_f}\right)^{-z\nu} \qquad \text{with } z\nu = 2 . \tag{29}$$

ξ is the correlation length and z the dynamic exponent.

Below T_f, however, the analysis predicts *algebraic decay* of the correlation function $q(t)$ (see eq. 18)

$$q(t) \propto (t/\tau)^{-\nu} \quad \text{for } T \leq T_f . \tag{30}$$

That means one has a *marginal* spin-glass transition in the SK model (Bray and Moore 1979), and the marginal stability of the spin-glass phase holds for all temperatures below T_f (Sompolinsky 1981). Sompolinsky and Zippelius (1981, 1982) obtain an exponent ν which decreases with temperatures below T_f:

$$\nu(T) = \frac{1}{2} - \frac{1}{\pi}(1 - T/T_f) \quad \text{for } T \leq T_f . \tag{31}$$

Fischer and Kinzel (1984) calculate the dynamic susceptibility $\chi(\omega, T, H)$ near T_f and determine the crossover for low frequencies from the expected analytic

behavior at high temperatures

$$\text{Im } \chi(\omega) \propto \omega \quad \text{at } T > T_f \tag{32}$$

to the behavior on the AT line:

$$\text{Im } \chi(\omega) \propto \omega^{1/2} \quad \text{at } T = T_f \tag{33}$$

which is consistent with the critical exponent $\nu = 1/2$ at T_f from eq. 31. The crossover relations also reproduce the sharp increase of Im $\chi(T)$ as measured in spin glasses.

4.4. *Transition in real spin glasses*

We saw above that the SK model has a transition at $T_f > 0$ with a complicated ordered state below T_f. It is of great interest to know how many of these features of the mean-field theory are confirmed in real systems in three dimensions ($d = 3$). This will be discussed in the next section where we will see that despite extensive experimental and theoretical studies several problems are still unsolved.

The question about the existence and nature of a spin-glass transition in $d = 3$ has remained controversial. The SK model does not answer the question since it is a mean-field theory, and the *upper critical dimension* d_u for spin glasses is $d_u = 6$ or for certain exponents even $d_u = 8$ (Fisher and Sompolinsky 1985).

Suggestions for the *lower critical dimension* d_l for Ising spin glasses range from $d_l = 2$ (Southern and Young 1977, Anderson and Pond 1978) to $d_l = 4$ (Fisch and Harris 1977, Sompolinsky and Zippelius 1983). In pure systems d_l for Ising spins is known to be lower than that for Heisenberg spins ($d_l = 1$ for Ising ferromagnets; $d_l = 2$ for XY or Heisenberg ferromagnets). Below d_l no transition occurs at finite temperature due to thermal fluctuations, and for $d = d_l$ one expects, e.g. a divergence of the exponent ν with $1/\nu = 0$.

The absence of a finite-temperature equilibrium transition of EA-Ising spin glasses in *two dimensions* has been inferred from transfer matrix calculations by Morgenstern and Binder (1979) which has been supported later by fitting the high-T Monte Carlo data (Young 1983a, McMillan 1983). Thus, Ising spin-glasses for $d = 2$ are now generally believed to have $T_f = 0$ and $1/\nu > 0$ (i.e. $d_l \neq 2$).

A similar concept of "$T_f = 0$-freezing" has been assumed to be valid in *three dimensions* as well (Kinzel and Binder 1983, 1984, Binder and Young 1984). More recently, however, finite-size scaling for "defect energies" for small lattices by Bray and Moore (1984, 1985a), McMillan (1984a), and Bhatt and Young (1985) has been interpreted as an indication for a *finite* T_f in $d = 3$. Monte Carlo simulations on a fast special-purpose computer by Ogielski and Morgenstern (1985) and Ogielski (1985) which exceed the previous ones by several orders of magnitude confirm the nonzero transition temperature for Ising spin glasses in $d = 3$. They obtain $T_f/\tilde{J} \approx 1.2$ and the following values of the critical exponents:

$$\nu = 1.3 \pm 0.1 \quad \text{for the correlation length } \xi \propto |T - T_f|^{-\nu} .$$

$$\gamma = 2.9 \pm 0.3 \quad \text{for the non-linear susceptibility } \chi_{SG} \propto |T - T_f|^{-\gamma} .$$

$$\eta = -0.22 \pm 0.05 \quad \text{for the decay of correlations} \tag{34}$$

$$G(r) = [\langle S_0 S_r \rangle^2]_{av} \propto \xi^{-d+2-\eta} g(r/\xi) .$$

$$z\nu = 7.2 \pm 1 \quad \text{for the correlation time } \tau \propto |T - T_f|^{-z\nu} .$$

The exponential decay of spin correlations at high T changes to an algebraic (power-law) decay as the system goes through T_f. There is a divergence of τ at T_f following the dynamical scaling hypothesis. The magnitude of critical exponents, and the rather unusual behavior of the spin-glass phase below T_f are not typical for a conventional phase transition to a state with long-range order. This suggests that $d = 3$ is *close to the marginal dimension* (i.e. $d_l \approx 3$). So far, the data are consistent with the hypothesis that the spin-glass phase is *always critical at all* $T \leqslant T_f$, i.e. that there is no true long-range order but rather that static and dynamic correlations decay algebraically (Bhatt and Young 1985, Ogielski 1985) – just as in the case of the Kosterlitz–Thouless (1973) transition in the two-dimensional XY ferromagnet. However, much greater lattice sizes and lower temperatures are required to clarify this last point.

5. Spin glasses at low temperatures

In this section characteristic properties of spin glasses at temperatures well below the freezing temperature T_f are discussed, T_f being determined, e.g. by the maximum of the low-field, low-frequency ac-susceptibility. A number of fascinating phenomena are known to occur in spin glasses at low temperatures and they had been well documented in dilute alloys such as *Cu*Mn and *Au*Fe (Owen et al. 1957, Schmitt and Jacobs 1957, Kouvel 1961, Tournier and Ishikawa 1964) long before these systems became objects of such intense and systematic studies.

5.1. *Irreversibilities*

In thermal equilibrium the magnetization of spin glasses is zero since the magnetic moments point into random directions (see e.g. property (b) in sec. 2.1). However, there exists a finite magnetization, called remanent magnetization, M_r, after an external magnetic field has been switched off at low temperature. The M_r value and the magnetization M in small fields are found to be dependent on temperature, field, time and on the "magnetic history" of the sample. Observations of such irreversibilities provide potentially useful information on low-temperature properties of spin glasses which will be discussed now.

The two most commonly "magnetic histories" used in experiments are the following (Tholence and Tournier 1974): the *zero-field-cooled* (*ZFC*) magnetization is obtained by cooling the sample to the measuring temperature $T^* < T_f$ in zero external field starting at high temperature $T > T_f$; then a field H is applied at T^* and M is measured (M_{ZFC}). After this ZFC procedure one can switch off the field H at T^* in order to obtain the so-called isothermal remanent magnetization (*IRM*). The second, *field-cooling* (*FC*) procedure is to turn on the field H already above T_f and then to cool the sample in this field H down to the measuring temperature $T^* < T_f$ where one measures either the magnetization M_{FC} or, after switching off H, the so-called thermo-remanent magnetization (*TRM*).

Susceptibilities, M/H, deduced from such measurements in low field H are shown in fig. 22 for two spin glasses $Cu_{1-x}Mn_x$ with concentration $x = 0.0108$ and 0.0202 (Nagata et al. 1979). One realizes that even in such a small field of $H = 5.90$ G, M_{FC} is different from M_{ZFC} (here the "zero" field is less than 0.05 G) below T_f. On heating, the FC-magnetization is reversible, whereas the ZFC-magnetization is not. If the ZFC-magnetization is cooled back down sufficiently below T_f, a reversible and relatively T-independent magnetization is obtained.

The field dependence of both sorts of magnetizations is displayed in fig. 23, taking as example data of the spin glass $Eu_{0.30}Sr_{0.70}S$ at 70 mK (Maletta and Felsch 1979b). The magnetization after ZFC exhibits a smaller slope versus H than $M_{FC}(H)$ below T_f which is consistent with the findings at very low fields

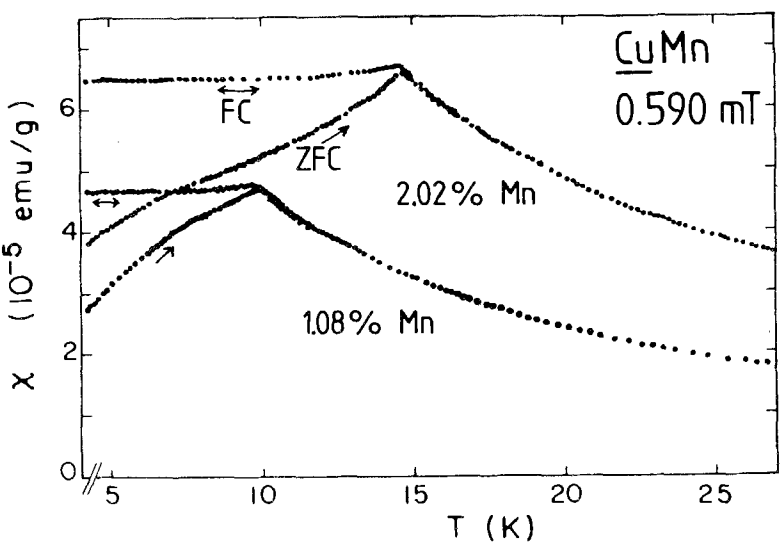

Fig. 22. Static susceptibilities M/H of *Cu*Mn spin glasses vs temperature for 1.08 atom% and 2.02 atom% Mn. After zero-field cooling ($H < 5 \times 10^{-3}$ mT) the initial susceptibilities (ZFC) were taken for increasing temperature in a field of 0.590 mT. The field-cooling susceptibilities (FC) were obtained in the field of 0.590 mT which was applied above T_f before cooling the sample, and they are reversible (from Nagata et al. 1979).

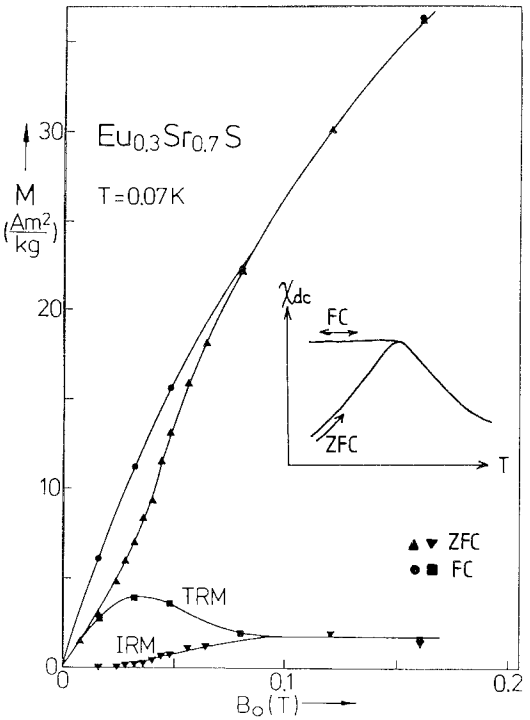

Fig. 23. Magnetization M of $Eu_{0.30}Sr_{0.70}S$ spin glass as function of the applied field at $T = 0.07$ K. Both the magnetization M_{ZFC} and isothermal remanent magnetization IRM, measured after zero-field cooling in increasing field, as well as the magnetization M_{FC} and thermoremanent magnetization TRM, measured after cooling in the field B_0, are shown. The inset displays schematically the corresponding ZFC- and FC-susceptibilities vs temperature (from Maletta and Felsch 1979b).

discussed above. An interesting feature is the S-shaped curvature of $M_{ZFC}(H)$ with an inflection point which moves downward in H with increasing T and disappears at about T_f (see also: Knitter and Kouvel 1980).

We now turn to the *remanent magnetization* which is only a small part of the total magnetization and is dependent on magnetic history, too, with

$$\mathrm{IRM}(H, T) < \mathrm{TRM}(H, T) \quad \text{for small fields} \tag{35}$$

as shown in fig. 23. The TRM starts out linear with the field H at small H, while the field dependence of the IRM is quadratic. There is no indication of a threshold field down to 0.5 Oe (Ferré et al. 1981) below which no remanent magnetization is observed as claimed by some authors (Tholence and Tournier 1974, Gray 1979). In high enough fields, both IRM and TRM saturate to the same value M_{rs} for $H \geqslant H_{cr}$. The IRM approaches it in a monotonous way, while the TRM passes through a maximum versus field. At fields exceeding $H_{cr}(T)$ where IRM and TRM merge, this history-dependence and hence irreversible effects are

negligible. The total magnetization, however, does not saturate even in pulsed fields up to 40 Tesla (Smit et al. 1979a, b, Rakoto et al. 1984). The temperature dependence of the saturated remanent magnetization obeys the relationship

$$M_{rs}(T) = M_0 \exp(-aT) \tag{36}$$

except at very low temperature (just where the TRM is found to be larger than M_{rs}, see fig. 23) as shown in fig. 24.

It has been well known from the beginning of these studies that the ZFC-magnetization and both types of remanent magnetizations show long-time, *non-exponential* variation in time (Tournier and Ishikawa 1964, Tholence and Tournier 1974, Guy 1975) typically of the form:

$$M(t) \propto \ln t\,. \tag{37}$$

On the other hand, the FC-magnetization has been generally assumed to yield information on the thermal equilibrium behavior of spin glasses because of its reversibility and time-independence (Malozemoff and Imry 1981, Chamberlin et al. 1982, Monod and Bouchiat 1982). Recently, several authors (Lundgren et al. 1982 and 1985, Wenger and Mydosh 1984a, Bouchiat and Mailly 1985, Kinzel and Binder 1984), however, question the validity of this assumption. We shall discuss this point in context with the time-dependent susceptibilities in sec. 6.1.

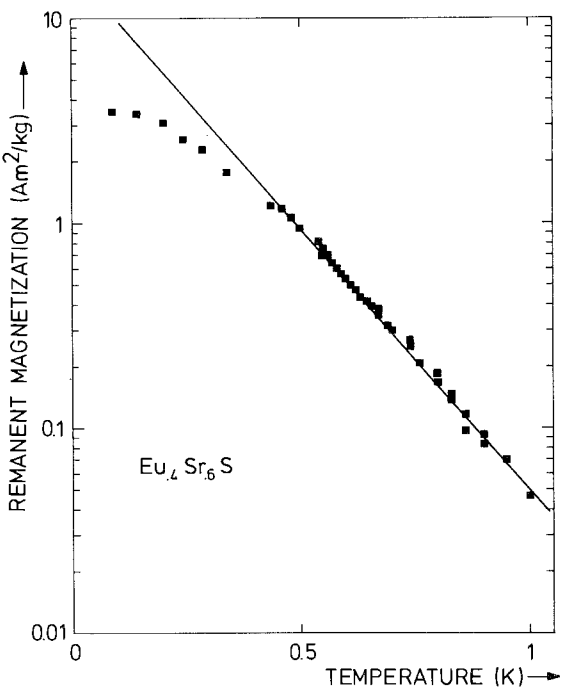

Fig. 24. Temperature dependence of the saturated remanent magnetization in $Eu_{0.40}Sr_{0.60}S$ (from Maletta and Felsch 1979b).

As first suggested by Tholence and Tournier (1974) one can decompose the FC-susceptibility $\chi = \lim_{H\to 0} M_{FC}/H$ into a reversible and an irreversible contribution at temperatures below T_f:

$$\chi_{rev}(T) + \chi_{irr}(T) = \chi(T_f) \quad \text{for } T \leq T_f \tag{38}$$

where the sum stays almost constant, and

$$\chi_{rev} = \lim_{H\to 0} \mathrm{d}M_{ZFC}/\mathrm{d}H \tag{39}$$

$$\chi_{irr} = \lim_{H\to 0} \mathrm{d}\,\mathrm{TRM}/\mathrm{d}H\,. \tag{40}$$

The ac-susceptibility as discussed later only measures the reversible part χ_{rev}. Equations (38) to (40) are consistent with the following relation (Maletta 1980c) between the magnetizations and remanent magnetizations measured after different magnetic histories, as is obvious from fig. 23, too:

$$M_{ZFC}(H, T) = M_{FC}(H, T) - \mathrm{TRM}(H, T) + \mathrm{IRM}(H, T)\,. \tag{41}$$

Thus, the S-shaped curvature of the virgin magnetization, $M_{ZFC}(H)$, is directly connected to the field dependence of the remanences.

The shape of the TRM(H) curve is a consequence of the importance of the measuring time as shown by Ferré et al. (1981). They demonstrate that the maximum in TRM versus H results from an increase of the magnetization decay rate with field H which can compensate the higher initial TRM value at higher fields (fig. 25).

The *time decay* of the TRM in spin glasses has been studied in great detail. First

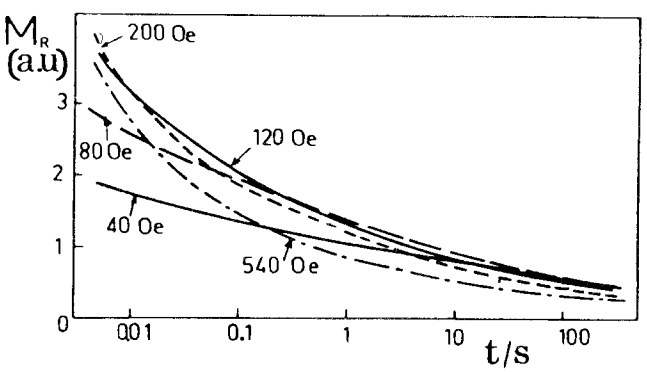

Fig. 25. Time decay of the TRM in $Eu_{0.40}Sr_{0.60}S$ for various fields at $T = 1.32$ K (from Ferré et al. 1981).

it was described by a logarithmic law, as already mentioned in eq. 37:

$$\mathrm{TRM}\,(t) \propto -S_{\mathrm{RM}} \ln t \tag{42}$$

where the coefficient S_{RM} is called "magnetic viscosity" (Guy 1977 and 1978). An example is shown in fig. 26: $M_{\mathrm{rs}}(t)$ is displayed for the spin glass $(La_{0.98}Gd_{0.02})Al_2$ at various temperatures below $T_{\mathrm{f}} = 520$ mK (von Löhneysen and Tholence 1979).

Measurements over two decades of time by Ferré et al. (1981) show that the data are better approximated by a power-law decay:

$$\mathrm{TRM}(t) \propto t^{\,a(T,H)}\,. \tag{43}$$

However, this power law fails for more than 3 decades of time, as already mentioned in that paper. A power-law decay is proposed by Monte Carlo simulations of an EA spin glass (Binder and Schröder 1976, Kinzel 1979, see fig. 27) which is nicely confirmed by the detailed Faraday-rotation measurements of $Eu_{0.40}Sr_{0.60}S$ by Ferré et al. (1981) as illustrated in fig. 28. As additional information, the experiment reveals a drastic change in the dynamics very near $T_{\mathrm{fo}} = 1.55$ K: there seems to be a divergence of the exponent a with T.

Very recently, Chamberlin (1985) pointed out that a better representation of his $M_{\mathrm{r}}(t)$-data for *Ag*Mn and *Cu*Mn is given by an exponential function of time raised to a fractional power (a "stretched exponential"):

$$\mathrm{TRM}(t) = M_{\mathrm{r}}(0)\exp(-(t/\tau_{\mathrm{p}})^{1-n}) \tag{44}$$

with a characteristic mean relaxation time τ_{p}. New $M_{\mathrm{r}}(t)$-data of $Eu_{0.40}Sr_{0.60}S$ over 5 decades of time (Ferré et al. 1986) and data of $Eu_{0.40}Sr_{0.60}Te$ (Börger-

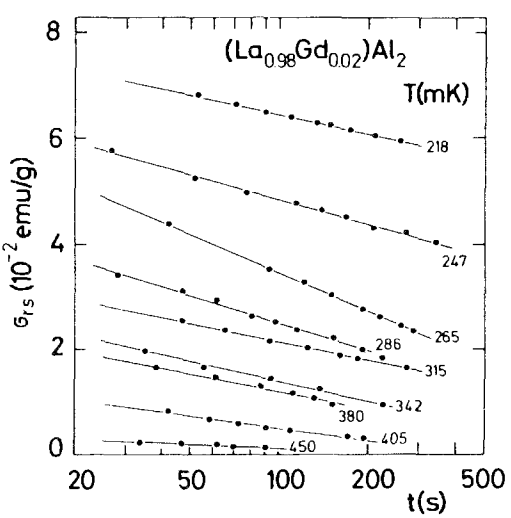

Fig. 26. Saturated remanent magnetization M_{rs} as a function of time (logarithmic) for $(La_{0.98}Gd_{0.02})Al_2$ at various temperatures (from von Löhneysen and Tholence 1979).

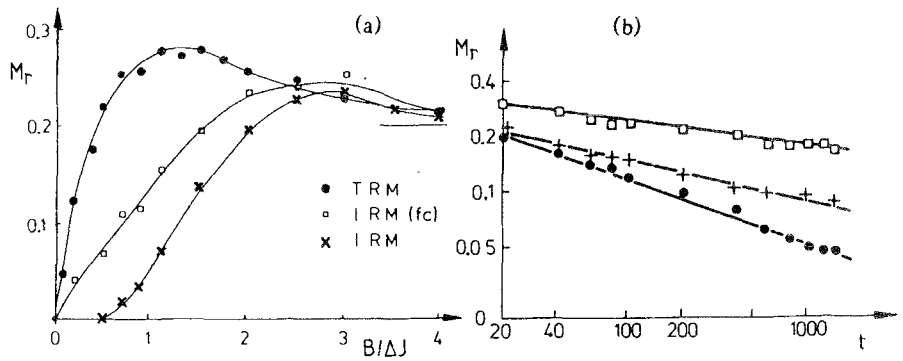

Fig. 27. Results from Monte Carlo simulations, like the data shown in fig. 14: (a) Remanent magnetization M_r obtained by cooling in a field (TRM) or shortly applying a field at constant temperature (IRM) as a function of the initially applied field. IRM (fc) is obtained by some mixed cooling procedure. M_r is measured at the temperature $T = \Delta J/4k_B$. (b) Remanent magnetization M_r as a function of time. The squares (TRM, $B = \Delta J$) and dots (IRM, $B = 1.5 \cdot \Delta J$) have the same initial energy, the dots and crosses (TRM, $B = \infty$) have the same initial magnetization ($T = 0.5 \cdot \Delta J$) (from Kinzel 1979).

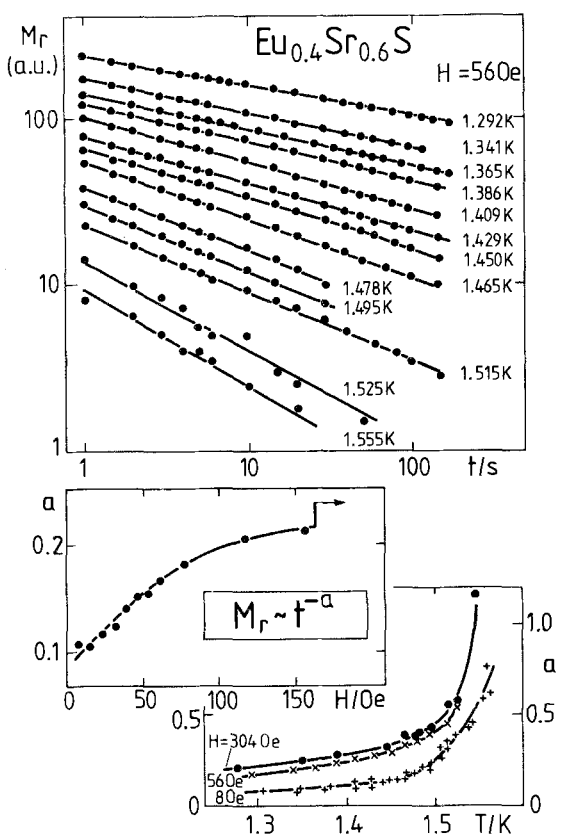

Fig. 28. Time decay of the TRM in $Eu_{0.40}Sr_{0.60}S$ spin glass close to $T_f = 1.55$ K (the initially applied field was $H = 56$ Oe), showing a power-law decay, t^{-a}, where the exponent a is dependent on the previously applied field H and on temperature (from Rajchenbach et al. 1981, and Ferré et al. 1981).

mann et al. 1986b) can also be fitted by eq. 44. In $Eu_{0.40}Sr_{0.60}Te$ the time decay depends on the waiting time t_w spent during cooling the sample from T_f to the temperature of measurement, similar to other spin glasses (Lundgren et al. 1983, Chamberlin 1985). Figure 29 shows data of $Eu_{0.40}Sr_{0.60}Te$ at $T = 0.890\ T_f$ which follows eq. 44 with the fitting parameters $M_r(0) = 0.60\ M_{FC}$, $n = 0.80 \pm 0.02$, and the waiting-time dependence $\tau_p(t_w)$ as displayed in the inset. The functional form of the time decay in eq. 44 appears attractive to be checked experimentally because it is based on a universal relation used to describe relaxation phenomena in glasses, polymers, dielectrics, etc. (Ngai et al. 1984). Recently, it has been predicted for glasses and spin glasses by Palmer et al. (1984) using models of hierarchically constrained dynamics and by De Dominicis et al. (1985) within the Parisi model extended to a dynamic context. Equation 44 holds only asymptotically for $t \gg \tau_p$. The problem, however, is the reliability of the three fitting parameters obtained with eq. 44, since they are generally rather correlated within the restricted time interval of the measurement.

One of the first phenomenological models to describe the irreversibilities in spin glasses is proposed by Tholence and Tournier (1974), following Néel's (1949) model for an ensemble of fine magnetic grains or particles. Their main assumption is the existence of well-defined "spin regions" or "*spin clouds*" *in a spin glass* which can relax between equilibrium orientations. For each cloud a potential barrier is determined by the dipolar anisotropy energy E_a which separates two

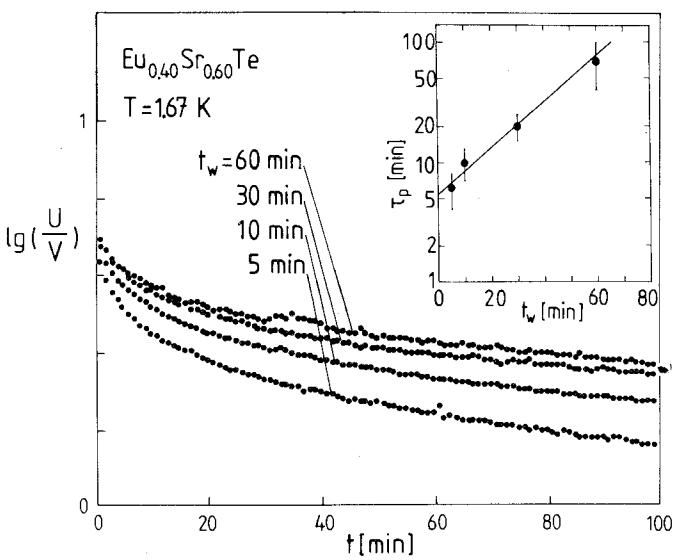

Fig. 29. Time dependence of the TRM in $Eu_{0.40}Sr_{0.60}Te$ spin glass as a function of the wait time t_w that the sample spent in the FC state at $T = 0.890 T_f$ before the field of 1.0 mT was removed, for $t_w = 5, 10, 30$ and 60 min. $M_r(t = 0)$ is not a function of t_w but M_r relaxes more slowly for longer t_w. The best fits to the data by the "stretched exponential" (eq. 44) give a characteristic mean relaxation time τ_p which increases with t_w exponentially, as shown in the inset (from Börgermann et al. 1986b).

easy orientations of its magnetization. Due to thermal fluctuations the magnetization can overcome the barrier within an average time τ given by the Arrhenius law

$$\tau = \tau_0 \exp(E_a/k_B T) \tag{45}$$

where τ_0 is some intrinsic time constant (τ_0^{-1} = attempt frequency). This implies that a particular cloud is blocked at a temperature T_B for which the relaxation time τ becomes equal to or larger than the measuring time t_m. As a consequence there appears a maximum in the ac-$\chi(T)$ at the freezing or blocking temperature T_B which is dependent on the measuring frequency $\omega = 2\pi/t_m$:

$$T_B^{-1}(\omega) = -(k_B/E_a)\ln(\tau_0\omega)\,. \tag{46}$$

Turning to the remanent magnetization M_r, this model provides a general relationship between the time and temperature dependence of M_r. Let $p(E_a)\,dE_a$ be the number of regions with an anisotropy energy between E_a and $E_a + dE_a$. Then the corresponding change of the remanent magnetization is

$$dM_r = -\tfrac{1}{2} M_g(E_a) p(E_a)\,dE_a \tag{47}$$

where $M_g(E_a)$ is the mean moment of those clouds and the factor $\frac{1}{2}$ takes into account the projection of M_g on the direction of field initially applied. By partial differentiation of M_r in eq. 47 with respect to $\ln t$ and T one obtains with eq. 45

$$\frac{\partial M_r}{\partial \ln t} = \frac{1}{\ln t - \ln \tau_0} \cdot T \cdot \frac{\partial M_r}{\partial T}\,. \tag{48}$$

For a number of years this concept of "spin clouds" has been very popular for analyzing experimental data of spin glasses (Tholence and Tournier 1974, Wohlfarth 1977, Préjean 1978, von Löhneysen and Tholence 1979). As an example, fig. 30 reproduces a plot according to eq. 48 for data of $(La_{0.98}Gd_{0.02})Al_2$ spin glass (with $\tau_0 = 10^{-6}$ s), which also follows eq. 36 and eq. 37 (fig. 26). von Löhneysen and Tholence (1979) claim that fig. 30 gives support to the model of "spin clouds".

Certainly, the "spin-cloud" model is based upon an oversimplified picture of spin glasses. It provides qualitative descriptions of several spin-glass properties, but thereby often unphysical fitting parameters are obtained. It is a correct, microscopic description of superparamagnetism, however, in spin glasses no evidence for independent domain structure is available. Let us give some examples to these statements.

Superparamagnetic behavior of independent spin clusters can be studied experimentally in dilute $Eu_xSr_{1-x}S$ with Eu concentrations x *below* the percolation threshold $x_p = 0.13$ (see discussion in sec. 2.2), as demonstrated by Eiselt et al. (1979a, b). Counting the number of all small, independent (since $x < x_p$) clusters

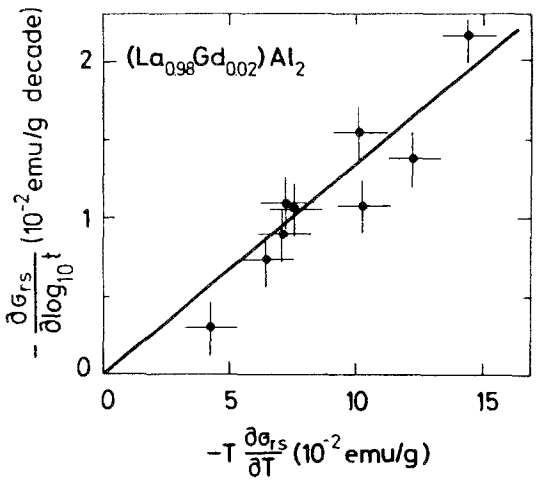

Fig. 30. Plot of the data from fig. 26, $M_{rs}(T, t)$, according to eq. 48 within the "spin cloud"-concept. The straight line yields $\tau_0 = 10^{-6}$ s (from von Löhneysen and Tholence 1979).

by computer with calculation methods known from percolation theory and calculating energy barriers due to intracluster dipolar anisotropy energy one gets time-dependent susceptibility maxima at $T_B(t)$ similar to eq. 46 and in good agreement with experiment *without* adjustable parameters (fig. 31). On the other hand, the frequency dependence of ac-susceptibility maxima $\chi(T)$ also observed in spin glasses, *cannot* be interpreted by means of the picture of blocking of superparamagnetic clouds, as done by von Löhneysen et al. (1978a); a description with eq. 46 leads to unphysical fitting parameters (Maletta 1980a, c). Experimental evidences for a distinction of spin-glass freezing from superparamagnetic

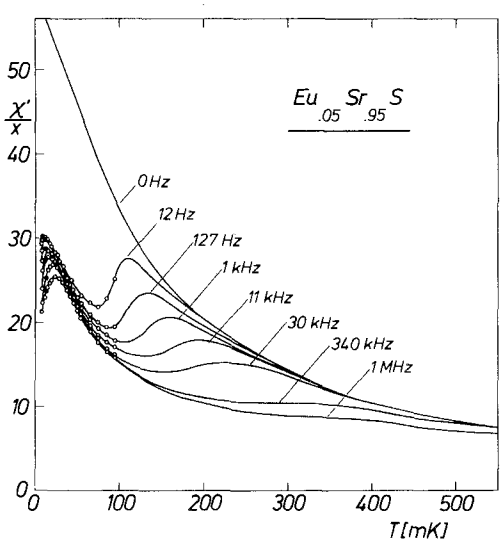

Fig. 31. Temperature dependence of the static (0 Hz) and ac susceptibilities of the superparamagnet $Eu_{0.05}Sr_{0.95}S$ for various measuring frequencies (from Eiselt et al. 1979a).

blocking are collected by Maletta (1981b) from systematic studies and comparison of superparamagnetic compounds ($x < x_p$) and spin-glass compounds ($x > x_p$) in the dilution system $Eu_xSr_{1-x}S$. Hence, the *interactions among* spin clusters (which are partially frustrated) play an essential role in spin glasses.

Such a model of interacting spin clusters can be reduced to a model of EA-type by reasonable approximations, as has been emphasized by Binder already in 1977. Indeed, Monte Carlo simulations of the 2-dimensional EA–Ising model (Kinzel 1979) yield reversible and irreversible susceptibilities and remanent magnetizations in excellent qualitative agreement with experimental data, as already mentioned in sec. 4.2 and shown in fig. 14. In addition, a power-law decay of $M_r(t)$ and even details like the maximum of the TRM versus H are reproduced in the simulations (fig. 27).

In this context one has also to report on a systematic experimental study by Bouchiat and Monod (1982) about the origin of the remanent magnetization in spin glasses. Analyzing data of *Ag*Mn spin glasses in the Mn concentration range 1% to 24% the authors come to the conclusion that remanent magnetizations are indeed an *intrinsic property* of the spin-glass state (and not some "parasitic" magnetic contribution). They show that the TRM and IRM data can be plotted on universal curves (independent of concentration) versus the reduced temperature T/T_f only, when they are normalized with $M_{rs}(T)$ and the field H is normalized with $H_{cr}(T)$. The same conclusion appears to hold in *Cu*Mn, *Au*Fe, (*La*Gd)Al_2, and (Eu, Sr)S spin glasses. The authors argue that the mechanism responsible for the existence of a remanent magnetization in metallic spin glasses exclusively involves exchange interactions (without additional dipolar anisotropy).

Finally, we refer to work by Alloul (1979a, b) on zero-field NMR on Cu in *Cu*Mn alloys (Mn concentrations from 0.4% to 4.7%) at low temperatures $T \leqslant 0.2\ T_f$, who finds *no evidence for independent domain structure*. The enhancement factor η of the rf-field and NMR signal intensity, associated with the rotation of domain magnetization, is found roughly proportional to the remanent magnetization M_r and is negligible when the sample is ZFC. These results contradict the independent "spin-cloud" model, for which η should be independent of M_r. A similar conclusion has also been reached from the square hysteresis loops observed well below T_f in *Cu*Mn (Monod et al. 1979) and is corroborated by computer simulations of *Cu*Mn alloys (Walker and Walstedt 1980).

Thus, a large amount of experimental data shows the intrinsic feature of irreversibilities of spin glasses at low temperatures. These distinct properties are obviously due to their enormous number of equivalent states below T_f. Hence, the picture of free-energy valleys in phase space (fig. 15) is useful to explain the effects phenomenologically. In the FC procedure the system can go immediately into the lowest valley. On the other hand, changing the field at a fixed temperature below T_f gives rise to pronounced irreversibility. After ZFC the system can be trapped in a local minimum before it relaxes slowly into the lower minimum. More detailed theoretical work, however, would be desirable in order to understand the nature of the "frozen state" in spin glasses at low temperatures.

5.2. *Anisotropy*

The very existence of a remanent magnetization, M_r, which maintains the direction of the field during cooling, is direct evidence of anisotropy in spin glasses (Alloul 1983). This property turned out to be independent of crystallographic directions in classical spin glasses like *Cu*Mn and (Eu, Sr)S for which single-ion crystalline anisotropy can be neglected. First, these properties were again assumed to be linked with an inhomogeneous description of the spin system, subdivided into domains or spin clouds. Recent experiments, however, have provided evidence for a *macroscopic* character of the anisotropy in spin glasses. Even a microscopic origin of anisotropy in metallic spin glasses has been proposed.

Measurements of the *transverse susceptibility* $\chi_\perp$ (Alloul and Hippert 1983) for instance allow the determination of the anisotropy energy $E_A(\theta)$ which keeps the remanent magnetization $\boldsymbol{M}_r$ aligned along the cooling field $\boldsymbol{H}_c(\|z)$, θ being the angle $(\boldsymbol{M}_r, z)$. In the standard method after inducing the remanent magnetization M_r along z, the response $\chi_\perp$ of M_r to a small alternating field h_{ac} ($\leqslant 1$ G, $\|y$) is measured in various static fields $\boldsymbol{H}_z \| z$ (fig. 32). In the most simple situation, assuming a collective response to a small field, one can define an anisotropy field

$$H_A = K/M_r \tag{49}$$

and the transverse susceptibility $\chi_\perp$

$$\chi_\perp - \chi_0 = \frac{M_r}{H_z + H_A} \,. \tag{50}$$

The decomposition of $\chi_\perp$ in eq. 50 into an isotropic part χ_0, measured after ZFC, and an anisotropic part is assumed to be reasonable since χ_0 is not modified by the presence of M_r within the experimental accuracy. Measurements on *Cu*Mn spin glass show perfect agreement with this concept in eq. 50 as illustrated in fig. 32. χ_0 is obtained after ZFC, and M_r is measured independently on the same sample, hence the anisotropy field H_A is the only fitting parameter.

From the experimental definition of a unique anisotropy field by these $\chi_\perp$ measurements and from the result of an *NMR* analysis (Alloul 1979a, b) that almost all local moments are involved in the magnetization rotation, Alloul and Hippert (1983) conclude that for $T \ll T_f$ small applied fields induce a *macroscopic rotation* of the spins in their metastable configuration. Further evidences for a macroscopic anisotropy in spin glasses are also found by ESR experiments (Monod and Berthier 1980) and measurements of the magnetic hysteresis (Monod et al. 1979).

One has to point out, however, that the anisotropy of spin glasses is not induced by the field. Although H_A depends on the magnitude of M_r (eq. 49), K has been found to be rather well defined. Measurements of both M_r and H_A at a given temperature for various cooling conditions and therefore for a large range

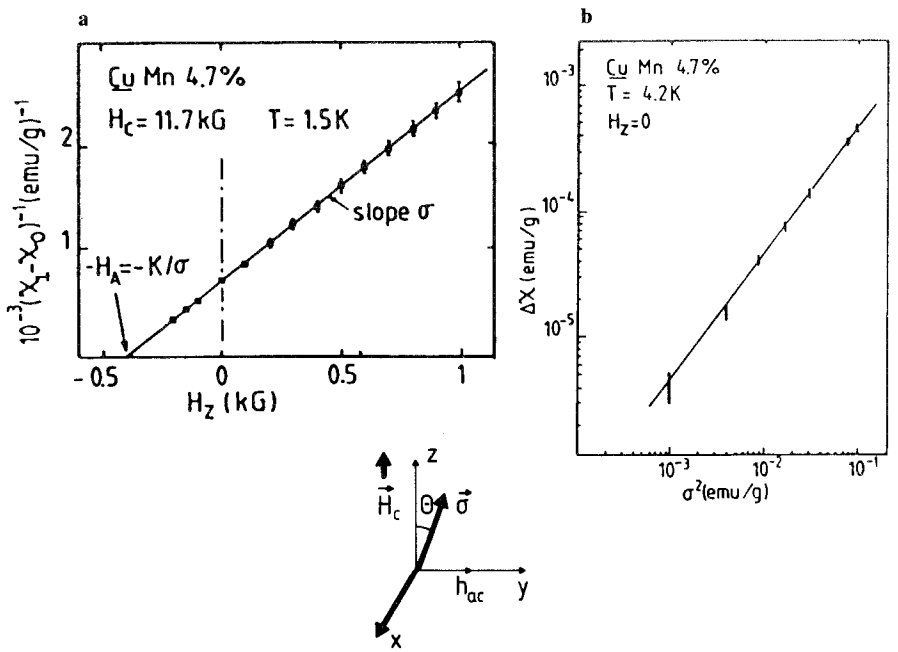

Fig. 32. Transverse susceptibility $\chi_\perp$: (a) Typical $\chi_\perp$ data of *Cu*Mn 4.7%, obtained at 1.5 K in the cooling field $H_c = 11.7$ kG, showing perfect agreement with eq. 50, the anisotropy field $H_A = K/M_r$ being the only parameter. The isotropic part χ_0 is measured after ZFC, while M_r ($\equiv\sigma$) is measured independently on the same sample (from Alloul and Hippert 1983). (b) $\Delta\chi = \chi_\perp - \chi_0$ as measured for $H_z = 0$, plotted versus M_r^2 ($\equiv\sigma^2$) for various values of the remanence. The straight line with slope unity perfectly fits the data, which allows one to conclude that $K = M_r^2/\Delta\chi$ from eq. 50 is independent of M_r (from Hippert and Alloul 1982).

of M_r values give a straight line with slope unity in the plot $\ln(\chi_\perp - \chi)$ vs $\ln M_r^2$, thus K is strictly independent of M_r for *Cu*Mn (Hippert and Alloul 1982), as well as for an insulating spin glass (Velu et al. 1981). Not only is K independent of M_r, but it remains meaningful even in a zero-field cooled state where no remanence exists as clearly evidenced by a *new* ESR signal for $M_r = 0$ (Schultz et al. 1980).

Figure 33 shows *both ESR signals* versus field corresponding to the large M_r (slope 1) and $M_r \to 0$ (slope 1/2) limits. In the presence of a large $M_r \gg \chi_0 H_z$ and for small enough fields $H_z \leqslant 2 H_A$, a ferromagnetic like ESR mode is detected by Monod and Berthier (1980) at frequencies

$$\omega/\gamma = \tfrac{1}{2}(H_z + 2H_i) \quad \text{with } H_i = \sqrt{K/\chi} \tag{51}$$

where H_A is found to be identical with that obtained from $\chi_\perp$ data (see eq. 50). Now even in a zero-field cooled state with $M_r = 0$ a second new ESR mode is predicted and found (Schultz et al. 1980) with frequency

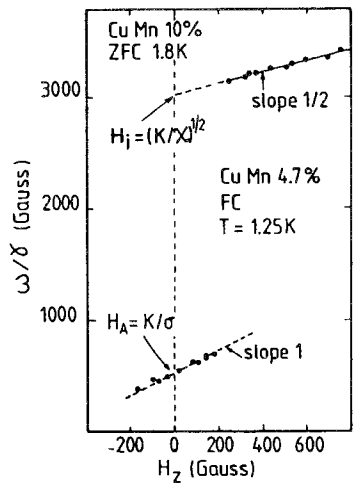

Fig. 33. ESR frequency in *Cu*Mn versus field in the two limiting cases of large M_r (slope 1) (Monod and Berthier 1980) and $M_r = 0$ (Schultz et al. 1980) ($M_r \equiv \sigma$).

$$\begin{aligned} \omega/\gamma &= \tfrac{1}{2}\,(H_z + 2H_i) \quad \text{with } H_i = \sqrt{K/\chi} \\ &\to \sqrt{K/\chi_0} \qquad \text{for } H_z = 0\,. \end{aligned} \tag{52}$$

Further ESR results are found in recent publications (Gullikson et al. 1983, Hoekstra et al. 1984) suggesting a breakdown of the rigid spin rotation at large field angles.

Thus the anisotropy constant K and hence $E_A(\theta)$ is an *intrinsic* property of the spin glass state. It defines a macroscopic anisotropy. Any rigid rotation of the spin system with respect to the lattice costs some anisotropy energy. However, due to the overall isotropy of the state, this energy $E_A(\theta)$ will be the same whatever the axis of the rotation is. Often it is called an "isotropic anisotropy". Therefore, the spin-glass state has to be characterized by an *anisotropy triad* (Saslow 1982) instead of an anisotropy axis.

The triadic character of the anisotropy shows up in an *unidirectional* angular dependence

$$E_A(\theta) = K_d(1 - \cos\theta) \tag{53}$$

rather than in an uniaxial dependence

$$E_A(\theta) = \frac{K_{ax}}{2} \sin^2\theta \tag{54}$$

which would result from a vector anisotropy. In principle the difference between both types of anisotropy should be seen from *hysteresis* cycles. While in the first case (eq. 53) a reversible reversal of M_r should occur at $H_d = -K_d/M_r$, in the second one (eq. 54) a hysteresis cycle around $H = 0$ with half width $H_{ax} = K_{ax}/M_r$

should be observed. Experimental hysteresis cycles of *Cu*Mn show a mixture of these two features, but H_A-values deduced from eqs. 53, 54 are not in agreement with values from $\chi_\perp$-experiments.

Another experiment, however, demonstrates the purely unidirectional character of the anisotropy in *Cu*Mn spin glass. Hippert et al. (1982) note that $\chi_\perp$ is sensitive to the ratio K_{ax}/K_d when being measured in the presence of a static field H_y applied in the direction of the susceptibility coil. The H_y *dependence of* $\chi_\perp$ is found to agree perfectly with $K_{ax} = 0$ (fig. 34). The authors argue that the disagreement with the hysteresis experiment stems from the fact that a rigid-body rotation of the spin system can only be produced on a limited angular range (in *Cu*Mn for $\theta \leqslant 40°$). This is fulfilled in the $\chi_\perp$-experiment but not in the hysteresis.

The triadic character of E_A has been directly detected first by *torque* experiments (Fert and Hippert 1982). The sequence of rotations of the anisotropy triad during the torque experiment can be followed in fig. 35. After a rotation of π around x induced by rotating an applied field from z to $-z$ in the yz-plane, the spin system does not have the same responses in the yz- and xz-planes [as would be the case for a vector anisotropy (fig. 35)]. Especially the torque $\Gamma_y = dE_A/d\varphi$ is found nearly zero for a further rotation of φ in the xz-plane, as the total rotation angle of the triad undertaken from the initial state is still π (the axis of rotation is different of course).

Microscopically, this type of anisotropy in metallic spin glasses is linked to the existence of *Dzyaloshinsky–Moriya interactions* (see sec. 3.2). This interpretation has been stimulated by hysteresis studies of ternary *Cu*Mn spin glasses by Préjean et al. (1980) where the third component is a nonmagnetic impurity of concentration x. Whereas M_r and T_f are found to be independent on x, the width of the hysteresis and hence the anisotropy constant K increases linearly with x (fig. 36). By taking different impurities the authors demonstrate that the *spin–orbit* interaction is responsible for the anisotropy.

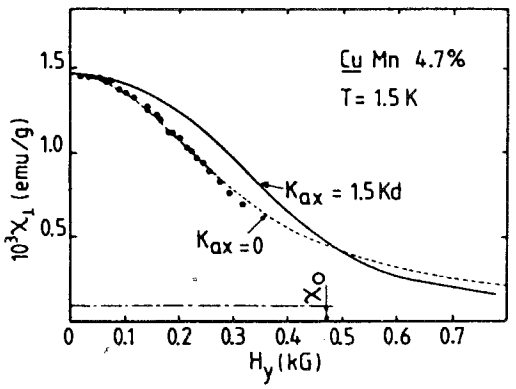

Fig. 34. Transverse susceptibility $\chi_\perp$ now measured versus H_y (compare with fig. 32) in *Cu*Mn 4.7% for $H_z = 0$. Excellent agreement is found with a purely unidirectional anisotropy energy ($K_{ax} = 0$, dotted line), while the data cannot be explained assuming the ratio K_{ax}/K_d given from $\chi_\perp$ experiments in the $\theta = 0$ and $\theta = \pi$ states (full line) (from Hippert et al., 1982).

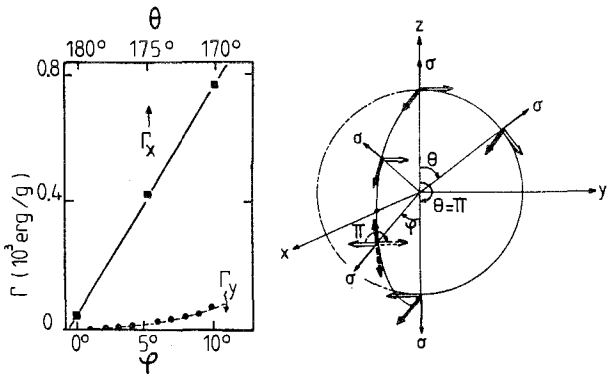

Fig. 35. Torque measurements in *Cu*Mn 20% at 1.5 K (Fert and Hippert 1982). The torques Γ_x and Γ_y measured after a π rotation of M_t ($\equiv\sigma$) in the yz-plane are displayed. These two responses are quite different and point out the triad character of the anisotropy. The sequence of rotations during the torque experiment can be followed in the right-hand part of the figure (from Alloul 1983).

Many experimental results in spin glasses have demonstrated that for $T \ll T_f$ a macroscopic anisotropy energy can be defined even in ZFC spin glasses. The spin-glass state is characterized by a triad and E_A is only specified by the rotation angle of the triad, as long as a rigid spin rotation can be assumed; deviations are detected for large angle rotations and at increasing temperature. In metallic spin glasses this anisotropy is associated with DM-interactions between the spins. In insulating (Eu, Sr)S no study of this kind has been performed up to now.

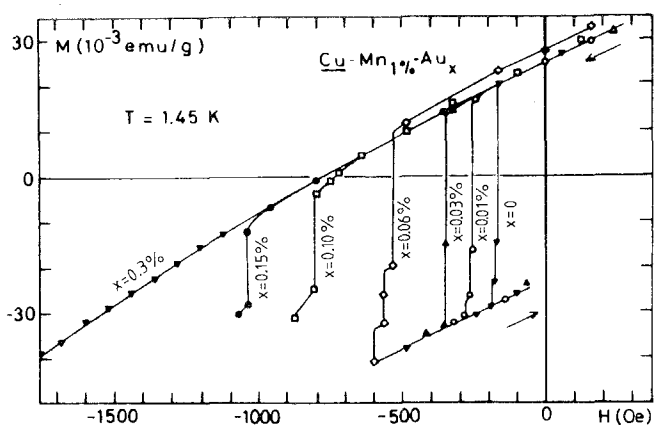

Fig. 36. Hysteresis cycles of various ternary *Cu*Mn 1%-Au_x spin glasses in low field. The remanent magnetization is obtained after removing a field of 18 kOe in which the sample was field-cooled down to 1.45 K. The time constant associated with the reversal increase with Au concentration x from ~1 sec for the more dilute to over hours for the most concentrated (from Préjean et al. 1980).

5.3. *Excitations*

Here we focus attention to the low-temperature excitations in spin glasses and especially to the question about the possible existence of spin waves in spin glasses. Low-energy excitations in disordered materials in general are far from being understood. Waves (phonons in glasses) are expected to propagate in disordered media as long as their wavelength is much larger than the scale of disorder. However, these excitations coexist at low temperature with other more or less localized modes which are still hard to characterize {two-level systems (Phillips 1972, Anderson et al. 1972), fractons (Alexander et al. 1983)}. In Heisenberg spin glasses both magnons with a linear dispersion relation at long wavelengths (Halperin and Saslow 1977) and diffusive modes (Dzyaloshinskii and Volovik 1978) have been proposed from hydrodynamic approaches depending on the choice of order parameter and dissipative processes. The most sophisticated macroscopic theory is that of Fischer (1980); he uses both the hydrodynamic and gauge theory approaches and is able to calculate spin-wave damping. Walker and Walstedt (1980) and Walstedt (1981) present data from numerical simulations in a harmonic approximation for a dilute Heisenberg spin glass with RKKY interactions and obtain well defined oscillating modes within one of the many local energy minima. Most of these modes are fairly delocalized but not necessarily propagating. Sample-size limitations have further restricted the information from computer simulations at low temperatures.

Up to now the most meaningful tests of the validity of these approaches have come from comparison between measured and calculated values of the *specific heat*. From calculations of the density $g(E)$ of spin excitations one can obtain the magnetic part $C_m(T)$ of the specific heat versus temperature at low T.

The magnetic specific heat, $C_m(T)$, of spin glasses exhibits three interesting features (see fig. 2):

(i) A rather broad maximum at a temperature exceeding the spin-glass temperature T_f by about 30%. Typically, about one third of the total magnetic entropy is attained by the spin glass when $T = T_f$.

(ii) At temperatures below T_f, C_m varies approximately linear with T.

(iii) $C_m(T)$ is progressively reduced in a magnetic field.

These properties of $C_m(T)$ are observed in metallic (e.g. *Cu*Mn: Wenger and Keesom 1976) as well as in insulating spin glasses ($Eu_xSr_{1-x}S$: Meschede et al. 1980), in spite of quite different types of magnetic couplings. The dependence (ii) at low T is not strictly linear. $C_m(T)$ can be represented as a power law in T with exponents ranging from 1.2 to 1.7 (Thomson and Thompson 1981, Caudron et al. 1981), or alternatively several authors (Martin 1979, Fogle et al. 1983, Sato and Miyako 1982) suggest the relation $C_m(T) = c_1 T + c_2 T^2$ where c_1, c_2 are constants.

The occurrence of a roughly linear T-term of $C_m(T)$ below T_f has been known for a long time, and in the early molecular-field theories was attributed to excitations of single spins submitted to essentially vanishing molecular fields (Wenger and Keesom 1975). Convincing arguments that this can occur in

Heisenberg spin-glasses with RKKY coupling have not been given. It reminds one to the linear specific heat of ordinary glasses which commonly is explained exclusively with the phenomenological concept of "two-level systems" introduced by Anderson et al. (1972) and Phillips (1972). Numerical studies by Walker and Walstedt (1977 and 1980) for classical spins and RKKY interactions demonstrate that in the cases of *Cu*Mn and *Au*Fe spin glasses the linear term of $C_m(T)$ can be explained quantitatively (fig. 37) by a high density of states of delocalized modes, i.e. magnon-like excitations of the spin system around either of its equilibrium configurations. For insulating spin glasses $Eu_xSr_{1-x}S$ the same conclusion is obtained by somewhat different numerical techniques of Krey (1980, 1981, 1982) and of Ching et al. (1980). Hence, it is not necessary to refer to the speculation of "two-level centers" for an explanation of the linear specific heat of spin glasses, in contrast to ordinary glasses.

In order to obtain further information about the magnetic excitations a comprehensive specific-heat study of $Eu_xSr_{1-x}S$ has been performed with x between 0.25 and 0.80 in magnetic fields up to 6 T (von Löhneysen et al. 1985, Wosnitza et al. 1986). The experimental results agree quantitatively with recent numerical calculations by Krey (1985) who has extended his earlier calculations to high fields. Figure 38 shows the specific heat C of the spin glass $Eu_{0.25}Sr_{0.75}S$ between 0.1 K and 30 K for various magnetic fields B between 0 and 6 T (Wosnitza et al. 1986) (the lattice contribution plays a negligible role at low T). A

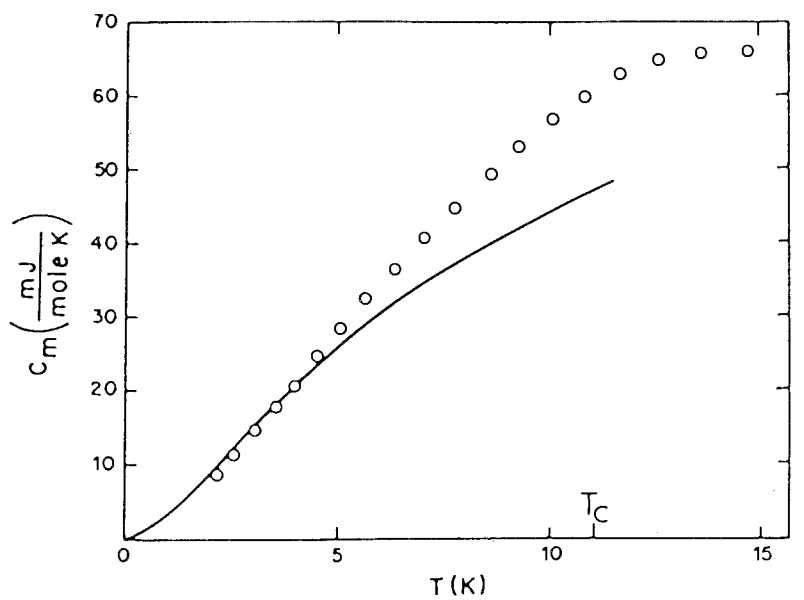

Fig. 37. Molar specific heat of a dilute RKKY-coupled spin-glass obtained by Walker and Walstedt (1977) by numerical simulations (solid curve). Circles are data for *Cu*Mn 1.2% spin glass from Wenger and Keesom (1976).

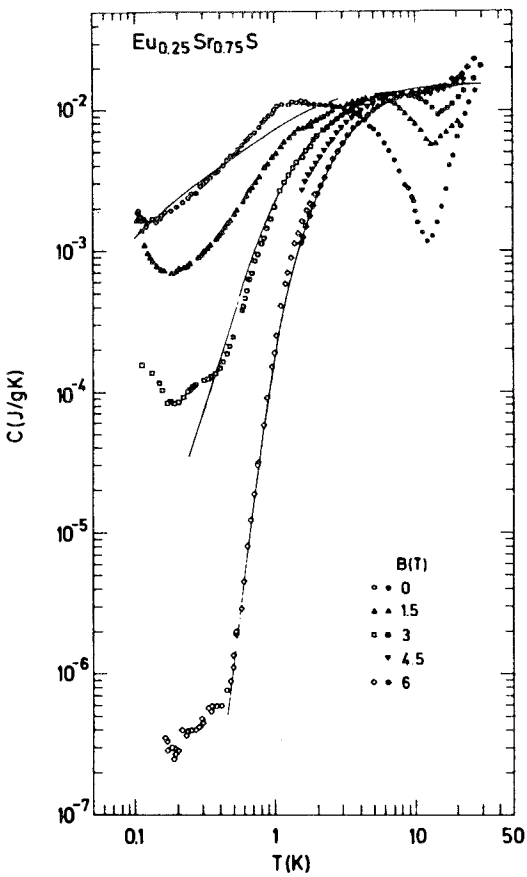

Fig. 38. Specific heat C of $Eu_{0.25}Sr_{0.75}S$ spin glass as a function of temperature T for various magnetic fields B between 0 and 6 T. Solid lines indicate the calculated specific heat by Krey for $B = 0, 3$, and 6 T (from Wosnitza et al. 1986).

strong depression of C is found at lower temperatures, with a crossing-over towards higher T where C is increased in a magnetic field. The up-turn of C below 0.2 K towards low T is due to the nuclear specific heat contribution C_N arising from the hyperfine splitting of Eu^{151} and Eu^{153} nuclei (the apparent decrease of C_N with B is discussed by von Löhneysen et al. 1985).

The most interesting observation in fig. 38 is the evidence for a gap in the excitation spectrum. The roughly linear T dependence of C in zero field below $T_f = 0.8$ K gradually turns steeper as the magnetic field is increased. For high fields, $B > 3$ T, however, the drop of C towards low T is quasi-exponential, indicating the opening of a *gap* (with energy ΔE) in the magnetic excitation spectrum at $E = 0$:

$$C_m(T) \propto \exp(-\Delta E/k_B T)$$
$$E = g\mu_B(B - B_0(x)) . \tag{55}$$

These data can be explained quantitatively, without any fit parameters (J_1 and J_2 are known), from a direct numerical calculation of the collective excitations of the system. In Krey's calculation (1985) the continued fraction method is used to obtain the density of magnon-like states, $g(E)$, as displayed in fig. 39 for various Eu concentrations at $B = 6.6\,\mathrm{T}$. The arrow denotes the Zeeman energy $E_B = g\mu_B B$. Treating the excitations as non-interacting bosons, i.e. in the RPA approximation, the magnetic specific heat C^* per Eu atom is deduced from $g(E)$ as

$$C^*/k_B = \int_0^\infty \mathrm{d}E\, g(E)\left(\frac{E}{k_B T}\right)^2 \frac{\mathrm{e}^{E/k_B T}}{(\mathrm{e}^{E/k_B T}-1)^2}\,. \tag{56}$$

The solid lines in fig. 38 represent some results of these calculations. The argeement with the experimental data is indeed excellent.

Three obvious trends of $g(E)$ with Eu concentration x can be inferred from fig. 39:

(i) With decreasing x, the energy range of $g(E)$ shrinks, i.e. the upper band edge decreases.

(ii) Simultaneously, a pronounced peak appears around E_B.

(iii) Finally, the lower band edge is separated from $E = 0$ by an energy gap whose magnitude ΔE depends on B and x as found experimentally, eq. 55. The effective field $B_0(x)$ is negligible small for the ferromagnetic samples, $0.70 \leqslant x \leqslant 1.0$, whereas in the reentrant and spin-glass regimes, $x < 0.70$, B_0 increases with decreasing Eu concentration x.

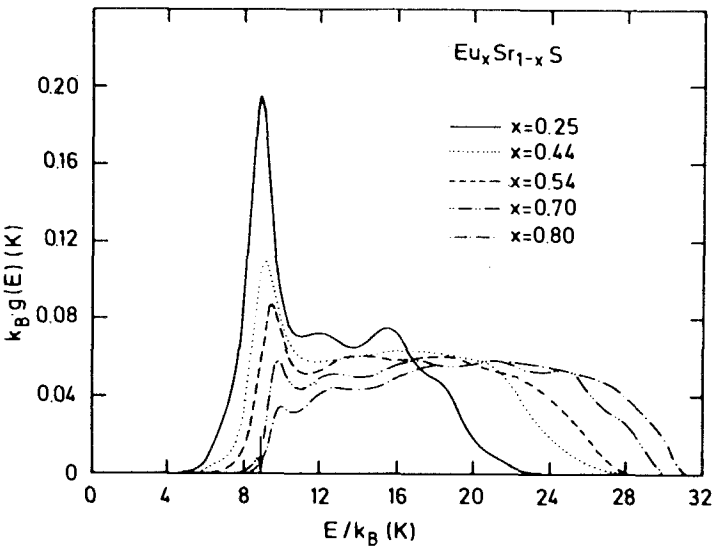

Fig. 39. Calculated spectral density of states $g(E)$ per Eu atom for magnetic excitations in $Eu_xSr_{1-x}S$ for various concentrations x in a field of 6.6 T (Krey 1985). The arrow indicates the Zeeman energy $E_B = g\mu_B B = k_B \cdot (8.87\,\mathrm{K})$ (from Wosnitza et al. 1986).

Hence, all these C_m data can be explained even quantitatively by dominant magnon-like excitations in (Eu, Sr)S spin glasses.

There have been other experimental attempts to study the nature of low-temperature excitations. Alloul and Mendels (1985) have recently measured the T dependence of the local magnetization in RKKY spin glasses (*Cu*Mn, *Ag*Mn and *Au*Mn) for $T \leqslant 0.2 \cdot T_f$, as obtained from the variation of the zero-field NMR frequency of Mn^{55}. It follows the T^2-dependence expected for magnon excitations with a linear dispersion relation, its spin-wave stiffness, however, does not agree with numerical estimates. Such an analysis implies, according to the authors, that the specific heat $C(T)$ should be attributed to modes which do not contribute to the $M(T)$ dependence. Obviously, more work is required to test this analysis and interpretation. Alloul et al. (1986) demonstrate that for $T \leqslant 0.1 \cdot T_f$ the T dependences of the local and macroscopic magnetization are quite identical within experimental accuracy, the latter being measured by the *remanent magnetization* M_r. The phenomena responsible for the time decay of M_r and its T dependence are shown to operate on completely different time scales. The authors speculate again on the nature of the excitations but the present data do not appear to be specific enough to distinguish between the various types of excitations.

Neutron scattering technique generally provides the most powerful probe of collective spin excitations. We recall that the cross section for magnetic neutron scattering from a system of N spins is given (Marshall and Lovesey 1971) by

$$\frac{d^2\sigma}{d\Omega\, d\omega} = N\left(\frac{\gamma e^2}{mc^2}\right)^2 \frac{k'}{k_0} \left(S_s(q)\delta(\omega) + S_D(q, \omega)\right) \tag{57}$$

where $S_s(q)$ is the static and $S_D(q, \omega)$ the dynamic structure factor, representing the elastic and inelastic/quasielastic scattering, respectively. The incident neutron beam with wavevector k_0 is scattered to give a beam with wavevector k', with wavevector transfer $q = k_0 - k'$ and energy transfer $\hbar\omega = \hbar^2/2m(k_0^2 - k'^2)$. The dynamic structure factor may be written in terms of the generalized susceptibility $\chi(q, \omega)$

$$S_D(q, \omega) \propto \frac{1}{1 - \exp(-\hbar\omega/k_B T)} \cdot \operatorname{Im} \chi(q, \omega) \tag{58}$$

which provides the information on spin dynamics. For a simple relaxational process with lifetime Γ^{-1} one measures a Lorentzian lineshape of the quasielastic line at $\omega = 0$ with

$$\operatorname{Im} \chi(q, \omega) \propto \frac{\omega\Gamma}{\omega^2 + \Gamma^2}\,, \tag{59}$$

while for ferromagnetic ordering with propagating spin waves one obtains two inelastic lines centered at $\omega = \pm\omega_q$ with the spectral shape function

$$\text{Im } \chi(q, \omega) \propto \frac{\omega\Gamma}{(\omega - \omega_q)^2 + \Gamma^2} + \frac{\omega\Gamma}{(\omega + \omega_q)^2 + \Gamma^2} \tag{60}$$

where Γ^{-1} is the lifetime of spin waves, and the spin-wave dispersion is quadratic at low wavevectors q

$$\omega_q = D \cdot q^2 . \tag{61}$$

Neutron studies have been performed extensively by Murani (see e.g. 1978b) on metallic spin glasses such as *Cu*Mn and reveal a distribution of relaxation times (see discussion in the next section). So far, no experimental evidence for spin-wave excitation exists in the typical metallic spin glasses. It is likely that in metals all modes are overdamped due to the strong Korringa relaxation of the spins to the conduction electron sea. In insulating spin glasses this mechanism is missing, and theories of the spin-glass dynamics might be more realistic.

In $Eu_xSr_{1-x}S$ considerable effort has been made in the search for spin waves in spin glasses by neutron inelastic scattering technique (Maletta et al. 1981a, Maletta 1982c). The idea in these experiments is to probe the dynamics of the spin-glass phase by studying the evolution of the spin waves from the ferromagnetic phase ($x \geq 0.70$), where the dynamics are resonably well understood, into the spin-glass phase. In a single crystal of pure EuS (enriched with ^{153}Eu to limit neutron absorption) the spin-wave dispersion over the whole Brillouin zone has been measured and analyzed by Bohn et al. (1980), the result is given in fig. 6a. The anisotropy of the spin-wave energies in EuS, in spite of the high symmetry of the rocksalt crystal structure and the isotropic exchange interactions, stems from the fact that the predominant exchange interactions to the first (J_1) and second (J_2) nearest neighbors have opposite sign.

The measurements on $Eu_{0.70}Sr_{0.30}S$ (in powder form) which orders ferromagnetically below $T_c = 8.5$ K show well-defined spin-wave excitations at 4.5 K (fig. 40a), and a quadratic form of the spin-wave dispersion at low q (eq. 61) similar to pure EuS. The stiffness constant D, related to the exchange constants in the non-diluted ferromagnet by the relation

$$D = 2a^2S(J_1 + J_2) \tag{62}$$

is found to be $D = 1.1$ meV$\cdot$ Å^2 in $Eu_{0.70}Sr_{0.30}S$, as compared to $D = 2.5$ meV$\cdot$ Å^2 in EuS at low temperatures (see inset in fig. 40a). Thus, D decreases much faster than linearly with dilution. One should note that there is a non-negligible broadening of the inelastic line which is only partly due to powder averaging. Figure 40a also demonstrates (see spectrum of $x = 0.70$ at $q = 0.6$ Å^{-1}) that one has to operate the spectrometer with a good energy resolution in order to resolve the inelastic line from the peak centered at $E = 0$.

Figure 40b displays spectra of $Eu_{0.52}Sr_{0.48}S$ measured for various wave vectors q at $T = 0.35$ K, i.e. in the spin-glass state. True inelastic scattering is present as evident by the asymmetry between the intensities for neutron energy gain ($E < 0$) and neutron energy loss ($E > 0$), i.e. the so-called detailed balance factor. As q decreases, the intensity shifts to lower energies consistent with the width of the

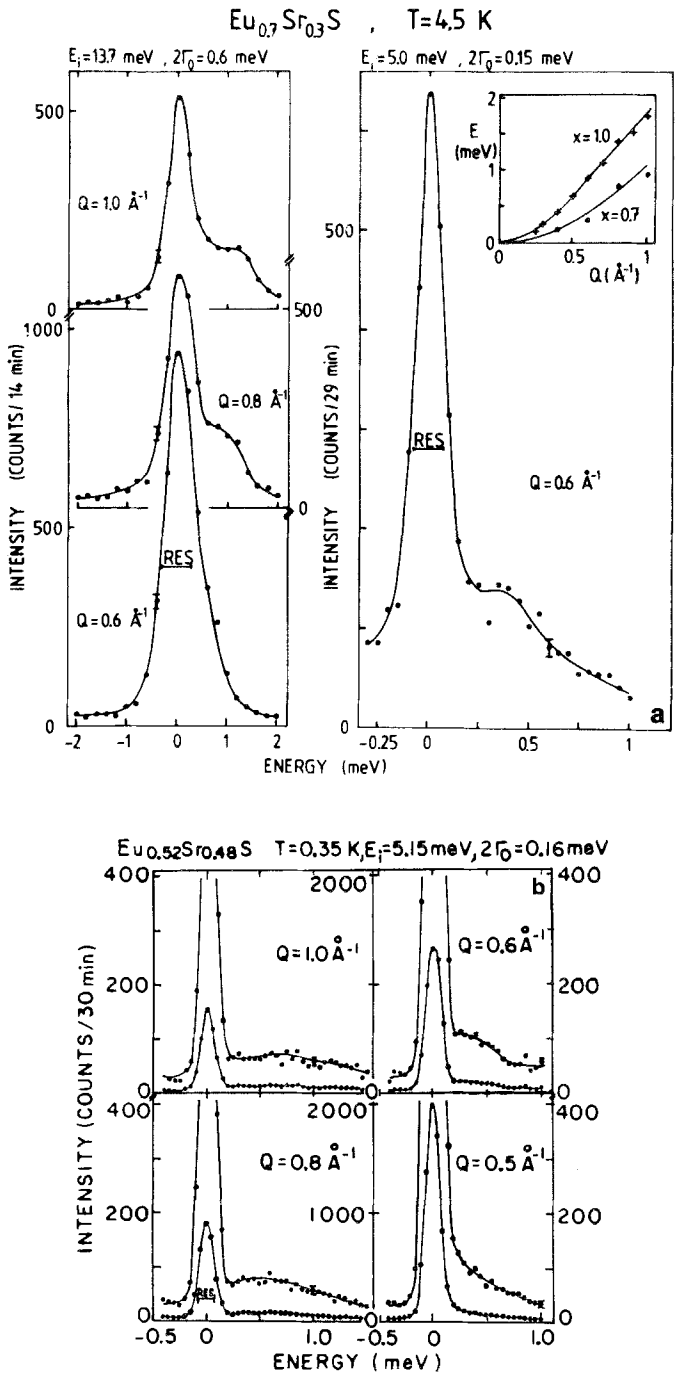

Fig. 40. Inelastic neutron spectra of $Eu_xSr_{1-x}S$ for various wave vectors q for (a) $x = 0.70$ at 4.5 K, and (b) $x = 0.52$ at 0.35 K. The inset in (a) shows the spin-wave dispersion $E(q)$ for $x = 1.0$ and 0.70 (from Maletta 1982c).

distribution and position of the intensity maxima shifting to lower energies. At the same time, the intensity at $E = 0$ increases dramatically.

The difficulty in interpreting these data is deciding which form of Im $\chi(q, \omega)$ gives a better representation of the data. The physics implicit in the forms of eqs. 59 and 60 may be different but the spectra will look similar at low temperatures: as described in eq. 58 the inelastic scattering intensity is proportional to Im $\chi(q, \omega)$ and to the Bose–Einstein factor, hence at low temperature if $\hbar\Gamma \gg k_B T$ the spectra will peak at a finite energy for *both* forms of Im $\chi(q, \omega)$ (eqs. 59 and 60). The authors convoluted the cross section using eq. 59 and 60 with the instrumental resolution function and performed a least-square fit to the data varying Γ, D and a normalization parameter. The χ^2 for the fit was slightly better using eq. 60. If one accepts the spin-wave like form for Im $\chi(q, \omega)$, a stiffness constant $D = 0.6 \pm 0.2\ \text{meV} \cdot \text{Å}^2$ for $x = 0.52$ is obtained formally, which is reasonable in magnitude compared with higher Eu concentrations. The line widths Γ obtained at high q are much broader than that expected for any powder broadening, and Γ decreases as q decreases. The additional strong intensity at $E = 0$ increases as q decreases. Only a small fraction of this is elastic incoherent scattering and background from the sample container and cryostat. Most of it is a true q dependent scattering with $E = 0$. Quite similar results are obtained with the spin-glass samples $x = 0.50$ and $x = 0.40$ at low temperatures where the inelastic scattering intensity is shifted to lower energies, thus the analysis is even more difficult.

The authors (Maletta et al. 1981a) prefer to attribute the inelastic lines to spin-wave like modes even in the spin-glass phase of (Eu, Sr)S. The accessible q-range, however, is restricted to large values $q \gtrsim 0.4\ \text{Å}^{-1}$ and the observed modes are highly damped. Probably these magnon-like excitations cannot be

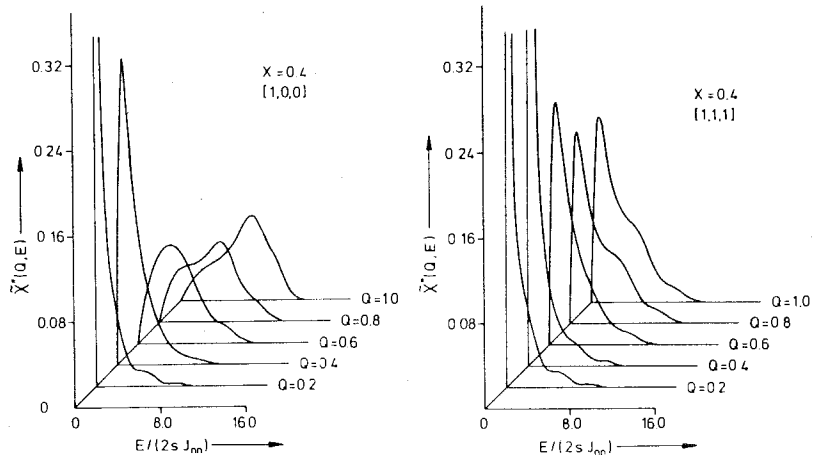

Fig. 41. Calculated neutron spectra for the $Eu_xSr_{1-x}S$ spin glass with $x = 0.40$ in two directions, [100] and [111], and for various wave vectors q at $T = 0$ K (from Krey 1981).

labelled by the quasi-momentum q, since one is dealing with a strongly disordered system. These modes are superposed by a quasielastic contribution centered at $E = 0$ with a high density of states attributed to diffusive modes of low energy. The results are in qualitative agreement with numerical model calculations by Krey (1981). As an example results for $x = 0.40$ for two directions of propagation are displayed in fig. 41: the theoretical neutron spectra for [100] (and [110]) show a "ferromagnetic like" spin-wave dispersion, whereas there is no dispersion along [111]. See also the calculated spectral density of states $g(E)$ for magnetic excitations in $Eu_xSr_{1-x}S$ in fig. 39 and discussions there.

6. Dynamics of spin-glass freezing

In spin glasses a freezing of spin motion occurs at low temperature in such a way that no conventional long-range magnetic order exists, as we have seen above. The upsurge of interest in spin-glass systems in the last decade appears to be related to two important events concerning this freezing process. First, the discovery by Cannella and Mydosh (1972) of a sharp maximum ("cusp") in the low-field, low-frequency ac-susceptibility of *Au*Fe spin glasses at the spin-glass temperature T_f leads to the theoretical interpretation by Edwards and Anderson (1975) in terms of a new kind of phase transition in such disordered systems. The second event, the observation of a particularly complicated spin dynamics near T_f seems to contradict the concept of a phase transition. Experimental studies on the spin freezing reveal a wide spectral distribution of relaxation times (Murani and Heidemann 1978c) extending even to macroscopic times around T_f (Maletta et al. 1978a, Maletta and Felsch 1979b). At present, however, the lack of corresponding reliable analytic theories hampers the interpretation of these and similar experiments. In this section, we will present data from different experiments which in principle might provide detailed insight into the dynamics of spin-glass freezing. Subsequently in sec. 7 attempts to interpret data at the transition into the spin-glass state in terms of a phase transition will be discussed.

6.1. *Time dependent susceptibilities*

One of the most prominent methods to study the onset of spin-glass freezing remains the low-field *ac-susceptibility* χ. Since the observation of a "sharp cusp" in $\chi(T)$ at T_f of *Au*Fe alloys in 1972, an ac mutual inductance technique is commonly used to measure $\chi(T)$ and to determine T_f, with a very small driving field (<1 Oe) and a rotation-frequency (normally <100 Hz) which should be large enough to prevent the appearance of long-time metastable effects. Thus the reversible susceptibility (see eq. 38) is generally believed to be measured by this ac-χ method, due to the long-time scale of the irreversible behavior especially in small fields.

One often also described the different susceptibilities (see sec. 5.1) phenomenologically by means of the picture of the many-valley structure of free

energy in phase space (fig. 15): the ac-χ measures the response of only one valley, whereas field-cooling is believed to correspond to averaging over all available states. These interpretations have to be taken with great precautions, as we will discuss below.

In 1978 Maletta et al. (1978a) and Maletta and Felsch (1979b) discovered the *frequency dependence of* T_f in (Eu, Sr)S spin glasses measured in a series of ac-χ experiments with various measuring frequencies ω. As an example the result of $Eu_{0.15}Sr_{0.85}S$ is shown in fig. 42a where a 15% increase of T_f is found by going from 10 Hz to 1000 Hz. Such a behavior is also observed in $(La\text{Gd})Al_2$ spin glasses (von Löhneysen et al. 1978a). It is less pronounced in other metallic spin glasses like *Cu*Mn (Tholence 1980, Mulder et al. 1981), but up to now at least a small frequency shift of χ in the range 1 Hz to 1 kHz has been measured for most spin glasses.

The frequency dependence in spin glasses cannot be explained with the simple picture of thermal blocking of superparamagnetic clouds, eq. 46, as already discussed in sec. 5.1. Ferré et al. (1981) pursued the time effect on T_f over 7 decades of frequency in $Eu_{0.40}Sr_{0.60}S$ (fig. 42b) by means of Faraday rotation measurements. One realizes in fig. 42b that now over such a broad frequency range even a formal description of $T_f(\omega)$ with eq. 46 does not work. The data are also incompatible with the Vogel–Fulcher law where one substitutes $T_B(\omega)$ in eq. 46 by $(T_B(\omega) - T_0)$. The law is proposed by Tholence (1980) to apply to $T_f(\omega)$ in spin glasses but the meaning of T_0 remains unclear. This phenomenological

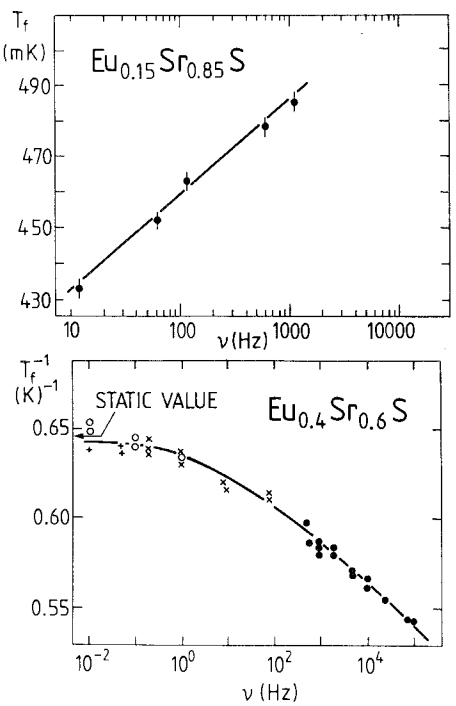

Fig. 42. Frequency dependence of the temperature T_f for the spin glasses $Eu_xSr_{1-x}S$ with $x = 0.15$ (Maletta and Felsch 1978b) and $x = 0.40$ (Ferré et al. 1981). $T_f(\omega)$ is determined from ac-susceptibility measurements at various measuring frequencies ω.

relation has long been known in the literature devoted to viscous fluids and glasses.

It is quite interesting, however, that the pronounced $T_f(\omega)$-effect in insulating spin glasses can be used to determine the limits in concentration of the spin-glass regime of a dilution system, as already shown in $Eu_xSr_{1-x}S$ (Maletta 1981b) where spin-glass freezing is distinguished experimentally from superparamagnetic blocking. Very recently, Börgermann et al. (1986a, b) established the phase diagram of $Eu_xSr_{1-x}Te$ (fig. 7b) in a similar way. The frequency shift of T_f, $\delta T_f(\omega)$, within the spin-glass regime is found to be *equal* in both systems, $Eu_xSr_{1-x}S$ and $Eu_xSr_{1-x}Te$: it is independent of the Eu concentration x and even equal in magnitude, $\delta T_f(\omega) \simeq 30$ mK per ω-decade within the frequency range displayed in fig. 43 (compare with fig. 42).

For Eu concentrations x above 0.50, $Eu_xSr_{1-x}Te$ shows $\delta T_f(\omega) \simeq 0$ (fig. 43) which coincides with the disappearance of irreversibilities (FC- and ZFC-magnetizations) as can be seen in fig. 44. Obviously these samples order antiferromagnetically. At low Eu concentrations, i.e. below the percolation threshold $x_p = 0.13$, the $x = 0.10$ compound for example exhibits no anomaly in dc-$M(T)$ (the lowest temperature of measurement was 20 mK) but an ac-$\chi(T)$ maximum at 150 mK for 5 Hz with a smaller $\delta T_f(\omega)$ compared to the spin-glass regime, which can now be explained quantitatively with eq. 46 similar to the $Eu_xSr_{1-x}S$ superparamagnetic compounds below $x_p = 0.13$ (Eiselt et al. 1979a). Such type of experiments obviously provides evidence for the *collective* character of spin-glass freezing around T_f (Maletta 1981b).

The unique properties of $\delta T_f(\omega)$ described above are a challenge to get more insight into the dynamics of spin-glass freezing. At present, however, no theory is available to be compared with. Nevertheless the data already demonstrate the

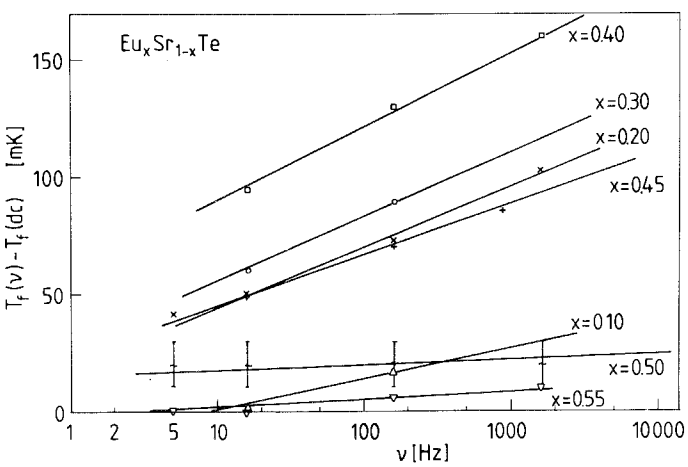

Fig. 43. Frequency dependence of T_f for $Eu_xSr_{1-x}Te$ with various Eu-concentrations x (from Börgermann et al. 1986b).

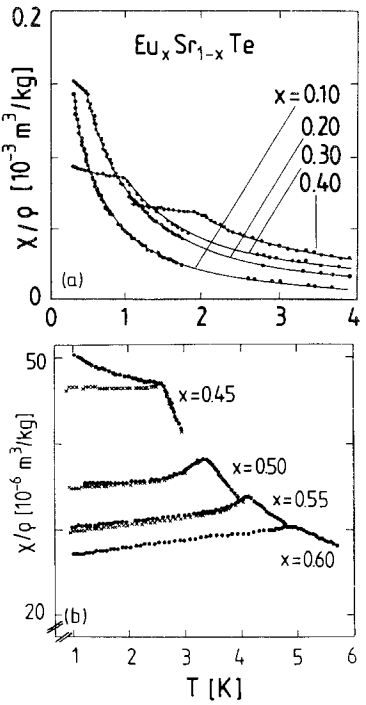

Fig. 44. Static susceptibility ($\chi = M/H$) data vs T for $Eu_xSr_{1-x}Te$ with various Eu-concentrations x: (a) Field-cooling χ in the earth's magnetic field (0.05 mT); (b) χ in 0.15 mT for "ZFC" (×: after cooling in 0.05 mT) and for FC (●: in 0.15 mT). The "ZFC" and FC curves coincide for $x = 0.60$ (from Börgermann et al. 1986a)

essential role played by the competing exchange interactions (frustrations) in producing the $\delta T_f(\omega)$ of spin glasses, because $Eu_xSr_{1-x}Te$ is based on the *antiferro*magnet EuTe (with $J_2/J_1 \simeq -2/1$) and $Eu_xSr_{1-x}S$ on the *ferro*magnet EuS (with $J_2/J_1 = -1/2$). Thus, it is misleading to consider $T_f(\omega)$ as a "cluster property" (Fischer 1985) since clusters are expected to be x-dependent and different in diluted ferro- and antiferromagnets. Apparently, the competing exchange interactions within the infinitely connected network of magnetic moments at the Eu ions create a constant frustration effect on spin dynamics in dilution systems above the percolation threshold, independent of concentration x as long as J_2/J_1 stays constant. The only necessary condition is a sufficiently high disorder (together with the frustration effects) in order to destroy long-range periodic magnetic order (note that the competition of J_1 and J_2 has no essential influence on magnetic ordering in the pure systems, $x = 1$). Obviously, both dilution series, $Eu_xSr_{1-x}S$ and $Eu_xSr_{1-x}Te$, exhibit an even quantitatively comparable behavior due to the same magnitude of competition relative to the different dominating exchange J_1 (>0) and J_2 (<0), respectively. It seems to us that competition in the exchange interactions is generally weaker in metallic spin glasses, consistent with a smaller frequency dependence of T_f.

Particularly valuable information on the dynamics of spin-glass freezing has recently been gained by experiments where both the real and *imaginary* component (χ', χ'') of the complex susceptibility $\chi(T, \omega)$ have been measured accurate-

ly. As regards metallic spin glasses, eddy currents in the material easily obscure an accurate observation of χ''. Such measurements, however, have been possible mainly for insulating spin glasses (Lundgren et al. 1981, Hüser et al. 1983b, Paulsen et al. 1984, Rajchenbach and Bontemps 1983, Baumann et al. 1984, Wenger 1983, Paulsen et al. 1986a, b).

The magnitude of the imaginary part χ'' of the complex susceptibility only amounts to a few percent of χ', but χ'' is directly indicative of the spectral distribution of relaxation processes because it singles out processes with relaxation times around the measurement time $\tau_m = 1/\omega$. In contrast, the real part χ' integrates over all relaxation processes which are fast compared with $\tau_m = 1/\omega$ and, therefore, is rather inconspicuous. The complex susceptibility, $\chi(T, \omega)$, of the $Eu_{0.20}Sr_{0.80}S$ spin glass is shown in fig. 45 as function of temperature for three different frequencies (Hüser et al. 1983b). At the highest temperatures, $T \gtrsim 1$ K, no difference is observed in the dispersion (χ') for the various measuring frequencies within the experimental accuracy. This feature plus the absence of any absorption (χ'') indicates the measured χ' is the isothermal susceptibility, χ_T, i.e. the spin system is in thermodynamic equilibrium.

On cooling one observes a nonzero absorption signal starting at the higher frequencies. Similarly, deviations in the dispersion signal from χ_T are evidenced. We also note that the temperature of the inflection point of $\chi''(T)$ corresponds to the temperature T_f of the $\chi'(T)$ maximum for each measuring frequency. Both features shift to higher temperatures with increasing frequency.

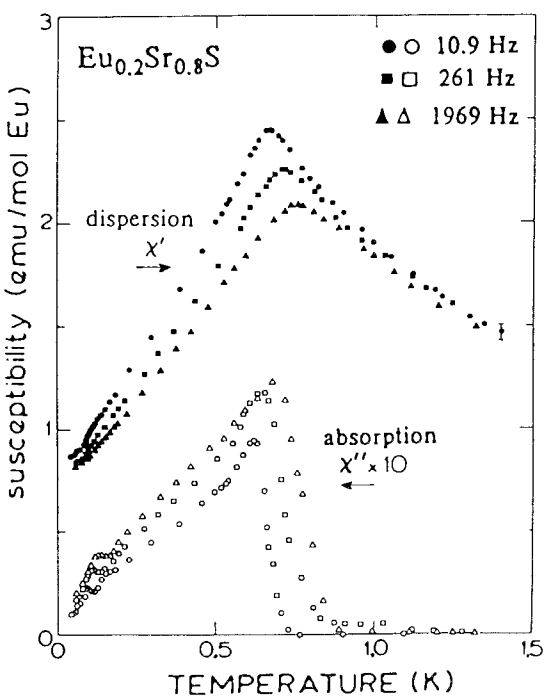

Fig. 45. Temperature dependence of the real (χ') and imaginary (χ'') part of the ac-susceptibility for $Eu_{0.20}Sr_{0.80}S$ spin glass with various frequencies (from Hüser et al. 1983b).

If the magnetization would relax with a single relaxation time τ, the frequency dependence of χ' and χ'' could be expressed by the Casimir and du Pré (1938) equations:

$$\chi'(\omega) = \chi_s + \frac{\chi_T - \chi_s}{1 + \omega^2\tau^2}$$
$$\chi''(\omega) = \omega\tau \frac{\chi_T - \chi_s}{1 + \omega^2\tau^2} \tag{63}$$

where χ_T is the isothermal susceptibility in the limit $\omega \to 0$ and χ_s the adiabatic one in the limit $\omega \to \infty$. Already from the results described above, however, one expects the relaxation of the magnetization in spin glasses to be governed by a distribution of relaxation times rather than a single one. Then, following Lundgren et al. (1981), equations (63) are generalized and one obtains for instance

$$\chi''(\omega) = \frac{1}{h_0} \int_{\tau_{min}}^{\tau_{max}} \frac{m_0(\tau)\omega\tau}{1 + \omega^2\tau^2} \, g(\tau) \, d \ln \tau \tag{64}$$

which reduces in the spin-glass state ($\tau_{min} \ll 1/\omega \ll \tau_{max}$) to

$$\chi''(\omega) \approx -\frac{\pi}{2} \cdot \frac{m_0(1/\omega)}{h_0} \, g(1/\omega) \, . \tag{65}$$

$m_0(\tau)$ is the magnetization of the magnetic entities with relaxation time τ in the field h_0 and in the limit $t \to \infty$; $g(\tau)$ their spectral distribution function and $m_0(\tau)g(\tau)$ their spectral weight. In order to reduce eq. 64 to eq. 65 one has to assume that

$$m_0(\tau)g(\tau) \approx \text{const.} \tag{66}$$

around the measuring frequency $\omega = 1/\tau$. Hence, in this approximation $\chi''(\omega)$ is directly proportional to the *spectral weight of relaxation processes* with relaxation times $\tau = 1/\omega$ (eq. 65). In a more complete treatment and using the same assumption, Lundgren et al. (1981) also obtain

$$\chi'' \approx -\frac{\pi}{2} \frac{\partial \chi'}{\partial \ln \omega} \, . \tag{67}$$

Relation (67) can be used to test the applicability of the approximation in eq. 65, and indeed good agreement is obtained with various samples (Lundgren et al. 1981, van Duyneveldt and Mulder 1982, Baumann et al. 1984, Paulsen et al. 1986a, b). We will come back to this point in sec. 7.1.

Thus, the absorption data $\chi''(T, \omega)$ provide important information about the relaxation spectrum of the freezing process in spin glasses. In fig. 46 such data of

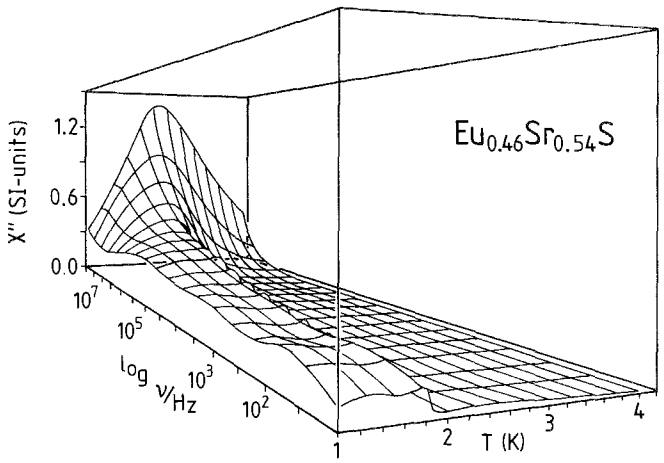

Fig. 46. Absorption χ'' in dependence of temperature and frequency, obtained from a fit to the measured data of the spin glass $Eu_{0.46}S_{0.54}S$ (from Baumann et al. 1984).

the $Eu_{0.46}Sr_{0.54}S$ spin glass are compiled in dependence of temperature and frequency on a logarithmic scale (Baumann et al. 1984). The measurements were performed in the frequency range 10 Hz to 50 MHz, the earth's magnetic field was compensated; however the results were not corrected for demagnetization effects which should have been done. At high temperatures, $T > T_f = 2$ K, the main part of the spectral weight is concentrated in the high-frequency relaxations. On cooling these relaxations shift to lower frequencies, their spectral weight function decreases and seems to broaden. Low-frequency relaxations suddenly appear in a narrow temperature interval on approaching T_f from above. Obviously, at least these low-frequency relaxations are incompatible with an Arrhenius-type description (eq. 45). It is reasonable to assume that their appearance around T_f is due to the collective nature of the freezing process.

In summary, the relaxation time spectrum in spin glasses is broad already above T_f, and it dramatically broadens at T_f, extending even to macroscopic times. This seems to occur in all spin glasses which have been studied by this technique so far. Hüser et al. (1983b) and Wenger (1983) try to analyze their data quantitatively via a plot of χ'' versus χ' with ω as a parameter which is a generalization of the "Cole–Cole plot" or the "Argand diagram" but no more information could be deduced as already described above by means of fig. 46 and eq. 65.

6.2. *Inelastic neutron scattering*

In the study of spin-glass phenomena during the last years neutron scattering measurements have made important contributions to our knowledge of spin glasses. First of all, *elastic* neutron scattering is an invaluable tool for asserting that conventional periodic long-range order in the spin system is really absent (see

point (b) of the defining properties of a spin glass in sec. 2.1). *Inelastic* magnetic neutron scattering techniques provide information about elementary spin excitations (see sec. 5.3) or via the quasielastic line $S(q, \omega)$ around $\omega = 0$ (eq. 58, 59) about spin relaxations. Typical results from this latter method will be presented now, and we emphasize that in the limit $q \to 0$, $\chi(q, \omega)$ in the cross-section eq. 58 reduces to the dynamic susceptibility discussed just above. Finally, measurements on the neutron spin-echo spectrometer will be reviewed where one measures directly the time correlation function.

Results of a detailed neutron scattering study of the metallic spin glass *Cu*Mn 8% by Murani and Tholence (1977) are given in fig. 47. Spectra at four different temperatures are shown for various wave vectors q (Å^{-1}) obtained on a time-of-flight spectrometer using a constant-q interpolation technique. Neutrons of incident energy 3.0 meV ($\lambda = 5.14$ Å) were selected by a multichopper system with an elastic energy resolution (FWHM) of 230 μeV. The spectra consist of a strong elastic line superposed over a broad quasielastic structure as shown on the reduced scale. The solid lines through the data points in fig. 47a represent the Lorentzian fits (eq. 59) to the quasielastic scattering intensity. Using the results of these fits, the integrated elastic and quasielastic cross-section as well as their sum (given as total cross-section) have been determined as shown in fig. 47b. Note that the elastic scattering begins to increase markedly with decreasing temperature below about 75 K, where simultaneously the quasielastic cross-section begins to diminish. In comparison, the temperature of the ac susceptibility peak is $T_f = 39$ K.

Two essential remarks, however, should be added to this analysis which are related to each other. We have seen above in sec. 6.1 that with decreasing temperature a whole spectrum of relaxation times develops. Therefore, fitting the quasielastic line by a simple Lorentzian becomes inadequate near T_f. Indeed, this has been demonstrated by Murani (1978a) who measured *Cu*Mn spin glasses of various Mn concentrations over a much broader energy range. Examples for a small $q = 0.08\ \text{Å}^{-1}$ in fig. 48 clearly reveal strong deviations from a simple Lorentzian spectral function already at high temperature, $T = 300$ K. The only exception is the spectrum for the 1.1 atom% Mn alloy where obviously the description with a single relaxation time works at high temperature. The problem of a proper description of the spin relaxation spectrum is even worse in metallic spin glasses where the Korringa relaxation of isolated spins mediated via their exchange coupling with the conduction electrons overlaps in an unknown fashion with the relaxation spectrum due to the solute–solute exchange interactions (Murani 1978a, b). The first mechanism if separated leads to a Lorentzian form, eq. 59, with a single q-independent relaxation time $\tau = h/\Gamma$.

The second severe difficulty in the analysis of neutron spectra of spin glasses is the separation of the elastic scattering from the inelastic/quasielastic scattering contribution, which is limited by the finite instrumental energy resolution. This has special relevance for spin glasses where with the evolution of correlations in the spin system with decreasing temperature a whole spectrum of relaxation time develops. A neutron spectrometer with energy resolution ΔE_0 can only resolve

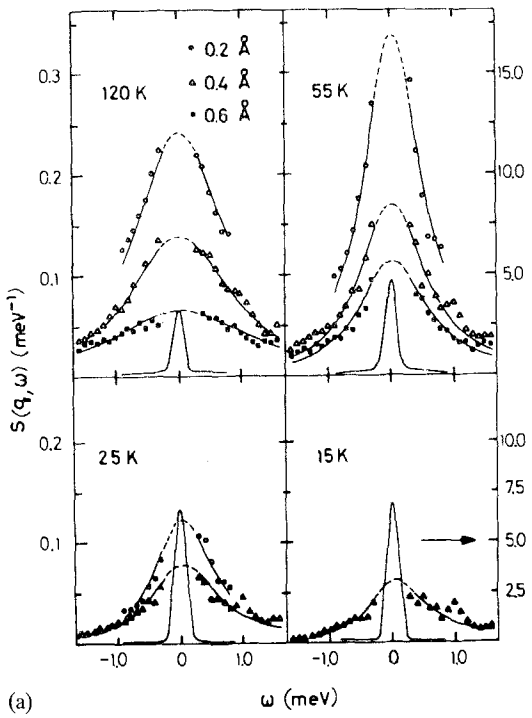

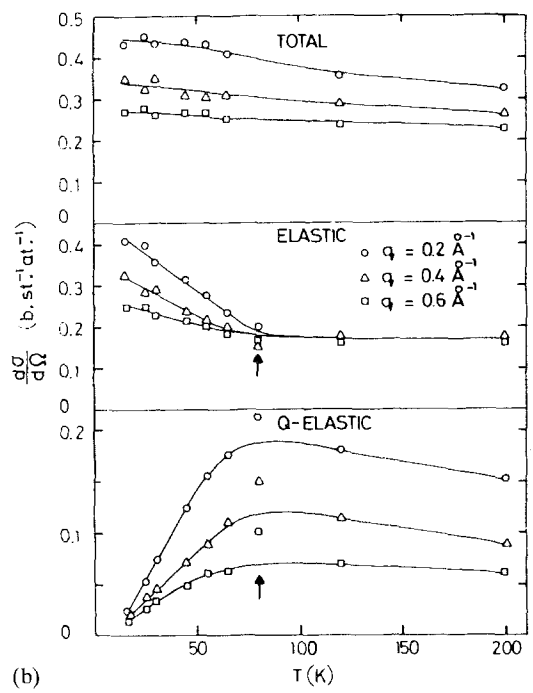

Fig. 47. Neutron scattering data of *Cu*Mn 8 atom%: (a) Spectra $S(q, \omega)$ vs energy $\hbar\omega$ for various q_0-values at four different temperatures. The solid lines through the data points represent the Lorentzian fits to the quasielastic scattering. (b) The scattering cross-section, $d\sigma/d\Omega$, as a function of temperature is given for the total, the elastic, and the quasielastic scattering from data in (a) The vertical arrows indicate the temperature where marked changes in the cross-sections become evident (from Murani and Tholence 1977).

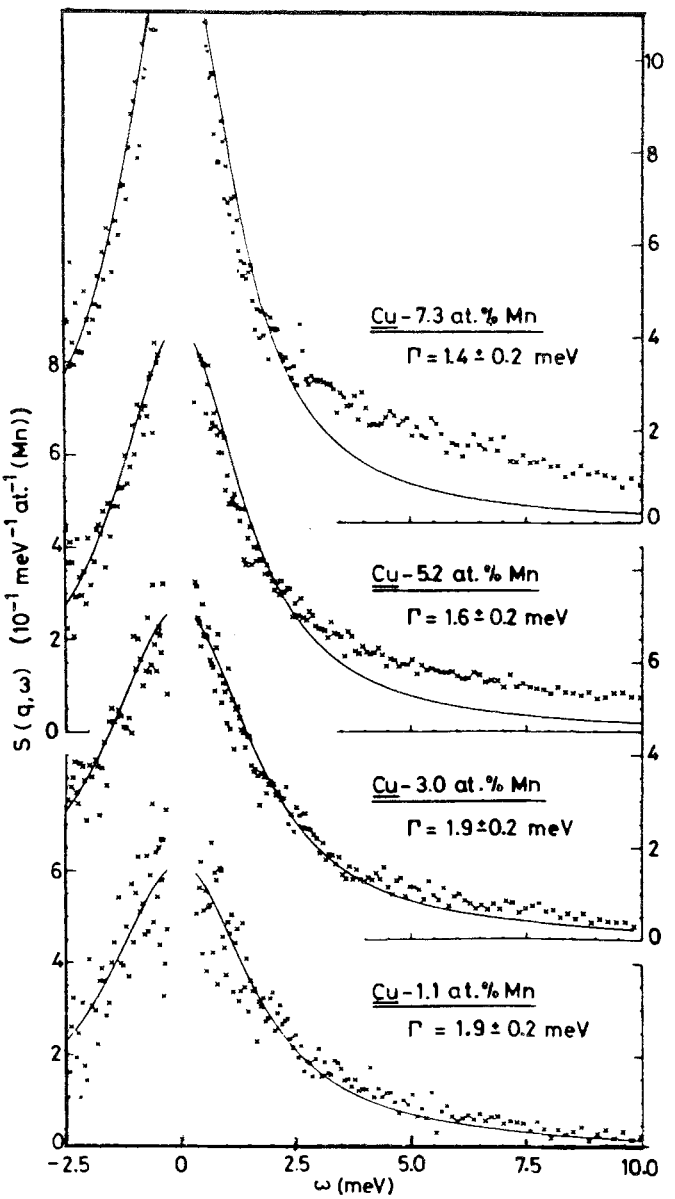

Fig. 48. Neutron scattering spectra, $S(q, \omega)$, vs energy $\hbar\omega$ for $q = 0.08$ Å^{-1} at $T = 300$ K, for *Cu*Mn alloys with Mn concentrations as indicated. The data points for elastic scattering are not shown in the figure. The continuous curves represent the best fits to the data using the Lorentzian form. Note the progressive narrowing of the spectra accompanied by increasing deviation from the fits in the high-energy wings with increasing concentration (from Murani 1978a).

processes with the longest relaxation times τ_0 given by $\tau_0 = h/\Delta E_0$, the rest with times longer than this would be indistinguishable from the truly elastic processes. It is obvious therefore that the apparent "elastic" scattering cross-section will depend on the instrumental energy resolution. This is clearly borne out by measurements of Murani and Heidemann (1978c) as shown in fig. 49. The temperatures, indicated by arrows in the figure, where the marked increase of the

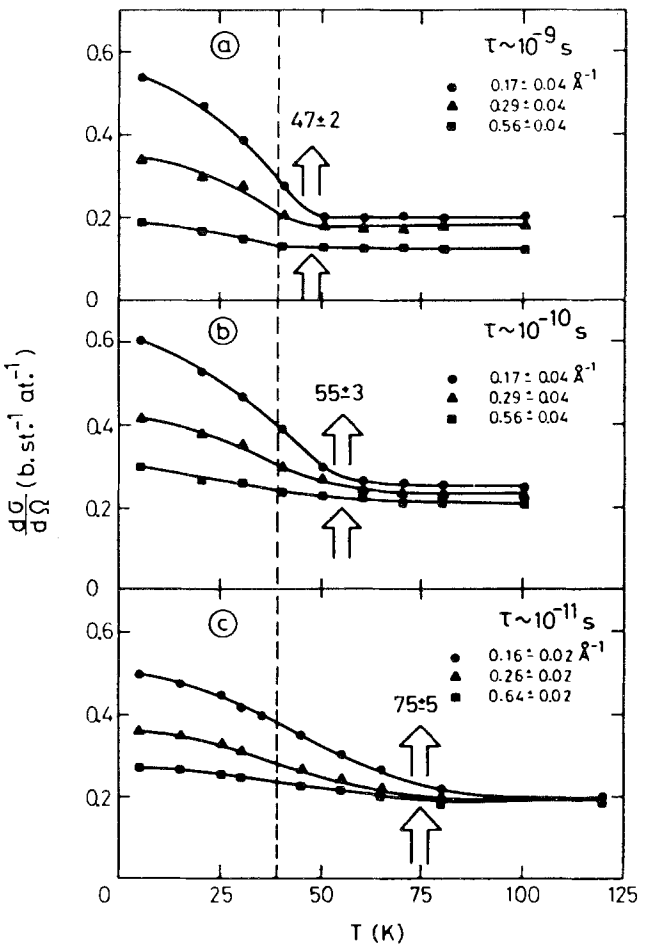

Fig. 49. "Elastic" scattering cross-section vs temperature for various q-values in *Cu*Mn 8 atom%, employing different energy resolutions: (a) Results from IN10 measurements with elastic energy resolution $\Delta E \sim 1.5$ μeV. (b) Total intensity within an energy window $\Delta E \sim 25$ μeV centered around $\omega = 0$ in the IN10 measurements. (c) Results from the IN5 time-of-flight measurements with elastic energy resolution $\Delta E \sim 230$ μeV. The arrows indicate the temperatures where marked increases in the cross-sections begin. The dashed vertical line marks the temperature of the ac susceptibility peak, measured with a time constant $\tau \sim 10^{-2}$ s. The statistical errors are smaller than the size of the data points and the curves are drawn to guide the eye (from Murani and Heidemann 1978c).

elastic scattering cross-section occurs depend strongly on the energy resolutions (ΔE) employed and hence on the measurement time constant $\tau = h/\Delta E$. All these temperatures, however, are systematically higher than the temperature T_f of the maximum of the ac-χ (time constant $\tau = 10^{-2}$ s) shown by the dashed vertical line in fig. 49.

In conclusion these measurements again have indirectly shown the presence of a wide spectrum of relaxation times near the spin-glass temperature (Murani 1981). The elastic magnetic scattering in the cross-section, eq. 57, of neutron scattering is formally related to the Edwards–Anderson order parameter q_{EA}

$$q_{EA} = [\langle S_i \rangle_T^2]_{av} = \frac{1}{N} \sum_q (S_s(q)/2F^2(q)) \tag{68}$$

where $F(q)$ is the magnetic form factor. Due to the finite measurement-time constant of any spectrometer, however, q_{EA} is not accessible (Murani and Heidemann 1978c), i.e. a decision about the existence of an equilibrium spin-glass state with this type of order parameter is impossible by these techniques.

The *neutron-spin-echo* (*NSE*) spectrometer invented by Mezei in 1972 detects the velocity change of the neutrons through the sample (inelastic scattering) by measuring the angle of the polarized neutron spins Larmor precessed around the external field. This spin-echo technique was used to decouple the energy resolution from the momentum resolution. Thus, one can look at much longer times, down to 5×10^{-9} s (higher energy resolution), without the loss of intensity inherent in conventional neutron techniques. The NSE-machine also has the advantage of measuring the spin auto-correlation function directly in the time domain which is the Fourier transform of $S(q, \omega)$ measured in conventional neutron spectroscopy:

$$s(q, t) = \int_{-\infty}^{\infty} \frac{S(q, \omega) \cos \omega t}{S(q)} \, d\omega \, . \tag{69}$$

Here $S(q) = \int_{-\infty}^{\infty} S(q, \omega) \, d\omega$ reflects the short-range order. By definition $s(q, t = 0) = 1$. This technique gives also information (in contrast to μSR) on the spatial correlations (Mezei 1983)

$$S(q, t) = S(q) \cdot s(q, t) \, . \tag{70}$$

It has been shown that the ac susceptibility and the function in eq. 70 are related in a good approximation for relaxation type dynamics by the equation (Mezei 1981):

$$\chi(\omega) \propto \lim_{q \to 0} \frac{1}{kT} S(q) \cdot [1 - s(q, t)] \tag{71}$$

where $t = 0.7/\omega$. This equation has a simple physical meaning: $[1 - s(q, t)]$ is the

fraction of the magnetic moments which can respond to an external field within time t.

Up to now it has been applied to three different spin glasses: *Cu*Mn with 1% and 5% (Mezei and Murani 1979, Mezei 1982), $La_{0.7}Er_{0.3}Al_2$ (Mezei et al. 1983), and $Eu_xSr_{1-x}S$ with $x = 0.40$ and $x = 0.54$ (Shapiro et al. 1985).

Figure 50 shows the result for the spin glass *Cu*Mn 5% ($T_f \approx 27$ K) by Mezei and Murani (1979) where the time-dependent correlation function $s(q, t)$ is plotted on a logarithmic scale. The thick continuous curve represents a simple exponential decay function, $\exp(-\Gamma t)$ for $\Gamma = 0.5$ meV, whereas the thinner lines are drawn to indicate the trend of the points. The data are found to be independent of q in the measured range $0.04\ \text{Å}^{-1} < q < 0.4\ \text{Å}^{-1}$, thus the results in fig. 50 indeed represent the spin autocorrelation function $\xi(t) = s(q, t)$. Data points beyond 10^{-6} s were calculated from ac-χ measurements. It is remarkable that at $T_f \approx 27$ K (from ac-χ measurement) at least half the spectral component has relaxation times below 10^{-9} s and that this fraction decreases slowly below T_f. The time-decay is distinctly slower than exponential already above and below T_f, indicating again a broad distribution of relaxation times which extend progressively to longer times with decreasing temperature. (It should be noted that on such a diagram a simple exponential function always maintains the same shape being only replaced laterally for different values of Γ.) At longer times the data can be approximated by a straight line in the plot which corresponds to

$$\xi(t) \propto \text{const.} - \ln t\,. \tag{72}$$

The authors of this experiment (Murani 1981, Mezei 1983) interpret their results as a clear evidence that the freezing in spin glasses is a purely dynamical gradual process, without any static phase transition.

In contrast, Heffner and MacLaughlin (1984) argue that the same data (fig. 50) can as well be fitted to the form

$$\xi(t) \propto \text{const.} + t^{-\nu} \tag{73}$$

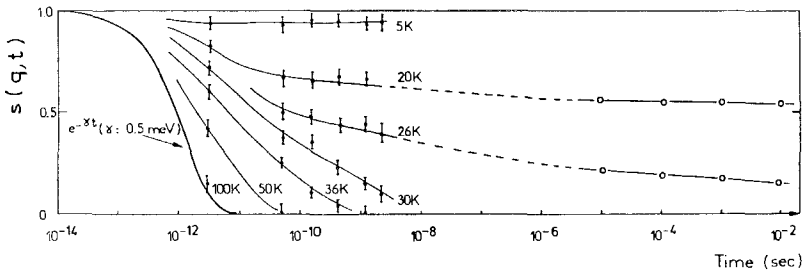

Fig. 50. Spin relaxation in *Cu*Mn 5 atom% spin glass at various temperatures. Data points at times shorter than 10^{-8} s were directly measured by neutron-spin-echo technique at $q = 0.093\ \text{Å}^{-1}$ (Mezei and Murani 1979), those beyond 10^{-6} s were calculated from ac susceptibility results (Tholence 1980). The lines are guides to the eye only (from Mezei 1983).

where the exponent $\nu \approx 1/4$ near T_f, and $\nu \approx 1/2$ for $T < T_f$. Curiously, the neutron-spin-echo data on the other sample, CuMn 1%, still yield $\nu \approx 1/2$ near T_f. The constant in this form (73) is non-zero only below T_f and thus would imply a truly static ordering.

Results from neutron spin-echo measurements on the insulating $Eu_xSr_{1-x}S$ compounds will be described briefly in sec. 8.

Remember that simulations of the nearest-neighbor two-dimensional Ising spin glass (Binder and Schröder 1976) yield logarithmic time-decay of the spin auto-correlation function while for the infinite-range three-dimensional Ising spin glass, Kirkpatrick and Sherrington (1978) find a power-law decay with an exponent $\nu = 1/2$. Sompolinsky and Zippelius (1981 and 1982) also obtain a power-law decay for the Heisenberg spin glass with infinite-range random exchange interactions at and below T_f (see eq. 31).

Recently, Murani (1985) again attempted to study the spin auto-correlation function and to see whether the infinite-range mean-field model may have direct application to relaxation dynamics in real spin-glass systems. He measured the *Cu*Mn 3% spin-glass alloy using unpolarized neutron-scattering techniques, namely the conventional time-of-flight spectrometer and the more sophisticated back-scattering spectrometer. Both these techniques permit measurements over a wide q-range. The slight disadvantage of the shorter time range covered by these "classical" techniques (8.8×10^{-9} s) compared to the neutron spin-echo method (5×10^{-9} s) is compensated by the greater statistical accuracy of the data, due to the higher neutron intensity using unpolarized neutrons and due to integrating over this wide q-range in order to obtain the correlation function. Murani shows in the paper that within a reasonable approximation for spin glasses the time correlation function $\xi(t)$ can be determined by these techniques from the "elastic" component using various energy resolutions ΔE. There is a direct relationship between the "elastic" scattering contribution, measured with finite resolution ΔE, and the local or auto-correlation function $\xi(t)$ at time $t = 1/\Delta E$. Including ac-χ measurements on the same sample he finds a power-law decay

$$\xi(t) \propto t^{-\nu} \tag{74}$$

with $\nu \approx 0.25$ at $T/T_f = 1.25$ (T_f is determined by ac-χ at 10 Hz), but $\nu = 0.1 \pm 0.02$ at and just below T_f. At lower temperatures ($T/T_f \approx 0.75$), $\xi(t)$ is best expressed as

$$\xi(t) \propto t^{-\nu} + \log t \quad \text{with } \nu = 0.4 \pm 0.1\,. \tag{75}$$

At still lower temperatures ($T/T_f \lesssim 0.5$), $\xi(t)$ can be expressed again as a power law with a value of $\nu = 0.5$ which is consistent with the theoretical predictions. The anomalously low value of ν close to T_f (see eq. 74 and 73), also found in muon spin relaxation measurements (Heffner and MacLaughlin 1984), is still unexplained and calls for further theoretical investigation.

6.3. *Muon spin relaxation*

Another new microscopic technique which can determine in principle $S(q, t)$ in spin glasses is the measurement of muon spin relaxation (μSR). Here the q dependences are not tunable as in the NSE method (eq. 70) but are broadly averaged over all q. The "window" of relaxation times seen by μSR spans the 10^{-11} s to 10^{-5} s regime, and hence partly overlaps with that of the neutron techniques (10^{-12} s to 10^{-8} s).

The technique was first applied to *Cu*Mn and *Au*Fe spin glasses by Murnick et al. (1976), who observed the spin precession of μ^+ around the applied transverse magnetic fields (*transverse-field μSR* or *TF-μSR*) and found a rapid increase of muon-spin depolarization rate on cooling towards T_f. Similar TF-μSR measurements were performed later in *Cu*Mn (Emmerich and Schwink 1981) and *Ag*Mn (Brown et al. 1981). It was not possible, however, to distinguish the effects of static inhomogeneous random fields from those of fluctuating dynamic fields since the TF-μSR experiment corresponds to the T_2-measurement of magnetic resonance. This difficulty also limited the information obtained from previous linewidth measurements in *NMR* (MacLaughlin and Alloul 1976, Levitt and Walstedt 1977) and *ESR* (Dahlberg et al. 1979, Salamon 1979, Wu et al. 1985, Baberschke et al. 1986). Furthermore, such experiments with external magnetic fields are not quite suitable for probing spin glasses in which the "cusp" of $\chi(T)$ is substantially rounded by a small H.

To overcome these difficulties Uemura et al. (1980) and Uemura (1981) have applied the *zero-field μSR* (ZF-μSR) to spin glasses. They have also made measurements on *Cu*Mn in *finite longitudinal magnetic fields* (LF-μSR) to separate the static and dynamic effects (Uemura and Yamazaki 1982). A review of these studies is given by Uemura et al. (1985).

In ZF-μSR the longitudinal muon spin relaxation function $G_z(t)$ is directly deduced from the time-differential measurement of the forward/backward muon decay asymmetry, without any disturbance of the spin-glass system by an external field. (No depolarization of the muon spin means $G_z = 1$, complete depolarization $G_z = 0$.) The observed time evolution $G_z(t)$ of muon-spin polarization reflects amplitudes, randomness, and fluctuations of local magnetic fields at muon sites in the specimen. There appear two essential problems in analyzing μSR experiments on spin glasses: (i) One has to make model assumptions about the shape of $G_z(t)$; (ii) Any relaxation slower than 10^{-5} s appears as a "static" component in μSR (lifetime of the muon is $\tau_\mu = 2.2 \times 10^{-6}$ s).

In the early stage of such studies on spin glasses (Uemura 1981) one assumed a simple exponential decay of spin correlation at all temperatures above and below T_f. With recent high-statistics data, as shown in fig. 51, Uemura et al. (1985) include a stochastic theory of spin relaxation to analyze the ZF-μSR data on *Cu*Mn spin glasses. Assuming a simplified autocorrelation function of the impurity spins (which is not in accordance with the experimental findings described above)

$$[\langle S(t)S(0)\rangle / \langle S(0)\rangle^2]_{av} = (1 - Q_{EA}) \exp(-\nu t) + Q_{EA} \tag{76}$$

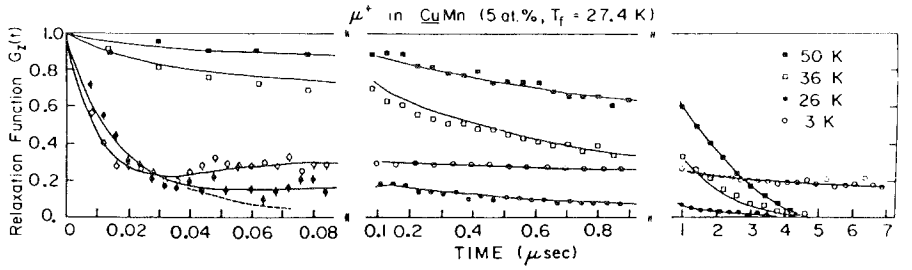

Fig. 51. Zero-field muon-spin-relaxation function, $G_z(t)$, observed in the spin glass *Cu*Mn 5 atom% ($T_f = 27.4$ K) at various temperatures. The solid lines represent the best-fit curves for eq. 76 with the values of a_s and λ_d given in fig. 52 (from Uemura et al. 1984).

the authors calculate $G_z(t)$ analytically. Best-fit curves to this form of $G_z(t)$ are shown in fig. 51 as solid lines. This ansatz leads to distinguish between "static" and dynamic random local fields at the muon site which are involved in $G_z(t)$. For the purely dynamic case where the averaged amplitude a_s of the "static" random fields is zero and $Q_{EA} = 0$, the $G_z(t)$ function exhibits a "root-exponential" decay, $G_z(t) = \exp(-\sqrt{\lambda_d t})$, similar to the ansatz in the early work (Uemura 1981). Here λ_d is the dynamic muon-spin depolarization rate which is proportional to the correlation time $\tau_c = 1/\nu$ above T_f. The "static" effect is reflected in the quick initial decay of $G_z(t)$ followed by the "$\frac{1}{3}$ tail" (for $a_s \neq 0$, $\lambda_d = 0$, $Q_{EA} = 1$). The only fitting parameters in fig. 51 are a_s and λ_d which are displayed in fig. 52. It turns out that a_s exhibits non-zero values only below T_f of each specimen. The λ_d value increases rapidly when T_f is approached both from higher and lower temperatures. The spin correlation time τ_c deduced from λ_d shows a rapid change

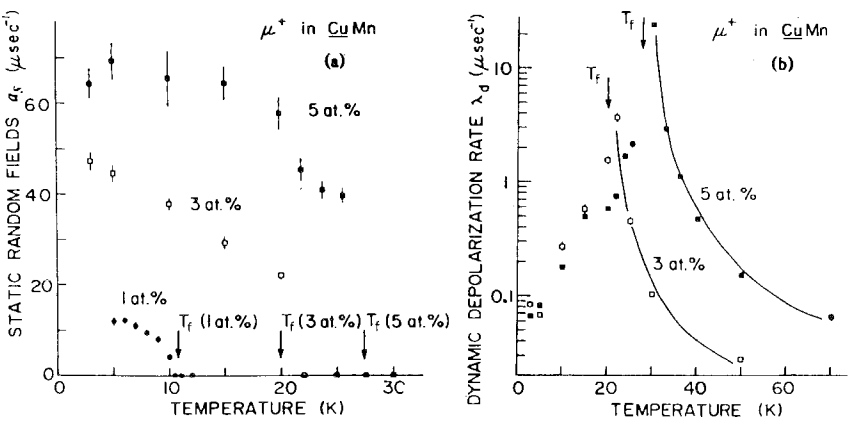

Fig. 52. Parameters from the best-fit curves in fig. 51: (a) Averaged amplitude a_s of static random local field at the muon site, and (b) the dynamic muon-spin depolarization rate λ_d. The solid lines of (b) correspond to the fit of λ_d to the power-law behavior of critical slowing down, eq. 77 (from Uemura et al. 1984).

from $\tau_c \approx 10^{-12}$ s at $T \geq 2T_f$ towards $\tau_c \approx 10^{-9}$ s at $T \approx T_f$ in all the specimens. Comparing λ_d or τ_c with the power-law behavior of critical slowing down

$$\tau_c = \tau_d(T/(T - T_f))^z \quad \text{for } T \geq T_f \tag{77}$$

the authors obtain values of $z = 2.9$ for *Cu*Mn 5% and $z = 2.6$ for *Cu*Mn 3% from the corresponding fit to λ_d, shown by the solid lines in fig. 52b. Below T_f "static" and dynamic effects are found to coexist. The broken line at 26 K in fig. 51 illustrates the decay of $G_z(t)$ assuming $a_s = 0$ (but assuming still only a single relaxation rate and eq. 76). By the way, this kind of coexistence has also been found by LF-μSR below T_f (Uemura et al. 1985). The values of the "average" relaxation time fitted to the *Cu*Mn 5% by μSR roughly agree with NSE above and below T_f. The authors also argue that they can rule out the extremely inhomogenous spin freezing {where for example 10 spins out of 100 are completely frozen ($Q_{EA} = 1$) while the remaining 90 spins are paramagnetic ($Q_{EA} = 0$)} (see also Emmerich et al. 1985).

The use of a single relaxation time and the ansatz, eq. 76, for the spin autocorrelation function in random systems like spin glasses is, of course, a very crude approximation, but Uemura et al. (1985) discuss that point and state, that "it is difficult to calculate $G_z(t)$ when the correlation times of impurity moments have a distribution in a more microscopic way", and hence, "it is difficult for μSR to directly determine the shape of $\xi(t)$". Nevertheless, a recent attempt is made in this direction by MacLaughlin et al. (1983) and Heffner and MacLaughlin (1984) with LF-μSR in *Ag*Mn spin glasses applying high external fields up to H_L = 5 kOe. The spectral distribution of the fluctuating field below T_f is "gated" by the Zeeman level $\omega = \gamma_\mu H_L$, and the authors claim to have evidence for an algebraic time dependence of $\xi(t)$ with $\nu = 0.24 \pm 0.02$ for $T/T_f = 0.92$, and $\nu = 0.54 \pm 0.05$ for $0.3 \leq T/T_f \leq 0.66$ (see eqs. 73, 74; NSE data). However, the studied time region is limited, and, in addition, the influence of the applied fields on the spin dynamics cannot be excluded.

6.4. $1/f$ *magnetic noise*

Recently two groups succeeded in observing equilibrium magnetic fluctuations or $1/f$ magnetic noise spectra (as distinguished from so-called Barkhausen noise) in various insulating spin glasses (Ocio et al. 1985, 1986, Reim et al. 1986), mainly due to the existence of relaxation times down to low frequencies in such disordered spin systems and the lack of contributions from eddy current noise (as for metallic samples). Here we present results obtained near the spin-glass temperature whereas effects of magnetic field and waiting time on the magnetic noise spectrum will be discussed in the next section (sec. 7.1).

Figure 53a displays typical noise power spectra of the $Eu_{0.40}Sr_{0.60}S$ spin glass at two different temperatures above and below $T_f = 1.54$ K, compared to the noise of the detection system alone (Reim et al. 1986). While the empty-system noise is white above 1 Hz and shows some $1/\omega$ component below 1 Hz, the noise level of the sample is up to three orders of magnitude larger and displays a $1/\omega^n$ behavior

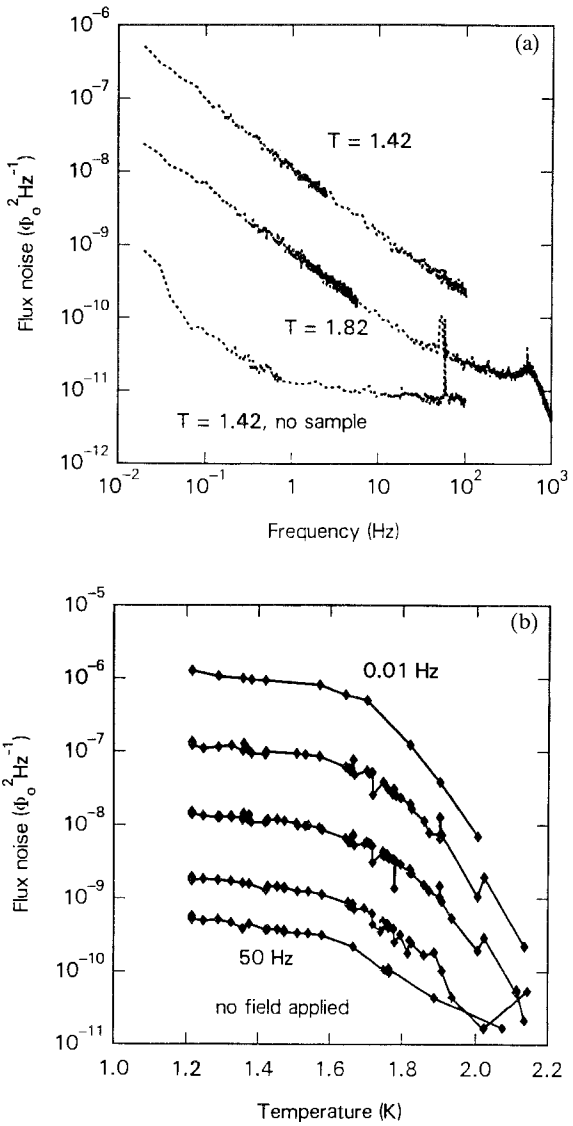

Fig. 53. Magnetic noise for the spin glass $Eu_{0.40}Sr_{0.60}S$: (a) as function of frequency at two different temperatures above and below $T_f = 1.54$ K, and (b) as function of temperature at five different frequencies 0.01, 0.1, 1, 10, and 50 Hz (at zero applied field). The data in (b) are obtained after subtracting the noise of the empty system at each temperature (the one at $T = 1.42$ K is shown in (a)) (from Reim et al. 1986).

in the whole frequency range with $n \leqslant 1$. The noise magnitude of the spin glass is obtained after subtracting the noise of the empty system at each temperature, the result is plotted versus temperature at five different frequencies in fig. 53b. Below 2 K, the amplitude of the magnetic fluctuations increases rapidly and levels off around $T = 1.6$ K (near T_f).

The *fluctuation dissipation theorem* states (Kubo 1966) a general relationship between the response of a given system to an external disturbance and the internal fluctuations in the absence of the disturbance at thermal equilibrium.

Applied to magnetic equilibrium fluctuations $S(\omega)$ this reads (Ocio et al. 1985):

$$S(\omega) = \alpha\chi''(\omega)4k_B T/\omega \tag{78}$$

where α is a geometry dependent conversion factor. Reim et al. (1986) prove unambiguously, by measuring the noise spectrum $S(\omega)$ and the imaginary part $\chi''(\omega)$ of the ac-χ simultaneously, that the fluctuation dissipation theorem is as accurately obeyed by the magnetic fluctuations below as well as above T_f. This is important because recent theories suggest that the spin-glass phase below T_f could be non-ergodic (see sec. 4.3).

Given the validity of eq. 78, measurements of the noise spectrum offer an alternative way to measure χ''. Two experimental advantages important in spin-glass research are that the noise measurement is done at zero field and conveniently as a function of frequency in the low-frequency regime. Therefore, Reim et al. (1986) studied the low-frequency dynamics of the $Eu_{0.40}Sr_{0.60}S$ spin glass near T_f. Figure 54 shows the temperature dependence of the noise exponent $n(T)$ in $S(\omega) \propto \omega^{-n}$ at five frequencies. The data exhibit a maximum slope in the vicinity of T_f, with the magnitude of the logarithmic slope decreasing both above and

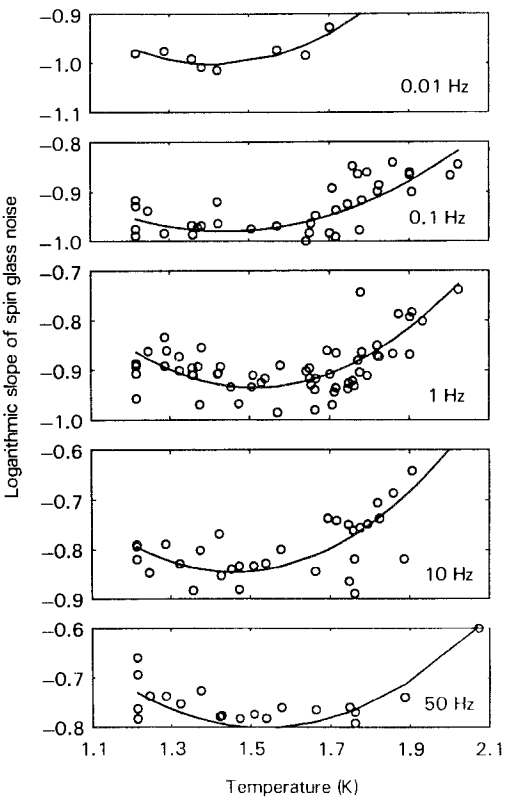

Fig. 54. Logarithmic slope of the noise power spectra (from fig. 53) versus temperature near T_f at five different frequencies. The solid curves show polynomial fits as guides for the eyes (from Reim et al. 1986).

below T_f. Most important, the slope at a fixed temperature is *frequency* dependent even at T_f. This second fact implies that it is not possible to describe the noise power or the imaginary part of the susceptibility by a simple power law, $\chi''(\omega) \propto \omega^{1-n}$, as derived in mean-field theory by Fischer and Kinzel (1984) (see eq. 33). The intriguing experimental result may be explained by the recent prediction (Fisher and Huse 1986) of a $1/f$ noise up to logarithmic corrections.

As another direct consequence of this finding, the time exponent of the magnetization decay $M(t)$ is expected to be also time dependent, an effect which should be noticeable already at $t \sim 1$ s. For instance a fit of $M(t)$ with the commonly used stretched exponential form (eq. 44) may lead to in some sense "*averaged*" values for the exponent $n(T)$. Indeed, Ferré et al. (1986) find for $Eu_{0.40}Sr_{0.60}S$ for Faraday rotation measurements of $M(t)$ and a fit with eq. 44 in the 10^{-3} to 10^{2} s time-interval an "averaged" exponent $n(T_f) = 0.9$, compared to the values of 1.0 at 0.01 Hz and 0.8 at 59 Hz in fig. 54.

7. Spin-glass transition

Let us now proceed to discuss the nature of the transition into the spin-glass state by reviewing experimental studies which have been devoted to analyzing the data in terms of a phase transition and to look for a static T_f. Hence, this section is intimately related to the results and discussions presented above.

7.1. *Search for a static* T_f

First we turn our attention to the *field-cooled magnetization*, M_{FC}, measured in a small field which has been applied already above T_f. Most important $M_{FC}(T)$ of the spin glass is often assumed to be the equilibrium magnetization (Malozemoff and Imry 1981, Chamberlin et al. 1982, Monod and Bouchiat 1982) because it does not seem to depend on time and is reversible as one moves up and down in temperature, as long as H_{FC} remains constant below T_f. In addition, $M_{FC}(T)$ usually developes a plateau below T_f, and a small "bump" ($\approx$10%) occurs around T_f for *Cu*Mn and *Ag*Mn spin glasses (Chamberlin et al. 1982), but for many other spin glasses there is a rather large peak in M_{FC} in the region of T_f. In spin glasses with dominating antiferromagnetic couplings, $M_{FC}(T)$ still increases below T_f on cooling but with a pronounced change in slope at T_f, as can be seen for instance in fig. 44a for $Eu_xSr_{1-x}Te$ spin glasses (Börgermann et al. 1986a, b). The field dependence of M_{FC} near T_f is often related to the mean-field prediction which gives M_{FC} independent of T below T_f (Parisi and Toulouse 1980, Sompolinsky 1981) as will be discussed below.

Recently, Lundgren et al. (1982, 1985) however questioned the validity of the assumption that the measured FC-susceptibility is the thermodynamic susceptibility of a spin glass. They studied the time variation of the relaxation rate in spin glasses by ac-χ measurements and showed that the time range can be

extended to consideably longer times utilizing ZFC-χ measurements, too. In this method a set of ZFC-χ curves is recorded each of which is obtained after various waiting periods t_w at constant temperature before the external field is applied. Figure 55 shows such ZFC-χ curves for the *Cu*Mn 4% spin glass at $T/T_f = 0.9$. In fig. 55a the curves are represented in a relative diagram with $\Delta\chi(t)$ arbitrarily displaced along the vertical axis. A relative change of the total χ of 1% is indicated. Figure 55b shows two curves $\chi(t)$ for $t_w = 0$ and $t_w = 270$ min in an absolute diagram. The data demonstrate that at a certain observation time t both the relaxation rate, S, and the time-dependent susceptibility, $\chi(t)$, markedly depend on the *waiting time* t_w at a constant temperature. Both are related to the ac-χ via

$$S(t) = (1/H)\Delta M(t)/\Delta \ln t \approx -(2/\pi)\chi''(\omega)$$
$$\chi(t) = (1/H)M(t) \approx \chi'(\omega) \tag{79}$$

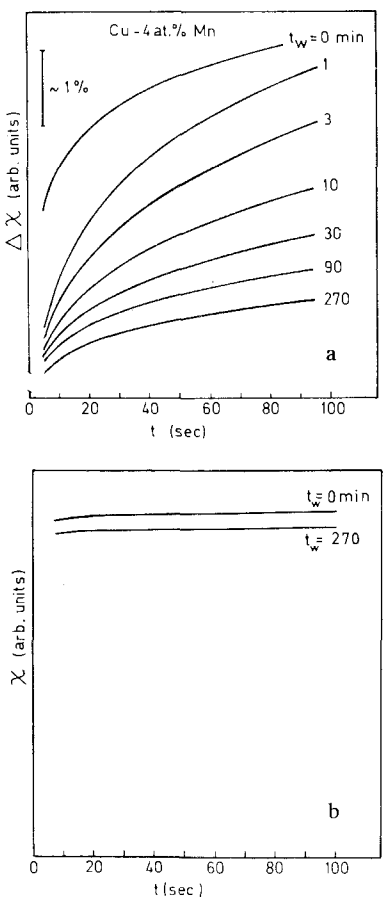

Fig. 55. Time dependence of the ZFC susceptibility for *Cu*Mn 4 atom% at $T = 0.9\,T_f$ ($T_f = 26$ K), obtained after different waiting times t_w before the external field is applied (at $t = 0$). Part (a) of the figure shows the curves arbitrarily displaced on the vertical axis, part (b) on an absolute scale. The estimated equilibrium χ coincides with the upper horizontal line of the frame of the figure (from Lundgren et al. 1985).

if $t = 1/\omega$. In a log t diagram these ZFC-χ curves display an inflection point at an observation time comparable to t_w at constant temperature. Although the experimental data only cover a limited range in observation time ($<10^3$ s) and waiting time ($<10^4$ s), the authors construct a diagram describing the evolution of $\chi(t)$ towards equilibrium. They claim that, independent of t_w, the time-dependent susceptibility attains equilibrium at the same observation time $t_{eq}(T)$. For example, for *Cu*Mn 4% at $T/T_f = 0.9$ (see fig. 55) they estimate $t_{eq} \approx 10^{15}$ s, or that the cusp of $\chi(t)$ coincides with the equilibrium susceptibility at T_f at an observation time of about 10^5 s. For shorter times, the data are interpreted as nonequilibrium or *aging phenomena* in the zero-field state of the spin glass.

The aging of the ZFC-state will be shown up analogously in the *thermoremanent* magnetization. For instance, these authors (Nordblad et al. 1986b) demonstrate that the t_w-dependence of the TRM-decay described by Chamberlin (1985) with the stretched-exponential form {eq. 44, where $\tau_p(t_w)$} is only an artifact caused by the influence of an aging process of the spin-glass state on the relaxation of the magnetization. Hence, according to Nordblad et al. (1986b) a stretched exponential only describes the relaxation in a specific time interval and does not accurately describe the total relaxation of the remanent magnetization. In contrast, Hoogerbeets et al. (1986) present new data of the temperature- and field-dependence of the TRM-decay which they analyze in "remarkable agreement" with predictions of De Dominicis et al. (1985) within the infinite-range mean-field model (eq. 44). (See also the results obtained from magnetic noise measurements as described in sec. 6.4.)

Following Nordblad et al. (1986a) further, they argue that the closely similar wait-time dependence of the TRM-decay to the ZFC-magnetization implies that a corresponding aging process also occurs in the *field-cooled* spin-glass state. The time effects, however, are drastically weaker in the $M_{FC}(t)$, as illustrated in fig. 56 (Note the striking feature of an inflection point at $t \approx t_w$ of the $M_{ZFC}(t)$ in the M–log t plot). According to these authors all the magnetizations measured in spin glasses below T_f probe the *non-equilibrium* state.

Similar time dependencies are observed in low-frequency magnetic *noise* measurements of the insulating spin glass $CsNiFeF_6$ at 4.2 K ($T_f = 5.4$ K) by Ocio et al.

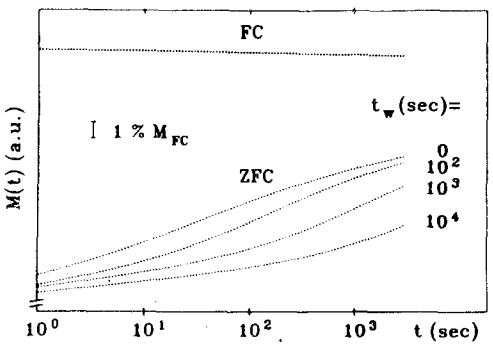

Fig. 56. ZFC magnetization of *Cu*Mn 5 atom% in H = 1 G after different wait-times t_w at $T = 0.9\ T_f$ ($T_f = 28.0$ K) plotted vs log t. The FC magnetization is also shown. 1% of the FC-magnetization value is indicated in the figure (from Nordblad et al. 1986a).

(1986). In the frequency range below 10^{-1} Hz the amplitude of the noise power strongly depends on the time t_w elapsed after cooling the sample (no field is applied!). The noise power measured for example at 3×10^{-3} Hz in the first five hours is 10 times above the value measured after 50 h. There seems to exist a characteristic frequency (which decreases with t_w), above which the $1/\omega$ noise spectrum is observed, but below which the spectrum presents a $1/\omega^x$ dependence with $1.5 < x < 2$. Spectra recorded for waiting times longer than 70 h are stationary and present a $1/\omega$ dependence between 2×10^{-4} Hz and 2×10^2 Hz.

Noise measurements were also performed in the presence of a small magnetic field of 0.3 Oe by Ocio et al. (1986). "Aging effects" are again observed in the ZFC state, but not after FC.

The "aging process" is possibly due to continuous rearrangements of the spin configuration caused by frustration phenomena. Very recently, Binder and Young (1986) argue that is is not absolutely certain that the findings described above really prove the non-equilibrium character of the spin-glass state. If states with spin-glass order exist *as thermal equilibrium states*, they are certainly highly degenerate (i.e. there are many order-parameter components). On cooling the system through its transition temperature one would expect that locally the system starts to form ordered regions of its various possible order-parameter components. As these regions grow there is misfit at their walls, and hence the growth of the domains might be *extremely slow*.

Several authors believe that in field-cooling experiments and using "*very slow*" *cooling rates* one measures the equilibrium susceptibility, or at least there is no time dependence observable in χ and on T_f when deduced from such FC-measurements. For instance, this tacit assumption is made in many experiments described in the following sections. Time effects on M_{FC} after slow cooling are generally tiny, and Chamberlin (1984) even speculates than any observed time dependence of M_{FC} may be a consequence of the fact that the sample is not cooled in a constant local field, due to a small temperature dependence of M_{FC} and the resulting corrections to the local field. Hence, it is important to establish whether there exists a static freezing temperature T_f.

Malozemoff and Imry (1981) were among the first who demonstrated with two spin-glass samples, *Cu*Mn 4.6% (with $T_f \approx 27$ K) and a-AlGd 37% (with $T_f \approx 17$ K), that no shift of the peak position of dc-$\chi(T)$ (defined by M_{FC}/H at a field of 4.5 Oe) can be detected over a long range of time delays from 6 min. to 2400 min. per temperature change $\Delta T = 0.2$ K. Further below the peak temperature, however, it is more difficult to achieve time-independence of M_{FC} in spin glasses. Results from recent experiments by Matsui et al. (1985) are displayed in fig. 57. The data on a-AlGd 37% in fig. 57a indicate that even at the lowest cooling rate applied χ ($= M_{FC}/H$ at 0.13 Oe) seems to be not yet independent of the cooling rate at the low temperature of 5 K (compared to $T_f = 17$ K). Nevertheless, the authors interpret the $\chi(T)$ curve in fig. 57b measured at the slowest cooling rate of 4×10^{-5} K/s as the "equilibrium curve" since at higher temperatures it is "common for all the other cooling rates". By means of this working definition one can determine a characteristic temperature T_{ne} at which a given curve in fig. 57b

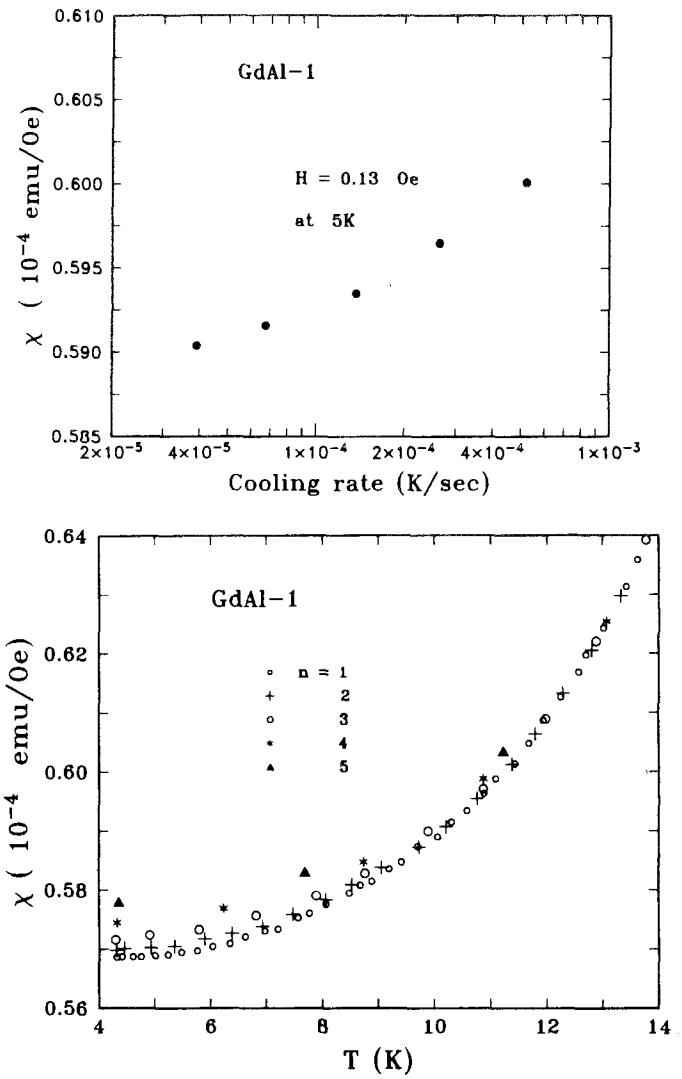

Fig. 57. Susceptibility, $\chi = M_{FC}/H$ at $H = 0.13$ Oe, of a-AlGd 37% spin glass ($T_f = 17$ K) after cooling from 23.5 K at different rates: (a) χ at $T = 5$ K; (b) χ at various T measured after different cooling rates; $n = 1, \ldots, 5$ correspond to 4×10^{-5}, 7×10^{-5}, 1.4×10^{-4}, 2.6×10^{-4}, 5×10^{-4} K/s (from Matsui et al. 1985).

"peels away" from the common curve. Then, a slower cooling rate determines a lower value of T_{ne}. The authors interpret T_{ne} as the lowest temperature for measuring an equilibrium susceptibility in field-cooling at a given cooling rate. For example, data of fig. 57 are in equilibrium for a cooling rate of 1.4×10^{-4} K/s down to 12 K (i.e. 5 K below T_f) when cooling in 0.13 Oe, and down to 11.5 K for 10 Oe.

Detailed dc-magnetization measurements on the spin-glass *Y*Er 1%, presented by Bouchiat and Mailly (1985), also reveal the existence of long-time relaxations of the FC-magnetization which, however, is not incompatible with the existence of a well-defined temperature, characteristic of the occurrence of thermal hysteresis, independent of the cooling rate. Figure 58 illustrates these findings: below $T_f = 0.59$ K strong irreversibility occurs in the magnetization when measured at 10 G along the *c*-axis (one can assume that the Er magnetic moment behave like Ising spins), the ZFC-magnetization differs from the FC one. As can be seen, both magnetizations measured at the warming or cooling rate of 0.15 mK/min are lower than at the higher rate of 10 mK/min, however, the onset of hysteresis occurs at T_f independent of the rate. This temperature is defined with an accuracy of better than 0.5% and coincides with the temperature at which the system deviates from the Curie law.

A completely different behavior is found in a cobalt aluminosilicate glass, $Al_2O_3 \cdot SiO_2 \cdot CoO$, by Wenger and Mydosh (1984a). A higher FC-magnetization is observed at a slower cooling rate (fig. 59), but apparently inconsistent with that, the magnetization stays constant at 4.4 K when monitored over a period of 8×10^4 s. They interpret the data as result of a "supercooling" effect, strongly analogous to the formation of ordinary glasses.

Guy and Park (1983) conclude that the FC-magnetization in *Cu*Mn 0.25% is in thermal equilibrium since the thermodynamic (Maxwell) relations are fulfilled for their magnetization data together with data from magneto-caloric and specific

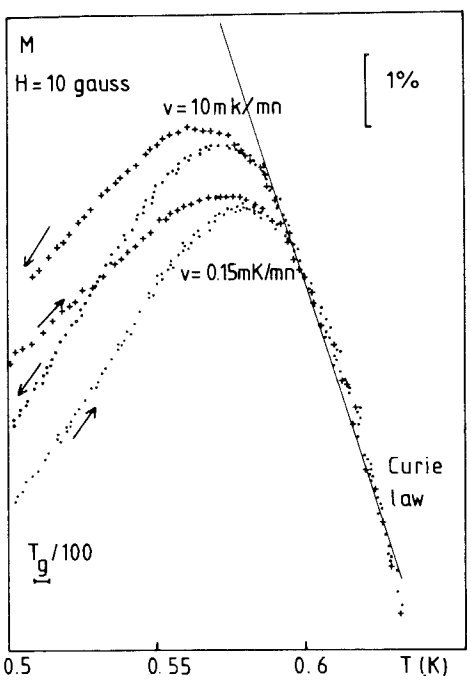

Fig. 58. Thermal hysteresis loops for *Y*Er 1 atom% obtained by cooling the sample from 0.7 K to 0.4 K and warming it under a field of 10 G with a constant speed equal to 10 mK/min (+) or 0.15 mK/min (●) (from Bouchiat and Mailly 1985).

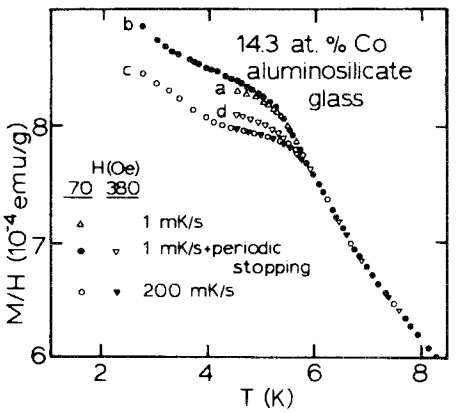

Fig. 59. Field-cooled susceptibility, M/H, of cobalt (14.3 atom%)-aluminosilicate glass versus temperature for various cooling rates and magnetic fields (from Wenger and Mydosh 1984a).

heat measurements. Duffield and Guy (1985) propose on the basis of a similar analysis where *Cu*Mn and $(La, Gd)Al_2$ spin glasses are compared that the equilibrium phenomenon is often obscured by secondary but large irreversible effects. They show that $(La, Gd)Al_2$ is an extremely reversible system that exhibits a relatively large amount of adiabatic cooling below T_f and little irreversibility. On the other hand, *Cu*Mn is much more irreversible and a definite observation of adiabatic cooling has not been made.

Another procedure to search for a static T_f is applied in the $Eu_xSr_{1-x}S$ spin glass with $x = 0.40$ where Ferré et al. (1981) observe a pronounced frequency dependence of the ac-$\chi(T)$ maximum, as shown in fig. 42b. $T_f(\omega)$ seems to saturate for low frequencies at a constant value near the temperature determined by static magnetization measurement. In order to obtain evidence that $T_f(\omega)$ for an infinite observation time really saturates at a nonzero temperature Paulsen et al. (1986b) propose the following extrapolation of the data to $\omega = 0$: first, careful measurements of the real (χ') and imaginary (χ'') part of $\chi(T, \omega)$ are performed in the frequency range $7\,\text{Hz} \leq \omega \leq 5\,\text{kHz}$. It is shown that the relation in eq. 67 between χ' and χ'' holds in zero and finite fields (examined up to 15 Oe). This is remarkable when one considers that the peak in χ' of $Eu_{0.40}Sr_{0.60}S$ shifts toward higher temperatures in moderate H while the χ'' response is moved toward lower temperatures in fields (Maletta and Felsch 1979b, Paulsen et al. 1986a). Then, the authors generalize the mean-field relation $\chi'' \propto \omega^{\nu}$ (eq. 33) via eq. 67 to obtain the functional form of $\chi(T, \omega)$:

$$\chi(T, \omega) = \chi' + i\chi'' = \chi_0 + (2A/\pi\nu)\omega^{\nu} + iA\omega^{\nu} \tag{80}$$

where $A(T)$ and $\nu(T)$ are shown to describe the data for the $Eu_{0.40}Sr_{0.60}S$ spin glass quite well at low frequencies near $T_f(\omega)$. Least-squares fits to the data of χ' and χ'', as illustrated in fig. 60 for a few representative frequencies, determine the parameters $A(T)$ and $\nu(T)$ displayed in fig. 61. Finally, eq. 80 and these parameters are used to calculate $\chi(T, \omega)$ in the limit $\omega \to 0$. The "static" limit is approached very slowly in fig. 60, with the peak in $\chi'(T)$ sharpening as it shifts toward lower temperatures. Also shown is the conventional dc susceptibility

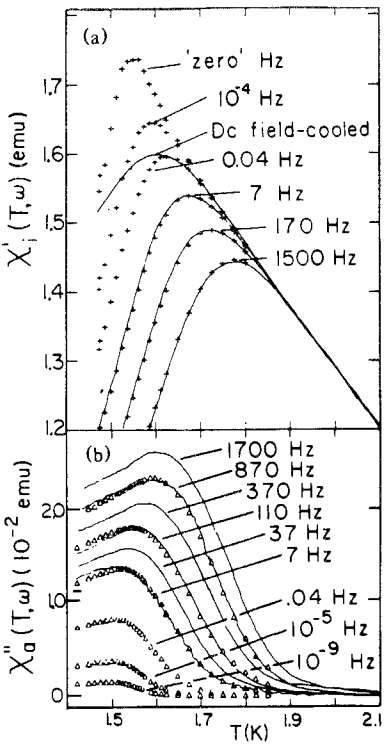

Fig. 60. Real and imaginary parts of the ac susceptibility as measured in $Eu_{0.40}Sr_{0.60}S$ spin glass for various frequencies, shown by solid lines in part (a) and (b), respectively. Eq. 80 describes the data quite well (crosses and triangles), obtaining the parameters $\nu(T)$ and $A(T)$ as shown in fig. 61. Then, χ' (crosses) and χ'' (triangles) can be predicted in the low-frequency range down to 0 Hz by using these parameters and eq. 80. In addition, the dc susceptibility (M_{FC}/H at $H = 0.5$ Oe) is shown for comparison (from Paulsen et al. 1986b).

obtained by cooling the sample at a rate of ~0.2 K per 10 min. in a field of 0.5 Oe. The departure from paramagnetic behavior above T_f is similar to that of the ac-χ for a frequency of 0.04 Hz, which is not inconsistent with the rate of field cooling. The zero-frequency behavior suggests that a phase transition occurs at $T_f(\omega = 0) = T_c = 1.54$ K for this sample. T_c is even somewhat below T_f(dc), but it is interesting to note that the exponent $\nu(T)$ levels off just at T_c (fig. 61). As this limit is approached in the extrapolation, χ'' decreases toward zero but at 10^{-9} Hz still has a small finite value (fig. 60).

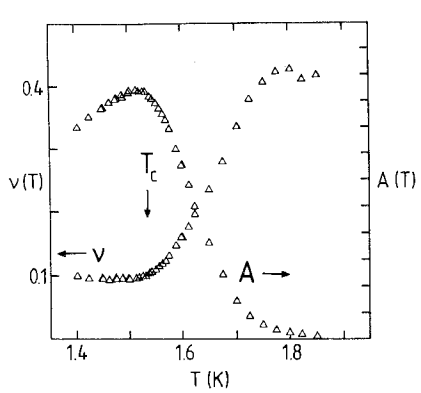

Fig. 61. The temperature dependence of the parameters $\nu(T)$ and A(T) extracted from least-squares fits to the data, shown and described in fig. 60 (from Paulsen et al. 1986b).

7.2. *H–T phase diagram; role of anisotropy*

AT-like lines: The mean-field theory of spin glasses predicts for Ising spins one and for Heisenberg spins two critical lines in the magnetic field–temperature plane (see sec. 4, eqs. 15 and 27). De Almeida and Thouless (AT) (1978) obtained in the mean-field Ising model of SK a transition line $H_f(T)$ below which the system becomes non-ergodic. This AT-line, separating the spin-glass phase from the paramagnetic phase (Parisi and Toulouse 1980), ends for $H \to 0$ at the freezing temperature T_f. Later on, the instability line is suggested to be also a critical line for the disappearance of macroscopic irreversibility (Sompolinsky 1981).

It is thus tempting to test this issue of the mean-field theory. Monod and Bouchiat (1982) perform measurements of the "equilibrium" magnetization in *Ag*Mn 10.6% by slow field cooling as function of temperature and magnetic field. Their data in fig. 62 reveal a deviation from the low-temperature plateau of $M(T, H)$ shifting to lower temperature with increasing field. The temperature of its onset, however, is experimentally ill defined, nevertheless by means of an (arbitrary) working criterion qualitative agreement of $T_f(H)$ with the AT-line (eq. 15) is obtained (see inset of fig. 62).

Chamberlin et al. (1982) present high-resolution SQUID measurements of the dc magnetization of two *Ag*Mn spin glasses containing 2.6 and 4.0 atom% Mn. They use the temperature derivative, $dM(H, T)/dT$ of the ZFC-curve near T_f for the identification of several characteristic temperatures associated with the paramagnetic to spin-glass transition in the presence of an external field. Only the temperature which defines the change of the slope dM/dT yields a power law with an exponent similar to the AT-line.

Berton et al. (1982) use the magnetocaloric effect to determine the H–T diagram of a *Cu*Mn 0.25% spin glass. Here, the variation of the temperature of an adiabatically isolated substance with external magnetic field is measured which is directly related to the magnetization via the Maxwell relation. Their result suggests the presence of two lines: the spin-glass to paramagnetic boundary line $H_c(T)$ and a cross-over line $H_m(T)$ separating a pure Curie paramagnet from a non-Curie paramagnet. The critical field $H_c(T)$, defined rather arbitrarily in the paper, is associated with the AT-line.

As already mentioned above, $T_f(H)$ is also predicted to be seen by the disappearance of irreversibility. Salamon and Tholence (1982) explore this possibility by examining the relaxation of the magnetization of zero-field-cooled samples (*Cu*Mn 0.24% and a-$Fe_{10}Ni_{70}P_{20}$) following the application of a step increase in magnetic field. They show that the magnetic viscosity $S(H, T) = dM(t)/d\ln t$ first increases with field at a fixed temperature, reaches a maximum at $H_m(T)$ and then tends toward zero at large fields. The values of $H_m(T)$ vary similar to the AT line, $\delta T_f \propto H^\eta$ with $\eta = 0.66$ and 0.55 for *Cu*Mn and a-FeNiP, respectively, but the amplitude of the field is much smaller than expected. Salomon and Tholence (1983) use as another criterion for a critical line in the H–T plane the disappearance of the dissipative part of the ac-susceptibility, $\chi''(\omega, T, H)$, in a-$Fe_{10}Ni_{70}P_{20}$ for two frequencies, 11.3 Hz and 11.3 kHz. Of

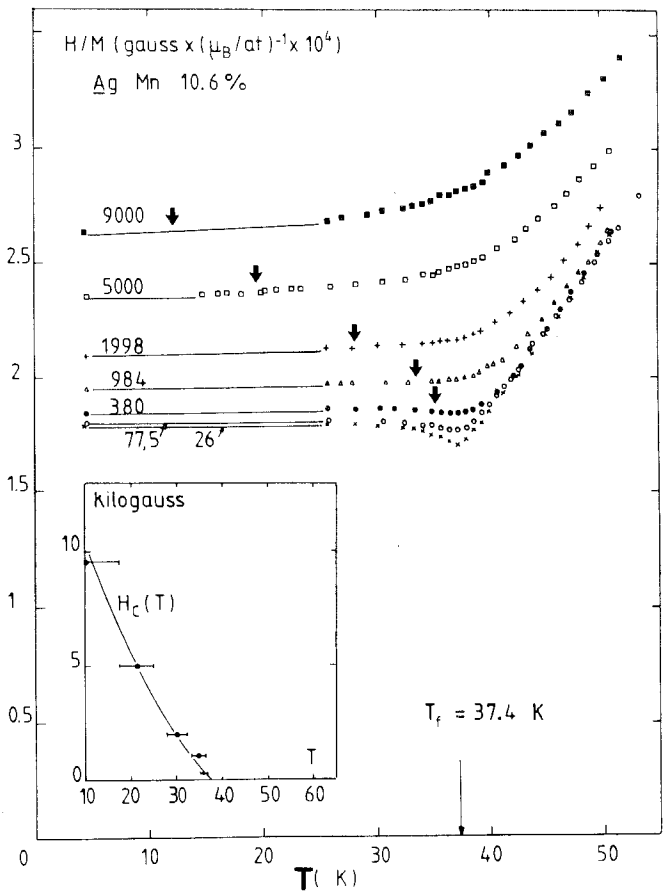

Fig. 62. Inverse of the susceptibility, $\chi^{-1} = H/M$, of AgMn 10.6 atom% as a function of temperature for various magnetic fields (indicated on each curve in G). Data points were obtained by slow cooling in constant field H. The onset of the plateau (marked by arrows) is defined arbitrarily by the point of the $M(T)$ curve departing by 3% from its low-temperature value. The resulting boundary for the spin-glass phase $H_c(T)$ is shown as an inset (from Monod and Bouchiat 1982).

course, such lines depend on the time scale of the measurement, and each of these arbitrary definitions defines a separate curve. Figure 63 summarizes these results, including the line for $S \to 0$. The characteristic field increases strongly with the frequency of the measurement, and the functional form changes. The exponent of T in $H_c(T)$ changes from 1.8 for the long-time data to 1.3 for 11.3 kHz, and the prefactor from 250 Oe to 3 kOe.

For the insulating spin glass $Eu_{0.40}Sr_{0.60}S$ characteristic $H_c(T)$ lines are obtained from the decay of the magnetization after a small field change (superimposed on a larger constant field) $\Delta M(T, H, t_m)$ for fixed time scales t_m, 1 ms $< t_m <$ 1 s (Bontemps et al. 1983), and from the imaginary part $\chi''(T, H, \omega)$ of the complex susceptibility at different frequencies (Paulsen et al. 1984, Rajchenbach

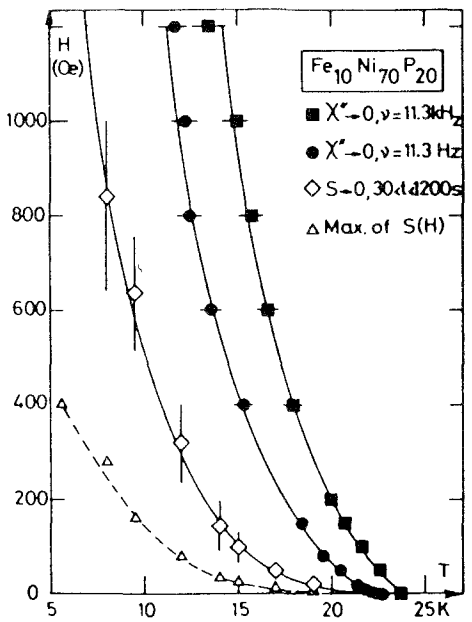

Fig. 63. Critical fields $H_c(T, \omega)$ {or $H_c(T, t)$} for a-$Fe_{10}Ni_{70}P_{20}$ spin glass, as defined by the disappearance of irreversibility (on different time scales) from different experiments. The dashed line represents the maximum of $S(H)$ for $30\,\mathrm{s} < t < 1200\,\mathrm{s}$ (from Salamon and Tholence 1983).

et al. 1984). Again, similarity with the AT-line is observed, but in the latter experiments a different structure at weak fields is detected, as illustrated in fig. 64: the $T_f(H)$ curves exhibit for higher frequency a low-field behavior of T_f nearly independent of H. The dynamic theory of the SK model (Fischer 1983b) confirms this crossover for lines of constant average relaxation time from analytic behavior for high frequencies, $\delta T_f \propto H^2$, to AT-like behavior for $\omega \to 0$, $\delta T_f \propto H^{2/3}$.

To summarize these few examples, the experimental data exhibit a fairly similar behavior to the AT-line of the mean-field theory, in spite of some arbitrariness in

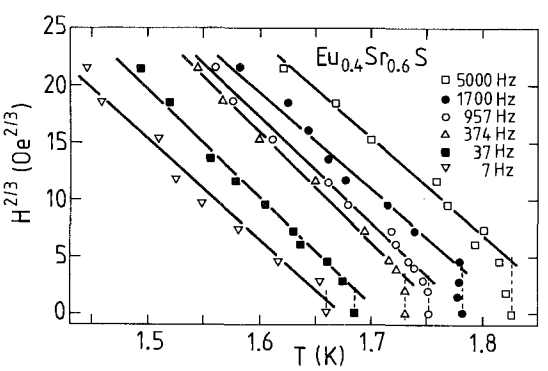

Fig. 64. Critical magnetic field (raised to the 2/3 power to check for the AT-behavior) plotted versus temperature for $Eu_{0.40}Sr_{0.60}S$, determined from the imaginary part $\chi''(T, H, \omega)$ of the complex susceptibility at various frequencies (from Paulsen et al. 1984).

the determination of the transition from the data. Nevertheless, two questions arise:

(i) Can one interpret the data only by assuming a nonzero transition temperature?

(ii) Why do experiments often show AT-like behavior rather than GT-lines, although most spin glasses are more Heisenberg-like than Ising-like?

The first question has been studied by computer simulations (Kinzel and Binder 1984). Even the *two*-dimensional EA–Ising model with a Gaussian distribution of nearest-neighbor interactions reproduces several experiments described above qualitatively in surprising many details (see also sec. 4.2). Since this 2D-model has a spin-glass transition at $T_f = 0$, the "$T_f = 0$-*hypothesis*" (Binder and Young 1984) has been used to describe even 3-dimensional Ising spin-glasses. We will discuss some examples here and also later in this section. These Monte Carlo simulations yield a temperature-independent plateau (fig. 14c) in the FC-susceptibility, M/H, which diverges for small fields as $H^{-1/\Delta}$ with $1/\Delta = 0.28$ (fig. 14d). The critical field, $H_{eq}(T)$, as determined from the onset of the plateau tends to zero as T^{Δ} (fig. 65). Both data are consistent with the scaling description for a static phase transition at $T_f = 0$:

$$\frac{M(T, H)}{H} = \frac{1}{T} \cdot g\left(\frac{H}{T^{\Delta}}\right). \tag{81}$$

The existence of the plateau appears as an effect of the non-linear susceptibility. Since the model has a zero-temperature transition, the linear equilibrium susceptibility should follow a Curie law ($\propto 1/T$) for all temperatures. Magnetizations measured after ZFC deviate from the plateau-value at low temperatures (fig. 14c). For a given field H and observation time t those ZFC curves merge with the equilibrium-plateaus at a temperature $T_f(H, t)$. This defines a line $T_f(H)$ below which for a given time scale t irreversible behavior is observed. $T_f(H)$ is shown in fig. 65 for different times t, and one can see in fig. 66 that the scaled curves, $T_f(H)/T_f(H=0)$, are similar to the AT-line in mean-field theory. However, this line should vanish for $t \to \infty$ (since $T_f = 0$).

Now, if one tries to interpret the FC-plateaus of *Ag*Mn in fig. 62 by means of this concept, one finds a rather different exponent, $1/\Delta = 0.03$, i.e. ten-times smaller than in the simulations for $d = 2$. This may well be taken as evidence for $d_1 \leq 3$ (see sec. 4.4).

The static critical fields, $H_{eq}(T)$, which separate the region of plateaus from the region of non-constant magnetizations behave quite different from the "dynamical" AT-line in the 2D-Monte Carlo-simulations (fig. 65): $H_{eq}(T) \propto T^{\Delta}$. Binder and Kinzel (1983) suggest that the experimental data on a-AlGd 37% (Barbara and Malozomoff 1983) shown in fig. 67 can possibly be interpreted similarly, but a fit then again implies a large value, $\Delta = 10^2$, which either means $T_f > 0$ or $d_1 = 3$. Matsui et al. (1985) extended recently these FC-measurements down to 0.01 Oe, using slow cooling rates (see fig. 57). The new, more precise data (fig. 68) rule out the $T_f = 0$ assumption since at low fields no shift is observed in the position

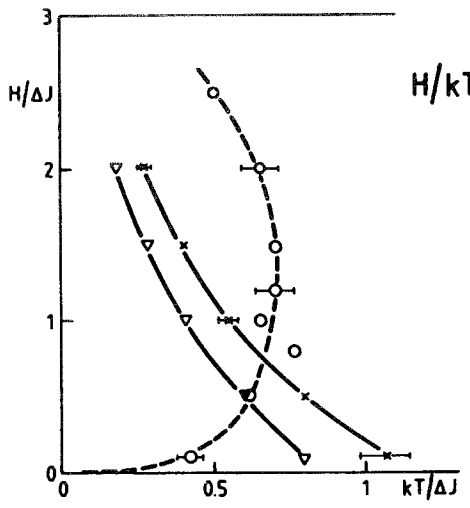

Fig. 65.

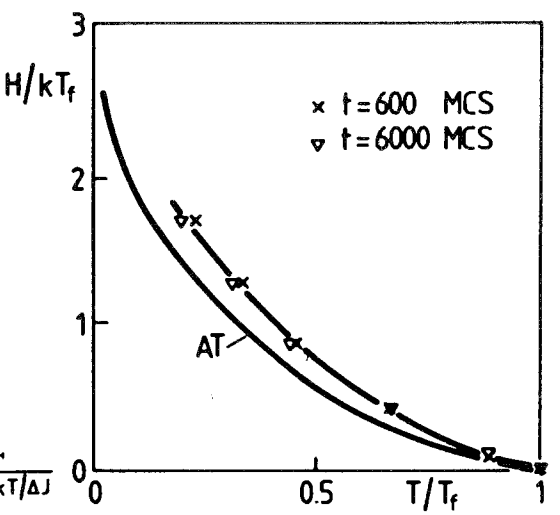

Fig. 66.

Fig. 65. Results from Monte Carlo simulations deduced from fig. 14c: static critical field $H_c^{eq}(T)$ (open circles) and dynamic critical fields $H_c(t)$ for $t = 600$ Monte-Carlo steps per spin (MCS) (crosses) and $t = 6000$ MCS (triangles) plotted versus temperature (from Kinzel and Binder 1984).

Fig. 66. Normalized dynamical critical fields, taken from fig. 65, where $T_f(t)$ is obtained from extrapolating $H_c(t)$ to $H = 0$, compared with the AT-phase boundary of the mean-field theory (SK) (from Kinzel and Binder 1984).

$T_p(H)$ of the maximum of the FC-$\chi(T)$. Thus, a fit to a nonzero-temperature transition

$$t_p = [T_p(H) - T_p(0)]/T_p(0) \propto H^p \tag{82}$$

with $p = 0.8$ is very satisfactory, as shown by the solid line in fig. 68.

Now we turn to the second question about the observation of AT-like lines even for typical Heisenberg systems. To reconcile this result with the mean-field

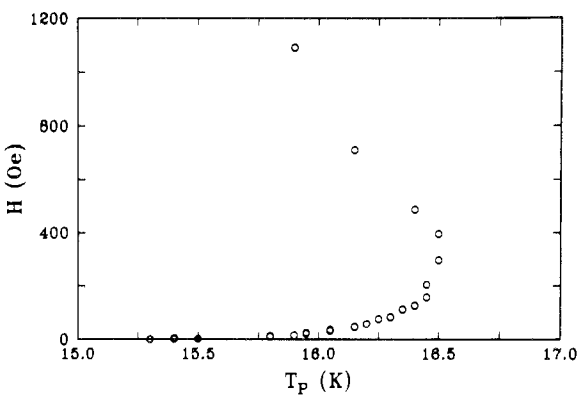

Fig. 67. Temperature $T_p(H)$ of a-*Al*Gd 37 atom% where the field-cooled magnetization has its maximum. It shows a vertical tangent at $H = 250$ Oe and $T - T_f = 0.07\ T_f$ (from Barbara and Malozemoff 1983).

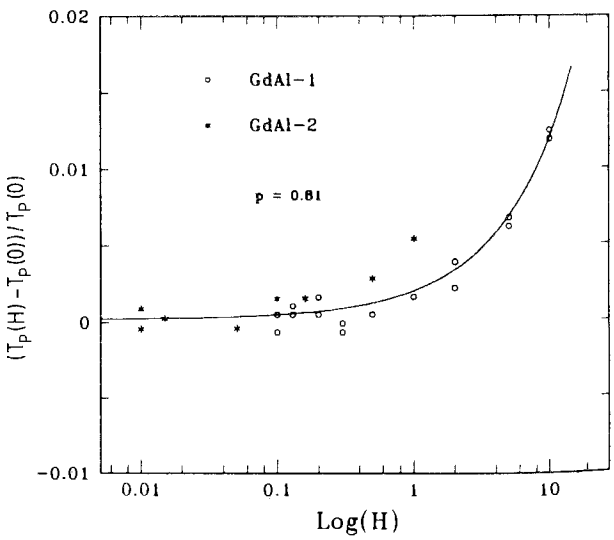

Fig. 68. Normalized peak-temperature, $t_p = (T_p(H) - T_p(0))/T_p(0)$ versus field H for two a-*Al*Gd 37 atom% samples. $T_p(0)$ was determined as the zero-field limit of a fit to eq. 82, shown by the solid line, which gives the exponent $p = 0.81$ (from Matsui et al. 1985).

predictions of Gabay and Toulouse (1981) (see sec. 4.3.2 and eq. 27), it has been argued that most of the experimental methods are weakly sensitive to transverse freezing and can detect only the crossover to strong irreversibility. However, AT-like lines have also been found recently by measurements of the transverse susceptibility which is supposed to be sensitive to transverse freezing (Ketelsen and Salamon 1984). An alternative explanation comes from Kotliar and Sompolinsky (1984). They show that random anisotropy forces, even when small, can mix the longitudinal and transverse components and hence the GT-phase diagram is changed. By a mean-field treatment of the SK spin glass with additional Dzyaloskinskii–Moriya interactions the authors predict an Ising-like transition at low fields; high enough fields (relative to the DM-interaction) restore the behavior expected for Heisenberg spin glasses without random anisotropy. Some indications of such a crossover behavior come from torque measurements (Campbell et al. 1983, 1984, de Courtenay et al. 1984), in which a nearly field-independent irreversibility line is observed. Further work for a clear verification of the GT-line is certainly necessary.

Anisotropic spin glasses: Anisotropy plays a crucial role in the freezing of real spin glasses. Isotropic Heisenberg spin systems are expected to show no spin-glass phase in three dimensions. Monte Carlo simulations on RKKY Heisenberg spin glasses by Walstedt and Walker (1981) suggest that (at least weak) microscopic anisotropy is necessary in order to obtain a cusp in the magnetic susceptibility $\chi(T)$.

The effect of single-ion anisotropy can be studied systematically in rare-earth spin-glasses (Baberschke et al. 1984). Those experiments with *uniaxial* anisotropic spin-glasses have attracted recent interest, and we will show how far the results can be compared with the magnetic phase diagram in fig. 21 (sec. 4.3.3) predicted within mean-field theory (eq. 28) by Cragg and Sherrington (1982b) and Roberts

and Bray (1982). Finally the behavior in applied magnetic fields will be discussed briefly.

Baberschke et al. (1984) report on magnetization measurements on single crystals of Y and Sc containing Gd, Tb, Dy, and Er impurities. The crystal-field parameters are well known. *Y*Er and *Sc*Er are expected to be Ising-like systems (longitudinal freezing for $D > 0$) while the alloys with Dy and Tb are expected to be XY-like (transverse freezing for $D < 0$). The ratio $D/\tilde{J}$ can be changed by varying the rare-earth concentration, which enables one to go from the Ising or XY limit at low concentrations to the most interesting intermediate situations at higher concentrations where at sufficiently small values of $/D//\tilde{J}$ the successive freezing of the two components at different temperatures is predicted; see the phases L, T and LT in fig. 21. For *Y*Gd and *Sc*Gd, D is small ($\sim 4 \times 10^{-3}$ K); their magnetic properties appear to be almost isotropic (Wendler et al. 1984).

In fig. 69 the experimental results are compiled in a plot of $D/\tilde{J}$ versus $T_f/\tilde{J}$ which can be compared directly to the theoretical phase diagram in fig. 21. The values of $D/\tilde{J}$ are calculated as explained in the paper (Baberschke et al. 1984), and T_f is chosen as the low-field limit of the temperature at which the FC- $\chi(T)$ curve departs from the ZFC curve. Typical experimental data of the Heisenberg-

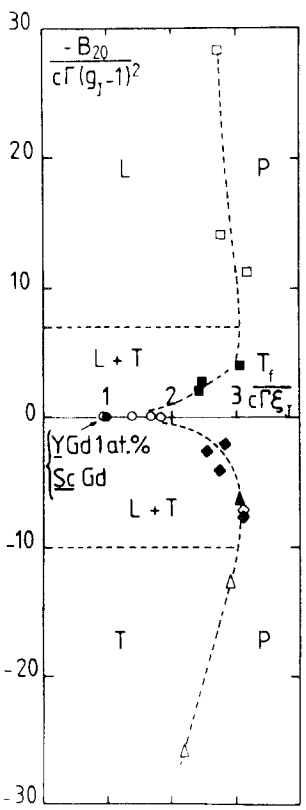

Fig. 69. Experimental phase diagram for *Sc*- and *Y*-based alloys (to be compared to the theoretical phase diagram of fig. 21). $-B_2^0/[c\Gamma(g_J-1)^2] \equiv D/\tilde{J}$ versus $T_f/(c\Gamma\xi_J) \equiv T_f/\tilde{J}$. The experimental data correspond to *Y*Er (□), ScEr (■), *Y*Dy (◇), *Sc*Dy (◆), *Y*Tb (△), *Sc*Tb (▲), *Y*Gd (○), and *Sc*Gd (●) alloys (from Baberschke et al. 1984).

spin system *Sc*Gd 15% (Wendler et al. 1984) and of the XY-spin system *Y*Dy 3% (Baberschke et al. 1984) are shown in figs. 70 and 71, respectively.

The most remarkable agreement of fig. 69 with fig. 21 is for the ratio of about 3 between the values of $T_f/\tilde{J}$ in the Ising ($D/\tilde{J} \gg 1$) and Heisenberg ($D/\tilde{J} = 0$) limits. In contrast, the ratio between the experimental values of $T_f/\tilde{J}$ in the XY and

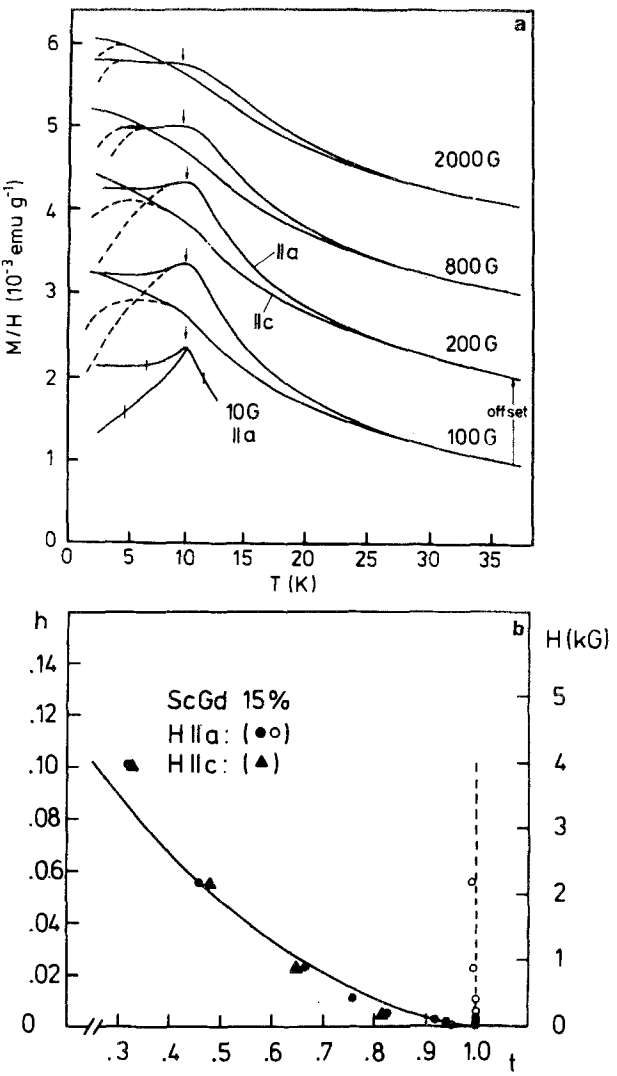

Fig. 70. (a) ZFC (dashed line) and FC (solid line) susceptibility, M/H, of *Sc*Gd 15 atom% for $\|a$ and $\|c$. The curve for 100 G corresponds to the scale of the vertical axis, the other curves are shown with the indicated offset. In the 10 G experiment the experimental error bars are indicated by vertical lines. The arrows indicate the cusp temperature. (b) Full symbols show the onset of irreversibility (T_f^{irr}), open symbols the temperature of the cusp (T_f^{x}) versus $h = g\mu_B(S(S+1)/m)^{1/2} \cdot (kT_{f0})^{-1}$. The temperatures are scaled with $T_{f0} = T_f^{irr}(10\,G) = T_f^{x}$. The solid curve is the AT line (eq. 15), with a scaling factor 1/12, and the dashed one the GT line (eq. 27) (from Wendler et al. 1984).

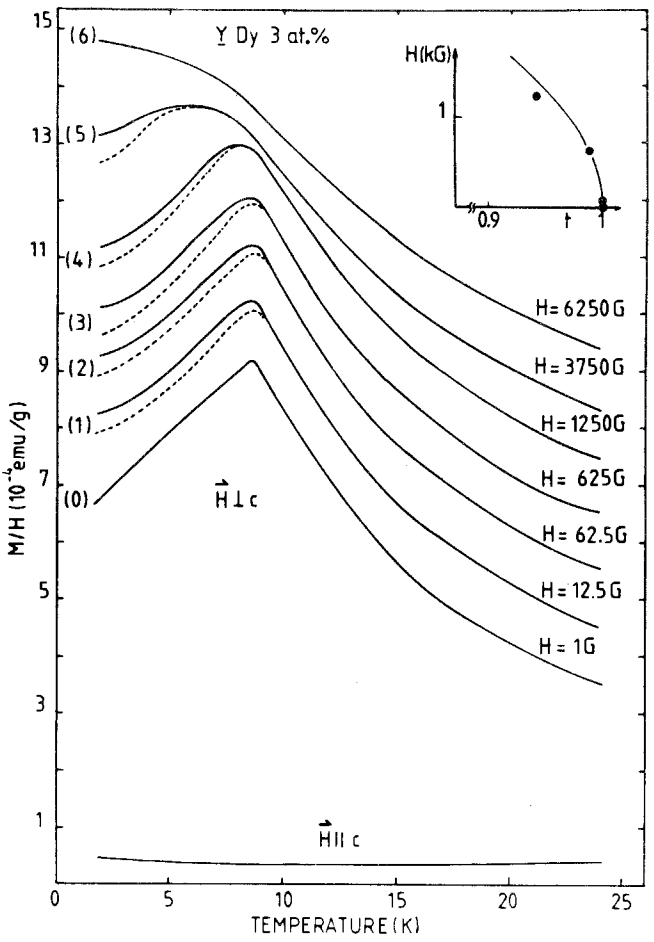

Fig. 71. ZFC (dashed line) and FC (solid line) susceptibility, M/H, of YDy 3 atom% for $\boldsymbol{H} \perp \boldsymbol{c}$ and $\boldsymbol{H} \| \boldsymbol{c}$. Inset: field H vs $t = T_f^{irr}/T_f$, where T_f^{irr} is defined as the temperature where the ZFC curve departs from the FC one. The full line corresponds to $H^2 \sim 1 - t$ (from Baberschke et al. 1984).

Heisenberg limits is definitely larger than the value 1.5 predicted by theory. At large values of $/D//\tilde{J}$ (=open symbols in fig. 69) irreversibility effects are observed only for longitudinal (or transverse) fields (see fig. 71). At small values of $/D//\tilde{J}$ (=full symbols in fig. 69) irreversibilities are observed in *both* directions below the *same* temperature (see fig. 70). Thus the two-stage freezing predicted by the theory (fig. 21) cannot be identified here.

Recently, Schröder et al. (1986) have succeeded in observing an anisotropic behavior with subsequent longitudinal and transverse freezing at *different* temperatures in a new anisotropic spin glass $Eu_xSr_{1-x}As_3$ whose phase diagram is displayed in fig. 9 (see sec. 3.3). The ac susceptibility $\chi(T)$ at 380 Hz of the $x = 0.24$ compound (fig. 72) exhibits a strong difference in $\chi_{\|}$ (=ac driving field

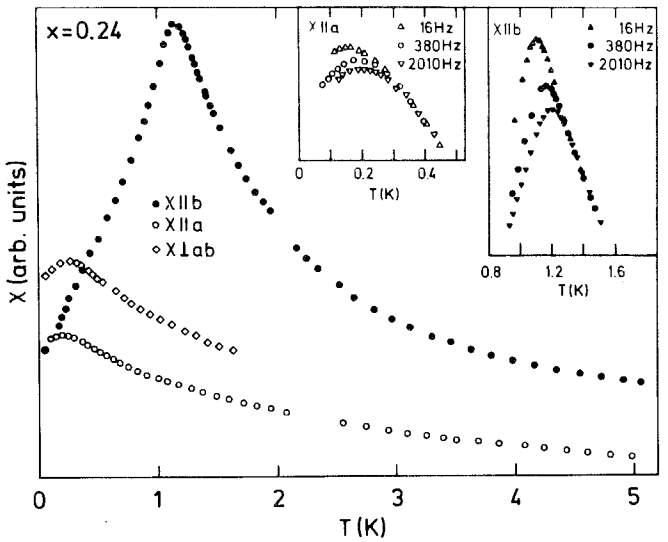

Fig. 72. Ac susceptibility χ (at 380 Hz) of $Eu_{0.24}Sr_{0.76}As_3$ in different crystallographic directions. Insets show the frequency dependence of χ (from Schröder et al. 1986).

parallel to the b direction) and $\chi_\perp$, the longitudinal spin components freeze at $T_f^{\parallel} = 1.17$ K, while $\chi_\perp$ continues to rise towards lower temperatures and shows a maximum at $T_f^{\perp} = 0.20$ K. The peaks in $\chi(T)$ at both temperatures are frequency dependent (see insets of fig. 72). The interactions in this system are predominantly short-ranged, and there are Eu^{2+} ions in an S-state where crystal-field effects are absent to lowest order. Probably a weak anisotropic contribution to the exchange interactions is the origin of the behavior of $\chi(T)$ shown in fig. 72. In this context it is interesting to note that Thalmeier (1986) proposes a realistic exchange Hamiltonian for pure $EuAs_3$ which is shown to lead to a proper incommensurate modulation of the spin order (see sec. 3.3) if the exchange interactions are sufficiently anisotropic.

Let us return to figs. 70, 71 in order to discuss the field dependencies of T_f. If one defines T_f^{irr} as the temperature where the ZFC-susceptibility departs from the FC one, Baberschke et al. (1984) find $\delta T_f^{irr}(H) \propto H^2$ for *XY* spin-glasses like *Y*Dy (fig. 71 and inset), in agreement with what is expected for the GT-line. In addition, a general feature observed for all XY-like alloys is that T_f^{irr} is always higher than the temperature T_f^{χ} of the maximum of the ZFC susceptibility (fig. 71). Both properties observed in the XY-like systems apparently follow the behavior predicted for Heisenberg spin glasses on the basis of the SK Hamiltonian (Sherrington 1983).

On the other hand, the also studied *Ising*-like *Sc*Er and *Y*Er alloys follow the behavior expected for Ising-spin glasses, with a splitting between the FC and ZFC susceptibility at the same temperature T_f^{irr} as T_f^{χ}, and with $\delta T_f^{irr}(H) \propto H^{2/3}$.

But surprisingly, Wendler et al. (1984) observe in the *Heisenberg*-like spin glass

*Sc*Gd (fig. 70) the characteristic temperature T_f^{irr} to be shifted to lower temperatures in the field with $\delta T_f^{irr}(H) \propto H^{2/3}$, while $T_f^{\chi}(H)$ stays constant ($\geqslant T_f^{irr}$). Thus, it is difficult to understand why the behavior predicted for Heisenberg spin glasses should be observed in XY-spin glasses and not in *Sc*Gd or in the classical Heisenberg-spin glasses such as *Cu*Mn, *Ag*Mn, etc.

Summarizing this subsection, there are extensive efforts in the comparing of experimental results with mean-field theory of spin glasses. Indeed, a great deal of theoretical information about the spin-glass transition has been provided by the mean-field theory but one has to keep in mind that it is only valid in high dimension. Even if in real three-dimensional systems the spin-glass freezing is a static phase transition, one should not expect that one can describe it quantitatively by mean-field theory. Fisher and Sompolinsky (1985) argue that several mean-field results for spin glasses apply only for $d > 8$. They show that for $d < 6$ in particular the exponent ψ of the finite-field transition lines, $\delta T_f \propto H^{\psi}$, if they exist, should be *equal for both* Ising and Heisenberg spins in short-range spin glasses and different from the mean-field exponents $\psi_{AT} = 2/3$ and $\psi_{GT} = 2$, respectively. Recent numerical estimates for a three-dimentional Ising-spin glass by Bhatt and Young (1985) and Ogielsky (1985) yield $\psi = 2/3.7 = 0.54$ and $\psi = 2/3.4 = 0.59$, respectively, thus the apparent agreement (see above) between the measured exponent ψ and the AT-mean-field exponent $\psi_{AT} = 2/3$ is *accidental*, as already suggested by Malozemoff et al. in 1983.

Clearly there is need for spin-glass theories *beyond mean-field*. One approach in this direction is presented by Malozemoff et al. (1983) and Malozemoff and Barbara (1985). They propose a *critical fractal cluster model* of spin glasses which is able to describe the essential features of the phenomena occurring near the spin-glass transition and to account for the static critical exponents. The basic assumption of this fractal model is the existence of a temperature- and magnetic-field-dependent characteristic cluster size s_ξ on which all relevant physical quantities depend and which diverges at the transition temperature T_f. It is related to the correlation length ξ and the cluster fractal dimension D by $s_\xi \propto \xi^D$. More recently, Continentino and Malozemoff (1986) extend this model to describe several aspects of spin-glass dynamics: stretched exponential relaxation, magnetic noise, and scaling above $T_f(T)$.

7.3. *Evidences for a phase transition*

In spin glasses critical behavior near T_f is not expected in the linear term χ_0 of the susceptibility M/H, but in the *nonlinear susceptibility* χ_{nl}. This is known from mean-field theory of spin glasses (Suzuki 1977) where the order parameter is not the magnetization but the quantity $q = \Sigma_i [\langle S_i \rangle^2]_{av}$ as suggested by Edwards and Anderson in 1975 (see sec. 4). Then, the field conjugate to the order parameter q is H^2 in spin glasses (instead of H which is coupled to the order parameter M in a ferromagnet). Above T_f this transition shows up in the susceptibility $\chi_{EA} \propto \Sigma_i [\langle S_i S_j \rangle_T^2]_{av}$ which diverges at T_f as

$$\chi_{EA} \propto t^{-\gamma}, \quad \gamma = 1 \tag{83}$$

where $t := |T - T_f|/T_f$. Furthermore, the magnetic field dependence of the susceptibility at T_f may be associated with the critical exponent δ (Chalupa 1977)

$$q(T_f, H) \propto (H^2)^{1/\delta} . \tag{84}$$

The nonlinear susceptibility χ_{nl} is defined by the second term in the expansion of the magnetization with respect to an external field as

$$M/H = \chi_0(T) - \chi_{nl}(T) \cdot H^2 + o(H^4) \tag{85}$$

where higher-order terms, $o(H^4)$, are usually neglected. The critical parts of χ_{nl} and of χ_{EA} are proportional (Binder 1982), for symmetric models we have simply

$$\chi_{nl}(T) = T^{-3}(\chi_{EA}(T) - 2/3) . \tag{86}$$

Hence, the nonlinear χ of spin glasses is one of the most important physical quantities characterizing the spin-glass transition, if it exists at all in the thermodynamic sense, and we will discuss experimental efforts in this direction now.

In spite of problems as discussed above to locate the static T_f in the zero field, numerous attempts have been made to estimate critical exponents for spin glasses. Table 1 contains a list of values for critical exponents obtained from measurements on various spin glasses either directly or via scaling relations. Monod and Bouchiat (1982) show in fig. 73 that their field-cooled magnetization data of the spin glass *Ag*Mn 10.6% (with $T_f = 37.4$ K) indeed exhibit a quadratic variation of M/H in H above T_f, thus $\chi_{nl}(T)$ is defined according to eq. 85.

Note the general feature and hence difficulty in this analysis that the field extension allowing a reasonable fit of the nonlinear susceptibility decreases rapidly when approaching T_f. The authors conclude that the resulting χ_{nl} is consistent with a power-law divergence

$$\chi_{nl}(T) \propto t^{-\gamma} \tag{87}$$

with a *critical exponent* γ of $1 < \gamma < 2$ as displayed in the inset of fig. 73.

Barbara et al. (1981) analyze their data by taking a free exponent $a(T)$ of the nonlinear term, $H^{a(T)}$, instead of the quadratic term in the expansion of eq. 85. Starting with $a(T) = 2$ at high temperatures they find a continuous decrease of $a(T)$ already in the paramagnetic regime (which does not fulfill the general law that the free energy has to be analytic in H) and a pronounced minimum of $a(T_f) \approx 0.7$ as well as a divergence of $\chi_{nl}(T)$ at T_f (eq. 87).

Chikazawa et al. (1983) analyze ac susceptibility data (80 Hz) of *Au*Fe 0.97% and claim that $\chi_{nl}(T)$ exhibits a logarithmic behavior rather than a power law (eq. 87). But after improving the signal-to-noise ratio in the ac-technique (discussing also the contributions of 3ω- and 5ω-terms induced by the ac-field amplitude $h = h_0 \sin \omega t$), the same group (Taniguchi et al. 1983) also obtains a critical power-law behavior for $\chi_{nl}(T)$ in *Au*Fe 1.5% with $\gamma = 1.1 \pm 0.2$. Taniguchi et al. (1985) recently studied the a-$Fe_{10}Ni_{70}P_{20}$ spin glass by the same method which shows $\gamma = 2.3 \pm 0.2$.

TABLE 1

Critical exponents obtained for various spin-glass systems. Some of the values are deduced from scaling laws (e.g. specific heat with $\alpha = 2 - \gamma - 2\beta$).

	δ	γ	β	ϕ	α	Range of T: $\Delta T/T_f$	Range of H: M_{n1} max/M	Remarks	Reference
*Ag*Mn (0.4, 0.5, 0.7, 20.5%)	3.1 ± 0.2	2.2 ± 0.2	1.0 ± 0.1	3.2 ± 0.1	−2.2	0.1	0.1	not s.-c.	Bouchiat 1986
*Ag*Mn (10.6%)		1.5 ± 0.5				0.4	0.1		Monod and Bouchiat 1982
*Ag*Mn (150 ppm)	6.6	3.8	0.7	4.5	−3.2			not s.-c.	Novak et al. 1986
*Cu*Mn (1%)	4.4	3.25 ± 0.10	0.75 ± 0.25	4.2	−2.7	2	0.5		Omari et al. 1983
*Cu*Mn (0.25%)	4.5	3.6 ± 0.3	1	4.5	−3.6	0.7			Berton et al. 1982
*Cu*Mn (4.6%)	4.15 ± 0.15	3.8 ± 0.5	1.2	5.0 ± 0.5	−4.1	1	0.5	not s.-c.	Barbara et al. 1981
*Cu*Mn (2%)	1.5 ± 0.3						0.02	AC	Mulder et al. 1981
*Au*Fe (1.5%)	2.0 ± 0.2	1.1 ± 0.2	0.9	2.0	−1	0.1	0.01	AC	Taniguchi et al. 1983
$Eu_xSr_{1-x}S$ ($x = 0.15, 0.25, 0.3, 0.4$)	4.1							AC	Maletta and Felsch 1979b
a-*Al*Gd (37%)	6.1 ± 0.2	3.4 ± 0.4	0.7	4.0 ± 0.5	−2.8	1	0.6	not s.-c.	Barbara et al. 1981
a-*Al*Gd (37%)	5.7 ± 0.2	2.7 ± 0.1	0.9 ± 0.6	3.3 ± 0.4	−2.1	0.16	0.3		Malozemoff et al. 1982
a-$Fe_{10}Ni_{70}P_{20}$	5.2 ± 0.5	2.3 ± 0.2	0.55	2.9	−1.4	0.3	0.15	AC	Taniguchi et al. 1985
a-AlMnSi	5 ± 1	0.9	0.2	1.1 ± 0.2	+0.7			AC, not s.-c.	Beauvillain et al. 1984a
a-AlMnSi	3.2	3.1 ± 0.1	1.4 ± 0.1	4.5	−3.9	0.4	0.05	AC	Beauvillain et al. 1984b
a-AlMnSi	3.4	3.4 ± 0.1	1.4 ± 0.1	4.8	−4.2			AC	Beauvillain et al. 1986
a-FMnP	5.5	3.6 ± 0.15	0.8 ± 0.1	4.4	−3.2			AC	Beauvillain et al. 1986
a-FMnP	5.5	3.6 ± 0.2	0.8 ± 0.1	4.4	−3.2				Beauvillain et al. 1986

AC = ac-technique

not s.-c. = treatment not self-consistent, as described in text.

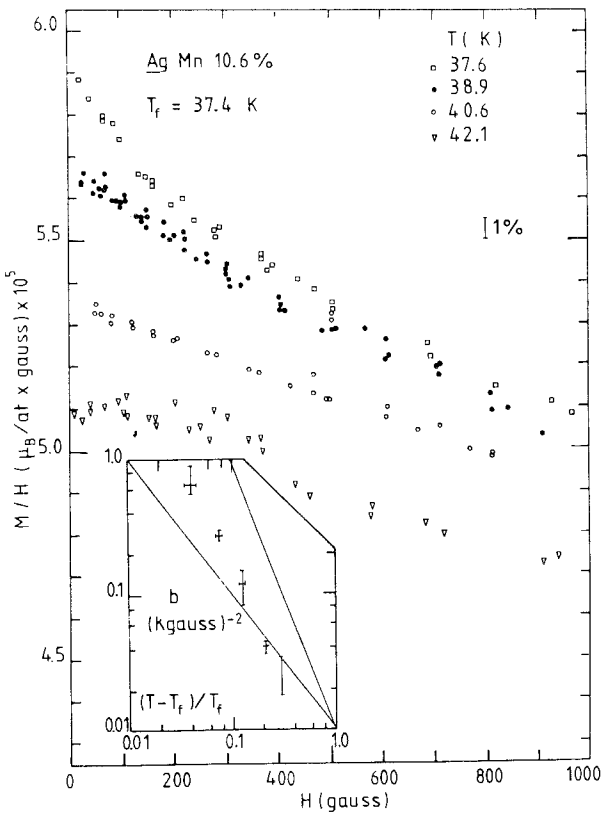

Fig. 73. Susceptibility, M/H, plotted vs magnetic field H in AgMn 10.6 atom% at four temperatures above T_f as indicated. Inset shows a log–log plot of the nonlinear susceptibility χ_{n1} vs the reduced temperature $t = (T - T_f)/T_f$. Straight lines indicate variations $\chi_{n1} = t^{-\gamma}$ with $\gamma = 1$ and $\gamma = 2$, respectively (from Monod and Bouchiat 1982).

Most other work yield somewhat higher values of γ (Berton et al. 1982, Barbara et al. 1981). Careful ac and dc susceptibility measurements were performed on the amorphous manganese aluminosilicate spin glass with 15 atom% Mn by Beauvillain et al. (1984b). The ac susceptibility data are fitted with a series expansion in even powers of an applied static field up to the fourth term in order to obtain $\chi_{n1}(T)$, resulting in $\gamma = 3.1 \pm 0.1$ and $\beta = 1.4 \pm 0.1$.

Fairly strong evidence in favor of the existence of a nonzero transition is provided by the measurement of *the magnetic equation of state* at $T > T_f$, as done with CuMn 1% by Omari et al. (1983). They analyze their static magnetization data in the ranges $T_f < T < 4T_f$ and $0 < H < 7$ T in terms of an expansion including higher-order nonlinear terms:

$$\frac{M}{\chi_0 H} = a_1 - \frac{1}{15} a_3 \cdot \left(\frac{\mu H}{kT}\right)^2 + \frac{2}{305} a_5 \cdot \left(\frac{\mu H}{kT}\right)^4 + \cdots \tag{88}$$

where the expansion coefficients a_1, a_3 and a_5 are related to the critical exponents β and γ by

$$a_1 = 1$$
$$a_m = \left(\frac{T - T_f}{T}\right)^{-n(\beta+\gamma)+\beta} \quad \text{for } m = 2n+1 > 1 \tag{89}$$

and are all normalized to 1 for $T \to \infty$. Note that Omari et al. use the nonlinear variable $(T - T_f)/T$ instead of t. The values of the parameters a_1, a_3, and a_5, obtained in a fit with eq. 88 for various temperatures above $T_f = 10.05$ K, are displayed in fig. 74b. While a_1 stays constant (=1) representing the non-interacting paramagnetic contribution, the other parameters, a_3 and a_5, vary by 3 and 7 orders of magnitude, respectively, between $4T_f$ and $1.1T_f$ and seem to diverge both at the same temperature T_f. Assuming $T_f = 0$, a power-law divergence of a_3 in T does not describe the $a_3(T)$ data (see inset of fig. 74b). Both coefficients are found to be related to each other by

$$a_5 \approx a_3^{2.25\pm0.05} \quad \text{for } T \geqslant 1.1\ T_f \tag{90}$$

shown in fig. 74a. The fact that $a_5 \neq (a_3)^2$ implies that two exponents, γ and β, are necessary to describe the transition with eq. 88. This eliminates the possibility of a transition occurring at $T_f = 0$. The divergence of both a_3 and a_5 can be described

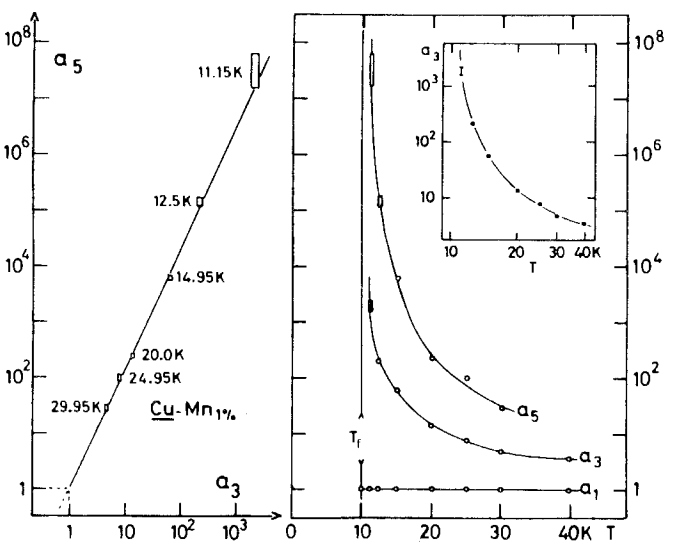

Fig. 74. The coefficients a_1, a_3, a_5 involved in the series expansion of the magnetization (eq. 88) for *Cu*Mn 1 atom% are displayed vs temperature in a semi-log plot on the right-hand-side (part b) of the figure. On the left-hand-side (part a), log a_5 is plotted vs log a_3 at the same temperatures. Note that the data extrapolate to a point where both a_3 and a_5 are equal to unity, which should be associated to the high-temperature paramagnetic limit. The straight line in part a of the figure yields the slope 2.25 ± 0.05 (eq. 90). The log a_3 vs log T plot shown in the inset stresses the failure of any attempt to describe the data with a power law in T ($T_f = 0$ hypothesis) (from Omari et al. 1983).

over the whole T range by the power law in $T/(T - T_f)$ with the exponents 3.25 ± 0.05 and 7.25 ± 0.05, respectively. Using eq. 89 implies $\gamma = 3.25 \pm 0.10$ and $\beta = 0.75 \pm 0.25$.

Quite recently Bouchiat (1986) performed magnetization measurements on *Ag*Mn spin glasses in a wide concentration range, $0.4\% < c < 24\%$, by means of an experimental set-up where the linear part of M is compensated in situ by a small coil mounted on the sample holder in order to increase the accuracy of the so directly measured nonlinear part $\Delta M/H$ $(= M_{n1}/H)$. A typical set of curves $\Delta M/M$ as function of H^2 in *Ag*Mn 20% is shown in fig. 75 for various temperatures above $T_f = 68.5$ K. The initial slope of each curve yields $\chi_{n1}(T)$ of the H^2-term in eq. 85, which is well described by a power law divergence (eq. 87) with $\gamma = 2.3 \pm 0.1$ for this sample with 20 atom% Mn in the temperature range between T_f and 1.1 T_f ($\gamma = 2.1 \pm 0.1$ for the 0.5% atom sample). An apparently higher value of $\gamma_{eff} = 3$ is obtained in an extended T-range between 1.1 and 1.5 T_f.

Turning over to the determination of the *critical exponent* δ (table 1), one of the first experimental attempts is performed for $Eu_xSr_{1-x}S$ spin glasses with $x = 0.15$, 0.25, 0.30 and 0.40 (Maletta and Felsch 1979b). They measure the dependence of the ac-χ-maxima (with 117 Hz) on a superposed static field up to 0.1 T. The normalized data, $\chi_{max}(H)/\chi_{max}(H = 0)$, fairly independent of concentration are associated with the putative order parameter q by the relation

$$q(T_f, H) \propto 1 - \chi_{max}(H)/\chi_{max}(H = 0) \tag{91}$$

and are indeed compatible with eq. 84 (fig. 76a), which gives an exponent $\delta = 4.1$. Moreover, good agreement is found (fig. 76b) with numerical simulations of the EA-order parameter at T_f by Stauffer and Binder (1978) yielding $\delta = 4.0$ in three dimensions.

Similar measurements of ac-χ (332 Hz) on *Cu*Mn 2% by Mulder et al. (1981) yield an anomalously small value of $\delta = 1.5 \pm 0.3$. Taniguchi et al. (1985) obtain $\delta = 5.2 \pm 0.5$ in a-$Fe_{10}Ni_{70}P_{20}$.

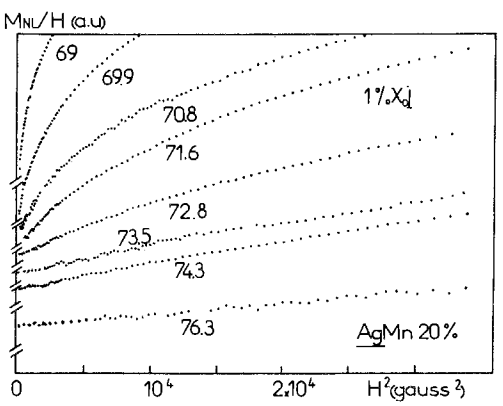

Fig. 75. Typical set of curves, $\Delta M/H$ as a function of H^2, in *Ag*Mn 20 atom% for various temperatures above T_f (from Bouchiat 1986).

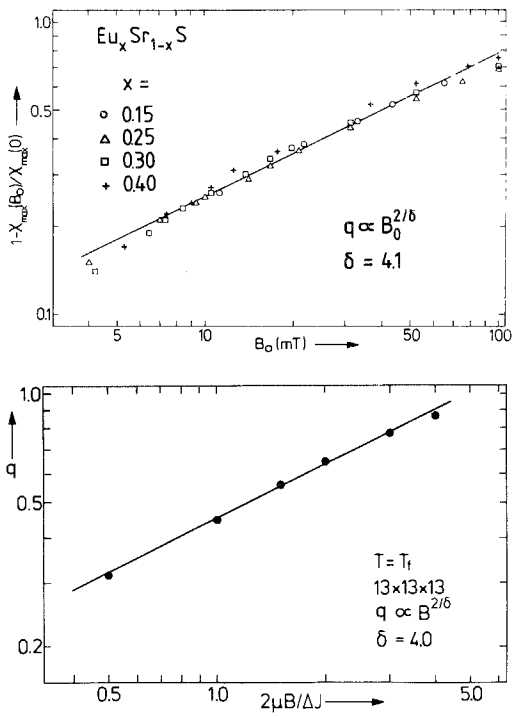

Fig. 76. (a) Depression of χ at the maximum of the ac-χ ($\omega = 117$ Hz) in $Eu_xSr_{1-x}S$ spin glasses as function of the external field, measured for various Eu-concentrations x as indicated. Straight line on this log–log plot gives an exponent $\delta = 4.1$ (from Maletta and Felsch 1979b). (b) Field dependence of the EA order-parameter at T_f, calculated from Monte Carlo simulations of a simple cubic Ising model with nearest-neighbor exchange distributed according to a Gaussian of width ΔJ. Data points are based on observations of 2000 MCS (from Stauffer and Binder 1978).

Bouchiat (1986) determined δ from the M_{n1} measurements. At the transition temperature T_f the data of AgMn 0.5% can be well fitted between 10 G and 400 G (where $M_{n1}/M < 0.1$) by a power law

$$M_{n1}/H \propto H^{2/\delta} \tag{92}$$

yielding $\delta = 3.1 \pm 0.1$ (independent of concentration) as shown in fig. 77. Deviations towards apparently higher values of δ occur at higher fields (see fig. 77).

If a phase transition at a nonzero temperature T_f exists in spin glasses, one expects that the nonlinear susceptibility should satisfy a static *scaling law*:

$$1 - \frac{M}{\chi_0 H} = t^{\beta} \cdot \tilde{M}\left\{\left(\frac{H}{T}\right)^2 \cdot t^{-\phi}\right\} \tag{93}$$

where $t = (T - T_f)/T_f$, $\tilde{M}$ being the appropriate scaling function with

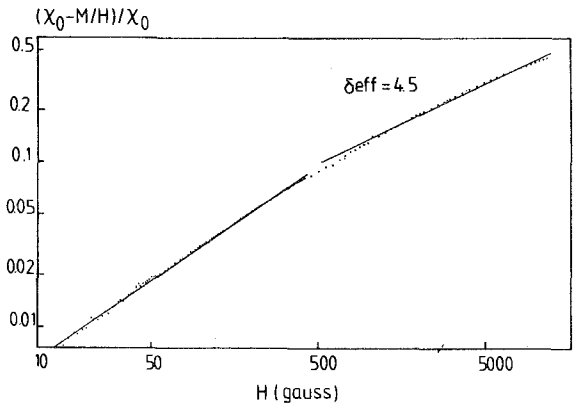

Fig. 77. Nonlinear magnetization versus magnetic field at T_f (log–log plot) for *Ag*Mn 0.5 atom% in the range of magnetic field where $M_{n1}/M < 0.5$. Note deviations towards apparent values of δ ($\delta_{eff} = 4.5$) which are higher than the value ($\delta = 3.1$) deduced when the analysis is restricted to the range of field where $M_{n1}/M < 0.1$ (from Bouchiat 1986).

$$\tilde{M}(x) \propto x \quad \text{for } x \to 0$$
$$\tilde{M}(x) \propto x^{1/\delta} \quad \text{for } x \to \infty \tag{94}$$

and scaling relations for the crossover exponent ϕ

$$\phi = \beta + \gamma$$
$$\phi = \gamma\delta/(\delta - 1) = \beta\delta. \tag{95}$$

Barbara et al. (1981) presented the first experimental demonstration of scaling in both field and temperature for the spin-glass susceptibility in *Cu*Mn 4.6% and a-*Al*Gd 37%. This first treatment is not self-consistent because they determine χ_0 from an expansion in H with a varying term $H^{a(T)}$ (as described above) which does not agree with eq. 93. The same criticism holds for the recent papers by Beauvillain et al. (1984a) and Novak et al. (1986). A self-consistent scaling analysis is performed by Malozemoff et al. (1982) of magnetization data on a-*Al*Gd 37%, the results of such a fit give $\phi = 3.3 \pm 0.4$, $\gamma = 2.7 \pm 0.1$, $\beta = 0.93 \pm 0.04$, and $\delta = 5.7 \pm 0.2$. They argue that the critical region extends from $T_f = 15.5$ K to about 22 K and in field up to about 15 kOe. Not all scaling relations for the various critical exponents are nicely satisfied, and low-field upturns fail to be described by the scaling. The authors suggest transition broadening due to sample inhomogeneity as a possible cause.

Beauvillain et al. (1986) measured the dc- and ac-susceptibility (69 Hz) of two insulating spin glasses, the amorphous manganese aluminosilicate (a-AlMnSi) with $T_f = 2.95$ K and the amorphous manganese fluorophosphate (a-FMnP) with $T_f = 2.80$ K in the field range up to 600 Oe near the freezing temperature. The

nonlinear parts of the ac-χ are well described by the series expansion up to the H^6-term, yielding the exponents $\gamma = 3.4 \pm 0.1$, $\beta = 1.4 \pm 0.1$ in a-AlMnSi and $\gamma = 3.6 \pm 0.15$, $\beta = 0.8 \pm 0.1$ in a-FMnP. Using these values of γ and β, all data in the whole field range fall onto a universal curve in a scaling plot with eq. 93. These results are in remarkable agreement with the scaling analysis of the static low-field magnetization measured on the same a-FMnP spin glass which gives identical values for γ and β.

Omari et al. (1983) present an impressive scaling plot as shown in fig. 78. All the data of *Cu*Mn 1% within the anomalous wide range $1.1T_f < T < 4T_f$ in fields up to 7 T superimpose to fit a unique function of the scaling variable with $\gamma = 3.25$ and $\beta = 0.75$ as deduced from the temperature dependence of a_3 and a_5 (eq. 88) in the $H \rightarrow 0$ limit (which is already described above). An even improved scaling is obtained with $\beta = 0.95$ (which yield $\delta = 4.4$). These values of the exponents are consistent with those deduced on the same spin glass, *Cu*Mn 0.25%, by a completely different technique using the magnetocaloric effect (Berton et al. 1982).

In a careful work by Bouchiat (1986) the nonlinear magnetization of various *Ag*Mn spin glasses is also analyzed in the framework of a phase transition. The transition temperature T_f is determined by three methods which give the same

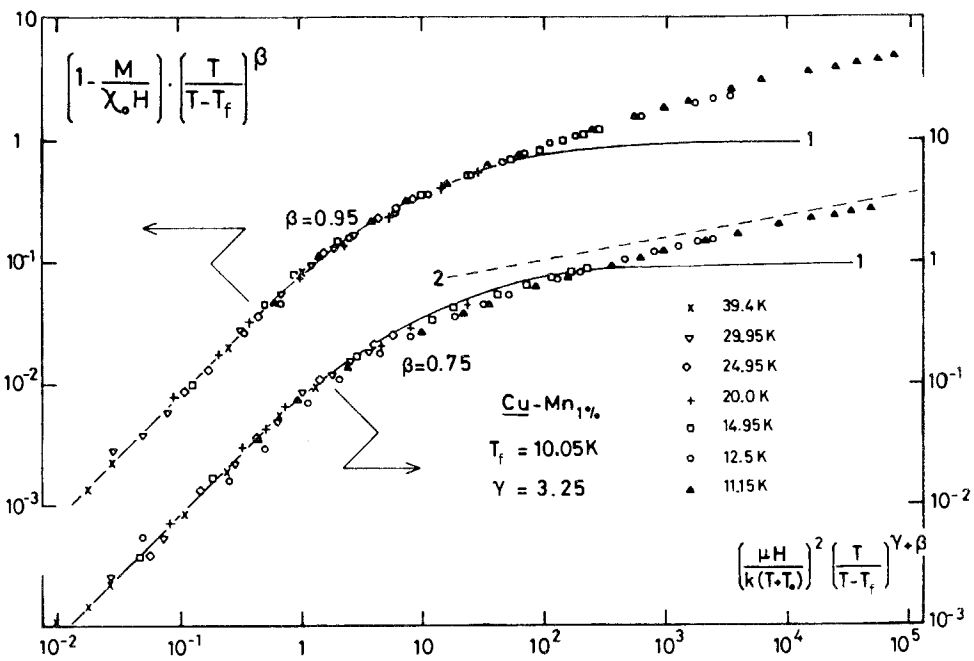

Fig. 78. Scaling plot of the magnetization data for *Cu*Mn 1 atom% using eqs. 88 and 89 for two choices of the exponent β (as indicated) and for $\gamma = 3.25$. Data at H up to 70 kOe and T up to 4 T_f are included (from Omari et al. 1983).

value within ±0.5%: ac-χ maximum (30 Hz); low-field magnetization; onset of irreversibility in the low-field magnetization (FC, ZFC). Then, Bouchiat uses three independent experimental criteria to determine the critical exponents among which only two are independent, assuming the T_f-value from above. When the analysis is restricted to the reduced temperature and magnetic field range where $(T - T_f)/T_f < 0.1$ and $M_{nl}/M < 0.1$, Bouchiat finds $\gamma = 2.2 \pm 0.2$, $\beta = 1.0 \pm 0.1$, and $\delta = 3.0 \pm 0.2$. (The determination of γ and δ was already discussed above.) It is also possible to describe all the data with a universal scaling function (eq. 93), as illustrated in fig. 79. The best fit is obtained for $\phi = 3.2 \pm 0.1$ and $\beta = 1.0 \pm 0.1$ independent of the Mn concentration. Note that the crossover exponent ϕ verifies the scaling relations $\phi = \beta + \gamma$. The asymptotic forms of the scaling function $\tilde{M}(x)$ (eq. 94) can also be checked in fig. 79 as indicated by the two straight lines. The three independent determinations of the critical exponents also verify the scaling relations in eq. 95. Extending the "critical range" leads to apparently higher values of the exponents as shown above (fig. 77), but the possibility of a real physical crossover occurring at $t > 0.1$ cannot be excluded. The different ranges of the critical region used in the various attempts to deduce critical exponents for spin glasses may explain the discrepancies existing between the different values obtained so far (see table 1).

Finally, let us consider the spin dynamics near T_f. Nonexponential decay of the dynamic correlation function and the rapid growth of correlation times on approaching T_f from above have been clearly established in spin glasses, as discussed in sec. 6. At present experiments, however, do not permit the determination of the exact shape of the dynamic correlation function. On the other hand the temperature dependence of the correlation times is analyzed carefully by

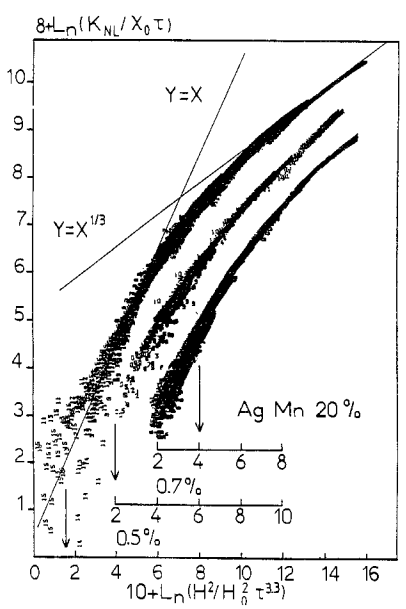

Fig. 79. Scaling of the nonlinear magnetization (eq. 93–95) for 15 different values of temperature between T_f and 1.1 T_f (τ denotes the reduced temperature t) and 200 values of magnetic field for which $M_{nl}/M < 0.1$. Note the shifted origins on the abscissa for the three alloys of *Ag*Mn with 0.5, 0.7, and 20 atom% Mn concentration (from Bouchiat 1986).

Bontemps et al. (1984, 1986) within the framework of *critical slowing down* applying two different dynamical scaling models:
(i) The *standard dynamic scaling* near the spin-glass temperature $T_c > 0$ which is considered as a second-order phase transition gives for the relaxation time τ and the correlation length ξ the relations

$$\tau/\tau_0 \propto \xi^z \propto t^{-z\nu} \tag{96}$$

where z is the dynamic exponent (Hohenberg and Halperin 1977). The field dependence of ξ generates the field dependence of τ:

$$\tau/\tau_0 \propto t^{-z\nu} \cdot \tilde{\tau}(h^2/t^{\beta+\gamma}) \tag{97}$$

$\tilde{\tau}$ being an appropriate scaling function.
(ii) The alternative picture of *logarithmic scaling* near a $T_c = 0$ phase transition (Binder and Young 1984) (see also eq. 81 and discussion there) assumes that thermal activation processes over free energy barriers ΔF controlled by $\xi(T)$ are important, hence

$$\ln(\tau/\tau_0) \propto \Delta F(\xi)/T \propto \xi^{z-1/\nu}/T \propto T^{-z\nu} \tag{98}$$

and similarly:

$$\ln(\tau/\tau_0) \propto T^{-z\nu} \cdot \tilde{\tau}(h/T^{\Delta}) \quad \text{with } \Delta = (\beta+\gamma)/2\,. \tag{99}$$

Bontemps et al. (1984, 1986) studied $T_f(\omega, H)$ lines of the $Eu_{0.40}Sr_{0.60}S$ spin glass for frequencies 10^4 Hz $< \omega < 10^{-2}$ Hz by means of Faraday rotation and SQUID measurements. In addition measurements of the remanent magnetization are performed by optical means in the 10 ms–1 s and 500 ms–25 s time ranges. Large demagnetizing-field corrections have to be made due to the platelet-shaped sample. The authors establish a dynamical criterion in order to extract a characteristic response time from the $\chi(\omega, T, H)$ data. Taking the response of a system in terms of a complex susceptibility $\tilde{\chi}(\omega) = \chi e^{i\phi}$, they define the zero-field freezing temperature T_f as the temperature where $\tan\phi = \varphi(\omega\tau)$ takes a given phase angle ϕ_0. The value of ϕ_0 has to be chosen as independent of ω and small but clearly above the noise of the signal. This defines $\tau = A/\omega$.

Bontemps et al. (1986) can fit the data with both scaling models, eqs. 97 and 99, as shown in figs. 80 and 81, respectively. The generalized reduced temperatures are $t = (T - T_c)/T$ and $t_f = (T_f - T_c)/T_f$ (following Omari et al. 1983) and the reduced field is $h = g\mu_B \cdot \sqrt{S(S+1)/3}\, H/kT$. They obtain the parameters summarized in table 2. Both fits are of comparable quality, which shows how difficult it is in practice to distinguish the two possibilities, but the parameters provide a strong support for the model of a nonzero-temperature transition in this insulating spin glass:

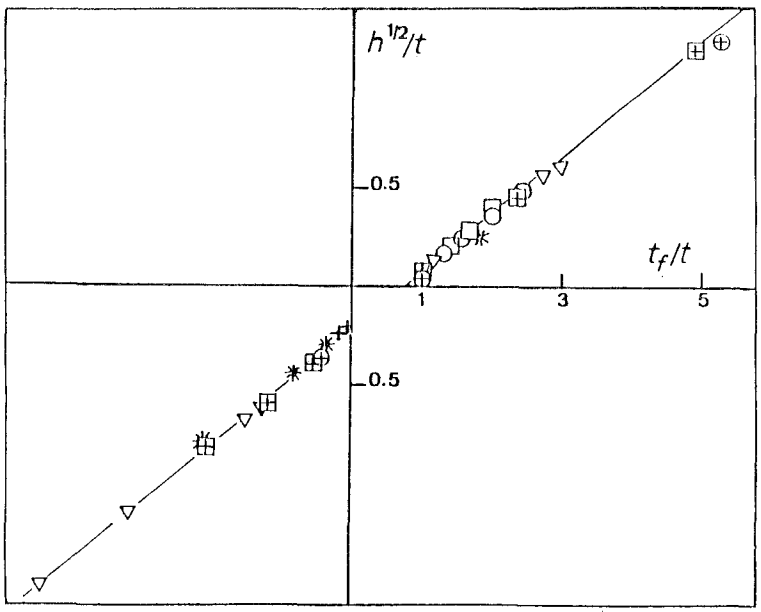

Fig. 80. Dynamic scaling of the $T_f(H, \omega$ or $t_m)$ lines for $Eu_{0.40}Sr_{0.60}S$ in the case of a nonzero-temperature transition ($T_c = 1.50$ K). Data are taken from χ-phase ($1\,\text{Hz} < \omega < 10^4$ Hz) and remanent-magnetization ($10\,\text{ms} < t_m < 25$ s) measurements (from Bontemps et al. 1986).

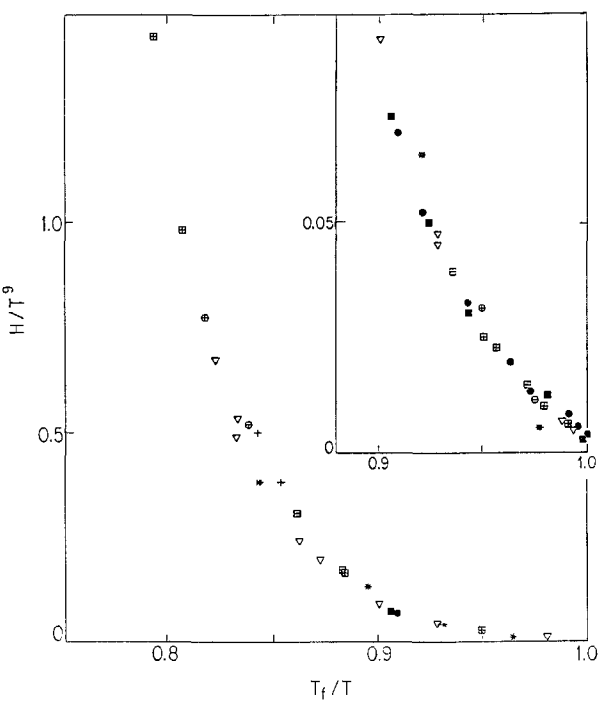

Fig. 81. "Logarithmic" dynamic scaling of the $T_f(H, \omega$ or $t_m)$ lines for the same data as in fig. 80, but now in the case of a zero-temperature transition ($T_c = 0$). The inset shows the low-field points with an extended scale (from Bontemps et al. 1986).

TABLE 2
Parameters obtained for the spin glass $Eu_{0.40}Sr_{0.60}S$ from two dynamic scaling models, eq. 97 with $T_c = 1.50$ K and eq. 99 with $T_c = 0$ (from Bontemps et al. 1986).

$T_c = 1.50$ K	$\tau_0 \approx 3 \times 10^{-12}$ s	$z\nu = 8.2 \pm 0.5$	$(\beta + \gamma) = 4$
$T_c = 0$	$\tau_0 \approx 10^{-8}$ s	$z\nu = 9 \pm 1$	$\Delta = (\beta + \gamma)/2 = 9$

– $T_c = 1.50$ K is consistent with the value of 1.51 K determined by dc-magnetization measurement on the same sample.
– $\tau_0 \approx 3 \times 10^{-12}$ s compares well with $\hbar/kT_c \approx 4 \times 10^{-12}$ s.
– $z\nu = 8.2$ is comparable to computer simulations by Ogielski (1985) which yield $z\nu = 7.2 \pm 1$ (see eq. 34).
– $(\beta + \gamma) = 4$ is in good agreement with the values found in other spin glasses both experimentally and by simulations. For instance, Bouchiat (1986) obtains $(\beta + \gamma) \approx 1.0 + 2.2 = 3.2$ (see table 1); Bhatt and Young (1985) $(\beta + \gamma) \approx 0.5 + 3.2 = 3.7$; and Ogielski (1985) $(\beta + \gamma) \approx 0.5 + 2.9 = 3.4$ (see eq. 34).

As consequence the scaling with eq. 97 leads to a divergence of the relaxation time along an "AT-line", $\delta T_f \propto H^{\psi}$, with $\psi = 2/(\beta + \gamma) = 1/2$ in $Eu_{0.40}Sr_{0.60}S$ (see discussion at the end of sec. 7.2 and in sec. 10).

Summarizing, the fairly convincing experimental demonstrations of static and dynamic scaling at a nonzero spin-glass temperature as reviewed above provide strong evidence for a *nonzero phase-transition* temperature in spin glasses, in good agreement with recent numerical results (see sec. 4.4).

8. Crossover to long-range periodic order

So far we have discussed the ordering behavior of diluted magnetic systems with competing ferro- and antiferromagnetic interactions which exhibit a transition from the paramagnetic to the spin-glass phase on lowering the temperature. By increasing the concentration of magnetic atoms (less dilution), the exchange couplings become stronger at the cost of less frustrated bonds between the magnetic moments on the average, thus one expects the evolution of long-range ferro- or antiferromagnetic order out of the spin-glass phase at a critical concentration x_c. Here, we are interested in the crossover regime which may be influenced by the interplay between spin-glass and long-range periodic order phenomena.

8.1. *Reentrant behavior*

One of the most fascinating aspects of these investigations has been the discovery of *reentrant spin glasses*. It has been claimed that within a small concentration regime a ferromagnetic-like state occurs at temperatures higher than the spin-glass state (see e.g. Maletta 1983b). This is an unusual property since ordered ferromagnetic states generally have a lower free energy than

manifestly disordered states. Nevertheless, many different systems are supposed to show such a behavior, the first studied examples are: Al–Fe (Shull et al. 1976), Pd–Fe–Mn (Verbeek et al. 1978), Au–Fe (Verbeek and Mydosh 1978, Crane and Claus 1981), Cr–Fe (Fincher et al. 1980), (Eu, Sr)S (Maletta and Convert 1979a, Maletta 1979c), and a-(Fe, Mn) PBAl (Yeshurun et al. 1980). The interpretation of the various experiments, however, are still highly controversial (Coles 1984).

Sherrington and Kirkpatrick (1975) were the first to predict a similar phenomenon of Ising spins for $J_0/\tilde{J} \geq 1$ within mean-field theory. It turned out, however, that one needs the Parisi solution (Vannimenus et al. 1981) of the SK model to get the exact solution at low-temperature. But then, reentrant spin-glass behavior does *not* occur (see fig. 18 and discussion in sec. 4.3): with decreasing temperatures, the system becomes first ferromagnetic (FM) with a spontaneous magnetization $M_0 \neq 0$ and subsequently goes into a "mixed phase" (F') with $M_0 \neq 0$ and with irreversibility (=a modified FM with SG-like features); the second transition is quite analogous to the AT-line of SG in a field. For Heisenberg spins, the mean-field theory (Toulouse 1980, Gabay and Toulouse 1981, Cragg et al. 1982a) predicts at the second transition (a GT-like line) a change from a collinear ferromagnet to a "canted ferromagnetic state" with $M_0 \neq 0$ and transverse-spin freezing (fig. 20). Thus, in both cases within the SK model the low-temperature state is a "*mixed phase*" where FM and SG orders coexist.

To date, bulk measurements like the *magnetization* and *ac-susceptibility* have mostly been performed in order to identify a second transition and a reentrant spin-glass (RSG) phase. This low-temperature transition at T_f manifests itself in a number of ways: drop of the demagnetization-limited ac susceptibility (fig. 82)

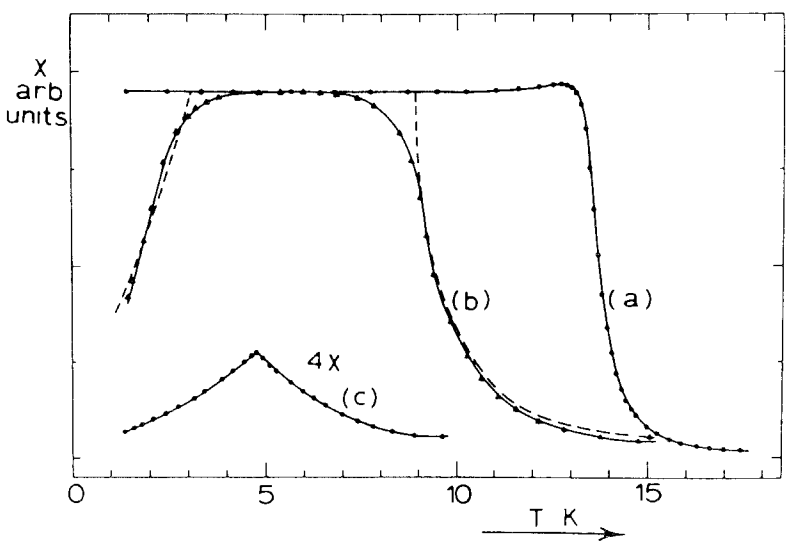

Fig. 82. Temperature dependence of the ac susceptibility for $(Pd_{0.9965}Fe_{0.0035})_{1-x}Mn_x$. Curve a: $x = 0.01$; curve b: $x = 0.05$; curve c: $x = 0.065$ (from Verbeek et al. 1978).

(Verbeek et al. 1978, Coles et al. 1978, Maletta and Felsch 1980d); field-dependent peak in the ac-susceptibility measured in the presence of a dc-field (fig. 83) (Maletta 1979c, Geohegan and Bhagat 1981); vanishing of the spontaneous magnetization (fig. 84) (Manheimer et al. 1983, Crane and Claus 1981); onset of magnetic viscosity (Yeshurun and Salamon 1981); onset of history-dependent effects (Carnegie and Claus 1979, Yeshurun and Sompolinsky 1982); change of hysteresis loop (Senoussi 1984).

Since all these experiments are performed in finite field and the sensitivity to the applied H is remarkable (see figs. 83 and 84) one has to work in really *low field* and has to introduce a reliable extrapolation procedure in order to obtain the spontaneous magnetization and to locate the temperature T_f. At first sight, one would expect only fields of the order of (kT_f/μ_B) or (kT_c/μ_B) to give significant effects, but the applied fields are several orders of magnitude smaller. For the a-$(Fe_xMn_{1-x})_{75}P_{16}B_6Al_3$ alloy with $x = 0.80$, for instance, Manheimer et al. (1983) locate $T_f(H \to 0)$ at 28 K, but an applied field of 10 Oe already suppresses to below 4 K any evidence of the low-T downturn of $M(T)$.

Manheimer et al. (1983) report such *low-field dc magnetization* measurements on a-$(Fe_xMn_{1-x})_{75}P_{16}B_6Al_3$ in the SG–FM crossover regime ($x = 0.65$, 0.70 and 0.80) at fields below 30 Oe. By reversing the field H and comparing field cooled and zero-field cooled states at low T they separate out the reversible (M) and irreversible (M_i) contributions to the magnetization. M is defined as that part of the measured magnetization which changes sign when the applied field H is reversed. Figure 84 shows the reversible (M) magnetization of the $x = 0.70$ alloy for various applied fields H: the system apparently exhibits reentrant behavior, one can define two characteristic temperatures in fig. 84: an effective freezing temperature $T_f^*(H)$ by extrapolating the linear part of the drop in M at low T to obtain $T_f^*(H)$ as the $M = 0$ intercept, and an effective Curie temperature $T_c(H)$

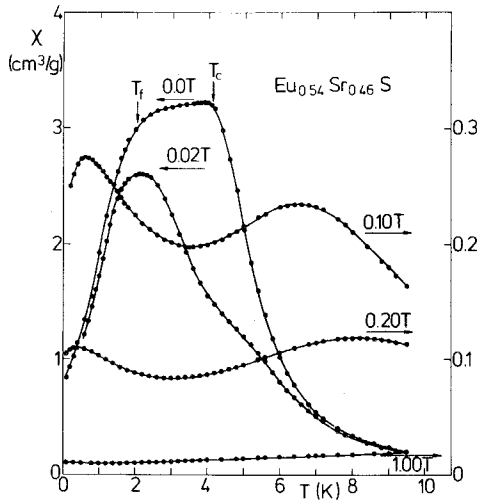

Fig. 83. Temperature dependence of the ac susceptibility (at 117 Hz) for $Eu_{0.54}Sr_{0.46}S$ in various magnetic fields. Note the change of scale between $B = 0.02$ T and 0.10 T (from Maletta and Felsch 1980d).

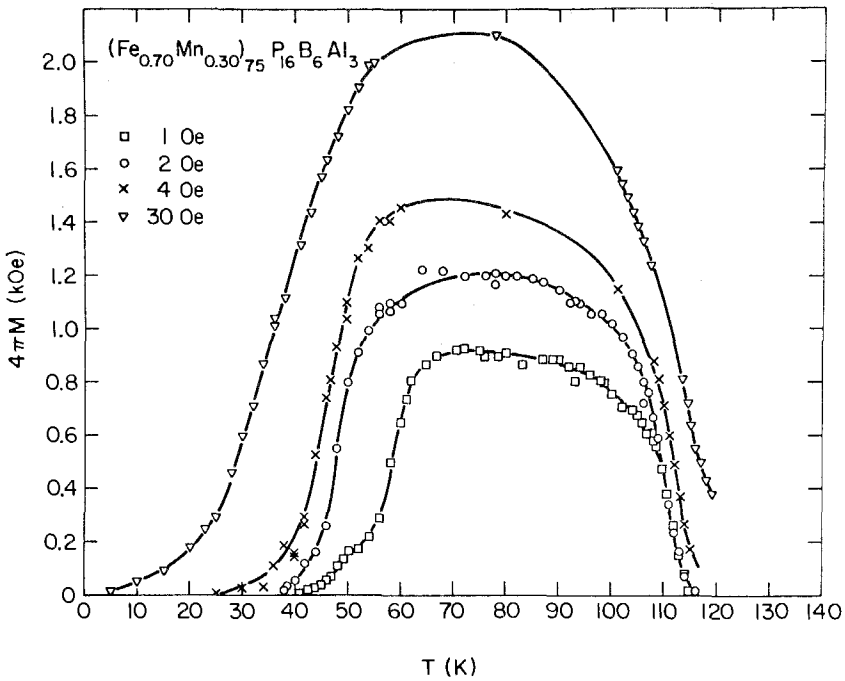

Fig. 84. Reversible magnetization as a function of temperature for amorphous $(Fe_{0.70}Mn_{0.30})_{75}P_{16}B_6Al_3$ at various applied fields (from Manheimer et al. 1983).

for the onset of the large increase of M. Increasing the applied field H favors the FM state, i.e. the rise in M near T_c shifts to higher T while the drop in M near T_f^* moves to lower T (fig. 84, see also fig. 83). $T_f^*(H)$ reduces as $\delta T_f^* \propto H^{1/2}$, thus by extrapolation the value of $T_f = T_f^*(H=0)$ can be determined ($T_f = 49$ K). The Curie temperature T_c is found by means of an Arrott plot; the applied fields have to be corrected for demagnetization ($T_c = 112$ K).

Here we want to call attention to the large magnitude of M measured at such low applied fields in the FM phase (fig. 84). For instance, the authors cite ferromagnetic resonance data taken at 3–10 kOe applied fields which give M values only about 50% higher than those at 30 Oe in fig. 84.

Figures 85a, b summarize the magnetic isotherm of the $x = 0.70$ alloy in the neighborhood of T_c and T_f, respectively. As expected, the curves in fig. 85a resemble those obtained near a PM→FM transition ($T_c = 122$ K), while in fig. 85b a similar behavior is observed except that now the role of temperature is reversed (i.e. the low-T data show less curvature). The authors demonstrate that the reversible part (M) of the magnetization can be described by the usual scaling laws for critical magnetic behavior

$$M = t^{\beta} \cdot \tilde{M}(H/t^{(\beta+\gamma)}) \tag{100}$$

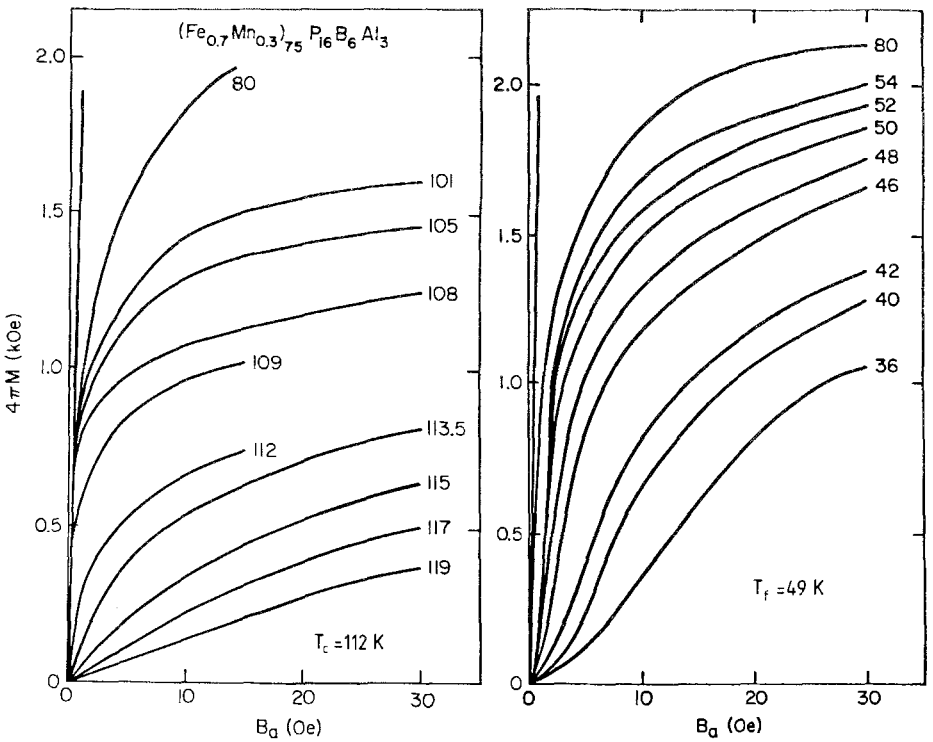

Fig. 85. Magnetic isotherms for a-$(Fe_{0.70}Mn_{0.30})_{75}P_{16}B_6Al_3$ in the vicinity of $T_c = 112$ K and $T_f = 49$ K. The left most (highest slope) line marks the demagnetization limit. The number labelling each curve is the temperature in K. Note that the role of temperature is reversed near T_c and T_f (from Manheimer et al. 1983).

not only at T_c but also at the FM→SG transition temperature T_f, yielding exponents as summarized in table 3. We note that a much smaller value of T_f (~30% lower) is obtained by a similar scaling analysis of high-field measurements (0.1 kG ≤ H ≤ 15 kG) by Salamon et al. (1981).

Below T_f no reversible magnetization M is left when extrapolating to $H \to 0$. The irreversible part (=frozen magnetization) M_i measured after field cooling is

TABLE 3

Critical exponents obtained from a scaling analysis (eq. 100) of low-field magnetization data of amorphous $(Fe_{0.70}Mn_{0.30})_{75}P_{16}Al_3$ at the PM–FM transition ($T_c = 112$ K) and at the FM–SG transition ($T_f = 49$ K) temperature (From Manheimer et al. 1983).

$T_c = 112$ K:	$\beta = 0.47$	$\gamma = 1.42$	$\delta = 4.0$
$T_f = 49$ K:	$\beta^* = 0.47$	$\gamma^* = 1.36$	$\delta^* = 4.7$

nonzero below T_f and vanishes approximately at T_f. Thus, relying on the separation (M, M_i) and extrapolation $(H \to 0)$ procedures Manheimer et al. (1983) provide experimental evidence for the existence of a RSG phase in a-(Fe-Mn)PBAl alloys.

The main problem in studying the RSG phenomenon remains the enormous sensitivity to applied fields, as illustrated in fig. 84. In order to really support the picture of a RSG with no spontaneous magnetization, a zero-field technique has to be applied. While *neutron diffraction* experiments do not share the resolution of bulk magnetization measurements, they can be performed in zero applied field and give microscopic information, for instance on the spatial spin correlations. Consequently, Maletta and co-workers (Maletta and Convert 1979a, Maletta and Felsch 1980d, Maletta et al. 1983a) have carried out detailed neutron diffraction studies of $Eu_xSr_{1-x}S$ which will be discussed now.

This insulating dilution system has been studied in great detail in the spin-glass regime, $0.13 \leq x \leq 0.51$, as described above. Early ac susceptibility measurements (Maletta and Felsch 1980d) displayed in fig. 86 can be taken as a first hint at a RSG behavior of the compounds with Eu concentrations $0.51 \leq x \leq 0.65$. Note that the different plateau values in fig. 86 are only due to different sample geometries in the various measurements, which is checked experimentally.

Turning now to the neutron diffraction measurements of $Eu_xSr_{1-x}S$ with $x = 0.52$ (Maletta et al. 1982b), typical data of elastic scans through the (002) reflection are shown in fig. 87a for three temperatures: $T = 6.0$ K in the PM regime, $T = 2.5$ K in the FM regime, and $T = 1.0$ K in the RSG regime. These results immediately suggest the existence of some unusual magnetic state. At high temperatures, the scattering consists of only the nuclear Bragg scattering centered at $q = 0$. As T is lowered, diffuse scattering appears whose width is a measure of the size of the ferromagnetically correlated regions. The diffuse scattering is seen to be very temperature dependent and exhibits even a broadening at the lowest temperature. Figure 88 shows the temperature dependence of the peak intensity of the (111) Bragg peak with various momentum resolutions. The following features of the data are especially important since they are in strict contrast with normal FM-ordering; (i) the magnetic signal normalized to the nuclear background decreases as the instrumental resolution is improved; (ii) the onset of the

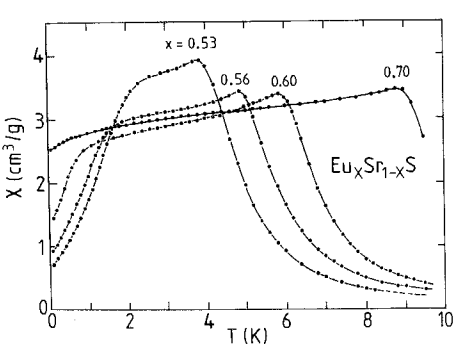

Fig. 86. Temperature dependence of the ac susceptibility for $Eu_xSr_{1-x}S$ with various Eu concentrations x, as indicated (from Maletta et al. 1980b).

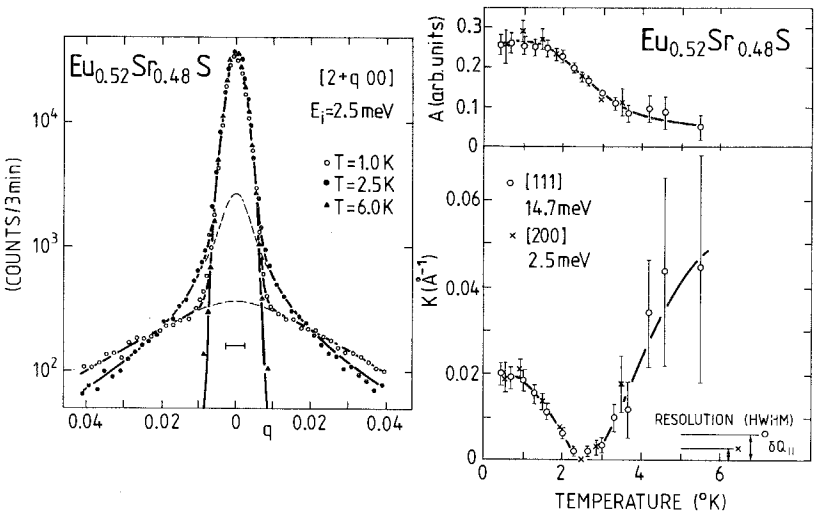

Fig. 87. Neutron-diffraction measurements of $Eu_{0.52}Sr_{0.48}S$ single crystal: (a) Elastic scans measured at $(2+q, 0, 0)$. The curve through the $T = 6$ K data is a resolution-limited Gaussian. For $T < 6$ K the solid line represents fits to the data using eq. 101, and the dashed line indicates the Lorentzian (non-Bragg) part of the scattering. (b) Temperature dependence of Lorentzian amplitude A and halfwidth κ obtained from the fits shown in part (a). The limits of instrumental resolution in q are indicated (from Maletta et al. 1982b).

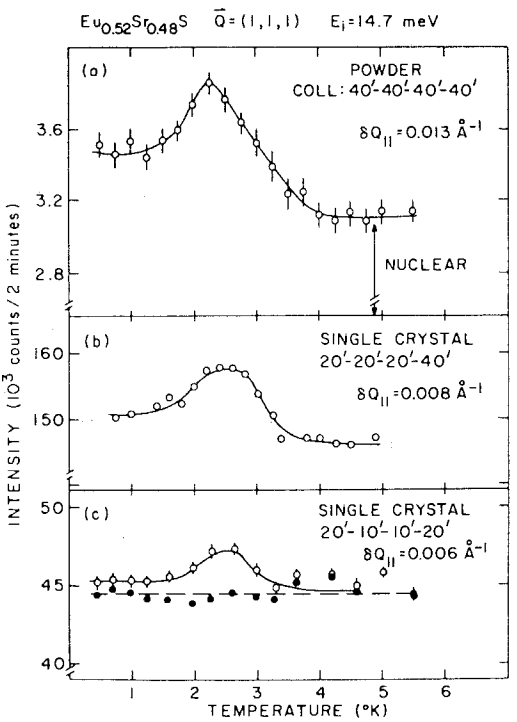

Fig. 88. Temperature dependence of (111) peak intensity (open circles) observed for $Eu_{0.52}Sr_{0.48}S$ for various experimental configurations. Filled circles in (c) represent Bragg intensity corrected for magnetic diffuse scattering (from Maletta et al. 1982b).

intensity increase shifts to lower temperatures with improved resolution; and (iii) the magnetic scattering is largest not at $T = 0$ but at the intermediate temperature $T = 2.5$ K. These observations indicate that the magnetic intensity is due primarily to diffuse scattering and not to the Bragg scattering which would arise if long-range FM order were present. As the instrumental resolution is improved different volumes of reciprocal space are sampled and the magnetic diffuse intensity will be decreased relative to the nuclear intensity.

The data can be described more quantitatively by assuming the following form for the scattering cross section:

$$S(\boldsymbol{Q}) = A/[(\boldsymbol{Q} - \boldsymbol{\tau})^2 + \boldsymbol{\kappa}^2]^{1-\eta/2} + B \cdot \delta(\boldsymbol{Q} - \boldsymbol{\tau}) . \tag{101}$$

The Lorentzian-like and δ-function terms represent the diffuse and Bragg scattering, respectively. τ is a reciprocal lattice vector and κ is the inverse correlation length ($\kappa = 1/\xi$). The solid lines in fig. 87a are the result of the least-squares fit to eq. 101 with $\eta = 0$ (=pure Lorentzian) after folding eq. 101 with the instrumental resolution function. The temperature dependence of A and κ are shown in fig. 87b. The amplitude A increases with decreasing T, which indicates that an increasing number of spins are becoming correlated. The Lorentzian linewidth κ becomes indistinguishable from *zero* around 2.5 K, and then *increases again at lower T* (the authors place a lower limit of 400 Å on the FM correlation length at 2.5 K, estimated from the high-resolution data).

These results contrast sharply with a normal Heisenberg FM where the correlation length remains infinite for all temperatures below T_c. In addition, the diffuse scattering below T_c would be almost entirely associated with the spin waves. In $Eu_xSr_{1-x}S$, the scattering is elastic on the scale of the instrumental energy resolution (30 μeV). Much higher resolution studies performed by the neutron spin echo technique (Shapiro et al. 1985) have shown that at low temperatures relaxation times are greater than 10^{-8} s. Since also the Bragg amplitude B stays constant at the nuclear level at low temperatures, the authors conclude that the state in $Eu_xSr_{1-x}S$ with $x = 0.52$ at the lowest T is a spin-glass phase, without a coexisting FM component.

The intermediate T regime where the correlation length diverges is studied (Maletta et al. 1983a) in detail in $Eu_xSr_{1-x}S$ with $x = 0.54$, since it is more extended here: $2\text{ K} \lesssim T \lesssim 4$ K. Line-profile analyses using eq. 101 reveal the same results as described for the $x = 0.52$-compound, except that now at intermediate temperatures the scattering profile shows clear deviations from the standard Lorentzian form (the maximum value of $|\eta|$ is $\eta = -0.6$ at 2.3 K; eq. 101) (see also: Maletta and Felsch 1980d). The magnetic Bragg scattering contribution (B_m) is weak (or even zero), as long as $\kappa \simeq 0$, and it vanishes at the lowest T where again κ becomes larger than the instrumental resolution width.

Due to the high amount of magnetic diffuse scattering the intermediate T regime with $\kappa \simeq 0$ is suggested to be called a "frustrated FM" state. Now it is plausible that such a highly distorted FM state (near the reentrancy point at $x_c = 0.51$) can change into a spin-glass state (RSG) at lower temperature. The

authors do not observe the "mixed phase" at the lowest T, as predicted in the mean-field model. Stimulated by these experimental data they present a phenomenological description of RSG systems (Maletta et al. 1983a, Aeppli et al. 1984), based upon the competition between two different ordering phenomena. Within the crossover regime, i.e. in $Eu_xSr_{1-x}S$ at Eu-concentrations just above $x_c = 0.51$, frustration leads to an effective decomposition of the spin system into a spin-glass-like and a ferromagnetic network (see also discussion in sec. 2.2). If the continuous network of "decoupled" spins undergoes a freezing transition, the frozen spins will impose a *random field* on the FM network through the exchange bonds also responsible for frustration. Hence, the order-parameter scattering, $B_m \cdot \delta(q)$, is converted into the sum of a Lorentzian and its square, similar to the structure factor with $\eta < 0$ in eq. 101, and finally the FM state is destroyed (see e.g. a recent review on random-field studies by Birgeneau et al. 1986).

This two-network model accounts for both the statics and dynamics of RSG systems, as observed in $Eu_xSr_{1-x}S$, Fe_xCr_{1-x}, Fe_xAl_{1-x} and a-$(Fe_xMn_{1-x})_{75}$-$P_{16}B_6Al_3$ (Aeppli et al. 1984, Shapiro et al. 1986). Figure 89 is a schematic

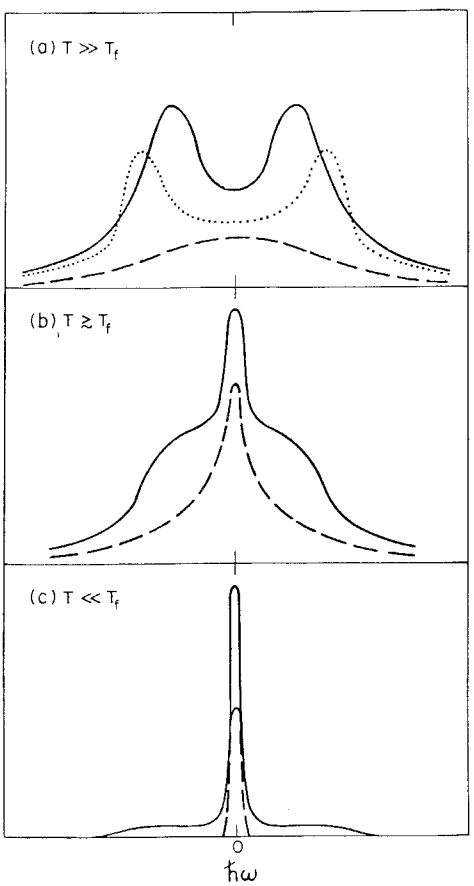

Fig. 89. Schematic constant-Q spectra of the magnetic response for the reentrant spin-glass problem. Dotted line represents spin-wave spectrum when the coupling between FM and SG network vanishes; dashed line represents spectrum for SG network, and solid line corresponds to spectra for FM network when it is coupled to SG spins (from Shapiro et al. 1986).

rendition of how the model describes the dynamics. At high T {frame (a)}, the dotted and dashed line represent the spin-wave spectrum for the related FM network and the relaxation spectrum for the SG spins, respectively. It is useful to think of the *time-varying random field* imposed on the FM spins at high T as an additional noise term, $\eta(t)$, in the semiclassical equations of motion for spin waves. The noise $\eta(\omega)$ has the property that its net weight, $\int|\eta(\omega)|^2\,\mathrm{d}\omega$, is weakly temperature dependent, while its bandwidth, γ, given by the inverse correlation time for the SG spins, can be a strong function of T. The primary effect of decreasing T will be to decrease γ, which initially will increase $|\eta(\omega)|^2$ at frequencies on the order of the spin-wave energies. Consequently, reducing T in such a RSG system above T_f has the same effect as increasing T in an ordinary FM: the occupation of the spin-wave modes increases, which leads to a decrease of M and a concomitant decrease in spin-wave stiffness D (see e.g. Fincher et al. 1980). The solid line in fig. 89a represents the net result of this process for T much larger than the temperature T_f where freezing occurs and $\gamma \to 0$.

For $T \ll T_f$ (fig. 89c), the SG network is entirely frozen, and a delta function at $\hbar\omega = 0$ exhausts most of the spectral weight of $\eta(\omega)$. Then, the SG network produces a *static random field* acting on the FM network and a pure RSG state is left. As consequence, the delta function domain scattering will coexist with weak sidebands (solid line in fig. 89c) associated with heavily damped spin waves "propagating" through a medium of static scattering centers. For intermediate T (fig. 89b), both the enhanced occupation of spin-wave modes and the domains commonly induced by static random fields must be taken into account.

Recently, the same group (Aeppli et al. 1986) started to study neutron diffraction of the reentrant system $Eu_{0.54}Sr_{0.46}S$ in magnetic fields $H \leq 60$ mT. Such magnitudes of H can easily induce some alignment of the Eu spins at the expense of the defective regions responsible for the magnetic diffuse scattering (fig. 90). That is observed in both FM and SG regimes, but while the net

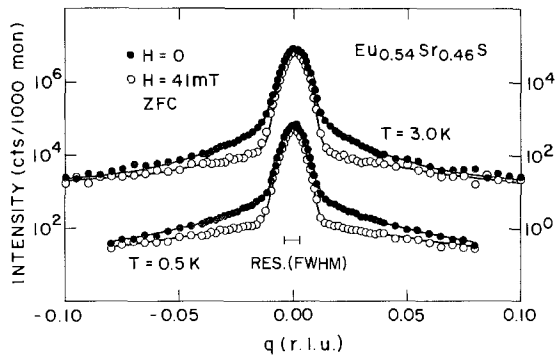

Fig. 90. Neutron scattering intensity of $Eu_{0.54}Sr_{0.46}S$ measured after zero-field cooling plotted as function of momentum transfer $(q, 0, 0) = Q - Q_0$ where $Q_0 = (2, 0, 0)$. Spectra at $H = 0$ and $H = 41$ mT are shown, each at a temperature in the FM-regime ($T = 3.0$ K) and in the RSG-regime ($T = 0.5$ K). The right- and left-hand vertical scales are for the 3 K (upper curves) and 0.5 K (lower curves) data, respectively. Solid curves correspond to eq. 101 (from Aeppli et al. 1986).

magnetization, monitored using the extinction-limited Bragg intensity, is history-dependent in both regimes, *remanence effects at microscopic length scales* (i.e. history dependences of the diffuse scattering) exist only in the SG regime (fig. 91). Thus, the authors have found a new distinction between FM and SG regimes in RSG systems. The latter effect is very dramatic: cooling to 0.5 K in a 41 mT field and then setting $H = 0$ results in a magnetic fluctuation length of less than 65 Å, well below the zero-field cooled value of 140 Å.

Shapiro et al. (1985) have performed *neutron-spin-echo* (NSE) experiments in $Eu_xSr_{1-x}S$ with $x = 0.40$ and $x = 0.54$ in order to further study the double transition PM→ FM and FM→ SG in $x = 0.54$. They observe no depolarization of the neutron beam for the SG sample ($x = 0.40$), but in the RSG sample ($x = 0.54$) the beam partly depolarizes near T_c. It becomes more depolarized on cooling further into the FM phase but less depolarized in the SG state. The incomplete depolarization of the scattered beam confirms the absence of true long-range FM order below T_c. Thus, there is sufficient neutron polarization of the incident beam to perform the experiment at all temperatures.

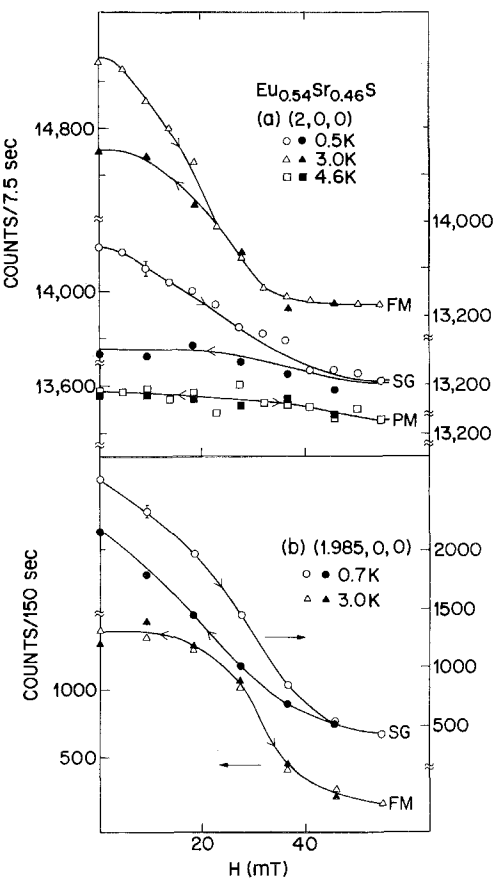

Fig. 91. Field dependence of (2, 0, 0) and (1.985, 0, 0) intensities for $Eu_{0.54}Sr_{0.46}S$ at fixed temperatures in the paramagnetic (4.6 K), ferromagnetic (3.0 K), and spin-glass (0.5 K and 0.7 K) regimes. Solid lines are guides for the eye (from Aeppli et al. 1986).

The NSE method (see sec. 6.2 and fig. 50 for the SG *Cu*Mn) measures directly the time dependence of spin correlations, $S(q, t)$, for times between $0.03\ \text{ns} \leqslant t \leqslant 5\ \text{ns}$. Figure 92 compares $S(q, t)$ in the SG sample ($x = 0.40$) with that in the RSG sample ($x = 0.54$), measured for $q = 0.072\ \text{Å}^{-1}$ at various temperatures. Both samples show similar behavior at low temperatures, the data in fig. 92 follow a straight line, i.e. $S(q, t) \propto A \cdot \ln t$, which implies that the spin correlations decay much slower than exponentially, typically for spin glasses. On heating the relaxation decay gets smoothly more rapid but no dramatic change of behavior is observable within our time interval of measurement at T_f in both samples. Similar behavior is observed in *Cu*Mn, except that the time spectrum for the decay in the insulating compounds is shifted towards (at least one order of magnitude) longer relaxation times compared to the metallic SG *Cu*Mn (see also fig. 50).

On further heating the RSG sample ($x = 0.54$) into the range of the Curie temperature T_c, $S(q, t)$ changes into an exponential form (fig. 92b): $S(q, t) \propto \exp(-\Gamma \cdot t)$. It is interesting to mention the also observed q dependencies. Relaxation effects in ordered magnets generally are q dependent, and indeed near T_c of the $x = 0.54$ sample the measurements are consistent with the behavior $\Gamma = D \cdot q^2$. Near T_f of both samples, however, the decay is nearly q independent.

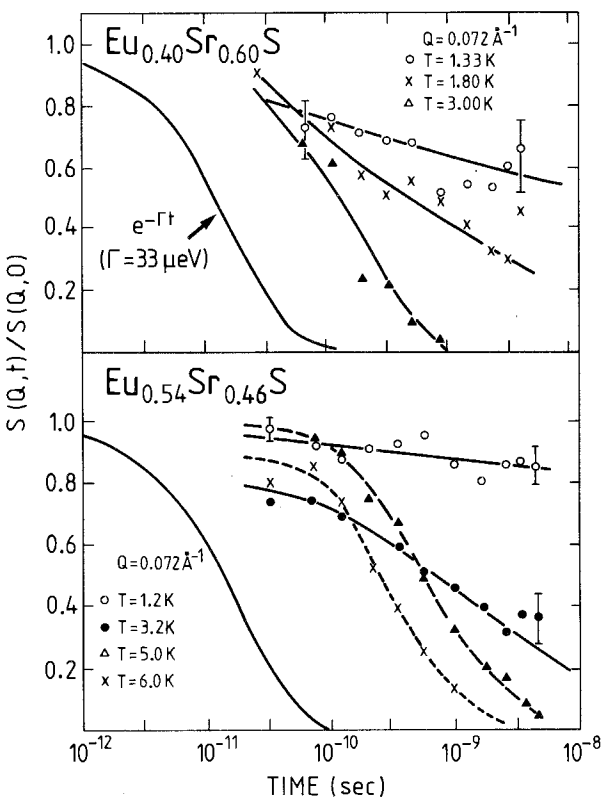

Fig. 92. Time correlation function, $S(q, t)/S(q, 0)$, for $Eu_xSr_{1-x}S$ as measured for the SG compound ($x = 0.40$) and the RSG compound ($x = 0.54$) for $q = 0.072\ \text{Å}^{-1}$ at various temperatures by the neutron spin-echo technique (from Shapiro et al. 1985).

This lack of kinematical slowing down near T_c may be interpreted by dipolar effects at the freezing process.

In conclusion, neutron scattering has played an important role in advancing our understanding of the magnetic behavior in RSG systems. The interpretation of some neutron experiments, however, is still controversial. From inelastic neutron scattering Fincher et al. (1980) find a spin-wave stiffness D in the RSG system $Cr_{1-x}Fe_x$ which after the usual increase below T_c decreases again within the intermediate FM regime and practically goes to zero in the RSG regime. In contrast, Hennion et al. (1983, 1984) and Murani (1983) observe more or less resolved spin waves in $Ni_{0.784}Mn_{0.216}$ and AuFe down to the lowest temperatures ($T < T_f$). The result on the constant D also depends on the ambiguity in choosing the proper spectral form for analyzing the spin-wave line (using either the "double Lorentzian" or the "damped harmonic oscillator" form). We want to emphasize, however, that contrary to their assertion the observation of well-defined spin waves at finite wave vectors does not demonstrate the existence of long-range FM order.

Among many other experiments which have been performed in order to elucidate the nature of RSG systems, two other microscopic techniques in addition to neutron scattering studies, ESR and Mössbauer effect, should be mentioned in this context. A careful study of the *electron spin resonance* (ESR) should provide valuable information about RSG systems, but one has to keep in mind the high resonance fields in this method. To date, many uncertainties remain already in the interpretation of experiments on SG samples near T_f. The origin of the dramatical change in the field for resonance (or g-shift) and linewidth while decreasing the temperature towards T_f is unclear. Recently, Monod et al. (1986) have studied ESR in $Eu_xSr_{1-x}S$ for $0.01 < x < 1$ in the high-T regime (also as function of frequency). They observe an exchange narrowed dipolar linewidth (proportional to $\sqrt{x}$), as proposed by Levy and Raghavan (1986), with a Lorentzian line shape (Deville et al. 1981a, b). For $x > 0.1$ the linewidth decreases when the resonance frequency increases.

Mehran et al. (1984) present an ESR study (at 9 GHz) of the RSG system $Eu_xSr_{1-x}S$ with $x = 0.56$ by comparing the data to measurements of a FM-sample ($x = 0.70$) (see fig. 93) and an SG-sample ($x = 0.40$: Deville et al. 1981a, b). In the FM-sample ($x = 0.70$) they find a sharp narrowing of the line near $2T_c$ (fig. 93, a2) and a g-shift to lower values (fig. 93, a1). Below T_c the ESR spectrum breaks up into several asymmetric lines, probably due to disorder. These findings are in contrast with those reported for the SG-sample ($x = 0.40$) where both g-value and linewidth are found to increase as T is lowered towards T_f. The behavior of the RSG-sample ($x = 0.56$) is qualitatively different from both others, as shown in fig. 93b. Although the linewidth in the PM phase narrows as T decreases no substantial asymmetry is detected in the $x = 0.56$ sample. For temperatures just above T_c the line starts to broaden and shifts to higher g-values. This broadening and shifting continue into the FM phase to the lowest temperatures measured (fig. 93, b1 and b2), as the FM$\rightarrow$SG transition is approached (similar variations have been observed in an a-FeMn RSG system by Rosenbaum

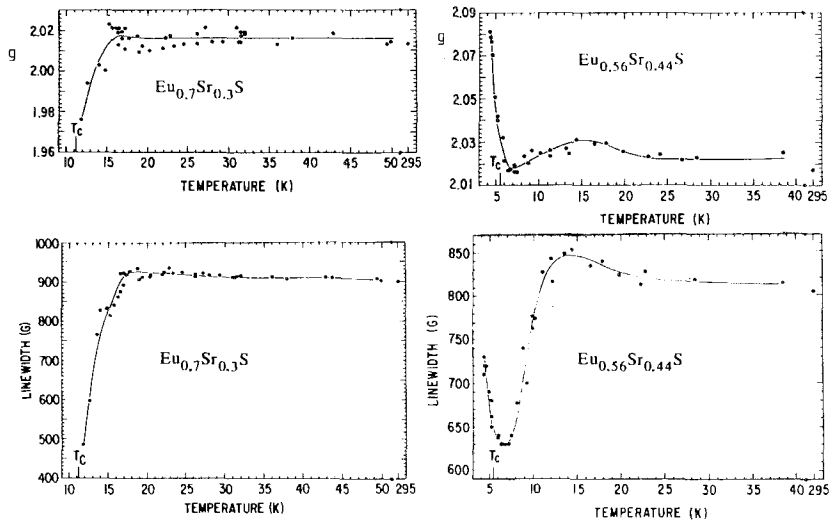

Fig. 93. Temperature variation of g-value and linewidth in $Eu_xSr_{1-x}S$ from ESR measurements. The left-hand-side (parts a1 and a2) shows the results for the FM compound with $x = 0.70$, the right-hand-side (parts b1 and b2) for the RSG compound with $x = 0.56$ (from Mehran et al. 1984).

et al. 1982). Probably, the line broadening and shift observed in the $x = 0.56$ sample near T_f in the intermediate FM regime as well as in the $x = 0.40$ sample just above T_f have the same origin. A detailed analysis of these data has not yet been published.

Now, considering *Mössbauer effect* studies on RSG systems, Lauer and Keune (1982) show in their pioneering ^{57}Fe Mössbauer effect measurements on *Au*Fe 16.8% at $H_{ext} = 20$ kOe that while essentially all the Fe spins are aligned parallel to H_{ext} below T_c (=165 K), the magnetic state below T_f (≈45 K) is no longer collinear: the average $\langle \sin^2\theta \rangle$ increases from zero below T_f, where θ is the angle between the magnetic Fe moment and the external field H_{ext}. This is deduced from the observation that the absorption lines with numbers 2 and 5 of the magnetic hyperfine pattern of ^{57}Fe (i.e., the $\Delta m = 0$ nuclear transitions) disappear in the FM state (only since all spins are aligned parallel to the γ-ray direction!), but become finite at lower T (below T_f), all spectra are measured at 20 kOe (see lower part of fig. 94). They also find at $H_{ext} = 0$ that the average hyperfine field $\bar{H}$ increases below T_f somewhat faster than in the (collinear) FM phase (see upper part of fig. 94), which is related to an increase in the average magnetic moment $\bar{S}$ in the RSG state. These two results are summarized by the authors in the *canting model*: in the FM phase, all moments are parallel to the external field H_{ext}. Spin components transverse to H_{ext} are free to rotate and do not contribute to the moment S (thermally averaged spin). At T_f, these components freeze out, canting the moment out of the direction of H_{ext}, and increasing its magnitude.

The analysis yields distribution functions of the hyperfine field, $P(H_{hf})$, with a double-peak structure in $P(H_{hf})$ at low T, as shown in fig. 95. The external field has little effect on $P(H_{hf})$ below T_f, but strongly suppresses the low hyperfine

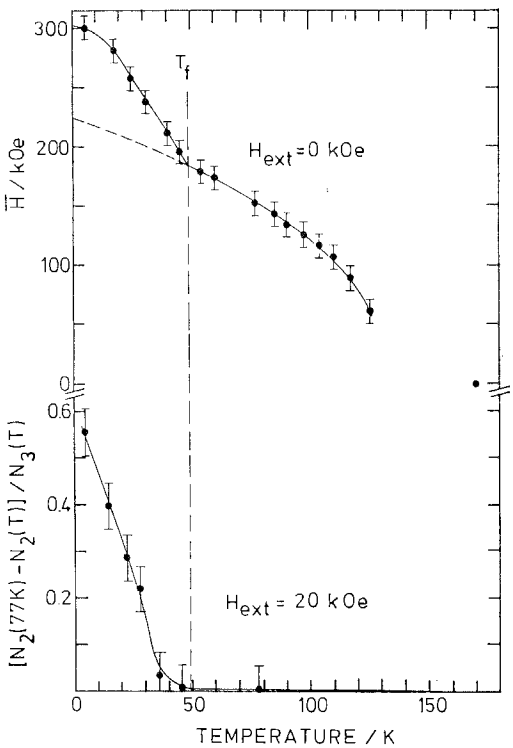

Fig. 94. Results from Mössbauer effect studies on the RSG system *AuFe* 16.8 atom%. Top: Average hyperfine field $\bar{H}(T)$ at zero applied field H_{ext}. Bottom: Peak-intensity ratio versus temperature measured at $H_{ext} = 20$ kOe (see text) (from Lauer and Keune 1982).

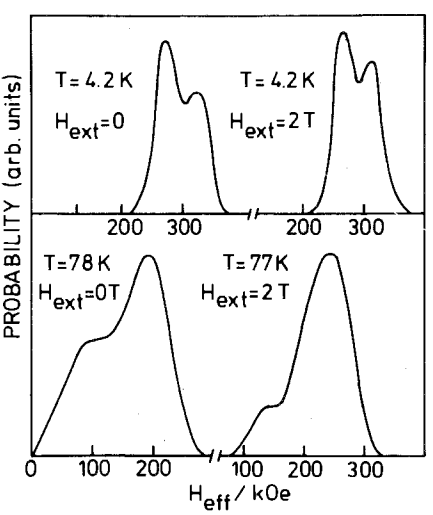

Fig. 95. Hyperfine-field distribution functions for *Au*Fe 16.8 atom% in the SG-state at 4.2 K (upper part of the figure) and in the FM-state at 78 K (lower part), both shown at $H_{ext} = 0$ and 20 kOe (from Brand et al. 1983).

fields which appear above T_f (Brand et al. 1983). The interpretation of such Mössbauer spectra of *Au*Fe has led to some controversy due to the known chemical short-range order (SRO) (Dartyge et al. 1982). The simple two-"phase" model proposed by Violet and Borg (1983, 1984), where SRO leads to phase segregation into Fe-rich platelets and remaining solid solution, is both erroneous and misleading as argued by Monod and Campbell (1984) and Brand and Keune (1984). The alloys seem to be magnetically homogeneous in the sense that $H_{hf}(T)$ disappears at one (x dependent) temperature within the resolution of Mössbauer spectroscopy, hence the magnetic correlation length is expected to be larger than the SRO-range.

Another severe problem is involved in the Mössbauer method itself since this "spin canting" can only be observed experimentally in the presence of a sufficiently high external field. Otherwise one cannot associate the variation of the line intensities (numbers 2 and 5) with "transverse spin freezing". Note that at zero external field the hyperfine patterns of a FM and SG are quite similar (see e.g. the recent detailed discussion on the Mössbauer effect analysis of the spin glass *Au*Fe 3% by Meyer et al. 1985, or: Maletta and Crecelius 1976). As an illustration, one may question the conclusion by Varret et al. (1982), from similar experiments on *Au*Fe 19% at a somewhat lower field of 6 kOe, that "spin canting" is already weak below T_c. Recently, Brand, Lauer and Keune (1985) attempt to analyze the spectra in *zero* external field by taking into account that the *electric quadrupole hyperfine* interaction defines locally an axis, and the orientation of the magnetic moments with respect to this local axis influences the spectrum line positions and profile. However, it is not convincing to us that by these means they can decide between a "canted" or collinear state at intermediate temperatures (FM phase).

In our opinion, Mössbauer effect measurements (as well as the ESR data presented above) reveal the existence of two different states in RSG systems, where the low-T state is hard to be aligned by external fields as is well known for spin glasses. As long as there is no experimental evidence for "spin canting" in zero field, we prefer this much simpler interpretation of the spectra. In any case, the Mössbauer method is a *local* one, thus global properties *cannot* be obtained easily such as the coexistence of transverse freezing with long-range FM order, as predicted for the zero-field GT state in mean-field theory at the lowest temperatures. We do not see any contradiction of the Mössbauer data to the model presented above in order to interpret the low-field magnetization and neutron-scattering data.

Very recently, Viana and Bray (1985) have proposed a *dilute* infinite-ranged SG model which can have such a RSG transition. Wolff and Zittartz (1985) present the phase diagram of the random-bond Ising model which quite generally exhibits reentrant behavior whenever there is a competition between a ferromagnetic coupling and a weaker antiferromagnetic one (or vice versa).

8.2. *Coexistence of spin-glass and Ising antiferromagnetic ordering*

Now we present experimental results of an Ising-type dilute antiferromagnet $Fe_{0.55}Mg_{0.45}Cl_2$ which give clear evidence for the *coexistence* of longitudinal

spin-glass and antiferromagnetic ordering (Wong et al. 1985a, b), as predicted by mean-field theory.

Pure $FeCl_2$ is an antiferromagnet ($T_N = 24$ K) with a strong uniaxial anisotropy ($D = 17$ K) which aligns the moments along the hexagonal c axis. There are ferromagnetic a-b planes that stack antiferromagnetically along the c axis. By dilution with Mg^{2+} ions, Bertrand et al. (1982, 1984) observe spin-glass behavior beyond 50% dilution as shown in fig. 96. The low-field dc-magnetization data measured along the c axis suggest a reentrant behavior in $Fe_{0.55}Mg_{0.45}Cl_2$, because the susceptibility shows a peak near $T_N \approx 8$ K and history-dependent behavior below $T_f = 3$ K (fig. 96, curve B). However, there are reservations with this interpretation because the applied field in the measurements produces site-random staggered fields which can also cause similar irreversibilities (see e.g. Birgeneau et al. 1986). Nevertheless, ac-susceptibility measurements by Wong et al. (1985b) confirm the existence of a spin-glass transition at $T_f \approx 30$ K: as displayed in fig. 97, a frequency-dependence gradually appears in $\chi'_{\parallel}$ below 5 K, with a corresponding onset of the imaginary part $\chi''_{\parallel}$. Below 3.0 K, $\chi'_{\parallel}$ shows a drop and $\chi''_{\parallel}$ rises rapidly, and simultaneously the frequency dependence becomes much stronger.

In order to decide between reentrance or coexistence, Wong et al. (1985a) carried out neutron-diffraction experiments. We recall that because the system is antiferromagnetic, the magnetic and nuclear Bragg peaks are separated in reciprocal (q-) space, and this allows one to study the magnetic order with little

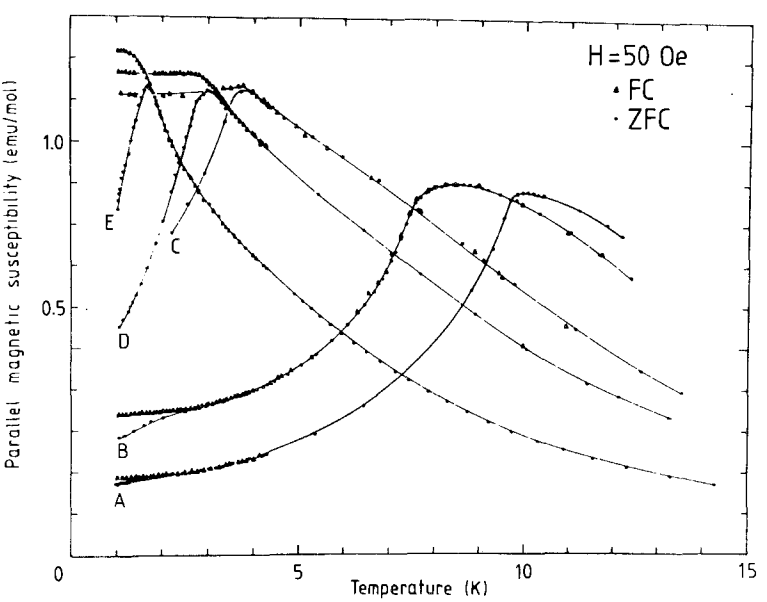

Fig. 96. ZFC- and FC-susceptibilities, M/H at $H = 50$ Oe, for $Fe_xMg_{1-x}Cl_2$ with the following Fe concentrations x: A: 0.610; B: 0.552, C: 0.495; D: 0.413; E: 0.286. The curves through the experimental data are guides for the eye (from Bertrand et al. 1984).

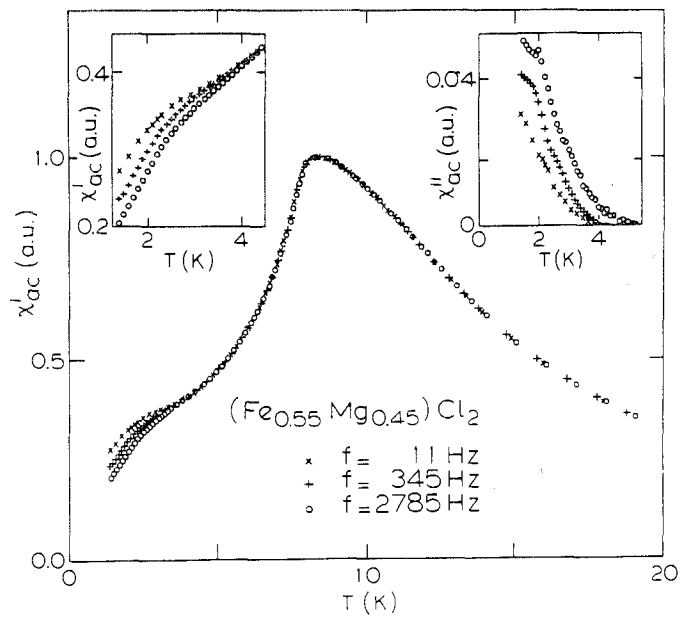

Fig. 97. Temperature dependence of the ac susceptibility $\chi'_{\|}$ for $Fe_{0.55}Mg_{0.45}Cl_2$ measured parallel to the easy axis at three different frequencies. Details of χ' and χ'' at low temperatures are displayed in the insets (from Wong et al. 1985b).

ambiguity. The scattering near the reciprocal lattice point $(0, 0, 3)$, which in principle gives information about the transverse spin component, is found to be independent of both T and q which implies no transverse components. Thus only a longitudinal component is present, and this is measured at $(1, 0, \bar{1})$. The temperature dependence of the peak intensity $I(1, 0, \bar{1})$ and the diffuse scattering $I(0.98, 0, \bar{1})$ slightly off the peak (fig. 98) indicates a well-defined Néel transition at $T_N = 7.5$ K, but remarkably there are no obvious signs for a SG transition at $T_f = 3$ K. In particular, $I(1, 0, \bar{1})$ increases smoothly down to 1.2 K, suggesting that the AFM order persists below T_f (in contrast to the behavior shown in fig. 88). However, the diffuse scattering is much higher than the background at low temperatures, which implies that not all the spins are antiferromagnetically ordered as $T \to 0$. Analyzing the line widths and shape, it turns out that the AFM order is of long range ($>10^3$ Å) below T_N and unaffected by the SG transition (obtained from the Bragg line), but simultaneously a Lorentzian magnetic diffuse peak appears underneath the Bragg peak whose width and amplitude are constant below 6.0 K. This frozen short-range correlation of approximately 10 Å is most likely the origin of the SG behavior observed in the ac and dc susceptibility experiments. There is no indication of atomic clustering in the sample.

In summary, the magnetic Bragg scattering demonstrates directly that the long-range AFM order is not destroyed by the SG transition, i.e. $Fe_{0.55}Mg_{0.45}Cl_2$ *does not reenter* into a disordered phase. Instead, combining all observations, the

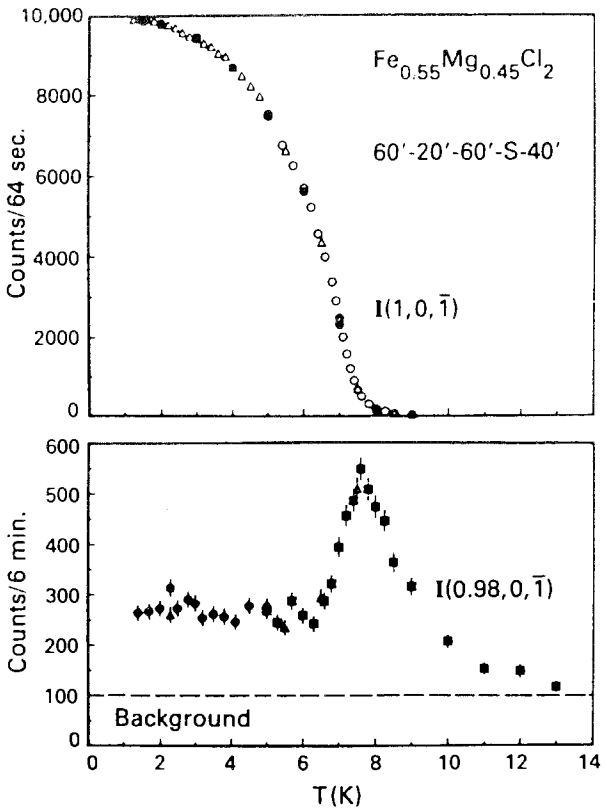

Fig. 98. Temperature dependence of the magnetic Bragg scattering at $(1, 0, \bar{1})$ and magnetic diffuse scattering at $(0.98, 0, \bar{1})$ for $Fe_{0.55}Mg_{0.45}Cl_2$. The open and solid symbols denote data taken on cooling and warming the sample, respectively (from Wong et al. 1985a).

authors (Wong et al. 1985b) conclude that the low-T phase of the system consists of *both* SG and long-range AFM order.

It is natural to question why coexistence is observed in a dilute Ising antiferromagnetic like $Fe_{0.55}Mg_{0.45}Cl_2$, but not in a dilute Heisenberg ferromagnet such as $Eu_{0.52}Sr_{0.48}S$ (see sec. 8.1). Since there is no existing theory that explains this difference the authors offer several conjectures. In any case, both observations are consistent with the phenomenological model of intrinsic random fields (Maletta et al. 1983a) described in sec. 8.1: the effect of random fields is to raise the lower critical dimension from 2 to 4 for Heisenberg systems, but only from 1 to 2 for Ising systems (see e.g. Birgeneau et al. 1986). As a consequence, one expects a coexistence of SG and long-range periodic order in 3-dimensional Ising systems, but a destruction of long-range periodic order, i.e. reentrancy, in 3-dimensional Heisenberg systems.

In order to further test this model of intrinsic random fields in the crossover regime to SG order, neutron diffraction experiments on the diluted Heisenberg antiferromagnetic system $Eu_xSr_{1-x}Te$ are underway (see its preliminary magnetic phase diagram in fig. 7b). As described in sec. 6.1, the borderline between SG and AFM behavior in $Eu_xSr_{1-x}Te$ has been determined up to now (Börgermann

et al. 1986a, b) only from bulk measurements: disappearance of the frequency shift of the ac-susceptibility maximum (fig. 43) and of the irreversibilities (FC, ZFC: fig. 44).

Westerholt and Bach (1985) have studied magnetic ordering in $Eu_xSr_{1-x}Se$ by ac-χ and specific heat experiments. EuSe is a Heisenberg antiferromagnet with rather complex magnetic behavior (see e.g. Wachter 1979), since the exchange interactions J_1 and J_2 are nearly equal in magnitude, but opposite in sign. It shows at $H = 0$ a first-order transition to AFM ordering at $T_N = 4.64$ K. The metamagnetic transitions in an applied field (from AFM to ferrimagnetic order and finally to FM alignment), mostly studied in $M(H)$ experiments, can also conveniently be observed by measuring the field dependence of the ac susceptibility {→ maxima in ac-$\chi(H)$}. Dilution of EuSe with SrSe leads to spin-glass behavior for $x \leqslant 0.70$, established by a frequency dependence of the ac-χ maximum and a broad maximum of the specific heat $C(T)$ at an even higher temperature. Compounds with $x \geqslant 0.85$ are definitely different: no frequency shift of the susceptibility, and the Néel temperature as derived from the position of the broadened maximum of the specific heat (see also Scherzberg et al. 1981) coincides with the maximum of $d\chi/dT$, as in normal antiferromagnets. The authors claim to have found evidence for the coexistence of SG effects and AFM order for the intermediate concentration range around $x = 0.80$ for $Eu_xSr_{1-x}Se$. This compound ($x = 0.80$) with a frequency shift of the χ-peak has a structure in the ac-$\chi(H)$ which resembles the response of metamagnetic transitions. There is a maximum in ac-χ versus field at finite H (similar to the more concentrated compounds), while for $x < 0.70$ (only shown for $x = 0.50$) the susceptibility decreases continuously with H similar to other spin glasses. Since a metamagnetic transition is a collective phenomenon of a large number of spins coupled rigidly, Westerholt and Bach (1985) argue that these experimental results indicate a coexistence of long-range AFM order and SG order. Again, neutron-diffraction studies would give more direct information on the behavior in the crossover regime.

Hiraoka et al. (1986) have found the onset of spin-glass order at the dilution concentration $(1 - x) \approx 0.11$ in similar compounds of the diluted antiferromagnetic system, $Eu_xYb_{1-x}Se$, by measurements of ac-χ and ^{153}Eu-NMR.

8.3. *Crossover via modulated spin structures*

Competing exchange interactions not only induce spin-glass ordering, but are also responsible for modulated spin structures as is well known for the lanthanide metals (see e.g. Koehler 1972, Elliott 1961). Dilution of heavy lanthanides with yttrium or scandium stabilizes the antiferromagnetic spiral structure at the expense of any ferromagnetic component or phase present in the lanthanide metal (Child and Cable 1969). The Néel temperature T_N decreases smoothly with dilution, while the interplanar turn angle ω of the helical structure increases (ω is also temperature dependent). Thus, one can expect to observe the crossover to spin-glass freezing upon further dilution.

An early study by Sarkissian and Coles (1976) has tried to find the *boundary*

concentrations between helical antiferromagnetic spin ordering and a spin-glass state in Y and Sc based alloys with 4f magnetic impurities. By measuring the ac susceptibility and resistivity, they propose a critical lanthanide concentration of 2.6 atom% for *Y*Gd and *Y*Dy alloys, 5 atom% for *Y*Tb, and about 23 atom% for *Sc* based alloys with Gd, Tb and Dy. In recent years there have been further attempts to distinguish experimentally between both types of magnetic ordering, which will be reviewed now. The studies reveal that spin-glass behavior in Y based alloys occurs probably at lower concentrations than previously believed.

Magnetization data (Wendler et al. 1984) of single crystals of *Sc*Gd (5 and 15 atom%) and *Y*Gd (1, 2 and 3 atom%) demonstrate different types of magnetic ordering. The *Sc*Gd system shows all the experimental features of a spin glass (fig. 70) (see also specific-heat data by Caudron et al. 1981), while *Y*Gd even at a Gd concentration as small as 1 atom% exhibits some kind of long-range antiferromagnetic order (fig. 99). Surprisingly both Gd systems are definitely anisotropic.

Figure 99a displays the dc susceptibility M/H as a function of temperature for the 1 atom% and 3 atom% Gd*Y* single crystals. The applied field ranges from $H = 10$ G to 15 kG and is applied both in directions parallel and perpendicular to the hexagonal c axis. When the field is perpendicular to the c axis, the susceptibility shows a cusp at a temperature T_c. For parallel fields only clear deviations from Curie–Weiss behavior are measured at low T. Important features of all these curves are the absence of "FC–ZFC" irreversibility effects, normally observed in spin glasses (see e.g. *Sc*Gd: fig. 70). In addition, a spin-flop transition is observed for $\boldsymbol{H} \perp \boldsymbol{c}$ in *Y*Gd 2% and 3% (fig. 99b). This observation is consistent with features shown in fig. 99a: below 7.5 kG there are large differences for $M_{\parallel}$ and $M_{\perp}$ of *Y*Gd 3%, while M is independent of the orientation of the crystal at higher fields. Similar effects are detected for the 2 atom% sample, but for the 1 atom% sample lower temperatures (<1.4 K) would be needed to establish the effect. The small magnetic hysteresis in $M(H)$ at the spin-flop transition (fig. 99b) also appears in the $M(T)$-curves of fig. 99a as a small difference between ZFC and FC at the spin-flop field (7.5 kG). These experiments rule out the existence of a spin-glass state in the *Y*Gd alloys down to 1 atom% Gd and strongly suggest the occurrence of an antiferromagnetic ordering with the Gd moments lying in the basal plane.

Neutron diffraction measurements confirm the existence of long-range magnetic helical order in dilute *Y*Gd alloys for Gd concentrations of 2 and 3 atom% (Brown et al. 1985) and 1.5 to 4.4 atom% (Wenger et al. 1986). For all Gd concentrations, the diffraction patterns reveal magnetic satellites at positions $(0, 0, 1 \pm \delta)$ where $\delta = 0.28c^*$ is the wave vector of the incommensurate periodic order (c^* is the reciprocal lattice vector). They correspond to a modulated spin state of about 20 Å wavelength with the Gd moment directions in the basal plane of the hexagonal structure (or very close to it) and the propagation wave vector along the c axis. The observed widths of the magnetic diffraction peaks are resolution limited, indicating that the scattering originates from a long-range ordered state. Below the ordering temperature, no shift in the position of the

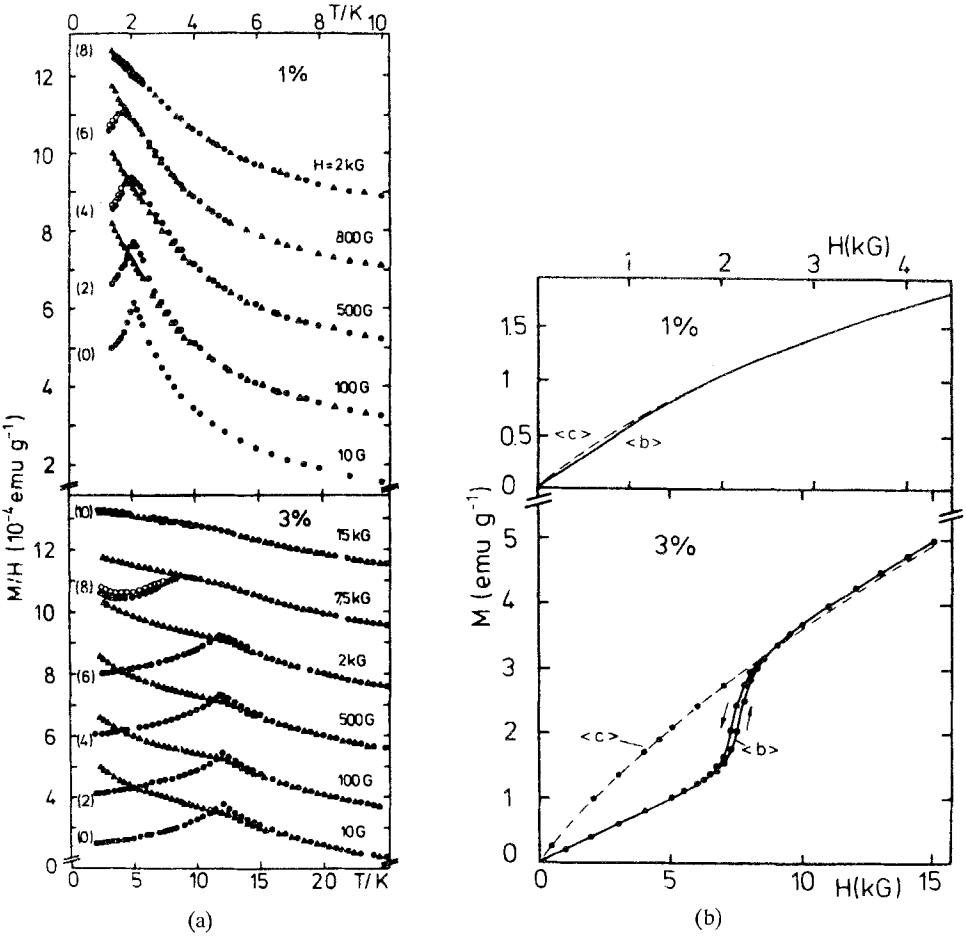

Fig. 99. (a) Susceptibility, M/H, at various fields H for two YGd single crystals, ●○$\|c$, ▲△$\|a$. Full symbols are ZFC, open symbols FC. In most cases the open and full symbols coincide. The curves are displaced vertically as indicated in parentheses. (b) Magnetization of YGd at $T = 1.5$ K. For $\boldsymbol{H}\|\boldsymbol{b}$ in YGd 3 atom% a small magnetic hysteresis in $M(H)$ is observed, the direction of the field scan is indicated by the arrows (from Wendler et al. 1984).

satellite peaks nor change in their width is measured. Figure 100 displays the temperature dependence of the satellite peak intensity (its position is shown in the inset) for the YGd 2.2 atom% single crystal as well as its ac susceptibilities and magnetic specific heat (Wenger et al. 1986).

The existence of such a long-range ordered magnetic structure down to at least 1.5 atom% Gd in YGd alloys implies a driving mechanism due to the electronic structure of the yttrium matrix. It has been proposed (Sarkissian and Coles 1976, Wenger and Mydosh 1984b) that the rare-earth moments stabilize the spin density wave (SDW) (Overhauser 1959, 1960) in the matrix. A somewhat different

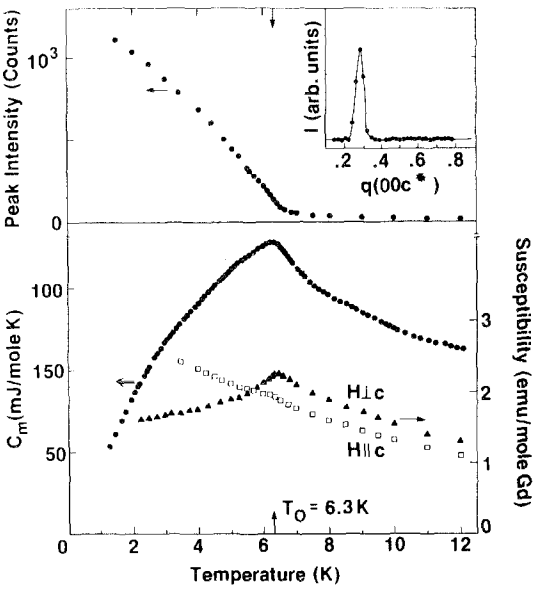

Fig. 100. The temperature dependence of the magnetic neutron scattering intensity at the satellite peak (0, 0, 0.28), the ac susceptibility, and the magnetic specific heat for $Y_{0.978}Gd_{0.022}$. Inset: The scattered neutron intensity for a scan along the (0, 0, 1) line at T = 4.5 K (from Wenger et al. 1986).

mechanism, first suggested by Freeman (1972) to explain the AFM ordering in 4f-metals, considers the nesting properties of the Fermi surface of the rare earths as giving a maximum to the electron gas susceptibility at a given ("nesting") vector $\boldsymbol{q}_0$. These result in a RKKY exchange integral $J(\boldsymbol{q}_0)$ which can explain the observed helical spin structures. The 4d conduction electrons of the Y matrix are expected to participate in both mechanisms of magnetic coupling. More accurate measurements of the Gd form factor are required in order to reveal a possible contribution of delocalized electrons.

Additional support for the SDW approach is obtained by Wenger and Mydosh (1984b) and Wenger et al. (1986). They present a quantitative interpretation of their *specific heat* data, also measured in applied fields, within a mean-field model of the SDW mechanism for AFM ordering. Note that already the bare data of $C_m(T)$ shown in fig. 100 demonstrate the non-SG-like behavior of the *Y*Gd alloy: the semicusp-like peak of the specific heat $C_m(T)$ appears at the temperature T_N of the $d(T\chi)/dT$ maximum, as common in antiferromagnets (in contrast to spin glasses where a broad maximum occurs at a temperature far above T_f).

Alloys of Y or Sc with small concentrations of *non-S*-state ions, like Tb, Dy or Er, are expected to exhibit an anisotropic ordering behavior strongly influenced by the low-symmetry crystal-field acting on the highly asymmetric 4f electron cloud of the magnetic impurity (see also sec. 7.2). A comparison between *Sc*Gd and *Sc*Tb alloys is given by Sarkissian (1977), reporting on static and ac-susceptibility measurements. At present there is some ambiguity of interpreting several bulk measurements either in terms of SG or long-range AFM ordering, as will be discussed now:

In the case of *Y*Tb alloys, Ketelsen and Salamon (1985) observe small

differences between the FC- and ZFC-magnetization at $H = 20$ Oe for Tb concentrations of 5 atom% and 3 atom%. Using neutron diffraction in addition, they demonstrate that *Y*Tb 5% is a helical antiferromagnet (similar as described above for the *Y*Gd alloys), despite the "SG-like" history dependence of its magnetization. In the other alloy *Y*Tb 3%, no magnetic satellites are found in the neutron-diffraction pattern. Hence, the authors conclude that only *Y*Tb 3% is a SG. They emphasize that irreversibility alone cannot be used to characterize the SG state. The same system has also been studied by Rainford et al. (1985). Their neutron-diffraction measurements on six single crystals of *Y*Tb with Tb concentrations of 2, 3, 4, 5, 6 and 7 atom% show the existence of long-range helical AFM for all the measured samples, in contradiction to the result above. Extrapolation of the Néel temperatures versus concentration would indicate a critical concentration for the disappearance of long-range AFM order near or below 1 atom% Tb in *Y*.

In the case of *Y*Dy alloys, a similar confusion exists in interpreting the data. Lecomte et al. (1986b) have studied three samples of Y based alloys with Dy concentrations of 2.5, 3.5 and 4.5 atom%. For all three alloys the characteristic temperatures deduced from the maximum in the specific heat, the dc and the ac susceptibilities coincide within experimental error. This behavior is not characteristic of a spin glass. In addition, the specific heat data can be used to estimate the entropy change between 0 K and T_N, which agrees to within 5% with the theoretical value of $Nk_B \ln(2J + 1)$ for $J = 15/2$. Hence, the authors rule out a SG freezing in these samples and suggest long-range AFM ordering. They also argue that the early experiments with *Y*Dy 2% by Wenger (1978) who found the ac-χ maximum even at a higher temperature than the maximum of the specific heat, are probably not properly analyzed.

The finding by Lecomte et al. (1986b) is consistent with results from neutron-diffraction measurements on *Y*Dy 3% by Rathmann and Touborg (1977) which reveal helical AFM ordering of the Dy moments below $T_N = 9$ K (again similar to the *Y*Tb and *Y*Gd alloys). In contrast, Baberschke et al. (1984) measure on a similar sample, *Y*Dy 3%, differences in the ZFC- and FC-magnetization (see fig. 71) below $T_f = 9.2$ K and field dependences of the remanences (IRM and TRM), similar to features in spin glasses.

*Y*Er alloys have been studied by Fert et al. (1982), Wendler and Baberschke (1983), Baberschke et al. (1984), Bonjour et al. (1984), and Bouchiat and Mailly (1985).

Much more work is still needed to clarify the question about the crossover to the spin-glass state by dilution of rare-earth metals. It is well known for a long time that *Y* and *Sc* based rare-earth alloys behave quite different. This has been explained by different spin-density wave effects: in Sc the congruence of the band structure with that of the 4f elements is weaker (Sarkissian and Coles 1976, Touborg 1977). Baberschke et al. (1984) estimate the ratio, $|D|/\tilde{J}$, between anisotropy D and exchange variance $\tilde{J}$ to be systematically smaller in the Sc- than in the Y-based alloys. Lanthanide impurities in the Sc host seem to behave as "good" spin glasses, while there is a strong tendency in the Y host to form a

helical or modulated magnetic structure. It could be that the strong SDW effect in Y-based alloys induces some kind of mixed state with long-range AFM correlations and SG irreversibilities {as directly observed in the diluted Ising AFM (Fe, Mg)Cl_2, see sec. 8.2}.

So far we have considered 4f systems but in principle similar effects may be expected in diluted 3d metals, too. Cable et al. (1984) have performed neutron measurements on *Cu*Mn single crystals containing 5, 10, 15 and 25 atom% Mn. Indeed, the results show the presence of a spin modulation with a period that varies continuously in terms of the edge of the fcc crystal cell from 6 a_0 at 5 atom% Mn to about 3 a_0 at 25 atom% Mn. For illustration, the intensity contours from nuclear and magnetic scattering are compared in fig. 101 for *Cu*Mn 25% at 10 K. In these systems, however, the correlation length associated with the modulation is of *finite* range (about 6 a_0) at all Mn concentrations. There are smaller regions of atomic short-range order in coexistence, which have net

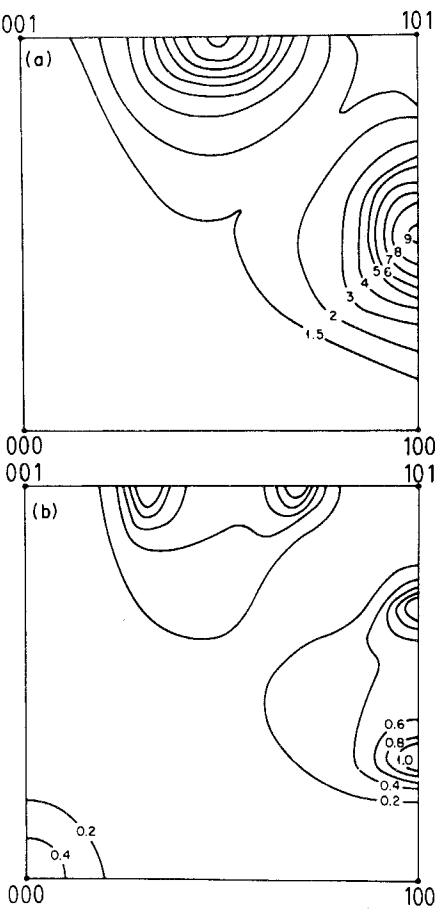

Fig. 101. Results from neutron-polarization analysis in *Cu*Mn 25 atom% at $T = 10$ K. The non-spin-flip or nuclear (in part a) and the spin-flip or magnetic (in part b) cross sections are displayed (from Cable et al. 1984).

ferromagnetic moments, and which complicates the studies because both effects are not independent from each other (see also a similar work by Gotaas et al. 1985).

In this context it is interesting to mention the recent work by Böni et al. (1986). They have studied the reentrant spin-glass system $Fe_{70.4}Al_{29.6}$ in applied fields by neutron scattering technique. In zero field the elastic scattering peaks at $Q = 0$ in the low-temperature RSG phase, whereas for an applied field parallel or perpendicular to Q the intensity peaks at finite Q (fig. 102). The peak position is field and temperature dependent and suggests a *field-induced modulated* spin structure within a *finite* correlation range of about 20 Å. This work opens a wide field of studying the field-dependence in other high-concentrated SG systems, which may help in further understanding the magnetic ordering in the crossover regime from SG to long-range FM or AFM order.

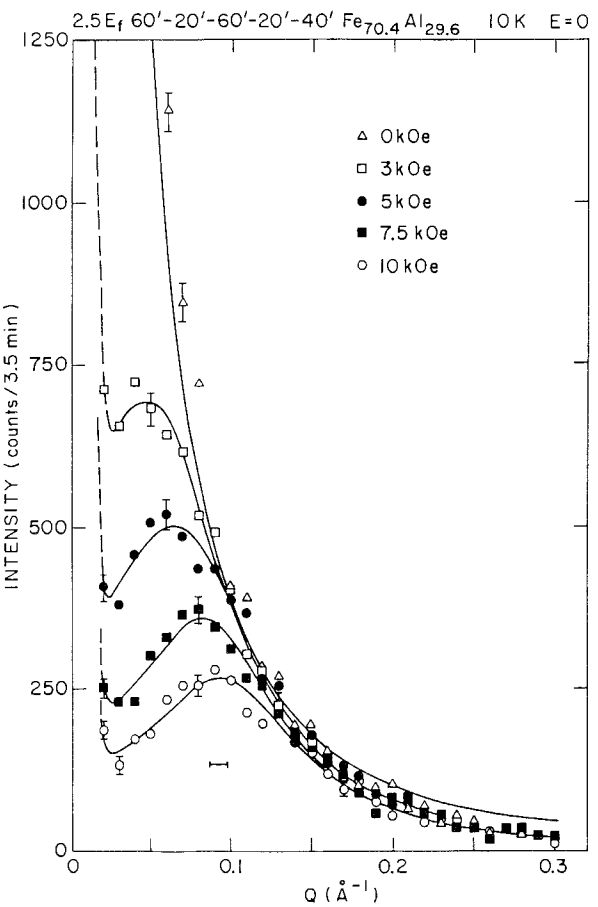

Fig. 102. Magnetic field dependence of the elastic scattering intensity for $Fe_{70.4}Al_{29.6}$ at 10 K. Note the good Q-resolution (~0.01 Å^{-1}, represented by the bar) as indicated by the steep increase of the intensity near $Q = 0$ (from Böni et al. 1986).

9. Systems with random anisotropy axis

Spin glasses are only one part in the issue of recent studies concerned with "frozen-in" disordered magnetic states. Random fields or random anisotropies also may destroy long-range ferro- or antiferromagnetic order. While it has been shown above that amorphous Gd–Al alloys (e.g. a-$Gd_{0.37}Al_{0.63}$, see fig. 13) are typical spin glasses like crystalline *Cu*Mn or (Eu, Sr)S, due to competing exchange interactions, amorphous alloys with non-S-state ions are characterized by single-ion anisotropy axes (eq. 6) which are distributed randomly in space. In this section we shall discuss briefly recent research concerning magnetic order in amorphous materials with significant local random anisotropy, emphasizing their similarities to spin glasses (see also Moorjani and Coey 1984). We shall use the term *speromagnet* to denote spin-glass-like magnetic structures that result from single-ion anisotropy to distinguish them from spin glasses which occur due to competing exchange interactions.

9.1. *RAM-model*

In order to describe the magnetic order behavior of amorphous intermetallic compounds containing rare-earth atoms with nonzero orbital momentum, such as a-$TbFe_2$, Harris et al. (1973) have introduced the "random anisotropy-axis" model (RAM) defined by the Hamiltonian

$$\mathcal{H} = -\sum_{ij} J_{ij} \boldsymbol{S}_i \cdot \boldsymbol{S}_j - D \sum_i (\boldsymbol{n}_i \cdot \boldsymbol{S}_i)^2 \tag{102}$$

where $\boldsymbol{S}_i$ is the total angular momentum at site i, and J_{ij} are the ferromagnetic exchange interactions of any range. The second term with a constant second-order anisotropy parameter D represents the local anisotropy where the unit vectors $\boldsymbol{n}_i$ point in random easy-axis directions. The properties of this model are still controversial.

The mean-field treatment of the RAM-model (eq. 102) with interactions $J_{ij} = J_0/N$ between all pairs $\boldsymbol{S}_i$, $\boldsymbol{S}_j$ predicts for all ratios D/J_0 a ferromagnetic state below T_c (see e.g. Derrida and Vannimenus 1980). But there is clearly a competition between the "aligning" effects of ferromagnetic exchange and the "scattering" effects of random anisotropy. Using renormalization-group techniques Aharony (1975) predicts that there is no ferromagnetism for dimensions $d < 4$. The result is in agreement with domain-wall arguments (Jayaprakash and Kirkpatrick 1980). It has been suggested by several authors (Chen and Lubensky 1977, Pelcovits et al. 1978, Bray and Moore 1985b) that a speromagnet (=spin-glass-like phase) may occur instead. Aharony and Pytte (1980), however, have found a novel "infinite-susceptibility phase" in which the magnetization vanishes (calculated to lowest order in D). This unusual property is obtained by an expansion in terms of M/H which becomes singular for $H \to 0$ and might be

incorrect. A low-temperature scaling theory by the same authors (Aharony and Pytte 1983) indicates for the case of small D/J_0 that χ should become large but not diverge. They suggest for T and $H \to 0$ that the maximum value of χ is given in $d = 3$ by

$$\chi_0 \propto (J_0/D)^4 \quad \text{for } T \leqslant T_c \,. \tag{103}$$

Chudnovsky and Serota (1983) recently have given a phenomenological theory for the RAM problem introducing into the model the length scale R_c of the spatial correlation of the easy axes. Then, the magnetic structure of amorphous magnets is shown to be strongly dependent on the parameter $\Lambda_r = \lambda_r (R_c/a)^2$, where $\lambda_r = D/J_0$ and a is the atomic spacing. For weak random anisotropy ($\Lambda_r < 1$) a new magnetic state is predicted: the "correlated speromagnet" (CSM). This state is characterized by a smooth rotation of the magnetization M over a ferromagnetic correlation length $R_D \gg R_c$, even though the net magnetization is zero. There are no domains separated from each other by thin domain walls, as it is in a crystalline ferromagnet. In the CSM, M is reversible and the zero-field susceptibility becomes large but remains finite

$$\chi_0 = \tfrac{1}{8} (\Lambda_r/4)^{-4} \propto (J_0/D)^4 \tag{104}$$

in agreement with eq. 103. In contrast to the CSM, for large random anisotropy ($\Lambda_t \ll 1$) the magnetization is irreversible as discussed by Callen et al. (1977).

9.2. *Properties in comparison to spin glasses*

Amorphous binary rare-earth alloys a-R_xX_{1-x} with non-magnetic X atoms are expected to show most clearly the influence of random anisotropy on magnetic properties. Hence, we mainly discuss here results from such materials with X = Cu, Ag, Au, or Al, which have been prepared in the amorphous state over a wide range of concentration by sputtering or evaporation.

It is always difficult to obtain saturation of the magnetization in these alloys even in the case of Gd, as demonstrated by pulsed-field measurements in fig. 103 (Boucher 1977, Moorjani and Coey 1984). $Gd^{3+}(4f^7, J = 7/2)$ is an S-state ion, thus single-ion anisotropy is expected to be negligible or very small (see also Nigh et al. 1963). The behavior in fig. 103 indicates the presence of antiferromagnetic interactions which prevent a complete parallel alignment of the moments favored by the generally stronger ferromagnetic interactions in these amorphous a-RX alloys. The corresponding crystalline RX alloys of CsCl-type structure are antiferromagnetic, which corroborates the statement. In the crystallized structure only the second nearest neighbors of a lanthanide ion are lanthanides again, while in the amorphous state they are randomly distributed with a finite probability of lanthanide ions to become first as well as second nearest neighbor. Thus, both ferro- and antiferromagnetic interactions are present in amorphous RX alloys

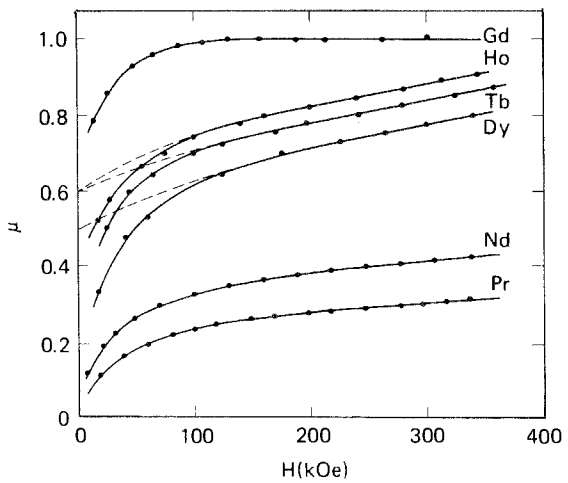

Fig. 103. High-field magnetization, $\mu = M/M_{sat}$, of amorphous RAg alloys at 4.2 K (R = lanthanides as indicated). Dashed lines are fits based on the RAM-model in mean-field approximation, eq. 102 (from Boucher 1977, Moorjani and Coey 1984).

with noble metals. In a-Gd_xX_{1-x} the competing exchange interactions lead to spin-glass behavior for sufficiently low Gd concentration x. Examples are a-Gd_xAl_{1-x} (fig. 13), a-Gd_xCu_{1-x} (McGuire et al. 1978), a-Gd_xAg_{1-x} (Boucher 1976) and a-$Gd_xLa_{0.80-x}Au_{0.20}$ (Poon and Durand 1978). For high Gd concentrations they become ferromagnets.

The approach to saturation in a-RX alloys when $R \neq Gd$ (fig. 103) is mainly governed by single-ion anisotropy. The dashed lines in fig. 103 are fits based on eq. 102 in the mean-field approximation (Ferrer et al. 1978). The analysis allows one to estimate the values for the random-anisotropy constant D and for the exchange interaction J_0, as summarized in table 4. For the light lanthanides (Pr, Nd: fig. 103) this simple model is inapplicable, influences of fourth- and sixth-order electrostatic fields obviously have to be invoked.

While there is good agreement between the RAM model description and the magnetization obtained at high fields, serious deviations are found (fig. 103) in

TABLE 4

Random-anisotropy parameter D and exchange coupling constant J_0 obtained from high-field magnetization data (using the model in eq. 102) of three amorphous RAg alloys (from Ferrer et al. 1978).

a-$Tb_{0.52}Ag_{0.48}$:	D = 4.0 K	$D/J_0 = 7.6$
a-$Dy_{0.50}Ag_{0.50}$:	D = 3.0 K	$D/J_0 = 22.0$
a-$Ho_{0.50}Ag_{0.50}$:	D = 1.5 K	$D/J_0 = 10.0$

the low-field region ($H \lesssim 100$ kOe). The deviations originate from the presence of sizable hysteresis loops and magnetic aftereffects. Most detailed information is available for a-TbAg (Boucher and Barbara 1979) and a-DyCu (Coey et al. 1981). Figure 104 displays hysteresis loops measured in a-$Dy_{0.41}Cu_{0.59}$ (anisotropy parameter $D = 3$ K) at two temperatures. Time-dependent effects are found in the dashed parts of the loop at 4.2 K. The measured value of the coercive field H_c is dependent on temperature and measurement time. H_c will be smaller the longer the time at which it is measured after the application of the field. The intrinsic coercivity (H_c extrapolated to zero temperature) is rather large: 8 kOe for a-DyCu and 23 kOe for a-TbAg. A quite remarkable feature appears in the 0.1 K loop (fig. 104). Instead of a smooth field dependence in the irreversible part of the loop (as measured at 4.2 K), the magnetization changes in a series of large discrete jumps, reminiscent of the Barkhausen effect in a sample containing about half a dozen domains. Each domain would have a volume of 10^{-2} mm^3 and contain some 2×10^{18} Dy ions.

The remanent magnetization in low fields invariably depends on the manner in which it is acquired. This is illustrated for a-DyCu in fig. 105, where the field dependences of the IRM and TRM are shown to be quite similar to the properties of spin glasses.

For the time dependence (magnetic aftereffect) a slow ln t-decay is measured, indicating a wide distribution of relaxation times or energy barriers. Low-field measurements of the magnetization reveal different behavior after ZFC or FC

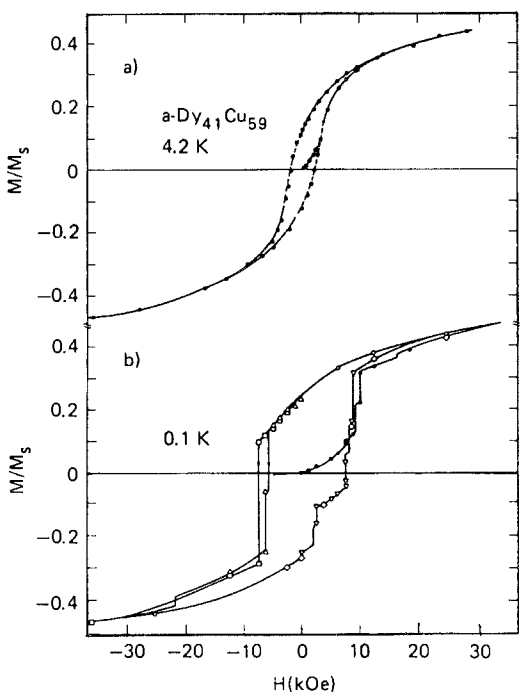

Fig. 104. Initial magnetization curves and hysteresis loops for a-$Dy_{0.41}Cu_{0.59}$ at two temperatures, 4.2 K and 0.1 K. The dashed parts of the loops at 4.2 K indicate the presence of time effects. Triangles, circles, and crosses denote different cycles at 0.1 K (from Coey et al. 1981).

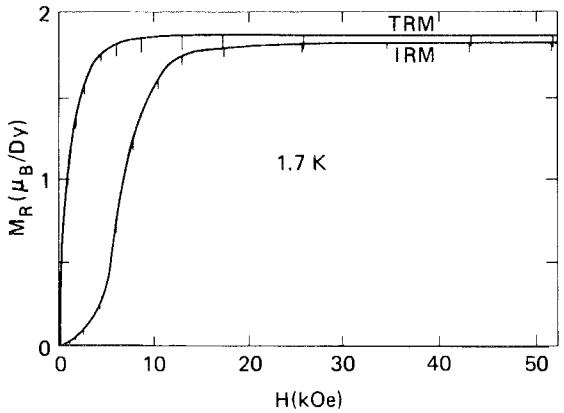

Fig. 105. Isothermal remanence and thermoremanence of a-DyCu at 1.7 K. Vertical lines indicate the time variation in one minute (from Coey et al. 1981).

(fig. 106). Below a well defined temperature one can define reversible and irreversible susceptibilities. Thus, the speromagnet a-DyCu, where random anisotropy dominates exchange, exhibits many properties which also characterize spin glasses, i.e. isotropic spin systems where competing exchange interactions are essential.

In a recent study von Molnar et al. (1982) present a comparison of random-anisotropy and spin-glass properties in the amorphous rare-earth alloys a-$Dy_{0.52}Cu_{0.48}$ (D/J_0 large), a-$Gd_{0.52}Ag_{0.48}$ (D/J_0 small), and a-$Gd_{0.37}Al_{0.63}$ (a well known spin glass). This work has also been stimulated by the theoretical prediction of Aharony and Pytte (1980) of an "infinite-susceptibility phase". Detailed measurements of the magnetization as a function of temperature and

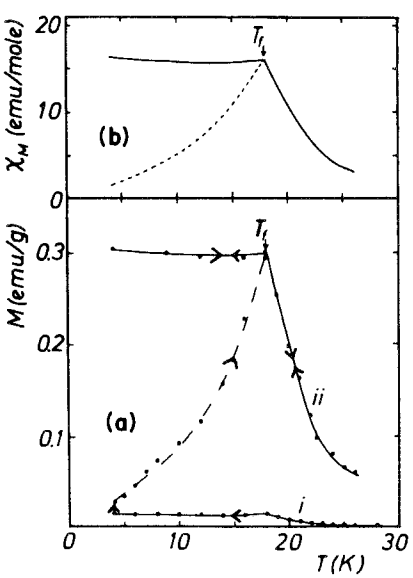

Fig. 106. (a) Magnetization of a-DyCu measured (i) in the earth's field and (ii) in 4.94 Oe applied at 4.2 K. The arrows indicate the sequence of measurements. (b) Reversible (solid lines) and irreversible (dashed line) susceptibilities, derived from these data (from Coey et al. 1981).

applied magnetic field are analyzed in the form of Arrott plots, i.e. M^2 vs H/M, as shown in fig. 107. The general features of the Arrott plot for a-DyCu (fig. 107a) are quite different from those of a-GdAg (fig. 107b). On the other hand, the behavior in fig. 107a is similar to the Arrot plot obtained for the spin-glass a-GdAl (fig. 107c). As in spin glasses and contrarily to the low-anisotropy case (fig. 107b), it is difficult to see on the plot in fig. 107a at which temperature the transition occurs. Low-field susceptibility measurements (similar to fig. 106), however, clearly indicate the transition at 23 K. Below $T_c = 23$ K the susceptibility remains large but finite ($\chi_0^{-1} = 0.69$) (intercept along the abscissa), and there is no spontaneous magnetization at any temperature (no intercept along the positive ordinate).

The disagreement with the theory of Aharony and Pytte (1980) can be ascribed to the fact that the prediction of the "infinite-susceptibility phase" is developed for $D/J_0 < 1$. Consequently, a-GdAg is also studied where the anisotropy is small. The data in fig. 107b show that the susceptibility approaches the demagnetizing limit, i.e. $\chi_0^{-1} \to 0$. In addition, a careful analysis of the low-field data indicates that the material may develop a small moment despite the apparent vertical drop in M^2 as $H/M \to 0$; although this conclusion depends critically on the magnitude of any possible extremely small demagnetizing field.

Finally, the spin-glass sample a-GdAl (fig. 107c) clearly exhibits no spontaneous magnetization, a small value for the initial susceptibility ($\chi_0^{-1} = 13.7$), and the curvature remains positive for all measured temperatures in the Arrott plot. Thus, the spin glass a-GdAl shows many similarities to the speromagnet a-DyCu.

It would be particularly interesting to know the magnetic behavior in systems with small anisotropy D/J_0. The random anisotropy should destroy ferromagnetic order, but a large or even diverging susceptibility is predicted (Aharony and Pytte 1980, 1983, Chudnovsky and Serota 1983). Barbara and Dieny (1985) have recently studied the properties of a-$Dy_xGd_{1-x}Ni$ (where Ni is nonmagnetic) for various concentrations x. Estimating D and J_0 for different x from high-field magnetization measurements, they find a dependence of χ_0 on the ratio D/J_0 (fig. 108) which can be represented by the power law of eq. 103 with the exponent 3.8 ± 0.2, in excellent agreement with the result (exponent 4) of non-mean-field theories (Aharony and Pytte 1983; Chudnovsky and Serota 1983). The problem of low-anisotropy systems, however, is still open. In particular, it is not known for the present, whether the transition to the infinite-susceptibility phase occurs at $D = 0$ as is theoretically predicted (Aharony and Pytte 1983) or at $D > 0$. Sellmyer and Nafis (1985) have also studied this problem. In a-$Gd_{0.72}Fe_{0.10}Ga_{0.18}$ they find no spontaneous magnetization and a completely reversible magnetization below T_c. They suggest that their data may be taken as evidence for the new CSM-state (fig. 109) predicted by Chudnovsky and Serota (1983). The same authors (1986) also analyze ac-χ data near T_c for a-$Dy_{0.60}Fe_{0.30}B_{0.10}$, taken in various applied fields, in terms of an Ising-type spin-glass transition, i.e. they deduce critical exponents γ and δ from the behavior of the nonlinear susceptibility ($\gamma = 2.4$; $\delta = 2.3$).

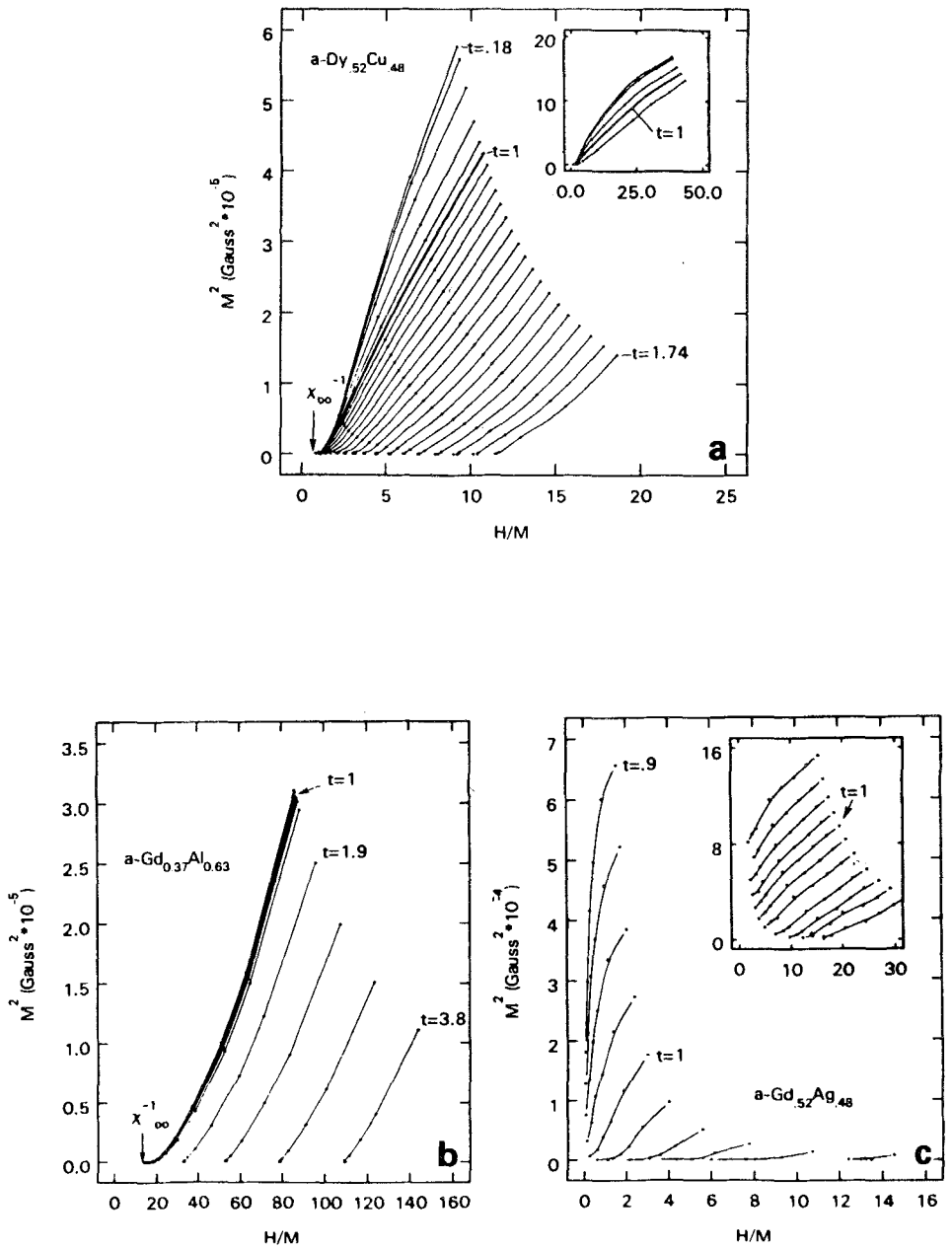

Fig. 107. (a) Arrott plot of a-$Dy_{0.52}Cu_{0.48}$ for applied fields up to 7 kOe. The inset is the same plot extended to 50 kOe. $t = T/T_c$, where $T_c = 23$ K. (b) Arrott plot of a-$Gd_{0.52}Ag_{0.48}$ for applied fields up to 400 Oe. The inset is the same plot for intermediate fields 500 Oe $\leq H \leq 6$ kOe. $t = T/T_c$, where $T_c = 83$ K. (c) Arrott plot of a-$GdAl_2$ for applied fields up to 48 kOe. $t = T/T_c$, where $T_c = 15.75$ K. (from von Molnar et al. 1982).

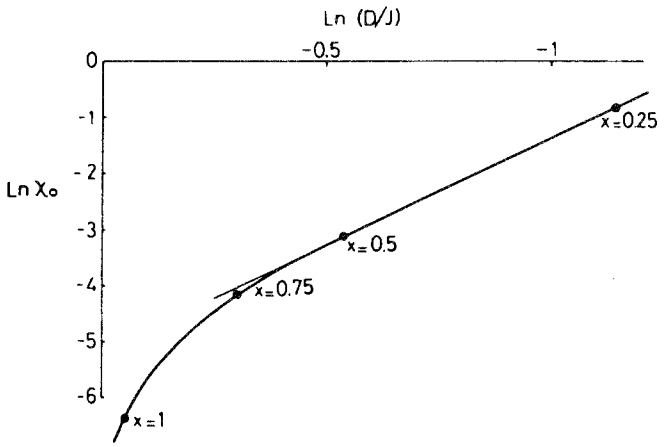

Fig. 108. Susceptibility χ_0 vs the ratio D/J_0 for a-$Dy_xGd_{1-x}Ni$ alloys. The straight line in the ln–ln plot for $D/J_0 < 0.7$ corresponds to eq. 103 with an exponent 3.8 ± 0.2 (from Barbara and Dieny 1985).

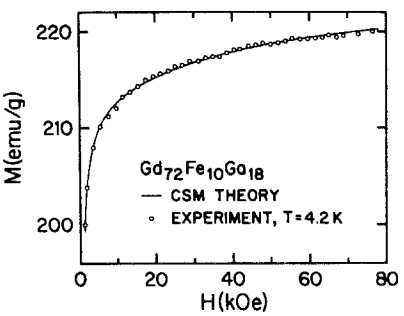

Fig. 109. Magnetization $M(H)$ of a-$Gd_{0.72}Fe_{0.10}Ga_{0.18}$ at 4.2 K and comparison (solid line) to CSM prediction (from Sellmyer and Nafis 1985).

10. Conclusions

Spin-glass behavior is an intrinsic effect of disorder and competition of the magnetic interactions (sec. 2). In such materials, several unusual properties are observed below the temperature T_f, and the transition at T_f appears as a complicated freezing process. Attempts to interpret this novel phenomenon of magnetic ordering has proved difficult, but in recent years progress has been substantial in our understanding of spin glasses.

Up to now no realistic model of a spin glass has been solved analytically. The simple model proposed by Edwards and Anderson (1975) (sec. 4.1), however, is shown by Monte Carlo simulations to reproduce many experimental findings on spin glasses remarkably well (sec. 4.2). Its *mean-field theory*, as realized in the Sherrington–Kirkpatrick (SK) model (1975) (sec. 4.3), is now fairly well understood (which has taken about eight years). The solution proposed by Parisi (1979) yields a rich structure in the ordered phases, described by an *infinite number* of

pure states related by an ultrametric topology. The onset of irreversibility at T_f is associated with a phase transition which also holds in an applied field. The critical H–T line is different for Ising (AT-line: eq. 15) or Heisenberg spins (GT-line: eq. 27).

A large amount of experimental data shows the intrinsic feature of irreversibilities of spin glasses at temperatures *below* T_f (sec. 5.1). The picture of the "many-valley structure" in phase space (fig. 15) is useful to explain the effects phenomenologically, independent of whether at T_f an equilibrium transition occurs. It would be desirable, however, to have more detailed theoretical work for instance on slowly relaxing metastable states. The concept of "isotropic anisotropy" (sec. 5.2), characterized by an anisotropy triad (Saslow 1982) and anisotropic interactions of the Dzyaloshinskii–Moriya-type, can explain successfully several distinct properties of metallic spin glasses well below T_f. The nature of low-energy excitations in spin glasses is far from being understood (sec. 5.3). In spite of observing a similar linear specific heat in glasses as well as in spin glasses, they are of different origin: the linear specific heat in spin glasses is accounted for by linear (oscillatory) spin excitations, while it is due to two-level tunneling systems in ordinary glasses. In addition, recent specific heat measurements (Martin 1985) on the spin glass *Cu*Mn 0.88 atom% show no time effects, in contrast to the behavior in ordinary glasses. Thus, there are little analogies between spin glasses and ordinary glasses, except the existence of slowly relaxing metastable states.

Most of recent experimental studies on spin glasses are concerned with the nature of the *spin-glass transition at* T_f (sec. 6 and 7). The appearance of a long relaxation phenomenon and the lack of corresponding reliable analytic theories hamper the interpretation of these experiments. Indeed, until recently no consensus existed as to whether spin glasses exhibit a phase transition at all. A number of experiments on various spin glasses, however, provides now fairly convincing evidence for a phase transition at a nonzero T_f (sec. 7.3). An understanding of the complicated spin dynamics near T_f, however, which includes macroscopic times, would be desirable. For the critical exponents, even numbers close to the Ising values determined from numerical studies are quoted.

Numerical studies of Ising spin glasses in three dimensions corroborate the experimental evidence that a phase transition takes place (sec. 4.4). However, similar studies of *Heisenberg* spin glasses indicate that there is no transition in short-range vector-spin systems in three dimensions. In a recent paper, Bray et al. (1986) demonstrate that vector-spin glasses with short-range couplings or RKKY couplings are in a different universality class, the lower critical dimension d_l is $d_l > 3$ or $d_l = 3$, respectively. In contrast, Ising spin-glasses have the same critical behavior for both types of couplings ($2 < d_l < 3$). The authors also show that the critical exponents associated with the Ising-type transition in anisotropic vector-spin glasses are always those of the short-range Ising spin-glass. The dependence of T_f on the anisotropy D in $d = 3$-Heisenberg spin glasses is such that as $D \to 0$, $T_f \to 0$, but so slowly that for realistic values of D/J ($\approx 10^{-2}$), the transition

temperature is still $T_f \approx J$ (see also; Morris et al. 1986). Thus, one can reconcile the numerical results with the experimental work, where most of the best-studied spin glasses are Heisenberg-type systems, by taking into account a very small anisotropy.

Much confusion, however, exists about the interpretation of spin-glass transitions in an *applied magnetic field*. As reported in sec 7.2, there have been extensive efforts in the comparing of experimental results with mean-field theory of spin glasses (AT- and GT-lines).

Such a comparison has to be done with great cautiousness (see sec. 7.2) as pointed out by Fisher and Sompolinsky (1985). In this context it is quite interesting that several authors (McMillan 1984b, Moore and Bray 1985, Bray and Moore 1986, Fisher and Huse 1986) have proposed a new picture of the Ising-spin-glass phase in short-range systems. In striking contrast to the results of the mean-field model (SK), they conclude that there is *only one phase* in three dimensions:

Bray and Moore (1986) present a theory, based on a "one-parameter-scaling" picture, the central concept being that of a scale-dependent coupling $J(L)$. The equilibrium properties in the ordered phase are determined from an exponent y which describes the scale dependence of $J(L)$ at zero temperature

$$J(L) \sim JL^{y} . \tag{105}$$

The sign of y determines whether the system scales to weak or strong coupling for $L \to \infty$, i.e. whether $d > d_l$ ($y > 0$) or $d < d_l$ ($y < 0$). They obtain $y = +0.19 \pm 0.01$ for $d = 3$, which again implies a phase transition at a nonzero temperature. Then, the exponent y determines the decay of correlations in the ordered state which is algebraic ($\sim r^{-y}$) for all $T < T_f$. This result was first suggested by Fisher and Huse (1986) on the basis of a droplet model. It implies that the ordered phase is described by a single pure state, and the short-range model does not exhibit "replica symmetry breaking", in contrast to the mean-field model. The exponent y also governs the response to a weak magnetic field. If the ordered phase is replica symmetric for short-range models, it follows that there can be *no AT line*; i.e. a magnetic field *destroys* the spin-glass transition. This would imply that experiments only observe "dynamic AT-lines", at which relaxation times become comparable with experimental observation time.

Summarizing, this new concept would mean that the ordered state of real spin glasses is *simpler* than the complicated structure obtained for the SK-mean-field theory. Further work will certainly be directed toward further studies on this central issue of the nature of the spin-glass phase.

Finally, systems where long-range periodic (FM, AFM) and spin-glass orderings compete exhibit magnetic properties which obviously are not in accordance with present theories (fig. 18 and 20). In sec. 8 we made a first attempt to classify the large amount of experimental data on this subject which now needs confirmation by theoretical work *beyond* the SK-mean-field theory.

References

Aeppli, G., S.M. Shapiro, H. Maletta, R.J. Birgeneau and H.S. Chen, 1984, J. Appl. Phys. **55**, 1628.

Aeppli, G., H. Maletta, S.M. Shapiro and D. Abernathy, 1986, to be published.

Aharony, A., 1975, Phys. Rev. B **12**, 1038.

Aharony, A., and E. Pytte, 1980, Phys. Rev. Lett. **45**, 1583.

Aharony, A., and E. Pytte, 1983, Phys. Rev. B **27**, 5872.

Alexander, S., C. Laermans, R. Orbach and H.M. Rosenberg, 1983, Phys. Rev. B **28**, 4615.

Alloul, H., 1979a, Phys. Rev. Lett. **42**, 603.

Alloul, H., 1979b, J. Appl. Phys. **50**, 7330.

Alloul, H., 1983, in: Heidelberg Colloquium on Spin Glasses, eds J.L. van Hemmen and I. Morgenstern (Springer, Berlin) p. 18.

Alloul, H., and F. Hippert, 1983, J. Magn. & Magn. Mater. **31–34**, 1321.

Alloul, H., and P. Mendels, 1985, Phys. Rev. Lett. **54**, 1313.

Alloul, H., P. Mendels, P. Beauvillain and C. Chappert, 1986, J. Magn. & Magn. Mater. **54–57**, 105.

Anderson, P.W., 1983, Proc. Natl. Acad. Sci. USA **80**, 3386.

Anderson, P.W., and C.W. Pond, 1978, Phys. Rev. Lett. **40**, 903.

Anderson, P.W., B.I. Halperin and C.M. Varma, 1972, Philos. Mag. **25**, 1.

Baberschke, K., P. Pureur, A. Fert, R. Wendler and S. Senoussi, 1984, Phys. Rev. B **29**, 4999.

Baberschke, K., C. Pappa, H. Mahdjour and R. Wendler, 1986, J. Magn. & Magn. Mater. **54–57**, 179.

Barbara, B., and B. Dieny, 1985, Physica B **130**, 245.

Barbara, B., and A.P. Malozemoff, 1983, J. Less-Common Met. **94**, 45.

Barbara, B., A.P. Malozemoff and Y. Imry, 1981, Phys. Rev. Lett. **47**, 1852.

Bauhofer, W., M. Wittmann and H.G. von Schnering, 1981, J. Phys. & Chem. Solids **42**, 687.

Bauhofer, W., E. Gmelin, M. Möllendorf, R. Nesper and H.G. von Schnering, 1985, J. Phys. C **18**, 3017.

Bauhofer, W., T. Chattopadhyay, M. Möllendorf, E. Gmelin and H.G. von Schnering, 1986, J. Magn. & Magn. Mater. **54–57**, 1359.

Baumann, U., D. Schubert, A. Schwotzer and G. Weber, 1984, J. Magn. & Magn. Mater. **45**, 179.

Beauvillain, P., C. Dupas, J.P. Renard and P. Veillet, 1984a, Phys. Rev. B **29**, 4086.

Beauvillain, P., C. Chappert and J.P. Renard, 1984b, J. Phys. Lett. **45**, 665.

Beauvillain, P., C. Chappert, J.P. Renard and J. Seiden, 1986, J. Magn. & Magn. Mater. **54–57**, 127.

Berton, A., J. Chaussy, J. Odin, R. Rammal and R. Tournier, 1982, J. Phys. Lett. **43**, 153.

Bertrand, D., A.R. Fert, M.C. Schmidt, F. Bensamka and S. Legrand, 1982, J. Phys. C **15**, L883.

Bertrand, D., F. Bensamka, A.R. Fert, J. Gelard, J.P. Redoulès and S. Legrand, 1984, J. Phys. C **17**, 1725.

Besnus, M.J., and J.P. Kappler, 1980, J. Magn. & Magn. Mater. **15–18**, 1237.

Bhatt, R.N., and A.P. Young, 1985, Phys. Rev. Lett. **54**, 924.

Binder, K., 1977, Z. Phys. B **26**, 339.

Binder, K., 1982, Solid State Commun. **42**, 377.

Binder, K., and W. Kinzel, 1983, J. Phys. Soc. Jpn. **52**, S-209.

Binder, K., and K. Schröder, 1976, Phys. Rev. B **14**, 2142.

Binder, K., and A.P. Young, 1984, Phys. Rev. B **29**, 2864.

Binder, K., and A.P. Young, 1986, Rev. Mod. Phys., in press.

Binder, K., W. Kinzel and D. Stauffer, 1979, Z. Phys. B **36**, 161.

Binder, K., W. Kinzel, H. Maletta and D. Stauffer, 1980, J. Magn. & Magn. Mater. **15–18**, 189.

Birgeneau, R.J., Y. Shapira, G. Shirane, R.A. Cowley and H. Yoshizawa, 1986, Physica B **137**, 83.

Bohn, H.G., W. Zinn, B. Dorner and A. Kollmar, 1980, Phys. Rev. B **22**, 5447.

Böni, P., S.M. Shapiro and K. Motoya, 1986, submitted for publication.

Bonjour, E., R. Calemczuk, R. Caudron, H. Safa, P. Gandit and P. Monod, 1984, Proc. of LT17 (North-Holland, Amsterdam) p. 643.

Bontemps, N., J. Rajchenbach and R. Orbach, 1983, J. Phys. Lett. **44**, 47.

Bontemps, N., J. Rajchenbach, R.V. Chamberlin and R. Orbach, 1984, Phys. Rev. B **30**, 6514.

Bontemps, N., J. Rajchenbach, R.V. Chamberlin and R. Orbach, 1986, J. Magn. & Magn. Mater. **54–57**, 1.

Börgermann, F.-J., H. Maletta and W. Zinn, 1986a, J. Magn. & Magn. Mater. **54–57**, 71.

Börgermann, F.-J., H. Maletta and W. Zinn, 1986b, Phys. Rev. B, submitted for publication.

Boucher, B., 1976, J. Phys. Lett. **37**, 345.

Boucher, B., 1977, IEEE Trans. Magn. **13**, 1601.

Boucher, B., and B. Barbara, 1979, J. Phys. F **9**, 151.

Bouchiat, H., 1986, J. Phys. **47**, 71.

Bouchiat, H., and D. Mailly, 1985, J. Appl. Phys. **57**, 3453.

Bouchiat, H., and P. Monod, 1982, J. Magn. & Magn. Mater. **30**, 175.

Brand, R.A., and W. Keune, 1984, Phys. Rev. Lett. **52**, 2097.

Brand, R.A., V. Manns and W. Keune, 1983, in: Heidelberg Colloquium on Spin Glasses, eds J.L. van Hemmen and I. Morgenstern (Springer, Berlin) p. 79.

Brand, R.A., J. Lauer and W. Keune, 1985, Phys. Rev. B **31**, 1630.
Bray, A.J., and M.A. Moore, 1979, J. Phys. C **12**, 1441.
Bray, A.J., and M.A. Moore, 1980, J. Phys. C **13**, L469.
Bray, A.J., and M.A. Moore, 1984, J. Phys. C **17**, L463.
Bray, A.J., and M.A. Moore, 1985a, Phys. Rev. B **31**, 631.
Bray, A.J., and M.A. Moore, 1985b, J. Phys. C **18**, L139.
Bray, A.J., and M.A. Moore, 1986, in: Heidelberg Colloquium on Glassy Dynamics and Optimization, eds J.L. van Hemmen and I. Morgenstern (Springer, Berlin) preprint.
Bray, A.J., M.A. Moore and A.P. Young, 1986, Phys. Rev. Lett. **56**, 2641.
Brown, J.A., R.H. Heffner, T.A. Kitchens, M. Leon, C.E. Olsen, M.E. Schillaci, S.A. Doods and D.E. MacLaughlin, 1981, J. Appl. Phys. **52**, 1766.
Brown, P.J., R. Caudron, A. Fert, D. Givord and P. Pureur, 1985, J. Phys. Lett. **46**, L-1139.
Bruss, F., K. Baberschke, M. Loewenhaupt and H. Scheuer, 1979, Solid State Commun. **32**, 135.
Cable, J.W., S.A. Werner, G.P. Felcher and N. Wakabayashi, 1984, Phys. Rev. B **29**, 1268.
Callen, E., Y.J. Liu and J.R. Cullen, 1977, Phys. Rev. B **16**, 263.
Campbell, I.A., D. Arvanitis and A. Fert, 1983, Phys. Rev. Lett. **51**, 57.
Campbell, I.A., N. de Courtenay and A. Fert, 1984, J. Phys. Lett. **45**, 565.
Cannella, V., and J.A. Mydosh, 1972, Phys. Rev. B **6**, 4220.
Carlson, N.W., S. Geschwind, G.E. Devlin, B. Batlogg, J.F. Dillon Jr, L.W. Rupp Jr and H. Maletta, 1984, J. Appl. Phys. **55**, 1679.
Carnegie Jr, D.W., and H. Claus, 1979, Phys. Rev. B **20**, 1280.
Casimir, H.B.G., and F.K. du Pré, 1938, Physica **5**, 507.
Caudron, R., P. Costa, J.C. Lasjaunias and B. Levesque, 1981, J. Phys. F **11**, 451.
Chalupa, J., 1977, Solid State Commun. **24**, 429.
Chamberlin, R.V., 1984, Phys. Rev. B **30**, 5393.
Chamberlin, R.V., 1985, J. Appl. Phys. **57**, 3377.
Chamberlin, R.V., M. Hardiman, L.A. Turkevich and R. Orbach, 1982, Phys. Rev. B **25**, 6720.
Chattopadhyay, T., P.J. Brown, P. Thalmeier and H.G. von Schnering, 1986, in press.
Chen, J.H., and T.C. Lubensky, 1977, Phys. Rev. B **16**, 2106.
Chikazawa, S., S. Taniguchi, H. Matsuyama and Y. Miyako, 1983, J. Magn. & Magn. Mater. **31–34**, 1355.
Child, H.R., and J.W. Cable, 1969, J. Appl. Phys. **40**, 1003.
Ching, W.Y., D.L. Huber and K.M. Leung, 1980, Phys. Rev. B **21**, 3708.
Chudnovsky, E.M., and R.A. Serota, 1983, J. Phys. C **16**, 4181.
Coey, J.M.D., T.R. McGuire and B. Tissier, 1981, Phys. Rev. B **24**, 1261.
Coles, B.R., 1984, Philos. Mag. B **49**, L21.
Coles, B.R., B.V.B. Sarkissian and H.R. Taylor, 1978, Philos. Mag. B **37**, 489.
Continentino, M.A., and A.P. Malozemoff, 1986, Phys. Rev. B **33**, 3591.
Cragg, D.M., and D. Sherrington, 1982b, Phys. Rev. Lett. **49**, 1190.
Cragg, D.M., D. Sherrington and M. Gabay, 1982a, Phys. Rev. Lett. **49**, 158.
Crane, S., and H. Claus, 1981, Phys. Rev. Lett. **46**, 1693.
Dahlberg, E.D., M. Hardiman, R. Orbach and J. Souletie, 1979, Phys. Rev. Lett. **42**, 401.
Dartyge, E., H. Bouchiat and P. Monod, 1982, Phys. Rev. B **25**, 6995.
De Almeida, J.R.L., and D.J. Thouless, 1978, J. Phys. A **11**, 983.
De Châtel, P.F., 1981, J. Magn. & Magn. Mater. **23**, 28.
de Courtenay, N., A. Fert and I.A. Campbell, 1984, Phys. Rev. B **30**, 6791.
De Dominicis, C., 1978, Phys. Rev. B **18**, 4913.
De Dominicis, C., 1983, in: Heidelberg Colloquium on Spin Glasses, eds J.L. van Hemmen and I. Morgenstern (Springer, Berlin) p. 103.
De Dominicis, C., and A.P. Young, 1983a, J. Phys. C **16**, L641.
De Dominicis, C., and A.P. Young, 1983b, J. Phys. A **16**, 2063.
De Dominicis, C., M. Gabay, T. Garel and H. Orland, 1980, J. Phys. **41**, 923.
De Dominicis, C., H. Orland and F. Lainée, 1985, J. Phys. Lett. **46**, 463.
De Gennes, P.G., 1962, J. Phys. **23**, 630.
Derrida, B., and J. Vannimenus, 1980, J. Phys. C **13**, 3261.
Deville, A., C. Arzoumanian, B. Gaillard, C. Blanchard, J.P. Jamet and H. Maletta, 1981a, Physica A **107**, 641.
Deville, A., C. Arzoumanian, B. Gaillard, C. Blanchard, J.P. Jamet and H. Maletta, 1981b, J. Phys. **42**, 1641.
Duffield, T., and C.N. Guy, 1985, J. Phys. F **15**, L17.
Dunlop, M.W., and D. Sherrington, 1985, J. Phys. C **18**, 1465.
Durand, J., and S.J. Poon, 1979, J. Phys. **40**, C5-231.
Dzyaloshinskii, I.E., 1958, J. Phys. & Chem. Solids **4**, 241.
Dzyaloshinskii, I.E., and G.E. Volovik, 1978, J. Phys. **39**, 693.
Edwards, S.F., and P.W. Anderson, 1975, J. Phys. F **5**, 965.
Eiselt, G., J. Kötzler, H. Maletta, D. Stauffer and K. Binder, 1979a, Phys. Rev. B **19**, 2664.
Eiselt, G., J. Kötzler, H. Maletta, K. Binder and D. Stauffer, 1979b, J. Magn. & Magn. Mater. **13**, 146.
Elliott, R.J., 1961, Phys. Rev. **124**, 346.
Emmerich, K., and Ch. Schwink, 1981, Hyperfine Interactions **8**, 767.
Emmerich, K., E. Lippelt, R. Neuhaus, H. Pinkvos, Ch. Schwink, F.N. Gygax, A. Hintermann, A. Schenck, W. Studer and A.J. van der Wal, 1985, Phys. Rev. B **31**, 7226.

Felsch, W., 1978, Z. Phys. B **29**, 203.
Ferré, J., J. Rajchenbach and H. Maletta, 1981, J. Appl. Phys. **52**, 1697.
Ferré, J., M. Ayadi, R.V. Chamberlin, R. Orbach and N. Bontemps, 1986, J. Magn. & Magn. Mater. **54–57**, 211.
Ferrer, R., R. Harris, D. Zobin and M.J. Zuckermann, 1978, Solid State Commun. **26**, 451.
Fert, A., and F. Hippert, 1982, Phys. Rev. Lett. **49**, 1508.
Fert, A., and P.M. Levy, 1980, Phys. Rev. Lett. **44**, 1538.
Fert, A., and P.M. Levy, 1981, J. Appl. Phys. **52**, 1718.
Fert, A., P. Pureur, F. Hippert, K. Baberschke and F. Bruss, 1982, Phys. Rev. B **26**, 5300.
Fincher, C.R., S.M. Shapiro, A.H. Palumbo and R.D. Parks, 1980, Phys. Rev. Lett. **45**, 474.
Finnemore, D.K., L.J. Williams, F.H. Spedding and D.C. Hopkins, 1968, Phys. Rev. **176**, 712.
Fisch, R., and A.B. Harris, 1977, Phys. Rev. Lett. **38**, 785.
Fischer, K.H., 1980, Z. Phys. B **39**, 37.
Fischer, K.H., 1983a, Phys. Status Solidi **116**, 357.
Fischer, K.H., 1983b, Z. Phys. **53**, 215.
Fischer, K.H., 1985, Phys. Status Solidi **130**, 13.
Fischer, K.H., and W. Kinzel, 1984, J. Phys. C **17**, 4479.
Fisher, D.S., and D.A. Huse, 1986, Phys. Rev. Lett. **56**, 1601.
Fisher, D.S., and H. Sompolinsky, 1985, Phys. Rev. Lett. **54**, 1063.
Fishmann, S., and A. Aharony, 1980, Phys. Rev. B **21**, 280.
Fogle, W.E., J.B. Boyer, R.A. Fisher and N.E. Phillips, 1983, Phys. Rev. Lett. **50**, 1815.
Freeman, A.J., 1972, in: Magnetic Properties of Rare Earth Metals, ed. R.J. Elliott (Plenum, New York) p. 245.
Gabay, M., and G. Toulouse, 1981, Phys. Rev. Lett. **47**, 201.
Geohegan, J.A., and S.M. Bhagat, 1981, J. Magn. & Magn. Mater. **25**, 17.
Gotaas, J.A., J.J. Rhyne and S.A. Werner, 1985, J. Appl. Phys. **57**, 3404.
Gray, E.M., 1979, J. Phys. F **9**, L167.
Gullikson, E.M., D.R. Fredkin and S. Schultz, 1983, Phys. Rev. Lett. **50**, 537.
Guy, C.N., 1975, J. Phys. F **5**, L242.
Guy, C.N., 1977, J. Phys. F **7**, 1505.
Guy, C.N., 1978, J. Phys. F **8**, 1309.
Guy, C.N., and J.G. Park, 1983, J. Phys. F **13**, 1955.
Halperin, B.I., and W.M. Saslow, 1977, Phys. Rev. B **16**, 2154.
Harris, R., M. Plischke and M.J. Zuckermann, 1973, Phys. Rev. Lett. **31**, 160.
Heffner, R.H., and D.E. MacLaughlin, 1984, Phys. Rev. B **29**, 6048.
Hein, R.A., R.L. Falge Jr, B.T. Matthias and C. Corenzwit, 1959, Phys. Rev. Lett. **2**, 500.
Hennion, B., M. Hennion, F. Hippert and A.P. Murani, 1983, Phys. Rev. B **28**, 5365.
Hennion, B., M. Hennion, F. Hippert and A.P. Murani, 1984, J. Phys. F **14**, 489.
Hippert, F., and H. Alloul, 1982, J. Phys. **43**, 691.
Hippert, F., H. Alloul and A. Fert, 1982, J. Appl. Phys. **53**, 7702.
Hiraoka, K., T. Hihara, K. Kojima and T. Kino, 1986, J. Magn. & Magn. Mater. **54–57**, 1295.
Hoekstra, F.R., G.J. Nieuwenhuys, K. Baberschke and S.E. Barnes, 1984, Phys. Rev. B **29**, 1292.
Hohenberg, P.C., and B.I. Halperin, 1977, Rev. Mod. Phys. **49**, 435.
Hoogerbeets, R., W.-L. Luo, R. Orbach and D. Fiorani, 1986, Phys. Rev. B **33**, 6531.
Hopfield, J.J., 1982, Proc. Natl. Acad. Sci. USA **79**, 2554.
Houghton, A., S. Jain and A.P. Young, 1983, J. Phys. C **16**, L375.
Huang, C.Y., 1985, J. Magn. & Magn. Mater. **51**, 1.
Hüser, D., M.J.F.M. Rewiersma, J.A. Mydosh and G.J. Nieuwenhuys, 1983a, Phys. Rev. Lett. **51**, 1290.
Hüser, D., L.E. Wenger, A.J. van Duyneveldt and J.A. Mydosh, 1983b, Phys. Rev. B **27**, 3100.
Jayaprakash, C., and S. Kirkpatrick, 1980, Phys. Rev. B **21**, 4072.
Kaneyoshi, T., 1975, J. Phys. F **5**, 1014.
Kasuya, T., 1956, Prog. Theor. Phys. **16**, 45.
Kasuya, T., 1973, CRC Crit. Rev. Solid State Sci. **3**, 131.
Ketelsen, L.J.P., and M.B. Salamon, 1984, Phys. Rev. B **30**, 2718.
Ketelsen, L.J.P., and M.B. Salamon, 1985, Solid State Commun. **55**, 237.
Kinzel, W., 1979, Phys. Rev. B **19**, 4595.
Kinzel, W., and K. Binder, 1981, Phys. Rev. B **24**, 2701.
Kinzel, W., and K. Binder, 1983, Phys. Rev. Lett. **50**, 1509.
Kinzel, W., and K. Binder, 1984, Phys. Rev. B **29**, 1300.
Kinzel, W., and K.H. Fischer, 1978, J. Phys. C **11**, 2775.
Kirkpatrick, S., and D. Sherrington, 1978, Phys. Rev. B **17**, 4384.
Kirkpatrick, S., C.D. Gelatt and M.P. Vecchi, 1983, Science **220**, 671.
Knitter, R.W., and J.S. Kouvel, 1980, J. Magn. & Magn. Mater. **21**, L316.
Köbler, U., and K. Binder, 1980, J. Magn. & Magn. Mater. **15–18**, 313.
Koehler, W.C., 1972, in: Magnetic Properties of Rare Earth Metals, ed. R.J. Elliott (Plenum, New York) p. 81.
Kosterlitz, J.M., and D.J. Thouless, 1973, J. Phys. C **6**, 1181.
Kotliar, G., and H. Sompolinsky, 1984, Phys. Rev. Lett. **44**, 1751.
Kouvel, J.S., 1961, J. Phys. & Chem. Solids **21**, 57.

Krey, U., 1980, Z. Phys. B **38**, 243.
Krey, U., 1981, Z. Phys. B **42**, 231.
Krey, U., 1982, J. Magn. & Magn. Mater. **28**, 231.
Krey, U., 1985, J. Phys. Lett. **46**, 845.
Kubo, R., 1966, Rep. Prog. Phys. **29**, 255.
Lauer, J., and W. Keune, 1982, Phys. Rev. Lett. **48**, 1850.
Lecomte, G.V., H. von Löhneysen, W. Bauhofer and G. Güntherodt, 1984, Solid State Commun. **52**, 535.
Lecomte, G.V., H. von Löhneysen, A. Schröder, W. Bauhofer and G. Güntherodt, 1986a, J. Magn. & Magn. Mater. **54–57**, 69.
Lecomte, G.V., N. Schubert, J.A. Heller and E.F. Wassermann, 1986b, J. Magn. & Magn. Mater., in press.
Levitt, D.A., and R.E. Walstedt, 1977, Phys. Rev. Lett. **38**, 178.
Levy, P.M., and R. Raghavan, 1986, J. Magn. & Magn. Mater. **54–57**, 181.
Levy, P.M., and Q. Zhang, 1986, J. Magn. & Magn. Mater. **54–57**, 133.
Lundgren, L., P. Svedlindh and O. Beckman, 1981, J. Magn. & Magn. Mater. **25**, 33.
Lundgren, L., P. Svedlindh and O. Beckman, 1982, Phys. Rev. B **26**, 3990.
Lundgren, L., P. Svedlindh, P. Nordblad and O. Beckman, 1983, Phys. Rev. Lett. **51**, 911.
Lundgren, L., P. Nordblad, P. Svedlindh and O. Beckman, 1985, J. Appl. Phys. **57**, 3371.
MacLaughlin, D.E., and H. Alloul, 1976, Phys. Rev. Lett. **36**, 1158.
MacLaughlin, D.E., L.C. Gupta, D.W. Cooke, R.H. Heffner, M. Leon and M.E. Schillaci, 1983, Phys. Rev. Lett. **51**, 927.
Maletta, H., 1979c, J. Appl. Phys. **50**, 7312.
Maletta, H., 1980a, J. Magn. & Magn. Mater. **15–18**, 100.
Maletta, H., 1980c, J. Phys. **41**, C5-115.
Maletta, H., 1981b, J. Magn. & Magn. Mater. **24**, 179.
Maletta, H., 1982a, J. Appl. Phys. **53**, 2185.
Maletta, H., 1982c, in: Excitations in Disordered Systems, Ser. B Vol. 78 (NATO Advanced Study Institutes, Plenum Press) p. 431.
Maletta, H., 1983b, in: Heidelberg Colloquium on Spin Glasses, Lecture Notes in Physics, Vol. 192 (Springer, Berlin) p. 90.
Maletta, H., and P. Convert, 1979a, Phys. Rev. Lett. **42**, 108.
Maletta, H., and G. Crecelius, 1976, J. Phys. **37**, C6-645.
Maletta, H., and W. Felsch, 1978b, J. Phys. **39**, C6-931.
Maletta, H., and W. Felsch, 1979b, Phys. Rev. B **20**, 1245.
Maletta, H., and W. Felsch, 1980d, Z. Phys. B **37**, 55.
Maletta, H., W. Felsch and J.L. Tholence, 1978a, J. Magn. & Magn. Mater. **9**, 41.
Maletta, H., W. Felsch, H. Scheuer and H. Pink, 1980b, J. Magn. & Magn. Mater. **15–18**, 167.
Maletta, H., W. Zinn, H. Scheuer and S.M. Shapiro, 1981a, J. Appl. Phys. **52**, 1735.
Maletta, H., G. Aeppli and S.M. Shapiro, 1982b, Phys. Rev. Lett. **21**, 1490.
Maletta, H., G. Aeppli and S.M. Shapiro, 1983a, J. Magn. & Magn. Mater. **31–34**, 1367.
Malozemoff, A.P., and B. Barbara, 1985, J. Appl. Phys. **57**, 3410.
Malozemoff, A.P., and Y. Imry, 1981, Phys. Rev. B **24**, 489.
Malozemoff, A.P., Y. Imry and B. Barbara, 1982, J. Appl. Phys. **53**, 7672.
Malozemoff, A.P., S.E. Barnes and B. Barbara, 1983, Phys. Rev. Lett. **51**, 1704.
Manheimer, M.A., S.M. Bhagat and H.S. Chen, 1983, J. Magn. & Magn. Mater. **38**, 147.
Maple, M.B., 1976, Appl. Phys. **9**, 179.
Marshall, W., and S.W. Lovesey, 1971, in: Theory of Thermal Neutron Scattering (Oxford University Press, Oxford).
Martin, D.L., 1979, Phys. Rev. B **20**, 368.
Martin, D.L., 1985, Phys. Rev. B **31**, 4708.
Matsui, M., A.P. Malozemoff, R.J. Gambino and L. Krusin-Elbaum, 1985, J. Appl. Phys. **57**, 3389.
Mattis, D.C., 1976, Phys. Lett. A **56**, 421.
McGuire, T.R., T. Mizoguchi, R.J. Gambino and S. Kirkpatrick, 1978, J. Appl. Phys. **49**, 1689.
McMillan, W.L., 1983, Phys. Rev. B **28**, 5216.
McMillan, W.L., 1984a, Phys. Rev. B **30**, 476.
McMillan, W.L., 1984b, J. Phys. C **17**, 3179.
Mehran, F., K.W.H. Stevens, F. Holtzberg, R.L. Melcher, W.J. Fitzpatrick and T.R. McGuire, 1984, Solid State Commun. **52**, 107.
Meschede, D., F. Steglich, W. Felsch, H. Maletta and W. Zinn, 1980, Phys. Rev. Lett. **44**, 102.
Meyer, C., F. Hartmann-Boutron, Y. Gros and I.A. Campbell, 1985, J. Magn. & Magn. Mater. **46**, 254.
Mézard, M., G. Parisi, N. Sourlas, G. Toulouse and M. Virasoro, 1984, Phys. Rev. Lett. **52**, 1186.
Mezei, F., 1972, Z. Phys. **255**, 146.
Mezei, F., 1981, in: Recent Developments in Condensed Matter Physics, Vol. 1, ed. J.T. Devreese (Plenum, New York) p. 679.
Mezei, F., 1982, J. Appl. Phys. **53**, 7654.
Mezei, F., 1983, J. Magn. & Magn. Mater. **31–34**, 1327.
Mezei, F., and A.P. Murani, 1979, J. Magn. & Magn. Mater. **14**, 211.
Mezei, F., A.P. Murani and J.L. Tholence, 1983, Solid State Commun. **45**, 411.
Mizoguchi, T., T.R. McGuire, S. Kirkpatrick and R.J. Gambino, 1977, Phys. Rev. Lett. **38**, 89.
Monod, P., and Y. Berthier, 1980, J. Magn. & Magn. Mater. **15–18**, 149.
Monod, P., and H. Bouchiat, 1982, J. Phys. Lett. **43**, 46.
Monod, P., and I.A. Campbell, 1984, Phys. Rev. Lett. **52**, 2096.

Monod, P., J.J. Préjean and B. Tissier, 1979, J. Appl. Phys. **50**, 7324.
Monod, P., A. Landi, C. Blanchard, A. Deville and H. Hurdequint, 1986, J. Magn. & Magn. Mater. **59**, 132.
Moore, M.A., and A.J. Bray, 1985, J. Phys. C **18**, L699.
Moorjani, K., and J.M.D. Coey, 1984, in: Magnetic Glasses (Elsevier North-Holland, New York).
Morgenstern, I., and K. Binder, 1979, Phys. Rev. Lett. **43** 1615.
Morgownik, A.F.J., and J.A. Mydosh, 1983, Solid State Commun. **47**, 321,325.
Moriya, T., 1960, Phys. Rev. Lett. **4**, 5.
Morris, B.W., S.G. Colborne, M.A. Moore, A.J. Bray and J. Canisius, 1986, J. Phys. C **19**, 1157.
Mulder, C.A.M., A.J. van Duyneveldt and J.A. Mydosh, 1981, Phys. Rev. B **23**, 1384.
Murani, A.P., 1978a, Phys. Rev. Lett. **41**, 1406.
Murani, A.P., 1978b, J. Phys. **39**, C6-1517.
Murani, A.P., 1981, J. Magn. & Magn. Mater. **22**, 271.
Murani, A.P., 1983, Phys. Rev. B **28**, 432.
Murani, A.P., 1985, J. Phys. F **15**, 417.
Murani, A.P., and A. Heidemann, 1978c, Phys. Rev. Lett. **41**, 1402.
Murani, A.P., and J.L. Tholence, 1977, Solid State Commun. **22**, 25.
Murnick, D.E., A.T. Fiory and W.J. Kossler, 1976, Phys. Rev. Lett. **36**, 100.
Nagata, S., P.H. Keesom and H.R. Harrison, 1979, Phys. Rev. B **19**, 1633.
Néel, L., 1949, Ann. Geophys. **5**, 99.
Ngai, K.L., A.K. Rajagopal and C.Y. Huang, 1984, J. Appl. Phys. **55**, 1714.
Nigh, H.E., S. Legvold and F.H. Spedding, 1963, Phys. Rev. **132**, 1092.
Nordblad, P., L. Lundgren and L. Sandlund, 1986a, J. Magn. & Magn. Mater. **54–57**, 185.
Nordblad, P., P. Svedlindh, L. Lundgren and L. Sandlund, 1986b, Phys. Rev. B **33**, 645.
Novak, M.A., O.G. Symko and D.J. Zheng, 1986, J. Magn. & Magn. Mater. **54–57**, 129.
Ocio, M., H. Bouchiat and P. Monod, 1985, J. Phys. Lett. **46**, 647.
Ocio, M., H. Bouchiat and P. Monod, 1986, J. Magn. & Magn. Mater. **54–57**, 11.
Ogielski, A.T., 1985, Phys. Rev. B **32**, 7384.
Ogielski, A.T., and I. Morgenstern, 1985, Phys. Rev. Lett. **54**, 928.
Omari, R., J.J. Préjean and J. Souletie, 1983, J. Phys. **44**, 1069.
Overhauser, A.W., 1959, Phys. Rev. Lett. **3**, 414.
Overhauser, A.W., 1960, J. Phys. & Chem. Solids **13**, 71.
Owen, J., M.E. Browne, V. Arp and A.F. Kip, 1957, J. Phys. & Chem. Solids **2**, 85.
Palmer, R.G., 1982, Adv. Phys. **31**, 669.
Palmer, R.G., D.L. Stein, E. Abrahams and P.W. Anderson, 1984, Phys. Rev. Lett. **53**, 958.
Parisi, G., 1979, Phys. Rev. Lett. **43**, 1754.
Parisi, G., 1983, Phys. Rev. Lett. **50**, 1946.
Parisi, G., and G. Toulouse, 1980, J. Phys. Lett. **41**, 361.
Paulsen, C.C., J.A. Hamida, S.J. Williamson and H. Maletta, 1984, J. Appl. Phys. **55**, 1652.
Paulsen, C.C., S.J. Williamson and H. Maletta, 1986a, J. Magn. & Magn. Mater. **54–57**, 209.
Paulsen, C.C., S.J. Williamson and H. Maletta, 1986b, submitted for publication.
Pelcovits, R.A., E. Pytte and J. Rudnick, 1978, Phys. Rev. Lett. **40**, 476.
Phillips, W.A., 1972, J. Low Temp. Phys. **7**, 351.
Poon, S.J., and J. Durand, 1978, Phys. Rev. B **18**, 6253.
Préjean, J.J., 1978, J. Phys. **39**, C6-907.
Préjean, J.J., M.J. Joliclerc and P. Monod, 1980, J. Phys. **41**, 427.
Rainford, B.D., H.B. Stanley and B.V.B. Sarkissian, 1985, Physica B **130**, 388.
Rajchenbach, J., and N. Bontemps, 1983, J. Phys. Lett. **44**, 799.
Rajchenbach, J., and N. Bontemps, 1984, J. Appl. Phys. **55**, 1649.
Rajchenbach, J., J. Ferré and H. Maletta, 1981, in: Recent Developments in Condensed Matter Physics, Vol. 2, eds J.T. DeVreese, L.F. Lemmens, V.E. Van Doren and J. van Royen (Plenum Publ. Coorp.) p. 253.
Rakoto, H., J.C. Ousset, S. Senoussi and I.A. Campbell, 1984, J. Magn. & Magn. Mater. **46**, 212.
Rathmann, O., and P. Touborg, 1977, Phys. Rev. B **16**, 1212.
Reim, W., R.H. Koch, A.P. Malozemoff, M.B. Ketchen and H. Maletta, 1986, Phys. Rev. Lett. **57**, 905.
Roberts, S.A., and A.J. Bray, 1982, J. Phys. C **15**, L527.
Rosenbaum, T.F., L.W. Rupp, G.A. Thomas, W.M. Walsh, H.S. Chen, J.R. Banavar and P.B. Littlewood, 1982, Solid State Commun. **42**, 725.
Roth, S., 1978, Appl. Phys. **15**, 1.
Ruderman, M.A., and C. Kittel, 1954, Phys. Rev. **96**, 99.
Salamon, M.B., 1979, Solid State Commun. **31**, 781.
Salamon, M.B., K.V. Rao and Y. Yeshurun, 1981, J. Appl. Phys. **52**, 1687.
Salomon, M.B., and J.L. Tholence, 1982, J. Appl. Phys. **53**, 7684.
Salomon, M.B., and J.L. Tholence, 1983, J. Magn. & Magn. Mater. **31–34**, 1375.
Sarkissian, B.V.B., 1977, J. Phys. F **7**, L139.
Sarkissian, B.V.B., and B.R. Coles, 1976, Commun. Phys. **1**, 17.
Saslow, W.M., 1982, Phys. Rev. Lett. **48**, 505.
Sato, T., and Y. Miyaka, 1982, J. Phys. Soc. Jpn. **51**, 2153.
Scherzberg, A., H. Maletta and W. Zinn, 1981, J. Magn. & Magn. Mater. **24**, 186.
Schmitt, R.W., and I.S. Jacobs, 1957, J. Phys. & Chem. Solids **3/4**, 324.
Schröder, A., H. von Löhneysen and W. Bauhofer, 1986, submitted for publication.

Schultz, S., F.M. Gullikson, D.R. Fradkin and M. Tovar, 1980, Phys. Rev. Lett. **45**, 1508.
Sellmyer, D.J., and S. Nafis, 1985, J. Appl. Phys. **57**, 3584.
Sellmyer, D.J., and S. Nafis, 1986, J. Magn. & Magn. Mater. **54–57**, 113.
Senoussi, S., 1984, J. Phys. **45**, 315.
Shapiro, S.M., H. Maletta and F. Mezei, 1985, J. Appl. Phys. **57**, 3485.
Shapiro, S.M., G. Aeppli, H. Maletta and K. Motoya, 1986, in: Frontiers of Neutron Scattering, Physica B **137**, 96.
Sherrington, D., 1983, in: Heidelberg Colloquium on Spin Glasses, eds J.L. van Hemmen and I. Morgenstern (Springer, Berlin) p. 125.
Sherrington, D., and S. Kirkpatrick, 1975, Phys. Rev. Lett. **35**, 1792.
Shull, R.D., H. Okamoto and P.A. Beck, 1976, Solid State Commun. **20**, 863.
Smit, J.J., G.J. Nieuwenhuys and L.J. de Jongh, 1979a, Solid State Commun. **31**, 265.
Smit, J.J., G.J. Nieuwenhuys and L.J. de Jongh, 1979b, Solid State Commun. **32**, 233.
Sompolinsky, H., 1981, Phys. Rev. Lett. **47**, 935.
Sompolinsky, H., and A. Zippelius, 1981, Phys. Rev. Lett. **47**, 359.
Sompolinsky, H., and A. Zippelius, 1982, Phys. Rev. B **25**, 6860.
Sompolinsky, H., and A. Zippelius, 1983, Phys. Rev. Lett. **50**, 1297.
Southern, B.W., and A.P. Young, 1977, J. Phys. C **10**, 2179.
Stauffer, D., and K. Binder, 1978, Z. Phys. B **30**, 313.
Suzuki, M., 1977, Prog. Theor. Phys. **58**, 1151.
Taniguchi, T., H. Matsuyama, S. Chikazawa and Y. Miyako, 1983, J. Phys. Soc. Jpn. **52**, 4323.
Taniguchi, T., Y. Miyako and J.L. Tholence, 1985, J. Phys. Soc. Jpn. **54**, 220.
Tatsumi, T., 1978, Prog. Theor. Phys. **59** 405.
Thalmeier, P., 1986, J. Magn. & Magn. Mater. **54–57**, 509.
Tholence, J.L., 1980, Solid State Commun. **35**, 113.
Tholence, J.L., and R. Tournier, 1974, J. Phys. **35**, C4-229.
Thomson, J.O., and J.R. Thompson, 1981, J. Phys. F **11**, 247.
Thouless, D.J., P.W. Anderson and R.G. Palmer, 1977, Philos. Mag. **35**, 593.
Touborg, P., 1977, Phys. Rev. B **16**, 1201.
Toulouse, G., 1977, Commun. Phys. **2**, 115.
Toulouse, G., 1980, J. Phys. Lett. **41**, 447.
Tournier, R., and Y. Ishikawa, 1964, Phys. Lett. **11**, 280.
Uemura, Y.J., 1981, Hyperfine Interactions **8**, 739.
Uemura, Y.J., and T. Yamazaki, 1982, Physica B **109–110**, 1915.
Uemura, Y.J., T. Yamazaki, R.S. Hayano and C.Y. Huang, 1980, Phys. Rev. Lett. **45**, 583.
Uemura, Y.J., D.R. Harshman, M. Senba, E.J. Ansaldo and A.P. Murani, 1984, Phys. Rev. B **30**, 1606.
Uemura, Y.J., T. Yamazaki, D.R. Harshman, M. Senba and E.J. Ansaldo, 1985, Phys. Rev. B **31**, 546.
van Duyneveldt, A.J., and C.A.M. Mulder, 1982, Physica B **114**, 82.
Vannimenus, J., G. Toulouse and G. Parisi, 1981, J. Phys. **42**, 565.
Varret, F., A. Hamzić and I.A. Campbell, 1982, Phys. Rev. B **26**, 5285.
Velu, E., J.P. Renard and J.P. Miranday, 1981, J. Phys. Lett. **42**, 237.
Verbeek, B.H., and J.A. Mydosh, 1978, J. Phys. F **8**, L109.
Verbeek, B.H., G.J. Nieuwenhuys, H. Stocker and J.A. Mydosh, 1978, Phys. Rev. Lett. **40**, 586.
Viana, L., and A.J. Bray, 1985, J. Phys. C **18**, 3037.
Violet, C.E., and R.J. Borg, 1983, Phys. Rev. Lett. **51**, 1073.
Violet, C.E., and R.J. Borg, 1984, Phys. Rev. Lett. **52**, 2098.
von Löhneysen, H., and J.L. Tholence, 1979, Phys. Rev. B **19**, 5858.
von Löhneysen, H., J.L. Tholence and R. Tournier, 1978a, J. Phys. C **6**, 922.
von Löhneysen, H., J.L. Tholence and F. Steglich, 1978b, Z. Phys. B **29**, 319.
von Löhneysen, H., R. van den Berg, G.V. Lecomte and W. Zinn, 1985, Phys. Rev. B **31**, 2920.
von Molnar, S., B. Barbara, T.R. McGuire and R.J. Gambino, 1982, J. Appl. Phys. **53**, 2350.
Wachter, P., 1979, in: Handbook on the Physics and Chemistry of Rare Earths, Vol. 2, eds K.A. Gschneidner Jr and L. Eyring (North-Holland, Amsterdam) p. 507.
Walker, L.R., and R.E. Walstedt, 1977, Phys. Rev. Lett. **38**, 514.
Walker, L.R., and R.E. Walstedt, 1980, Phys. Rev. B **22**, 3816.
Walstedt, R.E., 1981, Phys. Rev. B **24**, 1524.
Walstedt, R.E., and L.R. Walker, 1981, Phys. Rev. Lett. **47**, 1624.
Wendler, R., and K. Baberschke, 1983, Solid State Commun. **48**, 91.
Wendler, R., P. Pureur, A. Fert and K. Baberschke, 1984, J. Magn. & Magn. Mater. **45**, 185.
Wenger, L.E., 1978, J. Appl. Phys. **49**, 1630.
Wenger, L.E., 1983, in: Heidelberg Colloquium on Spin Glasses, eds J.L. van Hemmen and I. Morgenstern (Springer, Berlin) p. 60.
Wenger, L.E., and P.H. Keesom, 1975, Phys. Rev. B **11**, 3497.
Wenger, L.E., and P.H. Keesom, 1976, Phys. Rev. B **13**, 4053.
Wenger, L.E., and J.A. Mydosh, 1984a, J. Appl. Phys. **55**, 1717.
Wenger, L.E., and J.A. Mydosh, 1984b, J. Appl. Phys. **55**, 1850.
Wenger, L.E., G.W. Hunter, J.A. Mydosh, J.A. Gotaas and J.J. Rhyne, 1986, Phys. Rev. Lett. **56**, 1090.

Westerholt, K., and H. Bach, 1981a, J. Magn. & Magn. Mater. **24**, 191.
Westerholt, K., and H. Bach, 1981b, Phys. Rev. Lett. **47**, 1925.
Westerholt, K., and H. Bach, 1985, Phys. Rev. B **31**, 7151.
Westerholt, K., B. Gosh, K. Siratori, S. Methfessel and T. Petzel, 1977, Physica B **86–88**, 740.
Wohlfarth, E.P., 1977, Physica B **86–88**, 852.
Wolff, W.F., and J. Zittartz, 1985, Z. Phys. B **60**, 185.
Wong, P.-Z., H. Yoshizawa and S.M. Shapiro, 1985a, J. Appl. Phys. **57**, 3462.
Wong, P.-Z., S. von Molnar, T.T.M. Palstra, J.A. Mydosh, H. Yoshizawa, S.M. Shapiro and A. Ito, 1985b, Phys. Rev. Lett. **55**, 2043.
Wosnitza, J., H. von Löhneysen, W. Zinn and U. Krey, 1986, Phys. Rev. B **33**, 3436.
Wu, W.-Y., G. Mozurkewich and R. Orbach, 1985, Phys. Rev. B **31**, 4557.
Yeshurun, Y., and M.B. Salamon, 1981, J. Phys. C **14**, 1575.
Yeshurun, Y., and H. Sompolinsky, 1982, Phys. Rev. B **26**, 1487.
Yeshurun, Y., M.B. Salomon, K.V. Rao and H.S. Chen, 1980, Phys. Rev. Lett. **45**, 1366.
Yosida, K., 1957, Phys. Rev. **106**, 893.
Young, A.P., 1983a, Phys. Rev. Lett. **50**, 917.
Young, A.P., 1983b, Phys. Rev. Lett. **51**, 1206.
Zinn, W., 1976, J. Magn. & Magn. Mater. **3**, 23.

Handbook on the Physics and Chemistry of Rare Earths, Vol. 12
edited by K.A. Gschneidner Jr, and L. Eyring

Chapter 85

LIQUID METALS AND ALLOYS

J. VAN ZYTVELD
Physics Department, Calvin College, Grand Rapids, MI 49506, U.S.A.

Contents

Symbols

a	thermal diffusivity
A	surface area
$A(K)$	structure factor, pure liquid metal
$A_{ab}(K)$	partial structure factor, alloy
$A_{HS}(K)$	hard-sphere structure factor
c	atomic fraction of alloy component
c_a, c_b	atomic fraction of alloy constituent a, b
c_p	specific heat at constant pressure
c_v	specific heat at constant volume
C	Curie constant
D	self-diffusion coefficient
$D(E)$	electron diffusivity
e	electronic charge
E	electron energy
E_f	electron Fermi energy
E_J	4f energy level corresponding to J
E_v	activation energy
E^s	excess surface energy
F^s	surface Helmholtz free energy
g	Landé g-factor
$g(r)$	pair distribution function
$g_{ab}(r)$	partial pair distribution function, alloy
$\hbar$	$h/2\pi$, h = Planck's constant
J	total angular momentum quantum number
k	electron wave vector
k_B	Boltzmann's constant
k_f	electron Fermi wave vector

K	momentum transfer wave vector
$K_p^{(i)}$	value of K at the i^{th} peak in A(K)
K_{red}	$K/K_p^{(1)}$
l	orbital angular momentum quantum number
L_0	Lorentz number
m	electron mass
M	gram-atomic weight
$n(E)$	electron density of states
$n(r)$	number density
n_0	mean number density
n_c	effective number of conduction electrons per ion
n_e	number density of charge carriers
$n_d(E)$	electron d-density of states
$n_s(E)$	electron s-density of states
N_A	Avogadro's number
N_n	number of nearest neighbor ions
P	pressure
$P_l(\cos\theta)$	l^{th} Legendre polynomial
Q	thermoelectric power (thermopower)
Q_L	thermopower of a liquid phase
Q_S	thermopower of a solid phase
r	position vector
r_1	nearest neighbor separation
R	universal gas constant
RDF	radial distribution function
R_H	Hall coefficient
$R_H^{(0)}$	Hall coefficient, for nearly free electrons
S	entropy
S^s	excess surface entropy
S_s	entropy correction due to ion core softness
S_{el}	electronic contribution to entropy
S_{gas}	entropy of ideal ionic gas
S_{mag}	magnetic contribution to entropy
S_{pack}	entropy of packing of hard spheres
$t(K, E)$	transition matrix (t-matrix)
T	temperature
T_c	critical temperature
T_{mp}	melting temperature
T_t	solid–solid phase transition temperature
$U(K)$	electron–ion pseudopotential
v_f	electron Fermi velocity
v_s	velocity of sound
V	volume
x	packing fraction
Z	atomic number
α	linear thermal expansion coefficient
γ	surface tension
δ_l	phase shift associated with the lth partial wave
ΔH	enthalpy of mixing
$\overline{\Delta H}_R^{\infty}$	partial enthalpy of mixing at infinite R-metal dilution
Δn_{ws}	difference in electron densities at Wigner–Seitz cell boundaries between dissimilar ions in alloys.
$\Delta\phi^*$	difference in work functions between pure alloy constituents
ζ	thermopower parameter
η	shear viscosity
θ	Curie temperature
κ	thermal conductivity
κ_{el}	electronic thermal conductivity
κ_{ion}	ionic thermal conductivity
κ_T	isothermal compressibility
μ_B	Bohr magneton
μ_{eff}	effective magnetic moment
ρ	electrical resistivity
ρ_L	electrical resistivity of a liquid phase
ρ_0	mass density
ρ_{0i}	mass density of alloy component "i"
ρ_s	electrical resistivity of a solid phase
σ	hard-sphere diameter
σ_{xy}	transverse conductivity
τ	electron scattering lifetime
$\phi(r)$	effective interionic potential
χ	magnetic susceptibility
χ_{alloy}	total magnetic susceptibility of alloy
χ_A	total magnetic susceptibility
χ_d	Landau diamagnetism of conduction electrons
$\chi_{d\,0}$	χ_d for free electrons
χ_e	conduction electron susceptibility
χ_{4f}	paramagnetic susceptibility of 4f electrons
χ_{ion}	diamagnetic susceptibility of ion core
χ_n	magnetic susceptibility of atomic nuclei
χ_p	Pauli spin paramagnetism of conduction electrons
$\chi_{p\,0}$	χ_p for free electrons
Ω	molar volume
Ω_0	atomic volume

1. Introduction

Progress in the understanding of the properties of the liquid metals and alloys of the rare earths (R's), both theoretical and experimental, has been steady for more than two decades. The present chapter is an attempt to draw the threads of these studies together into a single fabric. A special attempt has been made to aid others in their work by providing a best estimate of each experimental parameter which has been measured to date, and also by providing some estimate of uncertainty for these. Those workers who are relatively unfamiliar with one or another research area should find the brief introductions which are provided for each topic to be useful; references to more complete presentations are made where these are available. Also, the list of references, while not thoroughly exhaustive, is meant to be more nearly exhaustive then representative.

A word should also be said about the units that have been utilized in this chapter. An attempt has been made to reduce the variety of units in use in many of the research areas represented, by expressing parameters in a limited set of units in most common use. In many cases, this has meant that non-SI units have been chosen. It is thought, however, that the employment of a limited set of common units will make the contents of this chapter more useful and accessible to interested workers.

2. Physical properties

2.1. *Density*

Perhaps the most basic of the physical properties of the liquid R's is their mass density. Knowledge of this parameter is of interest in itself, but is also essential to studies of a wide variety of other properties of these liquids, ranging from determinations of structural information from X-ray and neutron-diffraction experiments, to studies of electronic and of thermodynamic properties of pure R's and their alloys.

Densities, ρ_0, of all of the liquid R's, except Tm, have now been measured. Best estimates of these densities from presently available data are shown in table 1, along with $\mathrm{d}(\rho_0)/\mathrm{d}T$. Estimates of uncertainty are also shown, where possible. In cases in which the data are not reconcilable, more than one value are listed. Measurements of ρ_0 and $\mathrm{d}(\rho_0)/\mathrm{d}T$ for liquid Sc, Y, and the heavy lanthanides are particularly difficult, and much of the available data is due to the substantial work of Kononenko and his co-workers (Kononenko et al. 1984). Unfortunately, the "sessile drop" method they have employed, while being a method of choice for their surface tension studies, is subject to uncertainties in ρ_0 of about $\pm 2\%$ at higher temperatures (Crawley 1974). Moreover, this method may provide values of $\mathrm{d}(\rho_0)/\mathrm{d}T$ which are up to $3\times$ too large in magnitude, as can be seen in cases in which data from other methods are also available for comparison. (See Kononenko et al. 1984, Seerveld et al. 1983, and Wittenberg et al. 1963, for example.)

TABLE 1
Best estimates, from the literature, of experimental values of density, ρ_0, and $d(\rho_0)/dT$, of the liquid R's at their respective melting temperatures. Data from the references cited were used in making these estimates.

	ρ_0 (gm/cm^3)		$\frac{d(\rho_0)}{dT} \times 10^3$ (gm/cm^3 °C)	
Sc	2.80 ± 0.10	B, C, L	−0.5 ± 0.3	L
Y	4.24 ± 0.06	L	−0.25 ± 0.10	L
La	5.96 ± 0.01	B, C, E, L, M	−0.33 ± 0.10	B, E, L, M
Ce	6.68 ± 0.01	B, C, D, E, G L, M	−0.23 ± 0.05	B, D, E, G L, M
Pr	6.59 ± 0.05	B, E, L, M	−0.4 ± 0.2	E, L, M
Nd	6.72 ± 0.05	D, H, L, M	−0.7 ± 0.2	D, H, L, M
Sm	7.16 ± 0.10	L	−0.7 ± 0.2	L
Eu	4.87 ± 0.20	B, C, L	−0.24	B, C
			−2.8	L
Gd	7.4 ± 0.3	B, C, K, L	−0.6 ± 0.2	K, L
Tb	7.65 ± 0.20	B, C, L	−0.48	[9] in L
			−1.4	L
Dy	8.2 ± 0.2	H, L	−1.4	L
Ho	8.34 ± 0.15	H, L, [6] in L	−0.4	[6] in L
			−1.5	L
Er	8.6 ± 0.2	H, L	−1.6	L
Tm	—		—	
Yb	6.21 ± 0.03	A, B, C, J, L	−1.06 ± 0.15	A, B, C, J, L
Lu	9.3 ± 0.2	H, L	−2.0	L

(A) – Seerveld et al. (1983)
(B) – Quoted by Waseda and Tamaki (1977b)
(C) – Quoted by Waseda (1977)
(D) – Rohr (1966)
(E) – Wittenberg et al. (1963)
(F) – Crawley (1974)
(G) – Perkins et al. (1965)
(H) – Waseda and Miller (1978)
(I) – Lundin et al. (1965)
(J) – Stankus and Basin (1983)
(K) – Stankus et al. (1981)
(L) – Kononenko et al. (1984)
(M) – Kononenko et al. (1980)
[*i*] – *i*-th reference in article quoted

Some of these data must therefore be used carefully, until corroborating data are available.

The densities of the liquid lanthanides, at their respective melting temperatures, are shown as a function of atomic number in fig. 1. With the exception of the divalent liquid metals, Eu and Yb, the densities are seen to increase linearly with Z. It is also notable that the density increases at approximately twice the rate that the atomic weight increases, implying a contraction of the atomic core with increasing Z; this has been called the "lanthanide contraction".

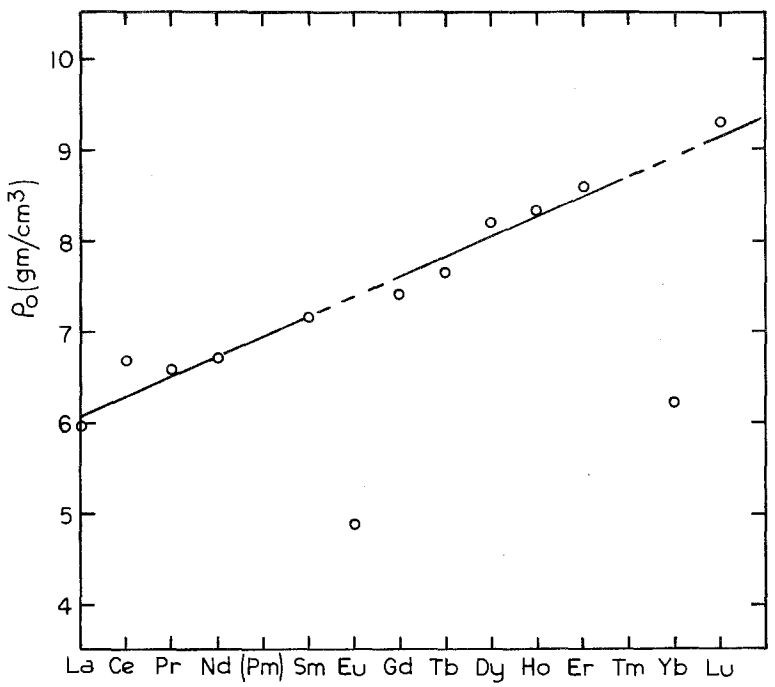

Fig. 1. Density, ρ_0, of the liquid lanthanides at their respective melting temperatures. Data are from table 1.

Kononenko et al. (1984) note that the change in density with melting is rather small for the R's, ranging from about -1.2% to about -1.5%. An interesting exception to this appears to be Ce, which exhibits an *increase* in density of about 0.4 to 0.6% upon melting. (See Wittenberg et al. 1963, Wittenberg and De Witt 1973, and Perkins et al. 1965.) This behavior may be related to a nearby electronic transition that has been induced in solid Ce by increasing temperature and pressure, and by alloying. This property is shared with the actinide Pu, which has the same solid structure as Ce, and perhaps with Bi as well.

The measured values of $\rho_0(T)$ for a large number of pure liquid metals, as analyzed by either of two semiempirical methods, separate these liquids into two distinct classes. (See Steinberg 1974, Grosse 1961, McGonigal 1962, and Hiemstra et al. 1977.) One class, having substantially smaller values of $\mathrm{d}(\rho_0)/\mathrm{d}T$, is made up of the Group IIA and IIB liquid metals; i.e. the divalent liquids. The other class, with larger $\mathrm{d}(\rho_0)/\mathrm{d}T$, includes a wide variety of non-divalent liquid elements. It is clear that the densities of the divalent R's, Eu and Yb, do not follow the trend established by the trivalent lanthanides (see fig. 1); the measured $\mathrm{d}(\rho_0)/\mathrm{d}T$ for liquid Yb does *not*, however, place it into the class of divalent liquid metals, but rather into the class of metals with larger values of $\mathrm{d}(\rho_0)/\mathrm{d}T$. So at least in this respect, Yb does not appear to belong to the class of divalent liquid metals. The remaining liquid R's have not yet been analyzed in this way, although

it has been commented that $d(\rho_0)/dT$ appears to be unusually small for liquid La, Ce and Pr (Wittenberg et al. 1963). X-ray diffraction data also imply a rather small temperature dependence, $d(\rho_0)/dT$, for these liquids; some care must be exercised in interpreting this observation, however, as this method also noted a very small temperature dependence for liquid Yb, whereas direct density measurements do not imply this. (Waseda and Tamaki 1977b, and Seerveld et al. 1983.)

Only minimal data have been reported on the density of liquid alloys containing R metals. Measurements of ρ_0 for the R–R alloy Pr–Nd indicate this to be an ideal substitutional alloy, one obeying Vegard's Rule:

$$\rho_0 = \rho_{01}c + \rho_{02}(1-c)\,, \tag{1}$$

where the ρ_{0i} is the density of the pure liquid constituent i, and c is the atomic fraction of species 1. (Lundin et al. 1965.) Measurements of the densities of liquid alloys of Ce–M, where M = Co, Cu, Mn or Ni, show significant deviations from ideality (in the case of CoCe, exceeding 10%), both positive and negative. (See Perkins et al. 1965.)

2.2. *Liquid structure*

Although a liquid metal can be considered to be a random assembly of ions, the fact that the density of such a metal changes little upon melting implies that the packing characteristics of the solid survive into the liquid, and impose a mean nonuniform short-range distribution on the liquid. This distribution can be described, for a pure liquid metal, in terms of the mean number, $n(r)\,dV$, of ions to be found in volume element dV at $\boldsymbol{r}$, given that an ion also resides at $\boldsymbol{r} = 0$. The pair distribution function, $g(r)$, is then given by

$$n(r) = n_0 g(r)\,, \tag{2}$$

where n_0 is the mean number density of ions. Also in common use is the radial distribution function, RDF, where

$$\mathrm{RDF} \equiv 4\pi r^2 n_0 g(r)\,. \tag{3}$$

$(\mathrm{RDF})dr$ is then the mean number of ions located in the spherical shell between r and $r + dr$. The number, N_n, of nearest neighbor ions to a given ion, is then

$$N_n = \int_{r_1}^{r_2} (\mathrm{RDF})\,dr\,, \tag{4}$$

where $r_1 < r < r_2$ spans the first peak in the RDF. Close packing implies $N_n = 12$.

The structure factor, $A(K)$, is more accessible experimentally, and is also

directly useful in studies of several other properties of liquid metals. $A(K)$ is given in terms of $g(r)$ as a Fourier transform:

$$[A(K)-1]=\frac{4\pi n_0}{K}\int_0^\infty [g(r)-1]r\sin Kr\,\mathrm{d}r\,, \tag{5}$$

which can be inverted to yield:

$$[g(r)-1]=\frac{1}{2\pi^2 n_0 r}\int_0^\infty [A(K)-1]K\sin Kr\,\mathrm{d}K\,. \tag{6}$$

K is the wave vector associated with momentum transfer. Thus, in principle at least, measurements of $A(K)$ can be used to determine $g(r)$; in practice, however, this is more difficult, since one cannot measure $A(K)$ to arbitrarily large values of K, and truncation errors must enter the integration, equation (6).

The structure of binary alloys can be handled similarly; the partial structure factor, $A_{ab}(K)$, and the partial pair distribution function, $g_{ab}(r)$, are related by:

$$[A_{ab}(K)-1]=\frac{4\pi n_0}{K}\int_0^\infty [g_{ab}(r)-1]r\sin Kr\,\mathrm{d}r\,. \tag{7}$$

Here $g_{ab}(r)$ is a measure of the distribution of type "b" ions about a central "a" ion. ("a" and "b" are dummy indices.) Three partial structure factors are needed: $A_{aa}(K)$, $A_{bb}(K)$ and $A_{ab}(K)$.

At least in the case of liquid simple metals, a knowledge of the effective pair potentials describing the interaction between the ions in the liquid metal can also be utilized to calculate $g(r)$ and $A(K)$. The most common such method involves the assumption of a hard-sphere potential in the Percus–Yevick (PY) equation; its solution provides the hard-sphere structure factor, $A_{HS}(K)$. (See Ashcroft and Lekner 1966.) The two parameters that must be provided for a calculation of $A_{HS}(K)$ are the hard-sphere diameter, σ, and the packing fraction, x. It is found that $x\simeq 0.45$ for most liquid metals at temperatures just above their melting points. A hard-sphere solution of the PY equation has also been obtained for binary liquid metal alloys, and provides estimates of the three partial structure factors describing the alloy structure (Ashcroft and Langreth 1967). To the extent that the hard-sphere approximation appears to be valid for the liquid R's, pair potentials should dominate these metals also, at least at short distances.

Excellent general reviews of liquid structure exist; the reader interested in a more thorough introduction is referred to them. (Waseda 1980, Shimoji 1977, and Enderby 1985). For a discussion of structure and forces in liquid metals, see March (1985).

Measurements of $A(K)$ for pure liquid metals are readily made by X-ray diffraction and neutron-diffraction techniques. The only direct determinations of

the partial structure factors, $A_{ab}(K)$, for any binary liquid alloys, to-date, have been made by isotopic enrichment, utilizing neutron-diffraction methods.

A summary of experimental data for $A(K)$ and of calculations of $g(r)$ for the liquid R's are shown in table 2. Best estimates of the positions of the first two peaks in $A(K)$ as well as the nearest neighbor separation, r_1 are shown. In those cases in which several groups have measured $A(K)$ for a given liquid, the positions of the first peak, $K_p^{(1)}$, agree well. The Saclay group, using neutron diffraction methods, did not to observe any oscillations in $A(K)$ beyond $K_p^{(1)}$, for liquid La, Ce, and Pr. (Breuil and Tourand 1969, and Bellissent and Tourand 1975). Other groups, however, using neutron diffraction (Rudin et al. 1977, Enderby and Nguyen 1975) and X-ray diffraction (Waseda and Tamaki 1977b, Waseda and Miller 1978) techniques did see oscillations at larger K, and agree rather well on the peak positions. It is assumed that oscillations at higher K do exist; the reason for the Saclay group's failure to observe them is not known.

TABLE 2

Experimental data from the literature on the static structure factor, $A(K)$, for the liquid R's near their melting points. $K_p^{(i)}$ is the position of the i-th peak in $A(K)$, and r_1 is the nearest neighbor separation, derived from the structure data. Data from the references cited were used in assembling the Table. "X" indicates that X-ray diffraction and "n" that neutron diffraction techniques were used.

	$K_p^{(1)}$ (Å^{-1})		$K_p^{(2)}$ (Å^{-1})		r_1 (Å)	
Sc	2.49	X – B, F	4.84	X – B, F	2.96	X – B, F
Y	—		—		—	
La	2.08 ± 0.01	X – B, F n – A, C, E	3.84 ± 0.10	X – B, F n – E	3.77 ± 0.10	X – B, F
Ce	2.14 ± 0.01	X – B, F n – C, D, E	3.97 ± 0.10	X – B, F n – E	3.57 ± 0.15	X – B, F n – D
Pr	2.11 ± 0.01	X – B, F n – D, E	4.04 ± 0.10	X – B, F n – E	3.58 ± 0.15	X – B, F n – D
Nd	2.10 ± 0.01	X – G n – E	4.04 ± 0.10	X – G n – E	3.45	X – G
Sm	—		—		—	
Eu	1.87	X – B, F	3.75	X – B, F	3.93	X – B, F
Gd	2.07	X – B, F	3.93	X – B, F	3.59	X – B, F
Tb	2.08	X – B, F	3.97	X – B, F	3.56	X – B, F
Dy	2.12	X – G	4.03	X – G	3.43	X – G
Ho	2.21	X – G	4.35	X – G	3.32	X – G
Er	2.24	X – G	4.38	X – G	3.28	X – G
Tm	—		—		—	
Yb	2.01 ± 0.01	X – B, F n – E	3.75	X – B, F	3.75	X – B, F
Lu	2.28	X – G	4.43	X – G	3.22	X – G

(A) Breuil and Tourand (1969)
(B) Waseda and Tamaki (1977b)
(C) Enderby and Nguyen (1975)
(D) Bellissant and Tourand (1975)
(E) Rudin et al. (1977)
(F) Waseda (1977)
(G) Waseda and Miller (1978)

In each case, the first peak in $A(K)$ is very nearly symmetric; the oscillations in $A(K)$ for $K > K_p^{(1)}$ are also consistent with a hard-sphere liquid model. (See fig. 2.) It does appear, however, that the hard-sphere approximation improves as one moves across the lanthanide series from La to Lu. The more rapid damping of the oscillations in $A(K)$ for the light R's implies a somewhat softer core (Waseda and Tamaki 1977b, Waseda and Miller 1978) (fig. 2). Rao and Sitpathy (1981) see this directly in their calculations of the effective interionic potentials, $\phi(r)$, where they use the $A(K)$ data of Waseda and co-workers. Fits of the experimental $A(K)$ to $A_{HS}(K)$ imply that the packing fraction, x, lies in the range of 0.42–0.43 for most R's; the range extends to 0.40–0.44 for some of the heavy R's, however.

The effect of changing temperature on $A(K)$ is shown schematically in fig. 3. The general effect of increasing temperature is to reduce the sharpness in the structure in $A(K)$, broadening and lowering the peaks. This temperature dependence of $A(K)$ is a leading contributor to the temperature dependence of several other properties of these liquid metals, and will be discussed in more detail in conjunction with them.

A direct relationship exists, also, between $A(K)$ at $K = 0$ and the isothermal compressibility, κ_T:

$$A(0) = n_0 k_B T \kappa_T \,, \tag{8}$$

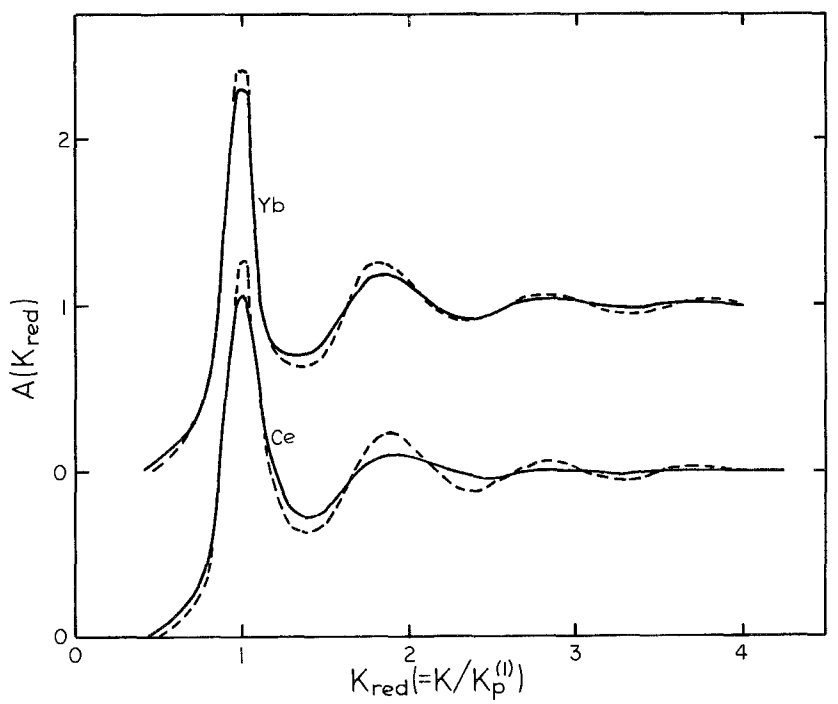

Fig. 2. The structure factors, $A(K_{red})$, for liquid Ce and Yb just above their respective melting temperatures. —— data from Waseda (1980), and Waseda and Tamaki (1977b); – – – $A_{HS}(K_{red})$ with $x = 0.43$.

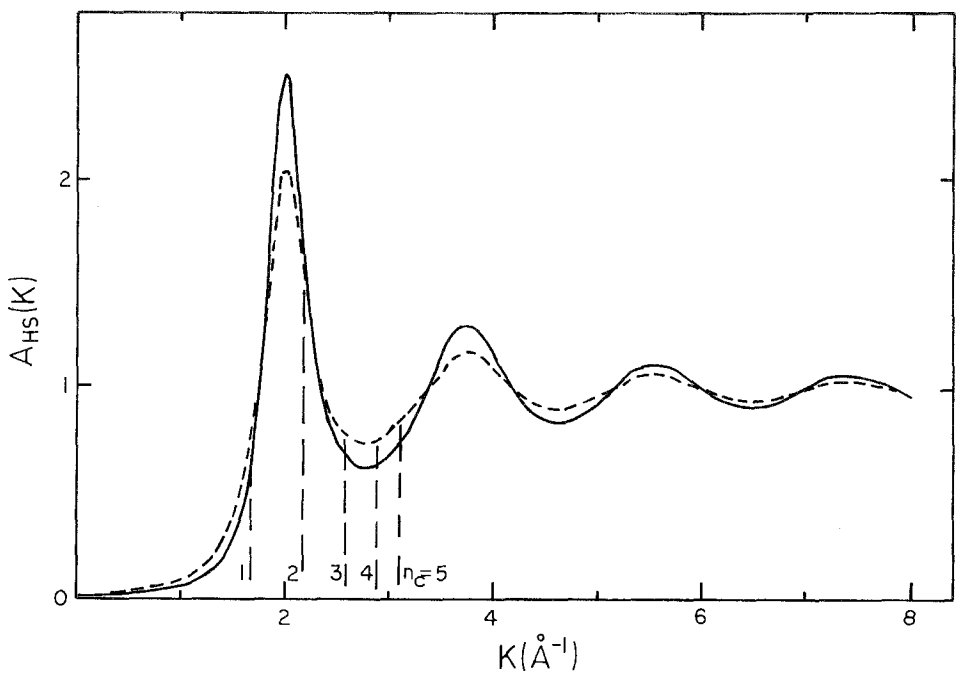

Fig. 3. Typical dependence of $A(K)$ upon temperature is indicated. —— $A_{HS}(K)$ at T_{mp}; - - - - $A_{HS}(K)$ at $T > T_{mp}$. The values of $K = 2k_f$ corresponding to the number of conduction electrons per ion, n_c, are also shown, with n_c ranging from 1 to 5.

where k_B is Boltzmann's constant, and T is absolute temperature. In a HS approximation, $A(0)$ depends only upon x; in the case of the PY equation, the form is:

$$A(0) = \frac{(1-x)^4}{(1+2x)^2} \,. \tag{9}$$

Here $x = 0.45$ gives a value $A(0) = 0.025$. κ_T, in this approximation, is then a function of $x(T)$, T, and $n_0(T)$. McAlister and Crozier (1981) have recently measured the velocity of sound, v_s, in liquid La, Ce, Pr, and Yb, and in Ce–10% Yb alloy, and have obtained a measure of κ_T from these data. (See table 3.) These data agree rather well with calculations of κ_T based on $A_{HS}(0)$; the agreement is improved further by incorporation of nearly free electron effects into the HS model. The anomalous sign of $(\partial v_s/\partial T)_P$ for liquid Ce may be associated with increasing delocalization of the 4f electron with increasing temperature; this will be discussed in more detail later (see sections 3.2. and 3.3.).

Estimates of the partial structure factors, $A_{ab}(K)$, have been obtained for the liquid alloys Ce–M (where M = Co, Cu, or Ni) by a combination of X-ray scattering techniques (Waseda and Toguri 1978, Waseda and Tamaki 1977a). These results can be summarized as follows: $A_{MM}(K)$, near $K_P^{(1)}$, is independent

TABLE 3
Data for the velocity of sound, v_s, for $(\partial v_s/\partial T)_P$, and for the isothermal compressibility, κ_T, for several liquid R's at their melting points. (Data from McAlister and Crozier 1981)

Metal	v_s (m/s)	$(\partial v_s/\partial T)_P$ (m/s·K)	κ_T (10^{-11}m^2/N)
La	2023 ± 5	−0.078 ± 0.004	4.24
Ce	1693 ± 4	+0.177 ± 0.005	5.30
Pr	1925 ± 5	−0.084 ± 0.007	4.17
Yb	1274 ± 7	−0.198 ± 0.003	11.69
Ce–10% Yb	1681 ± 5	+0.129 ± 0.005	—

of concentration, c; $K_P^{(1)}$ for $A_{CeM}(K)$ lies between that for $A_{CeCe}(K)$ and $A_{MM}(K)$ for all concentrations; and there is a shift of about 10% in $K_P^{(1)}$ for $A_{CeCe}(K)$ for the CeCo alloy, at about 60 atom% Co. This shift is also seen, (but is smaller in magnitude) at about 70 atom% Ni in the CeNi alloy, but is not seen in CeCu alloys. Anomalous behavior is observed at about the same concentrations in the magnetic susceptibility, χ, for CeCo and CeNi (Schlapbach 1974). It is suggested that this behavior results from a change in the electronic structure due to promotion of 4f electrons into a partially filled 3d band; this effect would not be seen in CeCu, since the d-band is filled for Cu. It is also noteworthy that the densities, $\rho_0(c)$, of both CeCo and CeNi show positive deviations from linearity, whereas the density of liquid CeCu is less than that predicted by Vegard's Rule (Perkins et al. 1965).

2.3. *Surface tension*

A discussion of the surface tension, γ, of the liquid R's must involve a discussion of mechanical, thermodynamic, and electronic properties. Nonetheless, we include it at this point in our review.

For a pure liquid metal, we may write the excess surface energy, E^s, of the liquid metal–vapor interface, as

$$E^s = F^s + TS^s , \tag{10}$$

where F^s is the surface Helmholtz free energy, and S^s is the excess surface entropy. We can write E^s in terms of γ;

$$E^s = A\left(\gamma - T\,\frac{\partial \gamma}{\partial T}\right), \tag{11}$$

where

$$\gamma = F^s/A , \tag{12}$$

and

$$S^s/A = -T\,\frac{d\gamma}{\partial T}\,. \tag{13}$$

Here A is the surface area; eq. (11) is called the Gibbs–Helmholtz equation. Thus it is possible to estimate E^s and the excess surface entropy per unit area, S^s/A, from a measurement of $\gamma(T)$.

Consistent with the recognition that the liquid–vapor surface vanishes as T approaches the critical temperature, T_c, implying that $\gamma \to 0$ as $T \to T_c$, we have Eötvos Law:

$$\gamma\Omega^{2/3} = k(T_c - T)\,, \tag{14}$$

where Ω is the molar volume, and k is a constant, about equal to 0.64 erg K^{-1} for many liquid metals (Grosse 1962). From eq. (14), we have:

$$\frac{d\gamma}{dT} = -n\,\frac{\gamma}{T_c - T}\,, \tag{15}$$

where

$$n \equiv 1 + \frac{2(T_c - T)}{3\Omega}\,\frac{d\Omega}{dT}\,. \tag{16}$$

One expects, therefore, to see $n \gtrsim 1$, since $d\Omega/dT > 0$ ($n \cong 1.27$ for many liquid metals at their melting temperatures (Tosi 1985), and $d\gamma/dT < 0$. Equations (14, 16) are completely equivalent to the common expression

$$\gamma = \gamma_0[1 - T/T_c]^n\,. \tag{17}$$

If one further takes the estimate, also from Grosse (1962)

$$T_c \cong 6.6\,T_{mp}\,, \tag{18}$$

eq. (14) becomes

$$\gamma \cong k' T_{mp} \Omega^{-2/3}\,, \tag{19}$$

where $k' \cong 3.6$ erg K^{-1}. Here T_{mp} is the melting temperature.

Values of γ for liquid metals tend to be about an order of magnitude larger than for nonmetallic liquids. This is true also for the liquid R's.

Measurements of γ and $d\gamma/dT$ have been reported for all of the liquid R's except T_m. These data are summarized in table 4 and fig. 4. Much of the data, especially for the heavy R's, Sc, and Y, are due to the work of Kononenko and his co-workers. (See Kononenko et al. 1980, 1984.) In most cases (including

TABLE 4
Best estimates, from the literature, of the surface tension, γ, and of $d\gamma/dT$, for the liquid R's just above their melting temperatures. Data from the references cited were used in making these estimates.

	γ (dynes/cm)		$\frac{d\gamma}{dT}\left(10^{-2}\frac{\text{dynes}}{\text{cm°C}}\right)$	
Sc	954 ± 15	C, [4]	−12.4	C
Y	871 ± 15	C, [4]	− 8.6	C
La	718 ± 10	A, B, C, E, [5]	−15	B, C, E
Ce	706 ± 10	A, B, C, E	− 4	B, C, E
Pr	707 ± 15	C, E, [5]	− 7.3	C, E
Nd	687 ± 15	C, D, E	− 7	C, E
Sm	431	C	− 7.2	C
Eu	264	C	− 5.0	C
Gd	664	C	− 5.8	C
	810	D		
Tb	669	C	− 5.6	C
	840	[5]		
Dy	648	C	−13.1	C
Ho	650	C	−12.3	C
Er	637	C	−12.1	C
Tm	—		—	
Yb	320	C	−10.3	C
Lu	940	C	− 7.3	C

References:
(A) Pulliam and Fitzsimmons (1955)
(B) Wittenberg et al. (1963)
(C) Kononenko et al. (1984)
(D) Allen (1972)
(E) Kononenko et al. (1980)
[*i*] reference "*i*" in (C)

Kononenko) a sessile drop method has been employed; "drop weight" and "maximum bubble pressure" techniques have also been used for Gd and Nd, respectively. Because impurities, especially non-metallic impurities, tend to accumulate at the liquid–vapor surface and lower γ, one tends to treat larger values of measured γ as being more nearly characteristic of the pure liquid, in cases in which multiple measurements for a given metal do not agree. It is possible that this may not be the case for the data in table 4 for Gd and Tb. The smaller values are consistent with data for other R's. (See fig. 4.) We should note that Kononenko et al. (1984) used Ta substrates for all of their measurements, except for liquid Sc and Y; for these two liquid metals W substrates were used. Moreover, the solubility of Ta and W in the liquid R's may be as large as 2–3 atomic % at the R-metal melting temperatures (see Dennison et al. 1966a, 1966b). The two metals for which the measured γ's are greatest, Sc and Lu, are also those for which the solubility of Ta and W are largest. It is possible that the introduction of Ta or W from the substrates into these samples may have contributed to the large values of γ that were observed. On the other hand, there

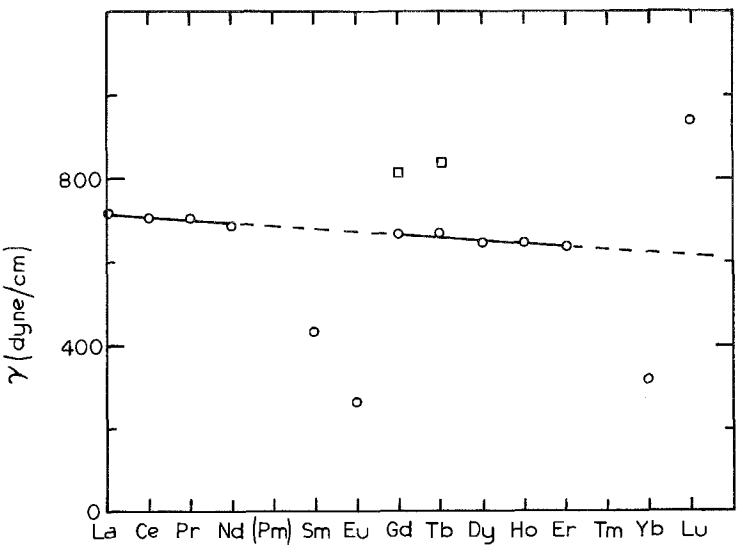

Fig. 4. The surface tension, γ, for the liquid lanthanides just above their respective melting temperatures. Data are from table 4.

is no clear relationship between the magnitude of γ and the solubility of Ta for the other liquid lanthanides. In general, an uncertainty of $\pm 5\%$ to $\pm 10\%$ should probably be assigned to measurements of γ and $\pm 50\%$ to measurements of $d\gamma/dT$ (Allen 1972). Unless otherwise noted, these uncertainties should be assigned to values in table 4. It has also been noted that measurements of $d\rho_0/dT$ by the sessile drop method tend to carry larger uncertainties than measurements via some other methods; the use of these data in determining $d\gamma/dT$ in table 4 brings an added measure of uncertainty to $d\gamma/dT$.

Kononenko et al. (1984) have used eq. (19) to analyze the data on γ for the liquid R's. They find that the R's are divided by this analysis into three groups; in each case, k' is less than 3.6 erg K^{-1} (eq. 19). One group contains Sc, Y, and Lu. These liquids may be considered transition metals in this regard, having either no f-electrons, or a filled f-band. A second group contains the trivalent lanthanides, except Sm, and the third group is made up of Sm, Eu, and Yb. This last group contains the divalent R's; it is suggested that the appearance of Sm in this group implies that the surface of liquid Sm is divalent, whereas the bulk remains trivalent in character. Additional evidence, both experimental and theoretical, also supports this suggestion. (Johansson and Mårtensson 1987). While earlier X-ray photoemission (XPS) studies could be interpreted as indicating an intermediate valence state both for the bulk and for the surface, more recent XPS, uv photoemission (UPS), and electron energy loss spectroscopy (EELS) studies rather clearly show a divalent surface for Sm. Moreover, a semiempirical theoretical treatment of the surface energy indicates that a divalent surface appears to be energetically preferred. (Johansson and Mårtensson 1987). Moreover, Sm appears to be unique in this respect, being the only element for which the surface is

divalent and the bulk trivalent. (See also fig. 4.) The analysis of the γ's for the trivalent lanthanide group is entirely consistent with eq. (19), except that the lanthanide contraction appears to have significant effect, resulting in $k' < 0$ actually.

Several attempts have been made to place the understanding of the surface energy (and γ) for liquid metals on a firm theoretical basis. Such a development must go beyond viewing excess surface energy as resulting from the breaking of ion–ion pair-wise bonds for ions at the surface, and must take explicit account of the metallic electrons as well. Lang and Kohn (1970) have applied psuedopotential methods to a study of the surface energy of solid metals, replacing the jellium model (constant positive background) of the metal with a lattice of pseudopotentials at the ion sites. Although the jellium model appears to do rather well in providing an estimate of the variation of the electron density across the surface, a full calculation of the surface energy in this model fails for metals with higher mean electron densities. Incorporation of the lattice of pseudopotentials (using the simple Ashcroft empty-core pseudopotential model) greatly improves the agreement with theory in the region where the jellium model breaks down. Evans (1974) complements the work of Lang and Kohn in developing a statistical–mechanical theory of the surface tension, specifically for liquid metals. In this formulation, Evans, assuming the bulk metal to be an assembly of pseudoatoms, finds that the electron and ion density profiles at the surface contribute substantially to γ. Shimoji, however, warns that care must be taken to ensure that the variation of electron density at the surface does not seriously compromise the use of the pseudopotential approach (Shimoji 1977). More recently, Hasegawa (1988) has coupled a semi-empirical approach to the screening effect with a first-order theory of the electron–ion interaction, to calculate successfully the surface density profile, and subsequently the surface tension, of a number of liquid simple metals.

Kononenko (1983) also uses a combination of pseudopotential theory and a variational method to calculate E^s specifically for the liquid lanthanide metals. These values are then compared with E^s obtained from measurements of γ and $d\gamma/dT$ (eq. 11) for these liquids. The trends in the measured E^s are reproduced by the calculated values, except for Sm, for which a transition of a small fraction of ions to the divalent state may have substantial effects not addressed in the calculations.

2.4. *Viscosity*

Only a few data exist for the shear viscosity, η, of the liquid R's. Those data which are available are summarized in table 5. It is noteworthy that measured values of η for these liquid R's are large when compared to values for most liquid non-transition metals; these range from about 0.5 to 2.5 centipoise at the melting temperature. All of the measurements on the R's were made utilizing an oscillating cup viscometer.

A theoretical understanding of η for liquid metals, while not yet fully satisfying,

TABLE 5
Experimental data for the viscosities, η, of the liquid R's at their melting temperatures.

Metal	η (centipoise)	references
La	2.65	A, B
	3.27	C
Ce	3.20	A, B
Pr	2.85	A, B
Yb	2.67	B

References:
(A) – Wittenberg et al. (1963)
(B) – Wittenberg and De Witt (1973)
(C) – Frohberg and Cakici (1978)

has progressed substantially in the last two decades. A good view of the theoretical picture as of 1972 is given in Faber (1972). Summaries of more recent advances can be found in Shimoji (1977) and Waseda (1980), and references therein. Only a few comments will be made here.

Early calculations of viscosity (and also of self-diffusion, D) of liquid metals employed the concept of an activation energy; experimental data were often compared to Andrade's Equation,

$$\eta = \eta_0 \, e^{E_v/RT} , \tag{20}$$

where E_v is the activation energy, and R is the universal gas constant. It now appears from experiments over a broader range in T that agreement with eq. (20) is the exception rather than the rule; molecular dynamics calculations also fail to support the idea of an activated process for η and D.

A hard-sphere model for D and η has been quite successful, especially as corrected for back-scattering, and where possible utilizing the results of molecular dynamics calculations (Faber 1972, Wittenberg and De Witt 1973, Ascarelli and Paskin 1968, Vadovic and Colver 1970, 1971). In each case one finds

$$\eta \sim (MT_{mp})^{1/2} \Omega^{-2/3} , \tag{21}$$

where M is the gram-atomic weight, and Ω is the molar volume. Recent attempts to include more realistic interionic potentials add a soft attractive long-range term to the hard repulsive term in the potential. Interestingly, it is suggested that the contributions of the soft term in the potential may actually be dominant both for η and for D (Waseda 1980), raising some questions about the apparent success of the hard-sphere approximation. In many cases, however, inclusion of the soft term has not improved comparison with experiment over the hard-spheres calculations. Analysis of η for a few R's was also done by Wittenberg and De Witt (1973), based on a hard-sphere model of diffusion, and using a result from molecular dynamics. Comparison with experiment was good, with deviations ranging from less than 7% (for La, Pr, and Yb) to 17% for Ce.

3. Electronic structure and magnetic properties

3.1. *Photoemission studies*

The electronic structure of the R metals is dominated by an s-band and a nearly empty d-band at the Fermi energy, E_f, and, for the lanthanides, a progressively filling narrow 4f band below E_f. Moreover, spin–orbit coupling has split this 4f level into two sublevels. X-ray (XPS) and uv photoemission studies have provided the best experimental picture of this structure. (X-ray studies have actually been more useful, because the oscillator strength for excitations of 4f electrons by X-rays is much greater than by uv light, making the 4f levels easily visible.) The filled 4f level in Yb is shown in fig. 5; the splitting of about 1.3 eV between the two sublevels is easily visible. Moreover, these peaks are well separated from one another and from E_f, since nearly all of the apparent line-width is due to instrumental broadening. (This spectrometer broadening is estimated to be 1.6 eV.) The spectra of La and Nd are shown in fig. 6. In both cases, the feature just below E_f has been identified as the 5d level; the lower 4f sublevel is about 4.8 eV below E_f for Nd, and no 4f level is seen in La. (The structure below −5 eV in La is from the 5p electrons.) Both figures show XPS results obtained on thin solid films of these metals. It is expected, however, that structures similar to these are also characteristic of the liquid R's. It is noteworthy that (except for Eu and Yb) the 4f level moves farther below E_f as the number of 4f electrons increases (Hedén et al. 1971). For those liquid metals for which the 4f level is far below E_f,

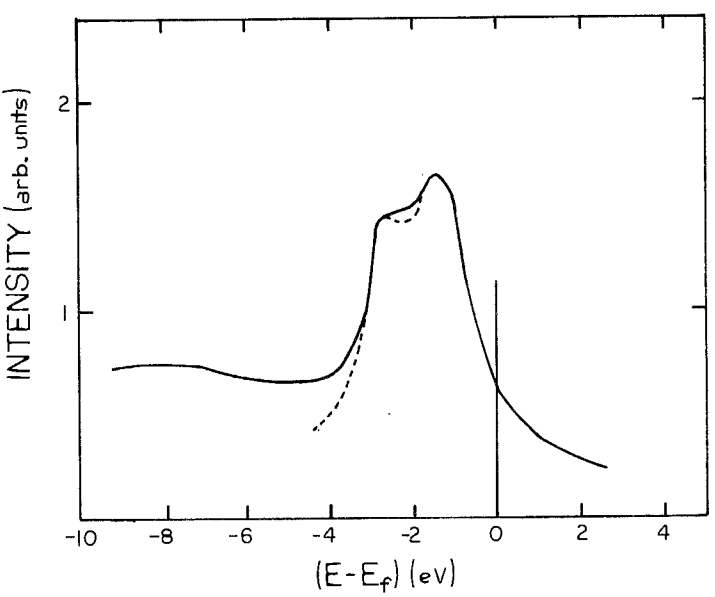

Fig. 5. X-ray photoemission spectrum for an Yb thin film. —— experimental data; – – – a fit to two Lorentzian curves, separated in energy by 1.30 eV. Data from Hagstrom et al. (1970).

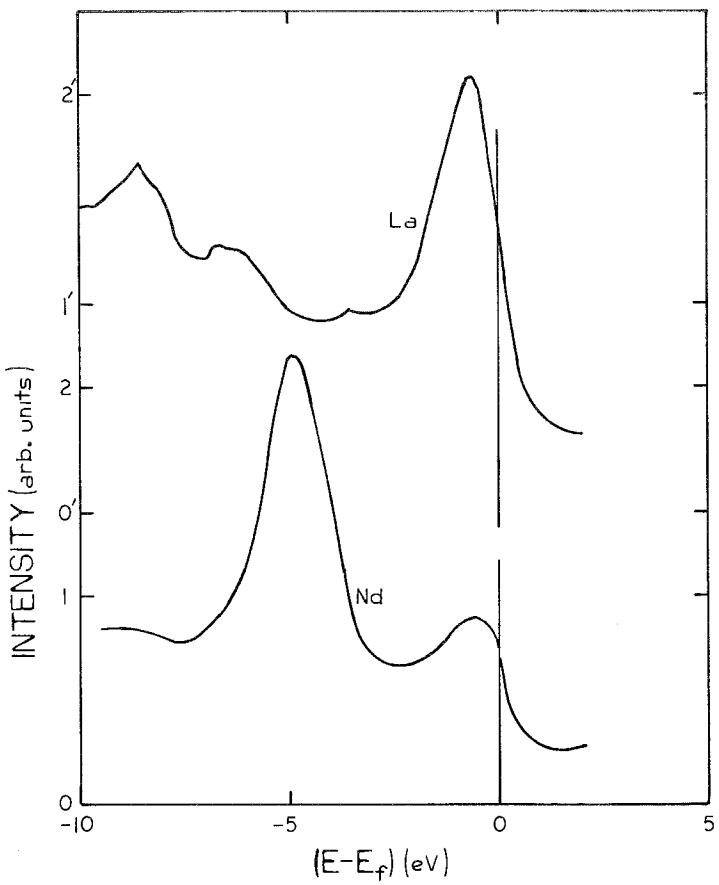

Fig. 6. X-ray photoemission spectra for La and Nd thin films. Data from Baer and Busch (1973).

the properties that depend on the 4f electrons can be described well by an ionic model; these have been called "normal". For those liquid R's for which the 4f level is near E_f, the interaction between the 4f electrons and the conduction electrons is often important; these R's have been called "anomalous". These metals tend to be the light R's.

3.2. *Magnetic susceptibility*

The total magnetic susceptibility, χ_A, of a pure liquid normal metal can be given as

$$\chi_A = \chi_{ion} + \chi_e + \chi_n \,. \tag{22}$$

(Throughout this discussion, we will use units of emu/mole for χ). Here χ_{ion} is the diamagnetic contribution due to the filled ion core states, χ_e is the contribu-

tion due to conduction electrons, and χ_n is the contribution of the atomic nuclei. χ_n is small, except at resonance, and will be neglected here. χ_{ion} can be obtained by calculation, or by measurement of χ_A for the ion of interest in a nonconducting compound. The latter method assumes that χ_{ion} does not change significantly when the ion is taken from a nonconducting to a metallic environment. This assumption is useful and adequate under the circumstances. Ignoring second order effects, χ_e can be written as

$$\chi_e = \chi_p + \chi_d \,, \tag{23}$$

where χ_p is the Pauli spin paramagnetism, and χ_d is the Landau diamagnetism of the conduction electrons. Both χ_p and χ_d depend upon the electron density of states, $n(E)$, at E_f:

$$\chi_p \sim \mu_B^2 n(E_f) \,, \tag{24}$$

and, at least in the limit of free electrons,

$$\chi_{d0} = -(1/3)\chi_{p0} \,. \tag{25}$$

χ_p can be measured directly by conduction electron spin resonance (CESR) methods, and thus can provide a direct measure of $n(E_f)$; these methods are limited to the lighter elements, with weak spin–orbit coupling, however, and are not of value for the R's. For the transition and R metals, $\chi_{ion} \simeq -1 \times 10^{-5}$ emu/mole, and measurements on liquid noble and polyvalent metals suggest that $\chi_e \simeq +1 \times 10^{-5}$ emu/mole. (See Güntherodt and Meier 1973).

In the case of certain of the R metals, the presence of localized moments due to partially filled f-levels on each atom results in another contribution, χ_{4f}, to χ_A. Where this contribution is present, it is also dominant. To the extent that these 4f states are localized and highly-correlated, the metallic ions approximate free ionic configurations well, and the Van Vleck theory of paramagnetism (Van Vleck 1932) can be applied to such states of well-defined angular momentum. For a system of interacting moments, a Curie–Weiss-law temperature dependence is to be expected:

$$\chi_{4f} = \frac{C}{T - \theta} \,; \tag{26}$$

here T is the absolute temperature, θ is the Curie temperature, and C is the Curie constant. C can be written in terms of the effective magnetic moment, μ_{eff}, of this state, as

$$C = \frac{N_A \mu_{eff}^2}{3k_B} \,, \tag{27}$$

where N_A is Avogadro's number, and k_B is Boltzmann's constant. In these cases

in which a single 4f multiplet, characterized by total angular momentum, J, is populated,

$$\mu_{\text{eff}} = \mu_B g\sqrt{J(J+1)}\,, \tag{28}$$

where g is the Landé g-factor, and μ_B is the Bohr magneton. This appears to describe a number of the liquid R's, especially the heavy lanthanides. (See below, also.) (The interested reader is referred to Dupree and Seymour 1972, Schlapbach 1974, and Güntherodt and Meier 1973, for more extensive introductions to this topic.)

The magnetic susceptibilities of most of the liquid R's have been measured (table 6). It has been observed that χ_A changes very little upon melting for these metals. Minor exceptions to this include Ce with an increase, $\Delta\chi_A$, of about

TABLE 6

Best estimates of the measured total susceptibility, χ_A, of the liquid R's at their melting temperatures. Experimental values of $d\chi_A^{-1}/dT$ at the melting point are also shown; μ_{eff} is derived from $d\chi_A^{-1}/dT$ via eqs. (26) and (27). The values of μ_{eff}^{4f} (Van Vleck) are calculated for R^{3+} ions in the ground state of the lowest multiplet (Taylor and Darby 1972), except for Sm and Eu, for which eq. (29) was employed.(*) Data from the references cited were used in assembling the table. (An (S) implies that data was from the solid at the melting temperature.)

	$\chi_A \times 10^4 \left(\frac{\text{emu}}{\text{mole}}\right)$		$\frac{d\chi_A^{-1}}{dT} \times 10^2 \left(\frac{\text{mole}}{\text{emu}\cdot\text{K}}\right)$		$\mu_{\text{eff}}(\mu_B)$ (exp)	$\mu_{\text{eff}}^{4f}(\mu_B)$ (Van Vleck)
Sc	—		—			
Y	—		—			
La	1.20 ± 0.03	C, I, K	0.0	C, I, K	0	0
Ce	9.37 ± 0.05	A, C, G, H, I	41 ± 5	A, C, I	4.4	2.56
Pr	17.3 ± 0.2	D, I	21 ± 3	D, I	6.1	3.62
Nd	18.7	E	22	E	6.0	3.68
Sm	18.3	F, M(S)	−4.6	F		1.55*
Eu	97	G	13.4	G	7.7	3.40*
Gd	67 ± 2	J, L(S)	10.7 ± 0.2	J, L(S)	8.6	7.94
Tb	82 ± 2	J, L(S)	9.7 ± 0.2	J, L(S)	9.0	9.70
Dy	95	L(S)	7.2 ± 0.2	J, L(S), N	10.45	10.6
Ho	88	E(S)	7.0 ± 0.2	J, E(S)	10.6	10.6
Er	69	E(S)	8.4 ± 0.2	N, E(S)	9.65	9.6
Tm	41.0	O(S)	14.0 ± 0.2	N, O(S)	7.5	7.6
Yb	—		—			4.5
Lu	—		—			0

References:

(A) Busch et al. (1970b)
(B) Dupree and Seymour (1972)
(C) Burr and Ehara (1966)
(D) Arajs et al. (1961)
(E) Arajs and Miller (1960)
(F) Arajs (1960b)
(G) Colvin et al. (1961)
(H) Doriot et al. (1971)
(I) Schlapbach (1974)
(J) Müller et al. (1979)
(K) Güntherodt and Schlapbach (1971)
(L) Arajs and Colvin (1961)
(M) Vedernikov et al. (1975)
(N) Müller and Güntherodt (1980)
(O) Arajs (1960a)

2–3%; Gd, with $\Delta\chi_A \cong 2\%$; and Sm, with $\Delta\chi_a \cong 5\%$. The change, $\Delta\chi_A$, in Ce can be fully explained by the effect of the small change of volume on the f-electron paramagnetism via crystal field effects, and on changes in Pauli paramagnetism (Burr and Ehara 1966). There is no need to postulate a 4f to 5d electron promotion for Ce upon melting. (See also section 3.3.) Typical data for χ_A for the light R's are shown in fig. 7 (La and Ce), and for the heavy R's in fig. 8.

It is expected that liquid Sc, Y, La, and Lu should have similar magnetic properties. All should be trivalent, exhibit no 4f character, and show some effect of the d-level at the Fermi energy. [Some differences in χ_A have been noted for these metals, at least at low temperatures ($T < 300$ K). In particular, while χ_A for Y and Lu are similar, and weakly temperature-dependent, χ_A for Sc shows some Curie–Weiss behavior. (See McEwen 1978.)] χ_A for liquid La has been measured. It is temperature independent, and is characteristic of Pauli paramagnetism,

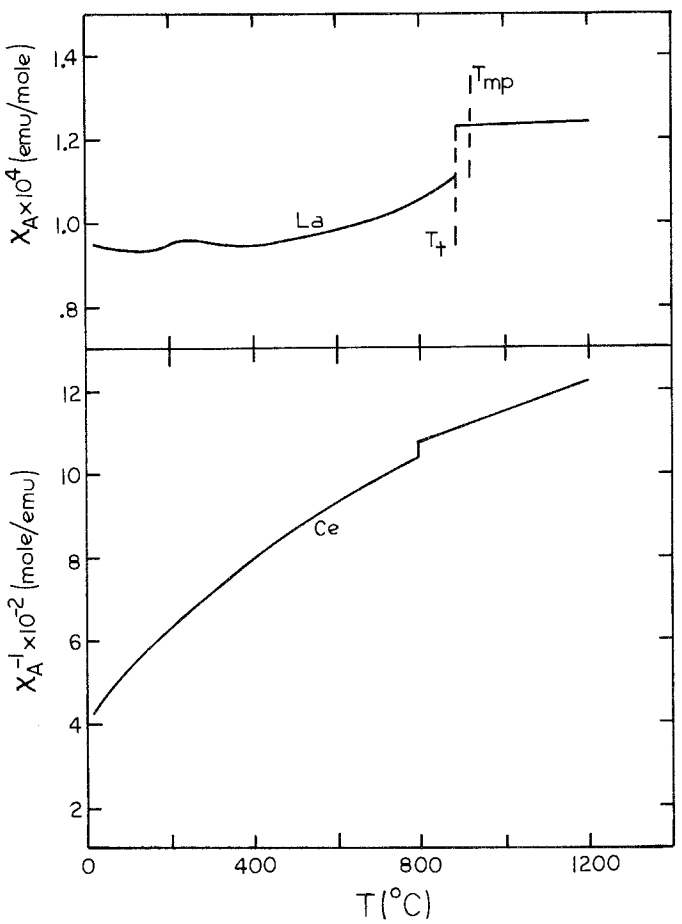

Fig. 7. The magnetic susceptibility, χ_A, for two of the light R's, La and Ce, as functions of temperature. (χ_A^{-1} is shown for Ce.) Data are from Schlapbach (1974).

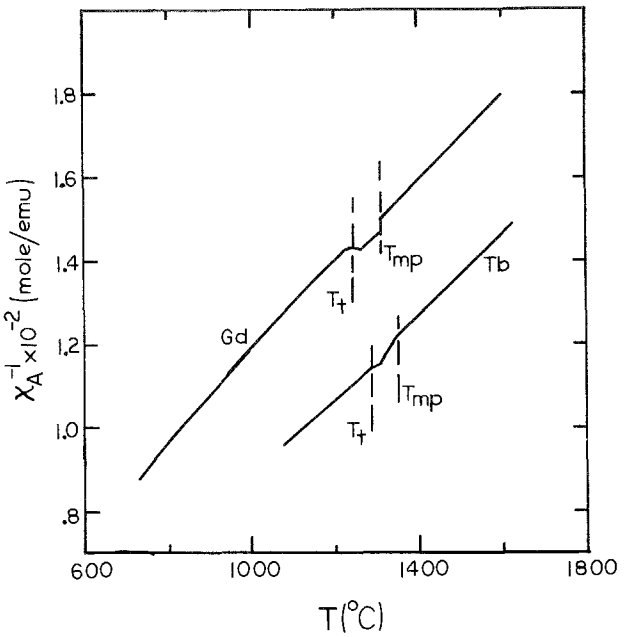

Fig. 8. The inverse of the magnetic susceptibility, χ_A^{-1}, for two heavy R's, Gd and Tb, as functions of temperature. Data are from Müller et al. (1979).

exchange enhanced by 10× above that for "normal" liquid metals. Some workers have made the reasonable assumption that $\chi_A(\text{Ce}) = \chi_A(\text{La}) + \chi_{4f}(\text{Ce})$, in order to extract $\chi_{4f}(\text{Ce})$ from a measurement of $\chi_A(\text{Ce})$. Arajs and Colvin (1961), studying Dy at high temperatures, attributed small deviations of χ_A from Van Vleck theory to conduction electron effects, and estimated $\chi_e \cong 1.9 \times 10^{-4}$ emu/mole, about the same magnitude as $\chi_A(\text{La})$. (See also Colvin et al. (1961), for χ_e for liquid Ce.) The magnetic properties of the R's, Ce through Yb, do show 4f character. χ_A for liquid Eu is consistent with a system of interacting Eu^{2+} ions (Colvin et al. 1961); no data are yet available for χ_A for liquid Yb. The remaining liquid R's clearly show trivalent character. χ_A for the heavy liquid R's (Gd→Tm) is nicely consistent with Curie–Weiss-law behavior; effective moments, μ_{eff}, estimated from measured values of $d\chi_A^{-1}/dT$ via eqs. (26) and (27), are also shown in table 6, and compare well with values obtained from Van Vleck theory assuming trivalent ions in the multiplet ground state. This indicates that the splitting between J multiplet levels, ΔE_J, for these liquid R's is $\gg k_B T$, leaving higher levels unpopulated. In those cases for which $\Delta E_J \cong k_B T$, higher levels will become populated, and χ_{4f} is described by the full Van Vleck formula:

$$\chi_{4f} = \frac{N_A \sum_J \left(\frac{g^2 \mu_B^2 J(J+1)}{3k_B(T-\theta)} - \alpha_J \right)(2J+1)\, e^{-E_J/k_B T}}{\sum_J (2j+1)\, e^{-E_J/k_B T}} . \tag{29}$$

There is good evidence, for example, that $\Delta E_J \cong k_B T$ for liquid Ce, and that

there is, as a result, a significant population in the $^2F_{7/2}$ spectroscopic level as well as in the $^2F_{5/2}$ ground state. Because the moments for the higher levels are larger, occupation of the higher levels enhances μ_{eff} above the ground state values. (μ_{eff} for the $^2F_{7/2}$ state for Ce is 4.5 μ_B; that for $^2F_{5/2}$ is 2.5 μ_B). There is also evidence that excited levels above the $^4I_{9/2}$ ground state are populated for liquid Nd (Arajs and Miller 1960), and that levels above the $^6H_{5/2}$ ground state (there are six levels in this lowest multiplet) are populated for liquid Sm (Arajs 1960b). Enhanced values of μ_{eff} above ground state values are noted for the light liquid R's (see table 6), and may, at least in part, be attributed to occupation of higher levels. It should also be noted that, for metals for which $\Delta E_J \cong k_B T$, the multiplet populations can be expected to change with temperature, so that $\chi_{4f}(T)$ will not follow a Curie–Weiss-law form. In fact, if the level spacing is especially small, so that the populations of excited levels increase rapidly with temperature, $d\chi_{4f}^{-1}/dT$ may even be negative. Perhaps this effect is being observed in the case of Sm (see table 6). Non-Curie–Weiss-law behavior does appear to be observed for liquid Sm, but data are scanty. The measured temperature range for χ_A for other liquid light R's is too limited to permit an adequate test of Curie–Weiss law behavior.

A considerable amount of effort has also gone into studies of the magnetic properties of binary liquid alloys in which at least one constituent is a R metal. Measurements of magnetic susceptibility on many such systems have been reported. The simplest of these involve binary systems for which χ_{alloy} is a linear function of concentration:

$$\chi_{alloy}(T) = c\chi_R(T) + (1 - c)\chi_M(T)\,; \tag{30}$$

here c is the atomic fraction of R ions in the alloy, and M denotes a non-R component. A number of systems have been studied for which M is a liquid simple metal: M = Cu (Busch et al. 1973, Busch et al. 1974, Schlapbach 1974, for CuCe, only; and Rigney et al. 1969); M = Sn (Busch et al. 1974, Schlapbach 1974, for CeSn only; and Ohno 1978); M = Ga (Zagrebin et al. 1975); M = In (Kakinuma and Ohno 1981); and M = Al (Stupian and Flynn 1968). Taking care to account for χ_e and for the contributions from χ_{ion} for each atomic species, one can extract χ_{4f} for the R ion from these data. One concludes that the R ion retains its local moment in the liquid alloy, and that these moments follow the free ion moments rather well. A summary of these results can be seen in fig. 9, where these moments are also compared with the free ion moments of table 6. Significant systematic deviations can be seen only for Sm, Eu and Yb. This is in contrast to the deviations noted for virtually all of the light pure liquid lanthanides. (See table 6.) We note that, for most of the liquid alloys (except that for which Cu is the host) the experimental temperature is significantly below the pure R-metal melting point, and one would expect to see reduced populations of excited 4f levels in the alloys. On the other hand, the results for the Cu host are consistent with those for the solvents at lower temperatures, suggesting that explanations based solely on differences in temperature are insufficient to explain this effect. We note here also that, because all of the data shown in fig. 9 were taken for dilute R-ion concentrations, significant changes are not expected to occur in the relative positions of E_{4f} and the Fermi level with alloying in these

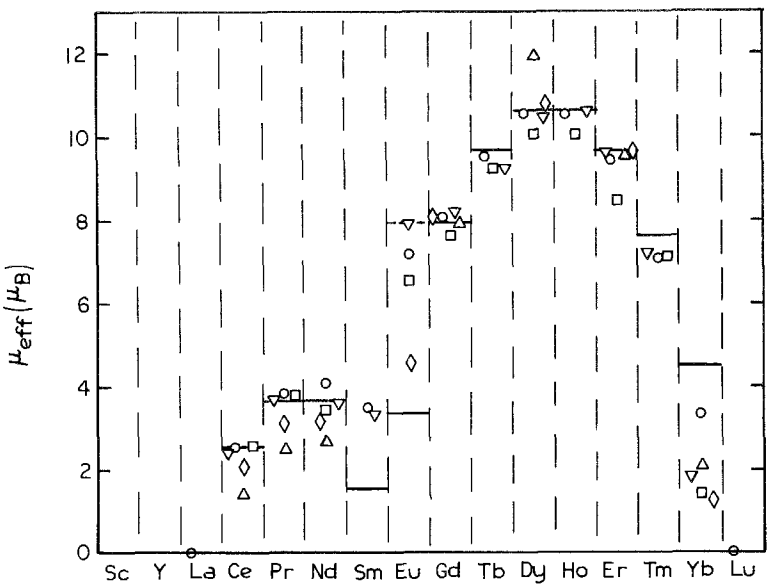

Fig. 9. Values of μ_{eff}^{4f} for the R's deduced from measurements of χ_A on dilute solutions of the R's in various liquid metal solvents. These solvents are: ∇ – Al: Stupian and Flynn (1968); ○ – Cu: Rigney et al. (1969); □ – Ga: Zagrebin et al. (1975); △ – Sn: Ohno (1978); ◇ – In: Kakinuma and Ohno (1981). The solid lines indicate μ_{eff}^{4f} (Van Vleck) from table 6; the broken line is for Eu^{2+} in the $^8S_{7/2}$ ground state.

cases. The 4f levels appear to be significantly closer to E_f in Eu and Yb, however, than in the other R's. (See the XPS results of Hedén et al. 1971.) One therefore expects more interaction between the 4f-electrons and the alloy conduction electrons for these solutes, and is not surprised to see solvent-dependent deviations in μ_{eff}, as are apparent in the figure. Linear concentration dependence, $\chi_{alloy}(c)$, is also seen for the liquid R–R alloys, CeLa and CePr (Busch et al. 1973, Busch et al. 1974, Schlapbach 1974). Here also the local moments are retained by the Ce and Pr ions in the alloys. Ohno (1978), in SmSn, and Zagrebin et al. (1975), in SmGa, also note the apparent effect of $\Delta E_J \cong k_B T$ for Sm in their work; this was discussed earlier in the context of pure liquid Sm.

Perhaps more interesting are the R–M liquid alloys which show a non-linear concentration-dependence for $\chi_{alloy}(c)$. These alloys which have been studied to date have M as a transition metal: Co, Fe, Ni and Rh. An example of this behavior is seen in fig. 10, where $\chi_A(c)$ and $d\chi_A^{-1}/dT(c)$ are shown for the liquid alloy CeCo. Not only is $\chi_A(c)$ strongly non-linear, $d\chi_A^{-1}/dT(c)$ also depends strongly on concentration, and, for CeNi, CeCo, and CeRh actually becomes negative for a range of concentrations, c. This has been interpreted to mean that both the 4f-paramagnetic moment of Ce and the d-paramagnetic moment of the transition metal have disappeared over this range of c (Schlapbach 1974). Using the CeCo system as a prototype, this behavior can be explained in the following way: as Ce is added to Co, the three valence electrons of Ce begin to fill the Co

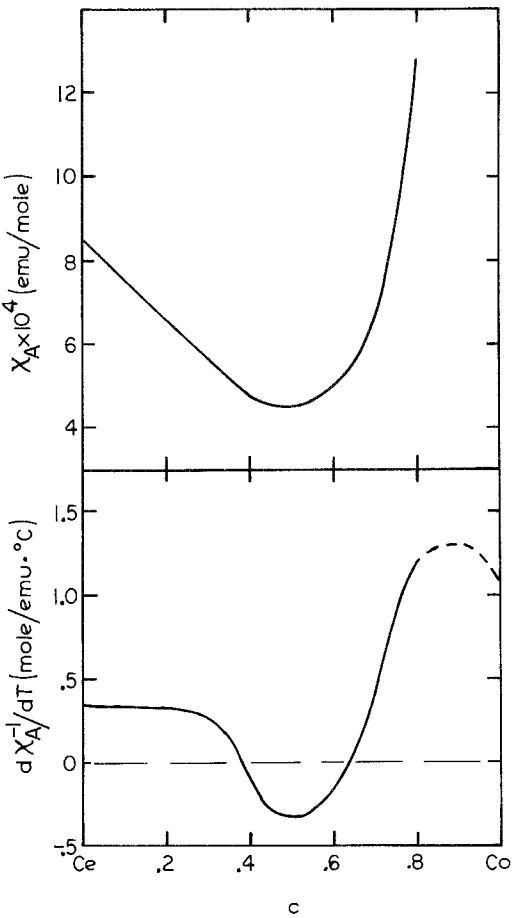

Fig. 10. The dependence of χ_A and $d\chi_A^{-1}/dT$ on concentration (atomic fraction) for the liquid alloy CeCo at 1100°C. Data are from Schlapbach (1974).

3d-level reducing the Co moment toward zero. Also, the alloy Fermi level lies below E_{4f} for Ce, at the Co-rich end, and the 4f-level of Ce is depopulated, reducing the Ce moment to zero as well. A similar effect occurs at the Ce-rich end of the concentration range, where the addition of Co progressively lowers E_f for the alloy towards E_{4f} (Ce), and eventually depopulates the 4f-level, the Co d-level being filled as before. It is estimated that the number of localized 4f electrons in Ce has gone to zero at 42 atom% Co (in CeCo), at 60 atom% Rh (in CeRh), and at 65 atom% Ni (in CeNi). Solodovnikov and co-workers have measured $\chi(c)$ for liquid CeNi and the electrical resistivity, $\rho(c)$, for liquid CeNi, CeFe and CeCo, and also conclude that the 4f-level of Ce is progressively depopulated as the concentration of the transition metal constituent is increased. (Solodovnikov et al. 1983a, Solodovnikov et al. 1983b, Solodovnikov et al. 1983c). Avignon and Falicov (1974) have studied CeNi theoretically, assuming a simplified picture of a Curie susceptibility for the Ce f-electrons, a Curie-like susceptibility of d-holes for Ni, and a Pauli susceptibility for the alloy conduction electrons. They find a

considerable charge exchange between the Ni and Ce ions, and the depopulation of the Ce 4f level, as discussed above. Bennemann (1976) also calculated χ, obtaining semiquantitative agreement for CeCo, CeNi, and CeRh, including the effects of the d-electrons in Ce at E_f in this calculation.

Other liquid alloys of Co with R's have also been studied: (LaCo – Busch et al. 1972, Schlapbach 1974; PrCo – Busch et al. 1974, Schlapbach 1974; and YCo – Kamp and Methfessel 1988). $d\chi_A^{-1}/dT$ becomes negative as La is added to Co, indicating loss of the d-paramagnetic moment of Co; in this respect, La behaves much like a trivalent simple metal when alloyed with Co. The concentration dependence of PrCo is also interesting, and can be described approximately by

$$\chi_{\text{alloy}} = c\chi_{\text{Pr}} + \chi(\text{Ge}_c\text{Co}_{1-c}) . \tag{31}$$

Apparently, the 3 valence electrons of Pr fill the d-level of Co very much as do those of the simple metal, Ge, but Pr retains its localized 4f electron with its associated moment. The 4f-level for Pr is farther below E_f than is the 4f-level for Ce; the 4f level is therefore not depopulated, as it is in Ce. In liquid CoY, Kamp and Methfessel (1988) report that Co retains its d-moment undiminished when alloyed with up to 30 atom% Y, at temperatures below 1775°C.

3.3. *Crystal field effects, and neutron scattering*

Recently, there has been some interest in the crystal electric field (CEF) in the liquid R's, and in its effect on the magnetic properties of these liquid metals. Two basic contributions to the CEF should be considered: effects due to neighboring triply-ionized R ions in the liquid; and contributions due to conduction electrons. These contributions can be of comparable magnitude in these liquid metals (Ray 1971). The action of the CEF is to lift some of the degeneracy associated with the 4f-electron multiplets; for example, if an axial crystal-field potential model is assumed, the $^2F_{5/2}$ ground state multiplet in liquid Ce will be split into three doublets. Millhouse and Furrer (1975) have looked for such a splitting, using thermal neutron inelastic scattering techniques, and see structure in the neutron energy spectrum, corresponding to level separations of about 3.3 and 6.9 meV for liquid Ce. The relative separation and relative peak heights are consistent with the predictions of the model. Structure, with separations of a few meV, is also observed in the scattering spectrum for liquid Pr, but it is less convincing. Rainford and Nguyen (1979), have also done neutron inelastic scattering measurements on liquid Ce; they suggest that the large spectral line widths, about 30 meV, make it unlikely that Millhouse and Furrer have seen CEF splitting. Rainford and Nguyen also infer from their data a value for the susceptibility χ_{4f}, independent of χ_e. (Neutron scattering methods do not sense the susceptibility due to conduction electrons.) It appears that the 4f electron in liquid Ce is ~15% delocalized at 840°C and ~26% delocalized at 950°C, presumably into the 5d conduction band. Earlier, Enderby and Nguyen (1975), in using neutron scattering techniques to obtain the magnetic form factor for liquid Ce, had estimated

that the 4f electron in Ce was about 20% delocalized. This analysis, however, was only approximate, in that it assumed no population of the $^2F_{7/2}$ spectroscopic state. Rudin et al. (1977), in another neutron scattering experiment on liquid Ce, also found the magnetic scattering ~30% reduced below what was expected for the $^2F_{5/2}$ state. Pr^{3+} and Nd^{3+} appeared to be fully in the $^3H_4$ and $^4I_{9/2}$ states, respectively, in scattering experiments on these liquid metals.

4. Thermodynamic properties

4.1. *Specific heat*

The specific heats at constant pressure, c_p, have now been measured for all of the liquid R's; values are listed in table 7. The experimental methods used include standard calorimetric and levitated drop calorimetric techniques (see Dokko and Bautista 1980), and dynamic, pulsed heating techniques (used by Filippov and

TABLE 7

Best estimates, from the experimental literature, of the thermodynamic parameters, c_p (specific heat at constant pressure), a (thermal diffusivity), κ (thermal conductivity), and L (Lorentz number). Data from the references cited were used in making these estimates. All values are for the liquids taken at the melting temperature. (*) Estimated from values for the solid at the melting temperature.

	c_p (cal/mole · K)		a (cm^2/s)		κ (W/cm · K)	L (W · Ω/K^2)
Sc	10.57*	N	—			
Y	10.30	N	—			
La	11.4 ± 0.5	A, C, E, J	0.116 ± 0.010	A, C, J	0.238	2.65×10^{-8}
Ce	8.9 ± 0.6	A, B, G, F L, [3, 4] in (G)	0.118 ± 0.010	[3, 4] in (G) A, G	0.210	2.56×10^{-8}
Pr	10.0 ± 0.8	E, J	0.128	J	0.251	2.89×10^{-8}
Nd	11.1 ± 0.5	A, B, D, M	0.090	A, D	0.195	2.27×10^{-8}
Sm	14.0	B	—			
Eu	9.11	N	—			
Gd	9.2 ± 0.6	H, I, K	0.082	K	0.149	1.83×10^{-8}
Tb	11.1	H	—			
Dy	10.3	J	0.086	J	0.187	2.34×10^{-8}
Ho	10.5	H	—			
Er	9.3	H	—			
Tm	9.9	H	—			
Yb	8.79	N	—			
Lu	11.45*	N	—			

References:

(A) Atalla (1972)
(B) Spedding et al. (1960)
(C) Mardykin et al. (1973)
(D) Mardykin et al. (1972)
(E) Novikov and Mardykin (1975)
(F) Kuntz and Bautista (1976)
(G) Novikov and Mardykin (1973)
(H) Dennison et al. (1966c)
(I) Novikov and Mardykin (1974)
(J) Banchila and Filippov (1974)
(K) Novikov et al. (1977)
(L) Dokko and Bautista (1980)
(M) Stretz and Bautista (1975)
(N) Hultgren et al. (1973)

co-workers – see Atalla 1972). Unfortunately, experimental difficulties are great enough that these values must still carry uncertainties of several percent. dc_p/dT is always measured to be ≤ 0, ranging from zero to about -3×10^{-3} cal/mole K^2. This reduction in c_p with increasing T is consistent with the fact that the liquid metal becomes more "gas-like" with increasing T, resulting in a reduction in the number of degrees of freedom per ion, and hence, by equipartition of energy arguments, in a reduction in c_p.

Calculations of c_v (and c_p) usually proceed from a calculation of the entropy, S, of the liquid metal. Choosing a hard-sphere model, we may write S as

$$S = S_{gas} + S_{pack} + S_{el} + S_{mag} , \tag{32}$$

where S_{gas} is the entropy of the ideal ionic gas, S_{pack} accounts for the finite packing of the hard spheres, S_{el} is the electronic contribution (which can be significant for the transition and R liquids, since it goes as the electronic density of states), and S_{mag} takes account of the magnetic contribution. (See Harder and Young 1977.) Then we can obtain c_v and c_p as:

$$c_v = T \left. \frac{\partial S}{\partial T} \right|_v \tag{33}$$

and

$$c_p - c_v = \alpha^2 \Omega T \beta_T . \tag{34}$$

Here α is the linear thermal expansion coefficient, Ω is the molar volume (for c_v, c_p as molar specific heats), and β_T is the isothermal compressibility. Direct comparison of values of S calculated on this model with values of S estimated from the measurements on the solid R's show close correlation (Harder and Young 1977). (Calculated values of S for liquid Pr and Nd fall somewhat below the observed values for these metals; this may be due to the fact that Harder and Young 1977 assumed in their calculations that only the ground state multiplet was occupied. This should tend to underestimate S for cases in which a significant population of excited states is realized. In this respect, however, it should be noted that Harder and Young's calculated value of S for liquid Ce is *not* below the observed value; in this case, also, only the ground state was assumed to be populated.)

Yokoyama et al. (1988) have recently calculated S and c_v along similar lines for the liquid R's, but have used a one-component plasma (OCP) model instead of the HS model. The results of their calculations of c_v are shown in table 8, and differ only slightly from results based on the HS model. One would wish to use eq. (34) to calculate c_p for a comparison with experiment, but α and β_T are not available for these liquids. Instead, we note that for a wide variety of liquid metals, c_p/c_v is in the range of 1.1 to 1.3. (See Khanna 1981, Hafner 1977, Faber 1972.) Taking $c_p/c_v = 1.2$ as a reasonable average for these liquid R's, we obtain c_p^{th} in table 8. Comparison with the experimental values is moderately good, and

TABLE 8
A comparison between calculated (c_p^{th}) and experimental values (c_p^{exp}) of c_p. c_v^{th} are from Yokoyama et al. (1988), and employ the OCP model. $c_p/c_v = 1.2$ is assumed. (See text.) c_p^{exp} are from table 7. (Units are cal/mole K.)

Metal	c_v^{th}	c_p^{th}	c_p^{exp}
La	6.7	8.0	11.4
Ce	6.9	8.3	8.9
Pr	6.7	8.0	10.0
Nd	6.9	8.3	11.5
Eu	6.5	7.8	—
Gd	7.9	9.5	9.2
Tb	8.1	9.7	11.1
Yb	6.5	7.8	—

may improve with increasing atomic number. Young (1977) notes that, at least in the HS context, S (eq. 32) always underestimates the entropy, and he attributes the difference, S_s, to the partial softness of the ion core, which has been neglected in this development. If this is the case, the fact that the HS approximation improves with increasing atomic number (see section 2.2) would be consistent with the apparent trend in table 8. On the other hand, dS_s/dT appears to be <0 (Young 1977), implying that introducing S_s would further lower c_p^{th}; this would make the difference between c_p^{th} and c_p^{exp} greater for the light liquid R's.

It is also interesting to note that c_p appears to be larger for liquid Sm than for the other liquid R's. We recall (section 3.2) that there is considerable evidence that the separation between 4f multiplet levels, ΔE_J, in liquid Sm is quite small ($\Delta E_J \simeq k_B T$), resulting in a significant thermal excitation to levels above the ground state. This additional contribution to S_{mag} and hence to c_p may result in the larger value of c_p that is observed.

4.2. *Thermal conductivity*

Measurements of thermal conductivity, κ, can be made by a variety of steady-state and dynamic methods. To date, all measurements on the liquid R's, however, have been made via a dynamic, radial, pulsed-heating method. (See Atalla 1972.) In this method, it is convenient to measure a, the thermal diffusivity, and from this to calculate κ:

$$\kappa = a\rho_0 c_p \,. \tag{35}$$

Best experimental estimates of a for several liquid R's are shown in table 7. Uncertainties, unfortunately, approach 10%. Values of da/dT carry greater uncertainty, but most fall within the range of $4\text{–}10 \times 10^{-5}$ cm^2/sec K. All are >0. Using the data of table 7 for c_p and a, and of table 1 for ρ_0, values of κ are obtained. These are also shown in table 7. Uncertainties in κ are $\geqslant 10\%$.

In liquid metals, two components to the heat current must be considered: heat carried by ions and heat carried by electrons. (It is also assumed that there is no net electron or ion flow.) Thermal conductivities due to each of these can be defined: κ_{ion}, κ_{el}. κ_{ion} can be calculated by methods similar to those used to calculate shear viscosity, η, and result in values of magnitude $\sim 10^{-3}$ W/cm · K. (For liquid argon, $\kappa_{el} = 0$, and values of κ_{ion} based on a HS model agree well with measurements of κ.) In a liquid metal, $\kappa_{el} \sim 1$ W/cm · K, implying that κ_{ion} can be neglected in κ to 1% or better. Thus it is possible to look on thermal conductivity for a liquid metal as an electronic property.

Proceeding via a solution of either the Boltzmann equation or the Kubo formula, one obtains the "Wiedemann–Franz law", relating κ_{el}, ρ, and T:

$$\frac{\kappa_{el}\rho}{T} = \frac{\pi^2 k_B^2}{3e^2} \equiv L_0 = 2.44 \times 10^{-8}\ \mathrm{W\Omega K^{-2}}\,. \tag{36}$$

(See Shimoji 1977.) Here T is the absolute temperature, and L_0 is called the Lorentz number. Equation (36) should be valid for a wide variety of conditions, but does require that the electron–ion scattering be elastic.

If we define

$$\frac{\kappa_{el}\rho}{T_{mp}} \equiv L\,, \tag{37}$$

and take $\kappa_{el}(=\kappa)$ from table 7 and ρ from table 9, we obtain the values of L also shown in table 7; these are to be compared with L_0. It appears that L and L_0 are equal for these liquid R's, except for Gd, within experimental error. Values of $L > L_0$ are particularly difficult to explain (should additional work for La, Ce, and Pr support the values listed here), since inelastic scattering effects would tend to lower L below L_0. It is also unlikely that such effects could lower L by more than perhaps a few %, or so. (see Rice 1970) On the other hand, the substantial experimental difficulties associated with measuring κ for liquid metals are broadly recognized (see Cook 1979); clearly more experimental work is needed.

4.3. *Alloys*

There has been considerable interest lately in the thermodynamic properties of liquid alloys, and in the relationship between these properties and evidence for clustering and short-range order in these liquids. Attempts to calculate excess energies for simple liquid alloys have been made that employ general methods (e.g.: Hafner 1976, Holzhey et al. 1982, Hafner et al. 1984). While moderate success has been realized for simple metal alloys, the added complexity resulting when at least one alloy component is a transition metal or R makes semi-empirical methods of greater use here. Much recent work for these binary alloys refers to a semi-empirical model developed by Miedema and co-workers. (See Miedema et al. 1980.) In this model, the enthalpy of mixing, ΔH, is given as a sum of three terms:

$$\Delta H \sim -P(\Delta\phi^*)^2 + Q(\Delta n_{ws}^{1/3})^2 - R\,. \tag{38}$$

The first term is attractive, and goes as the square of the electronegativity difference between the constituents (expressed in terms of the difference between the work functions, $\Delta\phi^*$ of the pure constituents); the second is repulsive, and depends on the difference between the electron densities, Δn_{ws}, at the Wigner–Seitz cell boundaries between dissimilar ions; and the third is attractive, depending on the types of ions involved (non-transition metal, transition metal, R-metal) and the alloy phase. P and Q are universal constants. The dependence on electronegativity difference is consistent with earlier fundamental work by Hodges and Stott (1972), and the recognition of a linear relationship between the electron chemical potential and the Pauling electronegativity. Murozzi et al. (1978), using self-consistent band structure calculations, have obtained interstitial electron charge densities which compare well with empirically derived values of n_{ws}, providing further support for Miedema's model. And values of ΔH calculated for many liquid alloys on this model follow the measured values very well. Heats of solution can also be obtained on this model.

Pasturel et al. (1983) have introduced another simple model, one which casts the partial enthalpy of mixing at infinite R dilution, $\overline{\Delta H}_R^\infty$, in terms of the change in E_f, the Fermi energy, and the change in volume, with alloying. This model addresses liquid alloys of R's with non-transition metals. These authors find that their measured and calculated values of $\overline{\Delta H}_R^\infty$, for the lanthanide series of R's in liquid Al, agree rather well, and, moreover, that both show the same dependence on atomic number as does the molar volume.

A number of experimental studies have been reported recently on a variety of liquid alloy systems involving R metals. Watanabe and Kleppa (1984) report measurements on liquid alloys of Sc, Y, La, and Lu in the monovalent liquid metal Cu. They find a maximum value for $-\Delta H$ of 13 to 24 kJ/mole at 33 to 50 atom% R component, providing evidence for clustering at the stoichiometric compositions Cu_2R and CuR. Additional evidence for this is provided by heat capacity measurements on liquid CuCe alloys. (Dokko and Bautista 1980). These show a maximum in c_p at the Cu_2Ce composition. Measurements of ΔH for the transition metal-based alloys, NiY (Batalin et al. 1977) and NiLa (Watanabe and Kleppa 1983) show somewhat stronger binding ($-\Delta H(\max) \sim 13$ to 30 kJ/mole) with a maximum corresponding to Ni_2R. And stronger binding yet is observed in the liquid polyvalent metal-R alloys, with $-\Delta H(\max)$ lying in the range of 70 to 75 kJ/mole for SiY (Esin et al. 1976) and AlLa (Kononenko et al. 1978). Again, preferred ordering for this limited number of examples favors Si_2Y and Al_2La. Data for an alloy from each of these groups are shown in fig. 11. Measurements of $\overline{\Delta H}_R^\infty$ are also reported for this class of alloys, and show evidence of strong bonding: GeCe (Nikolayenko et al. 1979), and SnR (Castanet et al. 1984). It is suggested that the 4f electrons play only a minor role in this interaction, but that transfer of electrons into the R d-band provides the major contribution (Pasturel et al. 1983, Batalin et al. 1977). Some work on ternary alloys has also been reported: (NiSi)Y – Stukalo et al. (1981); (FeSi)Y and (FeSi)La – Esin et al. (1983); (FeAl)R, where R = Y, La, Ce – Ermakov et al. (1982).

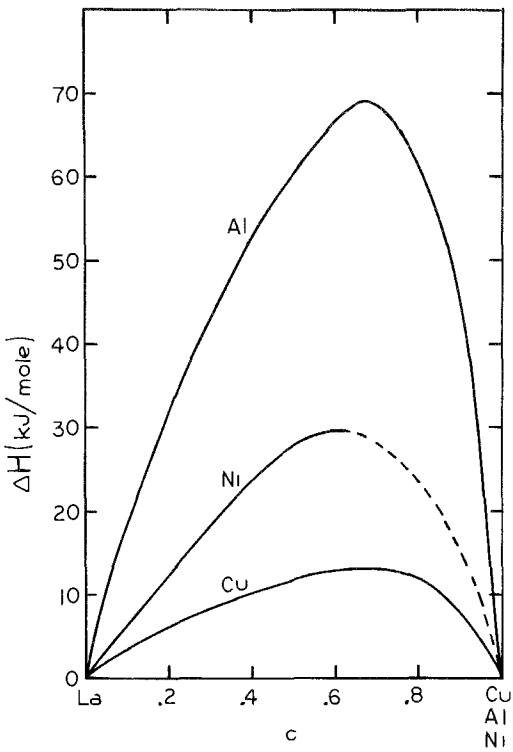

Fig. 11. Enthalpies of mixing, ΔH, as functions of concentration (atomic fraction), for the liquid alloys: LaCu, at 1100°C – Watanabe and Kleppa (1984); LaAl, at 1300°C – Kononenko et al. (1978); and LaNi, at 1103°C – Watanabe and Kleppa (1983).

5. Electronic transport properties

5.1. *Electrical resistivity and thermoelectric power*

5.1.1. *Experiment*

Best estimates of the experimental values for the electrical resistivity in the liquid, ρ_L, and solid, ρ_s, and of $d\rho_L/dT$ for the R's at their melting points, are shown in table 9. Similar values for the thermoelectric power, Q: Q_L, dQ_L/dT, and $(Q_L - Q_s)$ are displayed in table 10. Considerable difficulties have been encountered in containing these highly reactive liquid metals, and in maintaining their purity while their electronic properties are measured. For discussions of the ways these difficulties have been addressed, the reader is referred to the literature references cited.

The resistivities, ρ, of three characteristic trivalent R's are displayed in fig. 12. A tendency towards saturation with increasing T is noted in each case in the solid, and $d\rho_L/dT$ decreases and becomes negative as one goes through the sequence Pr → Dy → Lu. ρ for the divalent R's Eu and Yb, are shown in fig. 13. Although ρ_s for Eu shows some tendency toward saturation, ρ_s for Yb is linear. The thermopowers, Q, of two of the trivalent R's are shown in fig. 14. The concave downward $Q(T)$ seems to be characteristic of the light R's in the solid, and ΔQ

TABLE 9

Best estimates, from the literature, of experimental values of ρ_L, $d\rho_L/dT$, and ρ_L/ρ_S, all measured at the appropriate melting point. Data from the references cited were used in making these estimates.

Metal	ρ_L ($\mu\Omega$-cm)		$\frac{d\rho_L}{dT} \times 10^2$ ($\mu\Omega$ cm/°C)		ρ_L/ρ_s	
Sc	—		—		—	
Y	—		—		—	
La	133 ± 2	A, B, C, D, E, F, G, H	2.5 ± 0.7	A, B, C, D, E, G	1.06 ± 0.01	A, C, S
Ce	130 ± 2	B, C, D, F, H, I, J, V	1.7 ± 0.5	B, C, D	1.06 ± 0.01	C, S
Pr	139 ± 2	B, C, F, H, K, W	2.7 ± 1.0	B, C, K	1.07 ± 0.01	C, K
Nd	151 ± 2	B, C, D, E, F, K, L, W	2.4 ± 0.5	B, C, D, E, K, L	1.06 ± 0.01	B, C, D, K, T
Sm	182 ± 2	K	5.2 ± 0.4	K	1.07 ± 0.02	K
Eu	242 ± 2	B, M, N	−6.3 ± 0.5	B, M, N	1.30 ± 0.01	B, M, N
Gd	195 ± 6	B, O	0.0 ± 0.5	B, O	1.02 ± 0.02	O
Tb	193 ± 6	B, O	1.6 ± 0.5	B, O	1.02 ± 0.02	O
Dy	210 ± 6	B, P	0.0 ± 0.5	B, P	1.06 ± 0.01	B, U
Ho	221 ± 7	B, P	0 ± 1	B, P	1.04 ± 0.02	P
Er	226 ± 7	B	0.0 ± 0.5	B	1.02 ± 0.01	E, U
Tm	—		—		—	
Yb	113 ± 2	B, M, N	−2.3 ± 0.4	B, M, N	1.47 ± 0.01	B, M, N
Lu	224 ± 7	Q, R	−0.7 ± 0.5	Q	1.03 ± 0.02	Q

References:

(A) – Krieg et al. (1969)
(B) – Güntherodt et al. (1977)
(C) – Gaibullaev et al. (1969)
(D) – Atalla (1972)
(E) – Mardykin (1975)
(F) – Busch et al. (1973)
(G) – Mardykin et al. (1973)
(H) – Güntherodt and Künzi (1973)
(I) – Busch et al. (1970b)
(J) – Busch et al. (1970a)
(K) – Hiemstra et al. (1984)
(L) – Marydkin et al. (1972)
(M) – Güntherodt et al. (1976)
(N) – Ten Cate et al. (1980)
(O) – Güntherodt et al. (1974a)
(P) – Güntherodt et al. (1974b)
(Q) – Delley et al. (1978)
(R) – Delley et al. (1979a)
(S) – Spedding et al. (1957)
(T) – Vedernikov et al. (1977)
(U) – Habermann and Daane (1964)
(V) – Novikov and Mardykin (1973)
(W) – Burkov and Vedernikov (1984)

across the melting point is small. $Q(T)$ for the divalent R's is shown in fig. 15; again $Q(T)$ for solid Eu displays some of the characteristics of the solid trivalent R's, but the magnitudes are quite different; $Q(T)$ for solid Yb is nearly linear.

It is evident that no data for ρ_L are available for Sc, Y, and Tm; likewise, Q_L data are available for only seven R's. It is also clear that there is a considerable difference between the properties of the divalent R's (Eu and Yb) and the trivalent R's. In particular, we note that $d\rho_L/dT$ is negative for Eu and Yb, but is positive for the other (except Lu) R's; that ρ_L/ρ_s is in the range of 1.02 to 1.07 for the trivalent R's, but ρ changes by 30% to nearly 50% upon melting for Eu and Yb; and that $Q_L - Q_s$ for the trivalent R's is $\leq 1\mu V/°C$, whereas $Q_L - Q_s$ is in the

TABLE 10

Best estimates, from the literature, of experimental values of Q_L, dQ_L/dT, and $Q_L - Q_s$, all measured at the appropriate melting point. Data from the references cited were used in making these estimates.

Metal	Q_L (μV/°C)	$\frac{dQ_L}{dT} \times 10^2 \left(\frac{\mu V}{°C^2}\right)$	$Q_L - Q_S$ (μV/°C)
La	-7.5 ± 1.0 A	-1.1 ± 0.2 A	0.1 ± 0.2 A
Ce	-4.6 ± 0.3 A, B	-1.1 ± 0.2 A, B	1.0 ± 0.3 A
Pr	-7.8 ± 0.3 C, E	-0.75 ± 0.3 C	-0.3 ± 0.4 C
Nd	-8.8 ± 0.3 C, E	0.0 ± 0.3 C	-0.7 ± 0.4 C
Sm	-7.8 ± 0.6 F	-0.6 ± 0.4 F	0.0 ± 0.8 F
Eu	6.6 ± 0.4 D	$+2 \pm 2$ D	-24.5 ± 1.0 D
Yb	-12.2 ± 1.0 D	$+2 \pm 4$ D	-33 ± 2 D

References:

(A) – Howe and Enderby (1973)
(B) – Yatsenko and Golovin (1972)
(C) – Kooistra et al. (1988)
(D) – Ten Cate et al. (1980)
(E) – Burkov and Vedernikov (1984)
(F) – Evele et al. (1988)

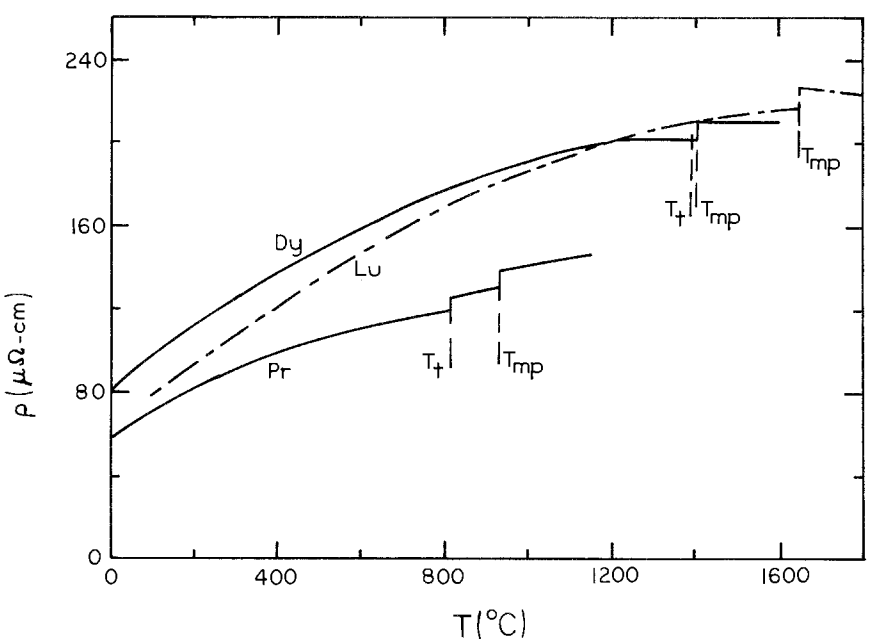

Fig. 12. Electrical resistivity, ρ, as a function of temperature, for a light (Pr), an intermediate (Dy), and a heavy (Lu) trivalent R. Data are from Hiemstra et al. (1984): Pr; Güntherodt et al. (1977): Dy; and Delley et al. (1978): Lu.

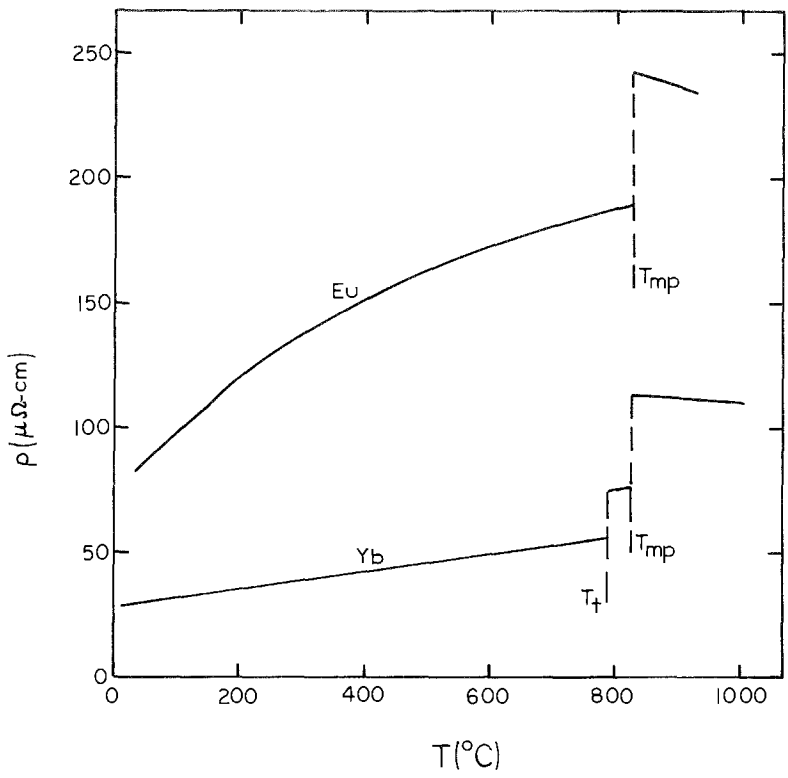

Fig. 13. Electrical resistivity, ρ, for the divalent R's, Eu and Yb, as a function of temperature. Data are from ten Cate et al. (1980).

range of 25–30 μV/°C for Eu and Yb. It will therefore be appropriate to discuss some of these properties for the divalent and trivalent R's separately in what follows.

5.1.2. *Theory and discussion*

The development by Ziman (1961, 1964) of a pseudopotential theory of the electronic properties of liquid metals provided a substantial impetus to this field. Within this formulation, based on first-order Born approximation and the Boltzmann equation, the electrical resistivity, ρ_L, can be cast as

$$\rho_L = \frac{12\pi\Omega_0}{e^2\hbar v_f^2} \int_0^1 |U(K)|^2 A(K) \left(\frac{K}{2k_f}\right)^3 d\left(\frac{K}{2k_f}\right), \tag{39}$$

where Ω_0 is the atomic volume, $U(K)$ is the electron–ion pseudopotential, $A(K)$ is the static structure factor, and v_f and k_f are the Fermi velocity and Fermi wave vector, respectively, and K is the wave vector corresponding to momentum transfer. The distribution of atomic scatterers thus enters this expression via

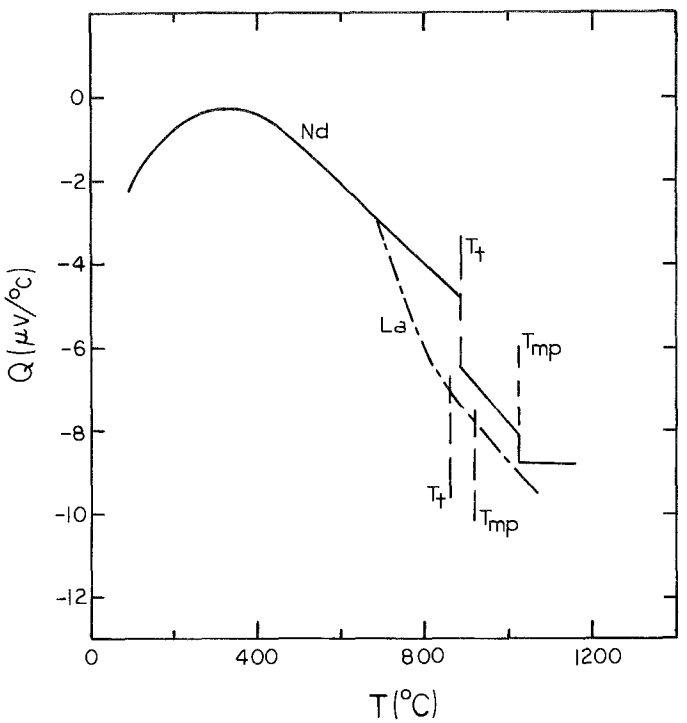

Fig. 14. Thermopower, Q, for two light trivalent R's, as a function of temperature. Data are from Howe and Enderby (1973): La; and Kooistra et al. (1988): Nd.

$A(K)$, which we encountered earlier in our discussion of liquid structure (section 2.2). Similarly, the thermoelectric power (thermopower), Q, takes the form

$$Q = \frac{-\pi^2 k_B^2 T}{3|e|E_f}\,\zeta\,, \tag{40}$$

where

$$\zeta \equiv -\frac{\partial \ln \rho_L}{\partial \ln E}\bigg|_{E_f}. \tag{41}$$

Here T is the absolute temperature, and E_f is the Fermi energy.

This theory, which is basically a weak-scattering theory, should not be expected to be directly applicable to the liquid rare-earth metals, since these clearly show evidence of strong electron–ion interactions (e.g. ρ_L tends to be quite large for these liquids). On the other hand, because of its considerable success in describing the properties of many simple liquid metals, it is not surprising that it has provided some basis on which to attempt to develop a theory for strong-scattering liquid metals as well.

The theoretical approach that has been used most extensively to-date for

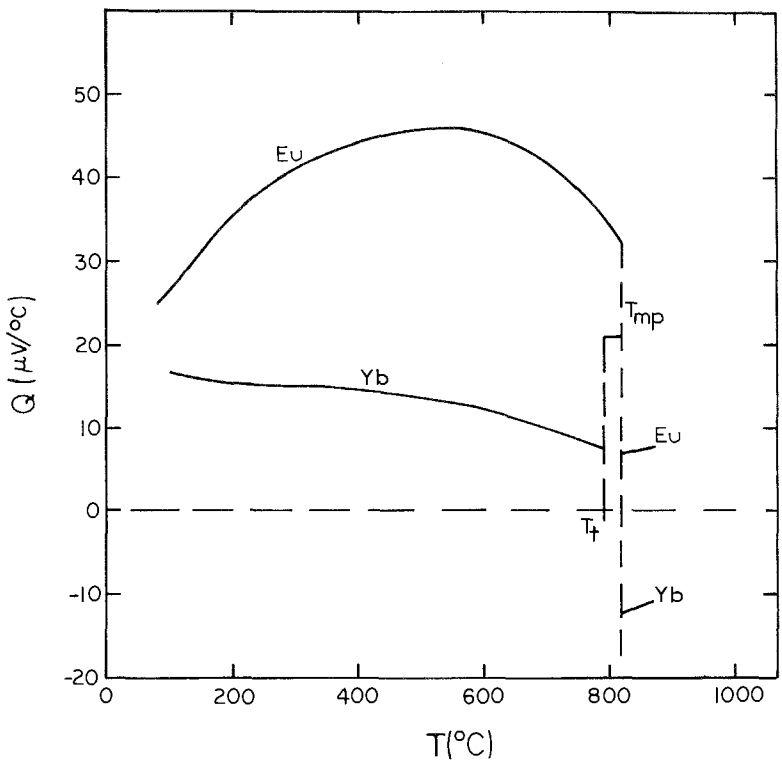

Fig. 15. Thermopower, Q, for the solid and liquid divalent R's, Eu and Yb, as a function of temperature. Data are from Ten Cate et al. (1980).

studies of the liquid R's is one developed initially for the liquid transition metals by Evans and his coworkers (cf: Evans et al. 1973). Beginning with general scattering theory and non-overlapping muffin-tin potentials, they found that within their "local approximation" they recovered the general form of Ziman's resistivity expression (eq. 39), with the pseudopotential replaced by the on-energy-shell components of the t-matrix:

$$\rho_{\mathrm{L}} = \frac{12\pi\Omega_0}{e^2\hbar v_{\mathrm{f}}^2} \int_0^1 |t(K, E_{\mathrm{f}})|^2 \, A(K) \left(\frac{K}{2k_{\mathrm{f}}}\right)^3 \mathrm{d}\left(\frac{K}{2k_{\mathrm{f}}}\right). \tag{42}$$

The t-matrix, $t(K, E)$ is given by

$$t(K, E) = \frac{-2\pi\hbar^3}{m\Omega_0(2mE)^{1/2}} \sum_l (2l+1) \exp(\mathrm{i}\delta_l) \sin\delta_l \, P_l(\cos\theta_{kk'}) \,, \tag{43}$$

where δ_l is the phase shift associated with the l-th partial wave, evaluated at E_{f}. The expression for Q (eqs. 40, 41) remains valid.

Waseda et al. (1978) have applied this method to a calculation of ρ_L, $d\rho_L/dT$, and Q_L for several of the liquid R's. In their work, they used experimental structure data to calculate the charge-density distribution and hence the muffin-tin potential; these same data provided $A(K)$ in eq. (42). These authors also assumed that the number of conduction electrons per ion, n_c, could be taken as 2 for Eu and Yb, and as 3 for the trivalent R's. Their calculated values for ρ_L (in $\mu\Omega$-cm) are reasonably close to measured values: 165 (La), 134 (Ce), 193 (Eu), 146 (Gd), and 137 (Yb). Calculated values for $d\rho_L/dT$ (in 10^{-2} $\mu\Omega$-cm/°C) also show the general trends that are measured: 2.0 (La), 5.4 (Ce), −1.2 (Eu), and 0 (Yb). While calculated values for Q_L (in μV/°C) for La (−2.42) and Ce (−6.34) fall reasonably close to measured values, those for the divalent R's, Eu (−2.64) and Yb (−0.87), differ widely from measured data. There are no experimental data with which to compare the calculated Q_L for Gd (3.35). Calculations of Q_L, involving energy derivatives, are certainly expected to present a more severe challenge to a theoretical method; this is clearly the case, here.

Delley, Beck, and collaborators (Delley et al. 1978, Delley et al. 1979a, Delley and Beck 1979a, Delley and Beck 1979b, Delley et al. 1979b) have taken a similar approach utilizing the single-site t-matrix, and have also taken Eu and Yb to have $n_c \cong 2$, but have assumed a monotonically increasing n_c (from about 0.5 for La to about 1.5 for Lu) across the trivalent lanthanide series. These assumptions appear to be consistent with band structure calculations in the solid (Duthie and Pettifor 1977). Duthie and Pettifor also note that this change in n_c is due to the change in ion core size across this series of metals. (See also section 2.1.) Their results for ρ_L for divalent Eu (about 225 $\mu\Omega$-cm) and Yb (about 125 $\mu\Omega$-cm) are quite close to measured values. Calculated values of ρ_L for trivalent liquid La, Gd, and Lu show some variation due to different choices of structure and scattering potential, but also follow the experimental data well.

Studies of the liquid transition metals using the t-matrix approach show large d phase shifts with strong energy dependence dominating the calculations of ρ_L and Q_L. These scattering properties can therefore be described by a d-resonance picture characterized by a resonance energy and half-width. Both Waseda et al. and Delley and his collaborators have found the energy dependence of δ_2 to be much weaker for the R's; the phase shifts δ_0 and δ_1 are also found to contribute significantly to the calculations. A resonance picture, therefore, is apparently not appropriate for these R's. (The 4f levels are assumed to be far enough below E_f to be passive.)

An examination of the apparent contribution of spin-disorder scattering to ρ_L is also interesting. A plot of ρ_L as a function of atomic number across the lanthanide series is shown in fig. 16. It is seen that, with the exception of the divalents Eu and Yb, ρ_L increases nearly linearly as the 4f band is filled. In contrast to this, a similar plot of ρ_s at room temperature shows a strong peak at Gd, presumably due to the peaking of the spin-disorder contribution when the 4f band is nearly half-full. The absence of any such dependence in the liquid is then striking. Delley, Beck, and collaborators have examined theoretically the importance of spin-disorder scattering on ρ_L and suggested that the contribution would be

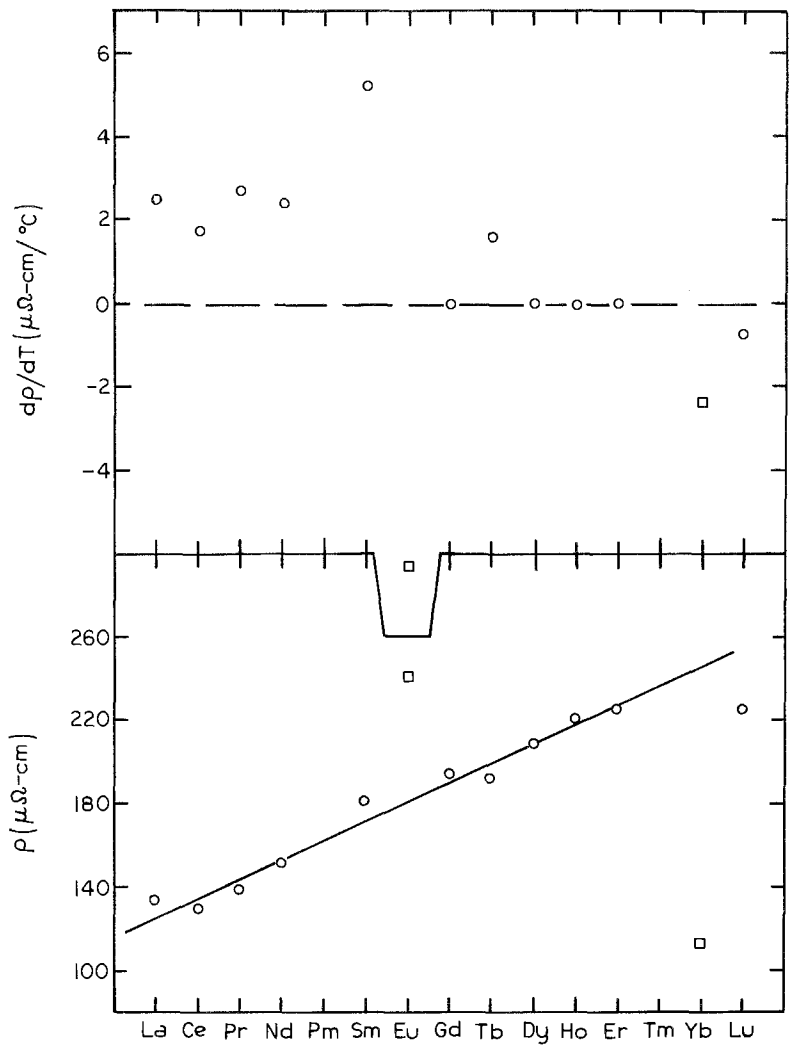

Fig. 16. ρ and $d\rho/dT$ for the liquid lanthanides at their respective melting temperatures. Data are from table 9.

minimal. Perrinello et al. (1977) have pointed out that, for these liquid metals, the Born approximation is no longer valid, and that a Hamiltonian incorporating both potential and exchange (spin-disorder) interactions must be utilized. In this case the apparent absence of spin-disorder scattering results from a breakdown of Matthiessen's rule, and an interference results between these scattering modes. (Harris and Shalom (1980) have taken the same approach to a calculation of ρ for solid R's at high temperatures.) Delley and Beck (1979b) have used the Hamiltonian of Perrinello et al. (1977) and included multiple scattering effects as well, to estimate the contribution of spin-disorder scattering to ρ_L in a careful study of liquid Gd, and have found it to be only about 5%.

The temperature dependence of ρ_L (i.e. $d\rho_L/T$) for the trivalent lanthanides tends to decrease toward zero with increasing Z, and for Lu actually becomes negative. This can be understood within the Evan's formalism as being due to the dependence of $\rho_L(T)$ upon $A(K, T)$ (eq. 42). If a major contribution to ρ_L in eq. (42) comes from the region near $K = 2k_f$, and if $A(K, T)$ behaves as shown in fig. 3, then one would expect $d\rho_L/dT$ to decrease as n_c increases from $1 \rightarrow 2$, even becoming negative at $n_c \simeq 2$. This is consistent with the trend seen in fig. 16. (See also the discussion of the divalent R's, section 5.1.3.) It is interesting to note that a decrease in $d\rho_L/dT$ with increasing ρ_L is also consistent with the Mooij rule, as formulated for solid amorphous alloys. (See Mooij 1973.)

Ballentine (Ballentine and Hammerberg 1983, Bose et al. 1983, Ballentine 1988) has recently suggested a new approach to the calculation of ρ_L and Q_L for strong-scattering (including R's) liquid metals. His method addresses the difficulty of assuming the validity of the Boltzmann equation, by beginning instead with the Kubo–Greenwood formula; it also treats on an equal footing the contributions of s and d states to the conductivity, eliminating the problem of estimating the number of conduction electrons, n_c, and also of estimating E_f. This is a problem which is not resolved in Evan's theory. (See also Esposito et al. 1978 on this point.) Ballentine uses a Monte Carlo method on a cluster of a few hundred atoms, adjusts the interionic interaction to reproduce the experimental structure, and uses a linear combination of atomic orbitals for the valence electrons to calculate the bulk density of states as a mean over sites near the cluster center. The resistivity is then given as

$$\frac{1}{\rho_L} = \frac{e^2}{\Omega_0} n(E_f) D(E_f) , \tag{44}$$

where $n(E_f)$ is the total density of states, and $D(E_f)$ is the diffusivity, both at the Fermi energy, E_f. In each case examined, the sd contribution to ρ_L was found to be small, making it possible to separate the ss and dd contributions to ρ_L:

$$\frac{1}{\rho_L} = \frac{e^2}{\Omega_0} [n_s(E_f) D_s + n_d(E_f) D_d] . \tag{45}$$

The thermopower, Q, can be calculated conveniently by performing the energy derivative, eq. (41), within the Kubo–Greenwood formula, resulting in

$$Q = -\frac{2\pi^2}{3} \frac{k_B^2 T}{|e|} \frac{\partial}{\partial E'} \ln D(E_f, E') \Big|_{E' = E_f} . \tag{46}$$

(See Ballentine 1988.) ρ_L for several liquid transition metals and for liquid La have been calculated, and the dd contribution to ρ_L was found to constitute about 80%–90%. This was due to the fact that the magnitude of $n_d(E_f)$ more than compensated for the reduced d-diffusivity. The calculated value for ρ_L for La (151 $\mu\Omega$-cm) compares reasonably well with experiment (Ballentine and Ham-

merberg 1983). Results of calculations of Q_L via this method have also been reported recently (Ballentine 1988). These calculated values include La (-6.7 μV/°C), Yb (-12.2 μV/°C) and Lu (-18 μV/°C). The values for La and Yb are close to measured values of Q_L; no data are presently available for Q_L for Lu. It appears that this method shows considerable promise in treating ρ_L and Q_L for the liquid R's. Other theoretical models have also been developed to permit a study of the electronic properties of strong-scattering liquid metals, but these have not yet been applied to the liquid R's. (See, for example, Mott 1972 and Itoh et al. 1984.)

5.1.3. *Divalent R's (Eu and Yb)*

The electronic structures of Eu and Yb metals are characterized by a half-filled (Eu) or a completely filled (Yb) 4f band, and two electrons distributed over the 5d and 6s bands. Spin–orbit coupling has split the two halves of the 4f band substantially; in Eu the filled half-band is below E_f and the empty half-band is above E_f; in Yb both filled half-bands are below E_f (see fig. 5). The electronic properties of liquid Eu and Yb are then expected to be dominated by a nearly filled s electron-band and a nearly empty d-band. The same situation exists for the liquid alkaline earth metals: Ca, Sr and Ba. Similar crystal structures in the solids suggest that liquid Yb and Sr should show similar electronic properties, and liquid Eu and Ba as well. This is, in fact, observed.

One parameter of special interest in this context is $d\rho_L/dT$. As noted earlier, if ρ_L is cast in the form of eq. (42), then the dominant contribution to the temperature dependence comes from $A(K)$. (Other contributions must be considered, however: see Delley et al. 1979b.) For a divalent liquid metal, the upper limit ($K/2k_f = 1$) of the integral, eq. (42), falls just above the first peak in $A(K)$. (See fig. 3.) If a major portion of the integral comes from the region of large K (as is the case for these metals) then the temperature dependence of $A(K)$ (see fig. 3) implies $d\rho_L/dT < 0$. [Negative $d\rho_L/dT$ have also been observed for many amorphous solid alloys, but apparently only divalent *pure* liquid metals (except for Lu) show this dependence. For a general discussion of this, see Harris et al. 1978.] Delley et al. (1978) have also argued that the value $n_c \cong 1.5$ for liquid Lu places it, for this discussion at least, nearly in the class of divalent R's, making its slightly negative $d\rho_L/dT$ reasonable as well. Waseda and Miller (1978) also note that their observed temperature dependence of $A(K)$ for liquid Lu is consistent with $d\rho_L/dT < 0$ on this model.

5.1.4. *Alloys*

Electrical resistivities, ρ_L, have been measured for a number of liquid alloys involving rare-earth metals. These results fall into three distinct classes: (1) Alloys of monovalent metals with R's; (2) alloys of polyvalent metals with R's; (3) alloys of R metals with other R's. An example of each class is shown in fig. 17. In the first class, measurements of ρ_L for liquid alloys of Cu with La, Ce, Pr, Nd, and Gd have been reported (Güntherodt et al. 1976, Busch et al. 1970a, Güntherodt et al. 1977, Ackermann et al. 1976, Güntherodt and Zimmermann

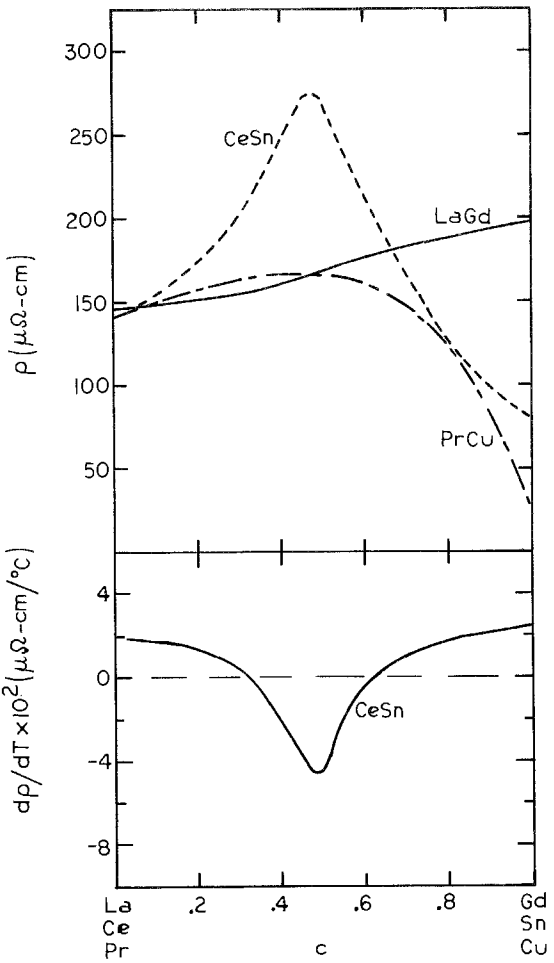

Fig. 17. ρ for three types of liquid alloys of R's as a function of concentration (atomic fraction), and $d\rho/dT$ for liquid CeSn. The data are from: LaGd, at 1320°C – Güntherodt et al. (1976); CeSn, at 1500°C – Ackermann et al. (1976); and PrCu, at 950°C – Busch et al. (1973).

1973, Busch et al. 1973). For these, the concentration dependence of ρ_L {i.e. $\rho_L(c)$} is roughly parabolic, and $d\rho_L/dT$ is small and positive for all concentrations. The liquid alloy CoCe also falls into this class (Ackermann et al. 1976). In class two, results for ρ_L for alloys of Sn with La, Ce, and Gd (Güntherodt et al. 1976, Delley et al. 1978, Güntherodt et al. 1977, Ackermann et al. 1976), and of InCe (Delley et al. 1978) have been reported. For these alloys, $\rho_L(c)$ is clearly peaked, and $d\rho_L/dT$ becomes negative over the concentration range of large ρ_L. (See fig. 17). Measurements of ρ_L for alloys in the third class include those for LaGd, LaCe, and CeEr (Güntherodt et al. 1976, Güntherodt et al. 1977, Ackermann et al. 1976). For these alloys, $\rho_L(c)$ is monotonic, approximately linear, and $d\rho_L/dT$ is small and positive for all concentrations.

The measurements of $d\rho_L/dT$ for all of these alloys are consistent with the

t-matrix theory of Evans and his co-workers. (See, for example, Güntherodt et al. 1977.) If one can assume that $d\rho_L/dT$ is influenced largely by structural effects, depending upon the temperature-dependence of $A(K)$, and if n_c for the pure liquid R's is ~ 1, then alloying R's with monovalent metals will not raise $2k_f$ to the region of K_p, the first peak in $A(K)$, and $d\rho_L/dT$ remains characteristic of simple monovalent metals (>0 and small). Alloying R's with other R's also leaves $n_c \sim 1$ for all concentrations, with the same effect. Alloying R's with polyvalent metals, however, sweeps n_c through 2, moving $2k_f$ across K_p, and results in $d\rho_L/dT < 0$ in this range. This is also a range in which ρ_L is large, consistent with the Mooij rule.

The t-matrix formulation of Evans and his co-workers can be extended readily to cover the case of liquid binary alloys. In this extension, $A(K)|t|^2$ in eq. (42) is replaced by

$$A(K)|t|^2 \rightarrow c_a|t_a|^2(1 - c_a + c_a A_{aa}) + c_b|t_b|^2(1 - c_b + c_b A_{bb}) + c_a c_b(t_a t_b^* + t_b t_a^*)(A_{ab} - 1)\,, \tag{47}$$

where the subscripts identify the individual constituents, and the A_{ab} are the partial structure factors. This method has also proven relatively successful in addressing the electronic properties of a variety of liquid alloys.

Also significant in this respect is the observation by Güntherodt and Zimmermann (1973) that $d\rho_L/dc$, for low R concentrations, is nearly the same for CuLa, CuLa, CuNd and CuGd. Ackermann et al. (1976) observe the same effects for the alloys SnLa, SnCe, SnGd for low R concentrations. The fact that the varying magnetic nature of these solutes is not seen in $d\rho_L/dc$ implies that magnetic contributions to ρ_L are minimal, and apparently can be ignored. (This is consistent with the discussion of the dependence of ρ_L upon n_c for the pure liquid lanthanides, above.) Ohno and his collaborators have also measured $d\rho_L/dc$ for many dilute alloys of the R's in Sn and In (Ohno 1978, Ohno and Kakinuma 1980, Kakinuma and Ohno 1981). They also find that magnetic contributions to ρ_L must be small, and that the t-matrix formulation via eq. (47) can adequately describe the behavior of $\rho_L(c)$ for these alloys.

In spite of the apparent consistency of the experimental results with calculations based on the t-matrix theory, the question of the validity of the application of this theory to strong-scattering liquid metals and alloys remains. Harris et al. (1978) have approached this question theoretically by means of a coherent-potential approximation displaying a Debye–Waller factor type of temperature dependence. They succeed by means of this strong-scattering model to reproduce, in semiquantitative fashion, the negative $d\rho_L/dT$ for liquid SnCe.

Minimal data on Q for liquid alloys of R metals exist. Enderby and Howe (1973) report measurements of Q for dilute alloys of Ce in liquid Al and Sn, and for liquid Ce_3Ni and $CeCu_2$. They find that $dQ/dc = +0.5$ and $+0.3$ (μV/°C-atom%) for Ce in Al and Ce in Sn, respectively. No theoretical work on Q for R-alloys has been reported.

5.2. *Hall effect*

5.2.1. *Experiment*

Hall coefficients, R_H, have been measured for only four of the pure liquid R's. The results of these measurements, at the respective melting temperatures of the metals, are: 6.15 (La), 7.8 (Ce), 9.3 (Pr), and 11.7 (Nd). The units are 10^{-11} m^3/A·s. $R_H(T)$, shown for La and Ce in fig. 18, is characteristic of these metals. R_H for several liquid alloys of R's have also been measured. These include R/non-R alloys (CuCe, CuPr, AgPr and AlCe), and one R/R alloy (LaCe). (See Güntherodt and Kunzi 1973.)

In spite of the relatively limited data on R_H for the liquid R's, the following common characteristics are seen to emerge. (1) R_H for each of the pure liquid R's is greater than zero; this is also characteristic of all binary liquid alloys of R's with more than about 40 atom% R concentration. {It appears that several pure liquid transition metals (Mn, Fe, Co) may have $R_H > 0$, as well.} (2) There is little or no change in R_H for the pure R's across the melting temperature, implying that little change has occurred in the electronic properties of these metals upon melting. (See Busch et al. 1971.) (3) R_H is independent of temperature for the pure R's and for the R-rich liquid alloys (Busch et al. 1970a, 1974). (4) R_H varies linearly with Z for the light liquid R's (see fig. 19.) and varies linearly with concentration for liquid LaCe. (Güntherodt and Kunzi 1973.) These dependencies appear naively to be similar to the dependences of electrical resistivity, $\rho_L(Z)$ for the pure liquid R's, and $\rho_L(c)$ for liquid R/R alloys. (See section 5.1.2.) It is also observed that, for each R/non-R liquid alloy, $R_H(c)$ varies linearly with atomic

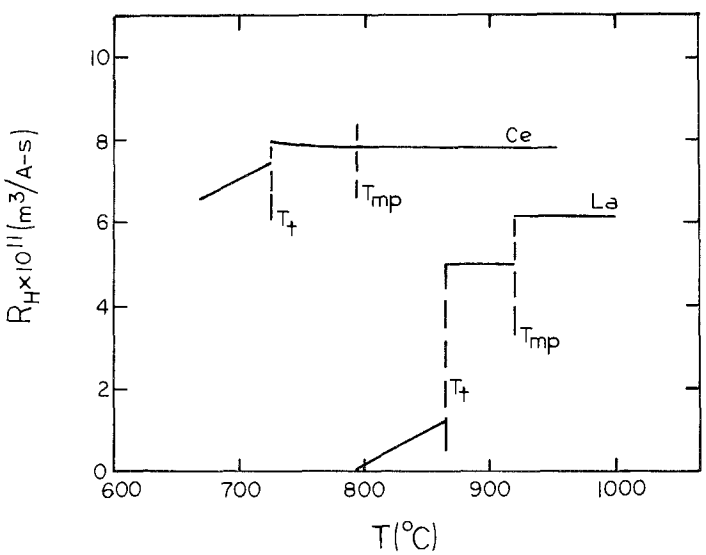

Fig. 18. The Hall coefficient, R_H, for solid and liquid La and Ce as a function of temperature. Data are from Güntherodt and Künzi (1973).

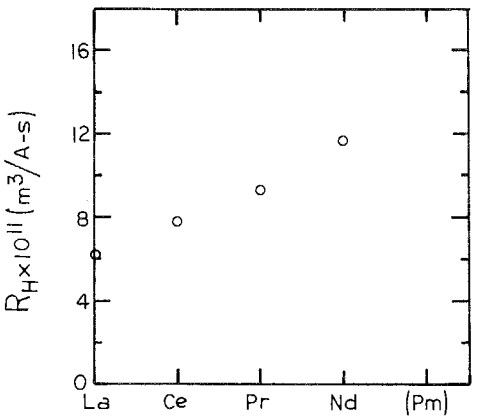

Fig. 19. Measured values of R_H for the liqht liquid R's at their respective melting temperatures, as a function of the number of 4f electrons. Data are from Güntherodt and Künzi (1973).

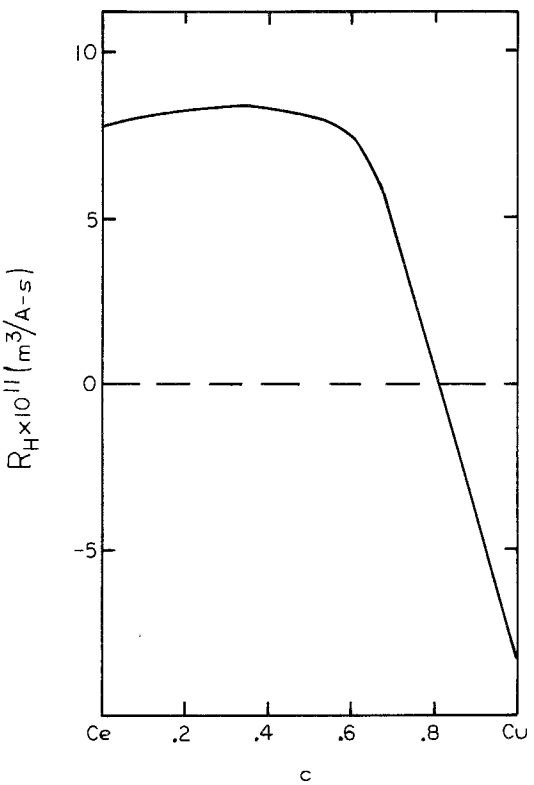

Fig. 20. Hall coefficient, R_H, for the liquid alloy, CeCu, as a function of concentration (atomic fraction), c. The $R_H(c)$ shown is characteristic of temperatures just above the alloy melting temperature. (R_H is nearly temperature-independent up to 300°C above T_{mp}.) Data are from Güntherodt and Künzi (1973).

fraction, $1-c$, of the R, from the negative value characteristic of the non-R to the positive value characteristic of the R, reaching this positive value by about 40 atom% R concentration. As $1-c$ then continues to increase, R_H remains nearly constant. (See fig. 20.)

5.2.2 *Theory and discussion*

A good review of the theoretical picture of the Hall effect in liquid metals has been presented by Ballentine (1980). We will only comment briefly on this here, and will identify advances that have occurred subsequently.

A zero-order theory of the Hall effect is easy to construct, and its results are well known. In a nearly-free-electron model, the Hall coefficient, $R_H^{(0)}$, is given as

$$R_H^{(0)} = \frac{1}{n_e e} , \tag{48}$$

where n_e is the number density of charge carriers, and $e = -|e|$ for conduction by electrons. Clearly, the predicted $R_H^{(0)} < 0$ is at variance with measurements of R_H for the liquid R's. Further progress beyond this zero-order theory has proven to be difficult.

It is well to note that there is little or no observed change in R_H across the melting temperature for these R metals; it appears, therefore, that a successful theory of R_H for the liquid should also be valid for the solid at high temperatures.

Some clear theoretical progress was made by Ballentine (1977): using random force correlation theory, he was able to demonstrate that the first correction to $R_H^{(0)}$ must be at least third order in the scattering. This will provide a useful test of various approaches to this problem.

Ten Bosch (1973) examined the effects of spin–orbit scattering on R_H, obtaining two spin–orbit-dependent terms; one was due to an additional transverse current, and the other due to a transverse polarization. Numerical estimates indicated that these anomalous contributions could result in $R_H > 0$. Ballentine and Hubermann (1977) suggest, however, that these two contributions may in fact be a single effect, appearing in two different guises, and therefore should not be summed.

Ballentine (1977) and Ballentine and Hubermann (1977) looked at the effect of the spin–orbit interaction on "skew-scattering", the nonreversibility of the transition probability between the initial and final states, due to the presence of an externally-applied magnetic field. Going beyond Born approximation, they obtained two correction terms to $R_H^{(0)}$: one involved the square of the ratio of the normal relaxation time to the skew-scattering relaxation time; the other went as the change in electron paramagnetic susceptibility due to electron interactions. This work showed that reasonably large deviations from $R_H^{(0)}$ could be obtained in this way, and qualitative success was seen in comparisons of calculated values with measured values. While this work focused on non-transition, non-R metals, it should be applicable to these as well. Ballentine (1982) speculated that, since the Fermi surface of solid La is dominated, at least in certain regions, by hole-like

behavior, perhaps some of these hole-like characteristics could survive into the liquid, making $R_H > 0$. This speculation was not supported by subsequent calculations (Ballentine 1982).

Weir et al. (1983) and Gallagher et al. (1983) examined the effects of s–d hybridization on R_H for amorphous transition metals and alloys. They suggested that anomalous dispersion ($dE/dk < 0$) may occur, implying negative group velocities, and a mechanism by which R_H could be >0. In other recent work, Bose et al. (1983) have questioned this method, however, finding no region of $dE/dk < 0$, and therefore placing this work in some doubt.

Very recently, Harris (1986) has employed the Kubo–Greenwood formalism and weak-scattering theory to evaluate the transverse conductivity in a magnetic field, σ_{xy}, and hence R_H. He finds

$$R_H = R_H^{(0)}\left(1 + \frac{2}{5}\frac{\partial \ln \tau}{\partial \ln E}\bigg|_{E_f}\right), \tag{49}$$

where τ is the electron lifetime. $R_H^{(0)} < 0$, but $d\tau/dE$ may be large and negative for E_f below a d-resonance energy, providing a mechanism by which positive R_H may be realized. This situation should describe the light liquid R's. On the other hand, a similar expression for thermopower, Q, would predict $Q > 0$, which is not observed (table 10). Harris (1986) notes, however, that the τ's entering the expressions for R_H and Q are not identical; this may contribute to the difference that is seen.

It is clear that considerable theoretical effort has been expended and progress has been made in understanding positive R_H for liquid metals; it is also clear that more work must be done before this effect can be considered well-understood.

Acknowledgments

I am happy to thank Professor W.H. Young for his helpful comments on the manuscript, and Professor J.E. Enderby for his reading of it as well. Partial support for the preparation of this chapter has been provided by the National Science Foundation via Grant No. DMR 86-03240.

References

Ackermann, K.P., H.J. Güntherodt, E. Hauser and H.U. Künzi, 1976, Phys. Lett. A **55**, 378.
Allen, B.C., 1972, in: Surface Tension of Liquid Metals, Liquid Metals, ed. S.Z. Beer (Dekker, New York) ch. 4.
Arajs, S., 1960a, J. Chem. Phys. **32**, 951.
Arajs, S., 1960b, Phys. Rev. **120**, 756.
Arajs, S., and R.V. Colvin, 1961, J. Appl. Phys. **32**, 336S.
Arajs, S., and D.S. Miller, 1960, J. Appl. Phys. **31**, 325S.
Arajs, S., R.V. Colvin and J.M. Peck, 1961, J. Chem. Phys. **34**, 1959.
Ascarelli, P., and A. Paskin, 1968, Phys. Rev. **165**, 222.
Ashcroft, N.W., and D.C. Langreth, 1967, Phys. Rev. **156**, 685.
Ashcroft, N.W., and J. Lekner, 1966, Phys. Rev. **145**, 83.

Atalla, S.R., 1972, High Temp.-High Pressures **4**, 447.
Avignon, M., and L.M. Falicov, 1974, J. Phys. F **4**, 1782.
Baer, Y., and G. Busch, 1973, Phys. Rev. Lett. **31**, 35.
Ballentine, L., 1977, in: Theory of the Hall Effect in Liquid Metals, Inst. Phys. Conf. Ser. No. 30, eds R. Evans and D.A. Greenwood (Institute of Physics, Bristol) p. 188–199.
Ballentine, L.E., 1980, The Hall Effect in Liquid Metals, in: The Hall Effect and Its Applications, eds C.L. Chien and C.R. Westgate (Plenum, London) p. 201–213.
Ballentine, L.E., 1982, Phys. Rev. B **25**, 6089.
Ballentine, L.E., 1988, Calculation of the Thermoelectric Power by the LCAO Recursion Method, in: Proc. 6th Int. Conf. on Liquid and Amorphous Metals, Z. Phys. C **157S**, 753–757.
Ballentine, L.E., and J.E. Hammerberg, 1983, Phys. Rev. B **28**, 1103.
Ballentine, L.E., and M. Huberman, 1977, J. Phys. C **10**, 4991.
Banchila, S.N., and L.P. Filippov, 1974, J. Eng. Phys. **27**, 839.
Batalin, G.I., V.A. Stukalo, N.Ya. Neshchimenko, V.A. Gladkikh and O.I. Lyoborets, 1977, Russ. Metall. **6**, 35.
Bellissent, R., and G. Tourand, 1975, J. Phys. **36**, 97.
Bennemann, K.H., 1976, J. Phys. F **6**, 43.
Bose, S.K., L.E. Ballentine and J.E. Hammerberg, 1983, J. Phys. F **13**, 2089.
Breuil, M., and G. Tourand, 1969, Phys. Lett. A **29**, 506.
Burkov, A.T., and M.V. Vedernikov, 1984, Sov. Phys.-Solid State **26**, 2211.
Burr, C.R., and S. Ehara, 1966, Phys. Rev. **149**, 551.
Busch, G., H.J. Güntherodt, H.U. Künzi, H.A. Meier and L. Schlapbach, 1970a, Mater. Res. Bull. **5**, 567.
Busch, G., H.J. Güntherodt, H.U. Künzi and L. Schlapbach, 1970b, Phys. Lett. A **31**, 191.
Busch, G., H.J. Güntherodt and H.U. Künzi, 1971, Phys. Lett. A **34**, 309.
Busch, G., H.J. Güntherodt, H.A. Meier and L. Schlapbach, 1972, 18th Conf. Mag. Mag. Mat'ls, AIP Conf. Proc. No. 10, 689.
Busch, G., H.J. Güntherodt, H.U. Künzi and H.A. Meier, 1973, Electronic Structure of Liquid Transition and Rare-Earth Metals and their Alloys, in: The Properties of Liquid Metals, ed. S. Takeuchi (Taylor and Francis, London) p. 263–276.
Busch, G., H.J. Güntherodt, H.U. Künzi, H.A. Meier and L. Schlapbach, 1974, J. Phys. Colloq. C4 **35**, 329.
Castanet, R., 1984, C.R. Acad. Paris Sci. **298**, 5.
Colvin, R.V., S. Arajs and J.M. Peck, 1961, Phys. Rev. **122**, 14.
Cook, J.G., 1979, The Wiedemann–Franz Ratio of Liquid Metals, in: Proc. 16th Int. Conf. on Thermal Conductivity, ed. D.C. Larsen (Plenum, New York) pp. 305–316.
Crawley, A.F., 1974, Int. Metall. Rev. **19**, 32.
Delley, B., and H. Beck, 1979a, J. Phys. F **9**, 517.
Delley, B., and H. Beck, 1979b, J. Phys. F **9**, 2231.
Delley, B., H. Beck, H.U. Künzi and H.J. Güntherodt, 1978, Phys. Rev. Lett. **40**, 193.
Delley, B., H. Beck, H.U. Künzi and H.J. Güntherodt, 1979a, J. Phys. Colloq. C5 **40**, 258.
Delley, B., H. Beck, D. Trautman and F. Rosel, 1979b, J. Phys. F **9**, 505.
Dennison, D.H., M.J. Tschetter and K.A. Gschneidner Jr, 1966a, J. Less-Common Met. **10**, 108.
Dennison, D.H., M.J. Tschetter and K.A. Gschneidner Jr, 1966b, J. Less-Common Met. **11**, 423.
Dennison, D.H., K.A. Gschneidner Jr and A.H. Daane, 1966c, J. Chem. Phys. **44**, 4273.
Dokko, W., and R.G. Bautista, 1980, Metall. Trans. B **11**, 511.
Doriot, P.A., H.J. Güntherodt and L. Schlapbach, 1971, Phys. Lett. A **37**, 213.
Dupree, R., and E.F.W. Seymour, 1972, in: Magnetic Properties of Liquid Metals, Liquid Metals, ed. S.Z. Beer (Dekker, New York) ch. 11.
Duthie, J.C., and D.G. Pettifor, 1977, Phys. Rev. Lett. **38**, 564.
Enderby, J.E., 1985, Diffraction Studies of Liquids, in: Amorphous Solids and the Liquid State, eds N.H. March, R.A. Street and M. Tosi (Plenum, New York) pp. 3–30.
Enderby, J.E., and R.A. Howe, 1973, The Thermoelectric Power of Liquid Metals and Alloys, in: The Properties of Liquid Metals, ed. S. Takeuchi (Taylor and Francis, London) pp. 283–287.
Enderby, J.E., and V.T. Nguyen, 1975, J. Phys. C **8**, L112.
Ermakov, A.F., Yu.O. Esin and P.V. Gel'd, 1982, Russ. Metall. **5**, 56.
Esin, Yu.O., M.G. Valishev, P.V. Gel'd and L.M. Tushkova, 1976, Russ. Metall. **1**, 19.
Esin, Yu.O., A.F. Ermakov, M.G. Valishev, P.V. Gel'd and E.S. Levin, 1983, Russ. Metall. **3**, 49.
Esposito, E., H. Ehrenreich and C.D. Gelatt Jr, 1978, Phys. Rev. B **18**, 3113.
Evans, R., 1974, J. Phys. C **7**, 2808.
Evans, R., B.L. Gyorffy, N. Szabo and J.M. Ziman, 1973, On the Resistivity of Liquid Transition Metals, in: The Properties of Liquid Metals, ed. S. Takeuchi (Taylor and Francis, London) pp. 319–331.
Evele, M., J. Kooistra and J.B. Van Zytveld, 1981, Phys. Lett. A **129**, 241.
Faber, T.E., 1972, An Introduction to the Theory of Liquid Metals (Cambridge University Press, London).
Frohberg, M.G., and T. Cakici, 1978, Z. Metallkd. **69**, 296.
Gaibullaev, F., A.R. Regel' and Kh.Khusanov, 1969, Sov. Phys.-Solid State **11**, 1138.
Gallagher, B.L., D. Creig, M.A. Howson and

A.A.M. Croxon, 1983, J. Phys. F **13**, 119.
Grosse, A.V., 1961, J. Inorg. Nucl. & Nucl. Chem. **22**, 23.
Grosse, A.V., 1962, J. Inorg. Nucl. & Nucl. Chem. **24**, 147.
Güntherodt, H.J., and H.U. Künzi, 1973, Phys. Kondens. Materie **16**, 117.
Güntherodt, H.J., and H.A. Meier, 1973, Phys. Kondens. Materie **16**, 25.
Güntherodt, H.J., and L. Schlapbach, 1971, Helv. Phys. Acta **44**, 575.
Güntherodt, H.J., and A. Zimmermann, 1973, Phys. Kondens. Materie **16**, 327.
Güntherodt, H.J., E. Hauser and H.U. Künzi, 1974a, Phys. Lett. A **47**, 189.
Güntherodt, H.J., E. Hauser and H.U. Künzi, 1974b, Phys. Lett. A **48**, 201.
Güntherodt, H.J., E. Hauser, H.U. Künzi, R. Evans, J. Evers and E. Kaldis, 1976, J. Phys. F **6**, 1513.
Güntherodt, H.J., E. Hauser and H.U. Künzi, 1977, Electrical Resistivity of Liquid Rare Earth Metals and their Alloys, in: Inst. Phys. Conf. Ser. No. 30, eds R. Evans and D.A. Greenwood (Institute of Physics, Bristol) pp. 324–336.
Habermann, C.E., and A.H. Daane, 1964, J. Less-Common Met. **7**, 31.
Hafner, J., 1976, J. Phys. F **6**, 1243.
Hafner, J., 1977, Phys. Rev. A **16**, 351.
Hafner, J., A. Pasturel and P. Hicter, 1984, J. Phys. F **14**, 2279.
Hagstrom, S.B.M., P.O. Hedén and H. Lofgren, 1970, Solid State Commun. **8**, 1245.
Harder, J.M., and W.H. Young, 1977, Phys. Lett. A **61**, 468.
Harris, R., 1986, J. Phys. F **16**, 53.
Harris, R., and M. Shalmon, 1980, J. Phys. F **10**, L77.
Harris, R., M. Shalmon and M.J. Zuckermann, 1978, Phys. Rev. B **18**, 5906.
Hasegawa, M., 1988, The Surface Tension and Surface Density Profile in Liquid Metals: A Semi-empirical Treatment of the Screening Effect, in: Proc. 6th Int. Conf. on Liquid and Amorphous Metals, Z. Phys. C **156S**, 445–450.
Hedén, P.O., H. Lofgren and S.B.M. Hagstrom, 1971, Phys. Rev. Lett. **26**, 432.
Hiemstra, C., P. Keegstra, W.T. Masselink and J.B. Van Zytveld, 1984, J. Phys. F **14**, 1867.
Hiemstra, S., D. Prins, G. Gabrielse and J.B. Van Zytveld, 1977, Phys. & Chem. Liq. **6**, 271.
Hodges, C.H., and M.J. Stott, 1972, Philos. Mag. **26**, 375.
Holzhey, C., F. Brouers, J.R. Franz and W. Schirmacher, 1982, J. Phys. F **12**, 2601.
Howe, R.A., and J.E. Enderby, 1973, J. Phys. F **3**, L12.
Hultgren, R., P.D. Desai, D.T. Hawkins, M. Gleiser, K.K. Kelley and D.D. Wagmann, 1973, Selected Values of the Thermodynamic Properties of the Elements (ASM International, Metals Park, OH).
Itoh, M., K. Niizeki and M. Watabe, 1984, Electronic Transport Theory of Liquid Non-Simple and Amorphous Metals, in: Proc. 5th Int. Conf. on Liquid and Amorphous Metals, eds C.N.J. Wagner and W.L. Johnson (North-Holland, Amsterdam) pp. 1267–1272.
Johansson, B., and N. Mårtensson, 1987, Thermodynamic Aspects of 4f Levels in Metals and Compounds, in: Handbook on the Physics and Chemistry of Rare Earths, eds K.A. Gschneidner Jr and L. Eyring (North-Holland, Amsterdam) ch. 69.
Kakinuma, F., and S. Ohno, 1981, J. Phys. Soc. Jpn. **50**, 3644.
Kamp, P.G., and S. Methfessel, 1988, Magnetic Susceptibility and Atomic Short Range Order in Molten Co and Co–Y Alloys, in: Proc. 6th Int. Conf. on Liquid and Amorphous Metals, Z. Phys. C **156S**, 575–579.
Khanna, K.N., 1981, Phys. Status Solidi b **103**, K15.
Kononenko, V.I., V.G. Shavchenko and A.L. Sukhman, 1978, Russ. Metall. **1**, 59.
Kononenko, V.I., A.L. Sukhman and V.G. Shavchenko, 1980, Russ. Metall. **2**, 45.
Kononenko, V.I., S.L. Gruverman and A.L. Sukhman, 1983, Russ. Metall. **6**, 49.
Kononenko, V.I., A.L. Sukhman, S.L. Gruverman and V.V. Torokin, 1984, Phys. Status Solidi a **84**, 423.
Kooistra, J., K. Dreyer and J.B. Van Zytveld, 1988, J. Phys. F **18**, 1225.
Krieg, G., R.B. Genter and A.V. Grosse, 1969, Inorg. & Nucl. Chem. Lett. **5**, 819.
Kuntz, L.K., and R.G. Bautista, 1976, Metall. Trans. B **7**, 107.
Lang, N.D., and W. Kohn, 1970, Phys. Rev. B **1**, 4555.
Lundin, C.E., A.S. Yamamoto and J.F. Nachman, 1965, Acta Metall. **13**, 149.
March, N.H., 1985, Structure and Forces in Liquids and Liquid Mixtures, in: Amorphous Solids and the Liquid State, eds N.H. March, R.A. Street and M. Tosi (Plenum, New York) p. 53.
Mardykin, I.P., 1975, Teplofiz. Vys. Temp. **13**, 211.
Mardykin, I.P., V.I. Kashin and A.A. Vertman, 1972, Izv. Akad. Nauk. SSSR Met. **6**, 96.
Mardykin, I.P., V.I. Kashin and P.P. Seitnev, 1973, Izv. Akad. Nauk. SSSR Met. **6**, 77.
McAlister, S.P., and E.D. Crozier, 1981, Solid State Commun. **40**, 375.
McEwen, K.A., 1978, Magnetic and Transport Properties of the Rare Earths, in: Handbook on the Physics and Chemistry of Rare Earths, eds K.A. Gschneidner Jr and L. Eyring (North-Holland, Amsterdam) ch. 6.
McGonigal, P.J., 1962, J. Phys. Chem. **66**, 1686.
Miedema, A.R., P.F. de Châtel and F.R. de Boer, 1980, Physica B **100**, 1.
Millhouse, A.H., and A. Furrer, 1975, Phys. Rev. Lett. **35**, 1231.
Mooij, J.H., 1973, Phys. Status Solidi a **17**, 521.
Mott, N.F., 1972, Philos. Mag. **26**, 1249.
Müller, M., and H.J. Güntherodt, 1980, J. Magn. & Magn. Mater. **15–18**, 1349.

Müller, M., E. Huber and H.J. Güntherodt, 1979, J. Phys. Colloq. C5 **40**, 260.
Murozzi, V.L., J.F. Janak and A.R. Williams, 1978, Calculated Electronic Properties of Metals (Pergamon, New York) p. 24.
Nikolayenko, I.V., E.A. Beloborodova and G.I. Batalin, 1979, Russ. Metall. **6**, 59.
Novikov, I.I., and I.P. Mardykin, 1973, High Temp. **11**, 472.
Novikov, I.I., and I.P. Mardykin, 1974, Sov. At. Energy **37**, 1088.
Novikov, I.I., and I.P. Mardykin, 1975, High Temp. **13**, 293.
Novikov, I.I., L.P. Filippov and V.I. Kostyukov, 1977, Sov. At. Energy **43**, 943.
Ohno, S., 1978, J. Phys. Soc. Jpn. **44**, 819.
Ohno, S., and F. Kakinuma, 1980, J. Phys. Colloq. C8 **41**, 527.
Pasturel, A., P. Hicter and F. Cyrot-Lackmann, 1983, J. Less-Common Met. **92**, 105.
Perkins, R.H., L.A. Geoffrion and J.C. Biery, 1965, Trans. Met. Soc. AIME (American Institute Mining, Metal Engineering) **233**, 1703.
Perrinello, M., N.H. March and M.P. Tosi, 1977, Nuovo Cimento **398**, 233.
Pulliam, G.R., and E.S. Fitzsimmons, 1955, Reactions of Cerium and Lanthanum with Ceramic Oxides, Report of the AEC (USA) ISC-659.
Rainford, B.D., and V.T. Nguyen, 1979, J. Phys. Colloq. C5 **40**, 262.
Rao, R.V.G., and B.M. Sitpathy, 1981, Indian J. Pure & Appl. Phys. **19**, 967.
Ray, D.K., 1971, in: Contributions of the Conduction Electrons to the Crystalline Electric Field in Rare Earth Metals, Rare Earths and Actinides, Inst. Phys. Conf. No. 3, (Durham, England) (Institute of Physics, Bristol) p. 15.
Rice, M.J., 1970, Phys. Rev. B **2**, 4800.
Rigney, D.A., J.A. Blodgett and C.P. Flynn, 1969, Philos. Mag. **20**, 907.
Rohr, W.G., 1966, J. Less-Common Met. **10**, 389.
Rudin, H., A.H. Millhouse, P. Fischer and G. Meier, 1977, in: Investigation of the Structure Liquid of Liquid La, Ce and Pr by Neutron Diffraction, Inst. Phys. Conf. Ser. No. 30, eds R. Evans and D.A. Greenwood (Institute of Physics, Bristol) p. 241.
Schlapbach, L., 1974, Phys. Condens. Matter **18**, 189.
Seerveld, J., S. Van Till and J.B. Van Zytveld, 1983, J. Chem. Phys. **79**, 3597.
Shimoji, M., 1977, Liquid Metals (Academic Press, London).
Solodovnikov, V.M., V.V. Singer, I.Z. Radovskii and P.V. Gel'd, 1983a, Sov. Phys. J. **26**, 643.
Solodovnikov, V.M., V.V. Singer, I.Z. Radovskii, P.V. Gel'd and V.E. Gusev, 1983b, Sov. Phys. J. **26**, 646.
Solodovnikov, V.M., V.V. Singer, I.Z. Radovskii and P.V. Gel'd, 1983c, Ikrayinss'kii Fizychnyi Zhurnal **28**, 1375.
Spedding, F.H., A.H. Daane and K.W. Herrmann, 1957, J. Met. Trans. AIME (American Institute, Mining, Metal Engineering) **9**, 895.
Spedding, F.H., J.J. McKeown and A.H. Daane, 1960, J. Phys. Chem. **64**, 289.
Stankus, S.V., and A.S. Basin, 1983, High Temp. **21**, 854.
Stankus, S.V., A.S. Basin and M.A. Revenko, 1981, High Temp. **19**, 213.
Steinberg, D.J., 1974, Metall. Trans. **5**, 1341.
Stretz, L.A., and R.G. Bautista, 1975, High Temp. Sci. **7**, 197.
Stukalo, V.A., N.Ya. Neshchimenko and G.I. Batalin, 1981, Russ. Metall. **3**, 18.
Stupian, G.W., and C.P. Flynn, 1968, Philos. Mag. **17**, 295.
Taylor, K.N.R., and M.I. Darby, 1972, Physics of Rare Earth Solids (Chapman & Hall, London) pp. 132ff.
ten Bosch, A., 1973, Phys. Kon. Mat. **16**, 289.
Ten Cate, J., J. Zwart and J.B. Van Zytveld, 1980, J. Phys. F **10**, 669.
Tosi, M.P., 1985, Liquid Surfaces and Solid–Liquid Interfaces, in: Amorphous Solids and the Liquid State, eds N.H. March, R.A. Street and M. Tosi (Plenum, New York) ch. 5.
Vadovic, C.J., and C.P. Colver, 1970, Philos. Mag. **21**, 971.
Vadovic, C.J., and C.P. Colver, 1971, Philos. Mag. **24**, 509.
Van Vleck, J.H., 1932, The Theory of Electronic and Magnetic Susceptibilities (Oxford University Press, New York).
Vedernikov, M.V., S.A. Kizhaev, A.V. Petrov and N.I. Moreva, 1975, Sov. Phys.-Solid State **17**, 212.
Vedernikov, M.V., A.T. Burkov, V.G. Dvunitkin and N.I. Moreva, 1977, J. Less-Common Met. **52**, 221.
Waseda, Y., 1977, The Structure of Liquid Transition Metals and their Alloys, in: Inst. Phys. Conf. Ser. No. 30, eds R. Evans and D.A. Greenwood (Institute of Physics, Bristol) p. 230.
Waseda, Y., 1980, The Structure of Non-Crystalline Materials (McGraw-Hill, New York).
Waseda, Y., and W.A. Miller, 1978, Philos. Mag. **38**, 21.
Waseda, Y., and S. Tamaki, 1977a, J. Phys. F **7**, L151.
Waseda, Y., and S. Tamaki, 1977b, Philos. Mag. **36**, 1.
Waseda, Y., and J.M. Toguri, 1978, The Charge Transfer Effect in Liquid Transition Metal Rare Earth Metal Alloys, in: Inst. Phys. Conf. Ser. No. 39 (Institute of Physics, Bristol) p. 432.
Waseda, Y., A. Jain and S. Tamaki, 1978, J. Phys. F **8**, 125.
Watanabe, S., and O.J. Kleppa, 1983, J. Chem. Thermodyn. **15**, 633.
Watanabe, S., and O.J. Kleppa, 1984, Metall. Trans. B **15**, 357.
Weir, G.F., M.A. Howson, B.L. Gallagher and G.J. Morgan, 1983, Philos. Mag. B **47**, 163.
Wittenberg, L.J., and R. De Witt, 1973, Vis-

cosity of Liquid Rare Earth and Actinide Metals, in: The Properties of Liquid Metals, ed. S. Takeuchi (Taylor and Francis, London) pp. 555–560.
Wittenberg, L.J., D. Ofte and W.G. Rohr, 1963, in: The Viscosity and Density of Molten La, Ce and Pr Metals, Proc. 3rd Rare Earth Conf., No. 2 (Gordon and Breach, New York) pp. 257–275.
Yatsenko, S.P., and O.P. Golovin, 1972, High Temp. **10**, 268.
Yokoyama, I., S. Naito and Y. Waseda, 1988, Entropies and Specific Heats at Constant Volume of Liquid Rare Earth Metals, in: Proc. 6th Int. Conf. on Liquid and Amorphous Metals, Z. Phys. C **156S**, 469–473.
Young, W.H., 1977, Interatomic Forces and Thermodynamic Properties of Liquid Metals: A Hard-Sphere Description, in: Inst. Phys. Conf. Ser. No. 30, eds R. Evans and D.A. Greenwood (Institute of Physics, Bristol) p. 1.
Zagrebin, B.N., S.P. Dovgopol and S.P. Yatsenko, 1975, Sov. Phys.-Solid State **17**, 2034.
Ziman, J.M., 1961, Philos. Mag. **6**, 1013.
Ziman, J.M., 1964, Adv. Phys. **13**, 89.

Handbook on the Physics and Chemistry of Rare Earths, Vol. 12
edited by K.A. Gschneidner, Jr. and L. Eyring

Chapter 86

THERMODYNAMIC PROPERTIES OF GASEOUS SPECIES

M.S. CHANDRASEKHARAIAH* and K.A. GINGERICH
Department of Chemistry, Texas A&M University, College Station, Texas 77843, USA

Contents

1. Introduction

Rare-earth elements, namely lanthanum through lutetium together with scandium and yttrium, are generally considered to display a predominantly trivalent cationic behavior. However, since 1960 the evidence began to accumulate that they display structural, electronic and energetic characteristics which are reflected in subtle differences in their chemistry. The thermodyamic properties of the rare-earth containing compounds also show this trend. Thermodynamic data for the rare-earth containing species support the view that the energetics of lanthanide species are dependent on electron configurations and structures of the metals and of the gaseous atoms. The enthalpies of vaporization of the rare-earth metals are an excellant example of this behavior.

Enthalpies of sublimation of lanthanides have been shown to decrease regularly from La to Eu, then again from Gd to Yb (Gschneidner 1961). This monotonic variation in property from La to Eu and again from Gd to Yb is often referred to

*Present address: *Water Chemistry Division, Bhabha Atomic Research Center, Bombay 400085, India.*

as "double periodicity of rare-earths." According to Brewer (1971), this anomalous behavior of the sublimation enthalpies is not due to the metallic phase but due to the abnormality of the gas. The crystal structures of most of these metals, except Sm, Eu and Yb, are similar and the metallic bonding is essentially trivalent and the cohesive energy, represented by the melting point of these metals, increases steadily with atomic number, the enthalpies of sublimation decreases steadily and sharply from La to Eu and again from Gd to Yb. This has been attributed to the vapor phase consisting of atoms of different valence character than in the solid metals. Similar behavior has been observed in the thermodynamic properties of many rare-earth gaseous species discussed in this chapter.

This review will be limited to certain thermodynamic properties of gaseous species of the elements yttrium, scandium, and lanthanum to lutetium. The dissociation enthalpies and enthalpies of formation are the two quantities which are evaluated and tabulated for all the species considered here. There have been two recent reviews by Gingerich (1980a, 1985) on this subject and should be referred to for literature references. In this review, the values reported in the literature have been recalculated in a large number of cases using newer data for reference systems.

2. Metal molecules containing rare-earth atoms

Rare earths, being strongly electropositive metals, are known to form stable compounds with most of the nonmetals. It has been shown that they also form stable intermetallic compounds (Gschneidner 1961). Recently mass spectrometric studies have established that gaseous metallic species with rare-earth atoms are also stable (Gingerich 1985). Some of them exhibit considerable stabilities. The dissociation energies are evaluated and are summarized here.

2.1. *Homonuclear diatomic molecules*

The rare-earth metals vaporize predominantly as monatomic species but the equilibrium vapors do contain small amounts of diatomic species (Gingerich 1980b). The dissociation enthalpies of these vapor species have been experimentally determined by Knudsen cell mass spectrometry. Then these data are combined with the standard enthalpies of formation of monatomic vapors to obtain the enthalpies of formation of the diatomic species.

The standard enthalpies of sublimation of rare-earth metals have been measured by a number of workers. Hultgren et al. (1973) have discussed the sources of data and error estimates in their tabulation. Later Morss (1976) has also briefly discussed these data in his comprehensive discussion on thermochemical properties of the lanthanides. Recently Bratsch and Lagowski (1985) have listed a set of values of the sublimitation enthalpies which are also listed in table 1. The values of ΔH_f° for rare-earth metals recommended in table 1 have been used in the recalculation of D^0 values.

TABLE 1
The standard enthalpies of formation (ΔH_f°) of gaseous rare-earth atoms and the homonuclear diatomic molecules (kJ/mol).

Rare-earth Element R	ΔH_f°(R, g, 298 K) (a)	ΔH_f°(R, g, 0 K) (This work)	δH_f°(R_2, g, 0 K)*	D_0°(R_2) (b)
La	431.0 ± 2.1	431.4 ± 2.1	620 ± 25	243 ± 21
Ce	420.1 ± 2.1	420.7 ± 2.1	603 ± 25	238 ± 21
Pr	356.9 ± 2.1	358.0 ± 2.1	590 ± 33	126 ± 29
Nd	326.9 ± 2.1	327.8 ± 2.1	576 ± 33	80 ± 29
Sm	206.7 ± 2.1	206.1 ± 2.1	362 ± 25	50 ± 21
Eu	177.4 ± 2.1	177.4 ± 4.1	326 ± 25	29 ± 17
Gd	397.5 ± 2.1	399.0 ± 2.1	626 ± 37	172 ± 33
Tb	388.7 ± 2.1	390.7 ± 2.1	653 ± 29	128 ± 25
Dy	290.4 ± 2.1	293.0 ± 4.1	519 ± 37	67 ± 29
Ho	300.6 ± 2.1	302.0 ± 2.1	523 ± 34	82 ± 30
Er	316.4 ± 2.1	317.6 ± 4.1	564 ± 37	71 ± 29
Tm	232.2 ± 2.1	233.4 ± 4.1	416 ± 25	50 ± 17
Yb	155.6 ± 2.1	156.1 ± 2.0	295 ± 21	17 ± 17
Lu	427.6 ± 2.1	427.8 ± 4.1	718 ± 41	138 ± 33
Y	421.3 ± 4.1	420.4 ± 2.1	685 ± 25	156 ± 21
Sc	377.9 ± 4.1	376.1 ± 4.1	593 ± 29	159 ± 21

*Calculated using ΔH_f°(R) of this work (column 3, table 1) and the D_0°(R_2) of the last column.
(a) Bratsch and Lagowski (1985).
(b) Gingerich (1980b).

The dissociation energies of the homonuclear diatomic molecules, $D_0^\circ(R_2)$, were calculated from the mass spectrometrically measured ion currents and the thermal functions evaluated for the gaseous species. The error limits shown in table 1 are upper limits and include those due to experimental uncertainties and also those due to the uncertainties in calculated thermal functions. The $D_0^\circ(R_2)$ values (last column, table 1) also show the "double periodicity" exhibited by the sublimation enthalpies. This "double periodicity" comes about because (1) in the thermodynamic calculations the ΔH_{subl}° of the pure rare-earth metals is needed, and (2) in the vaporization process the electronic configurations of both the solid rare-earth metal and the gaseous rare-earth metal need to be considered. For some of these there is a change from $(sd)^3 4f^n$ configuration in the metal to the $s^2 4f^{n+1}$ configuration in the gas and in others it does not change (La, Ce, Gd, Lu, Sc and Y remain "trivalent", and Eu and Yb remain "divalent") (Gschneidner 1971, Beaudry and Gschneidner 1978 and Cater 1978). The decrease in D_0° values from Gd_2 to Yb_2 is not as steep as is from La_2 to Eu_2 and it is also not as smooth as for La_2 to Eu_2. $D_0^\circ(Dy_2)$ is much smaller than that expected from a smooth, regular decrease with increasing atomic number. Either the experimental value for Dy_2 molecule has unusually large uncertainties or the enthalpy of sublimation value of Dy(g) has large error. As the dissociation reaction in each case involves only the gaseous species, namely R(g) and R_2(g), the thus observed "double periodicity" should be attributable to the electronic states of these species. This result thus further supports the hypothesis of Brewer (1971).

2.2. *Diatomic intermetallic rare-earth molecules*

Gaseous intermetallic molecules containing rare-earth atoms have interesting bonding characteristics. Several intermetallic diatomic species between rare-earth atoms and copper group metals as well as platinum metals have been observed (Gingerich 1980a, b). With gold, not only diatomic intermetallic species are observed but even polyatomic intermetallic species are identified and studied (Gingerich 1985, 1980a). In table 2, the enthalpies of formation and bond dissociation enthalpies of rare-earth-coinage group metal diatomic intermetallic species are summarized and in table 4 the atomization energies of polyatomic species are presented.

The bond dissociation energies for these intermetallic molecules vary between a low of 120 ± 19 kJ/mol for HoAg to a high of 346 ± 25 kJ/mol for LaAu. These values are a definite indication of true chemical bonding between the two atoms and not of Van der Waal's type molecules. The gold atom appears to form the strongest bonding among the three metals, namely copper, silver and gold, while silver forms the least stable molecules.

A number of diatomic intermetallic molecules containing a rare-earth and a platinum group metal have been observed and their bond dissociation energies

TABLE 2
The dissociation energies and the enthalpies of formation (ΔH_f°) of the rare earth–copper subgroup metals heterodiatomic molecules.

Molecule	D_0°(RB) kJ/mol	ΔH_f°(RB, 0 K) kJ/mol	Reference
LaAu	346 ± 25	453 ± 28	Gingerich and Finkbeiner (1970)
CeAu	318 ± 15	471 ± 18	Gingerich and Finkbeiner (1970)
PrAu	307 ± 25	419 ± 28	Gingerich and Finkbeiner (1970)
NdAu	290 ± 29	406 ± 32	Gingerich and Finkbeiner (1970)
EuAu	241 ± 12	304 ± 17	Cocke et al. (1975)
EuAg	123 ± 13	220 ± 18	Cocke et al. (1975)
TbAu	281 ± 33	478 ± 36	Kordis et al. (1974)
TbCu	187 ± 18	539 ± 21	Hilpert (1979)
DyAu	255 ± 24	406 ± 29	Hilpert (1977)
DyAg	124 ± 24	453 ± 29	Hilpert (1977)
DyCu	140 ± 18	489 ± 23	Hilpert (1979)
HoAu	263 ± 35	407 ± 38	Cocke and Gingerich (1971); Kordis et al. (1974)
HoAg	120 ± 19	466 ± 22	Cocke and Gingerich (1971); Gingerich et al. (1971)
HoCu	140 ± 19	498 ± 25	Hilpert (1979)
LuAu	328 ± 19	468 ± 25	Gingerich et al. (1971)
YAu	306 ± 12	482 ± 15	Gingerich and Finkbeiner (1971); Haque et al. (1980)
ScAu	276 ± 40	468 ± 45	Gingerich and Finkbeiner (1971)

TABLE 3
The dissociation energies and the enthalpies of formation (ΔH_f°) of the rare-earth and platinum metals heterodiatomic molecules (kJ/mol).

Molecule	D_0°(RA, 0 K)	ΔH_f°(RA, 0 K)	Reference
LaRh	546 ± 12	437 ± 18	Cocke et al. (1973a, b)
LaIr	573 ± 12	527 ± 20	Haque et al. (1979)
LaPt	501 ± 12	494 ± 15	Nappi and Gingerich (1981)
CeRu	490 ± 12	580 ± 18	Cocke and Gingerich (1978)
CeRh	541 ± 7	432 ± 13	Gingerich (1974)*
CePd	315 ± 21	481 ± 28	Cocke and Gingerich (1972)
CeOs	520 ± 20	688 ± 22	Cocke and Gingerich (1978)
CeIr	571 ± 9	518 ± 14	Gingerich (1974)†
CePt	546 ± 5	439 ± 8	Gingerich (1974)†
EuRh	234 ± 34	495 ± 40	Cocke et al. (1975)
LuPt	398 ± 34	594 ± 40	Gingerich (1971)
YRh	442 ± 11	530 ± 18	Haque and Gingerich (1980)
YPd	237 ± 15	433 ± 21	Ramakrishnan et al. (1984)
YIr	453 ± 15	636 ± 21	Haque et al. (1980)
YPt	470 ± 12	514 ± 15	Gupta et al. (1981)
ScRh	440 ± 11	488 ± 17	Haque and Gingerich (1980)
GeY	275 ± 11	522 ± 11	Kingcade and Gingerich (1986)
SiY	254 ± 17	625 ± 17	Kingcade and Gingerich (1986)

*The data were reevaluated using the latest data for D_0°(RhC) by Shim and Gingerich (1984).
†The data were reevaluated using the latest values for D_0°(IrC), and D_0°(PtC) by Gupta et al. (1981a).

have been determined experimentally (Gingerich 1985, 1980a). The data presented in table 3 show that the intermetallic bonds between platinum metals and the rare-earth elements are stronger than the corresponding values between the same rare-earth element and gold. There are indications that the bonds in rare-earth–platinum metals are multiple ones (Gingerich 1985). Gingerich (1973, 1974) and Miedema and Gingerich (1979) have suggested empirical models to describe these bonds.

TABLE 4
The atomization energies and enthalpies of formation (ΔH_f°) of polyatomic intermetallic vapors (kJ/mol).

Species	ΔH_{at}°	ΔH_f°(0 K)	Reference
Au_2Eu	549 ± 17	364 ± 21	Gingerich (1985)
Au_2Ho	533 ± 42	504 ± 46	Gingerich (1985)
Au_2Lu	602 ± 33	562 ± 39	Gingerich (1985)
Au_2Tb	582 ± 42	543 ± 48	Gingerich (1985)
Si_2Y	800 ± 23	528 ± 21	Kingcade and Gingerich (1986)

3. Oxides

Rare earths being good electropositive metals combine readily with all the nonmetal elements forming compounds in the solid state. However, with the exception of halides, only oxygen, carbon and sulphur have been observed to form stable gaseous vapors with the majority of rare-earth metals. We shall not be considering halides in this paper, but will review the gaseous species of rare-earth elements with other nonmetal elements.

Among these species, oxides are probably the best known and better studied molecules. All the 14 lanthanide elements, yttrium and scandium form gaseous oxides. Gaseous rare-earth oxide species of the general formulas, RO, R_2O, RO_2, and R_2O_2 where R is the rare-earth atom, have been observed (Gingerich 1980a). Among these, monoxides (RO) are the most abundant ones and have been studied more extensively (Pedley and Marshall 1983) athough data for other oxide species were reported by Gingerich (Gingerich 1980a).

3.1. *Rare-earth monoxides*

The lanthanide monoxides have been the subject of a number of thermodynamic investigations (Murad and Hildenbrand 1980, Ames et al. 1967, White et al. 1962, Ackermann et al. 1976, Ackermann and Rauh 1975, 1974, 1971). DeKock and Weltner (1971) have reported the spectroscopic results of a few spectra of these monoxides in argon matrix. But most of the thermodynamic results are based on the studies of high temperature vaporization of the solid oxides.

High temperature Knudsen effusion mass spectrometry had been the primary experimental method for these investigations. Vaporization of either pure sesquioxide (R_2O_3) or a mixture of sesquioxide and the corresponding metal ($R_2O_3 + R$) had been used as the source of the monoxide vapors. The sesquioxides vaporize predominantly according to the following reaction:

$$R_2O_3(s) = xRO(g) + (2 - x)R(g) + (3 - x)O(g)\,, \tag{1}$$

where $0 < x < 2.0$.

It has been generally assumed that the rare-earth sesquioxides vaporize congruently with almost stoichiometric composition though a few studies (White et al. 1962, Ackermann and Rauh 1971, 1975) have shown small deviations ($R_2O_{2.99}$ to $R_2O_{2.995}$) from ideal stoichiometry. But this approximation had insignificant contribution to the reliability of the thermodynamic data of monoxides.

One of the earliest systematic studies of the lanthanide monoxides was by White et al. (1962). They measured the vaporization rates of the sesquioxides and determined the enthalpies of formation of gaseous monoxides. Later, they extended this study by including a number of isomolecular equilibration studies (Ames et al. 1967) using high temperature mass spectrometry. Ackermann and Rauh (1975, 1974, 1971) have also studied the vaporization of some sesquioxides

and have reported the dissociation energies of monoxide vapors. Krause (1974) had reevaluated the then available data on the rare-earth monoxides and had recommended a set of best values. Since then there have been a few extensive studies (Murad and Hildenbrand 1980, Ackermann et al. 1976) which necessitates the revision of Krause's recommended values.

The standard enthalpy of formation, (ΔH_f°), and the dissociation energy, D_0°, are the two thermodynamic properties which have been deduced from the experimental results. The total mass effusion rates were combined with the vapor phase compositions derived from the mass spectrometric measurements to obtain the change in the enthalpies of the reaction (1). The second law values corresponded to the mean temperatures of measurements. The third law values corresponded to the standard temperature of either 298.15 K or 0 K.

In evaluating the enthalpy data at 0 K or at 298.15 K, it is necessary to calculate the Gibbs energy functions, $(G_T^\circ - H_0^\circ)/T$, of the monoxide vapors. In the absence of spectroscopic data for all molecules, the molecular parameters have been estimated. The models used to estimate these molecular constants were not always the same. Probably this difference in the estimation of the Gibbs energy functions may account for some of the scatter in the derived values of the dissociation energies. Recently Murad and Hildenbrand (1980) have discussed this point and the Gibbs energy functions used in this work are based upon their model.

The other important input data in the calculation of the dissociation energies, $D_0^\circ(\mathrm{RO, g})$, are the standard enthalpy of formation of atomic oxygen, the standard enthalpies of formation of the sesquioxides and the standard enthalpies of formation of rare-earth metal atoms. Among these, $\Delta H_{0,f}^\circ(\mathrm{O, g}) = 246.81 \pm 0.125$ kJ/mol (JANAF Table 1971), is known with sufficient accuracy that it will not contribute significantly to the uncertainties of the derived values for the monoxides. The values of the enthalpy of vaporization of rare-earth metals have been improved over the years. Yet the uncertainties in the values are not insignificant. The same is true of the enthalpies of formation of solid sesquioxides. Both sets of values have undergone significant changes since the work of Krause (1974). In order to have good internal consistency, many of the data of previous workers have been recalculated using the recent values for the auxiliary data. In table 1, we present the best values for the standard enthalpies of formation of gaseous atoms and in table 5 we present the corresponding values for the $\Delta H_f^\circ(\mathrm{R_2O_3, s})$.

The significant differences in calculating the Gibbs energy functions for these gaseous monoxides by different investigators have been largely due to the differences in the way the electronic contributions have been accounted for. Ames et al. (1967) have adopted the simple ionic model suggested by Brewer and Rosenblatt (1969). This was modified somewhat by Smoes et al. (1976). Murad and Hildenbrand (1980) have adopted this later model. Here the Gibbs energy functions for the monoxides were recalculated with minor changes using the model suggested by Murad and Hildenbrand (1980) and the values are summarized in table 6.

TABLE 5
The standard enthalpies of formation of rare-earth sesquioxides (kJ/mol).

R_2O_3(s)	$-\Delta H_f^\circ$(298 K) (This work)	$-\Delta H_f^\circ$(298 K)[a]	$-\Delta H_f^\circ$(298 K)[b,c]
La_2O_3	1794 ± 4.0	1973.3 ± 2.1	1794 ± 4.0
Ce_2O_3	1796 ± 4.0	1821.7 ± 3.8	1796 ± 4.0
Pr_2O_3	1824 ± 2.5	1825.5 ± 2.5	1823 ± 4.0
Nd_2O_3	1808 ± 5.0	1807.9 ± 5.0	1808 ± 4.0
Sm_2O_3	1828 ± 10	1832.2 ± 8.4	1824 ± 4.0
Eu_2O_3	1652 ± 10	1725.5 ± 10.5	1652 ± 4.0
Gd_2O_3	1816 ± 16	1815.9 ± 16.7	1816 ± 4.0
Tb_2O_3	1846 ± 20	1827.6 ± 8.4	1865 ± 4.0
Dy_2O_3	1863 ± 12	1863.1 ± 12.6	1863 ± 4.0
Ho_2O_3	1881 ± 8	1881.1 ± 8.4	1881 ± 4.0
Er_2O_3	1898 ± 4	1897.9 ± 4.2	1898 ± 4.0
Tm_2O_3	1889 ± 10	—	1889 ± 4.0
Yb_2O_3	1814 ± 6	1814.6 ± 6.3	1814 ± 4.0
Lu_2O_3	1871 ± 20	1881.9 ± 12.6	1861 ± 4.0
Y_2O_3	1905 ± 6	1905.4 ± 6.3	—
Sc_2O_3	1906 ± 6	1906.2 ± 6.3	—

[a]Kubaschewski and Alcock (1979).
[b]Ackermann and Chandrasekharaiah (1975).
[c]Gschneidner et al. (1973).

TABLE 6
The Gibbs energy functions and the electronic statistical multiplicities for the rare-earth monoxides.

Monoxide	Electronic Multiplicities	$\frac{-(G_T^\circ - H_0^\circ)}{T}$ (J K^{-1} mol^{-1})			
		2000 K	2200 K	2400 K	2600 K
LaO	2	271.83	275.22	278.28	281.16
CeO	6	280.37	284.09	287.15	289.99
PrO	8	283.47	286.86	289.95	292.80
NdO	10	285.52	288.91	292.00	294.85
SmO	12	287.57	290.91	294.01	296.85
EuO	16	290.12	293.47	296.56	299.41
GdO	9	285.73	289.07	292.17	295.01
TbO	20	292.50	295.89	298.95	301.79
DyO	12	288.53	291.92	294.97	297.82
HoO	12	288.74	292.09	295.18	298.03
ErO	10	287.40	290.58	293.84	296.69
TmO	8	285.68	289.03	292.13	294.97
YbO	6	280.59	286.94	290.03	292.88
LuO	2	274.51	277.90	280.96	283.80
YO	2	265.89	269.24	272.34	275.18
ScO	2	260.58	263.54	266.28	268.85

The primary sources of experimental data for the evaluation of the dissociation energies of the rare-earth monoxides have been the works of Ames et al. (1967), Ackermann et al. (1976) and Ackermann and Rauh (1975, 1974, 1971) and Murad and Hildenbrand (1980). Huber and Hertzberg (1979) list D_0° values which are in good agreement with the assessed values of Krause (1974). The latest measurements of Murad and Hildenbrand (1980) gave values that are somewhat different from those of Ames et al. (1967), but are in good agreement with the values evaluated by Ackermann and Chandrasekharaiah (1975).

The dissociation energies, D°(RO, g), and the standard enthalpies of formation, ΔH_f°(RO, g, 0 K) of the rare-earth monoxides have been recalculated using the recent values of the enthalpies of formation of solid sesquioxides (table 5) and of the gaseous metal atoms ΔH_f°(R, g, 0 K) (table 1). These recalculated values along with a few of the previous data are presented in table 7. In this reevaluation of D_0°(RO), we have made considerable use of the recent review by Pedley and Marshall (1983).

The nature of the bonding in these monoxides is not fully understood. Bonding in these oxides has been described in terms of the $R^{2+}O^{2-}$ ionic configuration with some success. (Ames et al. 1967, Ackermann et al. 1976, Guido and Guigli 1974). But Murad and Hildenbrand (1980) disagree with this model stating that the apparent success of ionic model could be due to a fortuitous adjustment of the

TABLE 7
The enthalpy of formation ($\Delta H_{f,0}^\circ$) and the dissociation enthalpies (D_0°) of rare-earth monoxides (kJ/mol).

Monoxide	$-\Delta H_{f,0}^\circ$	Dissociation enthalpy, D_0°				
		This work	(a)	(b)	(c)	(d)
LaO	121.0 ± 10.0	795 ± 9.6	797 ± 11	795 ± 9.6	794.9 ± 4.1	794.9 ± 10
CeO	117.0 ± 20.9	790 ± 17	801 ± 13	797 ± 9.6	786.6 ± 16.7	789 ± 10
PrO	133.9 ± 12.5	745 ± 9.5	743 ± 17	749 ± 9.6	736.4 ± 12.5	746.8 ± 10
NdO	125.5 ± 12.5	706 ± 12.5	698 ± 13	711 ± 9.6	698.7 ± 12.5	707 ± 10
SmO	117.0 ± 12.5	569 ± 9.6	567 ± 17	557 ± 9.6	569.0 ± 12.5	569 ± 10
EuO	46.0 ± 12.5	465 ± 15	479 ± 17	463 ± 9.6	468.6 ± 12.5	463.2 ± 10
GdO	66.9 ± 12.5	711 ± 12.5	710 ± 13	674 ± 9.6	711 ± 12.5	711.1 ± 10
TbO	54.4 ± 20.9	693 ± 21	704 ± 17	686 ± 9.6	690.4 ± 20.9	704.4 ± 10
DyO	75.3 ± 20.9	607 ± 21	611 ± 42	607 ± 9.6	610.8 ± 20.9	603 ± 10
HoO	54.4 ± 12.5	613 ± 9.6	607 ± 25	620 ± 9.6	602.5 ± 12.5	616.6 ± 10
ErO	37.7 ± 12.5	607 ± 9.6	604 ± 21	611 ± 9.6	602.5 ± 12.5	607.9 ± 10
TmO	31.4 ± 20.9	508 ± 9.6	507 ± 21	507 ± 9.6	510.5 ± 12.5	555.8 ± 10
YbO	−2 ± 21	401 ± 21	414 ± 8	406 ± 9.6	397.5 ± 20.9	355 ± 10
LuO	−8.4 ± 12.5	663 ± 9.6	671 ± 17	661 ± 9.6	665.3 ± 12.5	693.8 ± 10
YO	46.0 ± 9.6	715 ± 10	715 ± 10	—	—	—
ScO	54.4 ± 10	676 ± 10	676.5 ± 10	—	—	—

References:
(a) Pedley and Marshall (1983).
(b) Ackermann and Chandrasekharaiah (1975).
(c) Murad and Hildebrand (1980).
(d) Huber and Herzberg (1979).

estimated imputs such as the R^{2-} ion polarizabilities and the electron affinity of O^{2-}. According to them the bonding in these monoxides cannot be purely ionic and covalent bonding should also contribute significantly. They cite the example of the absence of double periodicity in the dissociation energies of the monofluorides for which the experimental data are available (Kleinschmidt et al. 1980, Zmbov and Margrave 1978) as the support for their argument.

The dissociation energies of these monoxides, $D_0^\circ(\mathrm{RO}, \mathrm{g})$, vary rather non-monotonically with the atomic numbers from La to Lu (fig. 1) exhibiting the "double periodicity" similar to the enthalpy of formation of the gaseous metal atoms. The non-monotonic variation in D_0° closely parallels the variation in the

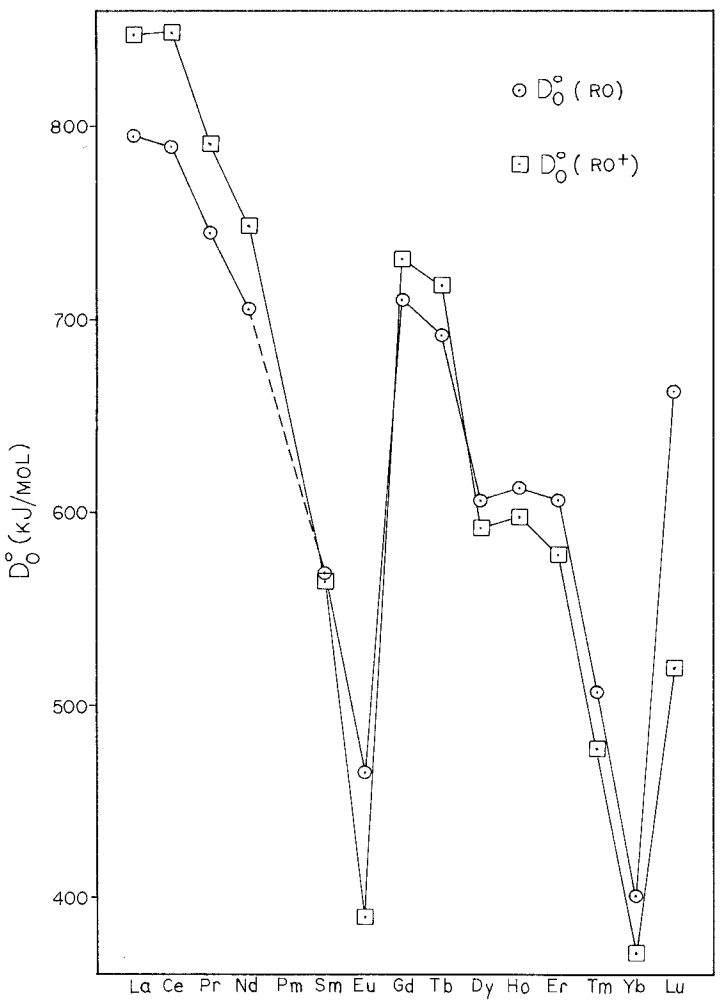

Fig. 1. Dissociation enthalpies of lanthanide oxides and oxide ions.

promotional energy of the $4f^n \rightarrow 4f^{n-1}5d$ electronic transitions. Thus the $4f^n \rightarrow 4f^{n-1}5d$ excitation energy plays a major role in determining the energetics of the lanthanide monoxide bonds. Ackermann et al. (1976) have observed a close similarity of the ionization potentials of the lanthanide metals and their monoxides. They showed that IP(R) and IP(RO) lie generally within 0.5 eV of each other. For La and the early members of the lanthanide sequence, the IP-values of the monoxides are less than those of the metals, but for europium and the members beyond terbium, the trend is reversed. Because the dissociation energies of the monoxide ions are related to those of the neutral monoxides $[D^\circ(RO^+) = D^\circ(RO) + IP(R) - IP(RO)]$, the values of $D^\circ(RO^+)$ will also show the same type of double periodicity. Hence, in the early lanthanides the ionized monoxides are more strongly bonded than the neutrals and the converse is true for the later members of the series. Thus the lanthanide monoxides ionization process, just as with the corresponding metal atoms, should involve the loss of a 6s electron (Martin et al. 1978) which in the monoxide must be nonbonding or slightly anti-bonding in the early lanthanide monoxides. Considering the importance of the $4f^n \rightarrow 4f^{n-1}5d$ excitation energy and the fact that at least one of the metal 6s electrons is not involved in bonding, it seems likely that the bonding in MO involves a metal s-d hybrid, or possibly a pure d orbital. The dissociation energies of (RO^+) are also calculated and are summarized in table 8.

TABLE 8
The dissociation enthalpies and enthalpies of formation (ΔH_f°) of lanthanide monoxide ions (kJ/mol).

Species	$\Delta H_{f,0}^\circ(R^+, g)$ (a)	$\Delta H_{f,0}^\circ(RO^+)$ ±17	$D_0^\circ(RO^+)$ ±15 (this work)	$D_0^\circ(RO^+)$ (b) ±9.6	$D_0^\circ(RO^+)$ (c) ±12.5
LaO^+	538.1	−62.2	847	842.4	857.7
CeO^+	527.5	−74.7	849	849.1	849.4
PrO^+	523.2	−22.0	792	794.1	790.8
NdO^+	529.6	+27.4	749	748.8	748.9
SmO^+	543.3	225.1	565	559.6	577.4
EuO^+	546.7	404.5	389	385.9	389.1
GdO^+	592.5	107.3	732	720.8	753.1
TbO^+	564.6	93.4	718	707.3	740.6
DyO^+	571.9	225.7	593	589.6	606.7
HoO^+	580.7	229.5	598	602.1	589.9
ErO^+	588.7	256.5	579	575.1	585.8
TmO^+	596.7	365.5	478	474.7	485.3
YbO^+	603.4	478.2	372	373.4	368.2
LuO^+	523.5	249.8	520	515.3	531.4

References:
(a) Morss (1976).
(b) Ackermann et al. (1976).
(c) Murad and Hildenbrand (1980).

3.2. *Polyatomic oxides*

Besides monoxides, other gaseous species of the formulas, R_2O, RO_2 and R_2O_2, R = rare-earth metal, have been observed as minor species in the rare-earth–oxygen systems at high temperatures (Smoes et al. 1965, Piacente et al. 1973, Pupp and Gingerich 1971, Staley and Norman 1969, Kordis and Gingerich 1977). They are about a factor of hundred to a thousand times less abundant than either the monoxide or the metal atom species. As such the thermodynamic data for these polyatomic oxides are very limited. The most extensive study of these polyatomic oxides was by Kordis and Gingerich (1977). The data presented here are taken primarily from this source and are recalculated using more recent data for the reference molecules presented in table 1.

The suboxides of the formula, R_2O, have been observed mass spectrometrically in a number of cases (Smoes et al. 1965, Kordis and Gingerich 1977). Quantitative data for the following reaction have been deduced from such measurements for La_2O, Eu_2O, Gd_2O, Ho_2O, Tb_2O, Lu_2O and Y_2O,

$$R(g) + RO(g) = R_2O(g). \tag{2}$$

From the measured ion intensities ratios, the equilibrium constants, and hence the Gibbs energy changes, for the reaction (2) were calculated. These reported equilibrium constants are combined with the corresponding values of monoxides (table 7) and of gaseous metal atoms (table 1), to evaluate the atomization energies for the $R_2O(g)$ species. Results are presented in table 9.

It was observed by Kordis and Gingerich (1977) that the ratios of the dissociation energy of the monoxide to the atomization energy of the corresponding suboxide lie within a narrow range. They have assumed this ratio to be constant. The available results support their conclusions, especially if one excludes the case of Lu_2O, and Eu_2O, and this ratio of atomization to dissociation was estimated to be 1.4 ± 0.2 which is slightly smaller than the value of 1.47 they have assumed. Assuming this value for the ratio of atomization energy of the suboxide to that of the corresponding monoxides, the atomization energies for those suboxides for which experimental values are not available are estimated. These estimated values are shown in parentheses.

The dimers, $(RO)_2$, have been observed in a few cases (Kordis and Gingerich 1977). The enthalpy of formation of the dimers were calculated from the mass spectrometrically determined equilibria of the reaction

$$2\,RO(g) = R_2O_2(g)\,. \tag{3}$$

The experimentally determined equilibrium constants were combined with the previously evaluated data for the corresponding monoxides to obtain the atomization energies of the dimers. In case of those dimers for which experimental data were missing, the atomization energies were estimated on the assumption that the ratio of atomization of dimeric oxide to its monomeric oxide is constant and equal

TABLE 9
The atomization energies (ΔH°_{at}) and the enthalpies of formation (ΔH°_f) of R_2O, RO_2 and R_2O_2 (kJ/mol).

Rare-earth Element	ΔH°_{at} (R_2O) (a)	$-\Delta H^\circ_f$ (R_2O)	$-\Delta H^\circ_{at}$ (RO_2) (b)	$-\Delta H^\circ_f$ (RO_2)	ΔH°_{at} (R_2O_2) (c)	$-\Delta H^\circ_f$ (R_2O_2)
La	1108 ± 40	−0.8 ± 25	(1511)	(587)	1920 ± 50	565 ± 50
Ce	(1124)	(37)	1435 ± 100	522 ± 100	1975 ± 100	642 ± 100
Pr	(1054)	(94)	1410 ± 100	560 ± 100	(1914)	(707)
Nd	(991)	(91)	(1328)	508 ± 100	(1800)	(653)
Sm	(799)	(139)	(1069)	(369)	(1452)	(545)
Eu	725 ± 40	123 ± 40	(885)	(214)	1349 ± 50	501 ± 50
Gd	990 ± 25	−51 ± 25	1312 ± 100	421 ± 100	1796 ± 50	508 ± 50
Tb	992 ± 40	−32 ± 25	(1307)	(425)	1762 ± 50	491 ± 50
Dy	(865)	(38)	(1157)	(373)	(1571)	(496)
Ho	864 ± 40	16 ± 25	1282 ± 100	488 ± 100	1624 ± 50	529 ± 50
Er	(860)	−(20)	(1151)	(341)	(1571)	(445)
Tm	(721)	(10)	(965)	(239)	(1310)	(352)
Yb	(571)	(13)	(764)	(115)	(1037)	(232)
Lu	1097 ± 40	−5 ± 20	(1259)	(338)	(1710)	361 ± 50
Y	1042 ± 30	−47 ± 40	—	—	1832 ± 50	496 ± 50

(a) Enthalpy change of the reaction: $R_2O(g) = 2R(g) + O(g)$.
(b) Enthalpy change of the reaction: $RO_2(g) = R(g) + 2O(g)$.
(c) Enthalpy change of the reaction: $R_2O_2(g) = 2R(g) + 2O(g)$.

to 2.58 (same as that assumed by Kordis and Gingerich (1977)). Estimated values are shown in parentheses.

The enthalpy of formation of dioxides, viz., CeO_2, PrO_2, NdO_2 and TbO_2, were determined (Pupp and Gingerich 1971, Staley and Norman 1969) from vaporization studies of their oxides. Kordis and Gingerich (1977) have extended this study to include GdO_2 and HoO_2. Atomization energies are calculated combining the measured equilibrium data with the corresponding dissociation energy of the monoxide. Estimated values are also listed in table 9 in parentheses.

4. Gaseous rare-earth carbides

The carbide systems are next to oxides in importance both in condensed state as well as in gaseous state. However, a few significant differences between the carbides and the oxides systems should be noted. Carbon, unlike the diatomic gaseous oxygen, not only is solid at ambient temperature, but even at high temperatures the carbon vapors in equilibrium with graphite contain many more species besides the diatomic carbon species. This difference between the carbide systems and the oxide systems is also found in the gaseous rare-earth carbides.

The gaseous carbide species containing rare-earth atoms are quite complex. The high temperature mass spectrometric data again are the primary source for

the thermodynamic data of these carbides. The enthalpies of formation and the atomization enthalpies have been evaluated from these mass spectrometric data.

In contrast to the rare-earth–oxygen systems, the rare-earth monocarbide vapors are exception rather than the rule. Only the CeC molecule has so far been observed in the gas phase (Gingerich 1969, Kingcade et al. 1983). On the other hand, dicarbides of the formula, RC_2, R = rare-earth atom, have been observed for most of the rare-earth elements (Gingerich 1980a, 1985). The recent review by Gingerich (1985) describes the complexity of gaseous rare-earth carbides. For primary references one should refer to this review.

4.1. *Rare-earth dicarbides*

Many of the thermodynamic data presented in the following tables have been re-evaluated. The enthalpies of formation of carbon vapors are those given in JANAF tables (Stull and Prophet 1971). For example, $\Delta H^\circ_{0,f}(C, g) = 709.5 \pm 1.9$ kJ/mol has been used in these reevaluations. The table 10 presents the enthalpies of formation and the enthalpies of atomization for the rare-earth dicarbide vapors. The listed uncertainties are the best estimates taking into account the inaccuracies in the experimentally measured quantities such as the temperature, ion currents, pressure calibrations, etc., of the mass spectrometric data, and also due to the estimated values of the Gibbs energy functions. All the

TABLE 10

The enthalpies of formation and the enthalpies of atomization (ΔH°_{at}) of rare-earth dicarbide molecules (kJ/mol)*.

Dicarbide	ΔH°_f (RC_2, 0 K)	ΔH°_{at} (RC_2, 0 K)	D°_0 (R–C_2) (a)	Reference
LaC_2	592 ± 9	1259 ± 5	669 ± 20	(Gingerich et al. 1981, 1982)
CeC_2	575 ± 10	1265 ± 5	675 ± 25	(Kingcade et al. 1983)
PrC_2	513 ± 36	1264 ± 30	674 ± 40	(Gingerich 1985)
NdC_2	509 ± 36	1238 ± 30	648 ± 40	(Gingerich 1985)
EuC_2	454 ± 36	1142 ± 30	553 ± 40	(Gingerich 1985)
GdC_2	563 ± 36	1255 ± 30	665 ± 40	(Gingerich 1985)
TbC_2	568 ± 41	1242 ± 35	652 ± 45	(Gingerich 1985)
DyC_2	557 ± 38	1155 ± 30	565 ± 44	(Gingerich 1985)
HoC_2	566 ± 36	1155 ± 30	565 ± 40	(Gingerich 1985)
ErC_2	574 ± 58	1163 ± 50	573 ± 64	(Gingerich 1985)
TmC_2	538 ± 38	1114 ± 30	524 ± 44	(Gingerich 1985)
LuC_2	609 ± 44	1238 ± 40	648 ± 48	(Gingerich 1985)
YC_2	585 ± 20	1254 ± 15	665 ± 25	(Haque and Gingerich 1980)
ScC_2	613 ± 20	1182 ± 20	592 ± 25	(Haque and Gingerich 1981)

*For RC_2, R = Pr to Lu, the D°_0 values were those reported by Gingerich (1985) but $\Delta H^\circ_{0,f}$ and D°_0(R–C_2) are calculated using the data shown in table 1 and $\Delta H^\circ_{0f}(C_2)$ given in JANAF Tables. The uncertainties are on the conservative side, and are larger than those estimated by Gingerich (1985).

(a) D°_0 is the enthalpy change for the reaction: $RC_2(g) = R(g) + C_2(g)$.

thermodynamic quantities tabulated in this report refer to the standard state of ideal gas at one standard atmosphere and zero kelvin unless otherwise specified.

Combining the values of $\Delta H_f^\circ(RC_2)$ and a value of 829.3 ± 3.9 kJ/mol for the standard enthalpy of formation of $C_2(g)$ (JANAF Tables), the bond dissociation enthalpies of $R-C_2$ bonds are evaluated and are presented in the 4th column of table 10. These bond dissociation enthalpies, $D_0^\circ(R-C_2)$, show a systematic variation with the atomic number. At first, the $D_0^\circ(R-C_2)$ shows a gradual decrease from LaC_2, CeC_2 to NdC_2 with rather a sharp decrease from NdC_2 to EuC_2. Another regular trend of decreasing values is observed from GdC_2 to YbC_2. Thus the bond dissociation energy, $D_0^\circ(R-C_2)$, of the dicarbide species also exhibit the "double periodicity", characteristic of the rare earths. This trend in dicarbides is very much reminiscent of the dissociation energies of the monoxide series though the magnitudes of the changes are not that pronounced. Figure 2 shows the plots of bond dissociation energies of monoxides and the

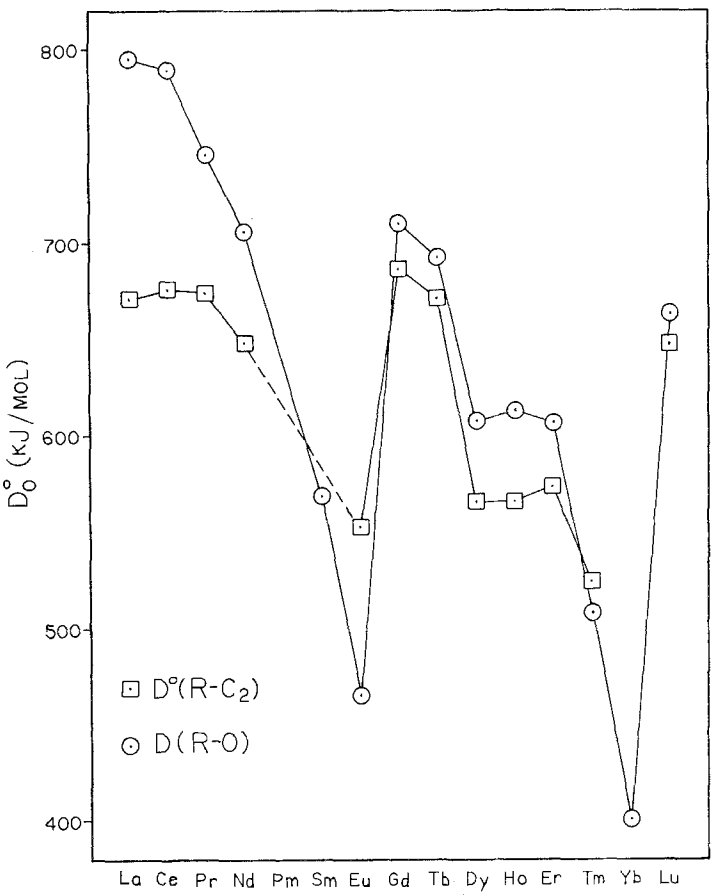

Fig. 2. Comparison of bond dissociation enthalpies of $R-C_2$ and R–O of lanthanide metals.

corresponding dicarbides. The similarity between the two groups of molecules, the monoxides and the dicarbides, and the scarcity of the gaseous rare-earth monocarbides, support the contention that the C_2 group behaves like a pseudo oxygen in its bonding with rare-earth metal atoms.

The similarity between the monoxides and the dicarbides of the rare-earth metals does not end at the existence of the parallel "double periodicity". The magnitude of the bond dissociation energies in both cases is large (except Eu–O, Yb–O, Eu–C_2 and Yb–C_2) to be purely that of a single bond. With the exception of Eu and Yb, in all other cases, the 5d is involved in the bonding even though only La, Ce, Gd and Lu have the ground electronic states of $4f^n5d$ configuration. In other cases, the electronic state of the rare-earth atom in bonding to oxygen or C_2 group is probably the excited $4f^{n-1}5d^1$ state. The supporting evidence for this conclusion is that the promotional energy for the transition $4f^n5d^0$ to $4f^{n-1}5d^1$ also shows the same "double periodicity". Murad and Hildenbrand (1980), Morss (1976), Ackermann et al. (1976), and Ackermann and Chandrasekharaiah (1975) have discussed this aspect in greater detail.

4.2. *Gaseous higher carbides*

The carbide systems are observed to be distinctly different from the corresponding oxide systems. In oxide systems, besides the monoxides, dioxides RO_2, $(RO)_2$ and suboxides, R_2O, are the only vapors observed. In those few cases where experimental results are available, the carbide vapor phase is much more complex (Gingerich 1985).

Most of the rare-earth elements have been observed to form tetracarbides of the formula RC_4. In the cases of La, Ce, Y and Sc carbon systems, in additions to di- and tetra-carbides, higher carbides of the formulae RC_n, $n = 1$–8, and R_2C_n, $n = 1 - 8$ have also been observed. Table 11 shows the thermodynamic data for

TABLE 11
The enthalpies of formation (ΔH_f°), atomization enthalpies (ΔH_{at}°) and dissociation enthalpies D_0°(R–C_4) of rare-earth tetracarbides (kJ/mol).

Carbide species	ΔH_f° (RC_4)	ΔH_{at}° (RC_4)	D_0° (R–C_4) ±60	$\Delta H'$ (a)	$\Delta H''$ (b)
LaC_4	754 ± 13	2515 ± 7	641	1336 ± 17	1338 ± 50
CeC_4	754 ± 15	2505 ± 9	631	1325 ± 19	1350 ± 50
PrC_4	627 ± 40	2569 ± 30	695	1390 ± 40	1348 ± 80
NdC_4	611 ± 40	2556 ± 30	682	1377 ± 40	1296 ± 80
DyC_4	719 ± 43	2412 ± 33	538	1232 ± 45	1130 ± 80
HoC_4	670 ± 44	2470 ± 34	596	1291 ± 45	1130 ± 80
LuC_4	752 ± 53	2514 ± 43	640	1334 ± 55	1296 ± 96
YC_4	735 ± 34	2523 ± 24	649	1344 ± 40	1330 ± 80
ScC_4	761 ± 32	2453 ± 22	579	1274 ± 38	1184 ± 50

(a) $\Delta H'$ is the enthalpy change of the reaction: $RC_4(g) = R(g) + 2C_2(g)$.
(b) $\Delta H''$ = two times the bond dissociation energy of the R–C_2 bond.

TABLE 12
The atomization enthalpies (ΔH°_{at}) and the enthalpies of formation (ΔH°_f) of lanthanum carbide molecules (kJ/mol).

Carbide Species	$\Delta H^\circ_{at}(LaC_n)$	$\Delta H^\circ_f(LaC_n, 0\,K)$	$D^\circ_0(La–C_n)$
LaC_2	1259 ± 5	592 ± 9	669 ± 30
LaC_3	2245 ± 7	746 ± 13	497 ± 40
LaC_4	2515 ± 7	754 ± 13	641 ± 50
LaC_5	3103 ± 45	875 ± 50	527 ± 65
LaC_6	3757 ± 45	931 ± 32	—
LaC_7	4310 ± 60	1088 ± 60	—
LaC_8	4976 ± 60	1131 ± 60	—

RC_4 species. In the absence of spectroscopic data for these carbide species, it is difficult to ascertain the accuracy of the estimated molecular parameters used in the calculation of Gibbs enthalpy functions. In fact, even to suggest the geometry of these complex molecular species is rather difficult. For example, carbides RC_n, $n > 3$, can have more than one geometrical disposition of the atoms. Thus, RC_3 species can be either $R–C_3$ or $C–R–C_2$ and RC_4 can be one of the following: $R–C_4$, $C_2–R–C_2$ or $C–R–C_3$. Further, these arrangements may be linear or bent. Though in the absence of complete spectroscopic data, it is not possible to delineate unambiguously the correct geometric form, in a very limited number of cases, one can use the experimental thermodynamic data to make a choice.

Table 11 lists all the RC_4 species for which the thermodynamic data are available. These carbide molecules could be represented equally by the two linear arrangements, namely $R–C_4$ and $C_2–R–C_2$. The bond dissociation energies of $R–C_2$ bonding is shown in table 10. A comparison of the calculated $2D^\circ(R–C_2)$ (last column of table 11) with the experimental value for the reaction (column 5, table 11).

$$RC_4(g) = R(g) + 2C_2(g) \tag{4}$$

TABLE 13
The atomization enthalpies (ΔH°_{at}) and the enthalpies of formation (ΔH°_f) of cerium carbide molecules (kJ/mol).

Carbide Species	$\Delta H^\circ_{at}(CeC_n)$	$\Delta H^\circ_f(CeC_n, 0\,K)$	$D^\circ_0(Ce–C_n)$
CeC	439 ± 12	692 ± 18	439 ± 30
CeC_2	1265 ± 5	575 ± 10	675 ± 25
CeC_3	1812 ± 11	737 ± 13	496 ± 35
CeC_4	2505 ± 9	754 ± 15	630 ± 40
CeC_5	3103 ± 25	865 ± 30	527 ± 45
CeC_6	3740 ± 30	936 ± 40	—

TABLE 14
The atomization enthalpies (ΔH°_{at}) and the enthalpies of formation (ΔH°_f) of yttrium carbide molecules (kJ/mol).

Carbide Species	$\Delta H^\circ_{at}(YC_n)$	$\Delta H^\circ_f(YC_n, 0\,K)$	$D^\circ_0(Y\text{-}C_n)$
YC_2	1254 ± 15	585 ± 20	665 ± 40
YC_3	1800 ± 40	749 ± 40	483 ± 55
YC_4	2523 ± 24	735 ± 34	649 ± 55
YC_5	3073 ± 45	895 ± 50	497 ± 60
YC_6	3772 ± 60	905 ± 60	—

shows that the most probable geometry for $R\text{-}C_4$ species is $C_2\text{-}M\text{-}C_2$. The $D^\circ(R\text{-}C_4)$ shown in the column 4 of table 11 also supports this conclusion.

In tables 12 to 15, the atomization enthalpies and enthalpies of formation of LaC_n, CeC_n, YC_n and ScC_n, $n = 1\text{–}8$, are presented. For species in which $n > 4$, the simplest linear geometry of the type $R\text{-}C_n$, has been assumed. In case of La and Ce, not only polyatomic vapors of formula RC_n were observed but also the carbide species of the formulae La_2C_n, Ce_2C_n, $n = 1\text{–}8$. The thermodynamic data for these molecules are presented in tables 16 and 17.

The information available at present for these complex carbide species is too limited to make any useful remark regarding the nature of bonding in them. But an interesting observation can be made. Gingerich and co-workers (Gingerich 1980a, 1985) have observed that the relative abundances of vapor species (LaC_n, CeC_n, YC_n, ScC_n) containing even numbers of carbon atoms (i.e., n = even) were higher than the corresponding species with n = odd. For example, CeC_2 is more abundant than either CeC or CeC_3 (Kingcade et al. 1983). This is just the opposite of the relative abundances of carbon species in equilibrium with graphite observed experimentally (Hultgren et al. 1973). In the case of graphite system, species with odd number of carbon atoms are more in abundance than the corresponding molecules of even number of carbon atoms. For example, $C_3(g)$ species are more abundant than either $C_2(g)$ or $C_4(g)$. This observation is also reflected in the observed bond dissociation energies of $R\text{-}C_n$ bonds. $D^\circ_0(La\text{-}C_2)$ is 669 ± 30 kJ/mol compared to $D^\circ_0(La\text{-}C_3) = 497 \pm 40$ kJ/mol. Similarly $D^\circ_0(Ce\text{-}$

TABLE 15
The atomization enthalpies (ΔH°_{at}) and the enthalpies of formation (ΔH°_f) of scandium carbide molecules (kJ/mol).

Carbide Species	$\Delta H^\circ_{at}(ScC_n)$	$\Delta H^\circ_f(ScC_n, 0\,K)$	$D^\circ_0(Sc\text{-}C_n)$
ScC_2	1182 ± 20	613 ± 20	592 ± 25
ScC_3	1777 ± 25	728 ± 25	460 ± 40
ScC_4	2453 ± 32	761 ± 22	579 ± 45
ScC_5	3131 ± 35	793 ± 40	556 ± 60
ScC_6	3766 ± 40	867 ± 45	—

TABLE 16
The atomization enthalpies (ΔH°_{at}) and the enthalpies of formation (ΔH°_f) of dilanthanum carbide molecules (kJ/mol).

Carbide Species	$\Delta H^\circ_{at}(La_2C_n)$	$\Delta H^\circ_f(La_2C_n, 0\,K)$	Remarks (a)
La_2C_2	1660 ± 30	616 ± 30	La–C–C–La
La_2C_3	2332 ± 35	660 ± 35	La–C_3–La
La_2C_4	3055 ± 25	646 ± 30	La–C_4–La
La_2C_5	3694 ± 45	716 ± 50	La–C_5–La
La_2C_6	4385 ± 45	735 ± 50	La–C_6–La
La_2C_8	5645 ± 50	894 ± 55	La–C_8–La

(a) The linear arrangements of atoms are assumed.

TABLE 17
The atomization enthalpies (ΔH°_{at}) and the enthalpies of formation (ΔH°_f) of dicerium carbide molecules (kJ/mol).

Carbide Species	$\Delta H^\circ_{at}(Ce_2C_n)$	$\Delta H^\circ_f(Ce_2C_n, 0\,K)$	Remarks(a)
Ce_2C	1046 ± 30	505 ± 30	Ce–C–Ce
Ce_2C_2	1687 ± 30	573 ± 30	Ce–C_2–Ce
Ce_2C_3	2340 ± 35	630 ± 35	Ce–C_3–Ce
Ce_2C_4	3075 ± 33	604 ± 35	Ce–C_4–Ce
Ce_2C_5	3660 ± 40	729 ± 45	Ce–C_5–Ce
Ce_2C_6	4336 ± 40	763 ± 45	Ce–C_6–Ce

(a) Linear arrangements of atoms as shown are assumed.

TABLE 18
The atomization enthalpies (ΔH°_{at})* and the enthalpies of formation (ΔH°_f) of ternary gaseous rare-earth carbides (kJ/mol).

Species	ΔH°_{at}	$\Delta H^\circ_f(0\,K)$
LaIrC	1027 ± 30	782 ± 40
LaC_2Ir[a]	1779 ± 25	740 ± 40
LaC_3Ir[a]	2344 ± 35	884 ± 51
LaC_4Ir[a]	2966 ± 35	972 ± 53
CeSiC[a]	1046 ± 42	—
CeCRh[a]	1031 ± 40	650 ± 50
CeCRu[a]	1109 ± 40	670 ± 50
$RhCeC_2$[a]	1674 ± 50	717 ± 62
$PtCeC_2$[a]	1695 ± 50	708 ± 62
YIrC	996 ± 33	802 ± 41
$YIrC_2$	1678 ± 33	829 ± 43
$RhYC_2$	1672 ± 50	719 ± 60
RhScC	1001 ± 40	636 ± 50
$RhScC_2$	1617 ± 50	723 ± 62

[a]Values based on linear geometry as written. Others average values from different assumed geometries.
*Gingerich (1985).

$C_2) = 675 \pm 25$ kJ/mol compared to $D_0^\circ(Ce–C) = 439 \pm 30$ kJ/mol or $D_0^\circ(Ce–C_3) = 496 \pm 35$ kJ/mol.

In addition to the carbide species such as LaC_n, La_2C_n, CeC_n, Ce_2C_n, $n = 1–8$, other gaseous carbide molecules containing La, Ce or Y and a platinum group metal atom (Ir, Pt, Rh or Ru) (Gingerich 1985) have been observed. Table 18 shows the thermodynamic data for these species.

5. Chalcogenides

Rare-earth chalcogenides are known to be quite stable compounds but stable gaseous species are less well known. Among these chalcogenides, sulphide systems have been observed to form a few complex vapors (Smoes et al. 1969, Gingerich et al. 1972, Steiger and Cater 1975, Cater and Steiger 1975). Diatomic selenides and tellurides for a few rare earths have also been observed (Gingerich 1980a, b).

5.1. *Sulphide vapors*

Gingerich et al. (1972) have observed a number of cerium sulphide species containing two cerium atoms per molecule. Smoes et al. (1977) have reported similar results for the eueropium–sulphur system. Table 19 summarizes the thermodynamic data of these sulphide species.

5.2. *Selenides and tellurides*

Several diatomic rare-earth selenides and tellurides have been observed and the atomization enthalpies were determined. The thermodynamic data for the known selenides and tellurides are presented in table 20.

TABLE 19
The atomization enthalpies (ΔH_{at}°) and the enthalpies of formation (ΔH_f°) of rare-earth sulphide molecules (kJ/mol).

Species	$\Delta H_f^\circ(0\,K)$	ΔH_{at}°	Species	$\Delta H_f^\circ(0\,K)$	ΔH_{at}°
LaS	137 ± 20	569 ± 16	CeS	3 ± 60	970 ± 50
CeS	128 ± 25	569 ± 20	Ce_2S	271 ± 60	845 ± 50
PrS	136 ± 30	468 ± 25	Ce_2S_2	−125 ± 75	1518 ± 50
NdS	133 ± 30	502 ± 25	Ce_2S_3	−317 ± 100	1987 ± 75
EuS	95 ± 30	359 ± 25	EuS_2	13 ± 60	718 ± 50
GdS	151 ± 30	520 ± 25	Eu_2S	−69 ± 60	700 ± 50
HoS	155 ± 30	423 ± 25	Eu_2S_2	−277 ± 60	1184 ± 50
LuS	201 ± 30	502 ± 25			
YS	172 ± 20	525 ± 16			

TABLE 20
The atomization enthalpies (ΔH°_{at}) and the enthalpies of formation (ΔH°_f) of rare-earth selenide and telluride vapors (kJ/mol).

Species	ΔH°_f(0 K)	ΔH°_{at}	Species	ΔH°_f(0 K)	ΔH°_{at}
LaSe	164 ± 30	473 ± 20	LaTe	250 ± 35	376 ± 20
NdSe	153 ± 30	381 ± 25	NdTe	222 ± 40	301 ± 25
EuSe	107 ± 35	276 ± 25	EuTe	135 ± 35	238 ± 20
GdSe	178 ± 30	426 ± 20	GdTe	256 ± 35	339 ± 20
HoSe	178 ± 35	330 ± 25	LuTe	301 ± 40	322 ± 25
LuSe	219 ± 35	414 ± 25	YTe	281 ± 35	335 ± 20
YSe	195 ± 30	431 ± 20	ScTe	277 ± 40	295 ± 25
ScSe	205 ± 35	377 ± 25			

TABLE 21
The atomization enthalpies (ΔH°_{at}) and the enthalpies of formation (ΔH°_f) of some rare-earth gaseous nitrides, borates and cyanides (kJ/mol).

Species	ΔH°_f(0 K)	ΔH°_{at}	Reference
CeN	382 ± 40	509 ± 46	Gingerich (1971c)
CeB	686 ± 50	301 ± 25	Gingerich (1970)
PrCN	193 ± 30	1344 ± 25	Guido and Guigli (1975a)
CeCN	229 ± 45	1372 ± 53	Guido and Guigli (1975b)
EuCN	182 ± 35	1176 ± 43	Cocke et al. (1973a)
NdBO	17 ± 50	1124 ± 40	Pupp and Gingerich (1971)
$NdBO_2$	−535 ± 50	1356 ± 50	Pupp and Gingerich (1971)

5.3. *Nitrides, cyanides, and borides and borates*

There are very few data for this class of molecules. Gingerich and co-workers have reported some mass spectrometric data for CeN (Gingerich 1971c), CeB (Gingerich 1970), EuCN (Cocke et al. 1973b) and NdBO, $NdBO_2$ (Pupp and Gingerich 1971). Guido and Guigli (1975a, 1975b) have reported the atomization enthalpies for PrCN and CeCN. These are summarized in table 21.

6. Conclusion

The rare-earth metals do form a number of gaseous molecules and the magnitude of the dissociation energies shows the presence of multiple bonds in many of them. This is true not only for molecules containing non-metallic elements such as oxygen or carbon but also for intermetallic species such as LaPt, CePt, LuPt, etc. Further, the equilibrium vapors over rare earth containing condensed systems are quite complex containing many types of gaseous species. Not only diatomic molecules but also multi-atomic species have been observed. Rare-earth–carbon systems appear to excell in the range of complex gaseous

molecules. The thermodynamic data confirm the pseudo-oxygen character of C_2 radical in the formation of gaseous carbides.

Presently Knudsen cell mass spectrometry is the one experimental method that has yielded most data. A wide open field remains for the spectroscopists and theoreticians to elucidate the electronic and molecular structure of these molecules.

Acknowledgements

The authors acknowledge the many able co-workers who have contributed to the results summarized here.

The preparation of the manuscript has been supported by the Robert A. Welch Foundation and the National Science Foundation. One of us, M.S. Chandrasekharaiah, thanks the authorities of the Bhabha Atomic Research Centre, Bombay for the grant of a study leave during this work.

References

Ackermann, R.J., and M.S. Chandrasekharaiah, 1975, Thermodynamics of Nuclear Materials, 1974, Vol. 2 (IAEA) p. 1.

Ackermann, R.J., and E.G. Rauh, 1971, J. Chem. Thermodyn. **3**, 445.

Ackermann, R.J., and E.G. Rauh, 1974, J. Chem. Phys. **60**, 2266.

Ackermann, R.J., and E.G. Rauh, 1975, Can. Metall. Quart. **14**, 205.

Ackermann, R.J., E.G. Rauh and R.J. Thorn, 1976, J. Chem. Phys. **65**, 1027.

Ames, L.L., P.N. Walsh and D. White, 1967, J. Phys. Chem. **71**, 2707.

Beaudry, B.J., and K.A. Gschneidner Jr, 1978, in: Handbook on the Physics and Chemistry of Rare Earths, Vol. 1, eds K.A. Gschneidner Jr and L. Eyring (North-Holland, Amsterdam) p. 173.

Bratsch, S.G., and J.J. Lagowski, 1985, J. Phys. Chem. **89**, 3310.

Brewer, L., 1971, J. Opt. Soc. Am. **61**, 1101,1666.

Brewer, L., and G.M. Rosenblatt, 1969, in: Advances in High Temperature Chemistry, Vol. 2, ed. L. Eyring (Academic Press, New York) p. 1.

Cater, E.D., 1978, J. Chem. Educ. **55**, 697.

Cater, E.D., and R.A. Steiger, 1975, High Temp. Sci. **7**, 288.

Cocke, D.L., and K.A. Gingerich, 1971, J. Phys. Chem. **75**, 3264.

Cocke, D.L., and K.A. Gingerich, 1972, J. Phys. Chem. **76**, 2332.

Cocke, D.L., K.A. Gingerich and J. Kordis, 1973a, High Temp. Sci. **5**, 474.

Cocke, D.L., K.A. Gingerich and J. Kordis, 1973b, J. Chem. Soc. Commun., 561.

Cocke, D.L., K.A. Gingerich and J. Kordis, 1975, High Temp. Sci. **7**, 61.

DeKok, R.L., and W. Weltner Jr, 1971, J. Phys. Chem. **75**, 514.

Gingerich, K.A., 1969, J. Chem. Phys. **50**, 2255.

Gingerich, K.A., 1970, J. Chem. Phys. **53**, 746.

Gingerich, K.A., 1971a, High Temp. Sci. **3**, 415.

Gingerich, K.A., 1971b, J. Cryst. Growth **9**, 31.

Gingerich, K.A., 1971c, J. Chem. Phys. **54**, 3720.

Gingerich, K.A., 1972, Chem. Phys. **13**, 262.

Gingerich, K.A., 1973, Chem. Phys. Lett. **23**, 270.

Gingerich, K.A., 1974, J. Chem. Soc. Faraday Trans. II, **70**, 471.

Gingerich, K.A., 1980a, Molecular Species in High Temperature Vaporization, in: Current Topics in Materials Science, Vol. 6, ed. E. Kaldis (North-Holland, Amsterdam) ch. 5, p. 345.

Gingerich, K.A., 1980b, Faraday Disc., Faraday Symp. **14**, 109.

Gingerich, K.A., 1985, J. Less-Common Met. **110**, 41.

Gingerich, K.A., and D.L. Cocke, 1978, Inorg. Chim. Acta **28**, L171.

Gingerich, K.A., and D.L. Cocke, 1979, Inorg. Chim. Acta **33**, L107.

Gingerich, K.A., and H.C. Finkbeiner, 1969, Chem. Commun., 901.

Gingerich, K.A., and H.C. Finkbeiner, 1970, J. Chem. Phys. **52**, 2956.

Gingerich, K.A., and H.C. Finkbeiner, 1971, Proc. 9th Rare Earth Conf., October 1971, p. 795.

Gingerich, K.A., and R. Haque, 1980, J. Chem Soc. Faraday Trans. II **76**, 101.
Gingerich, K.A., and J. Kordis, 1973, J. Phys. Chem. **77**, 700.
Gingerich, K.A., D.L. Cocke, H.C. Finkbeiner and R.J. Seyse, 1971, Proc. 19th Ann. Conf. of Mass Spectrometry, May 1971, p. 186.
Gingerich, K.A., C. Pupp and B.E. Campbell, 1972, High Temp. Sci. **4**, 236.
Gingerich, K.A., D.L. Cocke and J.E. Kingcade Jr, 1976, Inorg. Chim. Acta **17**, L1.
Gingerich, K.A., B.N. Nappi, R. Haque and M. Pelino, 1981a, Inorg. Chim. Acta **54**, L141.
Gingerich, K.A., B.N. Nappi, R. Haque and M. Pelino, 1981b, Proc. 29th Conf. of Mass Spectrometry, May 24–29, p. 89.
Gingerich, K.A., M. Pelino and R. Haque, 1981c, High Temp. Sci. **14**, 137.
Gingerich, K.A., M. Pelino and R. Haque, 1982, J. Chem. Soc. Faraday Trans. I, **78**, 341.
Gschneidner Jr, K.A., 1961, Rare Earth Alloys (Van Norstrand, Princeton) p. 24.
Gschneidner Jr, K.A., 1971, J. Less-Common Met. **25**, 405.
Gschneidner Jr, K.A., N. Kippenhan and O.D. McMasters, 1973, Thermochemistry of Rare Earths, 15-Ric-6, Rare Earth Information Centre (Iowa State University, Ames).
Guido, M., and M. Guigli, 1974, J. Chem. Phys. **61**, 4138.
Guido, M., and M. Guigli, 1975a, High Temp. Sci. **7**, 122.
Guido, M., and M. Guigli, 1975b, High Temp. Sci. **7**, 301.
Gupta, S.K., B.M. Nappi and K.A. Gingerich, 1981a, Inorg. Chem. **20**, 966.
Gupta, S.K., B.M. Nappi and K.A. Gingerich, 1981b, J. Phys. Chem. **85**, 971.
Haque, R., and K.A. Gingerich, 1979, J. Chem Soc. Faraday Trans. I, **75**, 985.
Haque, R., and K.A. Gingerich, 1980, J. Chem. Thermodyn. **12**, 439.
Haque, R., and K.A. Gingerich, 1981, J. Chem. Phys. **24**, 6407.
Haque, R., M. Pelino and K.A. Gingerich, 1979, J. Chem Phys. **71**, 2929.
Haque, R., M. Pelino and K.A. Gingerich, 1980, J. Chem Phys. **73**, 4045.
Hilpert, K., 1977, Ber. Bunsenges. Phys. Chem. **81**, 348.
Hilpert, K., 1979, Ber. Bunsenges. Phys. Chem. **83**, 161.
Huber, K.P., and G. Herzberg, 1979, Molecular Spectra and Molecular Structure IV, Constants of Diatomic Molecules (Van Nostrand, Princeton).
Hultgren, R., P.D. Desai, D.T. Hawkins, M. Gleiser, K.K. Kelley and D.D. Wagmann, 1973, Selected Values of the Thermodynamic Properties of the Elements, American Society for Metals (Metals Park, Ohio).
Kant, A., and S.S. Lin, 1972, Monatsh. Chem. **103**, 757.
Kingcade Jr, J.E., and K.A. Gingerich, 1986, J. Chem. Phys. **84**, 4574.
Kingcade Jr, J.E., D.L. Cocke and K.A. Gingerich, 1983, High Temp. Sci. **16**, 89.
Kingcade Jr, J.E., D.L. Cocke and K.A. Gingerich, 1984, Inorg. Chem. **23**, 1334.
Kleinschmidt, P.D., K.H. Lau and D.L. Hildenbrand, 1981, J. Chem. Phys. **74**, 653.
Kordis, J., and K.A. Gingerich, 1973, J. Phys. Chem. **77**, 700.
Kordis, J., and K.A. Gingerich, 1977, J. Chem. Phys. **66**, 483.
Kordis, J., K.A. Gingerich and R.J. Seyse, 1974, J. Chem. Phys. **61**, 5114.
Krause Jr, R.F., 1974, Thermodynamics of Chemical Species Important to Rocket Technology, AFOSR-TR-75-0596, NBS-IR-74-6000.
Kubaschewski, O., and C.B. Alcock, 1979, Metallurgical Thermochemistry, 5th edition (Pergamon, New York).
Martin, W.C., R. Zolubas and L. Hagan, 1978, National Standards Reference Data Series NSRDS-NBS60.
Morss, L.R., 1976, Chem. Rev. **76**, 827.
Murad, E., and D.L. Hildenbrand, 1980, J. Chem. Phys. **73**, 4005.
Nappi, B.M., and K.A. Gingerich, 1981, Inorg. Chem. **20**, 522.
Pedley, J.B., and E.M. Marshall, 1983, J. Phys. & Chem. Ref. Data **12**, 967.
Pelino, M., K.A. Gingerich, B.M. Nappi and R. Haque, 1984, J. Chem. Phys. **80**, 4478.
Pelino, M., R. Haque, K.A. Gingerich and J.E. Kingcade Jr, 1985, J. Phys. Chem. **89**, 4257.
Piacenta, V., G. Bardi, L. Malaspina and A. Desideri, 1973, J. Chem. Phys. **59**, 81.
Pupp, C., and K.A. Gingerich, 1971, J. Chem Phys. **54**, 3380.
Ramakrishnan, E.S., I. Shim and K.A. Gingerich, 1984, Faraday Trans. II, **80**, 395.
Shim, I., and K.A. Gingerich, 1984, J. Chem. Phys. **81**, 5937.
Smoes, S., J. Drowart and G. Verhaegen, 1965, J. Chem. Phys. **43**, 732.
Smoes, S., P. Coppens, C. Bergmann and J. Drowart, 1969, Trans. Faraday Soc. **65**, 682.
Smoes, S., J. Drowart and J.W. Walters, 1977, J. Chem. Thermodyn. **9**, 275.
Staley, H.G., and J.H. Norman, 1969, J. Mass. Spect. Ion Phys. **2**, 35.
Steiger, R.A., and E.D. Cater, 1975, High Temp. Sci. **7**, 204.
Stull, D.R., and H. Prophet, 1971, NSRDS-NBS-37.
White, D., D.N. Walsh, L.L. Ames and H.W. Goldstein, 1962, Thermodynamics of Nuclear Materials (IAEA) p. 417.
Zmbov, K.F., and J.L. Margrave, 1978, Mass Spectrometry in Inorganic Chemistry, in: Advance Chemical Series, No. 72, Amer. Chem. Soc. (Washington, D.C.).

Handbook on the Physics and Chemistry of Rare Earths, Vol. 12
edited by K.A. Gschneidner, Jr. and L. Eyring

Chapter 87

LASER SPECTROSCOPY

WILLIAM M. YEN
Department of Physics, University of Wisconsin, Madison, WI 53706, U.S.A.

Contents

List of Symbols

A_{12}	Einstein coefficient
B_{12}	Einstein coefficient
C	speed of light
e	electronic charge
f	oscillator strengths
f(ab)	oscillator strengths of a transition
g_a	degeneracy
h	Planck's constant
m	electronic mass
N_0	population
q	coupling parameter
S(ab)	matrix element
T_1, T_2	relaxation times
v, v_0	velocities
W_{nr}, W_r	relaxation probabilities
ΔE_{ij}	change in energy
ΔN	change in population
ΔR_{ij}	change in distance
Δt	time period
Δ	diffusion constant
$\Delta\alpha$	change in absorption
$\Delta\nu$	linewidth
$\Delta\nu_{FLN}$	FLN linewidth
$\Delta\nu_{INST}$	instrument resolution

$\Delta\nu_{\mathrm{INTR}}$	intrinsic linewidth	λ	wavelength
$\Delta\omega$	frequency change	ν	frequency
ε_0	dielectric constant	ρ_ν	radiation density
η	quantum efficiency	τ_{R}, τ	lifetimes
θ	angle	χ'	electrical susceptibility
κ	decay constant	ω_0	circular frequency

1. Introduction

Spectroscopy in its most general sense embraces all techniques in which radiation or particles are used as probes to investigate the structure of matter. We are all aware that many forms of spectroscopy have contributed to the evolution of our understanding of physical and chemical processes. These advances, resulting from experimental findings, are often intimately connected with the development of new sources, be they radiative or particulate, which produce refinements in the empirical methodology or give rise to entirely new techniques. In this review, we will limit our remarks to optical spectroscopy, i.e. techniques which utilize em radiation of less than ~10 eV, as applied to the rare earth elements. We shall focus specifically on the impact the introduction of stimulated or laser sources to the study of spectroscopic properties of these elements has had on our understanding of the latter systems.

This article is organized as follows: in the initial section we will make some general comments on spectroscopy and on the various properties of laser sources which have been found useful for spectroscopic purposes. We will then describe the various techniques of laser based spectroscopies which are being currently utilized and will follow this discussion with illustrative applications to rare-earth systems. We will conclude by making some comments on new prospects and directions these methodology indicate for the future.

2. Optical spectroscopy and laser spectroscopy

Spectroscopy of any system may be conducted using any number of techniques, the method used hinging simply on convenience and/or availability of instrumentation. The obvious requirement exists that results obtained through any method be consistent and complementary to those obtained by other means. Thus, for example, it is possible to conduct spectroscopic studies in the frequency or in the time domains; results obtained are in this case conjugated to each other through a Fourier transformation.

For the purposes of this article, we differentiate the study of optical properties into two general classifications. The first, which we term static spectroscopy, concerns itself with the determination of the structure of the spectrum of an optically active entity or a complex of such entities. The features of the spectrum are determined by interactions within the entity, i.e. intraelectronic, hyperfine,

etc., and by interactions with its environs provided that the latter is static in the motional sense. The spectral features are, of course, intimately connected with the quantized energy level structure of the system of interest. In general, however, it cannot be assumed that an atom or ion remains totally isolated and optically active entities may interact with a dynamic environment through collisions and other forms of coupling. A different type of spectroscopy, dynamic spectroscopy, is often required to probe into the manner in which these external interactions affect the spectral properties.

Conventional optical spectroscopy, i.e. techniques which use either incoherent line or broadband sources in conjunction with some form of optical analyzer or spectrograph, have of course contributed greatly to our understanding of optical properties in all phases. It is indeed through the findings of conventional optical spectroscopy that many of the advances in modern physical and chemical sciences find their foundation. It will be assumed that the reader is acquainted with the considerable background which has accumulated, for it provides the baseline for our discussion of the more refined and sophisticated laser based spectroscopies. For a pedagogical overview of conventional and other spectroscopic techniques, see for example Hollas (1982).

Since the conception and initial demonstration of the laser, the past two and a half decades have witnessed a rapid and impressive proliferation of these stimulated optical devices. Lasers are now available in an extremely broad range of designs, power levels, spectral coverage and sizes. It is not necessary to review either the principles or the developments of lasers, since in this article, we are principally concerned with the exploitation of the properties of laser radiation for spectroscopic purposes. Present day continuous wave (cw) lasers are available with unprecedented frequency resolution and stability while pulsed lasers have been developed with temporal durations of only a few light oscillations. Additionally, the high peak and average powers attainable by lasers, the phase coherence and the collimination intrinsic to stimulated sources have all been utilized in spectroscopic techniques to very good advantage. The evolution of tunable sources, represented by devices such as dye and color center lasers, has been of central importance to the maturation process of laser based spectroscopies as they now provide extensive and comprehensive coverage of the electromagnetic spectrum.

Needless to say, the spectroscopic virtues of laser radiation were recognized almost from the day of the conception of these devices. For example, the monochromacity and high power of gas discharge lasers served to make Raman scattering studies of sundry excitations into a practical analytic tool and allowed the discovery of the stimulated Raman effect in liquids and in solids. These developments have been reviewed by Anderson (1971, 1973) and by Wang (1975), for instance. Other early demonstrations of laser based techniques which exploited laser properties include the observation of two-photon absorption in solids by Kaiser and Garrett (1961), the extension of the concept of spin echoes to the optical region by Kurnit et al. (1964) and the demonstration of photo induced transparency by McCall and Hahn (1967). The laser also found im-

mediate early uses in conventional spectroscopic techniques, as an excitation source, for example. All the earlier experiments utilized monofrequency or discrete frequency lasers which were available then and because of this the growth of the nascent experimental techniques remained somewhat constrained until the development of the tunable laser. As an illustration, photon echoes in solids were first observed in 1964 but this technique did not come into its own as an analytic technique until a decade or so later, that is when tunable lasers became commercially available. Thus the advent of tunable sources constitutes a benchmark as it marks the origin from which the techniques of laser spectroscopy, of interest to this volume, have experienced an explosive growth and ever widening applications.

The spectra of all materials, be they in gaseous or condensed forms, all suffer to varying degrees from inhomogeneous broadening. The source of this spectral broadening is traceable to some extrinsic variation of statistical origin. In gases, for example, transitions are inhomogeneously broadened by the Doppler effect attributable to some velocity distribution. Similarly transitions in solids are influenced by unavoidable imperfections of the lattice as well as site variations of the active center. The statistical distribution in the external parameters does not affect the manner in which the transitions intrinsic to individual centers occur. A typical representation of inhomogeneous versus homogeneous broadening of a spectral line is shown in fig. 1. If the inhomogeneous broadening is severe in comparison to the intrinsic or homogeneous structure of the spectrum, it will serve to obscure features of transitions which might be of interest. One of the major contributions of laser spectroscopy has been to provide the means via which the extraneous contributions can be suppressed and the intrinsic spectrum derived.

Once again, spectroscopies which utilize incoherent sources can be manipulated to yield homogeneous features in certain circumstances, however, in general the experimental ease and elegance of laser based techniques make them the clear choice with which to conduct such measurements.

Depending upon the information sought, it is necessary to keep in mind that various types of spectroscopies place different requirements on the sources to be

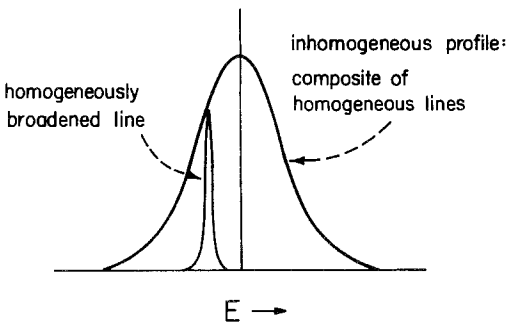

Fig. 1. Schematic representation of homogeneous and inhomogeneous broadening. Identical centers, i.e. atoms with the same velocity or ions in identical sites, have similar homogeneous characteristics. All centers contribute to make up the inhomogeneously broadened transition.

used. Generally, lasers of different capabilities might be required to provide complete experimental coverage of all our informational needs. It is often the case that static spectroscopic measurements can most conveniently be carried out using lasers with high frequency resolution while dynamic measurements are usually best served by pulsed sources with a high temporal (short) resolution. Because the frequency and time regimes are conjugated, the above cited requirements are oftentimes mutually exclusive in a single laser source.

3. Experimental methodologies in laser spectroscopy

In this section we will present a general outline of the experimental methodologies which are encountered in laser spectroscopy. The techniques described have evolved over the past fifteen years and many workers have contributed to these developments. Because of the nature of this review, we will not attempt to describe the developmental history nor delve into the many variations of the principal techniques which have evolved for this or that particular need. Our aim is to impart an idea as to the thrust and potential of this relatively new type of spectroscopy. As usual when dealing with fashionable techniques; several excellent reviews of laser based spectroscopic methods have appeared and the reader is referred to this literature for detailed description of the historical development and recent advances in this experimental discipline. These include reviews by Selzer (1981), Demtröder (1981), Steinfeld (1978) and Kliger (1983).

3.1. *Lasers as spectroscopic sources*

Lasers are of course nothing but a radiation source, consequently, they can simply be used as ordinary spectroscopic sources particularly if they are tunable. A typical optical absorption set-up, for example, is shown in fig. 2a when a conventional black-body source is used. Laser spectroscopy in its simplest form is shown in fig. 2b; a tunable laser source replaces the black body–monochromator combination to provide the absorption spectrum of the sample directly. The resolutions attainable using this simplest of laser techniques are limited only by the laser linewidth which in most instances surpasses the capabilities of ordinary monochomators. Additionally, spectroscopy conducted in this way is spectroscopy conducted with large effective apertures, and is in practice a convenient technique when small, irregular samples are encountered. The laser technique suffers, however, from the limitations placed on the scanning range of lasing media, typically 50–100 nm, so that often different media or different devices are required to span the complete range of interest.

Lasers can also be used as simple excitation sources for optical transitions. Mono or discrete frequency lasers, such as the ruby and argon discharge lasers, were used early on to excite various types of collective excitations through the Raman and Brillouin effects. Information on luminescence processes in a sample

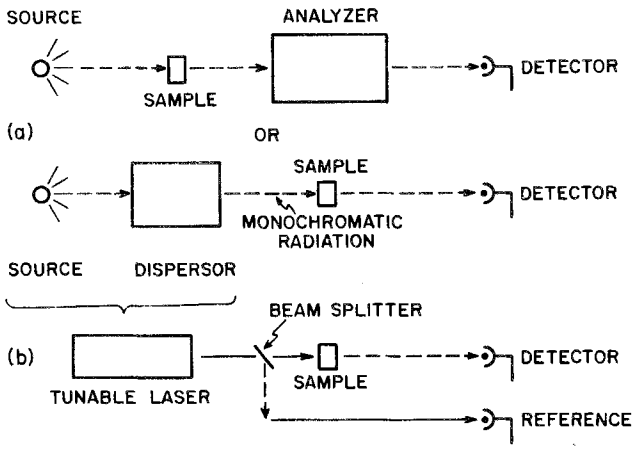

Fig. 2. a) Block diagram of a standard set-up used to conduct conventional optical absorption spectroscopy. The set-up is shown in two variations in which the analyzer and the sample change positions; the second variation is usually encountered in commercial instruments. b) The simplest utilization of tunable lasers for spectroscopic purposes. The laser output is, of course, monochromatic and thus replicates the set-up immediately above it. The resolution is determined by the laser linewidth.

may also be extracted provided that the discrete laser frequencies coincide with some excitation path for the emission. Once again, the advent of tunable lasers has made laser excitation techniques generally more useful by allowing us to cover, if not all, certainly a large portion of the optical spectrum. If a characteristic luminescence exists in the sample of interest, conventional or laser selective excitation spectroscopy provides us with a method to obtain the absorption spectrum of the species of interest. As fig. 3 illustrates, this method can be used to

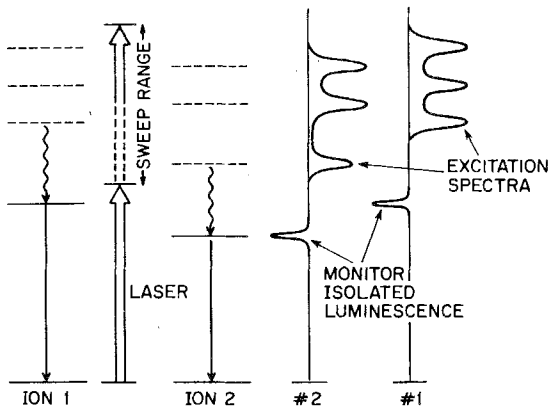

Fig. 3. A selective excitation scheme using a tunable laser. The inhomogeneously broadened spectrum consists of the sums of the spectra of ions #1 and #2. By monitoring an isolated feature specific to one or the other of the ions, the spectrum characteristic to that ion (sometimes called site selective) may be deconvoluted. See fig. 17 for experimental results. Reproduced from Yen (1986c).

deconvolute individual contributions from different species in complex spectra, this is already a simple form of homogeneous spectroscopy.

3.2. *Line narrowing and hole burning*

Simply using a laser as a source does not take advantage of the full range of laser properties that are useful for spectroscopic purposes. The past decade and a half have witnessed the evolution of a host of laser based techniques which either have no readily identifiable equivalent in conventional spectroscopy or are difficult to carry out using the latter means. Two complementary techniques, fluorescence line narrowing (FLN) and hole burning, have found widespread uses in the spectroscopy of all phases principally as a form of homogeneous spectroscopy.

As it has already been alluded to earlier, the optical spectra of materials reflect the effects of random or statistical variations. For dilute gases, for example, the linewidth of atomic transitions is determined by the Doppler effect rather than by the intrinsic uncertainty connected with the lifetime of the interacting states. In fig. 1, each intrinsic or homogeneous component of the broadened transition is shifted by the Doppler effect and thus each of these packages has a correspondence to a given thermal velocity. Various techniques involving atomic beams and lasers, and laser induced nonlinear saturation effects addressed to the suppression of the Doppler contribution are now in common usage. These techniques as applied to gaseous atomic or molecular spectroscopy comprised the initial and most visible successes of tunable laser based techniques. Basically, with allowance for modifications and variations, these techniques fall into two classifications, one which is linear and one which is nonlinear.

3.2.1. *Fluorescence line narrowing (FLN)*

Perhaps the technique most easy to visualize is laser induced fluorescence line narrowing (FLN), also known as site selective or velocity selective spectroscopy. Needless to say, in order for this technique to be applicable some feature of the system under study must radiate light and do so with a reasonable lifetime. These techniques were first developed by Feld and Javan (1969) for gases and by Szabo (1970) for solids.

We consider first the case of an ensemble of noninteracting or isolated optically active entities which experience some form of inhomogeneous broadening. Figure 1 is then a representation of the absorption of the system and since the atoms, ions or molecules depicted are isolated, the emission will be identical with the absorption, reflecting the inhomogeneous contribution. The homogeneous packets of isochromats have in the simplest case a width that is determined by the uncertainty connected with their lifetime, hence

$$\Delta\nu = (2\pi\tau_{\mathrm{R}})^{-1} . \tag{1}$$

Typically, an atomically allowed transition has a radiative lifetime, τ_{R}, of 10^{-9} s,

this translates to a linewidth of 0.3 GHz or 0.01 cm^{-1} in the frequency or energy domains. For partially forbidden transitions such as those encountered in crystals doped with trivalent rare earth ions, the lifetimes can be relatively long (μs–ms) resulting in linewidths as narrow as a few kHz or narrower.

To conduct FLN experiments, then, if a laser tuned to some portion of the absorption possessing a resolution comparable to the natural width of the isochromats is used to excite a finite subset of the constituents of the broadened transition, only those ions in resonance with the excitation will be capable of emitting luminescence. The resulting spectrum will differ from the emission observed through conventional broadband excitation, the luminescence is said to have been narrowed or FLN. This process is illustrated in fig. 4 where narrowing is demonstrated in the $^3P_0$ state of Pr^{3+} in LaF_3.

FLN techniques produce their most dramatic effects when a metastable electronic transition is pumped and the radiation resonant to the laser excitation is observed. Various additional sources of broadening remain in the FLN spectra if other excitation–emission schemes are followed. Thus, for example, little narrow-

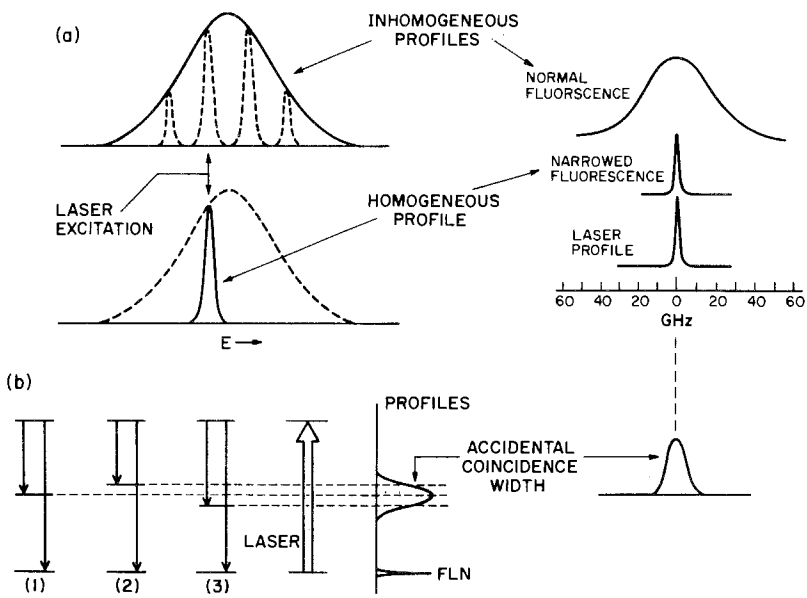

Fig. 4. a) Fluorescence line narrowing (FLN) results from the selective excitation of a subset of atoms or ions within an inhomogeneous distribution; in the limit of no inter-atomic interactions, only the excited subset will radiate, thus narrowing the spectrum. Figure also shows experimental traces of the $^3P_0 \rightarrow {}^3H_4(1)$ fluorescence in a 5% Pr^{3+} doped LaF_3 sample at low temperatures. Illustrated are the broadened and FLN signals, intrinsic information on the transition is obtained by deconvoluting the laser width, which is also shown. b) Only the resonant transition to the laser produces extreme narrowing. In general, transitions to intermediate states still suffer from residual inhomogeneous broadening if the broadening source is controlled by more than one parameter. This leads to the accidental coincidence effect illustrated here with the actual width observed in the FLN $^3P_0 \rightarrow {}^3H_6$ transition in $LaF_3:Pr^{3+}$ as the $^3H_4 \rightarrow {}^3P_0$ absorption is pumped. From Yen (1986c).

ing results when assisted transitions such as vibrational sidebands are excited. Similarly, if the fluorescence to an intermediate state is observed, fig. 4b shows additional broadening in this transition; this is termed the "accidental degeneracy width". This contribution is dependent on the mechanisms which produced the inhomogeneous broadening; in the case of crystals, the energy levels of ions are sensitive to small site to site variations of the electrostatic fields produced by the near neighbours resulting in the inhomogeneously broadened transition. Generally, the crystal field effects are describable by a set of parameters whose number depends on the symmetry of the field, a combination of these parameters may produce the same energy for a given state at non-equivalent sites thus producing an accidental degeneracy. Accidentally degenerate ions in one level are not necessarily degenerate in all their levels if they possess a complex spectrum and transitions involving these states will maintain a residual width which remains inhomogeneous in nature. As in the case of Doppler broadening, the parameters for ions in cubic crystal fields reduced to one, and it is possible to represent this effect schematically (fig. 5), the widths can be seen to depend on the laser excitation width, on the natural linewidth of the states involved and on the slope of the energy versus field diagram. See Selzer (1981) and Flach et al. (1977).

For resonant FLN, the narrowed line spectrum contains the intrinsic information sought. To a good approximation, the observed width

$$\Delta\nu_{\mathrm{FLN}} = 2\Delta\nu_{\mathrm{INTR}} + \Delta\nu_{\mathrm{INST}} \tag{2}$$

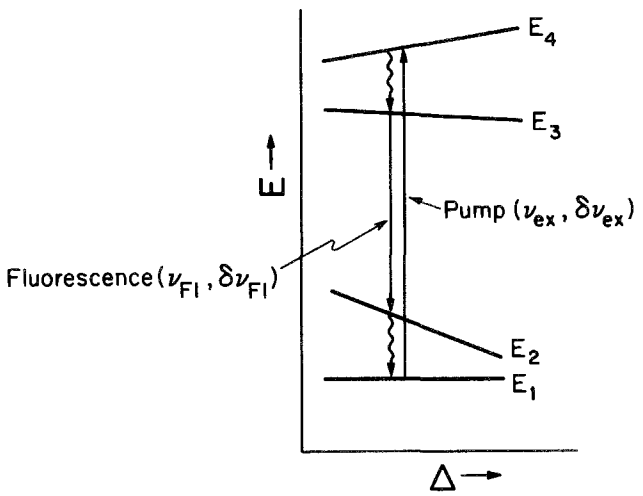

Fig. 5. Linewidths observable in intermediate transitions such as those encountered in the accidental degeneracy case may result in FLN fluorescences which are narrower than the excitation. The Δ parameter above is a measure of the inhomogeneity and can include many parameters. If one pumps the E_4 state from the ground E_1, a subset of width $\delta\Delta = \delta\nu_{ex}/|S_4 - S_1|$ will be excited and the fluorescence from E_3 to E_1 will possess a width given by $\delta\nu_{FL} = (|S_3 - S_2|/|S_4 - S_1|)\delta\nu_{ex}$. Here $S_i = dE_i/d\Delta$, and $\delta\nu$'s are the frequency widths. For the case shown in fig. 4, $E_3 = E_4$ and $S_1 = 0$ so that if a) $S_3 = S_1$, then $\delta\nu_{FL} \gg \delta\nu_{ex}$ no FLN will be observed, b) $S_1 \neq S_2 \neq S_3$, $\delta\nu_{FL} > \delta\nu_{ex}$, c) $S_1 = S_2 \neq S_3$, $\delta\nu_{FL} = \delta\nu_{ex}$ and d) $S_3 = S_2 \neq S_1$, $\delta\nu_{FL} < \delta\nu_{ex}$.

where $\Delta\nu_{INST}$ is the combined resolution of the excitation laser and the analytic equipment and $\Delta\nu_{INTR}$ is the homogeneous width of the transition. More sophisticated deconvolution procedures are required if the response function of the instruments is Gaussian or Voight in profile. See Kushida and Takeuchi (1975) and Hegarty et al. (1980).

A typical experimental set-up is shown in fig. 6. In these FLN experiments for gases or solids, a tunable laser source is used to pump some absorption in the sample resulting in luminescence. The fluorescence is then collected and analyzed with an appropriate monochromator or interferometer with resolving powers comparable to the laser linewidth; signals are then processed and displayed. Ultra high resolution cw lasers may be used in these experiments, however, analytic instruments of similar resolving powers are generally not as readily available and when intrinsic spectral features begin approaching widths of ~10 MHz, time domain experiments discussed below are easier to conduct. This limitation in frequency domain FLN is partially due to the fact that the narrowed signal consists of ordinary fluorescence which is emitted isotropically and hence it is relatively weak. This also produces practical problems particularly when the laser and the signal are resonant, scattered laser light tends to overwhelm the FLN signal and various procedures are necessary to remedy this situation. A common way to accomplish this is to use a pulsed laser source in combination with electronic or mechanical gating of the analytic equipment and/or detectors to prevent saturation effects on the detectors (Selzer 1981). These pulsed versions of FLN techniques are also helpful if spectral dynamics occur in the excited state, i.e. if the optically active centers interact with other entities; of course, pulsed laser sources have a lower resolution because of their own uncertainty limitations.

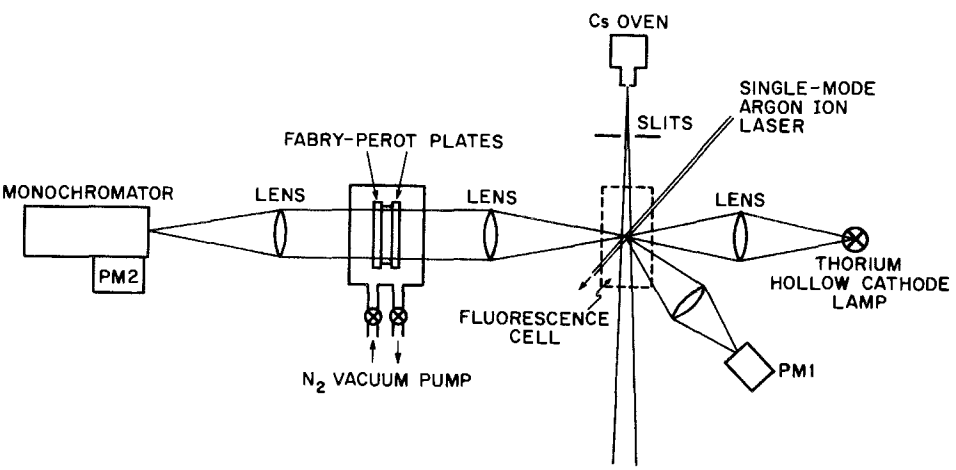

Fig. 6. A typical experimental apparatus used in sub-Doppler FLN laser spectroscopy of a molecular beam of Cs. In the above experiment photomultiplier PM1 monitors the total fluorescence emitted at the interaction region while PM2 records the narrowed fluorescence after dispersal through analyzers. In this case the monochromator acts as a narrow band filter for the Fabry–Pérot signals while the Th lamp serves as a frequency standard. After Demtröder (1981).

3.2.2. *Hole burning*

It is also possible to conduct homogeneous spectroscopy in absorption using laser techniques. These techniques which are complementary to FLN are known generically as "hole burning" or saturation spectroscopies. Basically the methodologies require that the pump laser depletes the ground state population in some part of the inhomogeneously broadened absorption to an extent that a decrease is observed in the absorptivity of the sample. The change of absorption is then interrogated by an auxiliary source. For narrowband laser excitation, a subset of isochromats resonant with the laser will be saturated by producing a hole in the absorption, hence the name hole burning. Under the proper conditions, the hole will carry information on the intrinsic properties of the transition.

Typically, for a simple two-level system with cw pumping, the percentage change in the absorption, α, is given by

$$\Delta\alpha = \Delta n/N_0 = \rho_\nu B_{12}/A_{12} \tag{3}$$

where $\Delta N/N_0$ is the fraction of active entities raised to the excited state, ρ_ν is the energy density of the laser source per unit frequency and A_{12}, B_{12} are the Einstein coefficients of the optical transition. For transitions in the visible and a laser linewidth of 10 MHz, an observable change in α of a few percent can be achieved with ρ of 10–100 mW/cm^2. Saturation can, of course, be achieved using pulsed sources, eq. (3) then becomes

$$\Delta\alpha_p = B_{12}\rho_\nu \Delta t \tag{4}$$

where Δt is the laser pulse width, generally peak powers of 0.1–1 MW/cm^2 are then required to produce equivalent degrees of saturation to those expressed in the cw case.

Typical experimental arrangements for hole burning are shown in fig. 7 for conducting gaseous and solid state spectroscopy. The apparatus is similar to that used in FLN except that in most cases a second laser is used to interrogate or probe the hole. The probe laser beam needs to have a resolution comparable or better than the pump laser and needs to have a relatively low power so as not to contribute further to the pumping. Hole burning techniques have experimental advantages in that one detects changes in transmission of a relatively strong and well characterized laser output. Though independently tunable laser sources for pump and probe beams are not required in all cases, for example in sub-Doppler gaseous spectroscopy a single laser is beam split to pump and probe the $v_0 = 0$ atomic bunch, the technical requirements of this methodology are more demanding than those encountered in FLN. For this reason, various clever techniques have been developed to probe the nature of the hole and/or to bypass the need for a second probe laser. For example, the primary pump laser can be frequency or amplitude modulated at high variable frequencies producing sidebands; the sidebands may then be used as interrogating probes as was done by Szabo (1975). Similarly if dynamic relaxation processes such as relaxation are slow, it is possible

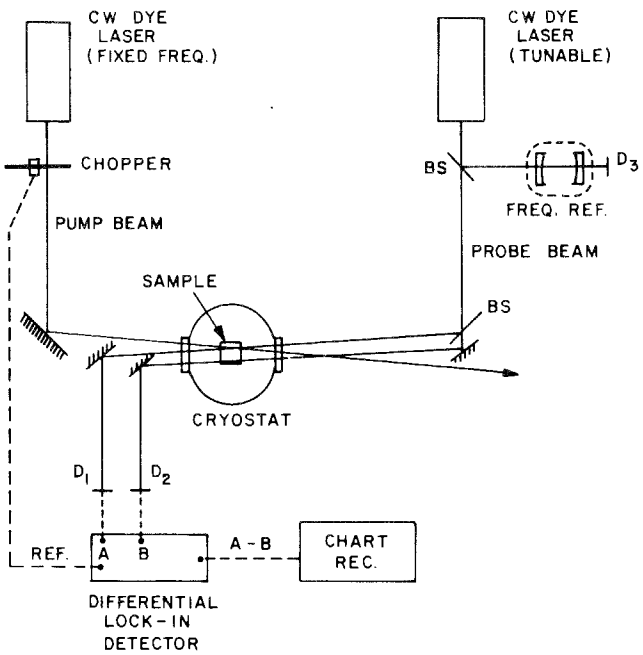

Fig. 7. A cw hole burning apparatus using a fixed frequency and a tunable laser. An interferometer is used as a frequency reference for the probe beam which is scanned in frequency. The probe beam then is split into a beam passing through an area which is hole burned and one which is not. This facilitates differential detection. After Selzer (1981).

to shift the hole using a Stark field and to use the primary pump laser as the probe laser as well, this method has been employed by Muramoto et al. (1977, 1978).

Generally, hole burning techniques are applicable to more transitions since relaxation processes induced by collisions in gases and lattice excitations in solids severely limit the states which can be studied through FLN techniques. However, hole burning methods are more demanding experimentally and care must be exercised in suppressing extrinsic effects inherent in non-linear techniques, such as power broadening. Hole burning in a transition can also arise from actual physical or chemical changes brought about by the laser irradiation; a change in the environment of the center being pumped (photophysical) or a chemical reaction induced by the laser (photochemical) both result in an entirely different optical spectrum for those sites experiencing excitation, the result is persistent or permanent holes. Carried to extremes, this process can produce the total "erasure" of a given absorption. See Moerner et al. (1983).

Regardless, it should be clear that FLN and hole burning are complementary approaches and thus the method of choice depends in great part on the experimental resources available and the nature of the spectroscopic problem at hand. As noted above, there are almost as many variations to these two basic techniques as there have been spectroscopic applications. Techniques such as

two-photon Doppler free saturation spectroscopy, polarization spectroscopy and various double resonant site selective (NMR, ESR) methods all fall into this category of variations. Detailed compendiums of all the techniques and applications have appeared in the literature (Demtröder 1981).

3.3. *Time domain and coherent spectroscopies*

Optical spectroscopy is generally thought to be carried out in the frequency domain and ultimately the limitation that one encounters is to be found in the resolution of the spectral analyzers which are available. Practically, analytic instruments of resolution of fractions of 1 GHz can be constructed without exerting herculean efforts. The analytic means are also available to resolve spectroscopic features in the MHz region but these methods generally require strong signals. In many cases such as in FLN the signals to be analyzed result from spontaneous luminescence and are in the scheme of things relatively weak, thus placing limitations of what can be achieved practically in frequency resolutions. Because of the conjugation of frequency and time, under the appropriate circumstances, it is indeed more convenient to conduct spectroscopy in the temporal domain. Again there are linear and non-linear methods applicable to these studies.

3.3.1. *Radiative lifetime studies*

Intrinsic information concerning a given energy level of a system of non-interacting atoms which radiate may be obtained through a direct measurement of the radiative lifetime, τ_R, appearing in eq. (1). These measurements are simple to conduct and are a traditional member in the arsenal of conventional spectroscopic techniques. A pulsed source is used to populate the excited state resonantly, as in optical pumping, or non-resonantly, while the resulting exponential decay of the luminescence is then measured following the turn off of the pump.

τ_R can be derived for the individual constituents of an inhomogeneously broadened line even using conventional non-stimulated sources provided that the source of the broadening does not affect the radiative parameters of the radiating entities. This is largely the case for Doppler broadening but not so for the case of broadening in solids. Pulsed FLN techniques combined with lifetime measurements can be used advantageously in this regard to obtain τ_R of the individual homogeneous components if a variation exists because of the inhomogeneously broadening mechanism. For example, in glasses large variations of lifetime are encountered in going from site to site (Yen 1986a).

The effectiveness of these types of measurements is limited since idealized isolated two-level systems are seldom encountered in practice. The pulsed nature of the laser sources which are used for excitation also places a limitation on the frequency width of the sources. The latter more often than not is broad enough to obscure features in the spectra, which are of interest, in which small energy splittings are involved. Examples of this are nuclear quadrupolar and magnetic

hyperfine splittings, to name but a few. In addition, if the emitting atoms interact with their environment various processes can induce relaxation and population loss of the excited state, thus shortening the observed lifetime; these lifetime limiting processes need to be properly deconvoluted in order to extract those static features of interest.

3.3.2. *Coherent studies*

A number of laser based temporal domain experiments have evolved in the past two decades which have no equivalents in conventional spectroscopic technique as they exploit the coherence inherent to stimulated sources. The origin of these methods traces directly to techniques which are widely utilized in NMR and ESR spectroscopy to determine various relaxation and dephasing times. In fact, much of the terminology from magnetic resonance processes has been carried over to laser driven coherent transient studies. See Shoemaker (1978), Levenson (1982) and Brewer and DeVoe (1984).

Many experimental variations of these coherent techniques have been developed but basically the experiments may be divided into two classifications, i.e. coherent transient technique and photon echo phenomena, the former requires high resolution, high stability sources while the latter relies on sequential pulse excitation with controlled delays.

In coherent transient measurements, fig. 8, a narrowband cw laser is tuned to be in resonance, ω_0, with a subset of centers within the inhomogeneous line. The centers which are excited are forced to radiate in phase with the laser. At a time $t = 0$ the laser frequency is switched rapidly to a new frequency, $\omega_0 + \Delta\omega_0$. The centers which were originally excited at ω_0 will continue to radiate coherently while simultaneously a population begins building up at the new laser frequency. If the laser switching time is much shorter than the relaxation times affecting the excited state and the switching process itself does not randomize the phase of the laser output wavefronts, the coherent emission of the centers at ω_0 and the laser radiation will interact in the forward direction and will produce a beat signal at the frequency, $\Delta\omega_0$. This signal will persist until the population of the excited state at ω_0 is depleted by the radiation process, yielding the radiative lifetime τ_R or T_1, or the excited state wavefunctions begin losing their coherence because of external perturbations. This latter is characterized by the spin-memory or spin–spin relaxation time T_2. The beat signal decays exponentially with a time constant, τ, given by

$$\frac{1}{\tau} = \frac{1}{T_2} + \frac{1}{2T_1} . \tag{6}$$

Generally $T_2 \ll T_1$ and T_2 dominates in determining the spectral linewidth through the use of eq. (1) with τ replacing τ_R.

Photon echo techniques may be described in a related way but in these experiments two or more resonant pulses are used to create an echo and T_2 is derived from the decay envelope of the echoes. The phenomena of echoes is

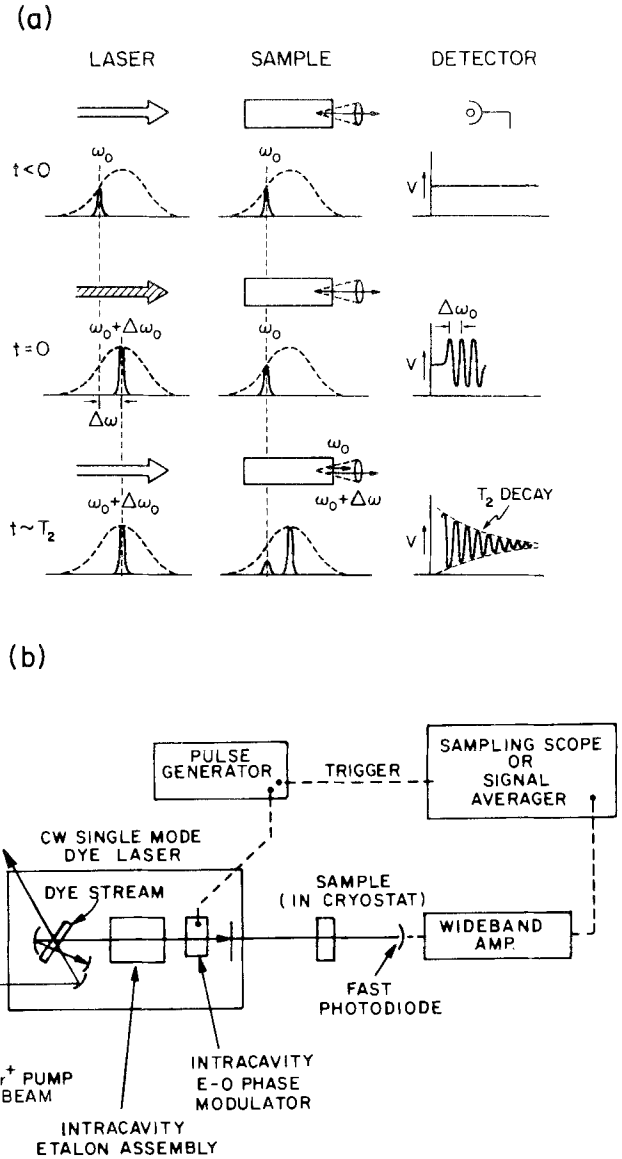

Fig. 8. a) Experimental sequence leading to the formation of transients. At $t<0$, the sample is induced to emit (cone and arrow) coherently with the laser at ω_0. At $t=0$, the laser is switched to a new frequency, $\omega_0+\Delta\omega_0$, while the sample continues to radiate at ω_0 provided that relaxation processes are slow; a beat signal at $\Delta\omega_0$ will be observed at the detector. As the population and/or coherence at ω_0 decays, the envelope of beats will show an exponential decrease with a decay constant equal to T_2; a population will, of course, build up a $\omega_0+\Delta\omega_0$ in resonance with the laser. b) Experimental apparatus for observing coherent transients. The E–0 device is an X-cut ADP (ammonia di-hydrogen phosphate) crystal which basically changes the dye laser optical path length, thus changing the output frequency. A pin diode of response ~ns is used to detect the signal. After Yen (1986c) and Selzer (1981).

connected with the quantum mechanical properties of two-level systems in general as the state of these systems may be represented by a state vector in a complex three-dimensional space rotating at the resonant frequency. See Feynman et al. (1957). An ensemble of two-level systems in their ground state is then represented by a vector pointed in the z-direction, an appropriate torque is produced by a pulsed resonant excitation centered at ω_0 which rotates the state vector into the $x - y$ plane. This represents a so-called super-radiant state, additional pulses are then applied at various delays to probe the decay of coherence.

In photon echo experiments, as in those experiments pioneering echo phenomena by Hahn (1950), the excitation source normally is broad enough to cover a considerable portion if not all of the inhomogeneously broadened transition. The coherence produced by the initial pulse or $\frac{1}{2}\pi$ pulse decays rapidly in the rotating frame since the state vector is composed of the inhomogeneous distribution of frequencies. This extrinsic loss in coherence may be recovered by applying a second pulse or π pulse at some later time t which reverses the phase accumulation of each of the constituents of the inhomogeneous distribution. A reconstruction of the state vector then occurs at $2t$ and a burst of radiation, the echo, is observed in a direction collinear with the excitation pulses. The echoes decrease in intensity as a function of delay, with the decay envelope of the heights yielding the relaxation time T_2. If the transition being studied is made up of unresolved components, all the components are excited coherently and the echo will show a complex beat structure which contains information on the unresolved splittings and which may be extracted. This is closely related to techniques known as quantum beat spectroscopy, see Demtröder (1981), Hollas (1982) and Levenson (1982).

Typical experimental set-ups for coherent transient spectroscopy and for photon echo experiments are shown in figs. 8 and 9. As alluded to earlier, many

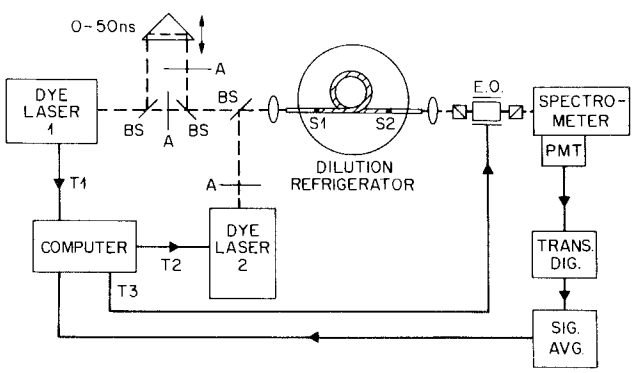

Fig. 9. A versatile set-up to detect photon echoes in an optical fiber at low temperatures. The pulsed dye lasers can be used independently or in a master–slave configuration. Dye laser 1 used in conjunction with the optical delay line can generate a $\pi/2 - \pi$ sequence or dye lasers 1 and 2 can be triggered to produce the proper pulse train. Combination of the above allows one to observe stimulated echoes; echoes remain trapped in fiber for detection. In the above: BS, beam splitter; A, attenuator; E.O., electro-optical shutter and T_i are synchronizing triggers. After Broer et al. (1986).

variations of these two methods exist. For example, the energy levels of the system may be switched in and out of resonance with a cw laser using a Stark field to produce the pulse sequences for photon echoes. Similarly a combination of photon echo and frequency switching transient techniques has been developed to minimize the effects or laser frequency jitter which is often troublesome in coherent transient experiments. See Hesselink and Wiersma (1981), Shelby (1983) and Shelby and Macfarlane (1984).

Transient spectroscopy is specially attractive whenever one deals with relatively long relaxation times. These techniques have allowed the resolution of spectral features with an equivalent frequency resolution of 1–10 kHz. It is generally advantageous to use this methodology down to relaxation times in the vicinity of 10^{-9} s, though subnanosecond coherent experiments have been carried out using mode-locked laser devices. In this latter regime, because of the complementary nature of temporal and frequency domain measurements, standard spectroscopic analytic techniques begin to be competitive. Again, here the method of choice is dictated by the availability of resources.

3.4. *Time resolved spectroscopies*

The above described methodologies have allowed us to conduct spectroscopic studies with a finesse which is not easily attainable using conventional techniques. These laser based techniques in some combination or variation have provided us with the means to resolve or to deconvolute intrinsic features connected with the energy level structure of the systems of interest. These features have so far been assumed to remain static as a function of time. This is, of course, not always the case as various interactions of centers with their environs produce dynamical changes in the excited state and lead to relaxation, optical energy dissipation and transfer. These processes are not generally radiative.

Some of the temporal spectroscopic methods already described yield evidence of the interactions affecting the excited states of optically active centers; the loss of coherence embodied in T_2 is but an example, however, oftentimes the information derived from these experiments is limited and additional techniques which probe spectral changes and spatial motion of the excitation are required.

The methods we discuss below rely on the temporal resolution achievable in pulsed lasers. These pulsed devices can be constructed with extremely short durations down to a few tens of femtoseconds (10^{-15} s), i.e. a finite number of light oscillations. These pulsed sources used as excitation in laser based time resolved experiments provide us with a way to study spectroscopic events occurring within the same framework as the laser pulse width.

3.4.1. *Spectral diffusion studies*

Processes affecting the optically excited state of active centers or entities can either interrupt the phase coherence of the excited state leaving the system in the same state or they can remove the excitation from that state entirely and transfer the energy elsewhere. In the case of simple loss of coherence, a measurement of

T_2 suffices to shed light on the interaction. A typical example of the latter case is illustrated in fig. 10 which shows a typical transfer process between an excited donor (D) atom and an unexcited acceptor (A). Figure 10 also shows the temporal change or dynamics which are expected in such transfer processes. For these measurements, the donor system is excited with a pulsed excitation and either the intensity of some luminescent feature or the total emission spectrum is monitored as a function of time. Time resolved methods have long been, of course, established in conventional spectroscopy and evidence of transfer and other nonradiative relaxation processes were demonstrated through the use of pulsed broadband sources.

Equivalent methods using pulsed laser sources have been developed; the time resolved version of FLN or TRFLN has been found to be particularly useful in unraveling the dynamics occurring in complex spectra and those occurring within a simple inhomogeneously broadened transition. See Yen (1983, 1985). The latter case is illustrated in fig. 11 showing the evolution of the FLN line in the presence of inter-center interactions within an inhomogeneous transition. Important information is contained in the manner in which the FLN signal evolves into the inhomogeneous background. Results derived in TRFLN have allowed us to identify microscopic mechanisms leading to transfer and have been instrumental in the quantification of macroscopic models of transfer by providing a means with which to monitor the dynamics of the donor system, see Huber (1981).

Similar time resolved techniques to study a host of transfer phenomena such as sensitization of luminescence, cross relaxation and optical trapping have been developed (Yen 1986b). Time resolved absorption or hole burning experiments are also possible but have been less common. In all of the above, the pulse length

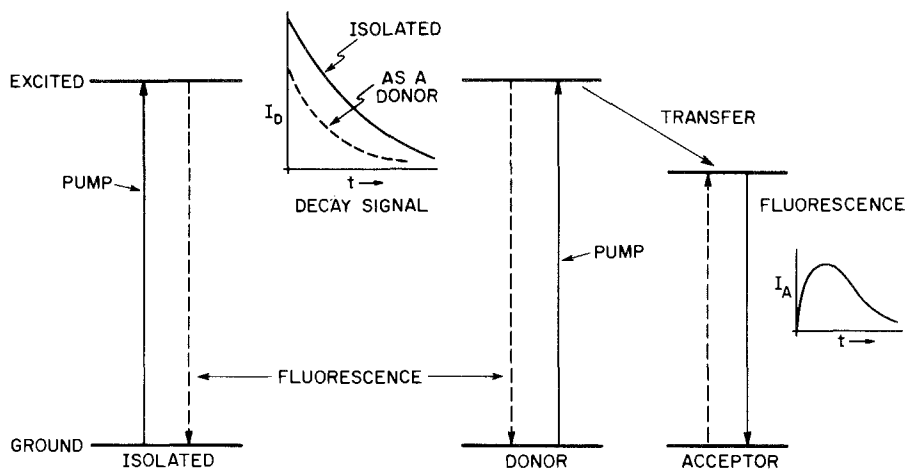

Fig. 10. Representation of the effects of transfer on the decay of the fluorescence or population of an optically excited state. The presence of transfer not only reduces the total light emitted by the state but also changes the characteristics of the decay. These changes can lead to complicated non-exponential decays that depend on the dynamics of the system.

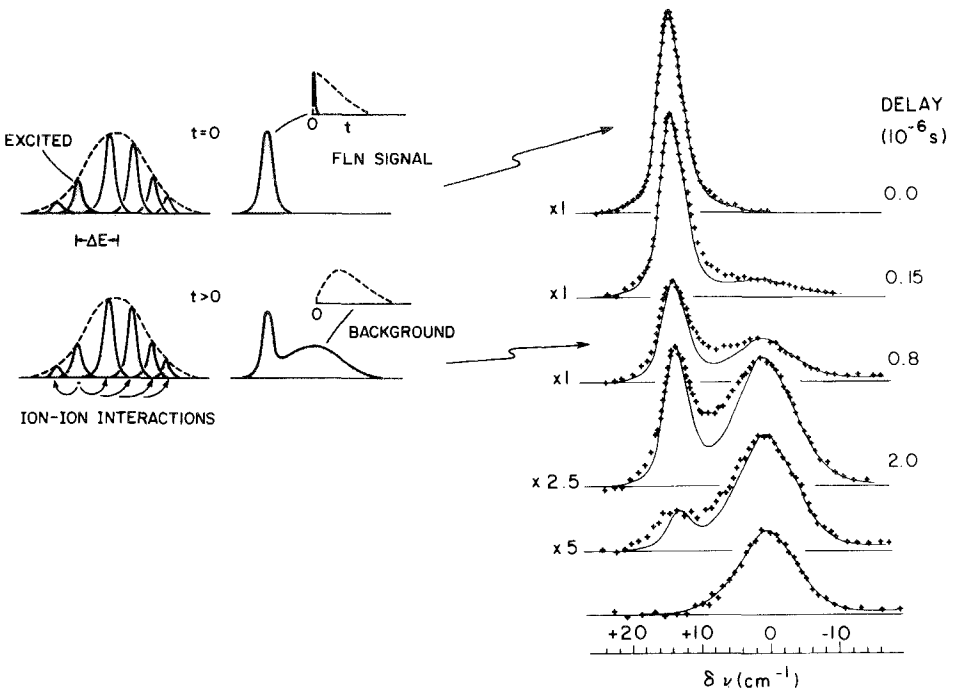

Fig. 11. Schematic representation of transfer processes observed within an inhomogeneously broadened line using pulsed TRFLN. Experimental traces illustrate the dynamics observed within the $^3P_0$ state of $Pr^{3+}:LaF_3$ as a function of time. Information on the microscopic interactions producing the transfer are carried in the manner in which the background develops. TRFLN has proven very useful in the study of like-ion or donor–donor transfer. Data from Huber et al. (1977).

of the excitation which is required is determined by the strength of the coupling between interacting centers. Analytic electronic equipment with temporal response of a few nanoseconds and longer are widely available. More recently this regime has begun expanding into the subnanosecond region and beyond.

3.4.2. *Spatial diffusion studies*

If spectral changes occur through dynamical processes between active centers, it necessarily implies that optical excitation is diffusing spatially. The converse is not also true always as it is possible to have energy migration in space without affecting the optical spectra observed. In these cases, the transfer process is resonant and the energy migration takes on characteristics of excitonic motion in which excited state coherence properties are for the large part maintained. Nonlinear laser spectroscopic methods using coherent interference properties of two or more laser beams have been devised to probe optically for spatial motion of excitation in a scale roughly comparable with the wavelength of light, Hellwarth (1977) and Salcedo et al. (1978).

The methods used to measure spatial diffusion are generically known as 4-wave mixing or grating experiments. They belong to a larger class of techniques which

exploit resonant and non-resonant properties of the electric susceptibilities, χ^i, of materials and which now have evolved into a literally alphabet soup of techniques, e.g. coherent anti-Stokes Raman spectroscopy (CARS) and resonantly induced Kerr effect spectroscopy (RIKES). As an excellent overview of the latter is available in a book by Levenson (1982) and as the emphasis of the present volume is centered elsewhere, the discussion here will focus on the application of spatial diffusion determinations only.

If two phase coherent waves are made to overlap in some medium, then constructive and destructive interferences will occur spatially depending upon the differences in the phases of the waves. Under the proper geometrical configurations, these two beams can be manipulated to produce a regular pattern of interferences. If in addition the intensity of the light affects the medium in some way so as to change the complex index of refraction of the medium a grating reflecting the pattern of interferences will result. There are a number of interactions which produce the required intensity dependent index changes, some of which are direct while others are not. Photorefractive materials fall in the first category while local heating produced by non-radiative processes can produce index changes indirectly, Eichler (1977) and Eichler et al. (1973).

In the case of our interest here, the two waves coincide in energy with some absorptive feature of the medium and thus create excited states in coincidence with the interference maxima. The change in the index of refraction is produced simply because the electronic charge distribution in the excited state differs from that in the ground state. The spacing of the regular array or grating produced by the alternate regions of excited and unexcited centers depends on the wavelength of the interacting or writing beams, λ_1 and λ_2, and on their crossing angle, θ. The simplest case results of course if $\lambda_1 = \lambda_2$.

If now a weak third wave is made incident upon the medium, this beam will encounter the optical grating and diffract into a fourth wave, hence 4-wave mixing. The diffracted wave has a peculiar phase relationship to the incident third wave and is said to be phase conjugated to the probe beam. This property is being actively exploited for image processing purposes in some interesting ways. Regardless, the intensity of the diffracted wave depends upon the contrast of the grating, i.e., the relative change in the index between regions where constructive and destructive interference occurs.

For a grating created with excited centers, if we now interrupt one of the writing beams, the excitation will remain for a time and the grating will persist but will gradually decay as the optical energy is dissipated through radiative or nonradiative processes, Phillion et al. (1975). The intensity of the diffracted wave will decrease with a decay constant equal to half the lifetime of the excited state. If in addition, there is energy diffusion so that the areas of excitation become spatially more extensive, the contrast of the grating will decrease and the diffracted wave will decay at an increased rate, see fig. 12a. The decay constant under the latter circumstances is given by

$$\kappa = 2\tau_R^{-1} + (32\pi D/\lambda^2)\sin^2\theta/2 \tag{6}$$

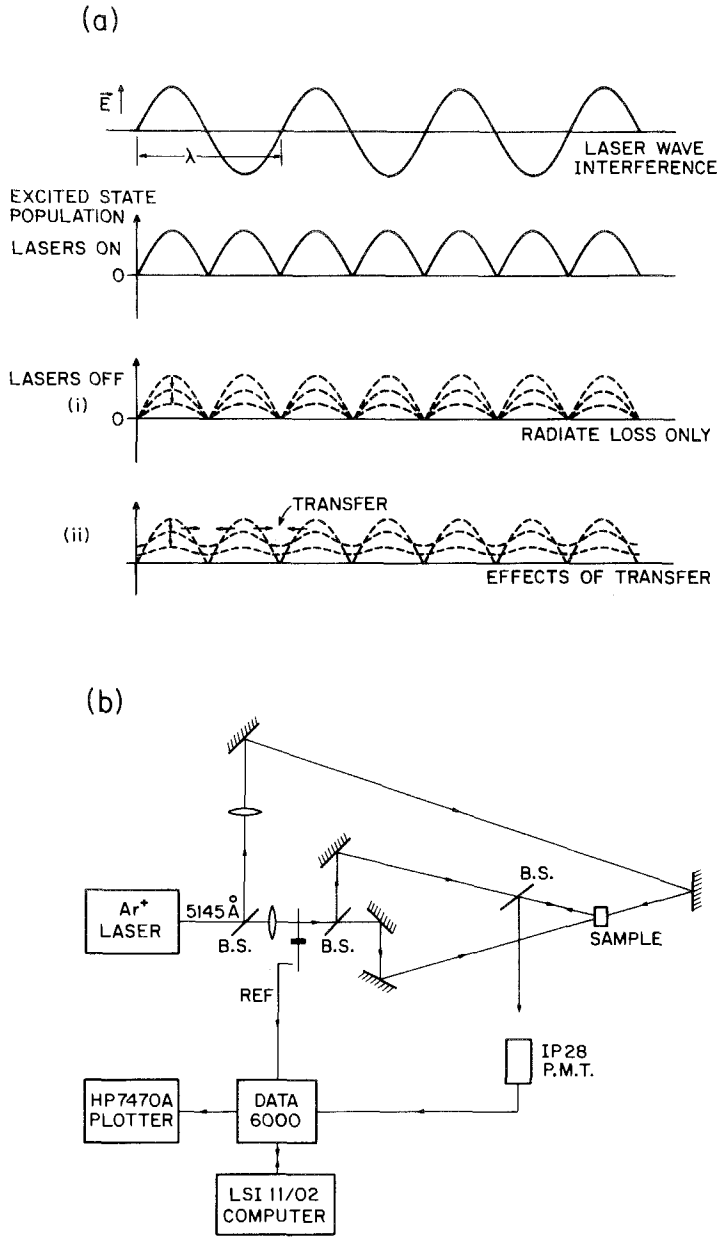

Fig. 12. a) Dynamic behaviour of the population in four-wave transient grating experiments. The constructive interference of two coherent waves produces a periodic population of excited states, causing a change in the index of refraction of the same periodicity. If one of the lasers is turned off, the grating will disappear as the excited state energy is radiated away (i). If in addition, transfer to other regions is present the contrast of the grating and hence the scattering from it will decrease more rapidly (ii). b) Typical experimental set-up for transient grating experiments. After Morgan et al. (1986b).

where τ_R, λ and θ are the lifetime of the excited states, the wavelength of the writing beams and the crossing angle respectively. D is the diffusion constant of the excitation and is, of course, the determining factor for how far the optical energy will propagate.

Experimentally, a typical set up for these measurements is shown in fig. 12b from Morgan et al. (1986b). A single laser beam is split and is used as both writing and probe beams. The diffracted fourth wave's behaviour as a function of time is then monitored and analyzed. For measurements entailing the spatial diffusion of optical energy, care must be taken to deconvolute and minimize effects produced by heating processes on the local level which have dynamics of their own. Additionally, any holographic method is inherently sensitive to environmental changes and to vibrations; care is thus also required to minimize these influences. In those cases where transfer is accompanied by spectral changes, the results of spatial and spectral diffusion measurements are correlated. Such a correlation has been demonstrated in a limited number of cases, see Broer et al. (1984).

In concluding this section, we emphasize that we have selected a few of the techniques and spectroscopic applications out of the multitude of methods which now comprise the experimental field of laser spectroscopy. The choice of laser based methods for description is biased by their general applicability to the subject of interest in this series of handbook volumes which is the elucidation of the physical and chemical properties of lanthanide systems.

4. Optical spectroscopy of lanthanide systems

In this section, we will present a sampling of actual experimental results obtained through the application of laser spectroscopic methods in the study of optical properties of the rare-earth group of elements with emphasis on the lanthanides. The optical properties of rare-earth atoms and ions have, of course, been the subject of active study since the discovery of these elements. Following the foundation of a quantum framework for the understanding of the spectra of complex atoms, the majority of the experimental work in this area has centered on the determination of various static aspects of their optical properties, i.e., the identification of their complex energy level schemes and the understanding of the nature of the optical transitions. Much of this work has been accomplished using conventional spectroscopic methods both in the case where the rare-earth atom or ion is found in a gaseous state or imbedded in some condensate. The spectroscopic data and our theoretical understanding of these systems has been tabulated and reviewed in a number of places and we will use this considerable volume of knowledge as our baseline for the discussion on laser spectroscopic studies in these systems. For example, see Musgrove and Zalubas (1985) for a bibliography, also see Dieke (1968).

For rare-earth systems, owing to a combination of experimental reasons, laser spectroscopic techniques have found their principal application in the study of

optical features and properties of these ions, particularly the divalent and trivalent lanthanides, doped into solids whence intraconfigurational transitions are only partially allowed. This is not to say that laser based methodologies have not contributed to our understanding of rare earths in the gaseous phase, it is simply that laser spectroscopy as applied to solids is in this case more illustrative of the advantages it presents; for a comprehensive review see Macfarlane and Kaplyanskii (1987).

4.1. *Laser spectroscopy of lanthanide systems in gases*

Historically, as already noted, much of the emphasis of spectroscopic studies of isolated atoms or ions of lanthanide has been placed in unraveling the very complex spectra of these systems. Because of La Porte's rule, transitions in question here entail the promotion of ground state electrons to configurations outside the 4f, 5d or 6s shells depending upon the state of ionization. These transitions generally fall in the high-energy end of the visible spectrum and beyond and extensive tabulations of the level structure of various configurations are available. Table 1 summarizes the status of these analytical studies in the lanthanides, Martin et al. (1979). A correlated effort involves the determination of the nature of the radiative transitions in these systems, these efforts center

TABLE 1
Status of analyses of lanthanide spectra.

Z	I	II	III	IV	V	VI
57 La	2	2	1	2	3	
58 Ce	2	1	1	2	4	4
59 Pr	2	3	1	1	2	
60 Nd	2	2	3			
61 Pm	3	3				
62 Sm	1	2	3			
63 Eu	2	2	2			
64 Gd	2	1	2			
65 Tb	2	3	2	2		
66 Dy	2	2	4			
67 Ho	2	3	2			
68 Er	2	2	2			
69 Tm	1	1	1			
70 Yb	2	1	1	1		
71 Lu	2	2	2	1	3	

Codes:
1. Spectrum has been thoroughly analyzed and the more important configurations calculated.
2. Comprehensive data has been obtained but analysis is not complete.
3. Observations have been carried out but important configurations are not known.
4. Only beginning analysis exists.

After: Martin et al. (1979).

upon the determination of the oscillator strengths, f, of various features of the spectrum; see Richter (1984).

The relative oscillator strength f, of a given level is related to the transition probabilities and to the Einstein coefficient A, see Imbusch and Kopelman (1981). For electric dipole transitions, one has

$$f(\mathrm{ab}) = \frac{1}{g_a} \cdot \frac{8\pi m\nu}{3he^2} S(\mathrm{ab}) \tag{7}$$

and the Einstein coefficient

$$A(\nu) = \frac{1}{4\pi\varepsilon_0} \cdot \frac{8\pi^2\nu^2e^2}{mc^3} f(\mathrm{ab}) . \tag{8}$$

In the above, S is the strength of the transition

$$S(\mathrm{ab}) = \sum_{a,b} |\langle \mathrm{b}|\boldsymbol{d}|\mathrm{a}\rangle|^2$$

between states a and b with $\boldsymbol{d}$ the general dipole operator; m and e are the electronic mass and charge, respectively, and g_a is the degeneracy factor of the initial state a. We have assumed that the medium under study has an index of refraction $n = 1$.

Combining eqs. (7) and (8) and using the definition that $A(\nu)$ is the inverse of the radiative lifetime or τ_R^{-1}, we have

$$f(\mathrm{ab}) \cdot A(\nu) = 1.5 \times 10^4 \lambda_0^2 \tag{9}$$

where λ_0 is the central wavelength of the transition in vacuum. The above may be generalized by introducing branching ratios into eqs. (7)–(9).

Equation (7) is also related to the integrated absorption coefficient or total emission strength of the transition in question and this has been the traditional way in which f has been evaluated. Laser spectroscopy has been used to good advantage in the measurement of lifetimes in lanthanide atomic systems from which f can be derived using eq. (9). In these measurements, a pulsed tunable laser populates a selected excited state in a few nanoseconds; the decay of the excited state is then monitored through its fluorescence or through other means such as the optogalvanic effect, see Duquette et al. (1981). General accuracies in the vicinity of 1% are common in lifetime measurements; this level of accuracy is considered to be excellent in comparison to the errors which accumulate in conventional absorption and emission methods. The status of lifetime measurements is summarized in fig. 13 which is reproduced from a general review by Richter (1984).

The experimental apparatus for lifetime measurements are similar to those shown in fig. 6. Recently, sputtering techniques have been employed to produce the atomic beam specially with metals with high evaporation temperatures, Rudolph and Helbig (1982). Photon counting and averaging techniques are also

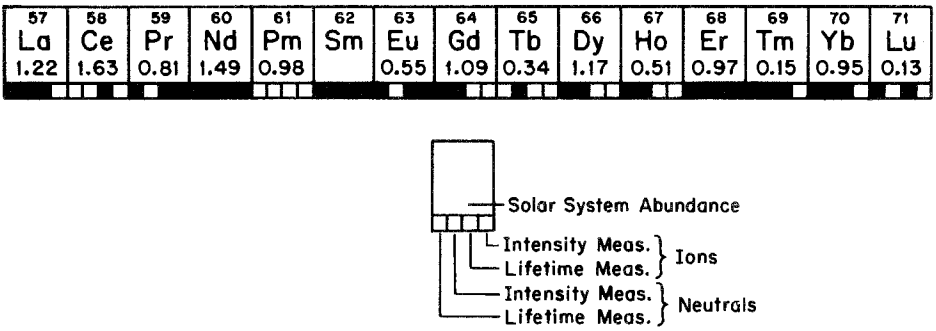

Fig. 13. Table of the lanthanide elements or ions showing whether intensity or lifetime measurements have been published. After Richter (1984).

routinely employed to analyze the resulting fluorescences. The lifetimes which can be measured with this technique range up to about ~2 μs; this upper limit results from excited atoms or ions drifting out of the field of view of the analyzing optics.

Cross atomic beam/laser excitation experiments using high-resolution single-mode tunable lasers have been used to obtain Doppler free fluorescences of neutral lanthanide atomic beams. These results have been used to analyze isotope shifts and hyperfine splittings of the lanthanide series, Clark et al. (1979). Additional variations of this technique exist, as we have noted. A laser–rf double resonance method has been employed to resolve small ground or excited state splittings and to determine these splittings to a high degree of accuracy, for example see Childs and Goodman (1981) and Childs et al. (1983). In these techniques, the laser beam is split into a strong pump and a weaker probe beam and both are tuned to a single hyperfine component of the optical line of interest. The population of the hyperfine component is largely depleted by using the pump beam to excite the atomic beam out of the lower state; the probe beam will thus produce little fluorescence if it intersects the atomic beam downstream from the pump region as there is a diminished population in the ground state. The lower state can however be repopulated by inducing rf or microwave transitions from neighbouring states to the ground state; if this adjustment is made in the region between the pump and the probe interactions, an increase in fluorescence at the probe site is observed whenever a resonance is produced by the rf in the ground state. Typical resolutions of a few tens of kHz may be obtained in this way, results are illustrated in figs. 14 and 15.

Spectroscopy conducted on ions which have been trapped by an appropriate configuration of fields leads to results void of inhomogeneous broadening sources and allows measurements with high spectral resolution. In a recent laser–microwave double resonance experiment conducted on Yb^+ trapped ions, Blatt and co-workers (1983) resolved the ground state hyperfine splitting of the 171 isotope with a Q-factor, i.e., $\Delta\nu/\nu_0$, of 10^{11}.

In the case of gases and because of the high resolution and brightness of lasers, selective excitation of a specific feature of the spectrum such as one belonging to a

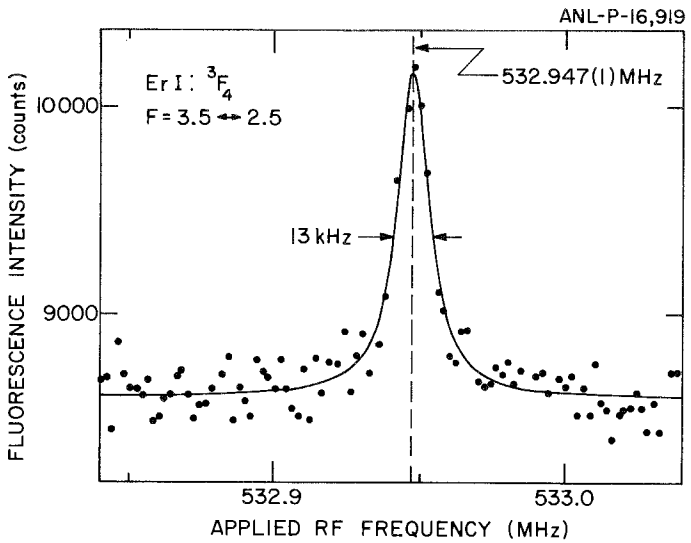

Fig. 14. Increase in resonance fluorescence observed in laser–rf double resonance experiment on one of the hyperfine levels of the $^3F_4$ state of ^{167}Er. After Childs et al. (1983). Using similar methods a hyperfine line as narrow as 33 mHz has been measured in trapped ^{171}Yb ions by Blatt et al. (1983).

given isotopic species can easily be accomplished. Sequential and preferential single or multiple laser excitation of an isotope leads to selective ionization of that species. This is, of course, the basis for laser induced isotope separation which is apparently the method of choice for various actinide elements. Similar methods are applicable to the lanthanides and these applications are now just beginning to appear, see Chopin et al. (1985).

4.2. *Spectroscopy of lanthanides in condensed phases*

Spectra from lanthanides were in fact first observed originating from a solid compound by Becquerel (1906), of course, the quantum theoretical framework was not in place at that time to allow analysis of the relatively unusual spectra observed in these materials. Since then due to the contributions of Bethe (1929), Kramers (1930) and Van Vleck (1937) the theory of the sharp line spectra of crystals containing lanthanides is now well established in terms of crystal field theory and its various extensions, see Hüfner (1978) and references therein.

Lanthanides in solids showing optical activity in the near and far IR, visible and near uv regions of the electromagnetic spectrum are invariably in the divalent and trivalent states. To arrive at these states of ionization the outer 6s and 5d shell and some of the 4f electrons are removed and the observed electronic transitions may be ascribed to the partially filled 4f shells. The closed shell 5s and 5p electrons remain in trivalent and divalent rare earths and serve to shield the active electrons from external perturbations, thus weakening the effects of the environs on the ions. The net result is that the energy levels of ions responsible for the

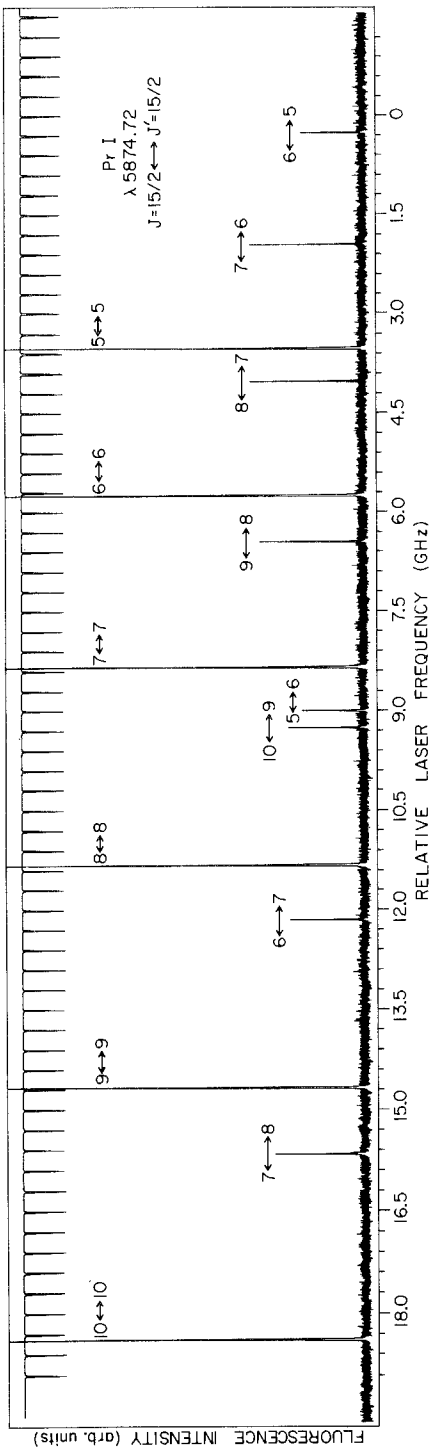

Fig. 15. A typical Doppler free laser induced fluorescence spectrum of Pr in the 5879 Å region, resolution is of the order of 5 MHz. The numbers in the transitions refer to hyperfine components. See Childs and Goodman (1981).

observed transitions in solutions and in crystals may be traced directly to their Russell–Saunders LS terms of a $(4f)^N$ configuration. The crystal field acts, in these cases, as a perturbation lifting the term degeneracies. Admixing of parities may also be produced through this interaction to allow electric dipole (forced) transitions to occur between states in the same $(4f)^N$ configuration though the admixing is such that transitions remain relatively weak as compared to transitions encountered in atomic beam experiments; radiative f-values for intraconfigurational $(4f)^N$ transitions range in the region of 10^{-4} to 10^{-6}. Allowed transitions involving the promotion of an inner 4f electron to empty 5d or 6s states are also observed in the lanthanide crystalline spectra, generally these transitions are in a higher energy region and are broadened by lattice effects.

Extensive compilations and reviews exist of the experimental data and theory of rare-earth spectra in solids, Wybourne (1965), Dieke (1968), Judd (1963), Carnall et al. (1978), and Conway (1985). Much of the rigorous work began with Hellwege and Hellwege (1952) and Dieke and their respective groups following World War II with a noticeable increase in activity and interest being created in this field because of the role rare earths have assumed in laser and phosphor technologies.

Because of the nature of intraconfigurational $(4f)^N$ transitions, principally their relative sharpness and longevity of metastable states, lanthanide ions in crystals have served as exemplary test systems for much of the laser spectroscopic methodology discussed in the earlier sections and much of the activity has focussed on the optical properties of trivalent ions in crystals and glasses. Detailed reviews of laser spectroscopy of solids have appeared recently so that we need only provide a prototypical sampling of the problems which have been delved with using these methods. See Yen and Selzer (1981), Macfarlane and Kaplyanskii (1987), and Yen (1986a).

4.2.1. *Static spectroscopy of lanthanides in solids*

As noted above, the energy levels of a given $(4f)^N$ configuration are sensitive to the nature of the electrostatic fields produced by their local environment in the condensed phases. Thus though no Doppler broadening occurs, the spectra of rare earths in solids contain sources of inhomogeneous broadening which can be microscopic or macroscopic in origin. The sources may be traced to various imperfections and random variations which invariably exist in even the most perfect of crystals. Additional sources of inhomogeneous broadening occur because of requirements for charge compensation, in the pairing and clustering of centers in a matrix and in the intrinsic disorder of the host lattice itself. The extent of this extrinsic broadening ranges from ~ 0.1 to several hundred wave numbers (cm^{-1}), fig. 16, and in many instances it is sufficient to obscure many of the static features required for analysis.

Laser spectroscopy has been extensively used in solids to suppress inhomogeneous contributions and to isolate features which are characteristic to a designated site or field distribution. In this, site selective excitation spectra (fig. 3) or FLN have been used to deconvolute the individual components of composite spectra. For example, when trivalent rare earths are doped into a divalent host such as

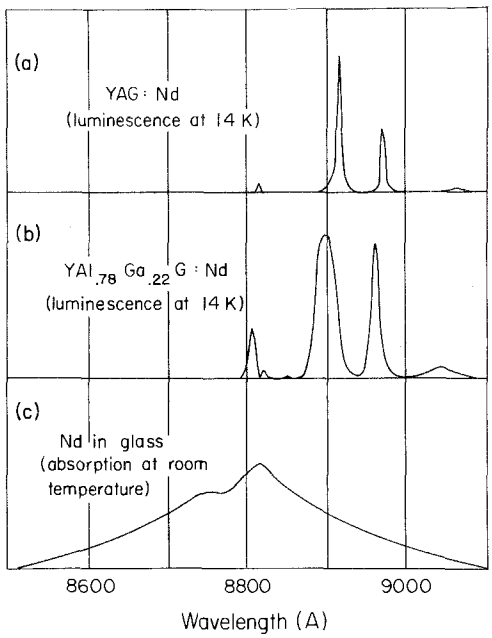

Fig. 16. Illustrative examples of extent of inhomogeneous broadening encountered in solids as they affect the spectra of lanthanide ions. Figure shows the strong $^4F_{3/2} \rightarrow {}^4I_{9/2}$ transition in Nd^{3+} in: a) a YAG crystal where the inhomogeneous broadening is produced principally by crystal imperfections. b) a mixed crystal of YAG (78%) and $Y_3Ga_5O_{12}$ (22%) which produces broadening through compositional disorder and c) absorption broadened by the total disorder inherent in amorphous materials. After Imbusch and Kopelman (1981).

CaF_2, charge compensation is required to maintain neutrality. The compensating charges may be located in a variety of positions either in the regular lattice array or as interstitial defects. If the compensating sites are near to a R^{3+} ion they will produce fields which differ from the normal orthohedral symmetry of Ca^{2+}, a range of splittings of the R^{3+} *LS* Stark manifold result sometimes, leading to a complex composite spectrum. As long as no interionic interactions occur, it is possible to extract individual constituents belonging to specific symmetries of the crystal field, such a deconvoluton is shown in fig. 17, see Wright (1985). Similarly, the spectra of rare-earth activated glasses suffer from large inhomogeneous broadening arising from the absence of any structural local order. FLN applied to these systems, when fluorescence occurs, has allowed the extraction of site specific spectral information and as a consequence have provided important information on the microscopic structural distributions prevalent in glasses. An illustrative FLN spectral study of a R^{3+} doped glass is shown in fig. 18, see Weber (1981, 1982).

The above examples are but two of the many possible applications of site selective laser spectroscopy. Many more examples for both small and large inhomogeneous broadening have been suppressed are to be found in the literature, see Yen and Selzer (1981). With the added dimension of time resolution,

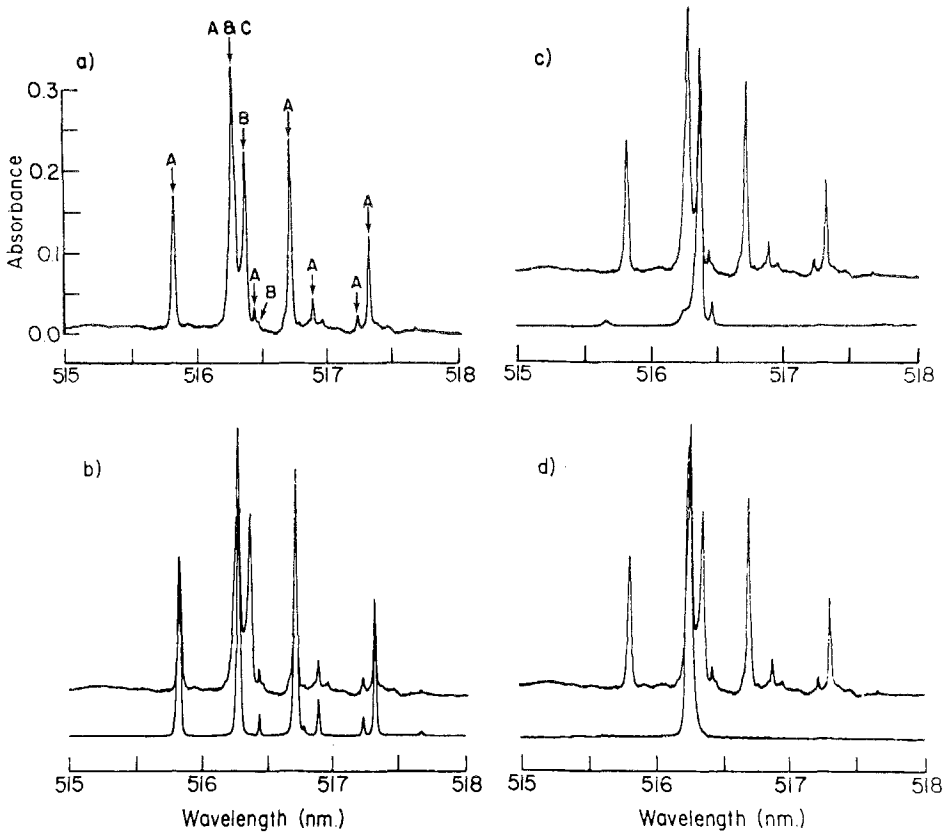

Fig. 17. a) Figure represents the absorption spectrum of $CaF_2:Er^{3+}$ observed using conventional spectroscopy; it consists of the sum of absorptions from all sites. Components from various sites are identified by A, B and C. These specific sites can be deconvoluted using selective laser excitation, fig. 3; the individual components, shown as b) to d), originate from clusters, trigonal and tetragonal symmetries respectively. Traces are for the $^4S_{3/2}$ absorption. No cubic sites are observed. From Wright (1985).

these techniques have also been demonstrated to be useful as analytic tools for chemical reactions in the condensed phases using lanthanides as probes where either the environment or the valence change because of a reaction, Wright (1977).

Further, because of the stability which can be attained in the frequency of the laser output, the frequency of spectra of sharp features can be determined to a high degree of accuracy. This feature of laser spectroscopy is so deeply entrenched through routine use that it needs no further ellucidation.

In this respect, non-linear applications of laser spectroscopy which exploit additionally the high output power of lasers have allowed the investigation of high energy states of the lanthanide ions in solids, both in the $(4f)^N$ and in higher configurations. These states are in general obscured by the conduction bands of the crystal or solid host and are not normally accessible to conventional spectros-

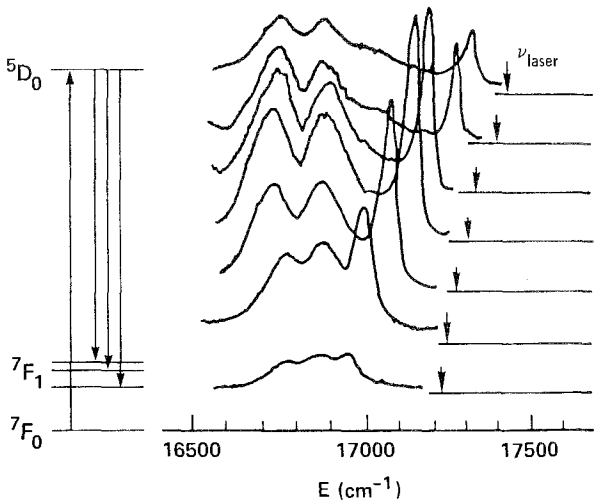

Fig. 18. FLN of the $^5D_0 \rightarrow {}^7F_1$ transition of Eu^{3+} in a silicate glass as a function of $^7F_0 \rightarrow {}^5D_0$ excitation (77 K). The observed spectra are affected by the accidental degeneracy effect. The large variation in the $^7F_1$ splittings are ascribable to changes in the site-to-site B_q^k parameters. Variations of these parameters are larger than the span of parameters encountered in all Eu^{3+} doped crystals. After Weber (1985).

copic sources though studies have been made using synchrotron radiation, see Heaps et al. (1976). The advantages of laser radiation in non-linear spectroscopy were realized early in the development of lasers by Kaiser and Garrett (1961). Using a ruby laser they were able to excite a blue transition in $CaF_2:Sm^{2+}$ through a two photon excitation where the intermediate state is virtual, i.e. no absorption exists at the laser frequency. An anachronism of this initial experiment is that the excited state in Sm^{2+} which was excited by these workers is in most instances two-photon forbidden because of parity rules. More recently, Gayen and Hamilton (1983) have shown that $4f \rightarrow 5d$ transitions in trivalent lanthanides are allowed only in those sites which have inversion symmetry or for which even crystal field terms have been admixed; two-photon absorption results for $CaF_2:Ce^{3+}$ obtained by the latter group are shown in fig. 19.

Following the initial experiments by Kaiser, Axe (1964) extended the theories of Judd (1962) and Ofelt (1962) to calculate selection rules and intensities of two-photon transitions in solids doped with lanthanides. The theoretical predictions with later extensions by Bader and Gold (1968) laid largely untested as an hiatus occurred in the experimental studies in this area, the emphasis having shifted in this period to the observation of $(4f)^N$ states buried in allowed (5d) or conduction bands. Interest has since returned following the work of Degenais (1981), Downer et al. (1982) and Down and Bivas (1983) on Gd^{3+} in LaF_3. As noted in fig. 20, these workers observed a number of violations of the selection rules developed by Axe in both the intensity and polarization dependence and were able to trace the descrepancies to various approximations necessary in the

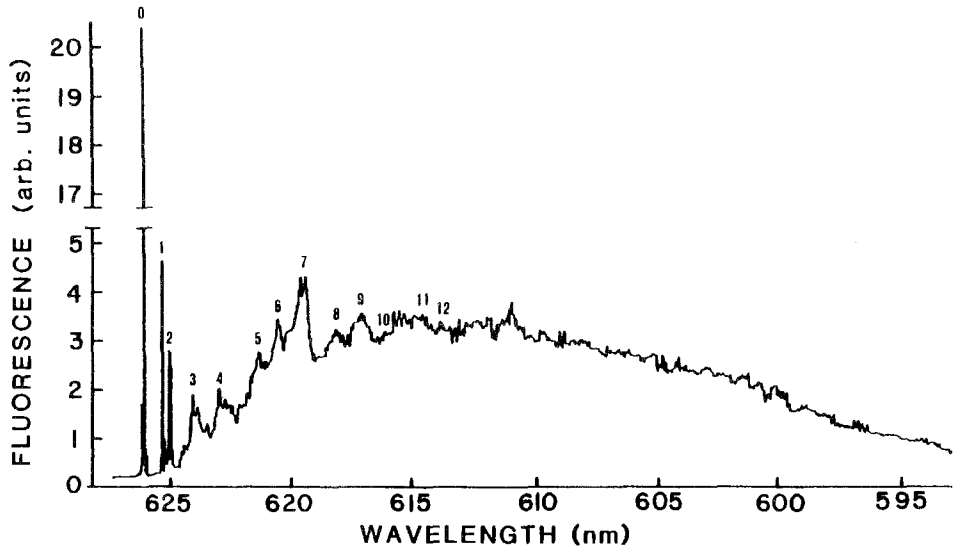

Fig. 19. Composite two-photon excitation spectrum of the 4f↔5d transition in 0.003% Ce^{3+} in CaF_2 at 6 K. The transition is studied by monitoring the 5d→4f, no phonon transition occurring at 313.1 nm. As noted in text this transition is normally two-photon forbidden because of parity selection rules, however, odd crystal-fields components admix parity to make the transitions partially allowed. The pure electronic transition of the state is labeled as 0; other excitations, 1 to 12, are identified as phonon or normal mode excitations of the lattice which couple to the pure transition. Selection rules for assisted transitions follow selection rules which differ from the one-photon case. After Gayen and Hamilton (1982).

Judd–Ofelt treatment to obtain closure; see Downer and Bivas (1983) and Judd and Pooler (1982). Similar work has been carried out on the $^1S_0$ state of Pr^{3+} in various hosts and once again the modifications of the first-order Judd–Ofelt theory by Downer seem to be applicable, see Levey (1984) and Cordero-Montalvo and Bloemberger (1984).

The advantages of using two-photon processes are, of course, that they allow us to extend laser spectroscopy far into the ultraviolet; in addition these techniques allow the investigation of states which are not accessible from the ground state because of parity selection rules and/or which are obscured by stronger allowed transitions. Further since commonly the intermediate state reached by one of the photons is virtual and thus no absorption exists there, the full power output of the laser can be brought to bear without risking damage to the crystals if applied within reason. The processes involved in two-photon absorption are closely related to those encountered in electronic Raman scattering as well as in those in which two ions cooperate to absorb one photon. The latter will be discussed in relation to dynamic spectroscopy. For a review of advances in this general area see Bloembergen (1984), Judd (1985) and Yen (1988).

A related process occurs when two lanthanide ions jointly participate in a transition. These cooperative processes were first reported by Varsanyi and Dieke (1961) in $PrCl_3$ and have been further investigated by Nakazawa and Shionoya

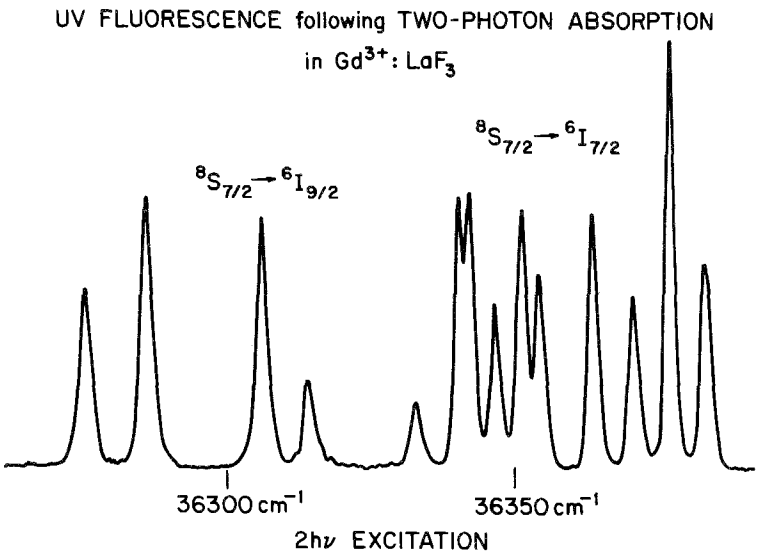

Fig. 20. Two-photon excitation spectrum of the $^6P_{7/2} \rightarrow {}^8S_{7/2}$ fluorescence in $LaF_3:Gd^{3+}$ from the $^6I_{7/2}$ and $^6I_{9/2}$ Stark manifolds, showing roughly equal transition strengths contrary to the selection rules of Axe (1964). These results have led to a re-examination of the theory as discussed by Bloembergen (1984).

(1970) in systems containing different lanthanides. Cooperative transitions are also of interest because they can provide insights on interionic coupling mechanisms, see Vial et al. (1979) and Lai et al. (1982).

4.2.2. *High resolution spectroscopy and relaxation processes*

The capabilities of laser spectroscopy have found a very demanding testing ground in studies of the intrinsic linewidths of 4f transitions in solids. The sharp line structure of the spectra of lanthanide ions in solids originates from atomically forbidden intra configurational transitions, consequently the radiative lifetimes of the diverse Stark manifolds which are excited are relatively long, reaching ms's in some instances. This merely implies that in the limit of no other lifetime limiting processes, the intrinsic frequency linewidth is extremely narrow, of the order of tens to a thousand Hz.

The active ions in solids are however not isolated but interact with their surroundings to produce not only the static splittings discussed in the preceeding section but which also lead to additional effects in the optical spectra including processes which produce relaxation and diffusion of optical energy. For ions in solids, these additional effects arise because of the presence of lattice vibrations or phonons and other collective excitations. These motions can, for example, change the symmetries of the active center and hence the strength of a transition; if the motion is harmonic, the spectra are altered by emergence of vibronic or phonon sidebands, for example see Di Bartolo (1968). Generally, because of the

relatively weak crystal field effects in the spectra of lanthanides in solids, sideband or assisted transitions are present but are weak. In the context of this review, the sidebands which normally appear as structure adjacent to a pure electronic transition add to the "accidental coincidence effect" by producing additional resonances with the laser. The sideband structure reflects all the inhomogeneous features of the parent electronic transition, thus if the no-phonon or pure transition is narrowed by laser spectroscopic techniques, the assisted transition will show narrowing as well, the degree of narrowing being in turn determined by the lifetime of the vibrations involved. Experiments of this type have been reported for Gd^{3+} compound by Hall et al. (1981) and in Ce^{3+} by Gayen and Hamilton (1983).

The presence of lattice excitations or phonons leads to relaxation processes which drastically affect the spectra of lanthanides in solids. The energy of optically excited states may be dissipated or altered through the emission or absorption of one or more phonons producing non-radiative relaxation and other temperature dependent effects, the latter through the influence of the thermal population of phonons, see Yen et al. (1964). The probability of phonon emission for energy dissipation purposes depends on the gap between states to be bridged (fig. 21) and on the maximum energy of the phonons involved, this probability is

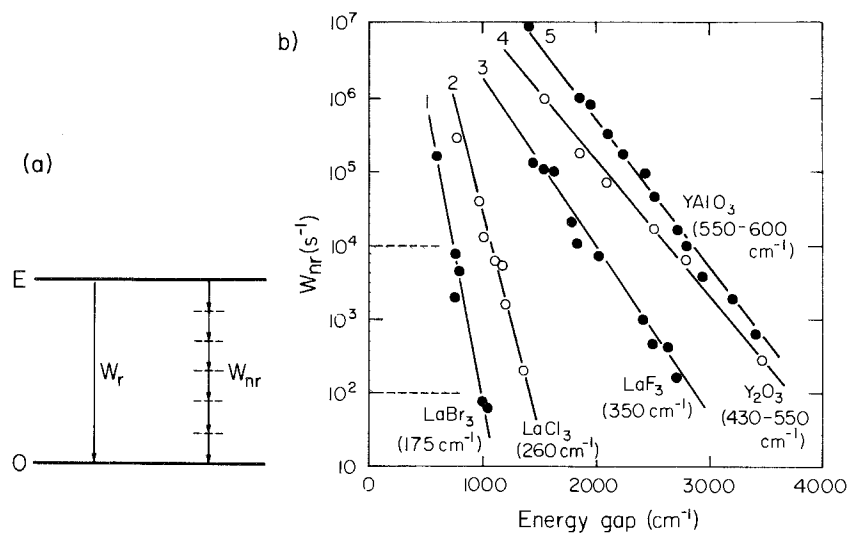

Fig. 21. a) Radiative and non-radiative processes dissipate energy competitively to bridge an energy difference or gap. The non-radiative processes require the emission of a number of phonons thus the non-radiative probability decreases as the number of phonons increases. b) Non-radiative decay rates plotted against the energy gap to the next lowest level for the excited states of various trivalent lanthanides in different hosts. The experimental gap law, eq. (10), is seen to apply. Hash marks denote the span of radiative decay rates encountered in these systems, thus if the non-radiative probability is below the hashed region fluorescence will be observed. After Riseberg and Weber (1976) and Imbusch and Kopelman (1981).

expressed by the gap law

$$W_{nr} = A \exp(-q\Delta E) \tag{10}$$

where A contains matrix elements coupling the initial and final states and q is a quantity proportional to $1/\hbar\omega_{ph}$ with $\omega_{ph} = \omega_{MAX}$, thus $q\Delta E$ becomes roughly equivalent to the number of phonons needed to bridge the gap and conserve energy, see Moos (1970). Measured results of W_{nr} for several rare-earth ions in various crystals are shown in fig. 21, similar results are applicable to glasses. The majority of the measurements depicted in the figure were obtained using conventional methods but it is clear that pulsed lasers can be used with good advantage here, see Riseberg and Weber (1976). The multiphonon relaxation process competes with radiative processes to dissipate optical energy; for crystals doped with lanthanides the non-radiation relaxation lifetime produced by a five-phonon process approximates radiative lifetimes encountered in these ions. This is, of course, the reason why fluorescence is observed from only a limited number of the many states of this series.

Non-radiative processes determine in part the so-called quantum efficiency of a transition. For a radiating state pumped resonantly from the ground state with a narrow band source such as a laser, the quantum efficiency is defined as

$$\eta = N_{out}/N_{in} \tag{11}$$

where N_{in} and N_{out} are the number of photons in the pump beam and the number of photons radiated respectively. Traditionally this quantity has been measured using an integrating sphere to gauge N_{out}. These conventional methods have proven to be extremely difficult to conduct as absolute calibration of sources and detectors are required. Laser spectroscopy in conjunction with photoacoustic or photothermal detection have been developed to provide more reliable values of η. In these techniques, a laser is used for excitation and one detects not the radiative flux but the energy left in the sample which degrades into heat; this is done by sensing a temperature change (photothermal), see Strauss and Seelert (1984) or by developing an acoustic wave in a cell while modulating the pump source (photoacoustic), see Quimby and Yen (1980). These techniques have been also reviewed recently by Tam (1983).

Another relaxation process involves the scattering of phonons from the excited state. These interactions do not remove energy from the excited state but serve to limit the coherence of the wavefunction resulting in a broadening of the state. The relaxation processes involve one or more phonons and are familiar to us from electron spin resonance (ESR) studies of the ground state of lanthanide compounds. These interactions have also been shown to be responsible for the thermal broadening of the spectra of trivalent lanthanides in crystals, see Di Bartolo (1968) and Hüfner (1978). These phonon induced effects are ultimately responsible for the thermalization of population of these systems. For a state that is metastable to a radiative process, the phonon relaxation processes vanish as

$T \rightarrow 0$ and the limiting linewidth is once again determined by the lifetime of the state. The thermalization of states within an excited Stark manifold may be monitored by selectively pumping one of the Stark components with a laser pulse and by then following the evolution of fluoresences from other components. Using this method, Broer et al. (1978) were able to extract a T_1 for the excited $^4S_{3/2}$ state of $LaF_3:Er^{3+}$ using a purely optical method. So-called optically detected magnetic resonance (ODMR) is closely related to these techniques, see Geschwind (1972).

As has already been noted even at low temperatures using conventional methods, fluorescing metastable states of $(4f)^N$ ions show a width which is much larger than the intrinsic width and which is inhomogeneous in nature. It is in attempting to obtain the intrinsic width of these transitions that the advantages of laser spectroscopic methods has been demonstrated most aptly. The progression of improvements in measurements have been detailed elsewhere and we need only to summarize the progress of events here, see Yen and Selzer (1981). Using FLN, Erickson (1975) and Flach and co-workers (1977) were able to show that inhomogeneous contributions could indeed be suppressed and measured widths for the $^1D_2$ and $^3P_0$ states of Pr^{3+} respectively to be in the MHz region, still much larger than the inverse lifetime. Using similar techniques, Pelletier-Allard et al. (1977) were also able to deconvolute the hyperfine states of Pr^{3+} in $PrCl_3$which are normally also obscured by the inhomogeneous contributions. Quadruple splittings were then resolved by Chen et al. (1980) through photon echo measurements and by Erickson (1979) using rf–FLN double resonance techniques. In a subsequent series of experiments using coherent transients and variations of rf and photon echo experiments, Brewer and DeVoe (1984) and Macfarlane and co-workers (1979, 1980, 1984) have succeeded in suppressing additional sources of inhomogeneous broadening including the effects of the magnetic dipolar fields of near-neighbour nuclear spins. The end result has been the observation of a linewidth for the transition of Pr^{3+} with

$$\Delta\nu = 1/2\pi\tau_{\mathrm{RAD}} \cong 5\ \mathrm{kHz}\,.$$

This is an impressive achievement as the Q-value for this transition, i.e. $\nu_0/\Delta\nu$, is 10^{12} and these measurements are in turn illustrative of the potential inherent in laser spectroscopic techniques. Figure 22 illustrates the progression of increases in spectral resolution for the $^1D_2(1)$ line of Pr^{3+} in LaF_3.

Both non-radiative and relaxation processes also affect lanthanide transitions in glasses. Generally, non-radiative processes in disordered systems are dominated not by zone boundary phonons but rather by the normal mode vibrations of molecular complexes which form the glass networks. Since these vibrations have on the average a higher energy than lattice phonons in crystals, the non-radiative probabilities are larger and thus the number of emitting states of lanthanides doped into glasses are fewer in number.

Inasmuch as linewidths of optical transitions of $(4f)^N$ are concerned, FLN studies revealed an anamolous behaviour of the width as a function of tempera-

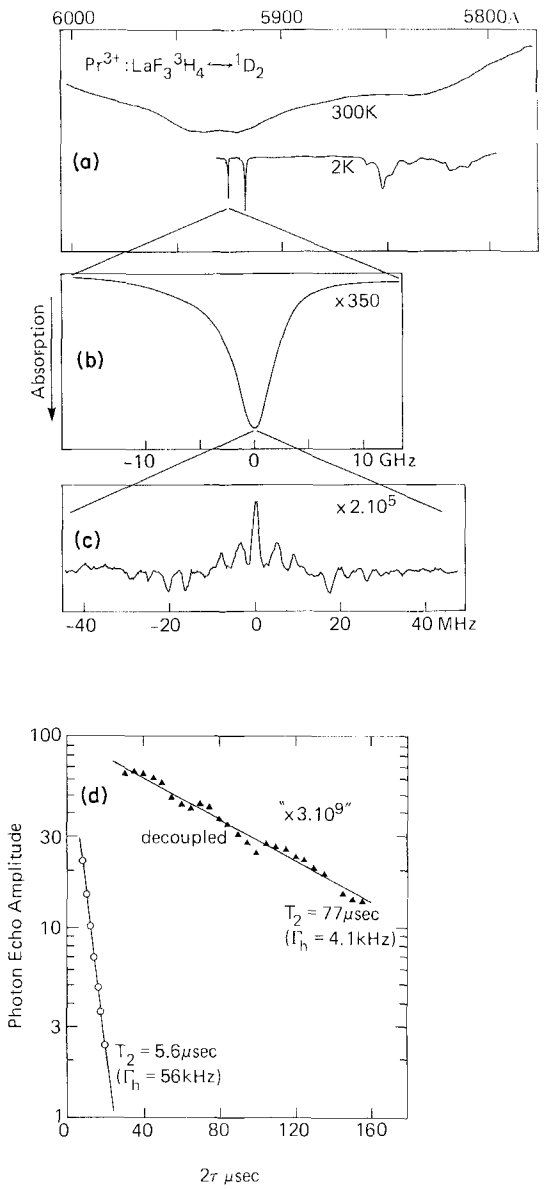

Fig. 22. Illustration of the increase in spectral resolution for the D1 line of $LaF_3:Pr^{3+}$ (0.05%) at 5925 Å using techniques which each remove an interaction leading to spectral broadening. (a) The 300 K spectrum broadened by phonons (the concentration was ~1% to produce measurable absorption). (b) At 2 K the linewidth of 6 GHz is limited by static inhomogeneous strain. In (c) this broadening is largely eliminated by spectral holeburning. The 1.5 MHz holewidth is limited by laser frequency jitter. This was significantly improved by time domain photon echo measurements as in (d) where the homogeneous width due to ^{19}F spin coupling is 55 kHz. By decoupling the fluorine spins, this was reduced to 4.1 kHz, a width which is $\sim 5 \times 10^{-9}$ of the room temperature value. The ultimate limit is set by T_1 which contributes 300 Hz. Courtesy of Macfarlane and Shelby (1986).

ture yielding a universal T^2 dependence from moderately low temperatures (~10 K) up to room temperature, see Hegarty and Yen (1979). Additionally as fig. 23 shows, an unusually large width is observed at low temperatures as compared to their crystal counterparts. More recently hole burning and photo echo experiments have been carried out in Pr^{3+}, and Eu^{3+} by Macfarlane and Shelby (1983) and in Nd^{3+} by Macfarlane and Shelby (1983) and in Nd^{3+} by Hegarty et al. (1983) and Eu^{3+} glasses extending to 0.1 K. Results in these studies implicate excitations intrinsic to disordered systems as the source of relaxation at low temperatures. The transition from the $T^{1.2}$ dependence of the linewidth observed by the majority of the latter experiments to the T^2 observed at higher temperatures has recently been reported in a Yb^{3+} doped glass by Brundage and Yen (1986). The developments here have drawn a great deal of attention as the findings appear to be applicable to transitions in all manners of disordered solids. Reviews have appeared in Zschöhke (1986) and a special issue of the *Journal of Luminescence* edited by Weber (1987) is addressed to the status of our understanding of these problems as of 1986.

It is interesting to note that persistent holes can be burned into the inhomoge-

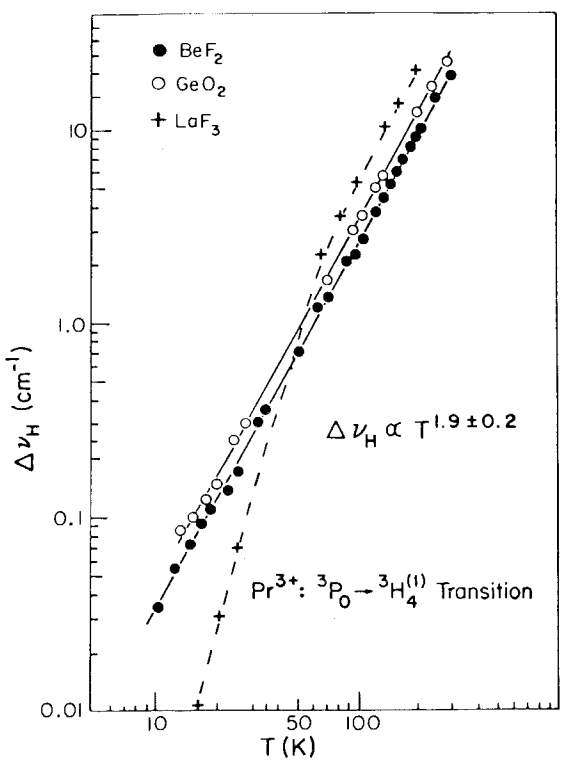

Fig. 23. Temperature dependence of the homogeneous linewidth of the Pr^{3+}, $^3P_0 \rightarrow {}^3H_4(1)$ transition in two glasses and a crystal (dashed lines). The plot shows the T^2 dependence discussed in text and the anomalous relaxation occurring in glasses at low temperature. From Hegarty and Yen (1979).

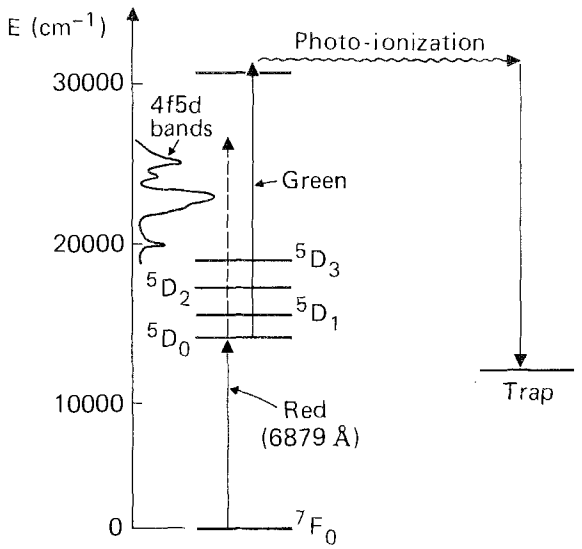

Fig. 24. Energy level diagram for BaClF:Sm^{2+} showing the mechanism which allows photon gated holeburning to be produced, after Winnaker et al. (1985).

neously broadened optical transitions of certain trivalent 4f ions in glasses. Macfarlane and Shelby (1983) have demonstrated this effect in an Eu^{3+} doped glass at low temperatures. The persistent hole is thought to be produced by actual physical changes of the environment surrounding the excited ion. These authors in collaboration with Winnaker (1985) also demonstrated that persistent holes could be produced by changing the valence of Sm^{2+} in solids. Persistent hole burning carries important technical consequences and has been one of the most visible contributions of laser spectroscopy methods. These processes which have allowed a detailed study of the spectra of Sm^{2+} in BaClF, see Macfarlane et al. (1986), are shown in fig. 24.

4.2.3. *Dyamical spectroscopy of lanthanide systems*

In addition to the relaxation processes described in the preceding section which affect the excited state, the optical energy may diffuse or be transferred out of a given ion to other neighbouring centers producing changes in the spectra which are time dependent. A number of processes such as fluorescence quenching, sensitization, optical trapping and upconversion belong to this classification. Lanthanide ions in their trivalent and divalent form have played an important role in the evolution of our understanding of these processes in solids. Historically, one of the first unequivocal demonstrations of energy transfer in solids was carried out in SrS co-doped with Gd^{3+} and Sm^{3+}. Since then these dynamical phenomena have been demonstrated in a very large number of singly doped or co-doped systems and many reviews of the literature are available, Wright (1976) and Yen (1986a, b) for example.

Briefly, our understanding of the inter-ion coupling mechanisms are traceable to the contributions of Förster (1946) and Dexter (1953) and to subsequent generalizations by Miyakawa and Dexter (1970) and by Holstein and co-workers

(1981). Förster and Dexter properly identified the microscopic interionic interaction leading to the communication between an excited and an unexcited ion as arising from the multipolar electrostatic fields produced by the excited state. In order to explain transfer in lanthanide doped systems where often there is no direct overlap in the sharp line spectra of acceptor and donor ions, it becomes necessary to invoke phonon assistance to conserve energy which entail the emission and absorption of one or more phonons. As in the case of relaxation, the various phonon mediated transfer processes have characteristic temperature dependences which allow their identification. The microscopic processes have also definite parametric dependences such as on R_{ij}, the distance between interacting centers, on ΔE_{ij}, the amount of energy to be taken up or supplemented by phonons, etc. The parametric dependences need to be translated to macroscopic observables in the laboratory. These observables are, for example, the precise form in which the excited state population decays following pulse excitation in the presence of energy transfer processes. In order to accomplish this translation averaging procedures over random variables are required and phenomenological models have been developed under sundry restrictions and approximations. The validity of a given transfer model depends on the relative magnitudes of the transfer probability between a donor and another like donor and the donor and the unlike acceptor as has been discussed by Huber (1981).

Conventional spectroscopic methods have been more than adequate to demonstrate the existence of donor to acceptor transfer and have allowed the extraction of the donor to acceptor transfer rates in a variety of lanthanide doped solids. In order to accomplish this extraction, a model is assumed to fit an observed decay. Implicit in this assumption is an estimate of the relative magnitude of the donor to donor transfer rate relative to the donor to acceptor rate. The former cannot be easily measured directly using broad band sources.

One of the main contributions of laser spectroscopy to these studies has been to provide us with a way to measure the donor to donor dynamics directly. The method of choice has been TRFLN within an inhomogeneously broadened line. Results obtained in an early study of the $^3P_0$ of $LaF_3:Pr^{3+}$ are shown in fig. 11, in this case a subset of ions is excited and transfer occurs to other ions through the $^3P_0$ state. The acceptor ion in this case is identical to the original donor in every respect except for the small, often negligible, variation in field produced by random strains. TRFLN has helped us identify various processes, all of which are phonon mediated, which lead to transfer within an inhomogeneously broadened line in 4f doped systems. This measurement complements conventional measurements of donor to acceptor dynamics by providing the value of donor to donor transfer probabilities as the whole donor inhomogeneously broadened line participates in the transferal to acceptors.

In a series of studies, Hegarty et al. (1981, 1982), Vial and co-workers (1979, 1982) and Morgan et al. (1986a) have studied concentration quenching, optical trapping and other transfer processes in Pr^{3+} and (Pr^{3+}, Nd^{3+}) doped systems. They have obtained consistency of results with a minimum of adjustable parameters and have been able in the process to quantify the limits of validity of

various prevalent phenomenological macroscopic models. Developments in this area have also been reviewed in a number of places recently, Yen (1988).

As noted earlier, TRFLN relies on changes in the spectral features. There are resonant processes however which produce transfer without spectral diffusion. These resonant transfer interactions maintain the coherence of the excited state wave functions in most instances. Then for these purposes it is necessary to utilize 4-wave transient grating methods to probe for spatial diffusion. A number of this type of studies exist on lanthanide systems mostly in stoichiometric materials such as NdP_5O_{14}, see Morgan et al. (1986a) where evidence of long-range coherent transfer has been reported by Lawson et al. (1982). Results obtained in spatial transfer have also been shown to be consistent with FLN in these materials, Broer et al. (1984). There is an intrinsic disadvantage in the spatial transfer studies and that is the relative coarseness of the probe. The latter is of the order of the laser wavelengths, thus these methods can be sensitive to transfers occurring over many lattice spacing. Again, a special volume of the *Journal of IEEE* edited by Eichler (1986) has been devoted recently to reviewing developments and applications of grating techniques.

A two-photon method which exploits the "accidental degeneracy effect" has been developed by Strauss and co-workers (1981) to probe directly for resonant transfer. As it may be recalled, in solids it is possible to have a subset of ions which have one level in resonance, this does not generate that other levels will also be in resonance so that transitions to intermediate states still have a degree of inhomogeneous broadening. Strauss et al. showed that by populating a metastable state and then stimulating part of the accidentally broadened intermediate transition, a hole could be produced in this fluorescence. The experiments are related to hole burning experiments conducted in laser glasses by Hall et al. (1984). Resonant transfer dynamics are then registered through the behaviour of the hole in the fluorescence. To date the preponderant experimental evidence is that transfer in lanthanide systems in the visible is generally phonon mediated and hence non-resonant and incoherent.

Relaxation processes of trivalent lanthanides in solids lead to the generation of narrowband phonons which can live for relatively long periods under the proper circumstances. This has allowed the possibility of study of not only the properties of phonons but also the properties of excited states using the generated phonons as probes, a form of spectroscopy which has been aided by laser spectroscopic methods. See Godfrey et al. (1979) and Meltzer and Macfarlane (1985).

4.3. *Spectroscopy in liquids and disordered systems*

Lanthanide ion doped disordered systems such as glasses have played an important role in the evolution of laser technology and thus there has been a concentration of efforts in those systems which have application to stimulated devices, see Stakowski (1982) and Weber (1982). In large part, lanthanide ions in glasses behave much as their similarly coordinated crystals and various laser spectroscopic studies of glasses have already been alluded to in the preceding

section. The study of energy transfer and other dynamical processes in disordered systems is more difficult to analyze in a macroscopic sense even as it has been demonstrated that the same microscopic interactions that exist in crystals are effective in glasses. The difficulty arises in the incorporation of all the randomly varying distribution of parameters, i.e. variation of oscillator strengths, distances etc., necessary in the translation of microscopic interactions to macroscopic observables. To then completely solve the problem of transfer leading to fluorescence quenching, cross relaxation and so on in disordered system requires additional theoretical development. Several reviews of this subject are available in the literature, Yen (1986a), Brundage (1985) and Weber (1987).

Not a great deal has been done in the application of laser spectroscopy of liquids in which lanthanide ions have been dissolved other than using lasers as excitation sources, see Conway (1985). Attempts have been made to observe narrowing in such systems using nanosecond duration lasers. These studies have been to no avail except near the freezing point of the solution whence the system approximates a glass. The likely reason for this negative result is that motion and vibrations are too rapid in liquids and in order to freeze this motion, faster temporal resolution is required. Studies in this area likely will begin appearing as subnanosecond techniques become more routinely available.

5. Summary

In the above, we have touched upon the methodology employed in those spectroscopies which exploit various laser properties. In an article such as this, we have had to be somewhat selective in our choice of subjects and methods which we could properly discuss and even then we have had to be overly brief and likely have not done proper justice to the many contributors to laser spectroscopy. Fortunately, as we have noted, detailed reviews which certainly are more comprehensive that this overview are available and have been cited in the bibliography.

In the development of these techniques, it is important to remember that lanthanide ions, specially those doped into solids, have played a leading role initially as laser sources themselves and later as prototypical optical systems on which to carry out and demonstrate laser spectroscopy technique. This is principally because $(4f)^N$ systems basically have attractive properties which are amenable to such studies.

Laser spectroscopy has in turn become a powerful and now routine tool with which to study systems of interest to this series of volumes. This has led to the characterization of lanthanide systems in much more detailed and fundamental ways. This additional understanding will in turn, of course, lead to improvements in the technologies which utilize optical materials. We note also that as new sources, detectors and materials are developed, additional opportunities invariable arise to improve experimental techniques and to find new ways in which spectroscopic applications can be advanced. We have no doubt that developments in this area will continue to occur rapidly.

Acknowledgments

The author has benefited from support from the National Science Foundation and from the U.S. Department of Energy. Writing of this article was initiated while the author held an A. von Humboldt U.S. Senior Scientist Award.

References

Anderson, A., 1971, The Raman Effect, Vol. 1 (Marcel Dekker, New York).
Anderson, A., 1973, The Raman Effect, Vol. 2 (Marcel Dekker, New York).
Axe Jr, J.D., 1964, Phys. Rev. A **136**, 42.
Bader, T.R., and A. Gold, 1968, Phys. Rev. **171**, 977.
Becquerel, J., 1906, C.R. Acad. Sci. **142**, 775.
Bethe, H., 1929, Am. J. Phys. **60**, 218.
Blatt, R., H. Schnatz and G. Werth, 1983, Z. Phys. A **312**, 143.
Bloembergen, N., 1984, J. Lumin. **31–32**, 23.
Brewer, R.G., and R.G. DeVoe, 1984, Laser Spectroscopy of Solids, in: Coherence and Energy Transfer in Glasses, NATO Conf. Ser., Vol. VI-9, eds P.A. Fleury and B. Golding (Plenum Press, New York) pp. 171–186.
Broer, M.M., J. Hegarty, G.F. Imbusch and W.M. Yen, 1978, Opt. Lett. **3**, 175.
Broer, M.M., D.L. Huber, W.M. Yen and W.K. Zwicker, 1984, Phys. Rev. B **29**, 2382.
Broer, M.M., B. Golding, W.H. Haenimerle, J.R. Simpson and D.L. Huber, 1986, Phys. Rev. B **33**, 4160.
Brundage, R.T., 1985, Fluorescence Line Narrowing in Yb^{3+} Doped Inorganic Glasses (Thesis, University of Wisconsin, Madison) unpublished.
Brundage, R.T., and W.M. Yen, 1986, Phys. Rev. B **33**, 4436.
Carnall, W.T., H. Crosswhite and H.M. Crosswhite, 1978, Energy Level Structure and Transition Probabilities of Trivalent Lathanides in LaF_3 (Argonne National Laboratory Report 60439, Argonne, IL) unpublished.
Chen, Y.C., K.P. Chiang and S.R. Hartmann, 1980, Phys. Rev. B **21**, 40.
Childs, W.J., and L.S. Goodman, 1981, Phys. Rev. A **24**, 1342.
Childs, W.J., L.S. Goodman and V. Pfeufer, 1983, Phys. Rev. A **28**, 3402.
Chopin, G.R., J.D. Navratil and W.W. Schulz, 1985, Actinide/Lanthanide Separation (World Scientific, Singapore).
Clark, D.L., M.E. Cage, D.A. Lewis and G.W. Greenlees, 1979, Phys. Rev. A **20**, 239.
Conway, J.G., 1985, Free Ion Spectra of Interest to Solid and Solution Spectroscopist, in: Rare Earths Spectroscopy, eds B. Jezowska-Trzebiatowska, J. Legendziewicz and W. Strek (World Scientific, Singapore).
Cordero-Montalvo, C.D., and N. Bloembergen, 1984, Phys. Rev. B **30**, 438.
Degenais, M., M. Downer, R. Neumann and N. Bloembergen, 1981, Phys. Rev. Lett. **46**, 561.
Demtröder, W., 1981, in: Laser Spectroscopy, Springer Series in Chemical Physics, Vol. 5 (Springer, Berlin).
Dexter, D.L., 1953, J. Chem. Phys. **21**, 836.
Di Bartolo, B., 1968, Optical Interactions in Solids (Wiley, New York).
Dieke, G.H., 1968, Spectral and Energy Levels of Rare Earth Ions in Crystals (Interscience, New York).
Downer, M., and A. Bivas, 1983, Phys. Rev. B **28**, 3677.
Downer, M., A. Bivas and N. Bloembergen, 1982, Opt. Commun. **41**, 335.
Duquette, D.W., S. Salih and J.E. Lawler, 1981, Phys. Rev. A **24**, 2847.
Eichler, H.J., 1977, Opt. Acta **24**, 631.
Eichler, H.J., 1986, Dynamic Gratings and Four Wave Mixing, IEEE-J. Quant. Electron. **QE-22**, No. 8.
Eichler, H.J., G. Salje and H. Stahl, 1973, J. Appl. Phys. **4**, 5383.
Erickson, L.E., 1975, Phys. Rev. B **11**, 77.
Erickson, L.E., 1979, Phys. Rev. B **19**, 400.
Feld, M.S., and A. Javan, 1969, Phys. Rev. **177**, 540.
Feynman, R.P., F.L. Vernon and R.W. Hellwarth, 1957, J. Appl. Phys. **28**, 49.
Flach, R., D.S. Hamilton, P.M. Selzer and W.M. Yen, 1977, Phys. Rev. B **15**, 1248.
Förster, T., 1946, Naturwissenschaften **33**, 166.
Gayen, S.K., and D.S. Hamilton, 1983, Phys. Rev. B **28**, 3706.
Geschwind, S., 1972, Electron Paramagnetic Resonance (Plenum, New York).
Godfrey, L., J.E. Rives and R.S. Meltzer, 1979, J. Lumin. **18–19**, 929.
Hahn, E.L., 1950, Phys. Rev. **77**, 297.
Hall, D.W., S.A. Brawer and M.J. Weber, 1981, Phys. Rev. B **25**, 2828.
Hall, D.W., M.J. Weber and R.T. Brundage, 1984, J. Appl. Phys. **55**, 2642.
Heaps, W.S., L.R. Elias and W.M. Yen, 1976, Phys. Rev. B **13**, 94.
Hegarty, J., and W.M. Yen, 1979, Phys. Rev. Lett. **43**, 1126.
Hegarty, J., R.T. Brundage and W.M. Yen, 1980, Appl. Opt. **19**, 1889.
Hegarty, J., D.L. Huber and W.M. Yen, 1981, Phys. Rev. B **23**, 6271.
Hegarty, J., D.L. Huber and W.M. Yen, 1982, Phys. Rev. B **25**, 5638.
Hegarty, J., M.M. Broer, B. Golding, J.R. Simpson and J.B. MacChesney, 1983, Phys. Rev. Lett. **51**, 2033.
Hellwarth, R.W., 1977, J. Opt. Soc. Am. **67**, 1.

Hellwege, A.M., and K.H. Hellwege, 1952, Z. Phys. **133**, 174.
Hesselink, W.H., and D.A. Wiersma, 1981, J. Chem. Phys. **75**, 4192.
Hollas, J.M., 1982, High Resolution Spectroscopy (Butterworths, London).
Holstein, T., S.K. Lyo and R. Orbach, 1981, Excitation Transfer in Disordered Systems, in: Laser Spectroscopy of Solids, Top. Appl. Phys., Vol. 49, W.M. Yen and P.M. Selzer (Springer, Berlin) ch. 2.
Huber, D.L., 1981, Dynamics of Incoherent Transfer, in: Laser Spectroscopy of Solids, Top. Appl. Phys. Vol. 49, eds W.M. Yen and P.M. Selzer (Springer, Berlin).
Huber, D.L., D.S. Hamilton and B.B. Barnett, 1977, Phys. Rev. B **16**, 4642.
Hüfner, S., 1978, Optical Spectra of Transparent Rare Earth Compounds (Academic Press, New York).
Imbusch, G.F., and R. Kopelman, 1981, Optical Spectroscopy of Electronic Centers in Solids, in: Laser Spectroscopy of Solids, Top. Appl. Phys. Vol. 49, eds W.M. Yen and P.M. Selzer (Springer, Berlin) ch. 1.
Judd, B.R., 1962, Phys. Rev. **127**, 750.
Judd, B.R., 1963, Operator Techniques in Atomic Spectroscopy (McGraw-Hill, New York).
Judd, B.R., 1985, Two-photon Rare Earth Spectroscopy, in: Rare Earth Spectroscopy, eds B. Jezowska-Trzepiatowska, J. Legendziewicz and W. Strek (World Scientific, Singapore) pp. 515.
Judd, B.R., and D.R. Pooler, 1982, J. Phys. C **15**, 591.
Kaiser, W., and C.G.B. Garrett, 1961, Phys. Rev. Lett. **7**, 229.
Kliger, D.S., 1983, Ultrasensitive Laser Spectroscopy (Academic Press, New York).
Kramers, H.A., 1930, Proc. Acad. **33**, 959.
Kurnit, N.A., I.D. Abella and S.R. Hartmann, 1964, Phys. Rev. Lett. **13**, 567.
Kushida, T., and E. Takeuchi, 1975, Phys. Rev. B **12**, 824.
Lai, S.T., S. Huang and W.M. Yen, 1982, Phys. Rev. B **26**, 2349.
Lawson, C.M., R.C. Powell and W.K. Zwicker, 1982, Phys. Rev. B **26**, 4836.
Levenson, M.D., 1982, Introduction to Nonlinear Laser Spectroscopy (Academic Press, New York).
Levey, C.G., 1984, Excitation of the $^1S_0$ State of Trivalent Praseodynium in Insulating Crystals (Thesis, University of Wisconsin, Madison) unpublished.
Macfarlane, R.M., and A.A. Kaplyanskii, eds, 1987, Spectroscopy of Solids Containing Rare Earth Ions, Modern Problems in Condensed Matter Sciences, Vol. 21 (North-Holland, Amsterdam).
Macfarlane, R.M., and R.M. Shelby, 1983, Opt. Commun. **45**, 46.
Macfarlane, R.M., and R.M. Shelby, 1986, in: Spectroscopy of Solids Containing Rare Earths Ions, Modern Problems in Condensed Matter Sciences, Vol. 21, eds R.M. Macfarlane and A.A. Kaplyanskii (North-Holland, Amsterdam).
Macfarlane, R.M., C.S. Yannoni and R.M. Shelby, 1980, Opt. Commun. **32**, 101.
Macfarlane, R.M., R.M. Shelby and A. Winnacher, 1986, Phys. Rev. B **33**, 4207.
Martin, W.C., R. Zalubas and L. Hagan, 1978, Atomic Energy Levels for the Rare Earth Elements, National Bureau of Standards NSRDS-NBS60 (U.S. Government Printing Office, Washington, DC).
McCall, S.L., and E.L. Hahn, 1967, Phys. Rev. Lett. **18**, 908.
Meltzer, R.S., and R.M. Macfarlane, 1985, Phys. Rev. B **32**, 1248.
Miyakawa, T., and D.L. Dexter, 1970, Phys. Rev. B **1**, 2961.
Moerner, W.E., A.R. Chraplyvy, A.J. Sievers and R.H. Silsbee, 1983, Phys. Rev. B **28**, 7244.
Moos, H.W., 1970, J. Lumin. **1–2**, 106.
Morgan, G.P., D.L. Huber and W.M. Yen, 1986a, J. Lumin. **35**, 277.
Morgan, G.P., S.Z. Chen and W.M. Yen, 1986b, Transient Grating Spectroscopy of LaP_5O^{14}:Nd^{3+} in: Dynamics Gratings and Four Wave Mixing, ed. H.J. Eichler, IEEE J. Quantum Electron. **QE-22**, 1360.
Muramoto, S., T. Nakamishi and T. Hashi, 1977, Opt. Commun. **21**, 139.
Muramoto, S., T. Nakamishi and T. Hashi, 1978, Opt. Commun. **24**, 316.
Musgrove, A., and R. Zalubas, 1985, Bibliography on Atomic Energy Levels and Spectra 1979-1983, NBS, Special Publication 363, suppl. 3 (U.S. Department of Commerce, Washington, DC) see also suppl. 1 and 2 this series.
Nakazawa, E., and S. Shionoya, 1970, Phys. Rev. Lett. **25**, 1710.
Ofelt, J.S., 1962, J. Chem. Phys. **37**, 511.
Pelletier-Allard, N., R. Pelletier and C. Delsart, 1977, J. Phys. C **10**, 2005.
Phillion, D.W., D.J. Kuisenga and A.E. Siegmann, 1975, Appl. Phys. Lett. **27**, 85.
Quimby, R.S., and W.M. Yen, 1980, J. Appl. Phys. **51**, 1780.
Richter, J., 1984, Phys. Scr. T **8**, 70.
Riseberg, L.A., and M.J. Weber, 1976, Prog. Opt. **14**, 91.
Rudolph, J., and V. Helbig, 1982, Phys. Lett. A **89**, 339.
Salcedo, J.R., A.E. Siegman, D.D. Dlott and M.D. Fayer, 1978, Phys. Rev. Lett. **41**, 131.
Selzer, P., 1981, General techniques and experimental methods in laser spectroscopy of solids, in: Laser Spectroscopy of Solids, Top. Appl. Phys., Vol. 49, eds W.M. Yen and P.M. Selzer (Springer, Berlin) ch. 4.
Shelby, R.M., 1983, Opt. Lett. **8**, 88.
Shelby, R.M., and R.M. Macfarlane, 1984, J. Lumin. **31–32**, 839.
Shelby, R.M., R.M. Macfarlane and R.L. Shoemaker, 1982, Phys. Rev. B **25**, 6578.
Shoemaker, R.L., 1978, Coherent Transient Infrared Spectroscopy, in: Laser and Coherence Spectroscopy, ed. J.I. Steinfeld (Plenum Press, New York) pp. 197–361.

Stakowski, S.E., 1982, Glass Lasers, in: Handbook of Laser Science and Technology, Vol. 1, ed. M.J. Weber (CRC Press, Boca Raton) pp. 215.
Steinfeld, J.I., 1978, Laser and Coherence Spectroscopy (Plenum Press, New York).
Strauss, E., and W. Seelert, 1984, J. Lumin. **31–32**, 193.
Strauss, E., W.J. Miniscalco, J. Hegarty and W.M. Yen, 1981, J. Phys. C **14**, 2229.
Szabo, A., 1970, Phys. Rev. Lett. **25**, 924.
Szabo, A., 1975, Phys. Rev. B **11**, 4512.
Tam, A.C., 1983, Photoacoustics: Spectroscopy and Other Applications, in: Ultrasensative Laser Spectroscopy, ed. D.S. Kliger (Academic Press, New York) ch. 1.
Van Vleck, J.H., 1937, J. Phys. Chem. **41**, 67.
Varsanyi, F., and G.H. Dieke, 1961, Phys. Rev. Lett. **7**, 442.
Vial, J.C., and R. Buisson, 1982, J. Phys. Lett. (France) **43**, L475.
Vial, J.C., R. Buisson, F. Madeore and M. Poirier, 1979, J. Phys. (France) **40**, 913.
Wang, C.S., 1975, The Stimulated Raman Process, in: Quantum Electronics: A Treatise, Vol. 1, eds H. Rabin and C.L. Tang (Academic Press, New York) ch.7.
Weber, J.J., 1982, J. Non-Cryst. Solids **47**, 117.
Weber, M.J., 1981, Laser Excited Fluorescence Spectroscopy in Glasses, in: Laser Spectroscopy of Solids, Top. Appl. Phys., Vol. 49, eds W.M. Yen and P.M. Selzer (Springer, Berlin) ch. 6.
Weber, M.J., 1985, Ceram. Bull. **64**, 1439.
Weber, M.J., ed., 1987, Optical Linewidths in Glasses, J. Lumin. **36**(4/5).
Winnaker, A., R.M. Shelby and R.M. Macfarlane, 1985, Opt. Lett. **10**, 350.
Wright, J.C., 1976, Energy Transfer in Rare Earth Systems, in: Radiationless Processes in Molecules and Condensed Phases, Top. Appl. Phys., Vol. 15, ed. F.K. Fong (Springer Berlin) ch. 4.
Wright, J.C., 1977, Anal. Chem. **49**, 1690.
Wright, J.C., 1985, Laser Spectroscopy of Point Defect Equilibria in Insulators Transitions of Insulators to Superionic State, in: Proc. Int. Conf. on Defects in Insulating Crystals, Cryst. Lattice Defects and Amorphous Mat., Vol. 12, ed. F. Lüthi (Gordon and Breach, New York) pp. 505.
Wybourne, B.G., 1965, Spectroscopic Properties of Rare Earths (Wiley–Intersciences, New York).
Yen, W.M., 1983, J. Phys. (France) C **44**, 6–333.
Yen, W.M., 1985, Spectral and Spatial Migration of Energy of Rare Earth Ions in Insulators, in: Rare Earth and Spectroscopy, eds B. Jezowska-Trzebiatowska, J. Legendziewicz and W. Strek (World Scientific, Singapore) pp. 484,501.
Yen, W.M., 1986a, Optical Spectroscopy of Ions in Inorganic Glasses, in: Optical Spectroscopy of Glasses, ed. I. Zschöhke (Reidel, Dordrecht) p. 23.
Yen, W.M., 1986b, Experimental Studies of Energy Transfer of Rare Earth Ions in Crystals, in: Spectroscopy of Solids Containing Rare Earth Ions, eds R.M. Macfarlane and A.A. Kaplyanskii (North-Holland, Amsterdam) ch. 4.
Yen, W.M., 1987, Spectroscopy Using Lasers, in: Spectroscopy of Solid State Laser Materials, ed. B. Di Bartolo (Plenum, New York) p. 503.
Yen, W.M., ed., 1988, Laser Spectroscopy of Solids II, Topics in Applied Physics (Springer, Berlin) in press.
Yen, W.M., and P.M. Selzer, 1981, in: Laser Spectroscopy of Solids, Top. Appl. Phys., Vol. 49, eds W.M. Yen and P.M. Selzer (Springer, Berlin).
Yen, W.M., W.C. Scott and A.L. Schawlow, 1964, Phys. Rev. A **136**, 271.
Zschöhke, I., ed., 1986, Optical Spectroscopy of Glasses (Reidel, Dordrecht).

SUBJECT INDEX